Synthesis, Characterisation, and Application of Novel Aluminium Initiators for the Ring-Opening Polymerisation of Cyclic Esters

Sami GESSLBAUER

Department of Chemistry

Imperial College London

April 2021

A thesis submitted in partial fulfilment of the requirements for the degree of Doctor of Philosophy in Chemistry.

If you do it right, you'll only do it once

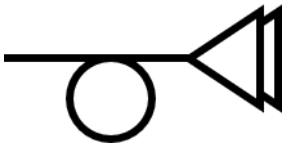


Table of Contents

Declaration **8**
Abstract **9**
Acknowledgements **10**
List of Publications **11**
List of Abbreviations **12**

Chapter 1 **16**

1.1 Bioplastics **17**
1.1.1 Introduction to Plastics 17
1.1.2 Introduction to Bioplastics 18

1.2 Poly-Lactic Acid **19**
1.2.1 Introduction to Poly-Lactic Acid 19
1.2.2 Synthesis of PLA 21
1.2.3 Other Bioplastics 22

1.3 Ring-Opening Polymerisation **23**
1.3.1 Thermodynamics of ROP 24
1.3.2 Mechanism of Metal-Catalysed ROP 25
1.3.3 Mechanism of ROP Catalysed by Organic Compounds 26
1.3.4 Living *vs.* Immortal Polymerisation 27

1.4 Desired Initiator Properties **28**
1.4.1 Activity 28
1.4.2 Molecular Weight Control 30
1.4.3 Polymer Microstructure 31
1.4.4 Stereocontrol 33

1.5 Previous Work **33**
1.5.1 Aluminium Initiators 34
1.5.2 The Catam Ligand 36
1.5.3 Differences Between Salen and Catam Ligands 40

1.6 Aims and Objectives **42**

1.7 References **43**

Chapter 2 **52**

2.1 Introduction **53**
2.1.1 Introduction to Chemical Bonding 53
2.1.1.1 Covalent Bonds 53
2.1.1.2 Ionic Bonds 53
2.1.1.3 Significance of Electronegativity in Bonding 54
2.1.1.4 Other Types of Bonding 54
2.1.2 Introduction to Non-Covalent Interactions 54
2.1.2.1 Aromatic Interactions 55
2.1.2.2 Van der Waals Forces 55
2.1.2.3 Hydrophobic Effect 56
2.1.2.4 Electrostatic Interactions 56

2.1.3 Non-Covalent Interactions in Catalysis 57
2.1.3.1 Underlying Principles 57
2.1.3.2 Selected Examples of NCI Exploitation in Catalysis 58
2.1.4 Non-Covalent Interactions in Polymerisation Catalysis 60
2.1.4.1 NCIs in Olefin Polymerisation 60
2.1.4.2 NCIs in ROP 61
2.1.5 Potential of the Catam Ligand 64

2.2 Pro-Ligand Synthesis and Characterisation 65
2.2.1 General Pro-Ligand Synthesis 65
2.2.2 Amine Moiety Modulation 65
2.2.2.1 Deuteration 65
2.2.2.2 *N*-Methylation 67

2.3 Complex Synthesis and Characterisation 69
2.3.1 Complexes of $H_2^{R}\mathbf{L_1}$ 69
2.3.1.1 Alkyl and Alkoxide Derivatives of $H_2^{H}\mathbf{L_1}$ 69
2.3.1.2 Deuterated Alkyl and Alkoxide Derivatives of $D_2^{D}\mathbf{L_1}$ 72
2.3.1.3 *N*-Methylated Alkyl Derivative of $H_2^{Me}\mathbf{L_1}$ 74
2.3.2 Complexes of $H_2^{R}\mathbf{L_2}$ 75
2.3.2.1 Alkyl and Alkoxide Derivatives of $H_2^{H}\mathbf{L_2}$ 75
2.3.2.2 Deuterated Alkyl and Deprotonated Derivatives of $H_2^{D}\mathbf{L_2}$ 80
2.3.2.3 *N*-Methylated Alkyl Derivatives of $H_2^{Me}\mathbf{L_2}$ 80

2.4 Polymerisation Results and Discussion 83
2.4.1 Polymerisation of *rac*-LA 83
2.4.1.1 Room-Temperature Polymerisations 83
2.4.1.2 Determination of the Order in Catalyst 87
2.4.1.3 Computational Studies Performed on $^{H}\mathbf{L_1}$Al(Et) (**2**) 88
2.4.1.4 Computational Studies Performed on $^{H}\mathbf{L_2}$Al(OBn) (**8c**) 93
2.4.1.5 Kinetic Isotope Effect Studies 95
2.4.1.6 Use of Methylated Analogues Bearing the $^{Me}\mathbf{L_1}$ and $^{Me}\mathbf{L_2}$ Ligands 97
2.4.1.7 Computational Studies Performed on $^{Me}\mathbf{L_1}$Al(Et) (**5**) 99
2.4.1.8 Solvent Effects on Polymerisation 101
2.4.1.9 Polymerisations at High Temperatures 102
2.4.2 Polymerisation of *L*-LA and *meso*-LA 103
2.4.3 Polymerisation of ε-CL and ε-DL 105
2.4.4 Polymerisation of Other Monomers 107
2.4.5 Reactions using $^{Me}\mathbf{L_2}$Al(Et) (**11**) 110
2.4.6 $H_2^{H}\mathbf{L_1}$ and $H_2^{H}\mathbf{L_2}$ as Organocatalysts 111

2.5 Conclusion 112

2.6 References 113

Chapter 3 123

3.1 Introduction 124
3.1.1 Pioneering Work on Chiral Aluminium Catalysts 124
3.1.2 Enantiotopic-Site Control *vs.* Chain-End Control Mechanism 126
3.1.3 Elucidation of Selectivity in Chiral Catalysts 127
3.1.4 Other Chiral Aluminium Catalysts 129
3.1.5 Aims and Objectives 133

3.2 Pro-Ligand Synthesis and Complex Characterisation **134**
3.2.1 Pro-Ligand Synthesis 134
3.2.2 Modification of Aromatic Substituents 136
3.2.3 Attempted Synthesis of the Alkyl Complexes of *rac*- and *cis*-$H_2^{H}L_3$ 139
3.2.4 Synthesis of the Benzyloxy Complexes of (*R*,*R*)-, (*S*,*S*)-, and *rac*-$H_2^{H}L_3$ 141
3.2.4.1 Attempted Synthesis of (*R,R*)-, (*S,S*)-, and *rac*-**14** 141
3.2.4.2 Synthesis and Characterisation of *rac*-**14** 145
3.2.5 Synthesis and Characterisation of (*R,R*)-, (*S,S*)-, *rac*-, and *cis*-**15** 147
3.2.6 Preliminary DFT Calculations on the Stability of Dimers 151

3.3 Polymerisation Results and Discussion **153**
3.3.1 Polymerisations with Enantiopure [(*R,R*)-**15** and (*S,S*)-**15**] and Racemic Catalysts (*rac*-**15**) 153
3.3.1.1 Polymerisation of an Achiral Monomer (ε-CL) 153
3.3.1.2 Kinetic Analysis of ε-CL ROP 156
3.3.1.3 Polymerisation of an Enantiopure Monomer (*D*- and *L*-LA) 159
3.3.1.4 Kinetic Analysis of *L*-LA ROP 162
3.3.1.5 Polymerisation of *meso*-LA 164
3.3.1.6 Polymerisation of a Racemic Monomer (*rac*-LA) 168
3.3.1.7 Computational Studies on LA ROP 172
3.3.1.8 Polymerisation of β-BL 177
3.3.1.9 Polymerisation of Other Monomers 180
3.3.2 Polymerisations with *cis*-**15** 181
3.3.2.1 Polymerisation of *rac*-LA, *L*-LA, *meso*-LA and ε-CL 182
3.3.2.2 Mechanistic Insight into ε-CL ROP by *cis*-**15** 183
3.3.2.3 Polymerisation of Other Monomers 184

3.4 Conclusion **185**

3.5 References **186**

Chapter 4 **192**

4.1 Introduction **193**
4.1.1 Artificial Switchable Catalysis 193
4.1.2 Photochemical-Controlled Switching 194
4.1.3 Chemical-Controlled Switching 196
4.1.4 Redox-Controlled Switching 197
4.1.4.1 Ferrocenyl-mediated redox catalysis 197
4.1.4.2 Metal-mediated redox catalysis 202
4.1.5 The Ph-Catam Ligand 204
4.1.6 Aim and Objectives 206

4.2 Pro-Ligand Synthesis and Complex Characterisation **206**
4.2.1 Synthesis of the alkyl complex of $H_2^{H}L_4$ and deprotonation behaviour 207
4.2.2 Synthesis of alkoxide complexes **17-a** to **17-b** 208
4.2.3 Synthesis and Characterisation of the chloro complex (**18**) 212
4.3.4 Electrochemical behaviour of **18** and oxidant choice 214

4.3 Reactivity of Complexes and Preliminary Polymerisation Studies **216**
4.3.1 Reaction of 18 with CHO 216
4.3.2 DFT calculations on the reaction of **18** with CHO 220
4.3.3 Other reactions of **18** 222

4.3.4 Preliminary polymerisation studies 224

4.4 Polymerisation Studies 228
4.4.1 Polymerisation of *rac*-LA 228
4.4.2 Polymerisation of CHO 234
4.4.3 Synthesis of block co-polymers 237
4.4.4 Polymerisation of other monomers by **18** and **18-ox** 239

4.5 Conclusion 240

4.6 References 241

Chapter 5 245

Chapter 6 254

6.1 General Considerations 255

6.2 Synthesis of Pro-Ligands 256
6.2.1 Chapter 2 256
6.2.2 Chapter 3 258
6.2.3 Chapter 4 260

6.3 Synthesis of Complexes 260
6.3.1 Chapter 2 260
6.3.2 Chapter 3 265
6.3.3 Chapter 4 268

6.4 General Procedure for Polymerisation Reactions 270

Appendices 272

Appendix A: NMR Data 273
A.1 Characterisation of Pro-Ligands 273
A.1.1 Chapter 2 273
A.1.2 Chapter 3 274
A.2 Characterisation of Complexes and Reactivity 276
A.2.1 Chapter 2 276
A.2.2 Chapter 3 285
A.2.3 Chapter 4 290

Appendix B: Kinetic and Molecular Weight Data Plots 298
B.1 Kinetic and Molecular Weight Data Plots 298
B.1.1 Chapter 2 298
6.7.2 Chapter 3 318
6.7.3 Chapter 4 342
B.2 Determination of Reaction Order 346
B.2.1 Determination of order in catalyst for ε-CL ROP: 346
B.2.2 Determination of order in catalyst for *rac*-LA/*L*-LA ROP: 348
B.2.3 Determination of order in ε-CL: 353

Appendix C: Homo- and Heteronuclear Decoupled NMR Spectra 354
C.1 General procedure 354
C.2 Chapter 2 Decoupled NMR Spectra 355

C.3 Chapter 3 Decoupled NMR Spectra 366
C.4 Chapter 4 Decoupled NMR Spectra 370

Appendix D: MALDI-ToF Mass Spectra 372
D.1 Chapter 2 372
D.2 Chapter 3 373
D.3 Chapter 4 374

Appendix E: DFT Calculations 375
E.1 General Considerations 375
E.2 Chapter 2 376
E.3 Chapter 3 378

Appendix F: Crystallography Data 381

Declaration

All work herein, unless stated otherwise, was carried out by the author between October 2017 and March 2021.

The copyright of this thesis rests with the author. Unless otherwise indicated, its contents are licensed under a Creative Commons Attribution Non-Commercial 4.0 International Licence (CC BY-NC).

Under this licence, you may copy and redistribute the material in any medium or format. You may also create and distribute modified versions of the work. This is on the condition that: you credit the author and do not use it, or any derivative works, for a commercial purpose.

When reusing or sharing this work, ensure you make the licence terms clear to others by naming the licence and linking to the licence text. Where a work has been adapted, you should indicate that the work has been changed and describe those changes.

Please seek permission from the copyright holder for uses of this work that are not included in this licence or permitted under UK Copyright Law.

Abstract

The salen and salan ligands are ligand families which have been extensively studied in the field of ring-opening polymerisation (ROP) catalysis. However, little is known about the behaviour of their *ortho*-aminophenol analogue in which the nitrogen atoms are directly connected to the aromatic moieties. This ligand scaffold (herein referred to as catam) has been previously complexed with early and late transition metals. Interestingly, no aluminium complexes bearing a catam ligand have been reported and little data exists on the use of catam complexes in the ROP of cyclic esters. Of those, the monomer lactide (LA) has been garnering considerable attention as it presents itself as a sustainable alternative to common polymers. This thesis describes the preparation and characterisation of aluminium complexes bearing catam ligands and their subsequent application in the ROP of *rac*-LA and other cyclic esters.

Even though aluminium complexes generally exhibit low activities in the polymerisation of cyclic esters, many of the described aluminium catam complexes were found to be highly active at room temperature with stereoselectivities ranging from slightly isoselective to highly heteroselective, placing them among the most active Al catalysts to date. Chapter 2 focusses on the catam ligands tethered by either 2,2-dimethyl-1,3-propanediamine or 1,2-ethanediamine and the synthesis and characterisation of their corresponding Al complexes. The NH moieties of the ligand were found to form beneficial non-covalent interactions with the substrate, which is thought to be at the root of the observed activity.

Seeking an improvement in isoselectivity, the synthesis and application of chiral aluminium complexes bearing a chiral catam ligand is detailed in Chapter 3. Neither the enantiopure nor the racemic catalysts afforded stereoregular polylactic acid. However, the enantiopure catalysts were able to polymerise enantiopure LA with unprecedented activities. The lack of selectivity in the polymerisation of *rac*-LA was traced back to polymeryl exchange events which lead to quasi-random insertions of LA. Furthermore, polymerisation of an achiral monomer (ε-caprolactone) was slower when the racemic catalyst was used which was traced back to aggregation being favoured when both enantiomers of a catalyst are present.

Chapter 4 describes the synthesis of aluminium complexes bearing a phenylene-tethered catam ligand. The corresponding Al chloro complexes was found to be redox-active. This feature was exploited in ROP. The reduced state was able to polymerise *rac*-LA with good activities whilst the oxidised state preferentially polymerised cyclohexene oxide. Using an oxidising (*e.g.* $FcBAr^F$) and reducing agent (*e.g.* $CoCp_2$), it was possible to readily switch the complex between both states and selectively polymerise one monomer over the other.

Acknowledgements

Throughout my studies, I was fortunate to be surrounded by people who wished to see me succeed. The bulk of my gratitude goes to Dr. Charles Romain, my supervisor. His guidance, encouragements, and unrelenting support have made this journey considerably less painful. I owe my skills and sanity to him, and for this I am grateful. Many thanks also go to my co-supervisor, Prof. George Britovsek, who has always kept an eye out for me and provided guidance when my research faced stagnation. I want to give special thanks to Prof. Nicholas Long and Dr. Antoine Buchard for taking the time to read through my doctoral thesis and being willing to discuss it with me.

The breadth of results detailed within this manuscript would not be noteworthy if it were not for the many excellent facility managers and technicians here in London. I thank Dr. Andrew White for analysing my sub-par crystals and readily discussing the intricacies of XRD with me. I thank Pete Haycock and Corey Fülöp, who have provided help in running various NMR experiments. I thank Dr. Lisa Haigh for her help in analysing my countless mass spectrometry samples. I thank Stephen Boyer for his swift elemental analysis and enthusiasm for my motherland. I thank Charlotte Rapley and Prof. Martin Heeney for allowing me to use their GPC when ours has met its maker.

I am grateful for the many friends that I have made within this department, without whom my lab days would have been indistinguishable from one another. I thank Richard, Sarah, Dillon, and Dom for their comradery and for making the department a better place. I thank Ryan, Greg, and Dani for their readiness to stop, drop, and drink. I thank Atanas for the entertaining discussions ranging from Jethro Tull to pyrophoric horror stories. I thank Flo for being a pleasure and honour to work with. To you particularly, I wish you all the best on your own journey. And of course, I thank the many other people in the Romain, Britovsek, Crimmin, Long, and Vilar group for enriching my time at Imperial College London.

However, my life did not start at the beginning of my PhD. There are countless people whom I owe my thanks to, without which I would not have been in my current fortunate position. My deepest gratitude goes to my loving parents for their many sacrifices. Many thanks to my sister for the entertaining phone calls while I was carrying out soporific lab work. Thank you Naomi for keeping me company and encouraging me during the final stretch of my PhD. Regarding my non-chemistry friends, I owe them recognition for which this page is too small to contain. Be aware that you have made a positive difference in my life by sharing your passions with me. Keep cool, but care.

List of Publications

Highly active aluminium catalysts for room temperature ring-opening polymerisation of rac-lactide

Gesslbauer, S.; Cheek, H.; White, A. J. P.; Romain, C.; *Dalton Trans.*, **2018**, 47, 10410-10414

Exploiting Noncovalent Interactions for Room-Temperature Heteroselective rac-Lactide Polymerization Using Aluminum Catalysts

Gesslbauer, S.; Savela, R.; Chen, Y.; White, A. J. P.; Romain, C.; *ACS Catal.*, **2019**, 9, 7912-7920

Chirality-Induced Catalyst Aggregation: Insights into Catalyst Speciation and Activity Using Chiral Aluminum Catalysts in Cyclic Ester Ring-Opening Polymerization

Gesslbauer, S.; Hutchinson, G.; White, A. J. P.; Burés, J.; Romain, C.; *ACS Catal.*, **2021**, 11, 4084-4093

List of Abbreviations

a.u.	atomic units
AgOTf	silver triflate
BnOH	benzyl alcohol
β-BL	β-butyrolactone
BnOH	benzyl alcohol
C_6D_6	benzene-d_6
cat.	catalyst
CD	circular dichroism
CD_2Cl_2	dichloromethane-d_2
$CDCl_3$	chloroform-d
CEC	chain-end control
CHO	cyclohexene oxide
ε-CL	ε-caprolactone
CO_2	carbon dioxide
$CoCp_2$	cobaltocene
Conv.	conversion
CTA	chain-transfer agent
CV	cyclic voltammetry
Cy	cyclohexyl
d	deuterium
Đ	dispersity
DCM	dichloromethane
DFT	density functional theory
ε-DL	ε-decalactone
DMAP	4-dimethylaminopyridine
DMSO	dimethyl sulfoxide
DOSY	diffusion-ordered spectroscopy
DOX	1,3-dioxolan-4-one
EA	elemental analysis
E_a	activation energy
EB	ethylene brassylate
equiv.	equivalents
ESC	enantiotopic-site control

Et	ethyl
$FcBAr^F$	ferrocenium tetrakis[3,5-bis(trifluoromethyl)phenyl]borate
FDA	U.S. Food and Drug Administration
FDE	framework distortion energy
ΔG_p	gibbs free energy of polymerisation
GPC	gel permeation chromatography
GS	ground state
HMF	(hydroxymethyl)furfural
HPLC	high-performance liquid chromatography
HRMS	high-resolution mass spectrometry
ΔH_p	enthalpy of polymerisation
I	initiator
^{i}PA	isopropyl alcohol
^{i}Pr	isopropyl
^{i}PrOD	isopropyl alcohol-OD
^{i}PrOH	isopropyl alcohol
IR	infrared
k_{app}	apparent rate constant
k_i	initiation rate constant
KIE	kinetic isotope effect
KO^{t}Bu	potassium *tert*-butoxide
k_p	propagation rate constant
k_t	termination rate constant
L	ligand
LA	lactide
LCA	life cycle assessment
m	meso dyad
M	monomer or metal
MALDI-ToF	matrix assisted laser desorption/ionisation-time of flight
Me	methyl
MeCN	acetonitrile
MeI	methyl iodide
MeOD	methanol-OD
MeOH	methanol
M_{eq}	monomer equilibrium concentration

M_n	number average molecular weight
M_n^{calc}	theoretical number average molecular weight
M_w	weight average molecular weight
MS	mass spectrometry
n	normal
ν	vibrational frequency
NCI	non-covalent interaction
NHC	*N*-heterocyclic carbene
NLE	non-linear effect
NLKE	non-linear kinetic effect
NMR	nuclear magnetic resonance
P	probability
P3HB	poly-3-hydroxybutyrate
PBAT	polybutylene adipate terephthalate
PBS	polybutylene succinate
PCL	polycaprolactone
PCHO	polycyclohexene oxide
ω-PDL	ω-pentadecalactone
PDL	polydecalactone
PDLA	poly-D-lactic acid
PET	polyethylene terephthalate
Ph	phenyl
PHA	polyhydroxyalkanoate
pK_a	negative log of the acid dissociation constant
PLA	poly-lactic acid
PLLA	poly-L-lactic acid
PP	polypropylene
PS	polystyrene
r	racemic dyad
rac	racemic
RDS	rate-determining step
ROH	alcohol
ROP	ring-opening polymerisation
RT	room temperature
ΔS_p	entropy of polymerisation

SEC	size exclusion chromatography
SQP	square pyramidal
time	t
T	temperature
TBP	trigonal bipyramidal
T_c	ceiling temperature
T_f	floor temperature
TFA	trifluoroacetic acid
T_g	glass transition temperature
T_m	melting point temperature
TMC	trimethylene carbonate
τ_5	five-coordinate structural parameter
^{t}Bu	tertiary-butyl
^{t}BuOH	*tert*-butanol
tert	tertiary
T_g	glass transition temperature
THF	tetrahydrofuran
TS	transition state
TSM	topographic steric map
δ-VL	δ-valerolactone
VTNA	variable time normalisation analysis
XRD	X-ray diffraction

Chapter 1

Introduction

1.1 Bioplastics

1.1.1 Introduction to Plastics

The discovery of Bakelite in 1907 marked the beginning of the plastic age. Already in 1856, Alexander Parkes synthesised nitrocellulose by treating cellulose with nitric acid. However, Bakelite was the first plastic that was made from synthetic components; formaldehyde and phenol.[1] In the 1920s, Hermann Staudinger began his research into polymer chemistry, postulating that macromolecules such as starch and cellulose are made up of repeating units of small molecules linked by covalent bonds.[2] Building on top of this work, Wallace Carothers synthesised various polymers (including neoprene, nylon-6,6, and polyesters) *via* step-growth polymerisation, demonstrating that different plastics with different physical properties can be readily prepared using simple organic reactions.[3, 4]

Plastics offer multiple advantages such as their ease of production, low cost of manufacture, as well as their versatility and durability. Their advantages soon made them popular, with global production increasing from 2 Mt in 1950 to 380 Mt in 2015 (Figure 1).[5] Nowadays, plastics have become ubiquitous in society, forming an integral component of modern living. They find their applications in sectors such as the textile, automotive, aeronautic, packaging, construction, and medical industry. Virtually every aspect of our life makes use of this material now and plastic usage is still increasing as of today, expected to grow steadily by 4% per year.[6]

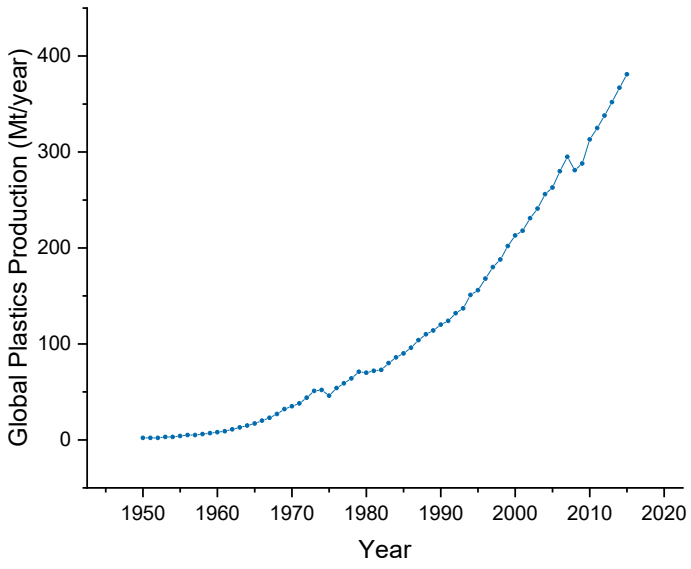


Figure 1. Global plastics production (in Mt) from 1950 to 2015. Data sourced from Geyer et al.[5]

Although, the world of plastics has its advantages, it comes with its drawbacks. The vast majority of polymers are derived petrochemically which raises concerns regarding their sustainability as oil and gas are non-renewable resources.[7] An estimate of 4% of all oil and gas produced is used to make plastics which is expected to grow to 20% by 2050.[8, 9] Although the petrochemicals used for the manufacture of plastics are sourced from the waste-streams of the refineries, the use of renewable resources would be optimal in making plastics a more sustainable material.[10]

Another drawback of plastics relates specifically to their end-of-life. Worldwide, only 9% of all plastic waste was recycled in 2015, whilst 12% was incinerated, and the remaining 79% accumulated in landfills or the natural environment.[5] This is particularly problematic for the marine environment as the stress induced by the tide breaks down the waste into microplastics which are virtually impossible to recover due to their small size.[11] While macroplastics pose an aesthetic issue while being detrimental to wild life, microplastics are difficult to spot with the naked eye and can be ingested by marine organisms and introduce toxins into the food-chain.[12, 13]

Solving these two major drawbacks would increase the sustainability of plastics as the use of renewable resources as well as waste prevention comprise two of the 12 principles of green chemistry.[14] Furthermore, the sustainable development goals recently set by the United Nations can be met by the employment of bioplastics.

1.1.2 Introduction to Bioplastics

In recent years, bioplastics have garnered a lot of attention by the research community as well as the media, offering potential solutions to the drawbacks of petrochemically derived plastics.[15]

In the context of this doctoral thesis, a bioplastic will be defined as any plastic that is either derived from biological sources (biomass) and/or which can be broken down completely into CO_2, water, and compost by microorganisms. Both characteristics are highly desirable in a commercial plastic:

-Bio-derived plastics offer a way to mitigate the use of non-renewable feedstocks by using biomass instead.[16]

-Biologically degradable plastics can prevent accumulation of waste in landfills and the

environment. While this is an advantage, most bioplastics require industrial facilities which operate at high temperatures to break down. As few cities have the necessary collection streams and infrastructure, bioplastics end up in landfills.

It is important to note that the biodegradability of a plastic is not dependent on whether the polymer is bio-derived or not. For example, bio-derived polyethylene does not readily bio-degrade even though 100% of the carbon content is bio-derived. A plastic is considered biologically degradable if more than 60% of the carbon is converted within 6 months and if 90% has been broken down into fragments smaller than 2 mm.[17]

Although bioplastics are very promising, they only make up 1% of total plastic production.[18] Producing plastics from bio-derived feedstocks may pose logistical challenges or may be financially unfeasible. Furthermore, bio-degradable plastics often do not have the physical properties desired for a particular use.

Apart from biodegradable starch blends, the most popular bioplastics are polyesters which includes poly-lactic acid (PLA), polycaprolactone (PCL), polyhydroxyalkanoates (PHA), polybutylene adipate terephthalate (PBAT) and polybutylene succinate (PBS).[19]

1.2 Poly-Lactic Acid

1.2.1 Introduction to Poly-Lactic Acid

Poly-lactic acid (PLA) is an aliphatic polyester made either from lactic acid or lactide (LA). It is entirely bio-derived and can be degraded biologically under industrial composting conditions, making it a promising candidate in replacing fossil-fuel derived plastics.[20] First synthesised by Carothers and co-workers in 1932, PLA was limited to medical applications as its production had a high cost associated with it. Advances in the field have allowed for cheaper and more reliable manufacturing which have led to a sharp increase in its production. NatureWorks LLC is the major producer of PLA with its US facility having a production capacity of 150,000 metric tons per year.[21] PLA's optical, mechanical, thermal, and barrier properties are similar to those of polypropylene (PP), poly(ethylene terephthalate) (PET), and polystyrene (PS), making its manufacture even more attractive as these plastics are among the

most produced ones.[22] The medical field makes extensive use of PLA due to its bio-compatibility with the human body, allowing it to be used in implants or surgical sutures.[23] On top of that, PLA is also suitable for applications as fibers, textiles, or packaging.[22] The potential applications make PLA particularly attractive as 36% of all plastics produced were used in packaging (Figure 2).[5] Coupled with the fact that packaging is often used only once, accumulating in landfills and the environment, it becomes clear why PLA is popular.

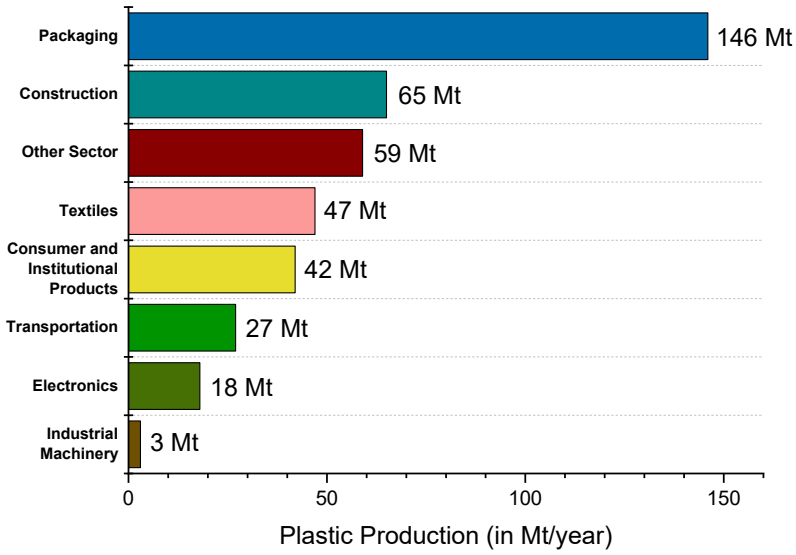


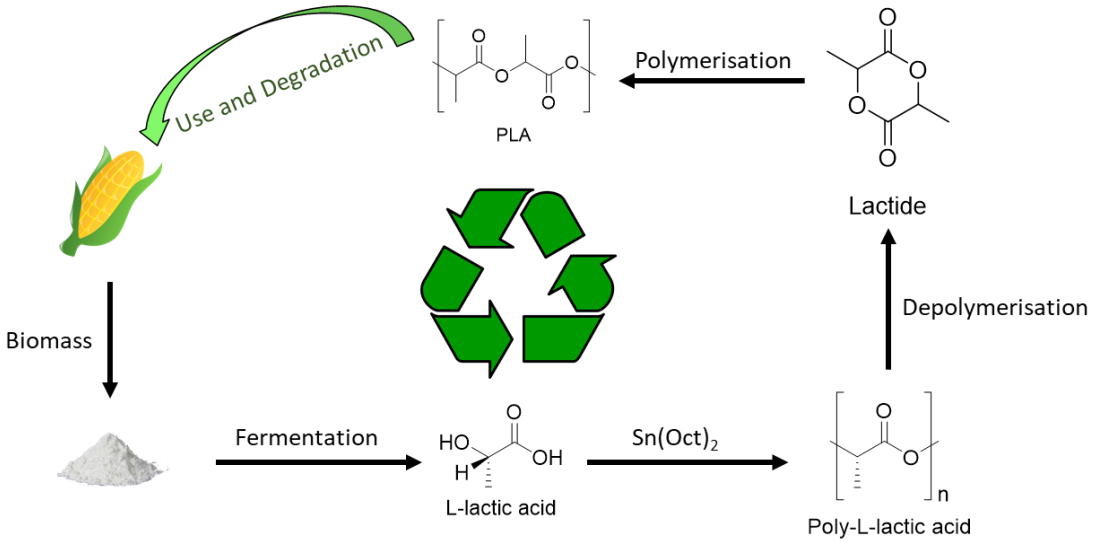
Figure 2. Global plastics production in 2015 by industrial sector (adapted from "Our World in Data")[5, 24]

A life cycle assessment (LCA) conducted by Groot and Borén demonstrated that the use of PLA results in significantly lower emissions of greenhouse gases, as well as less use of material resources and non-renewable energy.[25]

Degradation of PLA occurs in two steps:

- Through biodeterioration, the high molecular weight (M_w) polymers initially hydrolyse into smaller fragments by being exposed to abiotic factors (*e.g.* water, light, and heat). The speed at which this occurs is dependent on the structural properties of the PLA. For example, hydrolytic degradation of industrial PLA is faster than that of laboratory-made PLA.[26]
- Microorganisms present in the environment then break down the plastic further into oligomers and monomers through metabolic pathways. These are eventually either assimilated into the organism or expelled as waste (lactic acid).[27] Ultimately, the PLA is converted into CO_2 and water.

1.2.2 Synthesis of PLA



Scheme 1. Life-cycle of PLA

The life cycle of PLA is pictured in Scheme 1. Using sunlight as an energy source, plants sequester environmental CO_2 and water as starch. In industry, crops which have a high content of starch in their biomass such as corn, beets, and sugar cane are chosen as feedstocks for PLA production.[28] The starch is extracted and then converted to *L*-lactic acid *via* bacterial fermentation.

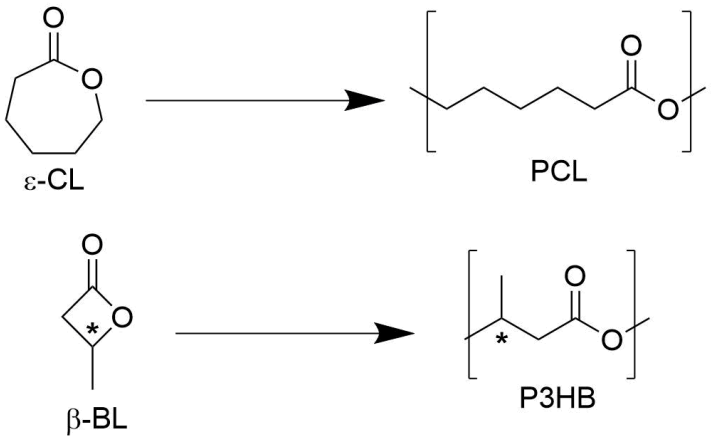
One method of PLA synthesis is the polycondensation of lactic acid, resulting in the polymer and water being formed. This must be carried out at temperatures below 200 °C to favour the formation of the polymer. Since the reaction is a step-growth polymerisation, each esterification step produces one equivalent of water. As this is a reversible process, it requires the continuous removal of water to shift the equilibrium towards the product and allow the reaction to proceed and generate high M_w species. Water can be removed through the use of a vacuum or azeotropic distillation to make polymers of up to 130 kDa.[29, 30] Due to the nature of the mechanism of step-growth polymerisation, a high conversion is needed to achieve high M_w polymers and dispersities (Đ) in the product are usually uncontrolled.

The preferred method of PLA synthesis is therefore *via* ring-opening polymerisation (ROP) in which the terminus of a polymer chain reacts with a cyclic monomer to continually grow. LA, the cyclic diester of lactic acid, can be synthesised by depolymerising low M_w oligomers of lactic acid at high temperatures *in vacuo* using an initiator [usually $Sn(Oct)_2$].[31] The monomer

can then undergo ROP in the presence of an initiator. The polymerisation is 100% atom economical, meaning that all atoms present in the reactants are incorporated into the product. Consequently, no by-products are generated, removing the need to eliminate water from the reaction mixture. ROP thus makes it much easier to synthesise high M_w polymers with low dispersities under mild conditions.

PLA can also be obtained directly through biosynthesis of glucose.[32] Zeolites were also used to produce LA from lactic acid at lower temperatures than conventionally employed.[33]

1.2.3 Other Bioplastics



Scheme 2. ROP of ε-CL (top) and β-BL (bottom) to form PCL and P3HB respectively

Polycaprolactone (PCL) is another aliphatic polyester obtained from the ROP of ε-caprolactone (ε-CL, Scheme 2). First synthesised in the 1930s, PCL is semi-crystalline, with a glass transition temperature (T_g) of -60 °C and a melting point of around 60 °C. PCL can be bio-degraded by enzymes and fungi, making it an attractive candidate for biomedical application as it readily hydrolyses in physiological conditions.[34, 35] Co-polymerisation of ε-CL with other monomers such as LA is an effective way to tailor degradation rates.[36]

ε-CL is currently produced through the Baeyer-Villiger oxidation of cyclohexanone. This organic redox reaction is generally a powerful method for the synthesis of various lactones from cyclic ketones. However, the ε-CL produced through this pathway is not bio-derived as the cyclohexanone is fossil fuel-based. A bio-based route has been proposed using 5-(hydroxymethyl)furfural (HMF) as a starting material, which can be readily synthesised from simple sugars.[37]

Polyhydroxyalkanoates (PHA) are polyesters that are naturally produced by microorganisms.[38] The most common PHA is poly-3-hydroxybutyrate (P3HB) which is synthesised by microorganisms in response to stress, acting as energy storage.[39] Although P3HB is bio-degradable, it is not soluble in water and resistant to hydrolytic degradation, which is not common in biodegradable plastics.[40, 41] Furthermore, P3HB exhibits thermoplastic properties and resists a wide temperature range (30 to 120 °C).[42] A drawback of the plastic is that biosynthetically produced P3HB is optically pure.[43] Perfectly isotactic P3HB is very brittle and decomposes at temperatures slightly above their melting transition, making them difficult to process. More desirable properties can be achieved by controlling the stereoregularity of P3HB from the stereoselective polymerisation of β-butyrolactone (β-BL, Scheme 2).[44] Particularly an isotacticity of 60 – 80 % generates properties that are conducive to elastomers and plastomers.[45] The ability to synthesise high molecular weight polymers is also important to make the promising plastic commercially feasible.[46] ROP is thus a sensible approach to synthesising high molecular weight polymers in a controlled fashion.[47] It is important to note however that β-BL is not a bio-derived monomer and a feasible route for such a synthesis has yet to be proposed.

1.3 Ring-Opening Polymerisation

Prior to discussing ROP, it is important to draw distinctions between the two main polymerisation mechanisms, namely step-growth and chain-growth polymerisation. In the former, pairs of multifunctional molecules combine to form a longer polymer chain. This occurs in a step-wise fashion where the average molecular weight of a polymer initially increases slowly. Towards the end of the reaction, the oligomers then combine to form larger chains (Figure 3, red). Step-growth polymerisation does not require an initiator, shows no termination, and can make use of multifunctional monomers to generate more intricate polymer architectures. However, the reaction is very sensitive to impurities, requiring highly purified starting materials and high conversion to reach a relevant degree of polymerisation (DP).

In chain-growth polymerisation, the reaction is initiated to form an active site with which monomer molecules can react to steadily grow the polymer chain one monomer at a time. The number of active sites is dependent on the quantity of initiator used. This leads to longer chains being formed at the beginning of the reaction (Figure 3, blue). As will soon be evident, ROP is

a form of chain-growth polymerisation, namely a living polymerisation. This method is characterised by an absence of chain termination and chain transfer reactions which leads to a more constant growth rate of the polymer chain (Figure 3, green).

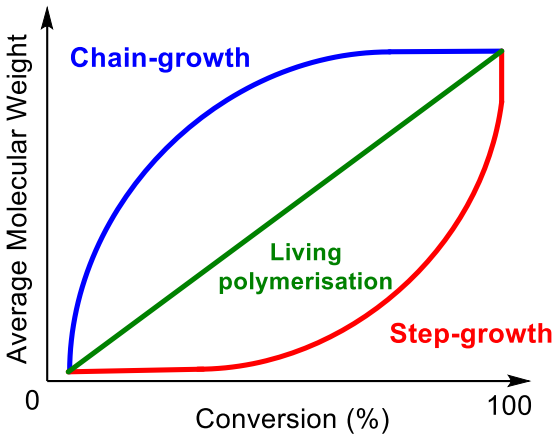


Figure 3. Graph depicting the increase in average molecular weight as a function of conversion for chain-growth (blue), living (green), and step-growth (red) polymerisation.

1.3.1 Thermodynamics of ROP

The thermodynamic driving force for the ROP of small cyclic monomers (4-7 membered rings) is the enthalpic release of ring strain upon opening.[48] This release in energy (ΔH_p) offsets the negative entropy of polymerisation (ΔS_p), keeping the Gibbs free change (ΔG_p) negative, and thus the polymerisation spontaneous.

$$\Delta G_p = \Delta H_p - T\Delta S_p$$

The total strain of a monomer is dependent on angle, conformation, and repulsion strain.[49] The ring strain of a monomer decreases as the ring size increases, resulting in an enthalpically unfavourable polymerisation. Instead, the reaction is driven entropically.[50] Macrocyclic lactones (8+ membered rings) are known to increase the entropy of a system upon opening, owing to an increase in their conformational degrees of freedom.

By running polymerisations at different temperatures, Duda and Penczek have determined ΔH_p and ΔS_p for *L*-LA to be -22.9 kJ mol^{-1} and -41.1 J mol^{-1} K^{-1} (starting from a 1 M monomer solution).[51] Given that polymerisation is a reversible reaction, the concentration of monomer at equilibrium ($[M]_{eq}$), where $\Delta G_p = 0$, can be given by the following equation:

$$[M]_{eq} = \exp\left(\frac{\Delta H_p}{RT} - \frac{\Delta S_p}{R}\right)$$

Thus, for *L*-LA, using the aforementioned values of ΔH_p and ΔS_p, $[M]_{eq}$ will adopt a value of 0.014 M at room temperature, corresponding to a total conversion of 98.6%. Thus, polymerisation is only favourable when the concentration of monomer is greater than $[M]_{eq}$ (conversion is less than 98.6 %).

For polymerisations that have a negative term for ΔH_p and ΔS_p, polymerisations can only be carried out under a so-called ceiling temperature (T_c).[50] This is due to the ΔS_p term being linked to temperature, which offsets the negative ΔH_p term as temperature is increased, ultimately leading to a positive ΔG_p. Thus, for a monomer solution of starting molarity $[M]_0$, the T_c is given by the following equation:

$$T_c = \frac{\Delta H_p}{\Delta S_p + R\ln[M]_0}$$

At a starting molarity of 1 M, a solution of *L*-LA will have a T_c of 557 K (284 °C). An important note to make that the equation also applies for polymerisations that result in a positive change of ΔH_p and ΔS_p (*e.g.* macrocyclic lactones), However, the resulting value is a floor-temperature (T_f) which denotes the minimum temperature at which a polymerisation can be carried out.

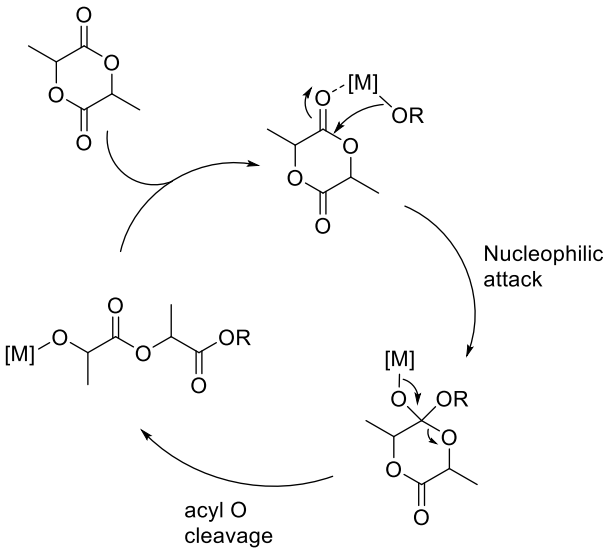
1.3.2 Mechanism of Metal-Catalysed ROP

The ROP of LA using metal-based catalysts has been studied extensively over the years, with $Sn(Oct)_2$ and aluminium isopropoxide [$Al(O^iPr)_3$] being amongst the first catalysts explored.[52, 53] Both compounds are synthesised easily and are stable to air/moisture and heat, which makes their employment and the study of their mechanism relatively uncomplicated. The polymerisation of metal-based catalysts proceeds through a three-step coordination-insertion mechanism (Scheme 3).[54] In the case of $Sn(Oct)_2$, a metal alkoxide complex is generated *in situ* by reaction with exogenous alcohol. The alkoxide moiety determines the end-group of a polymer as it is the initiating group of the ROP.

The Lewis acidic metal centre first coordinates onto the carbonyl oxygen of the monomer,

withdrawing electron density. This allows for nucleophilic attack by the alkoxide group onto the carbonyl which, after rearrangement, allows for the cleavage of the acyl oxygen bond. The ring-opening of the monomer yields a new metal alkoxide which can subsequently open another monomer unit until completion of the reaction or termination of the polymerisation. Upon consumption of all monomer, the metal-alkoxide bond hydrolyses to form a hydroxide end-group.[55]

There is a trend in which activity is correlated with Lewis acidity. However, it is important to note that more is not always better. Dagorne and co-workers have found that some cationic aluminium complexes do not insert any monomer which was attributed to the metal centre being too electron deficient.[56] These species prefer the formation of a chelate which is too stable to proceed with the polymerisation mechanism. Therefore, one must strike a subtle balance which favours both the nucleophilic attack as well as the subsequent acyl oxygen bond-cleavage.

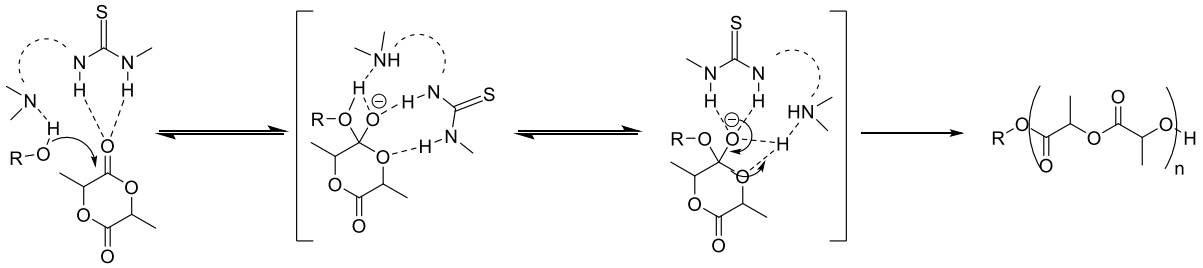


Scheme 3. Coordination-insertion Mechanism

1.3.3 Mechanism of ROP Catalysed by Organic Compounds

Pioneered by Waymouth and Hedrick, organocatalysis offers a metal-free alternative to ROP using accessible organic compounds.[57-60] Their ease of synthesis and purification, long shelf-lives (due to insensitivity to moisture and oxygen), and their broad scope of reaction conditions, solvents, and monomers, make them highly suitable candidates for industrial use. In 2001, Hedrick and co-workers reported that 4-dimethylaminopyridine (DMAP) was active in the

ROP of LA.[61] Following this discovery, a wide range of nucleophilic bases were subsequently investigated. *N*-heterocyclic carbenes (NHCs) were amongst the most successful and widely studied compound class.[59, 62] In 2005, the field of organocatalysis experienced a paradigm shift when a bifunctional catalytic system comprised of a thiourea and tertiary amine was reported.[63, 64] The system activates the monomer *via* the H-bond-donating thiourea moiety, and the exogenous alcohol *via* the H-bond-accepting tertiary amine. The mechanism of bifunctional activation is shown in Scheme 4. The LA carbonyl binds to the NH moieties of the thiourea component, forming a H-bond that acts as a Lewis acid and activates the LA carbonyl. Simultaneously, the tertiary amine forms a H-bond with the alcohol, making the oxygen more nucleophilic. Nucleophilic attack occurs, which results in a hemiacetal being formed. The reactive intermediate is stabilised by the catalyst and allows for migration of the alcohol proton, leading to the cleavage of the acyl-oxygen and opening of the LA ring.[58] Although simple on the surface, the pK_a of the systems needs to be highly tuned, making sure that the difference between the H-bond donor and H-bond acceptor is not too high.[65] Particularly fast catalysts haven been found to exhibit strong binding equilibrium constants (up to 4200) and strong H-bonds (1.79 Å).[66]This motif inspired the synthesis of many more supramolecular recognition catalysts including (-)-sparteine,[64] Me_6TREN,[67] as well as sulfonamides and fluorinated alcohols.[68-71]



Scheme 4. ROP catalysed by thiourea. (Adapted from Waymouth and Hedrick)[58, 63]

Although this doctoral work will focus on metal-based catalysis, organocatalysis was used to elucidate the mechanism of some metal complexes synthesised.

1.3.4 Living *vs.* Immortal Polymerisation

The living ROP of LA (and other lactones) exhibits an absence of chain-transfer agents (CTAs) and termination reactions, resulting in the polymer chains growing at a more constant rate.[72] Szwarc and co-workers termed this a living polymerisation.[73] The rate of initiation is much

faster than the rate of propagation, resulting in every polymer chain growing at the same rate. As a result, molecular weights are highly controlled, exhibiting a low dispersity in the product and thus allowing for predictable polymer synthesis.

This means that the chain length of a polymer can be estimated from the concentration of monomer that remains in the reaction mixture, due to the fact that the number average molecular weight (M_n) increases linearly with conversion.[74] Because of the absence of termination reactions, block co-polymers can be formed through sequential monomer addition such as diblock (A-B) or triblock (e.g. A-B-A or A-B-C) co-polymers.[73]

A similar yet different type of polymerisation is the immortal polymerisation (Figure 4). Building on top of Szwarc's work, Shohei Inoue discovered that the alkoxide group of aluminium porphyrin can undergo rapid exchange with exogenous alcohol during the alternating copolymerisation of epoxide and CO_2.[75] The chain transfer rate was thus much faster than the initiation, which led to a lower molecular weight of the polymer due to a greater number of propagating chains. Instead of terminating the polymerisation, the presence of a protic solvent formed more polymer chains.[76, 77] The dispersity of the polymer product remains narrow due to fast nature of the exchange.

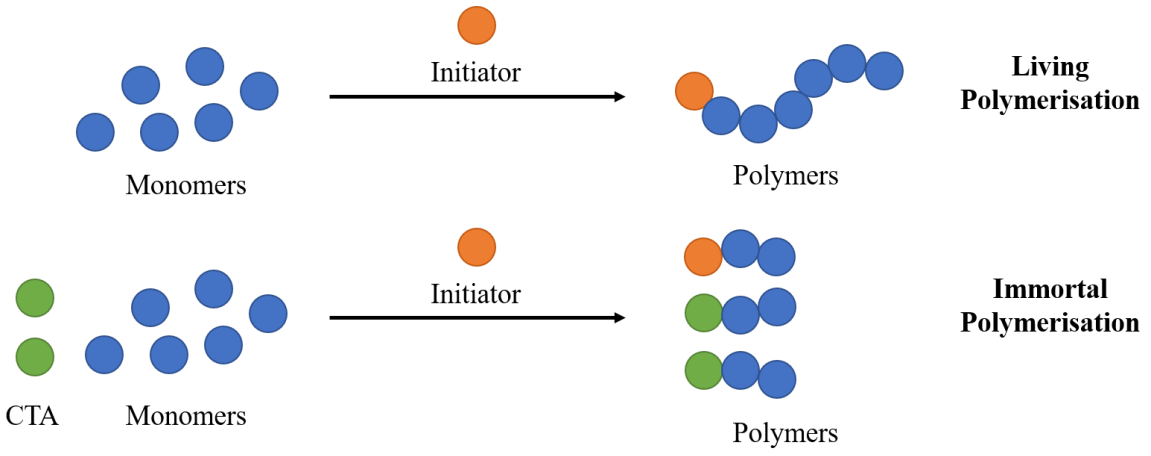


Figure 4. Representation of living and immortal polymerisation. The presence of CTAs increases the number of chains present in the latter.

1.4 Desired Initiator Properties

1.4.1 Activity

An important aspect of an initiator is its activity. A catalyst should be active at the desired

temperature as well as within the temperature ranges allowed by the thermodynamics of a particular monomer. However, a catalyst that is too fast may result in loss of control, possibly resulting in transesterification and thus an increase in dispersity.

The nature of living polymerisation allows for rigorous kinetic studies that can yield rate constants and order of reactants.[50] The rate law for the ROP of LA can be written as follows:

$$-\frac{d[LA]}{dt} = k_p[LA]^n[I]^m$$

Where k_p is the propagation rate constant, $[LA]_0$ and $[I]_0$ are the respective initial concentrations of lactide and initator, and n and m are their respective reaction order.

As the rate of initiation (k_i) in living polymerisation is much faster than the rate of propagation, it can be simply omitted as it does not contribute to the rate-determining step (RDS). In the same vein, the absence of any termination reaction means that a rate of termination (k_t) should not be present.

Assuming that the mechanism of polymerisation does not change with varying initiator concentration, one can express the above equation as a pseudo first-order rate law yielding an apparent rate constant (k_{app}) for a given $[I]_0$.

$$-\frac{d[LA]}{dt} = k_{app}[LA]_0$$

This can then be integrated to yield the following rate law:

$$\ln\left(\frac{[LA]_0}{[LA]_t}\right) = k_{app}t$$

Where $[LA]_0$ and $[LA]_t$ are the initial concentration of LA and the concentration at time t respectively. Plotting $\ln\left(\frac{[LA]_0}{[LA]_t}\right)$ as a function of time yields a linear plot with the gradient being conducive to the rate constant k_{app}. LA and other lactones usually exhibit a pseudo-first order rate dependence in monomer.

1.4.2 Molecular Weight Control

As previously mentioned in Section 1.3.4, a characteristic of a living polymerisation is the linear increase in M_n with conversion (%) as well as a narrow dispersity.

Consequently, plotting M_n (g/mol) as a function of conversion (%) should result in a linear plot, with the gradient being equal to the molecular weight of the monomer employed. For example, an M_n *vs.* conversion plot of a living lactide polymerisation ideally yields a gradient of 144.13 g/mol.

The dispersity of the polymer is also a good measure of polymerisation control. The molecular weight of a polymer can be measured either as the number average molecular weight (M_n) or the weight average molecular weight (M_w). The former is defined as the total weight of the polymer product divided by the total number of molecules.

$$M_n = \frac{\sum_{i=1}^{\infty} N_i M_i}{\sum_{i=1}^{\infty} N_i}$$

Where N_i is the number of molecules with weight M_i.

The weight average molecular weight also takes the weight of each polymer chain into account:

$$M_w = \frac{\sum_{i=1}^{\infty} N_i M_i^2}{\sum_{i=1}^{\infty} N_i M_i}$$

Using M_w and M_n, one can subsequently calculate the dispersity:

$$Đ = \frac{M_w}{M_n}$$

Where $Đ \geq 1$. The dispersity indicates the distribution of polymer molecular weights throughout the batch with the polymer chains approaching a uniform chain length as Đ approaches 1.[79] A living polymerisation typically exhibits dispersities between 1.0 and 1.3.[80]

Molecular weight control does not only depend on the ratio between the rate of propagation and initiation, but also on the extent of transesterification. This can occur either intramolecularly, leading to a macrocyclic polymer, or intermolecularly, leading to a redistribution of chains.[81, 82] These side-reactions result in a broader distribution of molecular

weights and thus a higher dispersity. The extent of transesterification depends on the nature of the initiator. The molecular weight and dispersity of a polymer product can be measured using gel permeation chromatography (GPC).

1.4.3 Polymer Microstructure

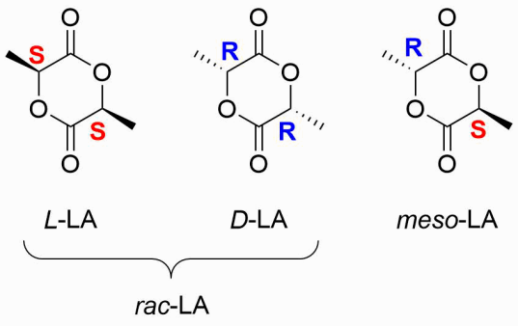
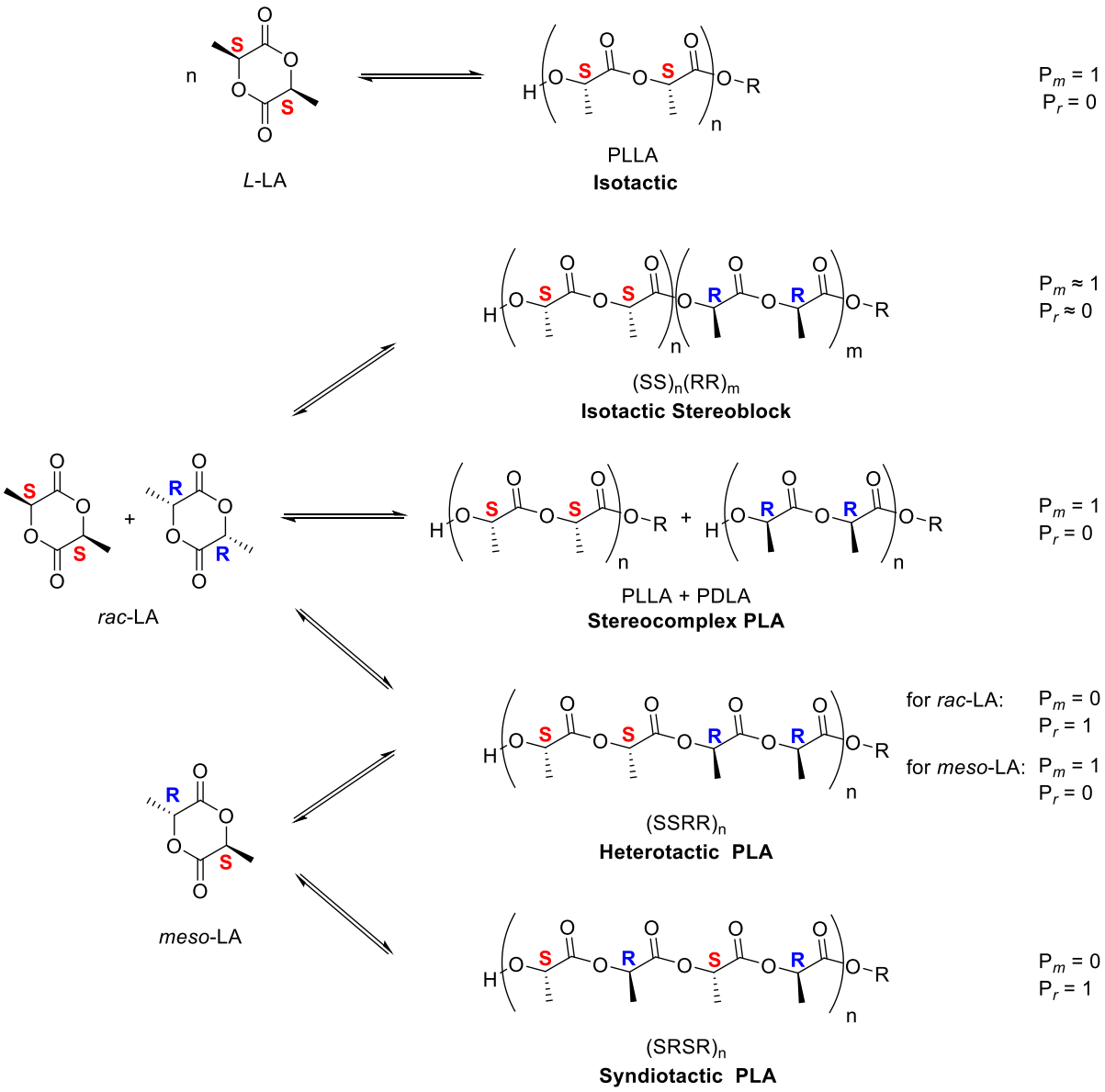


Chart 1. The stereoisomers of LA

The next two sections concern the stereocontrol in ROP and will almost exclusively describe it in the context of LA polymerisation. Lactide can be found as *L*-LA and *D*-LA (the racemic mixture of which is *rac*-LA), as well as its *meso* form *meso*-LA (Chart 1). Thus, a variety of microstructures can be exhibited in PLA depending on the monomers involved as well as the stereoselectivity of the catalyst. The physical properties of a polymer are heavily dependent on the tacticity.[83] Particularly the glass transition temperature (T_g) and melting point (T_m) are important as they dictate the processability and applications of a polymer.

Scheme 6 shows all possible stereochemical outcomes of LA polymerisation. Using either *L*-LA or *D*-LA alone will lead to isotactic poly-*L*-lactic acid (PLLA) or poly-*D*-lactic acid (PDLA) which are both semi-crystalline and have a melting point at around 175 °C.[84] Isotactic PLA can also be synthesised using *rac*-LA. However, the physical properties of the resulting polymer differ significantly from PLLA/PDLA, exhibiting a T_m of 230 °C.[85] This was initially attributed to the formation of a stereocomplex, where PLLA and PDLA chains form intermolecular interactions that are greater than those in PLLA/PDLA alone.[86] Ovitt and Coates demonstrated that the same high T_m can be achieved when forming stereoblock polymers. These contain both PLLA and PDLA segments in their main chain which result in the same co-crystallisation behaviour.[87] The isoselective polymerisation of *rac*-LA thus results in polymers with improved physical properties and has thus been of great interest to the research community. Particularly being able to control the length of the sequence blocks can allow the generation of polymers with tuneable properties.[88] Although the same effect can be achieved

by blending PLLA and PDLA together, a one-pot approach is more desirable.



Scheme 5. Possible outcomes of the stereoselective polymerisation of rac- and meso-LA

Another microstructure that can result from *rac*-LA is heterotactic PLA, which is semi-crystalline and thus exhibits a lower T_m (120 °C).[89]

Using *meso*-LA, the resulting microstructure may either be heterotactic or syndiotactic. The latter is semi-crystalline and has a T_m of 150 °C.[90]

A lack of any stereocontrol during the polymerisation of *rac*- and *meso*-LA results in an atactic polymer which does not exhibit stereoregularity. This polymer is amorphous due to a random configuration of stereocentres and cannot be used as a plastic.

1.4.4 Stereocontrol

Stereocontrol during the polymerisation can be achieved *via* two mechanisms: chain-end control (CEC) and enantiotopic-site control (ESC).[91]

In a CEC mechanism, the chirality of the chain end bound to the catalyst determines the preference of the next monomer insertion. This mechanism is generally applicable to achiral catalysts. In an ESC mechanism, the chirality of the catalyst dictates the preference for the enantiomer regardless of the chirality of the chain-end.

Whilst defects can be corrected in an ESC mechanism, in the case of CEC the introduction of a defect results in the propagation of that defect until another one is introduced. However, these mechanisms are not mutually exclusive. As will be discussed in Chapter 3, a combination of both mechanisms has been previously reported, and in some cases even more sophisticated stereocontrol mechanisms were observed.

The extent of sterocontrol can be quantified by the tacticity of the polymers in terms of the probabilities P_r and P_m (P_r = probability of racemic/syndiotactic enchainment; P_m = probability of meso/isotactic enchainment).[92] In the case of *rac*-LA, a perfectly isotactic polymer will have a $P_m = 1$ while a perfectly heterotactic polymer will have a $P_r = 1$. Conversely, in the case of *meso*-LA, a perfectly syndiotactic and a perfectly heterotactic polymer will have a value of 1 for P_r and P_m respectively. An atactic polymer will have a value of $P_m = P_r = 0.5$. These probabilities can be determined using Bernoullian statistic.[93]

1.5 Previous Work

Amongst other qualities, a ROP catalyst should ideally be easily synthesised, non-toxic, highly active, and highly isoselective. Industrially, PLA is produced using $Sn(Oct)_2$ in neat conditions at loadings of around 0.001 mol% and temperatures between 180 and 210 °C.[94] $Sn(Oct)_2$ offers no stereocontrol and thus is only used to polymerise the optically pure *L*-LA to produce PLLA. The system also results in both intra- and inter-molecular transesterification. Furthermore, the inherent cytotoxicity of tin makes its application in the medical industry rather unattractive.[95]

Although $Sn(Oct)_2$ is approved by the FDA,[96, 97] studies have shown that tin is incorporated in the final polymer at concentrations ranging from 20 to 50 ppm after processing.[98] This largely comes in the form of tin-hydroxyoctoate and tin-hydroxylactate.[99] Long-term liberation of tin in physiological conditions has not been studied yet and may impose more risks.[100]

Although numerous discrete catalysts have been reported,[101] aluminium-based complexes garnered considerable attention due to their high isoselectivity.[102] Aluminium's low toxicity as well as high availability in the earth's crust makes it an appealing metal centre.[103, 104] However, despite considerable efforts being made to design complexes that meet the aforementioned desirable criteria, a lack of rational design in ROP catalysts still persists.

1.5.1 Aluminium Initiators

Aluminium salen and salan complexes have found regular employment in the ROP of cyclic esters, particularly due to their ease of synthesis and high tuneability.[105] The salen ligand (Chart 2) can be easily prepared from commercially available reagents by condensation of two equivalents of 2-hydroxybenzaldehyde and one equivalent of a diamine to form the characteristic Schiff base backbone. The ligand is tetradentate, having an O'N'N'O-donor scaffold that binds to the metal ion, leading to a very stable complex in solution. Their ease of synthesis and ability to stabilise different metals at various oxidation has given this versatile class of ligands a "privileged" reputation.[106, 107]

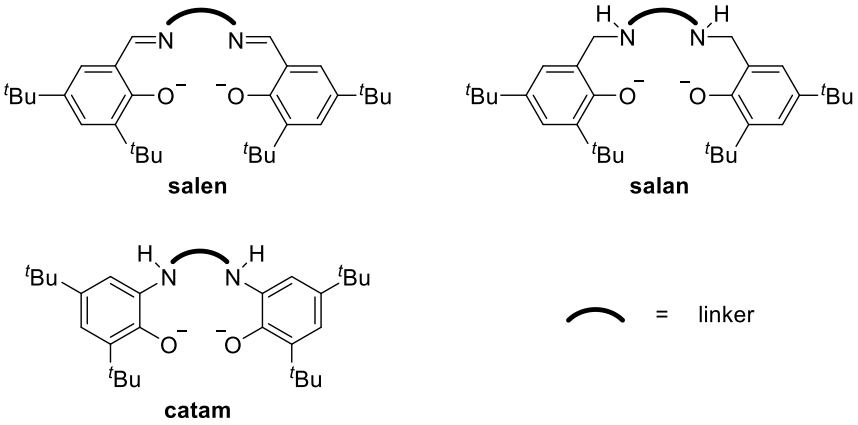


Chart 2. Representative structure of salen-, salan-, and catam-type ligand scaffolds

The first use of an aluminium salen complex for cyclic ester ROP was reported by Spassky in 1991, where an ethylene diamine bridged salen complex (Chart 3, left) was employed in the polymerisation of β-BL and LA at elevated temperatures (70 – 100 °C).[108-110] Results showed

high amounts of transesterification, but in the case of *rac*-LA, a slightly isotactic PLA was produced (P_m = 0.68).

Spassky then extended his work to chiral catalysts, reporting a (*R*)-BINAP-type aluminium salen complex (Chart 3, centre).[111] The introduction of a chiral component to the Schiff base scaffold allowed for higher activity alongside high stereoselectivity (70 °C, 1.3% catalyst loading). The catalyst was found to prefer the *D*-LA enantiomer and produced PDLA at low conversions. However, as *D*-LA was depleted, the insertion of the *L*-LA became possible (despite being less favourable than D-LA polymerisation), ultimately resulting in the formation of isotactic block polymers (PDLA-*b*-PLLA). These formed a stereocomplex with melting point temperatures (T_m = 187 °C) higher than what is expected with optically pure PLA.

As more salen complexes were synthesised and screened, a desire to understand the structure-activity relationship of the ligand emerged. In a landmark paper, Gibson and co-workers carried out a structural study which investigated the effect of varying substituents on the rate of reaction and selectivity of achiral salen catalysts.[112] They found that both the linker as well as the phenoxy substituents have an influence on the polymerisation. Electron-withdrawing substituents on the phenoxy groups resulted in an increase in activity, likely due to making the metal centre more Lewis acidic. Introducing bulky substituents on the *ortho* position generally slowed down the polymerisation rate, but resulted in an increase in isoselectivity (P_m up to 0.88) which confirmed previous findings by Nomura *et al.*[113] Interestingly, the vast majority of catalysts were isoselective with only one out of the 24 studied complexes exhibiting heteroselectivity (P_r = 0.63). Isoselectivity was found to increase with increased flexibility of the linker. The most active salen catalyst was found to be a 3,5-chlorosalen complex (Chart 3, right).

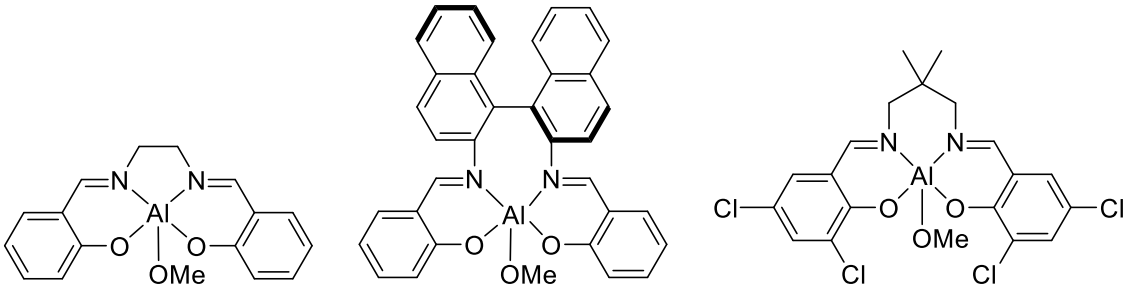


Chart 3. Structures of Et-salen-Al-OMe (left), (*R*)-SALBINapht-Al-OMe (centre), and 3,5-chlorosalen-Al-Me (right)

1.5.2 The Catam Ligand

Even though numerous aluminium catalysts have been reported with good isoselectivities, they traditionally suffer from poor activity, require high loading, and are sensitive to moisture/protic sources which limit their industrial employment. Whilst a wealth of research has been conducted on salen- and salan-based catalysts, not much is known about polymerisation catalysts using the corresponding catecholamine derivative (catam). This ligand scaffold features two rigid *ortho*-aminophenolate moieties tethered by a flexible linker (Chart 2) and was first discovered in the 1950s.[114] Although little came of that, the ligand scaffold experienced a revival in 1996 after a publication by Maslovskaya *et al*.[115] This section will outline the literature surrounding the catam ligand, with the many structures summarised in Chart 4.

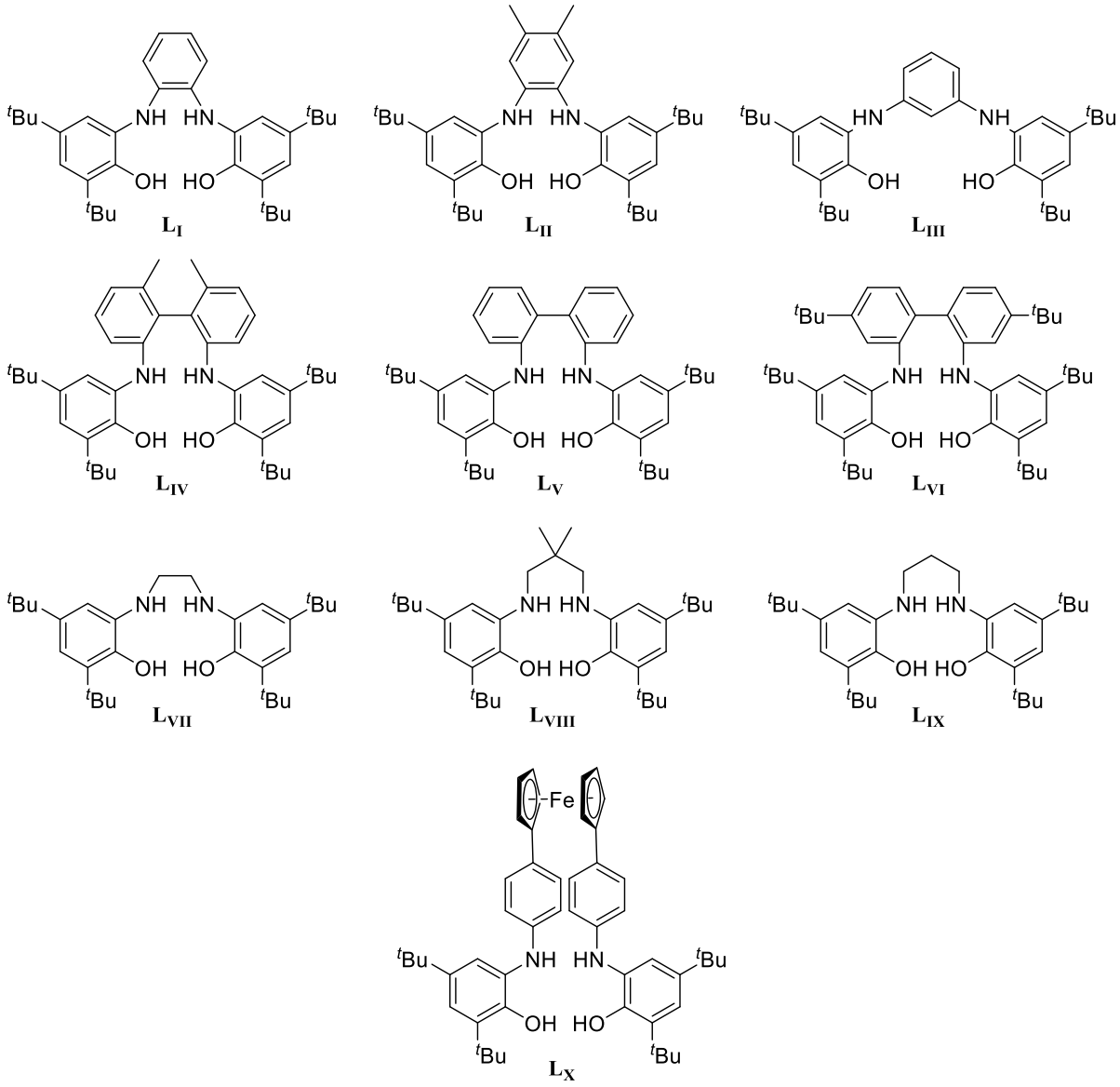


Chart 4. Structures of **L**$_{\mathbf{I}}$ - **L**$_{\mathbf{X}}$

a) Aromatic linker

In 1996, Wieghardt and co-workers synthesised a 1,2-phenylenediamine linked catam pro-ligand (**L$_{I}$**) as its structure was suspected to lend itself to redox activity. The complexation of **L$_{I}$** to Cu and Zn was carried out successfully and the group showed the complexes to have excellent redox properties, each displaying 2 successive reversible oxidations and reductions on their CV spectrum.[116] The complexes were at the time found to be the most stable and active ones concerning the selective oxidation of methanol and ethanol into their respective aldehyde. Nearly a decade later, Heyduk and co-workers employed **L$_{I}$** with Zr and found that the ligand's properties enabled the complex to catalyse the multielectron disproportionation of 1,2-diphenylhydrazine into azobenzene and aniline.[117] The group carried out further studies on the Zr as well as the Ti and Hf complexes of **L$_{I}$** and found that their reaction with Iodobenzene dichloride resulted in oxidative addition products in which the ligand supported the dicationic charge.[118] The interesting electronic properties of **L$_{I}$** drew the attention of other research groups with more structural and electronic studies being conducted on its complexes with Ti/Zr,[119] Co,[120, 121] Sn,[122] Mo,[123] W,[124] Fe,[121] Te,[125] V,[119] and Ni.[119]

Hanifpour *et al.* synthesised an analogue of **L$_{I}$** in which the 4 and 5 positions of the phenylene linker were methylated (**L$_{II}$**).[126] The complexation of **L$_{II}$** with Ti resulted in a fast and effective catalyst for the polymerisation of 1-decene. Dei *et al.* broadened the scope of phenylene linked catam ligands by synthesising a 1,3-phenylenediamine tethered catam ligand (**L$_{III}$**).[127] Coordination of **L$_{III}$** with Co and Fe resulted in complexes that displayed intra-ligand antiferromagnetic interactions. Electronic studies were also extended to the Ru analogue.[128] Chaudhuri and co-workers further studied the reactivity of **L$_{III}$** with Cu, Ni, Fe, Co, Cr, and Mn.[129] The Mn complex was found to catalyse the oxidation of catechols to their respective quinone under mild aerobic conditions, mimicking the function of the Cu-containing enzyme catechol oxidase.

Polyaromatic linkers as catam tethers were also explored. (*S*)-(-)-6,6'-dimethyl-2,2'-biphenyldiamine was used by Scott and co-workers to synthesise **L$_{IV}$**. La and Y complexes of **L$_{IV}$** were generated and used in the enantioselective hydroamination/cyclisation of aminoalkenes.[130, 131] The complexes were found to be more effective than their salen and salan counterparts. Chaudhuri and co-workers investigated the non-methylated counter-part of **L$_{IV}$** by synthesising a catam ligand linked by 2,2'-biphenyldiamine (**L$_{V}$**).[132] The coordination of **L$_{V}$**

was studied with Cu, Ni, Pd, Fe, and V and the complexes were found to undergo a redox-active disproportionation that yields active species for the oxidation of benzyl alcohol to benzaldehyde, mimicking the action of the Cu-centered metalloenzyme galactose oxidase. Gianino and Brown complexed **L**$_{\mathbf{V}}$ with Os and Ru for structural and electronic studies.[133] They found the complexes to exhibit highly covalent bonding between the ligand and metal centre, where the π-bond is slightly polarised towards the ligand in the case of Os, but slightly polarised towards the metal in the case of Ru. The ligand was modified by Brown and co-workers by including ^{t}Bu moieties on the linker (**L**$_{\mathbf{VI}}$). Complexation of **L**$_{\mathbf{VI}}$ with Mo resulted in a species that readily interconverted between different structural isomers due to the strong π-bonding of the ligand.[134, 135] The complexations were later extended to Ni, Pt, and Pd.[136] Structural an electronic measurements were performed and single-triplet gaps measured.

The fact that ligands **L**$_{\mathbf{I}}$ to **L**$_{\mathbf{VI}}$ were found to be highly redox active demonstrates how easily a redox-non innocent catam ligand can be synthesised. The breadth of positive results will eventually lead to the exploitation of **L**$_{\mathbf{I}}$ for polymerisation purposes (see Chapter 4).

b) Aliphatic linker

Having pioneered the use of aromatic catam ligands in inorganic chemistry, Wieghardt and co-workers moved onto the synthesis and use of alkyl-catam pro-ligands. The ethyl-tethered catam (**L**$_{\mathbf{VII}}$), which was previously discovered,[114, 115] was used with Ni and the resulting complex found to be paramagnetic.[137] Okuda and co-workers synthesised the Ti centred complex of **L**$_{\mathbf{VII}}$ and observed it to be inactive in the polymerisation of alkenes.[138] Interestingly, methylation of the NH moieties of **L**$_{\mathbf{VII}}$ and subsequent complexation with Ti, Zr, and Hf, led to active catalysts which indicates that, depending on the reaction, the NH moieties can have a detrimental effect. Given the simple C_2 linkage between the *ortho*-aminophenols, Bellemin-Laponnaz *et al*. found that a simple reaction of **L**$_{\mathbf{VII}}$ with triethyl orthoformate imbues the ligand with a carbene moiety.[139] The complexes of such NHC ligands have been studied further but are beyond the scope of this review.[140-142]

Another catam ligand explored by the Wieghardt group was one linked by a 2,2-dimethylpropane-1,2-diamine unit (**L**$_{\mathbf{VIII}}$).[137] Employed with Ni and Pd, the structural and electronic behaviour of the complexes was studied. They were found to be diamagnetic and electronic spectra also found that the electrochemically generated mono-cation and mono-anion forms have the unpaired electron delocalised over both halves of the ligand. An analogue

of **LVIII** lacking the *gem*-dimethyls (**LIX**) was reported by Sadr and co-workers. The corresponding Cu complex was synthesised and employed in the oxidation of benzyl alcohol to benzaldehyde in aerobic conditions.[143] The redox-behaviour of this complex was found to be quasi-reversible, likely due to the alkyl linker being employed.

An interesting approach was demonstrated by the Brown group in which a catam ligand, linked by a 1,1'-ferrocene-bis(*para*-phenylene) unit (**LX**).[144] The ligand was found to be tetradentate and bind to Pd in a planar fashion. Through electrochemical measurements, optical spectroscopy, and DFT calculations, the electronic interactions between the ferrocenyl moiety and the *ortho*-aminophenols were found to be minimal.

It needs to be mentioned that the use of linkers containing heteroatoms was also investigated for the synthesis of ligands with a denticity higher than 4. The use of sulfur-,[145-150] oxygen-,[151] and nitrogen-containing linkers was investigated to successfully generate penta- and hexa-dentate ligands.[142, 152, 153] As this thesis concerns itself with tetradentate ligands, they are not discussed.

Table 1. Summary of the synthesised catam ligands to-date, their respective names in the thesis (if applicable), as well as the metals they were complexed with and their respective literature reference

Pro-ligand	Pro-ligand name in this thesis	Metal	References
L$_{I}$	$H_2^{H}L_4$	Cu, Zn	[116]
		Ti, Zr, Hf	[117-119, 154]
		Co	[120, 121]
		Sn	[122]
		Mo	[123]
		W	[124]
		Fe	[121]
		Te	[125]
		V, Ni	[119]
L$_{II}$	-	Ti	[126]
L$_{III}$	-	Co, Fe	[127, 129]
		Ru	[128]
		Cu, Ni, Cr, Mn	[129]
L$_{IV}$	-	La, Y	[130, 131]
L$_{V}$	-	Cu, Ni, Pd, Fe, V	[132]
		Os, Ru	[133]
L$_{VI}$	-	Mo	[134, 135]
		Ni, Pd, Pt	[136]
L$_{VII}$	$H_2^{H}L_2$	Ni	[137]
		Ti	[138]
L$_{VIII}$	$H_2^{H}L_1$	Ni, Pd	[137]
L$_{IX}$	-	Cu	[143]
L$_{X}$	-	Pd	[144]

The catam ligands are summarised in Chart 4, and their employment with metals detailed in Table 1. Interestingly, there are no examples of their use with Group 13 metals which made the targeting of aluminium-based catam complexes attractive.

1.5.3 Differences Between Salen and Catam Ligands

Given that a breadth of research has been conducted on salen ligands in ROP, the catam ligand faces a very well-established ligand class (Chart 5). Although differences between salen and catam ligands initially appear to be minor, they are thought to change the behaviour of complexes significantly.

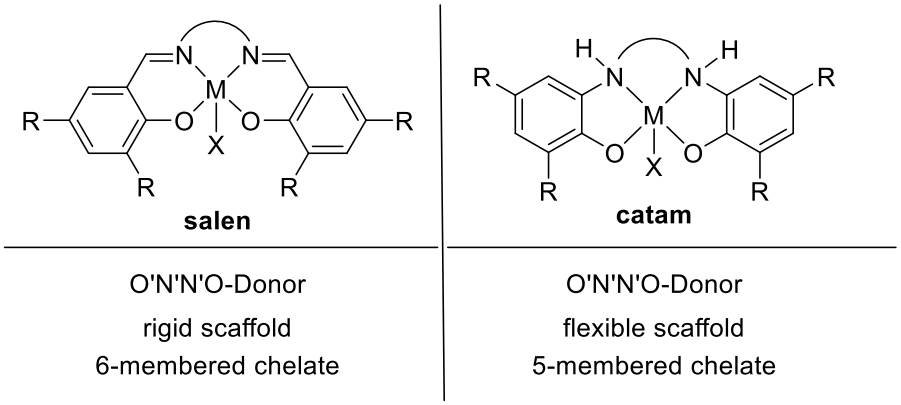
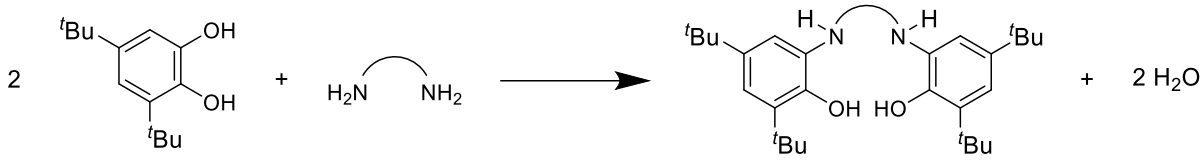


Chart 5. Comparison between the salen and catam ligand scaffold

Whilst both ligands are O'N'N'O-donors, the catam scaffold forms a rigid five-membered chelate between the *ortho*-aminophenols and the metal centre. Chen and co-workers have found this five-membered chelate system improved aluminium-mediated polymerisations of ε-CL, resulting in significantly higher polymerisation rates.[155] The catam ligands also replaces the Schiff base of the salen with NH moieties which are more acidic and thus can bind more strongly to the metal ions.[156] The amine is also sp^3 hybridized and thus a stereocentre which would bring a chiral environment to the immediate vicinity of the metal centre and possibly aid in mediating stereocontrol. Furthermore, the switch would lead to a more flexible scaffold which would allow the complexes to adopt structures closer to the ones of the transition states, leading to an overall lower activation energy and thus a higher rate of polymerisation. The synthesis of the catam ligand is also generally straightforward, occurring *via* a single step (Scheme 9).

As mentioned in Section 1.5.2, the catam ligand was never employed with Al or other Group 13 metals. Given that **L$_I$** was found to increase the activity of Ti in *rac*-LA ROP, studying aluminium-centred catam complexes could potentially counteract the sluggish reactivity of Al towards *rac*-LA. Given this vacant niche as well as the broad scope of the catam ligand, the scaffold is an ideal platform for the study of structure-activity relationships. Through the study of various aluminium-based catam complexes, this thesis aims to demonstrate the versatility of the ligand in the context of cyclic ester ROP. Different ligands were studied with the outlook of eventually gaining sufficient knowledge to implement a rational design approach.



Scheme 6. General reaction scheme for the synthesis of catam pro-ligands

1.6 Aims and Objectives

The principal aim of this project was to synthesise a range of new aluminium catalysts for the ROP of cyclic esters. The following selection criteria are used:

- **Activity**: The polymerisation should exhibit high activities in a broad range of conditions and offer reasonable conversions at low catalyst loadings
- **Control**: The polymerisation should display characteristics of a living polymerisation, including predictable molecular weights, linear increase of molecular weights, and narrow dispersities.
- **Selectivity**: The catalysts should be isoselective so that stereoblock PLA can be synthesised from *rac*-LA.
- **Stability**: The catalysts should be reasonably stable when mimicking industrial polymerisation conditions (neat, 200 °C, low loading).
- **Ease of synthesis**: The synthesis of the catalysts should be straightforward and require cheap commercially available starting materials with minimal synthetic steps.
- **Tuneability**: The backbone of the catalyst should be tuneable to allow for the preparation of analogues that can provide more insight on the structure-activity relationship. Furthermore, tuneability of the aminophenol groups can offer insight into the importance of substituents at the periphery of the ligand.

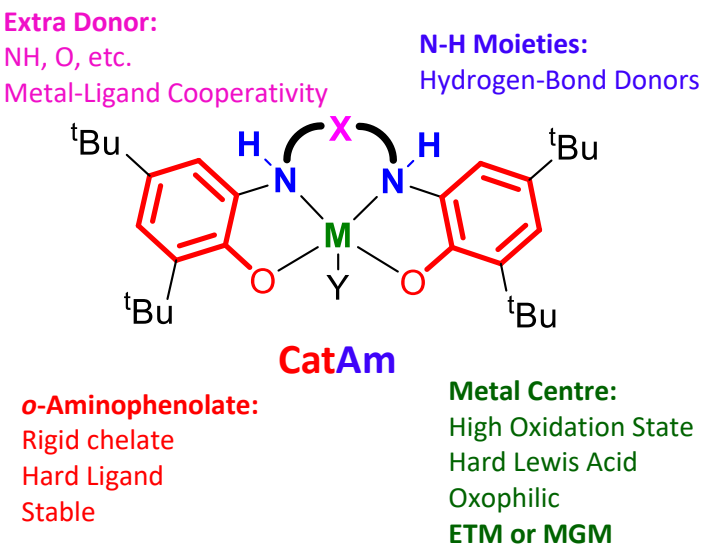


Figure 5. Representative structure of a catam complex highlighting its key properties

Aluminium complexes bearing the catam ligand scaffold will be investigated (Figure 5). The main modulation carried out will be on the linker to study its effect on the polymerisation behaviour. Chapter 2 will explore the importance of the NH moieties and non-covalent interactions (NCIs) in catalysis ($H_2^{H}L_1$ and $H_2^{H}L_2$). Chapter 3 will introduce a chiral component to the backbone of the ligand and investigate its effect on the polymerisation ($H_2^{H}L_3$). Chapter 4 will exploit the redox properties of the ligand with the aim to develop an electrochemically switchable catalyst ($H_2^{H}L_4$).

1.7 References

1. Baekeland, L. H. Insoluble product of phenol and formaldehyde. US942699, 1909.
2. Staudinger, H., *Ber. Dtsch. Chem. Ges.* **1920,** *53*, 1073-1085.
3. Carothers, W. H.; Hill, J. W., *J. Am. Chem. Soc.* **1932,** *54*, 1579-87.
4. Carothers, W. H.; Arvin, J. A., *J. Am. Chem. Soc.* **1929,** *51*, 2560-70.
5. Geyer, R.; Jambeck, J. R.; Law, K. L., *Sci. Adv.* **2017,** *3*, e1700782.
6. Narayan, R., *MRS Bulletin* **2011,** *36*, 716-721.
7. PetroleumUK An introduction to Petroleum. http://www.petroleum.co.uk/ (accessed 14/04/2020).
8. BritishPlasticsFederation Oil Consumption. https://www.bpf.co.uk/press/oil_consumption.aspx (accessed 14/04/2020).
9. Foundation, E. M. *The New Plastics Economy: Rethinking the future of plastics*; 2016.

10. Zhang, X.; Fevre, M.; Jones, G. O.; Waymouth, R. M., *Chem. Rev.* **2017,** *118*, 839-885.
11. Cole, M.; Lindeque, P.; Halsband, C.; Galloway, T. S., *Mar. Pollut. Bull.* **2011,** *62*, 2588-2597.
12. Teuten, E. L.; Saquing, J. M.; Knappe, D. R. U.; Barlaz, M. A.; Jonsson, S.; Björn, A.; Rowland, S. J.; Thompson, R. C.; Galloway, T. S.; Yamashita, R.; Ochi, D.; Watanuki, Y.; Moore, C.; Viet, P. H.; Tana, T. S.; Prudente, M.; Boonyatumanond, R.; Zakaria, M. P.; Akkhavong, K.; Ogata, Y.; Hirai, H.; Iwasa, S.; Mizukawa, K.; Hagino, Y.; Imamura, A.; Saha, M.; Takada, H., *Philos. T. Roy. Soc. B.* **2009,** *364*, 2027-2045.
13. Gregory, M. R., *Philos. T. Roy. Soc. B.* **2009,** *364*, 2013-2025.
14. Anastas, P.; Warner, J., *Green Chemistry: Theory and Practice*. Oxford University Press: 2000.
15. Saharan, B.; Sharma, D., *Int. J. Microbial Resource Technol.* **2012,** *11*, 11-23.
16. Gandini, A.; Lacerda, T. M., *Prog. Polym. Sci.* **2015,** *48*, 1-39.
17. Mecking, S., *Angew. Chem. Int. Edit.* **2004,** *43*, 1078-1085.
18. Florence Aeschelmann; Carus, M. *Bio-based Building Blocks and Polymers in the World*; 2013.
19. *Bio-based Building Blocks and Polymers in the World*; nova-institute: 2017.
20. Castro-Aguirre, E.; Iñiguez-Franco, F.; Samsudin, H.; Fang, X.; Auras, R., *Adv. Drug Deliver. Rev.* **2016,** *107*, 333-366.
21. Vink, E. T. H.; Davies, S., *Ind. Biotechnol.* **2015,** *11*, 167-180.
22. Auras, R.; Harte, B.; Selke, S., *Macromol. Biosci.* **2004,** *4*, 835-864.
23. Inkinen, S.; Hakkarainen, M.; Albertsson, A.-C.; Södergård, A., *Biomacromolecules* **2011,** *12*, 523-532.
24. Ritchie, H.; Roser, M. Plastic Pollution. https://ourworldindata.org/plastic-pollution (accessed 23/04/2020).
25. Groot, W. J.; Borén, T., *Int. J. Life Cycle Ass.* **2010,** *15*, 970-984.
26. Höglund, A.; Odelius, K.; Albertsson, A.-C., *ACS Appl. Mater. Inter.* **2012,** *4*, 2788-2793.
27. Lucas, N.; Bienaime, C.; Belloy, C.; Queneudec, M.; Silvestre, F.; Nava-Saucedo, J.-E., *Chemosphere* **2008,** *73*, 429-442.
28. LLC, N. How Ingeo is Made. https://www.natureworksllc.com/What-is-Ingeo/How-Ingeo-is-Made (accessed 17/04/2020).

29. Södergård, A.; Stolt, M., Industrial Production of High Molecular Weight Poly(Lactic Acid). In *Poly(Lactic Acid): Synthesis, Structures, Properties, Processing, and Applications*, 2010; pp 27-41.
30. Ajioka, M.; Enomoto, K.; Suzuki, K.; Yamaguchi, A., *J. Environ. Polym. Degr.* **1995,** *3*, 225-234.
31. Gruber Patrick, R.; Hall Eric, S.; Kolstad Jeffrey, J.; Iwen Matthew, L.; Benson Richard, D.; Borchardt Ronald, L. Continuous Process For The Manufacture Of A Purified Lactide From Esters Of Lactic Acid. US 5247059 A, 1992/08/24, 1993.
32. Jung, Y. K.; Kim, T. Y.; Park, S. J.; Lee, S. Y., *Biotechnol. Bioeng.* **2010,** *105*, 161-171.
33. Dusselier, M.; Van Wouwe, P.; Dewaele, A.; Jacobs, P. A.; Sels, B. F., *Science* **2015,** *349*, 78-80.
34. Tokiwa, Y.; Suzuki, T., *Nature* **1977,** *270*, 76-78.
35. Chandra, R.; Rustgi, R., *Prog. Polym. Sci.* **1998,** *23*, 1273-1335.
36. Nair, L. S.; Laurencin, C. T., *Prog. Polym. Sci.* **2007,** *32*, 762-798.
37. Buntara, T.; Noel, S.; Phua, P. H.; Melián-Cabrera, I.; de Vries, J. G.; Heeres, H. J., *Angew. Chem. Int. Edit.* **2011,** *50*, 7083-7087.
38. Lu, J.; Tappel, R. C.; Nomura, C. T., *Polym. Rev.* **2009,** *49*, 226-248.
39. Ackermann, J.-u.; Müller, S.; Lösche, A.; Bley, T.; Babel, w., *J. Biotechnol.* **1995,** *39*, 9-20.
40. Alves, M. I.; Macagnan, K. L.; Rodrigues, A. A.; de Assis, D. A.; Torres, M. M.; de Oliveira, P. D.; Furlan, L.; Vendruscolo, C. T.; Moreira, A. d. S., *Ind. Biotechnol.* **2017,** *13*, 192-208.
41. Steinbüchel, A.; Füchtenbusch, B., *Trends Biotechnol.* **1998,** *16*, 419-427.
42. Shen, K.; Haufe, J.; Patel, M. K. *Product Overview and Market Projection of Emerging Bio-Based Plastics. Final Report of Utrecht University to European Bioplastics.*; 2009.
43. Sudesh, K.; Abe, H.; Doi, Y., *Prog. Polym. Sci.* **2000,** *25*, 1503-1555.
44. Kricheldorf, H. R.; Eggerstedt, S., *Macromolecules* **1997,** *30*, 5693-5697.
45. Abe, H.; Matsubara, I.; Doi, Y.; Hori, Y.; Yamaguchi, A., *Macromolecules* **1994,** *27*, 6018-6025.
46. Chen, G.-Q., Plastics Completely Synthesized by Bacteria: Polyhydroxyalkanoates. In *Plastics from Bacteria: Natural Functions and Applications*, Chen, G. G.-Q., Ed. Springer Berlin Heidelberg: Berlin, Heidelberg, 2010; pp 17-37.

47. Zintl, M.; Molnar, F.; Urban, T.; Bernhart, V.; Preishuber-Pflügl, P.; Rieger, B., *Angew. Chem. Int. Edit.* **2008,** *47*, 3458-3460.
48. Olsén, P.; Odelius, K.; Albertsson, A.-C., *Biomacromolecules* **2016,** *17*, 699-709.
49. Dainton, F. S.; Ivin, K. J., *Q. Rev. Chem. Soc.* **1958,** *12*, 61-92.
50. Duda, A.; Kowalski, A., Thermodynamics and Kinetics of Ring-Opening Polymerization. In *Handbook of Ring-Opening Polymerization*, Wiley-VCH: 2009; pp 1-51.
51. Duda, A.; Penczek, S., *Macromolecules* **1990,** *23*, 1636-1639.
52. Kricheldorf, H. R.; Kreiser-Saunders, I.; Stricker, A., *Macromolecules* **2000,** *33*, 702-709.
53. von Schenck, H.; Ryner, M.; Albertsson, A.-C.; Svensson, M., *Macromolecules* **2002,** *35*, 1556-1562.
54. Kowalski, A.; Duda, A.; Penczek, S., *Macromolecules* **2000,** *33*, 7359-7370.
55. Dechy-Cabaret, O.; Martin-Vaca, B.; Bourissou, D., Polyesters from Dilactones. In *Handbook of Ring-Opening Polymerization*, Wiley-VCH: 2009; pp 255-286.
56. Dagorne, S.; Le Bideau, F.; Welter, R.; Bellemin-Laponnaz, S.; Maisse-François, A., *Chem. Eur. J.* **2007,** *13*, 3202-3217.
57. Dove, A. P., *ACS Macro. Lett.* **2012,** *1*, 1409-1412.
58. Kiesewetter, M. K.; Shin, E. J.; Hedrick, J. L.; Waymouth, R. M., *Macromolecules* **2010,** *43*, 2093-2107.
59. Kamber, N. E.; Jeong, W.; Waymouth, R. M.; Pratt, R. C.; Lohmeijer, B. G. G.; Hedrick, J. L., *Chem. Rev.* **2007,** *107*, 5813-5840.
60. Bourissou, D.; Moebs-Sanchez, S.; Martín-Vaca, B., *CR. Chim.* **2007,** *10*, 775-794.
61. Nederberg, F.; Connor, E. F.; Möller, M.; Glauser, T.; Hedrick, J. L., *Angew. Chem. Int. Edit.* **2001,** *40*, 2712-2715.
62. Connor, E. F.; Nyce, G. W.; Myers, M.; Möck, A.; Hedrick, J. L., *J. Am. Chem. Soc.* **2002,** *124*, 914-915.
63. Dove, A. P.; Pratt, R. C.; Lohmeijer, B. G. G.; Waymouth, R. M.; Hedrick, J. L., *J. Am. Chem. Soc.* **2005,** *127*, 13798-13799.
64. Pratt, R. C.; Lohmeijer, B. G. G.; Long, D. A.; Lundberg, P. N. P.; Dove, A. P.; Li, H.; Wade, C. G.; Waymouth, R. M.; Hedrick, J. L., *Macromolecules* **2006,** *39*, 7863-7871.
65. Ottou, W. N.; Sardon, H.; Mecerreyes, D.; Vignolle, J.; Taton, D., *Prog. Polym. Sci.* **2016,** *56*, 64-115.

66. Kazakov, O. I.; Datta, P. P.; Isajani, M.; Kiesewetter, E. T.; Kiesewetter, M. K., *Macromolecules* **2014,** *47*, 7463-7468.
67. Coady, D. J.; Engler, A. C.; Horn, H. W.; Bajjuri, K. M.; Fukushima, K.; Jones, G. O.; Nelson, A.; Rice, J. E.; Hedrick, J. L., *ACS Macro. Lett.* **2012,** *1*, 19-22.
68. Koeller, S.; Kadota, J.; Deffieux, A.; Peruch, F.; Massip, S.; Léger, J.-M.; Desvergne, J.-P.; Bibal, B., *J. Am. Chem. Soc.* **2009,** *131*, 15088-15089.
69. Koeller, S.; Kadota, J.; Peruch, F.; Deffieux, A.; Pinaud, N.; Pianet, I.; Massip, S.; Léger, J.-M.; Desvergne, J.-P.; Bibal, B., *Chem. Eur. J.* **2010,** *16*, 4196-4205.
70. Coulembier, O.; Sanders, D. P.; Nelson, A.; Hollenbeck, A. N.; Horn, H. W.; Rice, J. E.; Fujiwara, M.; Dubois, P.; Hedrick, J. L., *Angew. Chem. Int. Edit.* **2009,** *48*, 5170-5173.
71. Alba, A.; Schopp, A.; De Sousa Delgado, A.-P.; Cherif-Cheikh, R.; Martín-Vaca, B.; Bourissou, D., *J. Polym. Sci. Pol. Chem.* **2010,** *48*, 959-965.
72. Jenkins, A. D.; Kratochvíl, P.; Stepto, R. F. T.; Suter, U. W., **1996,** *68*, 2287.
73. Szwarc, M.; Levy, M.; Milkovich, R., *J. Am. Chem. Soc.* **1956,** *78*, 2656-2657.
74. Odian, G., *Principles of Polymerization*. 4th Edition ed.; Wiley-Interscience: 2004.
75. Inoue, S., *J. Polym. Sci. Pol. Chem.* **2000,** *38*, 2861-2871.
76. Asano, S.; Aida, T.; Inoue, S., *J. Chem. Soc., Chem. Commun.* **1985**, 1148-1149.
77. Aida, T.; Maekawa, Y.; Asano, S.; Inoue, S., *Macromolecules* **1988,** *21*, 1195-1202.
78. O'Keefe, B. J.; Breyfogle, L. E.; Hillmyer, M. A.; Tolman, W. B., *J. Am. Chem. Soc.* **2002,** *124*, 4384-4393.
79. Atkins, P.; De Paula, J., *Atkins' Physical Chemistry*. 9th Edition ed.; Oxford University Press: 2010.
80. Grubbs, R. B.; Grubbs, R. H., *Macromolecules* **2017,** *50*, 6979-6997.
81. Baran, J.; Duda, A.; Kowalski, A.; Szymanski, R.; Penczek, S., *Macromol. Rapid. Comm.* **1997,** *18*, 325-333.
82. Penczek, S.; Duda, A.; Szymanski, R., *Macromol. Symp.* **1998,** *132*, 441-449.
83. Chile, L.-E.; Mehrkhodavandi, P.; Hatzikiriakos, S. G., *Macromolecules* **2016,** *49*, 909-919.
84. Yin, H.-Y.; Wei, X.-F.; Bao, R.-Y.; Dong, Q.-X.; Liu, Z.-Y.; Yang, W.; Xie, B.-H.; Yang, M.-B., *CrystEngComm* **2015,** *17*, 4334-4342.
85. Ikada, Y.; Jamshidi, K.; Tsuji, H.; Hyon, S. H., *Macromolecules* **1987,** *20*, 904-906.
86. Tsuji, H.; Ikada, Y., *Polymer* **1999,** *40*, 6699-6708.
87. Ovitt, T. M.; Coates, G., *J. Polym. Sci. Pol. Chem.* **2000,** *38*, 4686-4692.

88. Fukushima, K.; Hirata, M.; Kimura, Y., *Macromolecules* **2007,** *40*, 3049-3055.
89. Kan, Z.; Luo, W.; Shi, T.; Wei, C.; Han, B.; Zheng, D.; Liu, S., *Front. Chem.* **2018,** *6*, 547-547.
90. Tsuji, H.; Arakawa, Y., *Polym. Chem.* **2018,** *9*, 2446-2457.
91. Stanford, M. J.; Dove, A. P., *Chem. Soc. Rev.* **2010,** *39*, 486-494.
92. Coudane, J.; Ustariz-Peyret, C.; Schwach, G.; Vert, M., *J. Polym. Sci. Pol. Chem.* **1997,** *35*, 1651-1658.
93. Chamberlain, B. M.; Cheng, M.; Moore, D. R.; Ovitt, T. M.; Lobkovsky, E. B.; Coates, G. W., *J. Am. Chem. Soc.* **2001,** *123*, 3229-3238.
94. Gruber, P.; O'Brien, M., Polylactides "NatureWorks® PLA". In *Biopolymers Online*, 2005.
95. Ganguly, B. B.; Talukdar, G.; Sharma, A., *Mutat. Res. Lett.* **1992,** *282*, 61-67.
96. Administration, U. S. F. D., Code of Federal Regulations. In *21*, 2019; Vol. 175.105.
97. Administration, U. S. F. D., Code of Federal Regulations. In *21*, 2019; Vol. 175.300.
98. Stjerndahl, A.; Finne-Wistrand, A.; Albertsson, A.-C.; Bäckesjö, C. M.; Lindgren, U., *J. Biomed. Mater. Res. A* **2008,** *87A*, 1086-1091.
99. Schwach, G.; Coudane, J.; Engel, R.; Vert, M., *Biomaterials* **2002,** *23*, 993-1002.
100. Hege, C. S.; Schiller, S. M., *Green Chem.* **2014,** *16*, 1410-1416.
101. Platel, R. H.; Hodgson, L. M.; Williams, C. K., *Polym. Rev.* **2008,** *48*, 11-63.
102. Jhurry, D.; Bhaw-Luximon, A.; Spassky, N., *Macromol. Symp.* **2001,** *175*, 67-80.
103. Gitelman, H. J., *Aluminium and Health*. CRC Press: 1988.
104. 7 - Aluminium, Gallium, Indium and Thallium. In *Chemistry of the Elements (Second Edition)*, Greenwood, N. N.; Earnshaw, A., Eds. Butterworth-Heinemann: Oxford, 1997; pp 216-267.
105. MacDonald, J. P.; Shaver, M. P., Aluminum Salen and Salan Polymerization Catalysts: From Monomer Scope to Macrostructure Control. In *Green Polymer Chemistry: Biobased Materials and Biocatalysis*, American Chemical Society: 2015; Vol. 1192, pp 147-167.
106. Yoon, T. P.; Jacobsen, E. N., *Science* **2003,** *299*, 1691-1693.
107. Cozzi, P. G., *Chem. Soc. Rev.* **2004,** *33*, 410-421.
108. Vincens, V.; Le Borgne, A.; Spassky, N., *Makromol. Chem. M. Symp.* **1991,** *47*, 285-291.
109. Le Borgne, A.; Vincens, V.; Jouglard, M.; Spassky, N., *Makromol. Chem. M. Symp.* **1993,** *73*, 37-46.

110. Wisniewski, M.; Borgne, A. L.; Spassky, N., *Macromol. Chem. Phys.* **1997,** *198*, 1227-1238.
111. Spassky, N.; Wisniewski, M.; Pluta, C.; Borgne, A. L., *Macromol. Chem. Phys.* **1996,** *197*, 2627-2637.
112. Hormnirun, P.; Marshall, E. L.; Gibson, V. C.; Pugh, R. I.; White, A. J. P., *Proc. Natl. Acad. Sci. U. S. A.* **2006,** *103*, 15343-15348.
113. Nomura, N.; Ishii, R.; Akakura, M.; Aoi, K., *J. Am. Chem. Soc.* **2002,** *124*, 5938-5939.
114. Freedman, H. H.; Frost, A. E., *J. Org. Chem.* **1958,** *23*, 1292-1298.
115. Maslovskaya, L. A.; Petrikevich, D. K.; Timoshchuk, V. A.; Shadyro, O. I., *Zh. Obshch. Khim.* **1996,** *66*, 1893-1898.
116. Chaudhuri, P.; Hess, M.; Müller, J.; Hildenbrand, K.; Bill, E.; Weyhermüller, T.; Wieghardt, K., *J. Am. Chem. Soc.* **1999,** *121*, 9599-9610.
117. Blackmore, K. J.; Lal, N.; Ziller, J. W.; Heyduk, A. F., *J. Am. Chem. Soc.* **2008,** *130*, 2728-2729.
118. Blackmore, K. J.; Lal, N.; Ziller, J. W.; Heyduk, A. F., *Eur. J. Inorg. Chem.* **2009,** *2009*, 735-743.
119. Salojärvi, E.; Peuronen, A.; Lahtinen, M.; Huhtinen, H.; Vlasenko, L. S.; Lastusaari, M.; Lehtonen, A., *Molecules* **2020,** *25*.
120. Lesh, F. D.; Lord, R. L.; Heeg, M. J.; Schlegel, H. B.; Verani, C. N., *Eur. J. Inorg. Chem.* **2012,** *2012*, 463-466.
121. Mondal, D.; Majee, M. C.; Kundu, S.; Mörtel, M.; Abbas, G.; Endo, A.; Khusniyarov, M. M.; Chaudhury, M., *Inorg. Chem.* **2018,** *57*, 1004-1016.
122. Cherkasov, V. K.; Piskunov, A. V.; Trofimova, O. Y.; Smolyaninov, I. V.; Fukin, G. K., *Dokl. Chem.* **2013,** *448*, 61-65.
123. Hänninen, M. M.; Paturi, P.; Tuononen, H. M.; Sillanpää, R.; Lehtonen, A., *Inorg. Chem.* **2013,** *52*, 5714-5721.
124. Hossain, M. K.; Haukka, M.; Hänninen, M. M.; Lisensky, G. C.; Paturi, P.; Nordlander, E.; Lehtonen, A., *Inorg. Chem. Commun.* **2018,** *93*, 149-152.
125. Petrov, P. A.; Kadilenko, E. M.; Sukhikh, T. S.; Eltsov, I. V.; Gushchin, A. L.; Nadolinny, V. A.; Sokolov, M. N.; Gritsan, N. P., *Chem. Eur. J.* **2020,** *26*, 14688-14699.
126. Hanifpour, A.; Bahri-Laleh, N.; Nekoomanesh-Haghighi, M.; Poater, A., *Green Chem.* **2020,** *22*, 4617-4626.

127. Dei, A.; Gatteschi, D.; Sangregorio, C.; Sorace, L.; Vaz, M. G. F., *Inorg. Chem.* **2003,** *42*, 1701-1706.
128. Fabrizi De Biani, F.; Dei, A.; Sangregorio, C.; Sorace, L., *Dalton Trans.* **2005**, 3868-3873.
129. Mukherjee, S.; Rentschler, E.; Weyhermüller, T.; Wieghardt, K.; Chaudhuri, P., *Chem. Comm.* **2003**, 1828-1829.
130. O'Shaughnessy, P. N.; Knight, P. D.; Morton, C.; Gillespie, K. M.; Scott, P., *Chem. Comm.* **2003**, 1770-1771.
131. O'Shaughnessy, P. N.; Gillespie, K. M.; Knight, P. D.; Munslow, I. J.; Scott, P., *Dalton Trans.* **2004**, 2251-2256.
132. Mukherjee, C.; Weyhermüller, T.; Bothe, E.; Chaudhuri, P., *Inorg. Chem.* **2008,** *47*, 11620-11632.
133. Gianino, J.; Brown, S. N., *Dalton Trans.* **2020,** *49*, 7015-7027.
134. Kopec, J. A.; Shekar, S.; Brown, S. N., *Inorg. Chem.* **2012,** *51*, 1239-1250.
135. Shekar, S.; Brown, S. N., *Dalton Trans.* **2014,** *43*, 3601-3611.
136. Conner, K. M.; Perugini, A. L.; Malabute, M.; Brown, S. N., *Inorg. Chem.* **2018,** *57*, 3272-3286.
137. Min, K. S.; Weyhermüller, T.; Bothe, E.; Wieghardt, K., *Inorg. Chem.* **2004,** *43*, 2922-2931.
138. Meppelder, G.-J. M.; Fan, H.-T.; Spaniol, T. P.; Okuda, J., *Organometallics* **2009,** *28*, 5159-5165.
139. Bellemin-Laponnaz, S.; Welter, R.; Brelot, L.; Dagorne, S., *J. Organomet. Chem.* **2009,** *694*, 604-606.
140. Nirmala, M.; Viswanathamurthi, P., *J. Chem. Sci.* **2016,** *128*, 9-21.
141. Harris, C. F.; Bayless, M. B.; van Leest, N. P.; Bruch, Q. J.; Livesay, B. N.; Bacsa, J.; Hardcastle, K. I.; Shores, M. P.; de Bruin, B.; Soper, J. D., *Inorg. Chem.* **2017,** *56*, 12421-12435.
142. Broere, D. L. J.; Plessius, R.; Tory, J.; Demeshko, S.; de Bruin, B.; Siegler, M. A.; Hartl, F.; van der Vlugt, J. I., *Chem. Eur. J.* **2016,** *22*, 13965-13975.
143. Sheykhi H., H. S. M., Soltani B., *Rev. Roum. Chim.* **2018,** *63*, 309-313.
144. Swanson, D. D.; Conner, K. M.; Brown, S. N., *Dalton Trans.* **2017,** *46*, 9049-9057.
145. Metzinger, R.; Demeshko, S.; Limberg, C., *Chem. Eur. J.* **2014,** *20*, 4721-4735.
146. Mondal, M. K.; Biswas, A. K.; Ganguly, B.; Mukherjee, C., *Dalton Trans.* **2015,** *44*, 9375-9381.

147. Ali, A.; Dhar, D.; Barman, S. K.; Lloret, F.; Mukherjee, R., *Inorg. Chem.* **2016,** *55*, 5759-5771.
148. Sarkar, P.; Tiwari, A.; Sarmah, A.; Bhandary, S.; Roy, R. K.; Mukherjee, C., *Chem. Comm.* **2016,** *52*, 10613-10616.
149. Maity, S.; Kundu, S.; Mondal, S.; Bera, S.; Ghosh, P., *Inorg. Chem.* **2017,** *56*, 3363-3376.
150. Sarkar, P.; Mondal, M. K.; Sarmah, A.; Maity, S.; Mukherjee, C., *Inorg. Chem.* **2017,** *56*, 8068-8077.
151. Mondal, M. K.; Tiwari, A.; Mukherjee, C., *Chem. Comm.* **2016,** *52*, 11995-11998.
152. Paul, G. C.; Sarkar, P.; Mukherjee, C., *Inorg. Chim. Acta* **2019,** *486*, 213-220.
153. Chun, H.; Verani, C. N.; Chaudhuri, P.; Bothe, E.; Bill, E.; Weyhermüller, T.; Wieghardt, K., *Inorg. Chem.* **2001,** *40*, 4157-4166.
154. Zelikoff, A. L.; Kopilov, J.; Goldberg, I.; Coates, G. W.; Kol, M., *Chem. Comm.* **2009**, 6804-6806.
155. Lee, C.-L.; Lin, Y.-F.; Jiang, M.-T.; Lu, W.-Y.; Vandavasi, J. K.; Wang, L.-F.; Lai, Y.-C.; Chiang, M. Y.; Chen, H.-Y., *Organometallics* **2017,** *36*, 1936-1945.
156. Pessoa, J. C.; Correia, I., *Coord. Chem. Rev.* **2019,** *388*, 227-247.

Chapter 2

Synthesis and Characterisation of Aluminium Complexes Bearing Alkyl Catam Ligands: On the Importance of Non-Covalent Interactions in Ring-Opening Polymerisation

2.1 Introduction

This chapter will describe the synthesis, characterisation, and application of catam complexes tethered by 2,2-dimethyl-1,3-propanediamine (H_2**^{H}L$_1$**) as well as 1,2-ethanediamine (H_2**^{H}L$_2$**). The complexes were found to be highly active at room temperature which was traced back to beneficial non-covalent interactions (NCIs) between the NH moieties of the catam ligand and the carbonyl moiety of the substrate. This introduction aims to outline the different types of bonding in chemistry and describes the occurrence and exploitation of NCIs in catalysis, particularly in cyclic ester ROP.

2.1.1 Introduction to Chemical Bonding

The IUPAC gold book defines a chemical bond as a lasting attraction between two atoms that leads to the formation of a stable independent molecular entity.[1] The governing principle of such an interaction is the reduction of the total potential energy at the expense of a small increase in kinetic energy. Covalent and ionic bonds are grouped into "primary bonds" and are amongst the strongest interactions.

2.1.1.1 Covalent Bonds

A covalent bond involves the sharing of electron pairs between atoms which (in most cases) allows the individual atom to attain a stable electronic configuration characterised by a full outer shell. As a pair of electrons is shared, it must be localised between both nuclei, meaning that the bond possesses directionality. Naturally, covalent bonding can be broken up into many more interactions including σ-bonding, π-bonding, agostic interactions, metallic bonds, bent bonds, three-center two-electron bonds, and three-center four-electron bonds.[2, 3] Whilst the most primitive form of a covalent bond is a single bond, σ- and π-bonds can combine to form double and triple bonds.

2.1.1.2 Ionic Bonds

Ionic bonding refers to an electrostatic attraction arising from the interaction between the electric charges of a cation and an anion. In this case, the involved atoms experience a stable electron configuration through the transfer of electrons from one atom to another. The ionic forces experienced between the atoms are generally much stronger than covalent bonds. Whilst covalent bonds incur a significant energy penalty when not adhering to the directionality of the bond, ionic bonds do not possess directionality resulting in efficient packing.

2.1.1.3 Significance of Electronegativity in Bonding

In both covalent and ionic bonds, valence electrons are actively involved in the bond formation. Thus, ionic bonds will always possess a covalent character as the proximity of the involved atoms will always result in a degree of electron sharing. Linus Pauling suggested the use of electronegativity (an atom's tendency to attract a pair of electrons) to characterise a bond.[4] Although multiple methods exist for calculating electronegativity, the Pauling scale is the most commonly used one.[5] In those terms, a bond is considered ionic if the difference in electronegativity between the two atoms is greater than 1.7. Anything less than that value is considered a covalent bond by traditional standards. The fact that electronegativity exists means that many covalent bonds will still possess an ionic character. In fact, a polar covalent bond is characterised by an electronegativity difference between 0.3 and 1.7.

2.1.1.4 Other Types of Bonding

A molecule is mainly characterised by the primary bonds that exist between its atoms. The covalent interactions act across a distance of 1 - 2 Å and their directionality leads to the molecule possessing a distinct structure.[6] However, unlike the name suggests, "secondary bonds" play an important role and are made up by different types of intermolecular forces. In this thesis, they are grouped into NCIs.

2.1.2 Introduction to Non-Covalent Interactions

In 1873, Johannes Van der Waals successfully defended his thesis wherein he first postulated the existence of non-covalent interactions.[7] Although initially a very rudimentary description, his theory was very much ahead of its time, and Van der Waals later became the namesake for a set of dipole forces.[1]

Nowadays, the importance of NCIs is undeniable and attributed to the very existence of the condensed phases and, furthermore, life.[8] NCIs are distinguished from covalent bonds by the fact that they do not involve a sharing of electron between atoms. The covalent bond is generally smaller than 2 Å and leads to the formation of the classical molecule as described earlier. NCIs however can act over distances of several angstroms and are thus considerably weaker (1-5 kcal/mol *vs.* 100+ kcal/mol).[9] These weak long-range interactions lead to the formation of supramolecular architectures such as the tertiary structure of proteins or double helix of DNA.[10]

Although many types of NCIs exist,[11] they can be classified into 4 distinct categories (Figure 1).

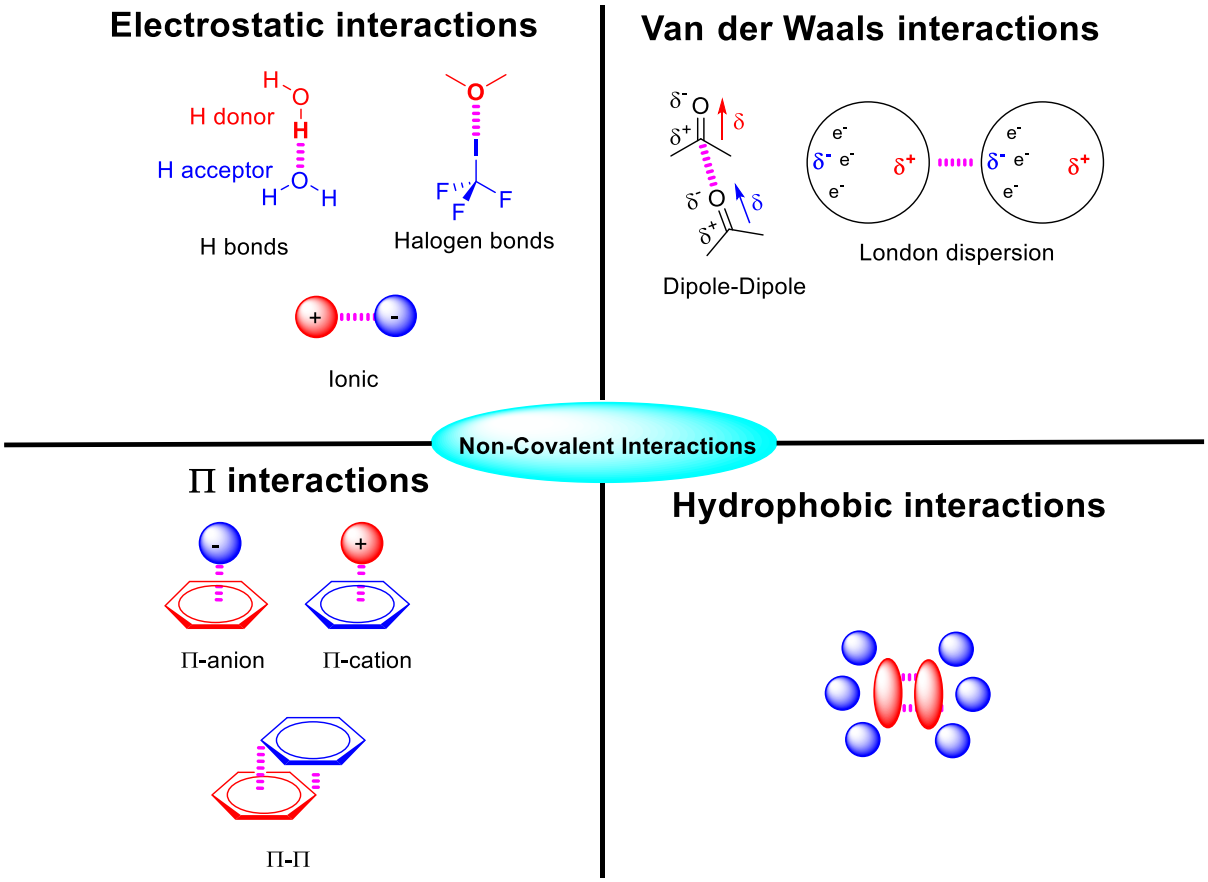


Figure 1. Summary of NCIs including electrostatic interactions (top left), Van der Waals interactions (top right), π interactions (bottom left), and hydrophobic interactions (bottom right)

2.1.2.1 Aromatic Interactions

These consist of interactions between molecules with conjugated π-systems (e.g. π-π interactions, π-cation interactions, etc.).[12] Due to the cyclic delocalisation in planar ring systems, the flat face of an aromatic compound will carry a partial negative charge.[13] The interacting residues are separated by a distance between 4.5 and 7 Å, with the interaction having a strength between 0.6 and 1.3 kcal/mol.[14]

2.1.2.2 Van der Waals Forces

Interactions involving permanent or induced dipoles such as dipole-dipole interactions or London dispersion forces. In the former, polar molecules interact *via* their partially charged regions. As these attractions occur over greater distances, their strength is relatively low, only amounting to 1.2 – 4.8 kcal/mol.[15] London dispersion forces arise from temporary fluctuations

in the distribution of electron density within an atom. This gives the atom a transient charge that may result in a non-specific and non-directional attraction.[16] These interactions are very weak, with a strength between 0.1 to 1 kcal/mol.

2.1.2.3 Hydrophobic Effect

In a polar medium such as water, non-polar molecules tend to form aggregates.[17] The medium usually "traps" the molecule in a clathrate cage, making the system more structured.[18] However, aggregation of hydrophobic molecules results in the displacement of the host-molecules. Whilst aggregation itself decreases entropy, the entropy increase from displacing the medium leads to an overall increase in ΔS, making hydrophobic interactions overall favourable.

2.1.2.4 Electrostatic Interactions

Attraction and repulsion between charged bodies including ion pairs, hydrogen bonding, and halogen bonding. The hydrogen bond owes its stability to Coulombic forces. A hydrogen atom bonded to an electronegative atom (such as O or N) will experience a partial positive charge (H-bond donor). This can attract a partial negative charge of a nearby nucleophile (H-bond acceptor) resulting in a directional long-range bond. The non-bonding orbital of the nucleophile donates electron density into the σ^* orbital of the proton donor.[19] Generally speaking, a hydrogen bond will generally have a strength between 2 and 15 kcal/mol (roughly 10% of the strength of a covalent bond).[20] Halogen bonds function in a very similar way to the H-bond, but instead of a hydrogen, a halogen atom acts as the donor. Although highly electronegative, the electron density of the halogen atom is located orthogonally to its covalent bond, resulting in a region of electron deficiency (σ-hole) on the axis of the covalent bond.[21] This σ-hole can consequently form attractive interactions with electron-rich atoms. Their strengths range from 1 to 43 kcal/mol. Note that these forms of interactions are not only limited between hydrogen, halogens, and other electronegative atoms. Chalcogens,[22] pnictogens,[23] and some metals have been found to participate in this type of bonding.[24] All in all, hydrogen- and halogen-bond interactions are the most impactful in nature and catalysis.[25, 26]

There has thus been great interest in harnessing NCIs to increase activity and selectivity in catalysis. However, although a plethora of research has been conducted on NCIs in catalysis, there is still a lack of rationale regarding their use in polymerisation catalysis.[12, 27] The

following section will briefly discuss the occurrence of NCIs in catalysis, with a focus on cyclic ester ROP.

2.1.3 Non-Covalent Interactions in Catalysis

2.1.3.1 Underlying Principles

NCIs are ubiquitous in enzyme catalysis and responsible for the tertiary structure of the enzyme and its ability to catalyse certain reactions.[28, 29] The classical explanation of a catalyst's efficacy is that the catalyst provides an alternative reaction pathway with an overall lower activation energy (E_a). While this is true, one can also view the efficacy of a catalyst through the lens of stabilisation. A catalyst can decrease the E_a of a reaction by either stabilising a transition state (TS), or by destabilising the ground state (GS). Both lead to a lower E_a overall (Figure 2).[30-32] The importance of NCIs in such stabilising/destabilising mechanisms in enzymes has first been suggested in 1925 by Sir Bayliss.[33]

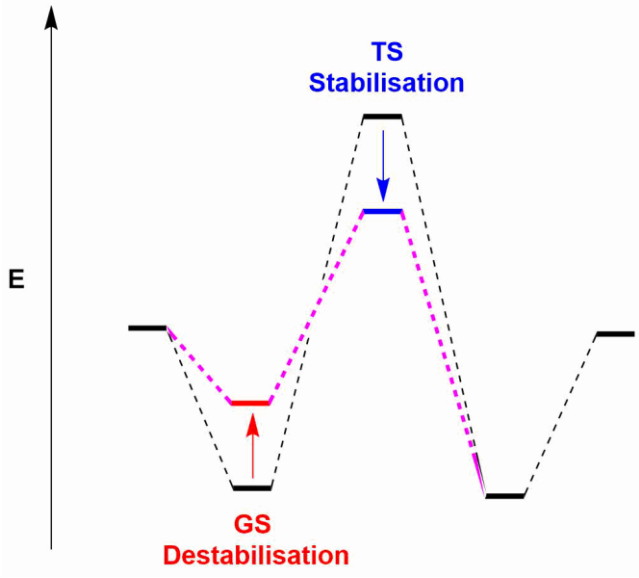


Figure 2. Energetic diagram depicting GS destabilisation and TS stabilisation, leading to a lower E_a

It is now obvious that the high activity and high control of an enzyme are due to the delicate balance of numerous NCIs throughout the reaction pathway.[34, 35] However, when applying such concepts to non-enzymatic small molecule catalysts, they do not come close to the performance of enzymes.[36] For example, comparing the enzyme triosephosphate isomerase with a primitive organic catalyst, the enzyme outperforms the small molecule by a factor of 10^{10}.[37] After all, nature did have a head start of a few billion years and we are just now starting to consider NCIs

in our catalyst design as new experimental and computational tools to quantify NCIs have emerged.[12, 26, 38, 39]

The physical essence of many NCIs is still disputed,[40] and controversy has been generated regarding how to characterise them.[41-43] Yet, particularly in the computational field, large strides have been made in quantifying and visualising NCIs.[8, 10, 44-49] Simpler reactions with organocatalysts can already benefit from the use of computational tools for catalyst design.[50] Raynal *et al.* outline a variety of interactions that can be exploited such as inter- and intra-molecular ligand-ligand interaction, as well as ligand-substrate interactions.[39] An overview of the interactions most relevant to this thesis is illustrated in Figure 3.

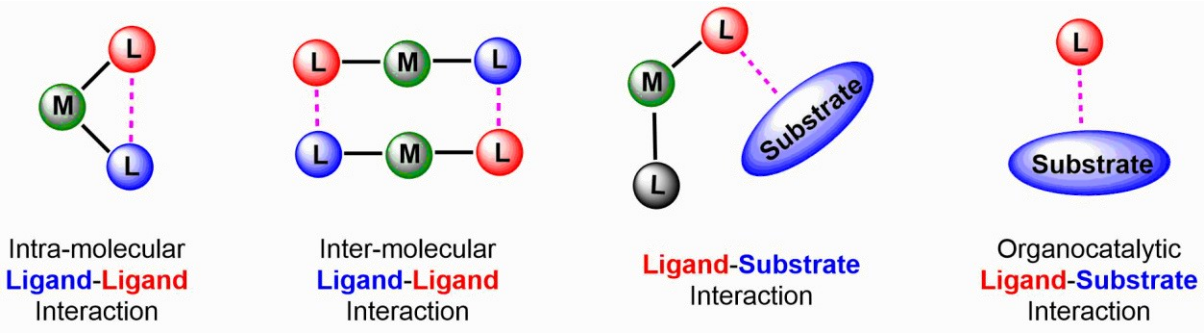
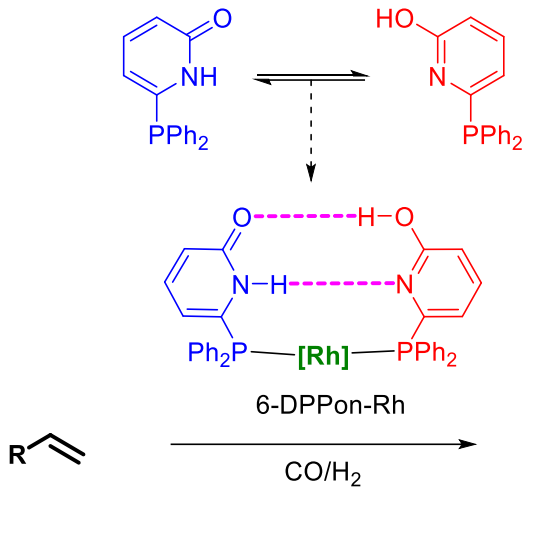


Figure 3. Ligand-Ligand and Ligand-Substrate interactions outlined by Raynal *et al.*

It should become clear how the interactions pictured in Figure 3 may result in profound changes in reactivity. For example, the thiourea catalysts mentioned in Section 1.3.3 depend on organocatalytic ligand-substrate interactions to proceed with LA ROP. By gaining control over the interactions in the second coordination sphere, one can achieve exquisite control over activity and selectivity. The use of H-bonding is particularly common, wherein they are exploited in the self-assembly of ligands, as well as the positioning of substrate in a specific conformation near the active site.[51] Examples of how these interactions are exploited are presented in the following section.

2.1.3.2 Selected Examples of NCI Exploitation in Catalysis

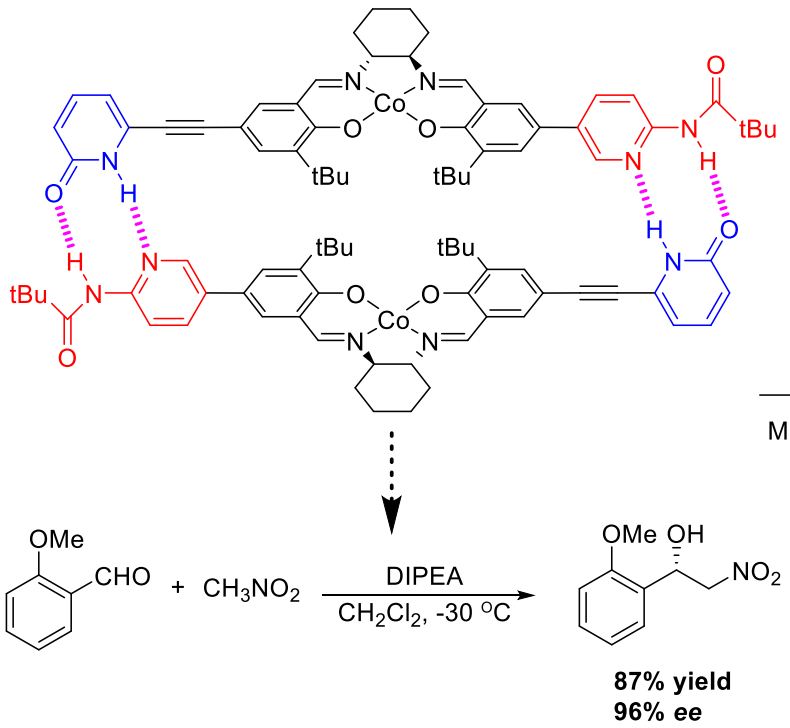
Breit and Seiche used intra-molecular H-bonding to assemble a 6-DPPon-Rh catalytic system (Scheme 1) for hydroformylation, yielding high activities and regioselectivities of 97%.[52]



	relative activity	selectivity (%)
^{t}Bu-XANTPHOS-Rh	1	98
PPh_3-Rh	3.7	73
6-DPPon-Rh	9.3	97

Scheme 1. Breit and Seiche's catalytic system consisting of the tautomers of 6-DPPon (red and blue). Self-assembly around a Rhodium metal centre through H-bonding led to a highly active and selective hydroformylation catalyst.

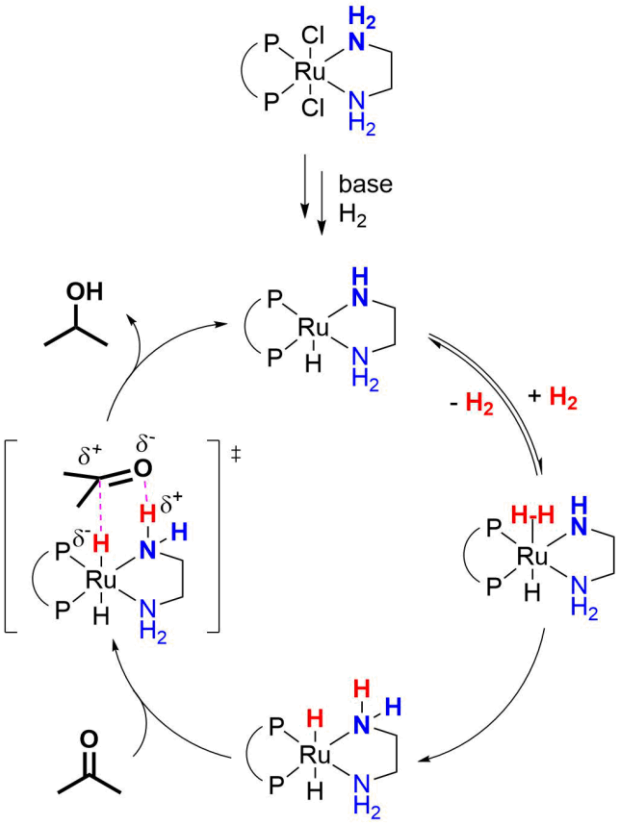
Hong and co-workers attached a 2-pyridone and a 2-aminopyridine unit to the backbone of a Co-salen complex leading to the formation of a head-to-tail dinuclear complex through inter-molecular H-bonding (Scheme 2).[53] The dinuclear catalyst was found to outperform the monomer in the Henry reaction, leading to higher activity (48-fold increase) and selectivity (96 *vs*. 55% ee). They have since expanded this concept to the hydrolytic kinetic resolution of epoxides.[54]



	k (M^{-1} h^{-1})	product ee (%)
Monomeric	6.02	55
Dimeric	289	96

Scheme 2. Hong's Co-salen complex consisting of a 2-pyridone (blue) and a 2-aminopyridine (red) moiety. Upon self-assembly, the dinuclear complex, catalysed the Henry reaction with a 48-fold increase in rate and higher selectivity compared to the monomer.

In terms of ligand-substrate interactions, Noyori and co-workers were the first to show that these interactions can be exploited to increase the activity of a catalyst for hydrogenation.[55-57] The NH functional groups on a Ru(diamine) catalyst can act cooperatively to activate carbonyl substrates (Scheme 3). Since then, the application of NH functionality in organometallic catalyst design has been widely discussed.[58-60]



Scheme 3. Proposed metal-ligand bifunctional system for Ru-NH catalysed hydrogenation

In the field of organocatalysis, dual H-bonding donors such as thiourea have received a lot of attention. Sigman and Jacobsen initially found that chiral thiourea derivatives were able to function as asymmetric catalysts.[61] This field has grown considerably since then as outlined in a variety of reviews.[62-68]

2.1.4 Non-Covalent Interactions in Polymerisation Catalysis

2.1.4.1 NCIs in Olefin Polymerisation

NCIs have been a very popular topic of discussion in olefin polymerisation catalysis. Particularly postmetallocene Ti catalysts with fluorine-containing phenoxy-imine chelate ligands have been shown to exhibit living characteristics, yielding highly controlled molecular

weights and narrow dispersities (Đ = 1.13).[69] Density functional theory (DFT) studies found non-covalent attractive C-H···F-C interactions between the fluorinated ligand and the β-hydrogen of the growing polymer chain (Figure 4) leading to a stabilisation of 7.2 kcal/mol. It was postulated that these interactions mitigate the reactivity of the β-hydrogen, preventing the termination of the polymerisation *via* β-hydrogen transfer.[70] An interesting aspect is the fact that these interactions prevent termination while still allowing propagation to occur. Further DFT studies conducted by Fujita and co-workers found that the arrangement of the polymer chain allows for a "back-side attack" by a monomer while maintaining the attractive C-H···F-C interactions.[71] As these interactions prevent termination, but allow for propagation, the living polymerisation can thus transpire. This effect is not exclusive to ethylene polymerisation and can also be applied to the propylene monomer.[72, 73]

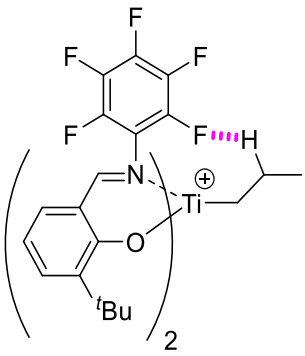


Figure 4. DFT-intermediate of the polymerisation of ethylene by Ti bearing a fluorine-containing phenoxy-imine chelate ligand. The attractive C-H···F-C interaction is thought to hamper β-hydrogen transfer

Talarico and co-workers were not convinced of these interactions and proposed that the living polymerisation can be explained by steric repulsion. The transition state of the β-hydrogen transfer is made bulkier by ancillary ligands and is thus more destabilised than the transition state of the propagation.[74]

Nevertheless, the living polymerisation of olefins was an exciting discovery and has been subsequently applied to Zr,[75] Ni,[76-79], and Pd.[79, 80] Given that olefin polymerisation catalyst-development traditionally involved trial-and-error,[81] these findings have led to the proposal of NCIs as a tool for rational catalyst design.[82]

2.1.4.2 NCIs in ROP

In the context of cyclic ester ROP, NCIs have been less discussed. In 2004, Gibson and co-workers discovered a decrease in heteroselectivity when switching from a 3,5-dimethyl-salan to the chloro derivative (Chart 1, **Al-1** and **-2**). From a first-order approximation the

substituents are sterically comparable .[83] They implied that the chloro substituents exerted an influence beyond a steric effect.

A computational analysis by Rzepa and co-workers suggested that the heteroselectivity of a β-diketiminate magnesium complex (Chart 1) arises from several steric interactions that may be reinforced by attractive C-H···π interactions between the methyl C-H of the Mg-lactate unit and the π-system of the *N*-aryl substituents of the ligand.[84]

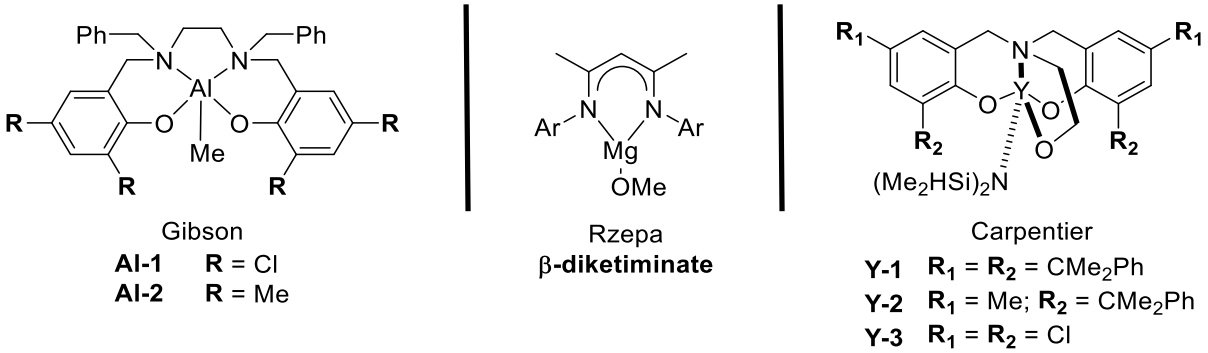


Chart 1. ROP initiators by Gibson (**Al-1, -2**), Rzepa (**β-diketiminate**), and Carpentier (**Y-1, -2, -3**) found to exhibit NCIs in catalysis

Carpentier and co-workers found H···π short-contacts in the solid-state structure of a series of methoxy-amino-bis(phenol) yttrium complexes and observed this interaction in solution through NOESY NMR spectroscopy (Chart 1, **Y-1**).[85-87] DFT computations (BP86-RI/fed-TZVP) for β-BL ROP were performed on a similar compound (Chart 1, **Y-2**) showed that C-H···π interactions between a methylene hydrogen of the butyrate moiety (H_a) and the *ortho*- and *meta*-carbon atoms of the phenyl ring of the cumyl substituent (H···C distances: 2.898 and 3.083 Å respectively) led to a stabilisation of 9.8 kcal/mol (Chart 2, left). Such interactions were thought to stabilise the active species during ROP and account for the high syndioselectivity of the catalyst.[88] Interestingly, no such interactions were observed in the computations of LA ROP. This suggests that NCIs are likely not a "be-all and end-all" solution and that they may need to be tailored specifically to a specific substrate. C-H···π interactions were also observed in the solid state of aluminium complexes but never linked to polymerisation behaviour.[89, 90]

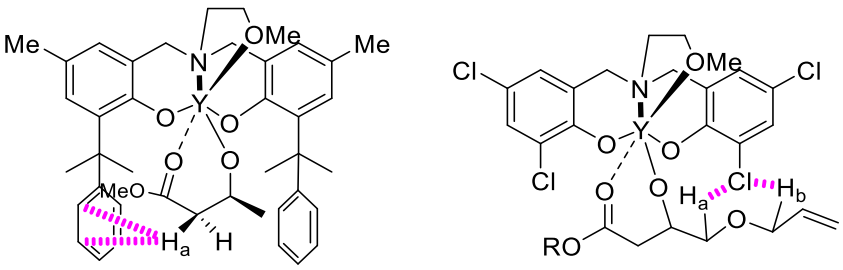


Chart 2. NCIs observed by Carpentier and co-workers during the ROP of β-lactones including C-H···π (left) and C-H···Cl (right)

Replacing the cumyl groups of the complex with chloro substituents (Chart 1, **Y-3**) resulted in a complete reversal of selectivity from syndio- to iso-selective in the ROP of functionalised β-BL.[91] This was traced back to strong C-H···Cl interactions between the acidic alkoxymethylene of the polymer chain and the chloro substituents of the ligand (Chart 2, right).[92] DFT studies (PBE/def2-SVP) showed the C-H_a···Cl and C-H_b···Cl interactions to act over a distance of 2.556 and 3.083 Å respectively.

Sarazin and Carpentier synthesised a series of cationic alkaline earth (Ae) metal complexes with fluorine containing ligands. The solid-state structures showed strong intramolecular Ae···F interactions between the metal and the ancillary ligand (Figure 5), leading to a calculated stabilisation of 25-40 kcal mol^{-1}.[93, 94] In terms of LA ROP, these complexes dissociate into monomeric fragments in solution and were highly active resulting in well-controlled polymers with excellent end-group fidelity. Interestingly, these complexes were slower than their non-fluorinated analogues which suggests that very strong NCIs may hamper activity by favouring the inactive aggregated form.[93]

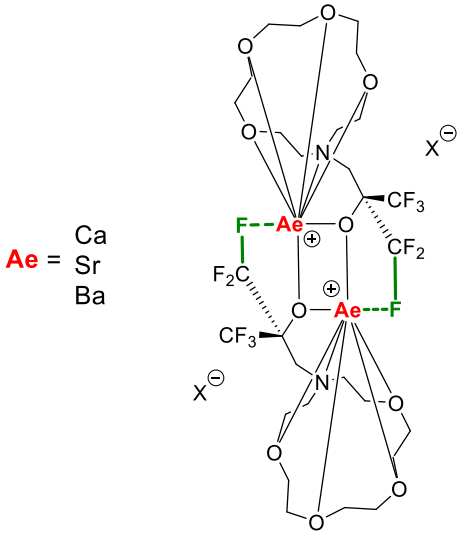
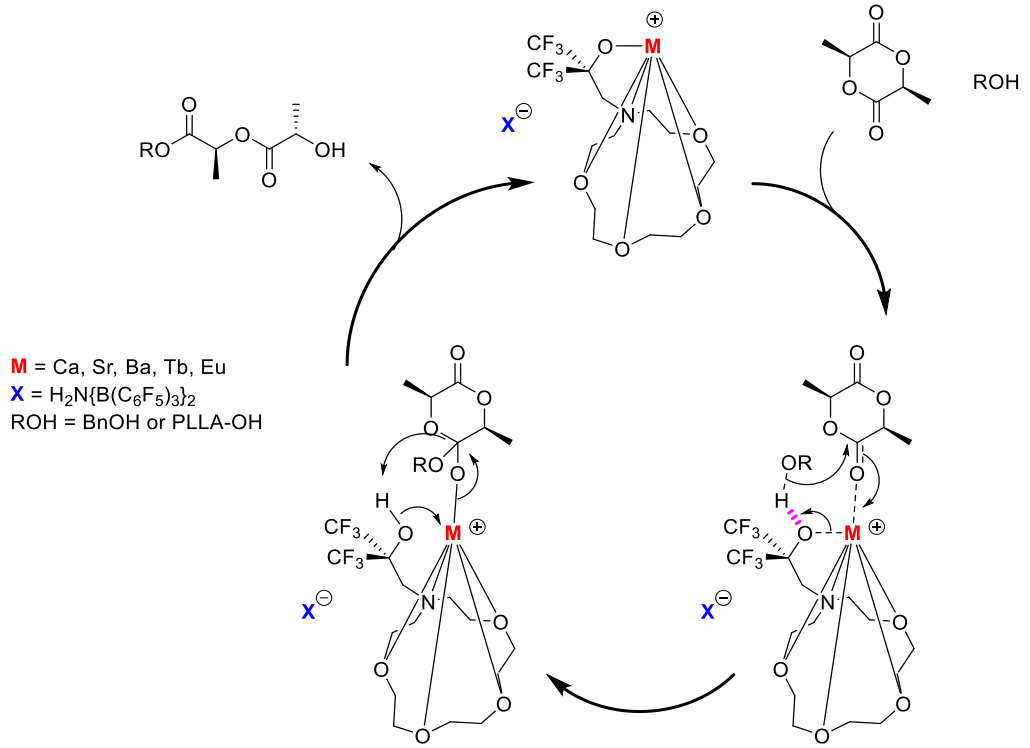


Figure 5. Structure of cationic Ae metal complexes with fluorine-containing ancillary ligands exhibiting Ae···F interactions

Traditional ROP mechanisms failed to provide conclusive insight, which prompted them to propose a modified ligand-assisted activated monomer mechanism in which the ancillary

ligand is not merely a spectator ligand (Scheme 4).[95, 96] Instead, it activates the nucleophile to facilitate attack onto the carbonyl.



Scheme 4. Proposed ROP mechanism by Sarazin postulating that the ligand is non-innocent in the mechanism

As discussed in Section 1.3.3, ROP using organocatalysts such as thioureas proceeds through a very similar activated monomer mechanism and relies heavily on NCIs. However, as the focus of this doctoral thesis is on metal-based catalysts, they will be omitted from discussion.

2.1.5 Potential of the Catam Ligand

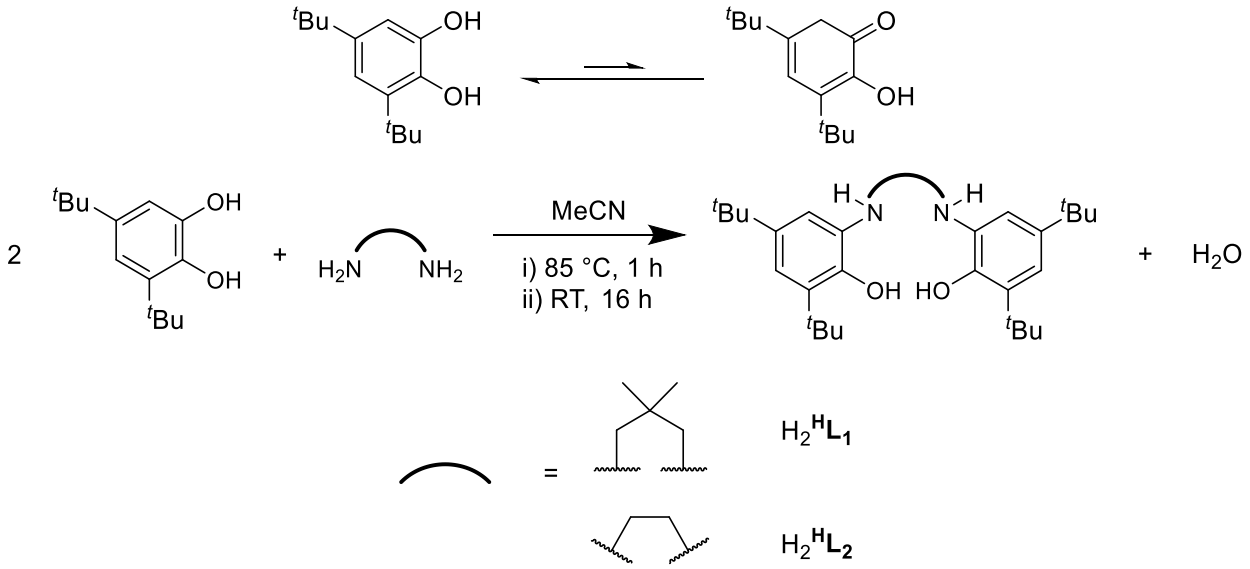
Clearly, NCIs have been used to describe trends in selectivity in cyclic ester ROP. However, there are little examples highlighting the importance of NCIs in main-group metal catalysis. Organocatalysis benefits from the formation of H-bonds by bringing the substrate closer and activating the monomer for nucleophilic attack. NH moieties near the metal center could act as H-bond donors and open up avenues for metal-ligand cooperation.[97] The catam ligand is a great candidate to test out such a hypothesis. The NH moieties would be close to the metal and any H-bonding event would be vicinal to the active site. The rationale consists of bringing the ideas applied to organocatalysis into metal-catalysis, with the hopes of merging the benefits of both and obtain a system that is greater than the sum of its parts.

2.2 Pro-Ligand Synthesis and Characterisation

This section will discuss the general synthesis of the $H_2{}^{H}L_1$ and $H_2{}^{H}L_2$ pro-ligands previously described by Wieghardt and co-workers (Section 2.2.1) along with examples of modulations offered by the NH groups on the catam scaffold (Section 2.2.2).

2.2.1 General Pro-Ligand Synthesis

The tethered *o*-aminophenol pro-ligands $H_2{}^{H}L_1$ and $H_2{}^{H}L_2$ were prepared according to a standard literature procedure exploiting the keto-enol equilibrium of the 3,5-di-*tert*-butylcatechol reagent (Scheme 5, top).[98] Two equivalents of 3,5-di-*tert*-butylcatechol react with one equivalent of a primary diamine (2,2-dimethyl-1,3-propanediamine or 1,2-ethanediamine) to afford $H_2{}^{H}L_1$ and $H_2{}^{H}L_2$ respectively in acetonitrile (Scheme 5, bottom).[99] Filtering and washing the precipitate with *n*-hexane, afforded the pro-ligands in good yields (> 60 %).

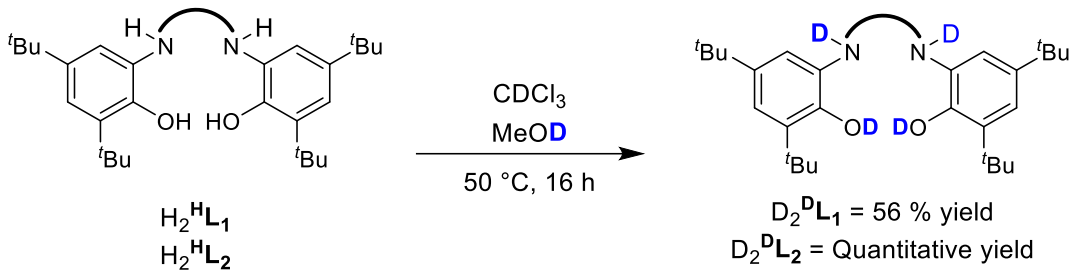


Scheme 5. Keto-enol equilibrium exhibited by 3,5-di-*tert*-butylcatechol (top) allowing for synthesis of pro-ligands $H_2{}^{H}L_1$ and $H_2{}^{H}L_2$ (bottom).

2.2.2 Amine Moiety Modulation

2.2.2.1 Deuteration

The NH moieties on the backbone of the ligand allow for multiple modulations on the pro-ligand. For example, the NH and OH groups can be deuterated by recrystallising the pro-ligands from a mixture of $CDCl_3$ and MeOD that has been stirred under an inert atmosphere at 50 °C overnight, yielding the deuterated pro-ligands $D_2{}^{D}L_1$ and $D_2{}^{D}L_2$ (Scheme 6).



Scheme 6. Deuteration of pro-ligands $H_2^{H}L_1$ and $H_2^{H}L_2$ to form $D_2^{D}L_1$ and $D_2^{D}L_2$

Analysis of the ^{1}H NMR spectrum (DMSO-d$_6$, 298 K) of $H_2^{H}L_1$ and $D_2^{D}L_1$ indicates a disappearance of the NH and OH peaks, suggesting that the deuteration was successful (Figure 6). Furthermore, the IR spectra show a characteristic shift of the vibrations associated with OH and NH stretching. Both peaks shift to lower wavenumbers upon deuteration (~3200 cm^{-1} to ~2380 cm^{-1}; ν_D/ν_H = 0.74; Figure 7) which is consistent with the expected vibrational isotope effect (ν_D/ν_H = 0.73).[100] The formation of the deuterated pro-ligand $D_2^{D}L_2$ from $H_2^{H}L_2$ was also confirmed in that manner (Figures A1 and A2). These pro-ligands were eventually useful in the study of kinetic isotope effects, shedding light on the importance of the NH moieties in ROP catalysis.

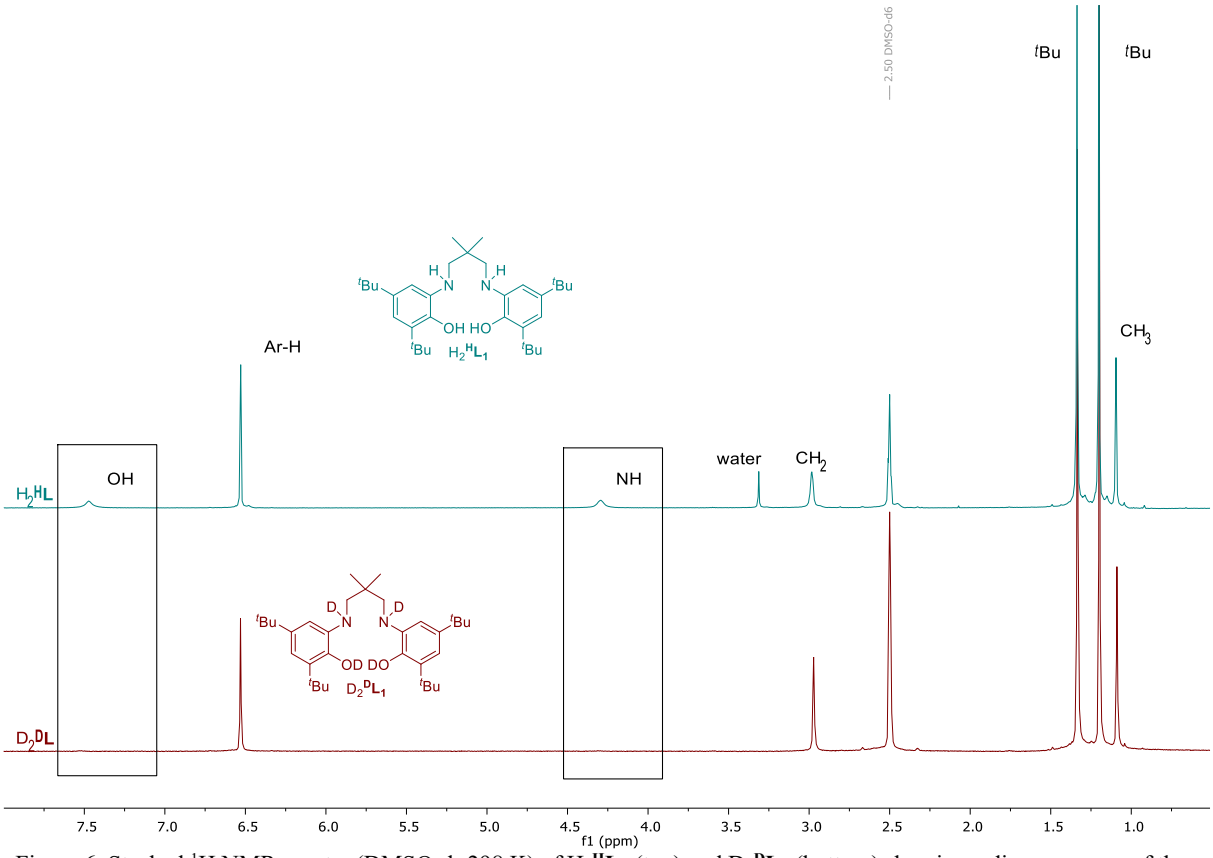


Figure 6. Stacked ^{1}H NMR spectra (DMSO-d$_6$,298 K) of $H_2^{H}L_1$ (top) and $D_2^{D}L_1$ (bottom) showing a disappearance of the OH and NH peaks, corresponding to a successful deuteration.

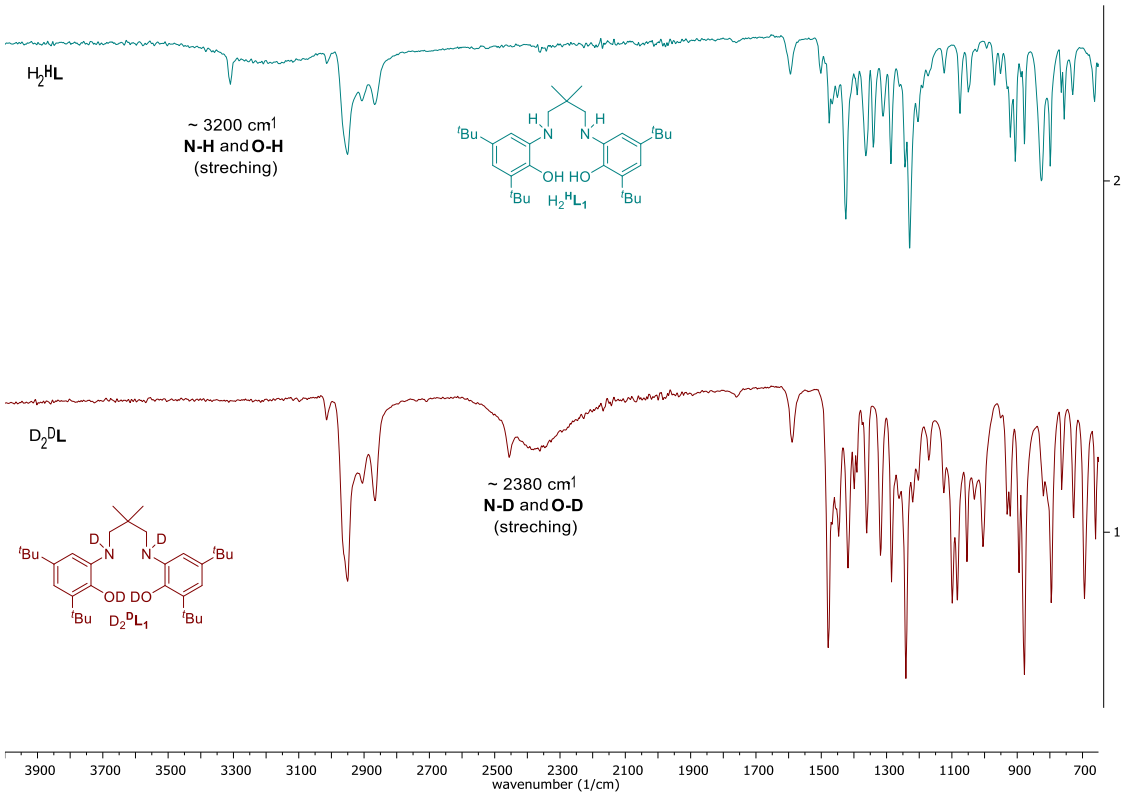
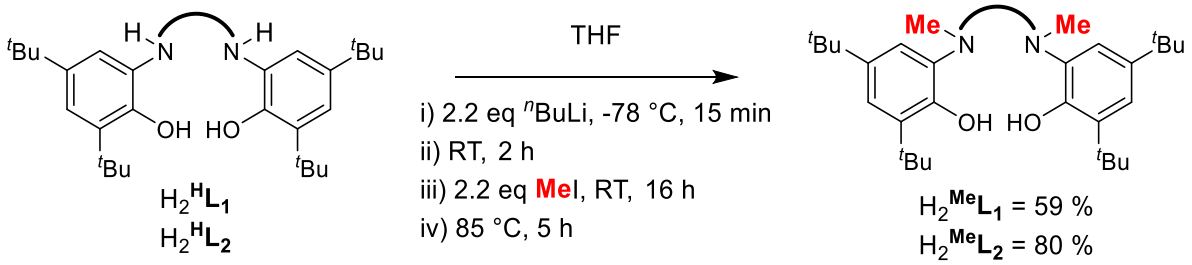


Figure 7. Stacked IR spectra of $H_2^{H}L_1$ (top) and $D_2^{D}L_1$ (bottom) showing a shift of the OH and NH stretching frequencies to lower wavenumbers.

2.2.2.2 *N*-Methylation

Another ligand modulation that was carried out on $H_2^{H}L_1$ and $H_2^{H}L_2$ was the methylation of the NH groups to yield $H_2^{Me}L_1$ and $H_2^{Me}L_2$ respectively (Scheme 7).

The *N*-methylation of $H_2^{H}L_2$ was successfully carried out according to a procedure by Okuda and co-workers.[101] The pro-ligand was first treated with 2.2 equivalents of *n*-butyllithium at low temperatures (-78 °C) followed by the addition of methyl iodide (MeI) which, after purification, afforded the methylated analogue. The synthesis was then adapted for $H_2^{H}L_1$.



Scheme 7. Methylation of pro-ligands $H_2^{H}L_1$ and $H_2^{H}L_2$ to form $H_2^{Me}L_1$ and $H_2^{Me}L_2$

In the case of $H_2^{Me}L_2$, the product was quite easily recrystallised from methanol, yielding the expected product with a ^{1}H NMR spectrum consistent with the literature . However, due to the high solubility of $H_2^{Me}L_1$ in most common solvents (including THF, methanol, acetonitrile, pentane, and diethyl ether), the ligand was purified by column chromatography, ultimately lowering the yield to 59 % compared to a yield of 80 % for $H_2^{Me}L_2$.

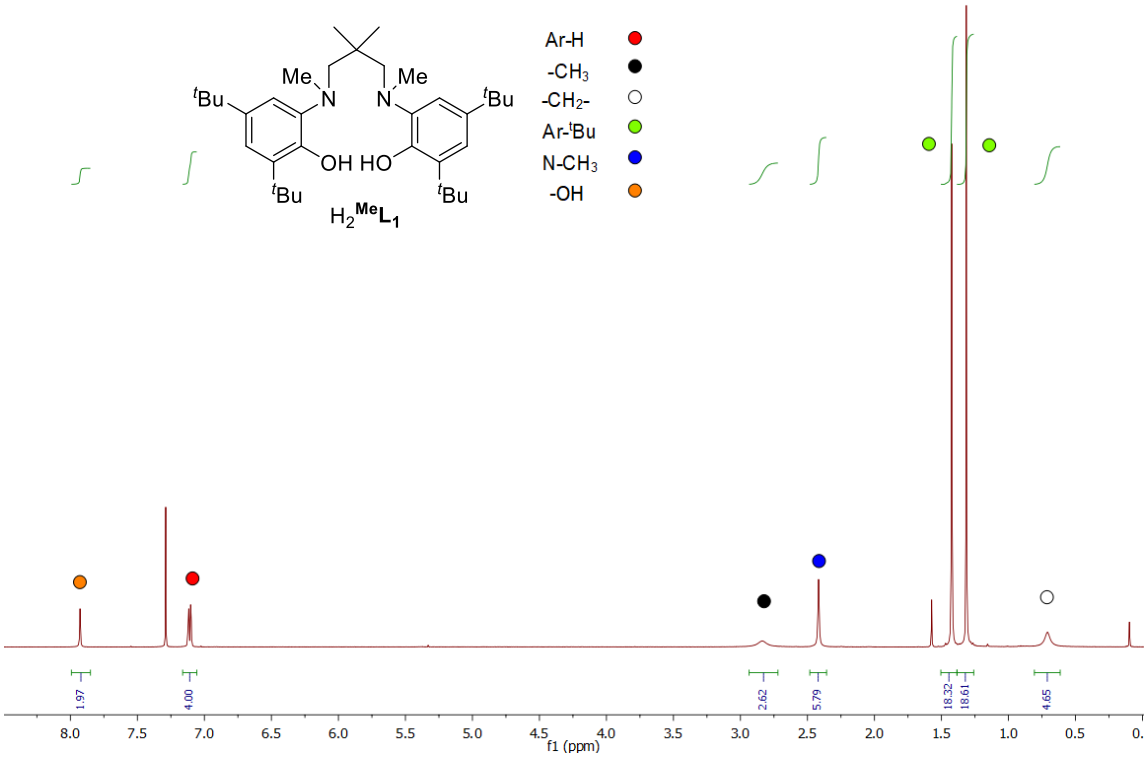


Figure 8. ^{1}H NMR spectrum ($CDCl_3$, 298 K) of pro-ligand $H_2^{Me}L_1$.

The ^{1}H NMR spectrum ($CDCl_3$, 298 K) of $H_2^{Me}L_1$ shows a C_2-symmetric structure in solution (Figure 8). The N-Me groups appear as a singlet at 2.41 ppm while no trace of a NH group can be found. Furthermore, the presence of the OH groups at δ^1_H 7.90 ppm indicate that only the NH moieties were methylated, meaning that the desired product was obtained.

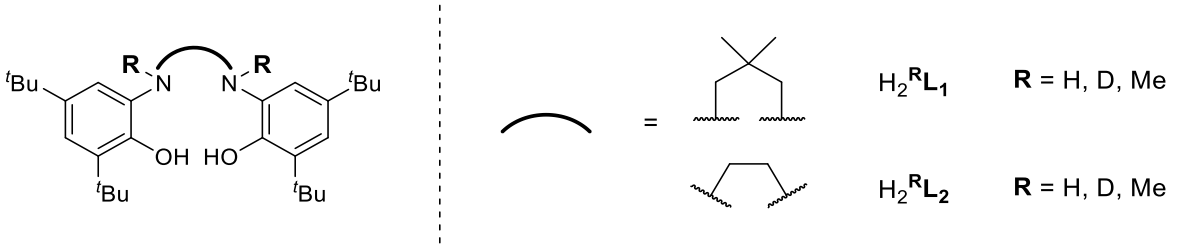


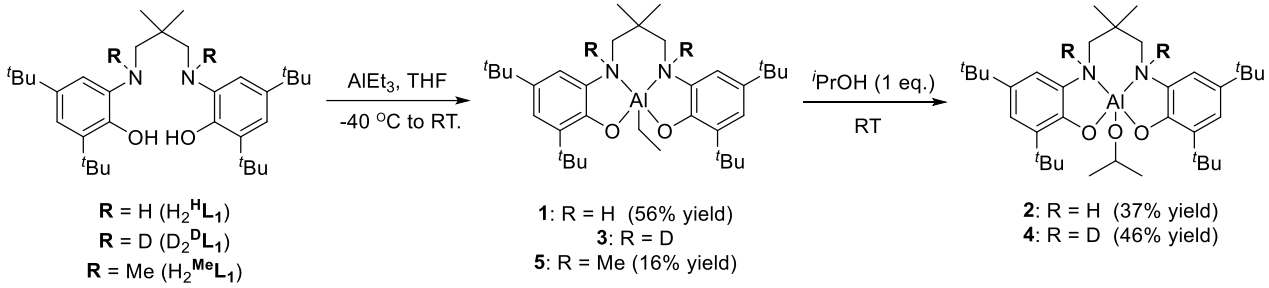
Chart 3. Overview of the synthesised pro-ligands in this chapter

To sum up, the pro-ligands $H_2^{H}L_1$ and $H_2^{H}L_2$, as well as their deuterated and methylated analogues were successfully synthesised (Chart 3). The pro-ligands were characterised using NMR and IR spectroscopic techniques, which allowed the project to proceed with the complexation reactions.

2.3 Complex Synthesis and Characterisation

This section will discuss the Al complexes synthesised from the pro-ligands $H_2^{R}L_1$ (Section 2.3.1) and $H_2^{R}L_2$ (Section 2.3.2). The complexes were successfully characterised using a variety of methods including NMR spectroscopy, IR spectroscopy, and XRD.

2.3.1 Complexes of $H_2^{R}L_1$



Scheme 8. Synthesis of complexes **1**-**5** from pro-ligands $H_2^{H}L_1$, $D_2^{D}L_1$, $H_2^{Me}L_1$

2.3.1.1 Alkyl and Alkoxide Derivatives of $H_2^{H}L_1$

$H_2^{H}L_1$ reacts with 1 equivalent of $Al(Et)_3$ in THF to afford the corresponding aluminium ethyl complex $^{H}L_1Al(Et)$ (**1**) in good yields (56 %) after purification from a mixture of THF and pentane (Scheme 8). The ^1H NMR spectrum (C_6D_6, 298 K) shows a C_s-symmetric structure in solution with characteristically shielded triplet and quartet peaks corresponding to the aluminium ethyl group (δ^1_H 1.19 and −0.05 ppm) (Figure 9).

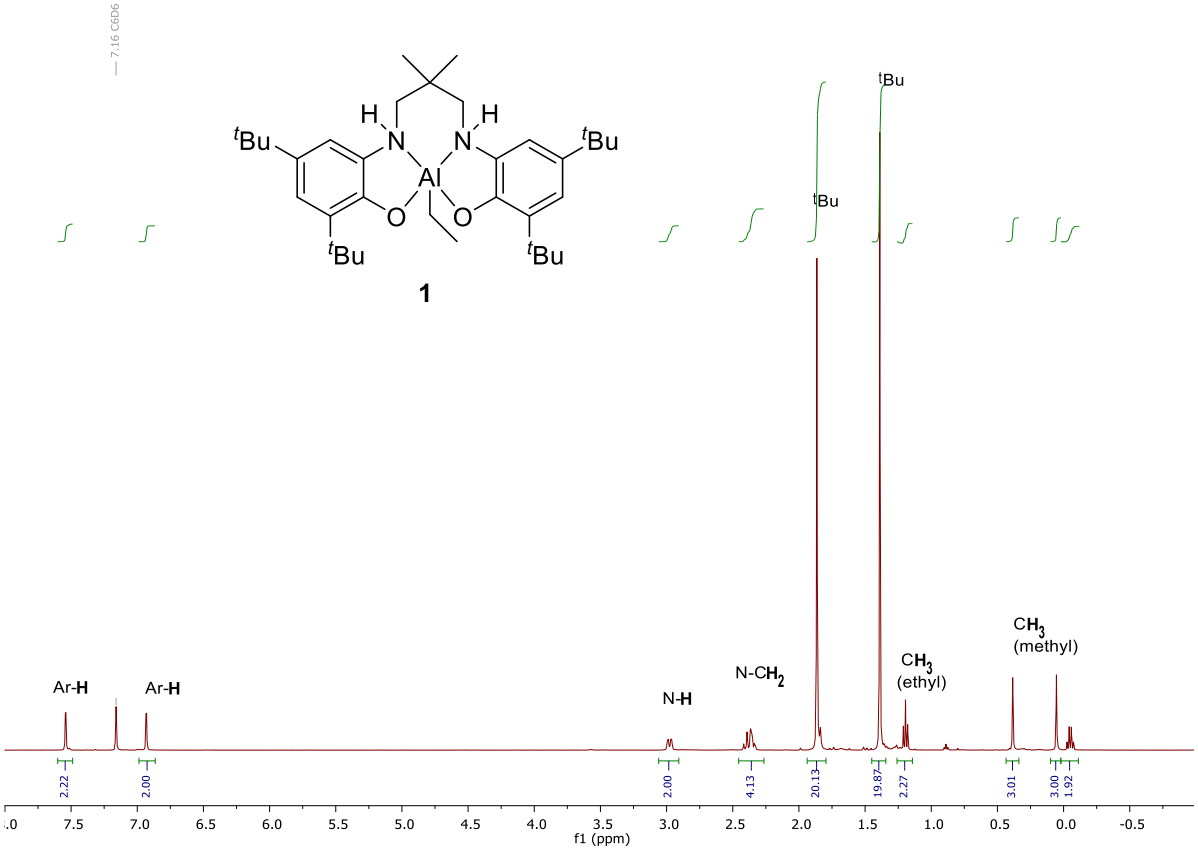


Figure 9. ^{1}H NMR spectrum (C_6D_6, 298 K) of **1** showing the presence of the ethyl chain.

A single crystal of **1** was grown by diffusion of pentane into a concentrated THF solution, and the molecular structure determined by X-ray diffraction (XRD). The molecular structure of **1** (Figure 10) shows a penta-coordinate aluminium complex, exhibiting near-perfect square pyramidal geometry (τ_5 = 0.03) as per the 5-coordinate geometry index proposed by Addison *et al*.[102] The tetradentate catam ligand is coordinated in a planar fashion, with the alkyl chain occupying the apical position. The N_2Al chelate forms a six-membered ring that adopts a chair conformation, with both NH bonds pointing axially in the same direction. Wieghardt and co-workers found a similar arrangement of the ligand around a square-planar Pd(II) metal centre,[99] although the N_2Pd chelate in this case adopts a half-chair conformation. Furthermore, the H-bond donors Wieghardt's complex are spaced apart by 3.077 Å, which is considerably larger than in the case of **1** (2.789 Å) and was attributed to aluminium being a smaller atom and thus forming a "tighter" chelate. Interestingly, the H-bond donor spacing of **1** is similar to that of well-studied squaramide-type organocatalysts (Figure 11).[103] Squaramides were found to be stronger H-bond donors than ureas, attributed to their electron-withdrawing backbone offering an aromatic component to their binding energies.[104, 105] The H-bond donor capabilities of **1** can already be observed in its molecular structure, where two THF molecules are seen forming a

H-bond with the NH groups (H7···O40 = 2.231(4) Å and H11···O50 = 2.181(4) Å). These distances are characteristic of strong H-bonds with a covalent character.[106]

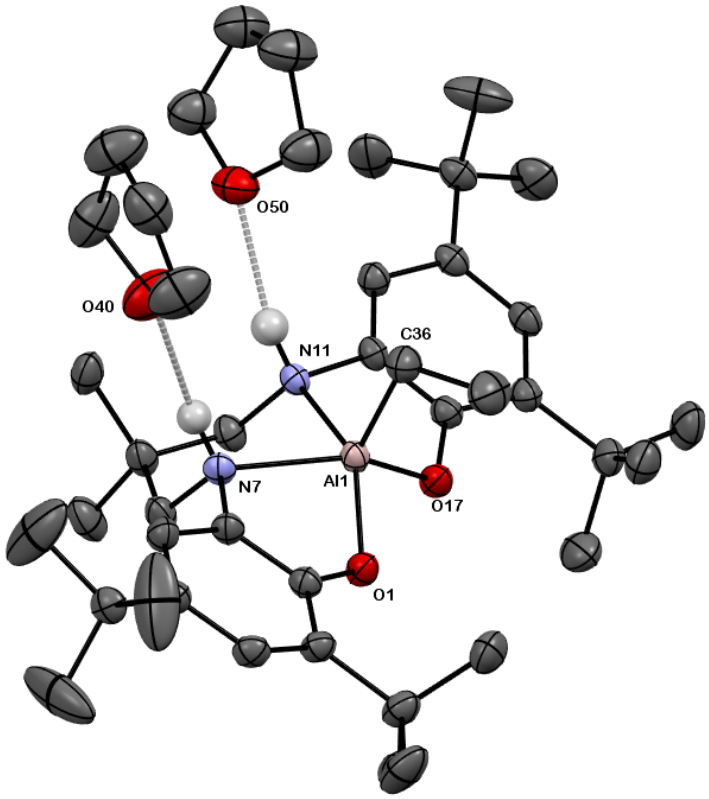


Figure 10. Crystal structure of **1** (ellipsoid plot, 50% probability) showing the N-H···O hydrogen bonds to the included THF solvent molecules.

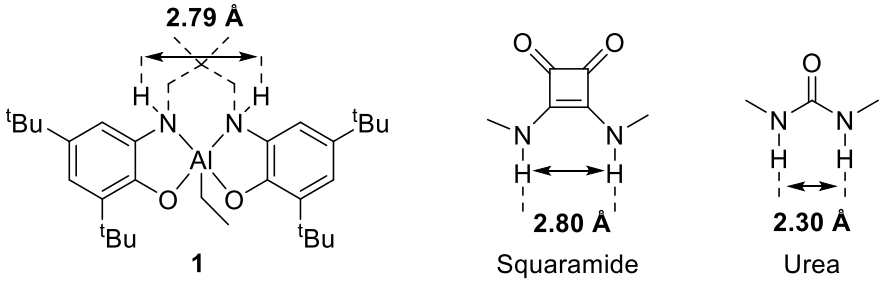


Figure 11. Directionality and distance of H-bond donors of **1** (left), Squaramides (centre), and Ureas (right).

The reactive nature of the Al-Et bond allows for the straightforward reaction of **1** with an alcohol to form the corresponding alkoxide. Thus **1** was found to react cleanly with 1 equivalent of isopropyl alcohol (^{i}PrOH) in THF at room temperature to afford ^{H}**L**$_1$Al(O^{i}Pr) (**2**) at a yield of 37 % (Scheme 9). The ^{1}H NMR spectrum (C_6D_6, 298 K) of **2** initially showed the presence of multiple species, suggesting a slow exchange in solution (Figure A7). This was substantiated

using DOSY NMR analysis (C_6D_6, 298 K) which shows the presence of two species, suggesting a mononuclear-dinuclear equilibrium (Figure A18).

In the presence of coordinating molecules such as THF, the aggregation behaviour of **2** changes. The ^{1}H NMR spectrum in THF-d_8 (298 K) shows a single set of peaks (Figure A8). The DOSY NMR (THF-d_8, 298 K) confirms that the structure is monomeric in solution and suggests the coordination of THF as a contributing factor to the mononuclearity of **2** (Figure A19). Similarly, NMR analysis (C_6D_6, 298 K) was carried out in the presence of 10 equivalents of ^{i}PrOH, meant to mimic immortal polymerisation conditions (Figure A9). The spectrum was clean despite being in the non-coordinating C_6D_6 solvent, suggesting the formation of a species of **2** with coordinated ^{i}PrOH molecules. The DOSY NMR (C_6D_6, 298 K) confirms the formation of a mononuclear complex with possible coordination of ^{i}PrOH (Figure A20).

2.3.1.2 Deuterated Alkyl and Alkoxide Derivatives of D_2**^{D}L$_1$**

The deuterated analogues of **1** and **2** were synthesised from D_2**^{D}L$_1$** using a similar procedure as per above. The NMR spectrum (C_6D_6, 298 K) of the deuterated alkyl complex **^{D}L$_1$**Al(Et) (**3**) shows a disappearance of the NH peak, confirming its formation (Figure A10). The corresponding isopropoxy-analogue **^{D}L$_1$**Al(O^{i}Pr) (**4**) was thus synthesised from the reaction of **3** with one equivalent of ^{i}PrOD. The ^{1}H NMR spectrum (THF-d_8, 298 K) of **4** indicates a disappearance of the NH peaks at δ^1_H 5.02 ppm (Figure 12, bottom). Furthermore, the methylene signals at δ^1_H 2.95 ppm indicate an absence of ^3J coupling with the NH moieties which confirms the formation of **4**.

The IR spectrum shows a characteristic shift of the vibrations associated with NH stretching. The peak of **4** is shifted to lower wavenumbers compared to **2** (~3200 cm^{-1} to ~2390 cm^{-1}; ν_D/ν_H = 0.75; Figure 13) which again is consistent with the expected vibrational isotope effect.

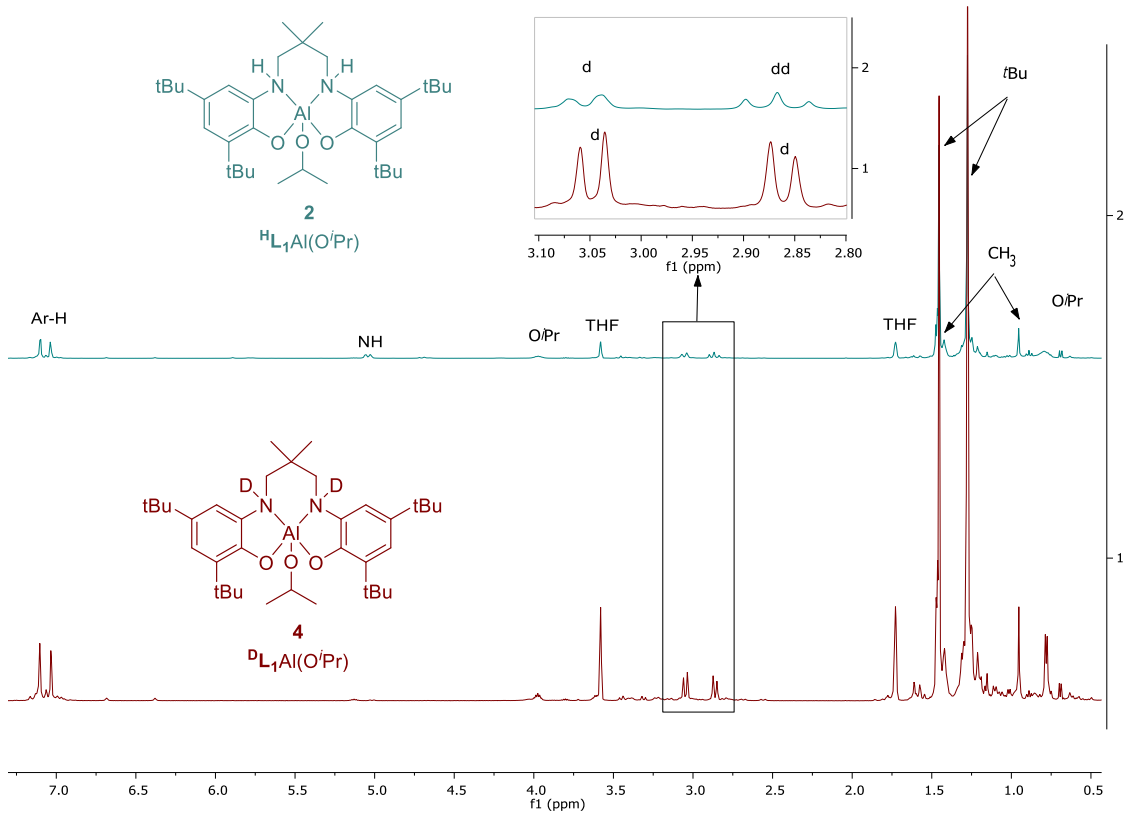


Figure 12: Stacked ^{1}H NMR spectra (THF-d$_8$, 298 K) of ^{H}**L**$_1$Al-(OiPr) (**2**) (top) and ^{D}**L**$_1$Al-(O^{i}Pr) (**4**) (bottom) showing the absence of NH signals and ^{3}J coupling for methylene signals (2.80 - 3.10ppm) in the ^{D}**l**$_1$Al-(O^{i}Pr) (**4**) spectrum.

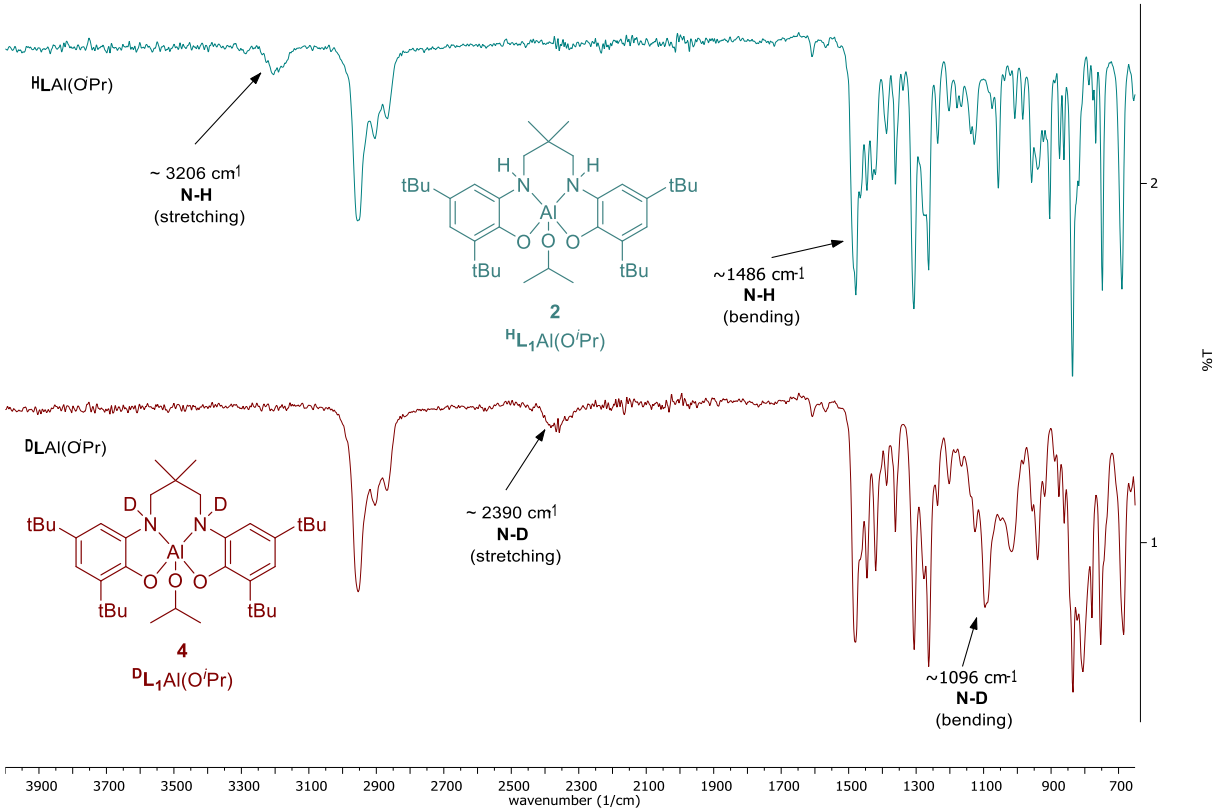


Figure 13: Stacked IR spectra of ^{H}**L**$_1$Al-(O^{i}Pr) (**2**) (top) and ^{D}**L**$_1$Al-(O^{i}Pr) (**4**) (bottom) showing a characteristic shift of the vibrations assigned to the amine.

2.3.1.3 *N*-Methylated Alkyl Derivative of H_2**^{Me}L$_1$**

To further study the importance of the NH group, the *N*-methylated complex **^{Me}L$_1$**Al(Et) (**5**) was synthesised by reacting H_2**^{Me}L$_1$** with one equivalent of $Al(Et)_3$ in THF. The ^{1}H NMR spectrum (C_6D_6, 298 K) shows **5** to be C_2-symmetric in solution showing a singlet at δ^1_H 2.58 ppm corresponding to the N-Me groups (Figure A11). An interesting aspect of the spectrum is the peak corresponding to the CH_2 group of the ethyl chain (δ^1_H 0.65 ppm) which splits into what appears to be a doublet of quartets; likely due to a restricted rotation of the ethyl chain resulting in the *gem*-protons being magnetically inequivalent. Each CH_2 proton couples once with the geminal proton (^2J = 23.2 Hz) and thrice with the CH_3 protons (^3J = 8.0 Hz). Although the NMR suggested the complex to be free of [1], the sample repeatedly failed to pass elemental analysis. This was attributed to the presence of inorganic salts (*e.g.* lithium iodide) that were carried over from the ligand synthesis which were eventually removed by dissolving **5** in a minimal amount of pentane and passing the solution through a 0.2 µm syringe filter.

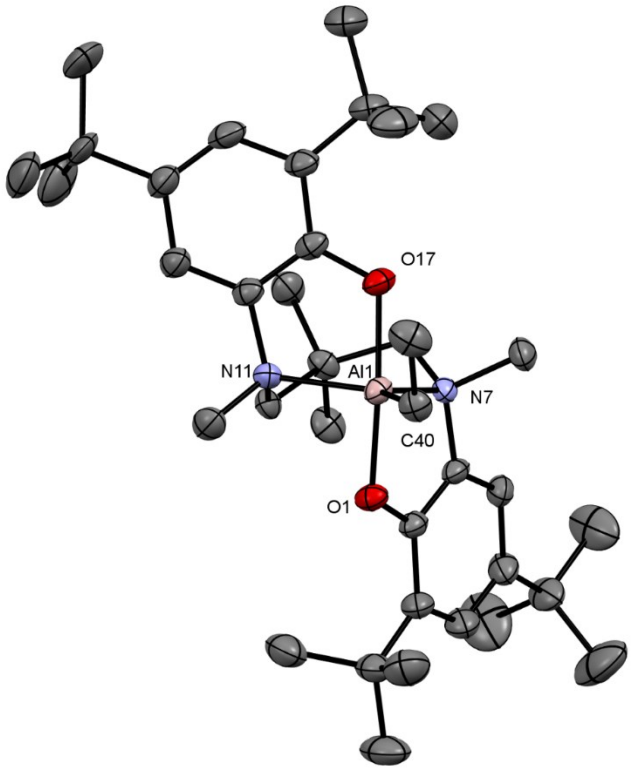
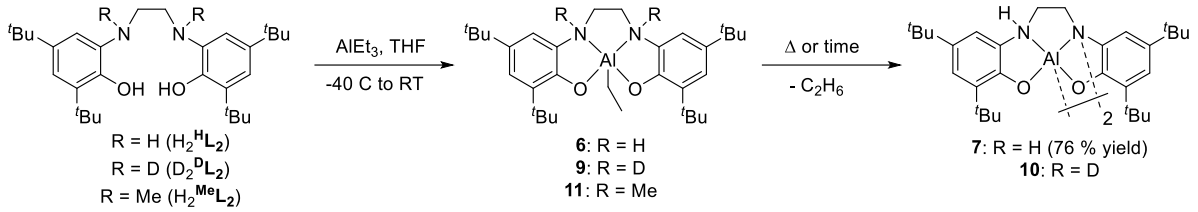


Figure 14. Crystal structure of **5** (ellipsoid plot, 50% probability).

A single crystal of **5** was obtained from a cold mixture of THF/pentane (-40 °C). The molecular structure of **5** differs considerably from that of **1** (Figure 14). The complex exhibits a distorted trigonal bipyramidal geometry (τ_5 = 0.63) with a *cis*-α wrapping around the penta-coordinate

aluminium metal centre.[107] Instead of a planar conformation of the ligand, the N atoms occupy the equatorial position while the phenolate moieties are orientated *trans* to one another (O-Al-O = 169.2(11)°). The N_2Al six-membered chelate adopts a distorted twisted boat conformation, with both *N*-methyl groups at the equatorial position, pointing away from each other which is in stark contrast to the molecular structure of **1** (Figure 10).

2.3.2 Complexes of $H_2^{R}L_2$



Scheme 9. Synthesis of complexes **6**-**11** from pro-ligands $H_2^{H}L_2$, $D_2^{D}L_2$, $H_2^{Me}L_2$.

2.3.2.1 Alkyl and Alkoxide Derivatives of $H_2^{H}L_2$

As previously observed with $H_2^{H}L_1$, the pro-ligand $H_2^{H}L_2$ was found to react cleanly with $Al(Et)_3$ in THF to yield the alkyl aluminium complex $^{H}L_2Al(Et)$ (**6**) (Scheme 10). The ^1H NMR spectrum (C_6D_6, 298 K) of the crude product shows **6** to be C_i-symmetric in solution with two peaks in the aromatic region (δ^1_H 7.42 and 6.62 ppm), two *tert*-butyl peaks at δ^1_H 1.71 and 1.46 ppm, and one peak corresponding to the NH (δ^1_H 2.36 ppm) (Figure 15, top). Furthermore, the characteristically shielded triplet and quartet peaks corresponding to the aluminium ethyl group (δ^1_H 1.51 and 0.24 ppm) confirm the formation of **6**.

The purification of the complex was attempted using cold pentane only, since the crude product was soluble in all common solvents. This resulted in the precipitation of a new aluminium complex as determined by NMR spectroscopy. The ^1H NMR spectrum (C_6D_6, 298 K) shows the formation of a different compound, with a C_i-symmetric structure in solution and thus essentially a doubling of the number of peaks (Figure 15, bottom). This includes four signals in the aromatic region, as well as four signals corresponding to the *tert*-butyl groups. The fact that the ethyl chain was no longer present, and that the NH signal integrated to one proton (instead of two), suggest that the new compound was formed from the deprotonation of a NH group by the ethyl chain. Every subsequent purification attempt *via* different techniques (such

as recrystallisation or precipitation in cold solvent) of **6** led to the formation of the deprotonated complex ^{H}**L**$_2$Al (**7**).

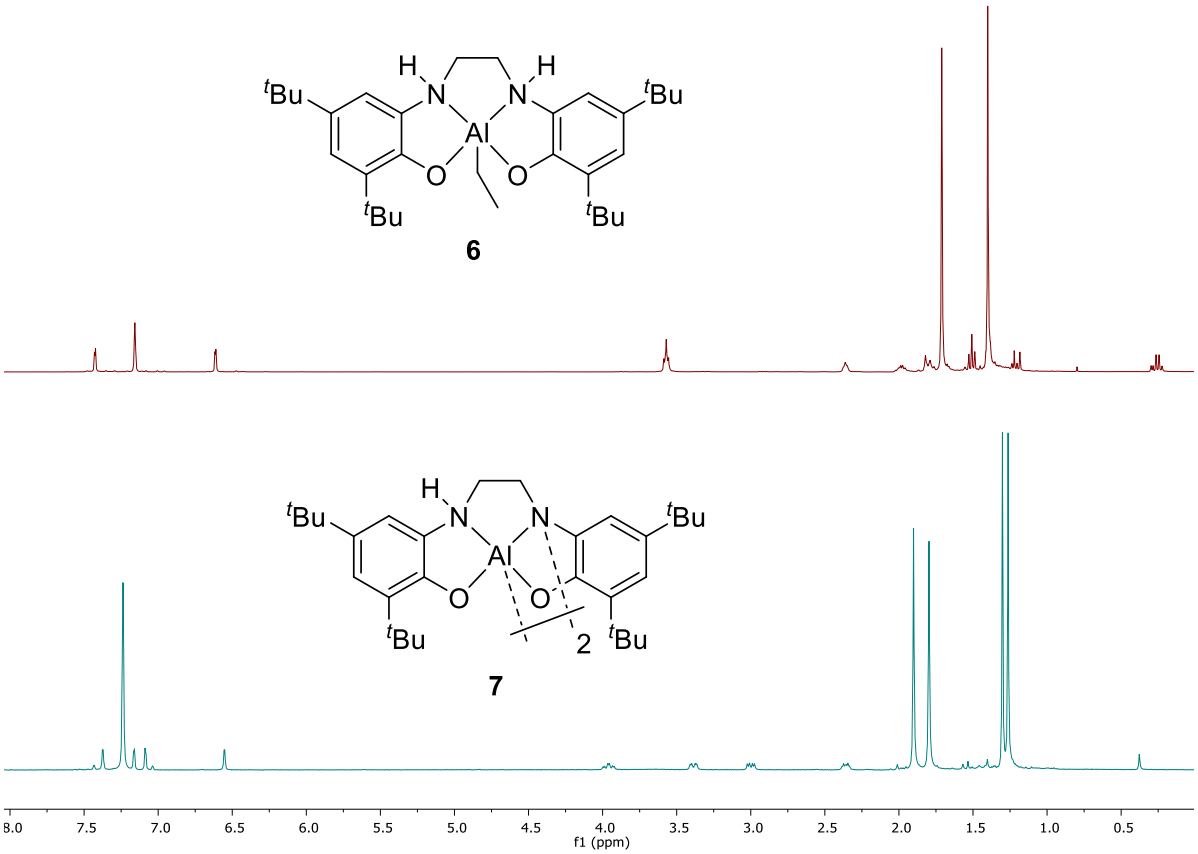


Figure 15. Stacked ^{1}H NMR spectra (C_6D_6, 298 K) of **6** (top) and **7** (bottom) showing a disappearance of the ethyl chain and a doubling of signals upon deprotonation.

NMR studies performed in the group by Stanley Ng have shown the deprotonation of complex **6** to be significantly slower in THF-d_8, which was attributed to the coordination of the solvent molecules to the NH groups. As was seen in the crystal structure of **1** (Figure 10), the NH moieties likely form H-bonds with the THF, preventing their deprotonation by the ethyl chain. However, the addition of a non-coordinating solvent into the mixture may decrease the favourability of such interactions, leading to the formation of complex **7**. The volatility of ethane, as well as the general insolubility of **7**, provide the thermodynamic driving force that allows this reaction to proceed.

A single crystal of **7** was grown from a THF/pentane mixture of **6**, and the molecular structure determined using XRD (Figure 16). The complex is a centrosymmetric dimer, consisting of two units of complex **7**. The two aluminium centres are connected to each other through the deprotonated N atoms, forming an Al_2N_2 quadrangle containing a centre of inversion in the

middle. The aluminium centres are both pentacoordinate, exhibiting a near perfect square pyramidal geometry ($\tau_5 = 0.05$) as was seen with complex **1**. The tetradentate O'N'N'O-ligand itself is coordinated in a planar fashion, which forms the base of the pyramid with the bridging N atom sitting at the apical position. The ethyl chain is not present which is in line with the NMR spectrum.

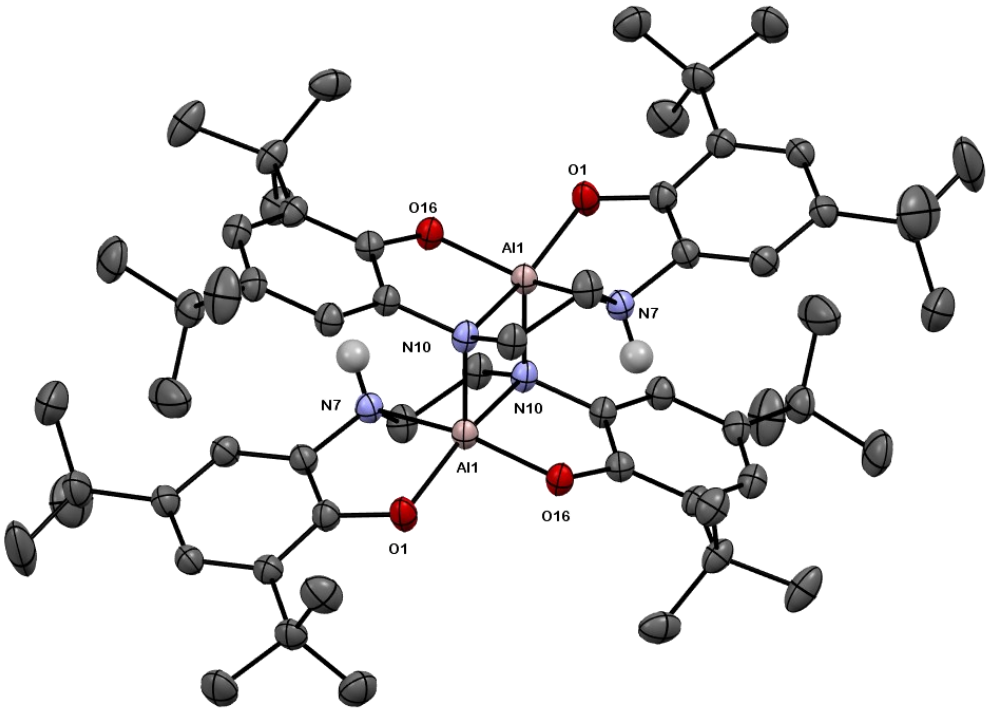
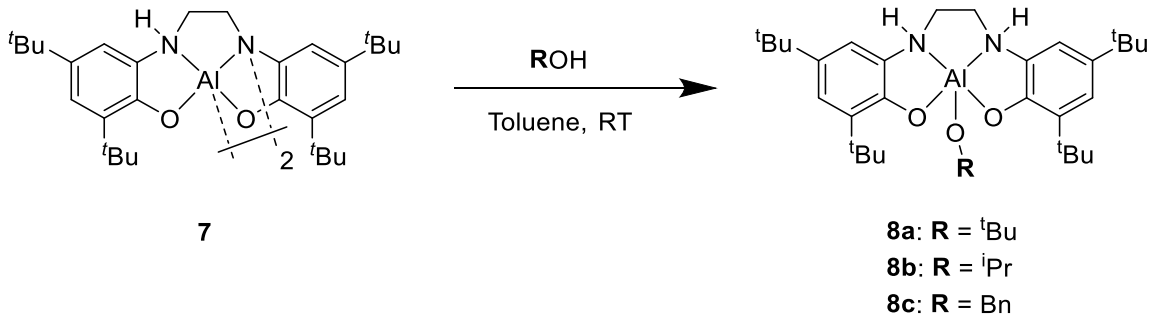


Figure 16. Crystal structure of **7** (ellipsoid plot, 50% probability).

Just like the addition of ^{i}PrOH to **1** form the isopropoxy-complex **2**, an alcohol can be added to **7** to form the corresponding alkoxide complex. This was tested with a primary [benzyl alcohol (BnOH)], secondary (^{i}PrOH), and a tertiary alcohol [*tert*-butanol (^{t}BuOH)] (Scheme 10). The ^{1}H NMR spectra (C_6D_6, 298 K) show that the addition of 2 equivalents (1 equivalent per metal centre) of BnOH or ^{t}BuOH leads to the formation of a new well-defined compound. This was characterised mainly by a change of the chemical shifts of the complex, the appearance of the new alkoxy group on the spectrum, as well as the NH peaks integrating to a total of 2 protons.

In the case of **7** + ^{t}BuOH, the NMR spectrum (C_6D_6, 298 K) shows the formation of a new complex (**8a**). The compound exhibits a C_i-symmetric structure in solution, with 2 peaks each corresponding to the aromatic protons and the ^{t}Bu groups. A broader peak is present (δ^{1}_{H} 1.65

ppm) which can be attributed to the new *tert*-butoxy group formed (Figure 17). Although easily formed, the new complex was difficult to purify, which led to inconsistent EA results. Furthermore, the high solubility of the complex made growing a single crystal for XRD analysis impractical.



Scheme 10. Synthesis of alkoxide complexes **8a** (R = ^{t}Bu), **8b** (R = ^{i}Pr), and **8c** (R = Bn) from complex **7** by addition of one equivalent of the corresponding alcohol.

The addition of ^{i}PrOH to **7** led to the formation of a mixture of products as seen on the NMR spectrum (C_6D_6, 298 K). Even after purification using a mixture of THF/pentane, the spectrum remains largely unchanged (Figure 17). This can be due to a slow monomer-dimer exchange of the complex and/or the adoption of different conformations in solution as previously observed for **2**. Heating of the mixture at 60 and 80 °C was attempted to force the formation of a single species and thus resolution of the NMR spectrum. The resulting spectra showed minimal change in the composition of the product. Furthermore, numerous attempts of growing a single crystal for XRD turned out fruitless. However, EA indicated the formation of the desired complex (**8b**).

The effect of a primary alcohol was finally explored by synthesising **8c** through the addition of BnOH to **7**. The ^{1}H NMR spectrum of the crude indicated that a new product was formed as new peaks appeared in the aromatic region which were eventually attributed to the aromatic protons of the benzyloxy moiety (Figure 17). Furthermore, two peaks characteristic of the benzyl protons can be seen at δ^1_H 4.55 and 4.83 ppm (Figure A16). It was found that **8c** was soluble in THF but easily purified using pentane, which made the synthesis and purification of this complex feasible (79 % yield). A single crystal of **8c** was obtained from a concentrated C_6D_6 solution and analysed by XRD. The molecular structure shows a centrosymmetric dinuclear structure containing two Al metal centres connected by the bridging μ-O atoms of the two benzyloxy co-ligands (Figure 18). The centre of inversion sits in the middle of the

Al_2O_2 quadrangle. Each Al atom is hexacoordinate, exhibiting a distorted octahedral geometry. The wrapping of the ligand around the metal centre is conducive to a *cis*-β conformation as three atoms (O, N, and N atoms) occupy the equatorial position while one O atom can be found at the apical position. Both benzyloxy moieties occupy an equatorial and axial position around the metal centre.

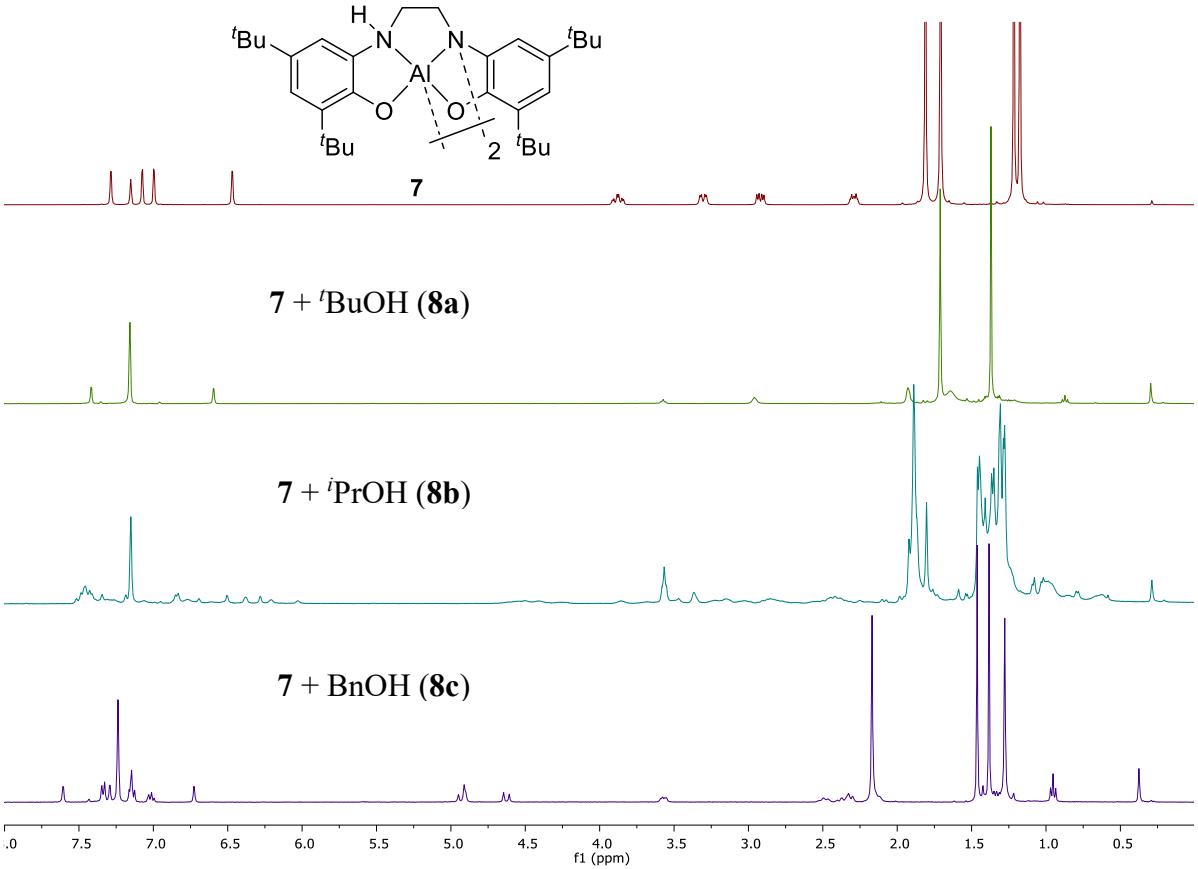


Figure 17. Stacked ^{1}H NMR spectra (C_6D_6, 298 K) of complexes **8a**, **8b**, and **8c** compared to complex **7** showing a reaction between the deprotonated complex and different alcohols.

The dimeric nature of **8c** was an interesting property. Particularly since the octahedral geometry of the metal centre saturates the coordination sphere and thus would hinder the catalysis of ROP reactions. Through DOSY NMR it was sought to determine whether **8c** is only dimeric in the solid state or if the aggregation is also maintained in solution. The DOSY NMR run in C_6D_6 (298 K) in fact shows the complex to be dimeric in solution which can be attributed to the stability gained by the formation of the dimer (Figure A21). However, in a coordinating solvent such as THF-d_8, the DOSY shows the complex to be monomeric in solution (Figure A22). The coordination of the THF onto the metal centre or the NH moieties may stabilise the monomeric species and thus help the breakdown of the dimer. Because of ease of synthesis and

straightforward purification of **8c**, as well as its monomeric nature in a coordinating solvent, the complex was chosen as the main initiator for the H_2**^{R}L$_2$** series.

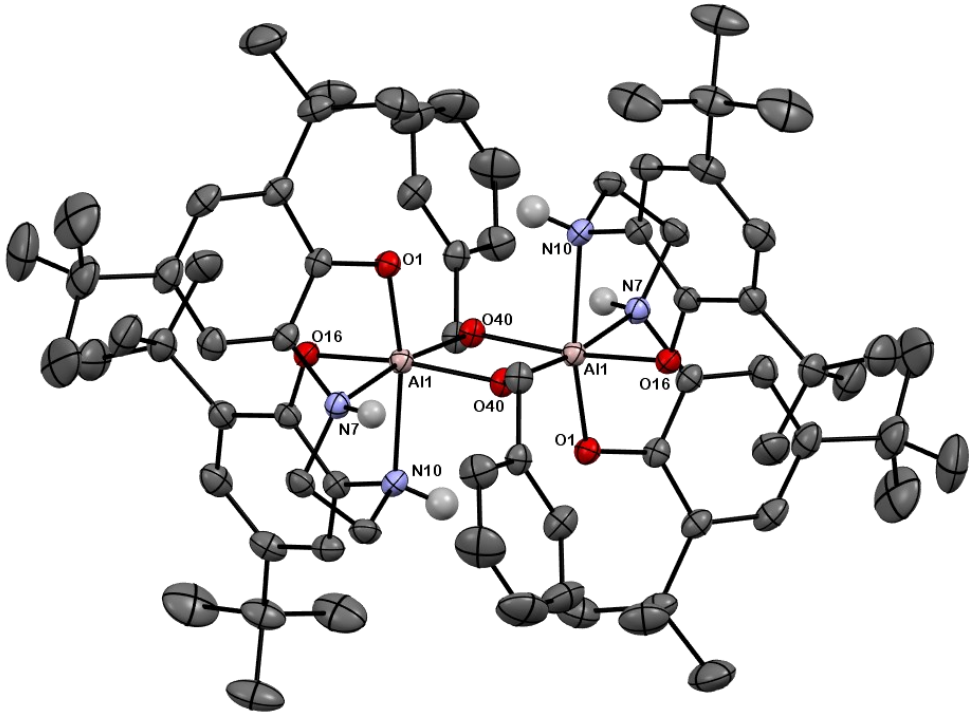


Figure 18. Crystal structure of **8c** (ellipsoid plot, 50% probability)

2.3.2.2 Deuterated Alkyl and Deprotonated Derivatives of H_2**^{D}L$_2$**

The deuterated analogues of **6** and **7** were synthesised from D_2**^{D}L$_2$** using similar procedures as above. The ^{1}H NMR spectrum (C_6D_6, 298 K) of the deuterated alkyl complex **^{D}L$_2$**Al(Et) (**9**) shows a disappearance of the NH peak, confirming its formation (Figure A17). It was thought that the deprotonation of **9** might be problematic due to the increased strength of the N-D bond. However, stirring **9** in pentane overnight yielded pure **^{D}L$_2$**Al (**10**) after purification. The difference between the N-H and N-D bond strength is thus not large enough to overcome the formation of the thermodynamically favourable dimer. Given that the benzyloxy analogue **8c** was found to be an easily synthesised and well-defined complex, the synthesis of its deuterated analogue from **10** was sought. However, sourcing deuterated benzyl alcohol (BnOD) proved difficult and instead the generation of the active species *in-situ* was sought through the addition of ^{i}PrOD to **10** prior to polymerisation.

2.3.2.3 *N*-Methylated Alkyl Derivatives of H_2**^{Me}L$_2$**

The *N*-methylated analogue of **6** was synthesised by reacting H_2**^{Me}L$_2$** with one equivalent of Al(Et)$_3$ in toluene. Recrystallisation from pentane afforded clean **^{Me}L$_2$**Al(Et) (**11**). The ^{1}H NMR

spectrum (Figure 19, C_6D_6, 298 K) showed the complex to be C_2-symmetric in solution with two peaks in the aromatic region (δ^1_H 7.55 and 7.05 ppm), a single peak corresponding to the N-Me groups (δ^1_H 2.76), as well as a shielded multiplet corresponding to the CH_2 group of Al-Et (δ^1_H -0.15).

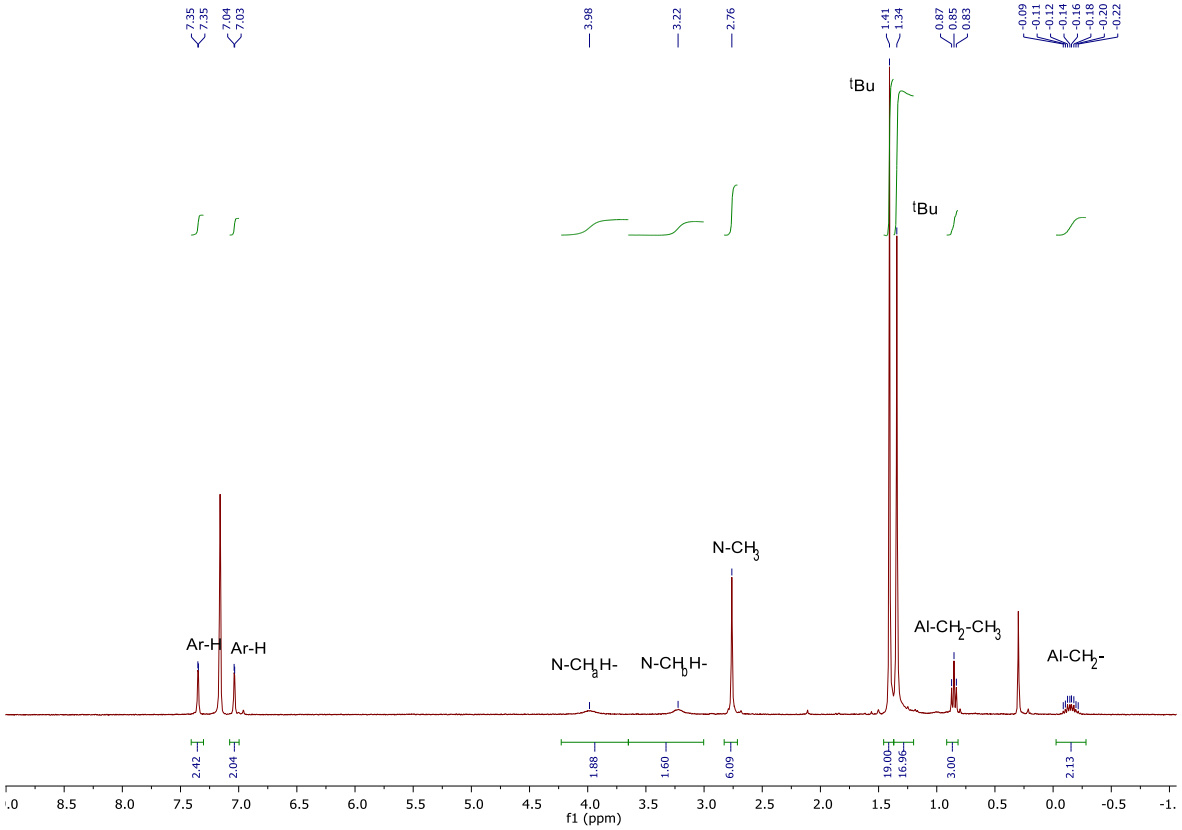


Figure 19. ^{1}H NMR spectrum (C_6D_6, 298 K) of complex **11** showing the ethyl chain as well as broad peaks corresponding to the tether, indicating a slow exchange

A single crystal of **11** was grown from a concentrated C_6D_6 solution and analysed through XRD (Figure 20). The molecular structure of **11** shows the complex to be dinuclear, containing two aluminium metal centres. Due to the absence of an alkoxide co-ligand, the complex was found to bridge *via* the oxygen atom of the *o*-aminophenolate moiety, resulting in each ligand bearing both metal centres. This is in contrast to the benzyloxy-bridged dimeric structure of **8c** and the mononuclear structure of **5**. Each aluminium centre is pentacoordinate, exhibiting a near-perfect square pyramidal geometry on one centre (τ_5 = 0.03) and moderately square-pyramidal geometry on the other (τ_5 = 0.24). In each case, both catam ligands are coordinated in a *trans*-planar fashion, with the ethyl chain sitting at the apical position. What was interesting is the lack of symmetry within the molecule which is not in line with the C_2-symmetric structure

exhibited in the NMR spectrum. Particularly the large difference between the τ_5 value for each metal centre indicates that the geometry the complex adopts in solution is vastly different.

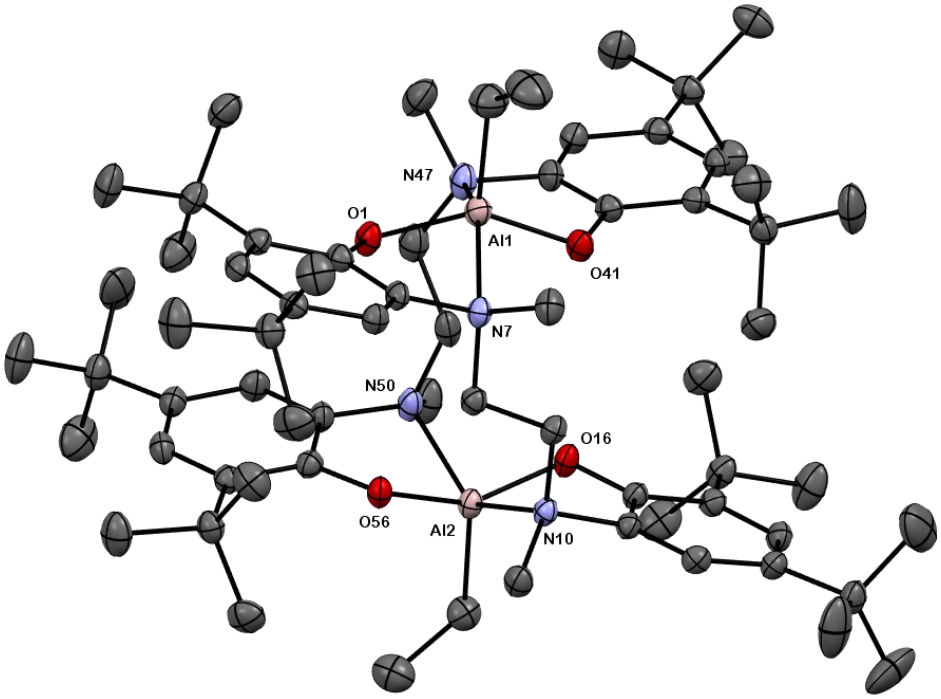


Figure 20. Crystal structure of **11** (ellipsoid plot, 50% probability)

DOSY NMR analysis run in C_6D_6 (298 K) shows that the **11** remains dimeric in solution (Figure A23). Interestingly, carrying out a DOSY in THF-d_8 (298 K) shows the complex adopting a monomeric structure, which was attributed to the coordinating solvent favouring the formation of the mononuclear species *via* coordination to the Lewis acidic metal centre (Figure A24).

To examine whether the presence of a coordinating solvent changes the solid-state geometry of **11**, a single crystal was grown by evaporation from a concentrated THF solution. However, preliminary XRD experiments show the unit cell of the crystal to be the same as in the previous case.

2.4 Polymerisation Results and Discussion

This section discusses the employment of the $^{R}L_1$ and $^{R}L_2$ complexes in ROP with a strong focus on *rac*-LA polymerisation. The mechanism was studied carefully using computational and experimental methods to elucidate the underlying processes. Other monomers were eventually tested in order to establish a substrate scope.

2.4.1 Polymerisation of *rac*-LA

2.4.1.1 Room-Temperature Polymerisations

The $^{H}L_1$ isopropoxide complex, **2**, was found to be active for the ROP of *rac*-LA at room temperature in THF (Table 1, Entry 3). At a catalyst loading of 1 mol%, **2** polymerised 91 % of the starting material in 90 minutes with the PLA being highly heterotactic ($P_r = 0.91$). The polymerisation itself is conducive to a living polymerisation:

1. The molar mass of the polymer increases linearly with conversion (Figure B6).
2. The polymerisation is well-controlled, leading to a low dispersity (Đ).
3. The rate law is pseudo first order in monomer with a $k_{app} = (4.75 \pm 0.29) \times 10^{-4}$ s^{-1} (Figure B5).

A MALDI-ToF mass spectrum of the polymer was obtained and exhibits metal ion peaks ($M + K^+$) that are equally spaced by 144 a.u. and with exact masses consistent with linear PLA with the presence of an isopropoxide group on the ester end (Figure D1). This is in line with the coordination-insertion mechanism outlined in Section 1.3.2. A particularly interesting feature is the complete lack of transesterification reactions, which can be attributed to the polymerisation being run at low temperatures and thus exhibiting more control. Furthermore, the lack of peaks conducive to cyclic polymers indicates that back-biting reactions do not take place during polymerisation. This contributes to the particularly low Đ of the polymer (1.3).

The active species **2**, can also be generated *in-situ* by the addition of one equivalent of ^{i}PrOH to the alkyl complex **1** prior to the addition of *rac*-LA (Table 1, Entry 1), with very similar activities. Furthermore, the P_r and Đ of the polymer are virtually unchanged which indicates that the conversion of **1** to **2** occurs rather quickly and cleanly, with minimal formation of unwanted by-products.

The analogous salen and salan complexes of **2**, which feature the same 2,2-dimethyl-1,3-propanediamine backbone, were previously synthesised in the group and shown to be lower in activity despite being employed at elevated temperatures (Table 1, Entries 8 and 9).

The $^{H}L_2$ complexes were found to be particularly active too. The crude alkyl complex **6** was tested by generating the active species *in-situ* through the addition of 1 equivalent of BnOH (Table 1, Entry 4). The complex showed remarkable activity at room-temperature (k_{app} = 3.48 × 10^{-4} s^{-1}, Figure B7) , converting 84 % over the course of 90 minutes and affording PLA with an isotactic bias (P_m = 0.62).

Table 1. *rac*-LA polymerisations at room temperature using $^{H}L_1$ complexes **1** and **2** as well as $^{H}L_2$ complexes **6**, **7**, and **8c**. Polymerisations using their salan and salen analogues are included for comparison.

Entry	Cat.	ROH	Cat./ROH/ LA (equiv.)	Solvent	T (°C)	Time (min)	Conv.[a] (%)	$M_{n(SEC)}$(Đ)[b] (kg/mol)	P_r[c]	$M_{n(calc.)}$[d] (kg/mol)
1	**1**	^{i}PrOH	1/1/100	THF	25	90	92.5	10.8 (1.3)	0.90	13.3
2[e]	**1**	^{i}PrOH	1/1/100	THF	25	15 + 120	85.3	7.3 (1.2)	0.89	12.3
3	**2**	-	1/0/100	THF	25	90	91.4	9.5 (1.3)	0.91	13.2
4	**6**	BnOH	1/1/100	THF	25	90	84	10.8 (1.2)	0.62	12.2
5[f]	**6**	BnOH	1/1/100	THF	25	15 + 90	72	6.6 (1.2)	0.59	10.3
6	**7**	BnOH	1/1/100	THF	25	90	80	8.7 (1.1)	0.62	10.2
7	**8c**	-	1/0/100	THF	25	90	96	14.3 (1.2)	0.60	13.8
8	**1-^{H}salan**[g]	^{i}PrOH	1/1/100	Toluene	90	960	46.1	5.7 (1.3)	0.54	6.6
9[108]	**1-salen**[h]	-	1/0/100	Toluene	70	300	94	21.2 (1.1)[j]	0.08	-
11[109]	**6-salen**[i]	BnOH	1/1/100	Toluene	70	4320	19	5.3[j] (1.1)	0.79	2.7
12[83]	**6-salan**[i]	BnOH	1/1/100	Toluene	70	7200	77	11.3[j] (1.1)	0.39	10.1

Reaction conditions: $[LA]_0$ = 1 $mol.L^{-1}$; a) Determined by ^{1}H NMR by relative integration of signals at 5.06 ppm (monomer) and 5.20 ppm (polymer); b) Determined by SEC calibrated with polystyrene standards in THF and corrected (see ESI); c) Probability of racemic linkages determined by ^{1}H NMR spectroscopy (see ESI); d) Calculated using the conversion; e) **1** was generated *in-situ* by stirring $AlEt_3$ and $H_2{}^{H}L_1$ in THF for 15 minutes prior to addition of LA and ^{i}PrOH (see ESI); f) **6** was generated *in-situ* by stirring $AlEt_3$ and $H_2{}^{H}L_2$ in THF for 15 minutes prior to addition of LA and BnOH (see ESI); g) salan derivative of **1** (see ESI); h) salen derivative of **1** with BnO instead of OiPr,[110] i) examples of salen and salan Al complexes, analogous to **6**; j) as per reference, not corrected.

The deprotonated complex **7** was tested by adding an equivalent to BnOH prior to polymerisation, which proceeded with similar activities and selectivities (Table 1, Entry 6). This shows that the active species can be generated quickly from the deprotonated complex **7** without significant losses in activity (k_{app} = 2.41 × 10^{-4} s^{-1}; Figure B10). However, comparing Entries 4 and 6 in Table 1, the fastest initiator was the alkyl complex **6**, which can be attributed to the high reactivity of the Al-C bond resulting in fast generation of the active species upon addition of an alcohol.

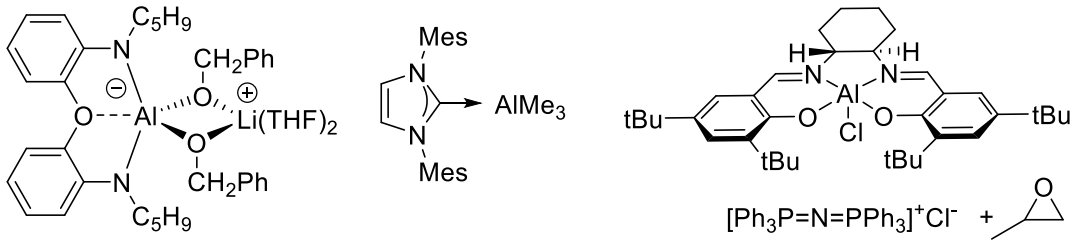
The dimeric benzyloxy complex **8c** was tested as a triplicate in THF and found to convert an average of 96 % of starting material over 90 minutes (Table 1, Entry 7), showing that the complex is active in THF despite its dinuclear solid state structure (Figure 18). The k_{app} was found to be (5.47 ± 0.22) × 10^{-4} s^{-1} (Figure B12), which is slightly higher than that of **2** (*c.f.* 4.75 × 10^{-4} s^{-1}). Polymerisations with **6-8c** all proceeded in a living fashion with the molar mass

of the polymers increasing linearly with monomer conversions while maintaining low dispersities (Figures B7-B13). MALDI-ToF analysis of the polymer from Entry 7 shows metal ion peaks ($M + K^+$) that are equally spaced by 144 a.u. and with exact masses consistent with linear PLA capped with a benzyloxy group on the ester end (Figure D2). Neither transesterification nor cyclisation has taken place, indicating that the polymerisation is rather controlled, and contributing to the low Đ of the polymers (~1.2). **8c** also outperformed its salen and salan analogues, which required a reaction temperature of 70 °C and several hours to proceed with the polymerisation (Table 1, Entries 11 and 12).

It was investigated whether the active species **2** and **8c** can be generated *in-situ* starting from their respective precursors. This was carried out by stirring the pro-ligands H_2**L1** or H_2**L2** with one equivalent of $Al(Et)_3$ for 15 minutes, prior to the addition of *rac*-LA and either ^{i}PrOH or BnOH (Table 1, Entries 2 and 5). Although this led to a noticeable decrease in activity for the *in-situ* generated **2** (85 % conversion over 120 minutes), the heteroselectivity of the species was still high ($P_r = 0.89$) while dispersity of the polymer remained low (Đ = 1.2). However, in the case of the *in-situ* generated **8c**, the polymerisation still proceeded, although with lower activities and a slight loss in isoselectivity (Table 1, Entry 5). Comparing the k_{app} of Entries 5 and 7, there was a 30% decrease in activity ($k_{app} = 3.48$ *vs.* 2.36×10^{-4} s^{-1}; Figures B2 and B8) which was attributed to incomplete generation of the active species.

These results are rather promising as the *in*-situ generation of the catalyst may ease the use and translation of the catalyst to industrial application. The fact that both active species **2** and **8c** can be generated in minutes from the ligand makes the applicability of such a complex more feasible.

A remarkable feature of these complexes is the high activity in ambient conditions. As mentioned in Section 1.5.1, aluminium complexes often require high temperatures (> 70 °C) as well as high loadings (> 1 mol%) to be significantly active, which is not the case for the catam complexes.



Dagorne
P_r = 0.67

Dagorne
atactic PLA

Thomas
P_m = 0.65

Chart 4. Room temperature active aluminium complexes by Dagorne (left, centre) and Thomas (right)

Compared to other Al catalysts reported in the literature, the complexes were found to be significantly more active than Dagorne's heteroselective anionic aluminium alkoxide complex (Chart 4, left), with the k_{app} being an order of magnitude higher (10^{-4} *vs.* 10^{-5} s^{-1}).[111] Further to this, **2** is considerably more heteroselective (P_r = 0.90 *vs.* 0.67). However, the activity does not parallel that of the catalytic systems used by the groups of Thomas and Balasanthiran (Chart 4, right).[112-114] These *in-situ* generated anionic aluminium complexes require the addition of a co-catalyst (PPNCl) as well as an epoxide in order to proceed with the room-temperature polymerisation of *rac*-LA. Admittedly, the system often requires a long pre-activation time (up to 16 h) but can in turn achieve full conversion in as little as 30 minutes under similar conditions to **8c** (TOF = 200 *vs.* 64 h^{-1}).

In addition, the NHC-Al adduct developed by Dagorne and co-workers also exhibited faster activities than the catam complexes,[115] though the polymerisation itself resulted in a high degree of transesterification, with the polymer being atactic (Chart 4, centre). However, it needs be mentioned that such a polymerisation does not occur through a coordination-insertion mechanism.

It is thus evident that the high activity of the catam complexes is a remarkable result, which reinforces the favourable features of the catam ligand highlighted in Section 1.5.3. The *o*-aminophenolate moieties that form a rigid 5-membered N,O,Al chelate are important to the high activity; a finding initially discovered by Chen and co-workers for the ROP of ε-CL.[116] The proximity of the NH groups to the aryl moiety increases the polarity of the N-H bond, allowing it to act as a strong H-bond donor. This is due to the carbon atoms in the phenyl ring being sp^2-hybridized, which increases their s-character which manifests itself as a strong electron-withdrawing effect of the aromatic group.

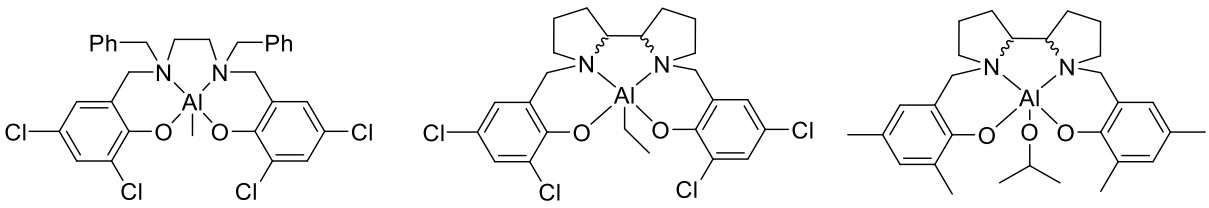


Chart 5. Highly heteroselective aluminium catalysts Gibson (left), Kol (centre), and Jones (right)

Regarding the heteroselectivity of complex **2**, there are few examples of aluminium complexes that lead to highly heterotactic PLA. The vast majority of aluminium-based catalysts tend to be isoselective which is a reason why this metal-centre is attractive.[117] Gibson and co-workers initially reported an alumium salan complex which yielded PLA with a P_r value of 0.96, which was attributed to the chloro-substituents on the aryl backbone (Chart 5, left).[83] Twelve years later, Kol *et al.* published the synthesis of a chiral salan catalyst built around a 2,2-bipyrrolidine core which yielded PLA with a P_r value of up to 0.98 (Chart 5, centre).[118] Shortly after Kol's discovery, Jones and co-workers reported a structural analogue to Kol's complex that produced PLA with a P_r of up to 0.87 (Chart 5, right).

2.4.1.2 Determination of the Order in Catalyst

To gain an understanding of the high activity of **2** and **8c**, as well as the high heteroselectivity of **2**, further studies were conducted using variable time normalisation analysis (VTNA) and DFT.

VTNA is a normalised time scale method that allows for determination of the kinetic order of a catalyst or a substrate in a reaction.[119, 120] Whilst the order in catalyst can be determined using initial rates or continuous rates, the normalised time scale method allows for faster and more accurate handling of data. Given that this has been successfully applied to similar polymerisation reactions,[121-124] this method was employed to determine the order in catalyst and thus elucidate the mechanism of *rac*-LA polymerisation when using **2** and **8c** (see Appendix B for details).

For complex **2**, an order in catalyst close to 1 was observed (Figure B100). This means that the mechanism solely occurs *via* either a monometallic or bimetallic mechanism. Given that the crystal structure of **1** is monomeric, and that DOSY NMR analysis showed complex **2** to be monomeric in THF-d_8, the order of 1 suggests that the rate-determining step proceeds through

a monomeric active species. Thus, the stereocontrol proceeds through a CEC mechanism in which the chirality of the last inserted LA molecule determines the preference for the next insertion.

For complex **8c**, the order in catalyst was also found to be close to 1 (Figure B102). Despite the dinuclear crystal structure of **8c**, DOSY NMR analysis showed the complex to be monomeric in THF-d_8 which indicates that the rate-determining step proceeds through a monomeric active species. To further elucidate the mechanism DFT calculations were carried out on a ωB97xD level of theory with a split valence double zeta 6-31G(d,p) basis set.

2.4.1.3 Computational Studies Performed on ^{H}L$_1$Al(Et) (**2**)

The structure of **2** was deduced the molecular structure of **1** by replacement of the ethyl co-ligand with a methoxide group (for computational efficiency). This mechanism was previously calculated in the Romain group but will be discussed as it provides valuable insight as to how the polymerisation proceeds and will serve as comparison for the calculations performed on other catalysts.

Initiation Mechanism of **2** and the role of NCIs

In the coordination step, it was found that one molecule of *L*-LA can displace two molecules of THF, leading to a stabilisation by 1.5 kcal/mol (Figure E1).[84] The carbonyl of the LA interacts favourably with one of the NH moieties, leading to the formation of a strong H-bond with a length of 1.92 Å. A considerably weaker H-bond was also formed between the acyl oxygen atom and the other NH moiety (Figure 21, left). This was supported by the NCI surfaces calculated for the structure, which show the presence of H-bonds as a bright blue disc (Figure 21, right).[45] The NCIs are shorter and possibly stronger than the C-H···π and C-H···Cl contacts reported by Carpentier and co-workers (See Section 2.1.4.2).[85-88, 91, 92]

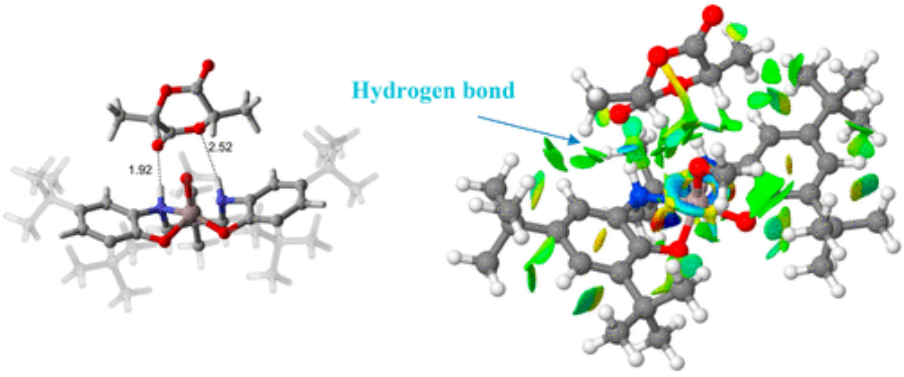


Figure 21. Complex formed between L-LA and **2** (left) and NCI surfaces (right). A Hydrogen bond is depicted as a blue disc.

These NCIs possibly contribute to suitably orient the monomer prior to the nucleophilic attack. Furthermore, the NHs withdraw electron density from the LA carbonyl, which activates the monomer similarly to the mechanism of H-bond activated organocatalyst ROP (See Section 1.3.3).[125-128] The steric and electronic influence of NCIs thus contribute to lower the barrier for nucleophilic attack by the Al-OMe bond shown by the transition state **2-III(t)-TS** with $\Delta\Delta G_{298}$ = 6.9 kcal/mol (Figure 22). The subsequent rearrangement of the monomer from **2-IV(t)** to **2-V(t)** is facilitated by the formation of a H-bond between an oxygen atom of the hemiacetal and a NH moiety of the ligand. This interaction is maintained in the transition state **2-VI(t)-TS**, which stabilises it and thus contributes to its low barrier ($\Delta\Delta G_{298}$ = 9.2 kcal/mol). The overall energy barrier for the initiation step is 11.8 kcal/mol, indicative of a room temperature active reaction (≤ 19 kcal/mol).[129]

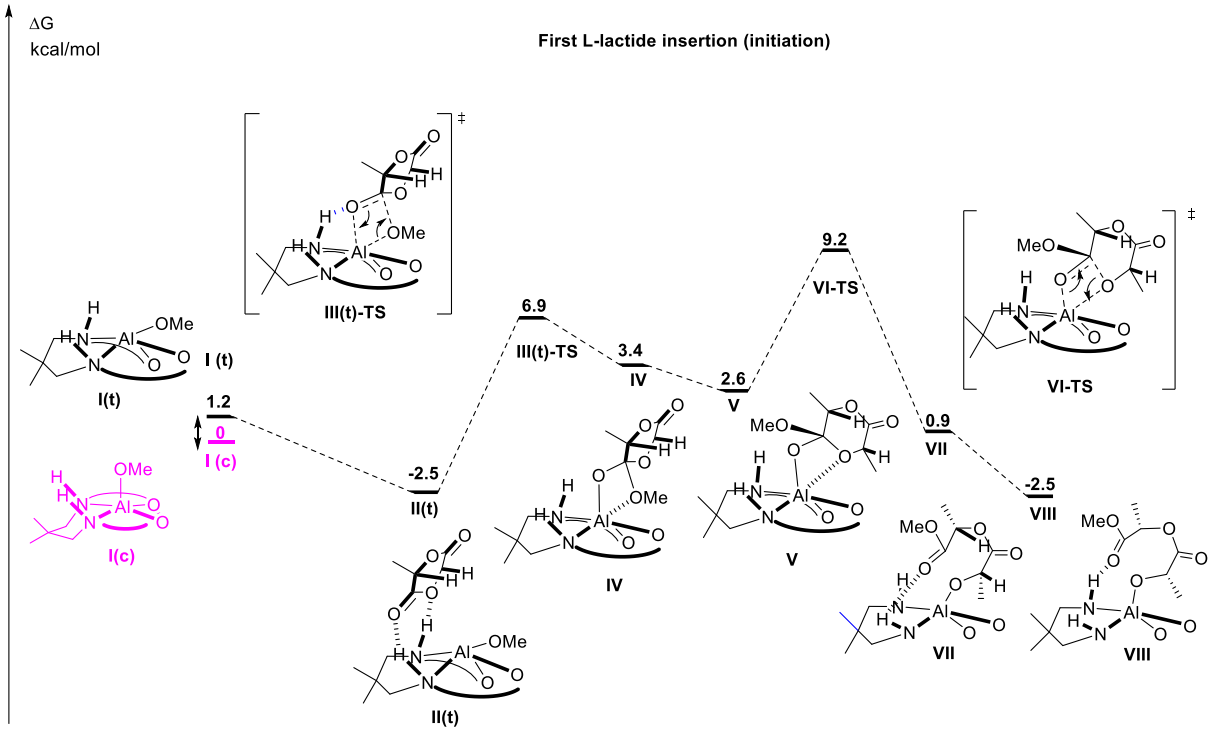


Figure 22. PES showing first insertion of a LA monomer into complex **2**-I(t). DFT protocol: # ωB97xD/6-31g(d,p) scrf=(cpcm, solvent = THF) nosymm integral=grid=ultrafine

Influence of the backbone geometry on polymerisation

A look at the 2,2-dimethyl-1,3-propanediamine tether reveals that the 6-membered N_2Al chelate can adopt multiple conformations – chair (**2-I(c)**), twisted boat (**2-I(t)**), and half-chair (**2-I(h)**) (Figure 23). Although the chair conformation is the most stable, the room temperature active initiation step occurs *via* the twisted boat conformation. This conformation does not lead to a significant energy penalty and likely arranges the propyl backbone in a way that minimises

steric repulsion between the ligand and the monomer. To further probe the importance of the backbone, the initiation mechanism was calculated for the **2-I(c)** and **2-I(h)** conformations (Figure E3). The mechanism proceeding *via* the stable chair-configuration interestingly was the least favourable, with an overall energy barrier of $\Delta\Delta G_{298}$ = 20.4 kcal/mol (*c.f.* 11.8 for **2-I(t)**). Additionally, the half-chair conformation **2-I(h)** led to an overall energy barrier of $\Delta\Delta G_{298}$ = 14.8 kcal/mol, putting it between **2-I(c)** and **2-I(t)** in terms of energetics.

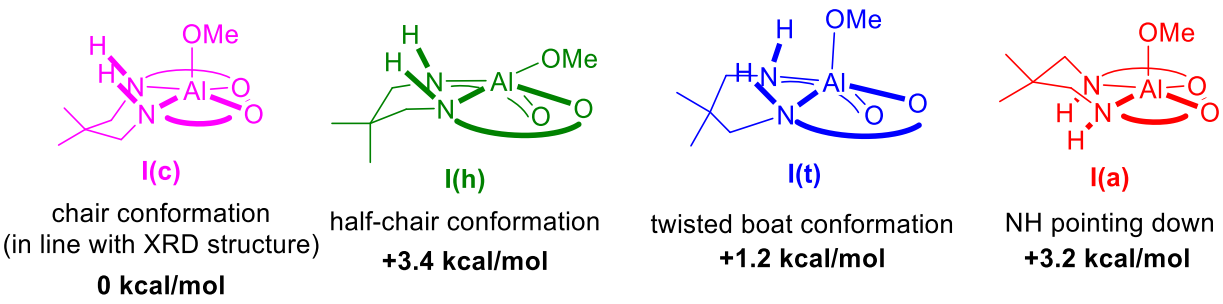


Figure 23. Relative Gibbs free energies ΔG_{298} of different conformations of complex **2**-I.

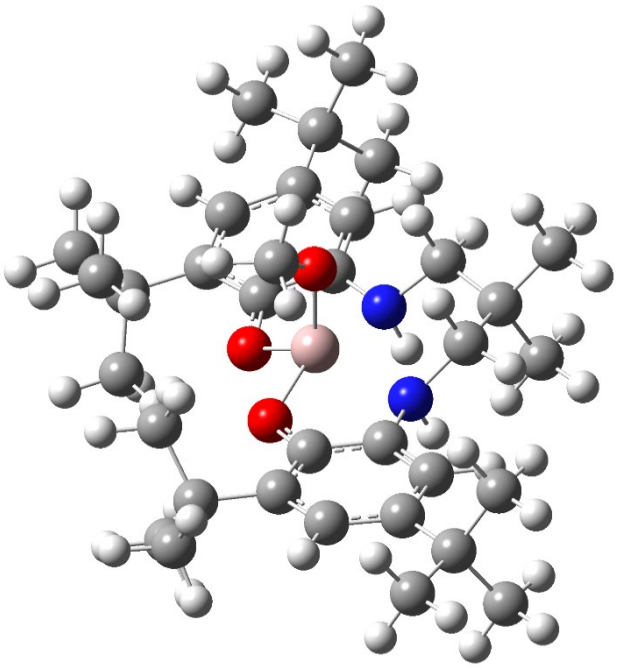


Figure 24. DFT structure of **2**-I(a) as deduced from the crystal structure of **2-Cl** through DFT optimisations

To highlight the importance of the NH moieties, a mechanism was calculated in which the two hydrogen bond donors point away from the catalytic pocket. This was observed in a chloro analogue of **2**, synthesised by Dr. Charles Romain within the group, which exhibited a similar SQP structure but with the NH moieties pointing down relative to the apical position and thus

being shielded from the reactive centre. The crystal structure (**2-Cl**) was used (See Appendix F) and the chloro group replaced with a methoxy group which led to the structure **2-I(a)** (Figure 24). The lowest energy pathway was subsequently calculated for the polymerisation of LA by **2-I(a)**, which was found to have an overall energy barrier of $\Delta\Delta G_{298}$ = 21.4 kcal/mol, roughly 10 kcal/mol higher than **2-I(t)** (Figure E2). As the NH groups do not take an active part in the polymerisation, this difference in energy points to the moieties having a profound impact on the rate of reaction. However, the geometry of the NH will incur a significant energy penalty when the complex adopts an octahedral structure, which may be a contributing factor to the high energy barrier.

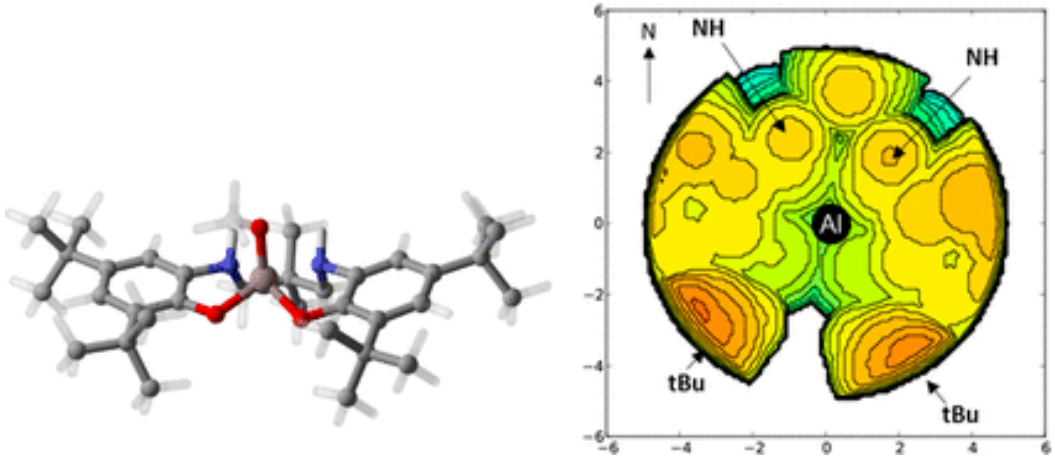


Figure 25. Structure of the resting species of **2**-I(c) (left) and its TSM (right) showing the NH groups and bulky ^{t}Bu groups sticking out from the plane of the complex.

Topographic steric map

To depict the shape of the catalytic pocket, Cavallo and co-workers introduced the concept of topographic steric maps (TSM).[130, 131] These maps estimate the molecular surface that is accessible and provide the user with a shape of the catalytic pocket. This method was previously used to rationalise the highly controlled ROP of β-BL by a pentacoordinated aluminium complex.[132] The TSM for **2-I(c)** show a flat space around the catalytic pocket, facilitated by the planar coordination of the ligand around the metal centre (Figure 25). The NH moieties can be found sticking out from the surface in a manner that facilitates the formation of H-bonds. A particularly interesting aspect of this map are the bulky ^{t}Bu groups found in the southern quadrant. These essentially hinder the advance of the monomer and force the LA to approach from the northern quadrant and thus take part in H-bonding, which may be at the origin of the experimentally observed binding isotope effect (see Section 2.4.1.5).[133]

Propagation mechanism of **2** and observed stereoselectivity

To gain an understanding of the high stereoselectivity observed, the propagation step after the first insertion of a *L*-LA molecule was calculated. The final structure of the first insertion, **VIII** (Figure 26), was considered and the second insertion calculated with a molecule of *D*- and *L*-LA. In both cases, docking of the monomer on the NH moieties was observed leading to a stabilisation of $\Delta\Delta G_{298}$ = -9.7 and -8.0 kcal/mol for *D*- and *L*-LA respectively. The NCI surfaces show the same H-bonding interactions observed in the initiation step (Figures E4 and E5). The rate-determining step was the acyl oxygen cleavage, leading to a total energy barrier of $\Delta\Delta G_{298}$ = 24.0 and 26.0 for *D*- and *L*-LA respectively. The insertion of *D*-LA is thus favoured by 2 kcal/mol which would correspond to a selectivity of around 95%.[134] This is in good agreement with the experimentally observed heteroselectivity (P_r = 0.90). The results thus show that a CEC mechanism devoid of polymeryl exchange events can lead to the high stereoselectivity observed for **2**.

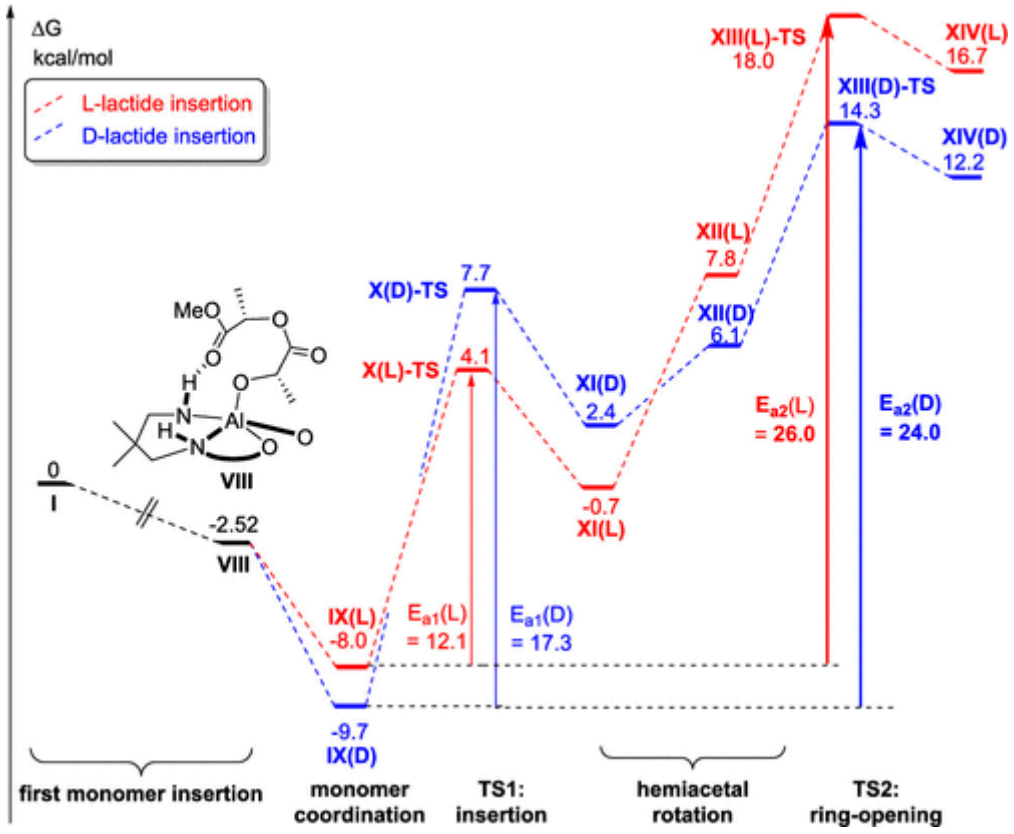


Figure 26. PES showing second insertion of a lactide monomer (red = L-lactide, blue = D-lactide) after initial insertion of L-lactide as per initiation step in Figure S35. DFT protocol: # ωb97xD/6-31g(d,p) scrf=(cpcm, solvent=THF) NoSymm grid=integral=ultrafine.

2.4.1.4 Computational Studies Performed on $^{H}L_2Al(OBn)$ (**8c**)

Given the fact that molecular structure of **8c** was dimeric, but that DOSY experiments showed the complex to be monomeric in THF, assumptions had to be made regarding its monomeric form. The monomeric form of **8c** was deduced by breaking the dimer into its components and optimising the monomers to a TBP structure. The benzyloxy moiety was subsequently replaced by a methoxy group for computational efficiency.

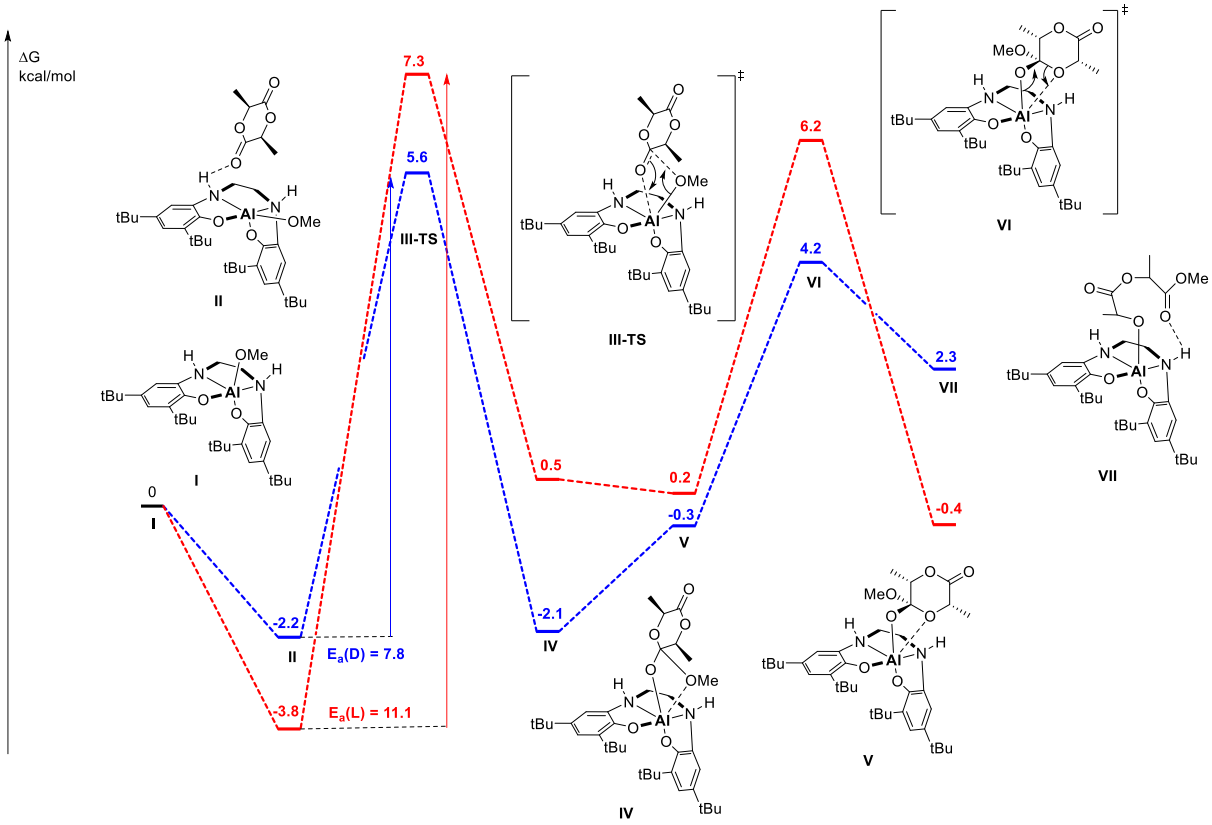


Figure 27. PES showing first insertion of a lactide monomer (red = L-lactide, blue = D-lactide) *via* a "top-down" approach. DFT protocol: # ωb97xD/6-31g(d,p) scrf=(cpcm, solvent=THF) NoSymm grid=integral=ultrafine.

Initiation mechanism of **8c**

The initiation mechanism for **8c-I** was calculated for an axial approach (referred to as "top-down" approach) of the pro-R and pro-S faces of the *D*- and *L*-LA molecules (Figure 27). The lowest overall energy barrier was found to be for the insertion of a *D*-LA molecule ($\Delta\Delta G_{298}$ = + 7.8 kcal/mol) which is lower than what was found for **2-I** (*c.f.* $\Delta\Delta G_{298}$ = + 11.8 kcal/mol for **2-I**). The insertion of *D*-LA was favoured over that of *L*-LA by 2.3 kcal/mol. As was the case for **2-I**, the mechanism was found to incorporate NCIs in some of its steps which likely also were a contributing factor to the low energies. So far, only the axial approach of the monomer (refer to as "top-down" approach) was considered as it allows for the favourable NCIs to occur

throughout the mechanism. An equatorial approach of the monomer (referred to as "side-on" approach) was also considered, which resulted in increased energy barriers of ΔG_{298} = + 9.1 kcal/mol (Figure 28). This was rather expected, mainly due to the TSM of **2-I(c)** (Figure 25) showing that the ^{t}Bu groups at the 3-position of the aromatic ring offer a considerable amount of steric bulk, and thus hinder such an approach. However, the polymerisation through a "side-on" approach can still occur favourably at room temperature. Given that the energy barriers between the insertion of a *D*- and *L*-LA monomer in a "side-on" approach have only a slight difference (0.3 kcal/mol), it could rationalise the reduced stereoselectivity observed during polymerisation.

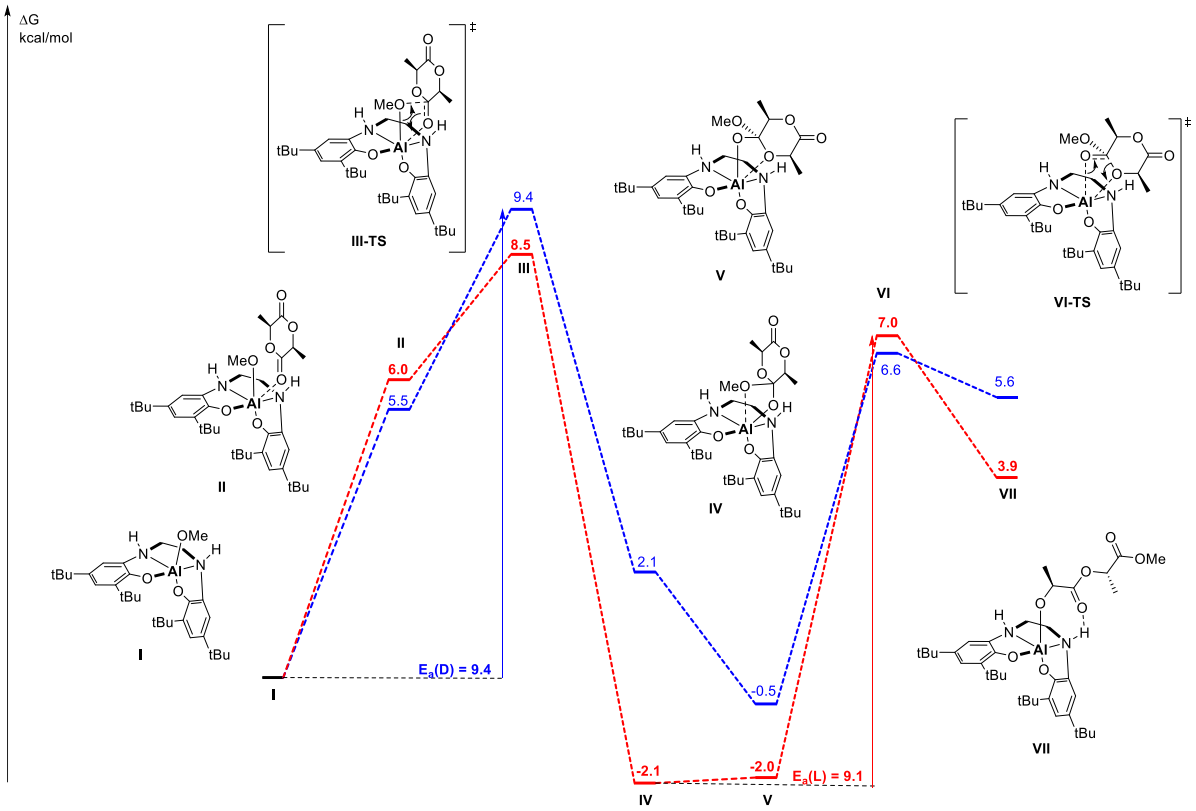


Figure 28. PES showing first insertion of a lactide monomer (red = L-lactide, blue = D-lactide) via a "side-on" approach. DFT protocol: # ωb97xD/6-31g(d,p) scrf=(cpcm, solvent=THF) NoSymm grid=integral=ultrafine.

Propagation mechanism of **8c** and observed stereoselectivity

Given that the considered isomer **8c-I** preferentially inserts a *D*-LA molecule at the initiation stage, the propagation was calculated to gain insight into the stereoselectivity of the complex. Thus, using **8c-VII**, the insertion of *D*- and *L*-LA *via* various approaches was considered (Figure 29). Interestingly, **8c-VII** favours the insertion of another *D*-LA molecule over *L*-LA with an energy difference of $\Delta\Delta G_{298}$ = + 5.3 kcal/mol. While this is in line with the experimental formation of isotactic polymers (P_m = 0.60), an energy difference of 5.3 kcal/mol

should lead to much higher tacticity control. This suggests that other mechanisms may take place that lower the stereoselectivity. This includes but is not limited to "side-on" approaches which were found to be favourable in the initiation step but result in little stereoselectivity, as well as interconversion of the active species between conformational isomers which exhibit different selectivities.

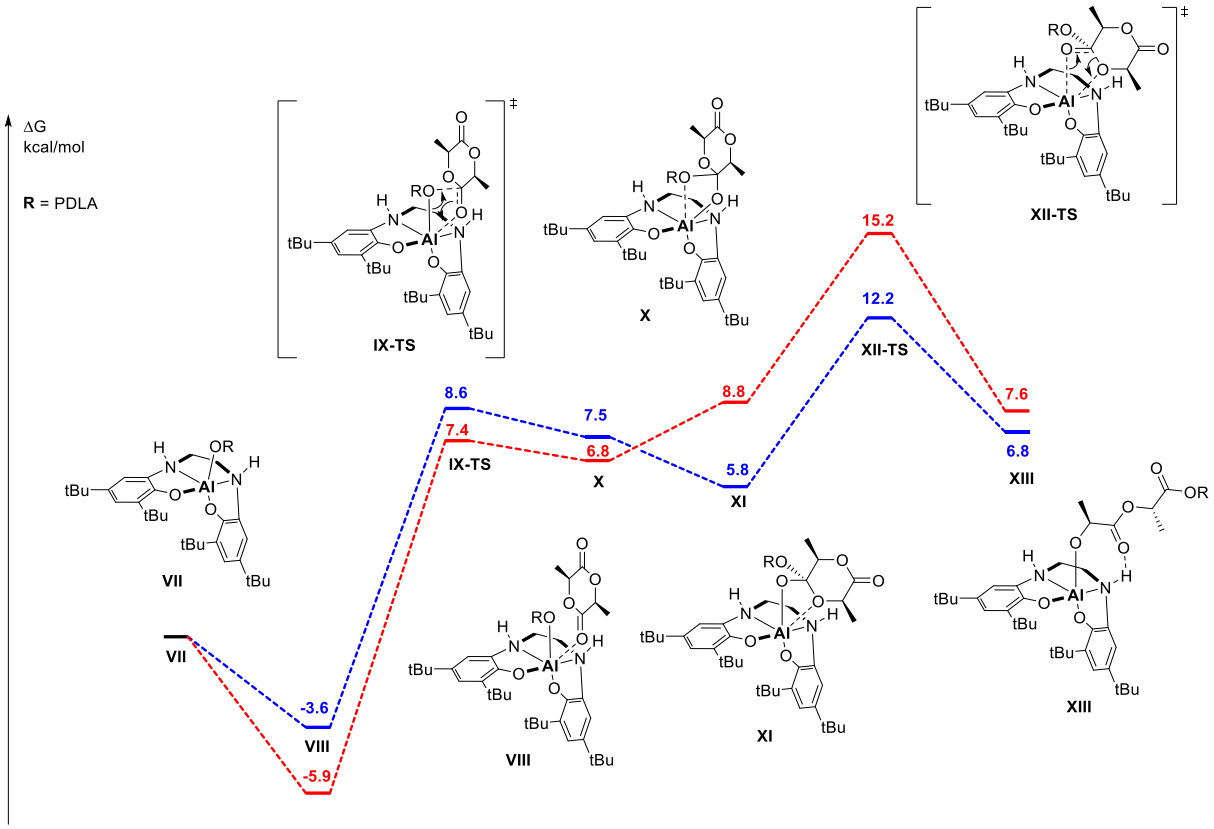


Figure 29. PES showing second insertion of a lactide monomer (red = L-lactide, blue = D-lactide) after insertion of a *D*-LA monomer. DFT protocol: # ωb97xD/6-31g(d,p) scrf=(cpcm, solvent=THF) NoSymm grid=integral=ultrafine.

2.4.1.5 Kinetic Isotope Effect Studies

Table 2. *rac*-LA polymerisations at room temperature using $^{H/D}$**L1** complexes **2** and **4** as well as $^{H/D}$**L2** complexes **7** and **10**.

Entry	Cat.	ROH	Cat./ROH/ LA (equiv.)	Time (min)	Conv.[a] (%)	$M_{n(SEC)}$(Đ)[b] (kg/mol)	P_r[c]	$M_{n(calc.)}$[d] (kg/mol)
1	**2**	-	1/0/100	90	91.4	9.5 (1.3)	0.91	13.2
2	**4**	-	1/0/100	90	83.9	16.5 (1.3)	0.91	11.8
3	**7**	^{i}PrOH	1/1/100	90	80	8.7 (1.1)	0.62	10.2
4	**10**	^{i}PrOD	1/1/100	90	85	-	-	-

Reaction conditions: $[LA]_0$ = 1 mol.L^{-1}, 25 °C, THF; a) Determined by ^{1}H NMR by relative integration of signals at 5.06 ppm (monomer) and 5.20 ppm (polymer); b) Determined by SEC calibrated with polystyrene standards in THF and corrected (see ESI) c) Probability of racemic linkages determined by ^{1}H NMR spectroscopy (see ESI); d) Calculated using the conversion

To elucidate the importance of the NH moieties, polymerisations were carried out with the deuterated analogue of **2**, ^{D}**L**$_1$Al(O^{i}Pr) (**4**). Complex **4**, was found to still be a highly active *rac*-LA ROP catalyst at room temperature, resulting in an 84 % conversion over 90 minutes, while keeping the high heteroselectivity (Table 2, Entries 1 and 2). However, the k_{app} of **4** is lower (2.52×10^{-4} s^{-1}, Figure B14) than that of **2** (4.75×10^{-4} s^{-1}, Figure B5), resulting in a kinetic isotope effect (KIE). In fact, **2** is almost twice as fast as **4** ($k_H/k_D \approx 1.9$) which confirms that the NH moieties on the ligand are important to the activity of the catalyst (Figure 30). The KIE value is too small to be considered a primary KIE, meaning that the N-H bond is not broken during the RDS. A secondary KIE adopts a value up to 1.2,[135] putting the observed value in a similar range. However, the fact that the value of 1.9 is still considerably large for a secondary KIE suggests that it likely arises from equilibrium or binding isotope effects, which is indicative of the monomer binding to the NH moieties in the catalytic pocket.[133] This agrees with the DFT calculations outlined in Section 2.4.1.3 in which NCIs were found to be present during the monomer's approach to the catalytic pocket.

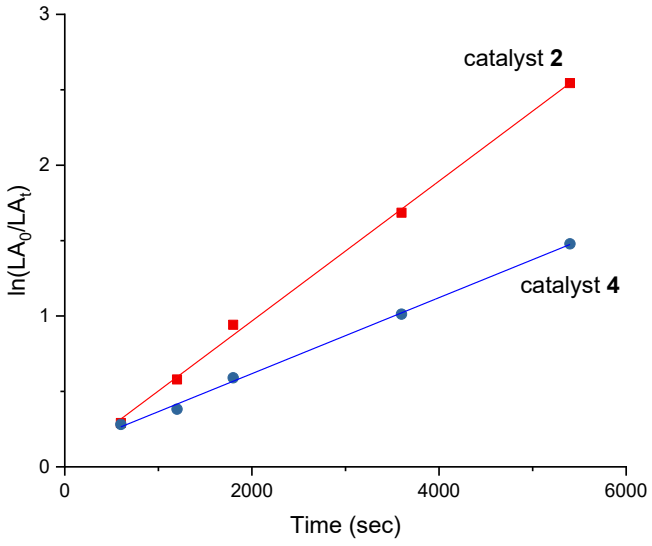


Figure 30. First-order plots of rac-LA ROP initiated by **2** and **4** showing a clear isotope effect.

The KIE was probed for the complexes bearing a ^{R}**L**$_2$ ligand by testing **7** and its deuterated analogue **10**. The initiating alcohols used were ^{i}PrOH and ^{i}PrOD respectively, given the fact that BnOD was difficult to source. The polymerisation with the protonated complex **7** (+ ^{i}PrOH) was run as a triplicate and yielded the average $k^{H}_{app} = 3.93 \times 10^{-4}$ s^{-1} (Figure B15). This was higher in activity than the polymerisation of **7** + BnOH which can be attributed to the isopropoxide being a secondary alcohol, giving the complex a propensity to remain

monomeric. The deuterated complex **10** (+ ^{i}PrOD) was subsequently tested as a duplicate, yielding an average k^{D}_{app} = 3.72 × 10^{-4} s^{-1} (Table 2, Entry 4; Figure B16). This translates to a KIE of $k_H/k_D \approx 1.06$ which is negligible, suggesting that the NH moieties are not as impactful as for complex **2** (Figure 31). It is worth mentioning that the ^{R}**L**$_2$ complexes are less selective and only exhibit a slight isotactic bias (P_m = 0.60). This is in contrast to the ^{R}**L**$_1$ complexes which exhibit high heteroselectivity (P_r = 0.90). The NCIs thus may not play a significant role in the polymerisations using ^{R}**L**$_2$. Given that DFT calculations found a "side-on" approach to be favourable, it could well be that the NH moieties are not as involved in **8c** as they are in **2**. Furthermore, it was outlined in Section 2.3.2.1 that the isopropoxy complex generated from **7** shows multiple species in the ^{1}H NMR spectrum (Figure 17). As it is difficult to attribute a KIE to multiple species and the results thus remain inconclusive.

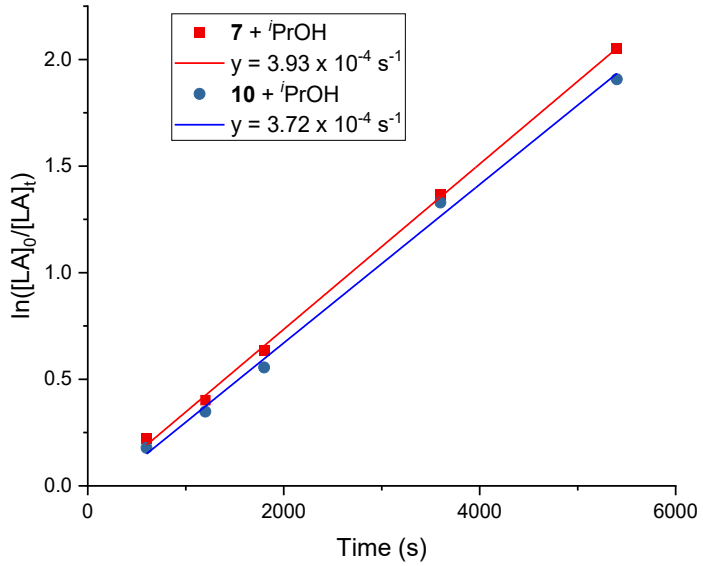


Figure 31. First-order plots of rac-LA ROP initiated by **7** and **10** showing a negligible isotope effect.

2.4.1.6 Use of Methylated Analogues Bearing the ^{Me}**L**$_1$ and ^{Me}**L**$_2$ Ligands

Table 3. *rac*-LA polymerisations at room temperature using ^{Me}**L**$_1$ complex **5** and ^{Me}**L**$_2$ complex **11**.

Entry	Cat.	ROH	Cat./ROH/ LA (equiv.)	Solvent	T (°C)	Time (min)	Conv.[a] (%)	$M_{n(SEC)}$(Đ)[b] (kg/mol)	P_r[c]	$M_{n(calc.)}$[d] (kg/mol)
1	**5**	^{i}PrOH	1/1/100	THF (THF) [Toluene]	25 (50) [90]	180 (240) [960]	0 (0) [39]	- - 8.4 (1.0)	- - 0.43	- - 5.6
2	**11**	BnOH	1/1/100	THF	25 (50)	90 (16 × 60)	0 (20)	-	0.28	-

Reaction conditions: $[LA]_0$ = 1 $mol.L^{-1}$; a) Determined by ^{1}H NMR by relative integration of signals at 5.06 ppm (monomer) and 5.20 ppm (polymer); b) Determined by SEC calibrated with polystyrene standards in THF and corrected (see ESI); c) Probability of racemic linkages determined by ^{1}H NMR spectroscopy (see ESI); d) Calculated using the conversion;

Having established the importance of the NH moieties in the room temperature activity of *rac*-LA polymerisation, methylated analogues were tested. Complex **5** bearing the ^{Me}**L1** ligand was employed in *rac*-LA ROP in THF at 25 and 50 °C (Table 3, Entry 1). In either case, no conversion was observed, even when left to react for up to 4 hours. Running the reaction in toluene at 90 °C resulted in a 39 % conversion after 16 hours, with an activity close to the salan analogue previously outlined (Table 1, Entry 8). The stereoselectivity changed dramatically as well, with the P_r of 0.43 indicating a slight isotactic bias. This outlines the profound impact that the NH moieties may have on activity and selectivity of the catam series. It was initially thought that the low activity of **5** was due to it not being reactive to ^{i}PrOH. The active species would thus not be generated, and polymerisation would not proceed. However, ^{1}H NMR studies (C_6D_6, 298 K) confirm that **5** reacts with ^{i}PrOH and that the low activity must arise from somewhere else (Figure A12). The NH moieties are thus likely important to the polymerisation activity which could be due to them allowing the complex to adopt a favourable geometry in solution. Comparing the molecular structure of **1** and **5**, the former adopts a square pyramidal geometry while the other exhibits a *trans*-phenolato trigonal bipyramid, which can have a profound effect on activity and selectivity (Figures 10 and 14). A change of geometry was also observed by Jones and co-workers where salan ligands were found to wrap differently around the Al centre because of weak interactions between a NH moiety of the ligand and O atom of the O^{i}Pr group.[136] A change in reactivity was observed by Mehrkhodavandi and co-workers who reported indium complexes that exhibit a change in activity when substituting a secondary amine in the ligand with a tertiary amine.[137] The latter was found to be less active by two orders of magnitudes compared to the secondary amine analogue. Although weak H-bonding has been observed in the solid-state structures, Mehrkhodavandi could not fully attribute the higher activity to such interactions.

Complex **11** bearing the ^{Me}**L2** ligand was found to be inactive in THF at room temperature. However, heating the mixture at 50 °C overnight resulted in a 20 % conversion (Table 3, Entry 2). As elucidated in Section 2.3.2.3. the unusual dimeric structure of **11** breaks down into its monomeric form in THF. Despite this occurring, the complex requires elevated temperatures to proceed with the polymerisation, indicating that the NH moieties are important to the catam scaffold regardless of the linker involved. As was previously seen with **5**, the polymer formed by **11** was found to have a different stereoregularity to its non-methylated counterparts, exhibiting moderate heterotacticity (P_m = 0.28 *vs.* 0.60 for **8c**). This inversion of stereoselectivity highlights that the NH moieties have an impact that extends beyond activity.

2.4.1.7 Computational Studies Performed on ^{Me}**L**$_1$Al(Et) (**5**)

Initiation Mechanism of **5**

As shown in the previous section, the polymerisation using the methylated analogue **5** was found to only occur at high temperatures (90 °C), albeit at sluggish rates (Table 3, Entry 1). Using the molecular structure of **5**, the alkyl chain was replaced with a methoxy group to yield **5-I** and DFT calculations were subsequently carried out to elucidate the mechanism of polymerisation and thus explain the slow activity (Figure 32). Interestingly, the total energy barrier was found to be $\Delta\Delta G_{298}$ = 8.4 kcal/mol, considerably lower than the barrier found using the protonated structure **2-I(t)** (11.8 kcal/mol). This can be attributed to the starting structure, which adopts a TBP configuration. This puts the system closer to the octahedral transition states of the polymerisation and thus less energy is required for these to be adopted. Furthermore, the *trans*-phenolato coordination of the ligand may be more efficient in withdrawing electron-density from the metal centre, making it more Lewis acidic. However, the disparity between experimental and computational evidence remains, and points to other mechanisms taking place during the reaction which ultimately hamper **5** from carrying out the polymerisation.

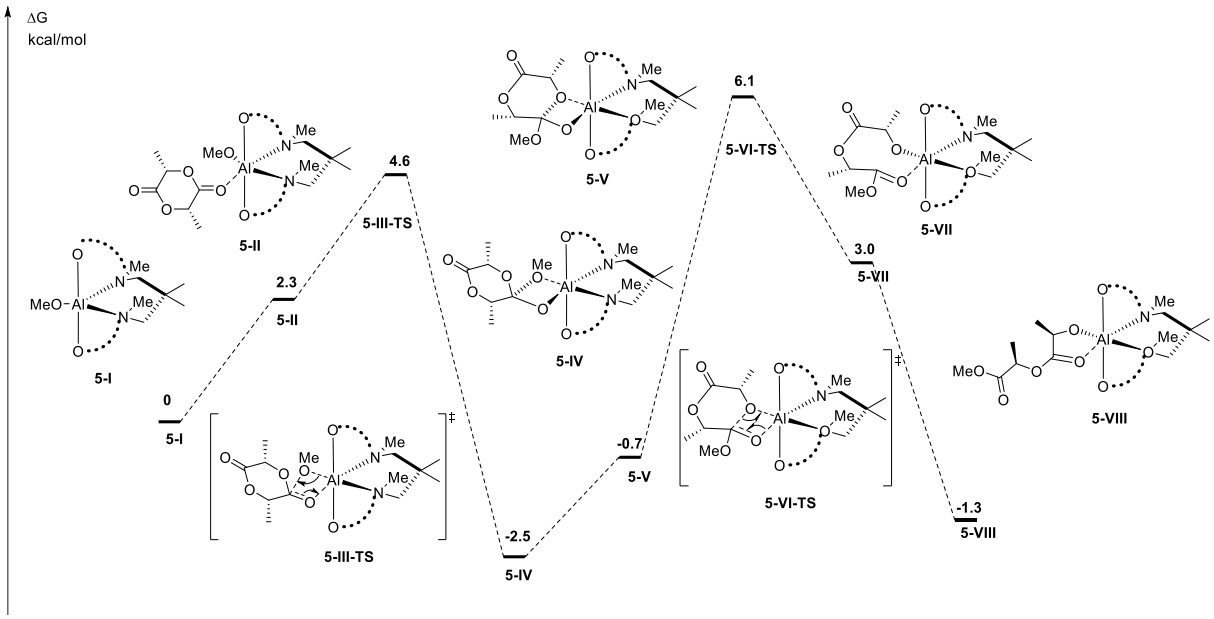


Figure 32. PES showing first insertion of a LA monomer into complex **5**-I. DFT protocol: # ωB97xD/6-31g(d,p) scrf=(cpcm, solvent = THF) nosymm integral=grid=ultrafine

Framework Distortion Energies and their relation to Activation Energy

Table 4. FDEs calculated for complexes **2-I(t)**,**(c)**,**(h)**,**(a)**, and **5** as well as their calculated activation energies

Entry	Complex	Activation Energy (kcal/mol)	FDE (kcal/mol)
1	**2-I(t)**	11.8	5.8
2	**2-I(c)**	20.4	8.0
3	**2-I(h)**	14.8	11.0
4	**2-I(a)**	21.4	21.0
5	**5-I**	8.4	2.1

Having calculated the activation energies for the initiation *via* **2-I(t)**,**(c)**,**(h)**,**(a)** (Figure 23) and **5-I**, framework distortion energy (FDE) calculations were carried out to elucidate the importance of backbone conformation. Tolman and Cramer found that the ease at which a ligand can be distorted can dictate activity of a catalyst in cyclic ester ROP.[138-142] The FDE indicates the energy penalty that is incurred when the ligand geometry of the resting species is distorted to that of the rate-determining step. For each of the complexes, their optimised structure was used as the GS and compared to their largest TS. The alkoxide co-ligand and LA molecule are removed to remove any steric or electronic influence of the substrate. The resulting structures were optimised and the energy difference between GS and TS used as the FDE. The favourable polymerisation mechanism, carried out by **2-I(t)**, features a low FDE of 5.8 kcal/mol (Table 4, Entry 1) which is among the lowest FDE values reported for cyclic ester ROP by similar Al complexes. This is in good agreement with the low energy barriers that were calculated ($\Delta\Delta G_{298}$ = 11.8 kcal/mol). Backbone conformation must play an important role in the FDE, as other conformations such as the chair conformation (Table 4, Entry 2) and the half-chair conformation (Table 4, Entry 3) were found to exhibit higher FDE values (8.0 and 11.0 kcal/mol respectively). The twisted conformation thus allows for the complex to adopt a suitable TS structure while minimising steric factors, which ultimately leads to the low activation energy of polymerisation. The orientation of the NH groups has a profound impact, with the structure **2-I(a)** featuring a FDE of 21.0 kcal/mol (Table 4, Entry 4), a big outlier in the series. Interestingly, the FDE for the methylated analogue **5-I** is surprisingly low (Table 4, Entry 5), showing an energy penalty of 2.1 kcal/mol for the adoption of the TS geometry. Nonetheless, experimental results show the ROP mediated by **5** to be slow, which hints that other mechanisms may be present during the reaction which deactivate the species.

Plotting the activation energy as a function of the FDE, shows that there is a positive relationship between the two variables (Figure 33). Despite the usefulness of such a method, one should not reduce the polymerisation mechanism to such a primitive form. Given that NCIs

and aggregation can play a role in determining activity and selectivity, the FDE should be used *ad hoc* as a complementary tool only.

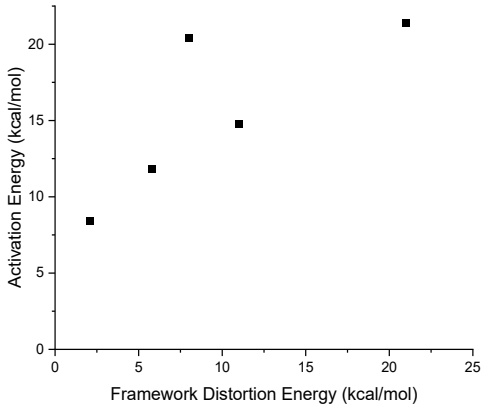


Figure 33. Scatter plot of activation energy as a function of FDE showing a positive correlation between both variables

2.4.1.8 Solvent Effects on Polymerisation

Table 5. *rac*-LA polymerisations at room temperature using **2** and **8c** in different solvents

Entry	Cat.	Solvent	T (°C)	Time (min)	Conv.[a] (%)	$M_{n(SEC)}$(Đ)[b] (kg/mol)	P_r[c]	$M_{n(calc.)}$[d] (kg/mol)
1	**2**	THF	25	90	91.4	9.5 (1.3)	0.91	13.2
2	**8c**	THF	25	90	96	14.3 (1.2)	0.60	13.8
3	**2**	DCM	25	90	66.5	9.5 (1.2)	0.69	9.6
4	**8c**	DCM	25	90	50	12.1 (1.3)	0.57	7.2
5	**2**	Dioxane	25 (90)	240 (60)	0 (0)	- -	- -	- -

Reaction conditions: Al/LA = 1/100, $[LA]_0$ = 1 mol.L^{-1}; a) Determined by ^{1}H NMR by relative integration of signals at 5.06 ppm (monomer) and 5.20 ppm (polymer); b) Determined by SEC calibrated with polystyrene standards in THF and corrected (see ESI); c) Probability of racemic linkages determined by ^{1}H NMR spectroscopy (see ESI); d) Calculated using the conversion

Complexes **2** and **8c** were also briefly tested in solvents other than THF to examine whether they can influence performance. Interestingly, using DCM as the polymerisation solvent for **2** led to a lower activity and selectivity when compared to THF (Table 5, Entry 1 *vs*. 3). In fact, the k_{app} was essentially halved (2.15 *vs.* 4.75 × 10^{-4} s^{-1}) and the P_r was lowered from 0.90 to 0.70. This attributed this to the fact that DCM is a non-coordinating solvent. It was outlined in Section 2.3.1.1 that **2** was in a slow monomer-dimer equilibrium at room temperature in C_6D_6 (Figure A12). In DCM, **2** is likely not completely monomeric, with a fraction of it being in its inactive dimeric form at any given time, resulting in a lower activity overall. This however does not explain the decrease in heteroselectivity observed, which is not as straightforward. A possible explanation for the change in stereoselectivity may be that the dimeric species formed

is still active in the polymerisation but not as selective as its monomeric counterpart, leading to an overall lowering of the P_r value. As was discussed previously in this chapter, the H-bonds that the NH moieties form with the monomer are integral to both, the activity and stereoselectivity. It has been previously shown that H-bonds are weakened in less polar solvents.[143] Given that the polarity index of DCM is lower than THF (3.1 *vs.* 4.0),[144] one may consider DCM a H-bond disruptor which could result in lower stereoselectivities as well as lower activities. It must be stated that this is purely speculative, and that further studies must be conducted to elucidate this drastic shift in stereoselectivity.

Using **8c** in DCM resulted in a considerably slower polymerisation (50 % in 90 min; Table 5, Entries 2 *vs.* 4) which is akin to what was found for **2**. Given that **8c** was found to be dimeric in the non-coordinating C_6D_6, the lower activity may be attributed to a slow breakdown of the dimer into the active species. This would also explain the high discrepancy between the predicted M_n and that measured by SEC.
Polymerisations with **2** were also conducted in 1,4-dioxane at both, 25 and 90 °C (Table 5, Entry 5). In either case, no conversion was observed which was attributed to the dioxane being able to coordinate strongly with either the NH moieties or the metal centre of the catalyst. Its ability to crowd the secondary coordination sphere of the complex can thus hinder the monomer approach.

2.4.1.9 Polymerisations at High Temperatures

The potential of the catalysts was explored by carrying out polymerisations at higher temperatures. Preliminary studies outlined in Section 2.3.1.1 indicated that complex **2** was stable in immortal polymerisation conditions (Figure A9). Indeed, immortal polymerisation was found to proceed without any deactivation at low loadings (0.1 and 0.2 mol%) and high temperatures (50 and 90 °C) in both THF and toluene (Table 6 Entries 1, and 2). Even though the molecular weight control was maintained (Đ = 1.1), the stereoregularity of the polymer was found to decrease with increasing temperature, which is known to decrease monomer selectivity. Polymerisation using complex **2** was also found to proceed in molten monomer (130 °C), converting 41 % within 3.5 minutes (Table 6, Entry 3). This contrasts with the salen analogue and aluminium isopropoxide which were found to be significantly slower in the melt (Table 6, Entries 4 and 5).

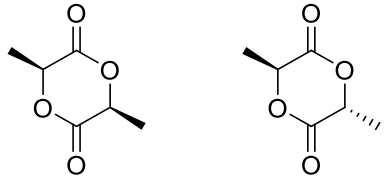
Table 6. *rac*-LA polymerisations at elevated temperatures complexes **2** and **8c**

Entry	Cat.	ROH	Cat./ROH/ LA (equiv.)	Solvent	T (°C)	Time (min)	Conv.[a] (%)	$M_{n(SEC)}$(Đ)[b] (kg/mol)	P_r[c]	$M_{n(calc.)}$[d] (kg/mol)
1	**2**	^{i}PrOH	1/9/1000	Toluene	90	30	90	11.5 (1.1)	0.61	13.0
2	**2**	^{i}PrOH	1//4/500	THF	50	60	56	7.0 (1.2)	0.85	8.0
3	**2**	-	1/0/250	Bulk[e]	130	3.5	41	4.3 (1.1)	0.61	5.9
4	**1-salen**[f,145]	-	1/0/300	Bulk[e]	130	30	25	14.3 (1.1)[g]	0.09	-
5	**Al(O^{i}Pr)$_3$**[146]	-	1/0/2085	Bulk[e]	110	45 × 60	80	-	-	-
6	**8c**	BnOH	1/4/500	THF	50	60	86	10.7 (1.1)	0.61	12.4
7	**8c**	BnOH	1/9/1000	Toluene	90	15	98	14.3 (1.6)	0.55	14.1
8	**8c**	BnOH	1/9/1000	Bulk[e]	130	4	77	4.9 (1.6)	0.51	11.2
9	**8c**	-	1/0/500	THF	50	60	60	45.9 (1.1)	0.56	43.5

Reaction conditions: $[LA]_0$ = 1 mol.L^{-1}; a) Determined by ^{1}H NMR by relative integration of signals at 5.06 ppm (monomer) and 5.20 ppm (polymer); b) Determined by SEC calibrated with polystyrene standards in THF and corrected (see ESI); c) Probability of racemic linkages determined by ^{1}H NMR spectroscopy (see ESI); d) Calculated using the conversion; e) in molten monomer; f) salen derivative of **2** as per reference; g) Determined by SEC calibrated with polystyrene standards in $CHCl_3$, value not corrected.[145]

8c was stable when employed at high temperatures in THF and toluene under immortal conditions (Table 6, Entries 6 and 7) but resulted in a less stereoregular polymer. This was particularly the case at 90 °C in toluene where a near-atactic polymer was obtained. Furthermore, the polymerisation in the absence of any solvent resulted in an atactic polymer with a high discrepancy between the calculated and observed molecular weights (Table 6, Entry 8). This can be attributed to slow mass transfer during the reaction. The ability of **8c** to produce high M_n polymers was also investigated by omitting any further addition of the BnOH initiating species (Table 6, Entry 9). The high conversion, as well as the good agreement of the M_n with what is expected, show that the complex can produce high molecular weight polymers with ease.

2.4.2 Polymerisation of *L*-LA and *meso*-LA



***L*-LA** ***meso*-LA**

Chart 6. Structures of *L*-LA and *meso*-LA

Table 7. Polymerisation of *L*-LA and *meso*-LA using **2** and **8c**

Entry	Complex	Monomer	Time (min)	Conv.[a] (%)	$M_{n(SEC)}$ (Đ)[b] (kg/mol)	$M_{n(calc).}$[d] (kg/mol)	k_{app} (s^{-1})
1	**2**	*L*-LA	150	66	12.8 (1.1)	9.4	9.44×10^{-5}
2	**8c**	*L*-LA	60	96	17.5 (1.1)	13.8	9.17×10^{-4}
3	**2**	*meso*-LA	40	89	10.5 (1.1)	12.8	9.06×10^{-4}
4	**8c**	*meso*-LA	40	99	11.3 (1.1)	14.2	1.98×10^{-3}

Reaction conditions: Al/LA = 1/100 $[LA]_0$ = 1 mol.L^{-1}, 25 °C, THF; a) Determined by ^{1}H NMR by relative integration of signals at 5.06 ppm (monomer) and 5.20 ppm (polymer); b) Determined by SEC calibrated with polystyrene standards in $CDCl_3$ and corrected (see ESI); c) Probability of racemic linkages determined by ^{1}H NMR spectroscopy (see ESI); d) Calculated using the conversion;

Given that **2** is a heteroselective catalyst, the polymerisation for *L*-LA proceeded slower than for *rac*-LA (Table 7, Entry 1), resulting in a 5-fold decrease of the k_{app} (*c.f.* 4.75×10^{-4} s^{-1} for *rac*-LA). This reinforces the notion that the selectivity arises through a CEC mechanism. On the other hand, when using **8c**, the polymerisation was about twice as fast as with *rac*-LA (Table 7, Entry 2). This can be traced to the initiator being slightly isoselective and therefore preferring subsequent insertion of the same monomer.

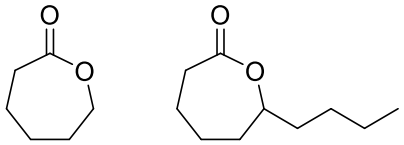
To gain a further understanding regarding the mechanism of polymerisation of an enantiopure substrate, the catalyst order was determined *via* the use of the normalised time scale method. Compared to *rac*-LA polymerisation, the order in catalyst did not change much. Complexes **2** and **8c** exhibited an order of 0.9 and 1.0 respectively, indicating that the rate-determining step proceeds through a largely monomeric species (Figures B101 and B103). In the case of **2**, this is a further indicator of the polymerisation proceeding through a CEC mechanism.

Polymerisations of *meso*-LA using **2** proceeded twice as fast as for *rac*-LA (Table 7, Entry 3) which was unusual. When Kricheldorf and co-workers first polymerised *meso*-LA using Al(III) and Sn(II) initiators, they observed a substantially lower rate compared to the polymerisation of *rac*-LA.[147, 148] This was attributed to the *trans* configuration of the methyl groups lending the monomer increased thermodynamic stability. This was observed experimental studies carried out by the groups of Coates and Feijen,[149-151] and highlighted with computational studies by Jitonnom and Meelua.[152] The inverse is true for **2**, which could be attributed to the *meso*-LA possessing two centres of opposite chirality, giving the initiator a greater freedom of choice. Not only does **2** polymerise *meso*-LA faster than *rac*-LA; previously reported Al-based catalysts require temperatures above 60 °C for the polymerisation to occur. However, the high

stereoselectivity of **2** was not carried over. The polymers exhibited a P_m of 0.54, conducive to a slight heterotactic bias (See Appendix C).

As was the case with **2**, the activity of **8c** with *meso*-LA was unprecedented, approaching full conversion within 40 minutes, which is twice as fast as **2** (Table 7, Entry 4). The resulting polymer was slightly heterotactic, exhibiting a P_m of 0.58.

2.4.3 Polymerisation of ε-CL and ε-DL



ε-CL **ε-DL**

Chart 7. Structures of ε-CL and ε-DL

The polymerisation of ε-CL was explored to probe the effect of ring-size on the polymerisation. Furthermore, upon opening, the polymer chain forms a primary alkoxide which may lend itself to different reactivities for subsequent insertions. The polymerisation of ε-DL was also tested, having the same ring size as ε-CL. However, the butyl chain present at the ε-position of the ring results in the formation of a secondary alcohol which may result in different overall reactivities to ε-CL. ε-DL has received relatively little attention in the polymer industry,[153-155] despite being a naturally occurring monomer that can be produced through fungal technology.[156, 157] It has been shown that ε-DL can be used as a comonomer to increase thermal resilience and elasticity of the resulting copolymer.[158, 159]

Table 8. Polymerisation of ε-CL and ε-DL using **2** and **8c**

Entry	Complex	Monomer	Time (min)	Conv.[a] (%)	$M_{n(SEC)}$ (Đ)[b] (kg/mol)	$M_{n(calc).}$[c] (kg/mol)	k_{app} (s^{-1})
1	**2**	ε-CL	1260	61	44.7 (1.4)	7.0	2.07×10^{-5}
2	**8c**	ε-CL	1260	60	10.8 (1.3)	6.9	1.24×10^{-5}
3	**2**	ε-DL	1395	86	21.7 (1.1)	14.6	2.38×10^{-5}
4	**8c**	ε-DL	660	89	28.4 (1.2)	15.1	6.16×10^{-5}

Reaction conditions: Al/M = 1/100, $[M]_0$ = 1 mol.L^{-1}, 25 °C, THF; a) Determined by ^{1}H NMR by relative integration of signals at 5.06 ppm (monomer) and 5.20 ppm (polymer); b) Determined by SEC calibrated with polystyrene standards in $CDCl_3$ and corrected (see ESI); c) Calculated using the conversion;

Complexes **2** and **8c** can polymerise ε-CL, albeit with a significant loss in control (Table 8, Entries 1 and 2). The polymerisation using **2** was considerably active at the beginning, converting 34 % within 4 hours, but eventually slowed down with time. After 21 hours a conversion of 61 % was achieved, and the resulting polymer showed high discrepancies between the expected and measured M_n (7.0 *vs*. 44.7 kg/mol) as well as a high dispersity (1.4). This may be due to the opening of the ε-CL forming a primary alkoxide on the metal centre, as opposed to a secondary alcohol obtained from the opening of LA, which can give the complex a propensity to dimerise as it reduces the steric bulk around the metal centre. Previous results within the group have shown that the benzyloxy-analogue of **2** is a dimer that cannot be broken in solution and thus does not polymerise any monomer. It is suspected that the opening of ε-CL slowly deactivates the catalytic species in solution, eventually leaving only a small number to proceed with polymerisation. This explains the high difference between the expected and measured M_n. Complex **8c** did not exhibit such discrepancies, but it is thought that the primary alkoxide formed by the opened ε-CL molecule still hampers polymerisation.

The order in catalyst for **8c** was determined using the normalised time scale method and was found to be 0.65. As previously observed by others, this is indicative of the formation of an inactive dimeric species which must break down prior to continuing with the polymerisation. The importance of the alkoxide can thus not be understated as it can have a profound impact on activity.

The polymerisation of ε-DL (Chart 7) was thus probed as its opening results in the formation of a secondary alkoxide upon opening of the monomer, which should prevent the deactivation of the catalyst. As a matter of fact, the polymerisation of ε-DL by **2** proceeds without any sign of catalyst deactivation (Table 8, Entry 3; Figure B31), with the resulting polymer M_n being closer to what is expected. Likewise, polymerisation using **8c** resulted in a 5-fold increase in activity, polymerising 89 % in 11 hours (Table 8, Entry 4). This indicates that the nature of the alkoxide is an important aspect to consider when employing **2** and **8c**. It must be added that these, to my knowledge, are the first aluminium-based catalysts reported for polymerisation of ε-DL.

2.4.4 Polymerisation of Other Monomers

Further testing was carried out on other monomers to get a clearer picture of the scope in which **2** and **8c** can be employed (Chart 8).

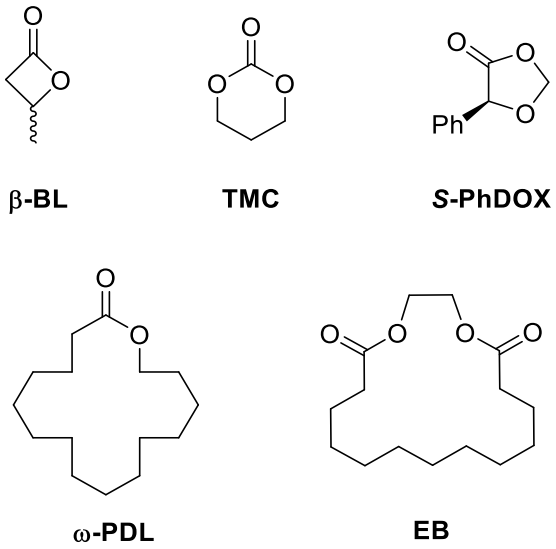
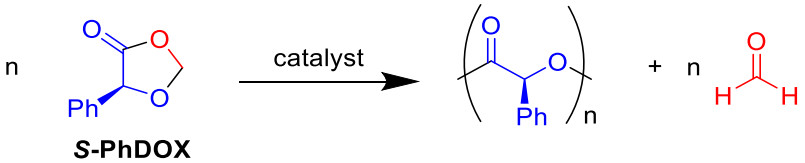


Chart 8. Other monomers employed for this scope test

As discussed in Section 1.2.3, β-BL is an attractive monomer that is interesting to investigate due to its low reactivity with aluminium complexes despite its high ring strain. Macrolactones (n > 10) were investigated since their low ring strain makes their polymerisation particularly difficult, and thus entropy-driven as opposed to enthalpy-driven. These are derived from fatty acids and the properties of the resulting polymers mimic those of polyethylene,[160-163] which has garnered attention in the research community. The chosen macrolactones were ω-pentadecalactone (ω-PDL) and ethylene brassylate (EB). Finally, monomers bearing different functional groups were included. One being trimethylene carbonate (TMC), a six-membered carbonate ester which is bio-degradable and finds its applications in the biomedical industry.[164, 165] Another interesting monomer class were 1,3-dioxolan-4-ones (DOX), developed by the Shaver group, which upon polymerisation produce poly(α-hydroxy acid)s and release an equivalent of formaldehyde or ketone, hence driving the reaction (Scheme 13).[166, 167]



Scheme 11. ROP of S-PhDOX showing formation poly(α-hydroxy acid) and release of formaldehyde

Table 9. Polymerisation of β-BL, TMC, PDL, EB, and *S*-PhDOX using **2** and **8c**

Entry	Complex	Monomer	Solvent	T (°C)	Time (min)	Conv.[a] (%)	$M_{n(SEC)}$ (Đ)[b] (kg/mol)	$M_{n(calc).}$[c] (kg/mol)	k_{app} (s^{-1})
1	**2**	β-BL	THF	25	600	74	5.3 (1.1)	6.4	3.74×10^{-5}
2	**8c**	β-BL	THF	25	240	57	4.1 (1.1)	5.8	7.32×10^{-5}
3	**2**	TMC	THF	25	90	56	11.4 (2.3)	5.7	1.03×10^{-4}
4	**8c**	TMC	THF	25	1400	74	22.3 (1.4)	7.5	1.63×10^{-5}
5	**2**	ω-PDL	Toluene	100	360	15	14.4 (1.5)	3.6	-
6	**8c**	ω-PDL	Toluene	100	360	6	5.2 (1.6)	1.4	-
7	**2**	EB	Toluene	90	960	0	-	-	-
8	**8c**	EB	Toluene	90	960	0	-	-	-
9	**2**	*S*-PhDOX	Toluene	100	960	0	-	-	-
10	**8c**	*S*-PhDOX	Toluene	100	960	0	-	-	-

Reaction conditions: Al/M = 1/100, $[M]_0$ = 1 mol.L^{-1}; a) Determined by ^{1}H NMR by relative integration of monomer and polymer signals (see ESI); b) Determined by SEC calibrated with polystyrene standards in $CDCl_3$ and corrected (see ESI); c) Calculated using the conversion;

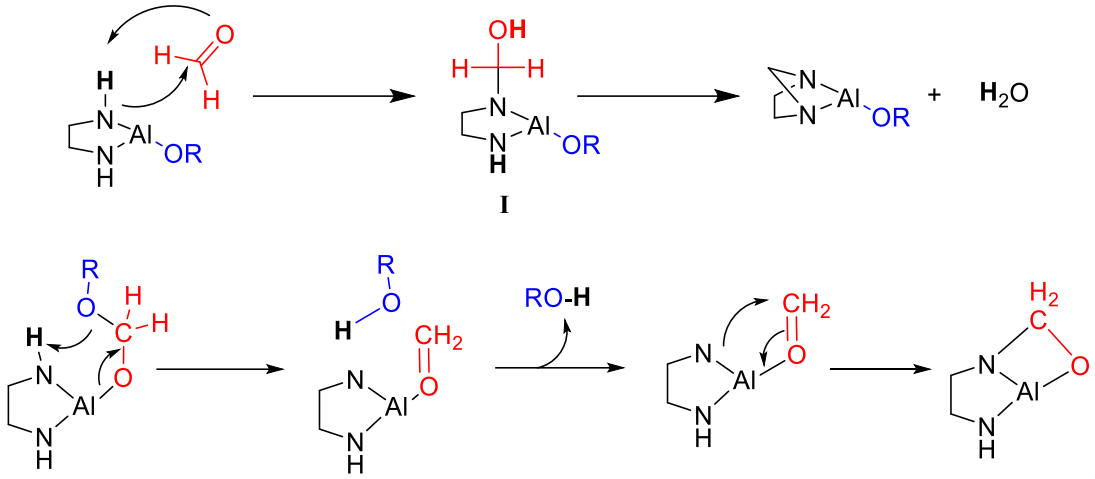
The results concerning β-BL were surprising, with **2** and **8c** showing moderate activity at room temperature (Table 9, Entries 1 and 2). Complex **8c** was twice as fast as **2**, converting 57 % in 4 hours and yielding a k_{app} of 7.32×10^{-5} s^{-1} (*c.f.* 3.74×10^{-5} s^{-1} for **2**). A look at the log plot however reveals a considerable lag time, indicating that the dimeric structure of **8c** may have trouble breaking down in the presence of the monomer (Figure B37). The high activity exhibited by **2** and **8c** comes with a cost: the resulting polymer exhibits little stereoregularity (P_r = 0.47 and 0.57 respectively; See Appendix C).

While the monomer has been continuously employed to tune thermal properties or biodegradability,[132, 168-173] homo-polymerisations using Al-based complexes were less investigated as they can result in undesirable properties (See Section 1.2.3). Generally, the polymerisation of β-BL proceeds slower than that of *rac*-LA and requires higher temperatures. Nomura and co-workers found that aluminium complexes bearing a phenoxy-imine ligand required 6 days at 70 °C to reach 82 % conversion.[174] Another group with the same name conducted structure activity relationship studies with this scaffold and found that minor changes in the structure can lead to loss of its propensity to polymerise β-BL.[175] Unpublished results by Carpentier and Guillaume showed that a $Al(OTf)_3$/BnOH system can function at 60 °C leading to 35 % conversion in 30 minutes.[176]

Regarding the polymerisation of TMC, not many aluminium catalysts have been reported. Most require temperatures above 70 °C to proceed,[177-179] except for a complex reported by Dagorne and co-workers.[180] The N'O'N-supported tetracoordinate aluminium complex can reach up to 90 % conversion in 5 minutes with good control. Complex **2** was capable of polymerising TMC at room temperature, albeit at lower activities (Table 9, Entry 3). The discrepancy between calculated and measured M_n, as well as the very high dispersity of the polymer, indicate that similar deactivation processes as in the case of ε-CL might be in place. A look at the log plot (Figure B39) reveals a sharp drop in activity after the first data point, suggesting that the primary alkoxide formed by the opening of the TMC may promote the dimerisation and subsequent deactivation of the catalyst. This notion was reinforced using **8c** (Table 9, Entry 4), which formed polymers that differ highly from the expected M_n (22.3 *vs.* 7.5 kg/mol). The log-plot shows a straight line that passes through the origin, indicating that the primary alcohol merely slows down the polymerisation rate and does not deactivate the catalytic species (Figure B40).

Interestingly, complexes **2** and **8c** were only able to polymerise ω-PDL out of the entropy-driven monomers (Table 9, Entries 5-10), requiring a temperature of 100 °C to proceed with the polymerisation. These polymerisations only reached conversions up to 15 % with the polymer having substantially higher molecular weights than was expected. The high dispersity (Đ > 1.5) suggests that the complexes may also form stable dimeric complexes due to the primary alkoxide formed upon ring-opening of ω-PDL.

EB and *S*-PhDOX were not polymerised at either room temperature or elevated temperatures (up to 90 °C). The monomers differ from the ones previously tested in the sense that the thermodynamic driving force of their polymerisation is an increase in entropy as opposed to a release in enthalpy. The macrolactones may be too big to take full advantage of the NH moieties of the complexes. Furthermore, while smaller lactones adopt a cisoid conformation, macrolactones lack ring strain which results in them adopting a transoid conformation.[181] This can make the ester moiety less accessible for NCI formation, resulting in low activities. A further increase in temperature may facilitate polymerisation by helping to overcome the activation energy as well as increasing the contribution of entropy towards the spontaneity of the reaction ($\Delta G = \Delta H - T\Delta S$).



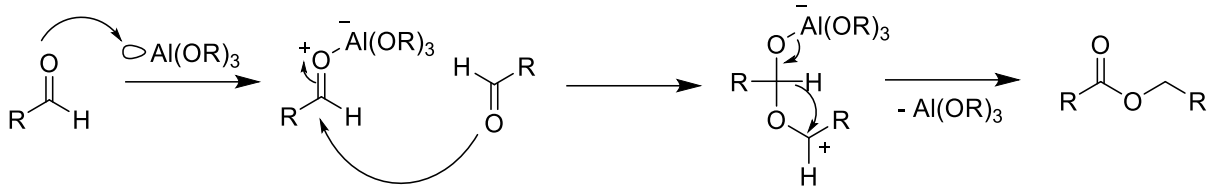
Scheme 12. Possible deactivation pathways of aluminium complexes by formaldehyde

The inactivity towards *S*-PhDOX was particularly interesting. Polymerisations of this monomer run by Shaver and co-workers used an aluminium salen complex tethered by a 1,3-propanediamine.[167] It was suspected that the NH moieties on **2** and **8c** were the reason why these catalysts were inactive. The opening of one equivalent of *S*-PhDOX results in the release of one equivalent of formaldehyde which may react with the acidic NH groups in a similar fashion as in the Mannich reaction (Scheme 14). Not only does this reaction lead to the loss of the NH moiety, but the intermediate (**I**) can react with another equivalent of the secondary amine to form a methylenebisamine which would also result in a drastic change in reactivity. Indeed, research conducted by Fernandez and Butler,[182] as well as Wagner,[183] show this to be a feasible route at room temperature. The release of an equivalent of water may react with the aluminium metal centre to form a hydroxo complex, leading to a complete deactivation. This theory of deactivation was tested by adding 20 equivalents of benzaldehyde to a polymerisation mixture of **2** and *rac*-LA. If the polymerisation does not proceed, then that indicates a decomposition reaction between the catalyst and the benzaldehyde. However, over multiple runs, no deactivation occurred. This indicates that benzaldehyde is either not reactive enough, or that another process is responsible for the deactivation of the complex.

2.4.5 Reactions using ^{Me}**L**$_2$Al(Et) (**11**)

Due to the lack of reactive NH moieties, the use of the methylated analogue **11** on *S*-PhDOX was investigated. However, employing **11** at temperatures of 25, 50, and 90 °C did not result in any conversion of the starting material. Given that the complex was not reactive towards *rac*-LA, it is still unclear whether the general lack of reactivity of the catam complexes towards

S-PhDOX stems from a side-reaction of the NH groups with the produced formaldehyde, or from general incompatibility.



Scheme 13. Mechanism of the aluminium catalysed Tishchenko reaction

To study this further, **11** was employed in the Tishchenko reaction which involves the disproportionation of 2 equivalents of an aldehyde to form the corresponding ester (Scheme 15).[184] Aluminium-based complexes are particularly effective in the catalysis of this transformation.[185] The reaction was thus used to probe whether the aldehydes deactivate **11**. Using **11** in C_6D_6 with 50 equivalents of benzaldehyde and one equivalent of ^{i}PrOH, the reaction was found to have reached 88% conversion in 5 minutes at room temperature, making this complex particularly active (Figure A13). The aldehyde functionality thus does not appear to be reason for the inactivity of **11** towards *S*-PhDOX and points to an incompatibility of another kind being present.

2.4.6 $H_2^{H}L_1$ and $H_2^{H}L_2$ as Organocatalysts

Given that complexes **2** and **8c** were found to form favourable NCIs during polymerisation, the pro-ligands $H_2^{H}L_1$ and $H_2^{H}L_2$ were tested as organocatalysts for the ROP of *rac*-LA. The solvent that was predominantly used was DCM as the coordinating abilities of THF may hamper the rate of polymerisation. In addition to being a H-bond donor, the systems also require the addition of an alcohol (^{i}PrOH) and a base [(-)-sparteine]. In the absence of a pro-ligand, polymerisations of *rac*-LA were slow, converting only 7 % of the monomer after 24 hours at room temperature (Table 10, Entry 1). Furthermore, the polymerisations were not found to occur in the absence of either ^{i}PrOH or sparteine (Table 10, Entries 2 and 3). However, when all components of the catalytic system were present, an enhancement in activity was observed in which a conversion of 27 % was achieved after 24 hours for $H_2^{H}L_1$ (Table 10, Entry 4). This activity almost doubled when $H_2^{H}L_2$ was employed (Table 10, Entry 5). The catam ligand is thus an interesting molecule as the use of the salan analogue of $H_2^{H}L_1$ hampered the polymerisation (Table 10, Entry 7). Therefore, the presence of NH moieties alone is not

enough to cause activity in the polymerisation. Likely, the distance between the NH groups as well as their arrangement in space is considerably more favourable in the catam ligands, allowing them to mimic the mechanism of thioureas and squaramides.

As expected, when the polymerisation was carried out in THF, the conversion dropped to 4 % indicating that the choice of solvents is crucial in the organocatalysis (Table 10, Entry 6).

Table 10. *rac*-LA ROP catalysed by H_2-^{H}**L1**, $H_2{}^{H}$**L2**, and H_2-salan.

Entry	Cat	Cat./^{i}PrOH/sparteine/LA	Solvent	T (°C)	Time (h)	Conv.[a]	$M_{n(SEC)}$ (Đ)[b] (kg/mol)	$M_{n(calc)}$[c] (kg/mol)
1	-	0/1/1/20	DCM	25	24	7	0.8 (1.3)	1.1
2	$H_2{}^{H}$**L1**	1/0/0/20	DCM	25	67	0	-	-
3	$H_2{}^{H}$**L1**	1/1/0/20	DCM	25	67	0	-	-
4	$H_2{}^{H}$**L1**	1/1/1/20	DCM	25	24	27	1.0 (1.1)	3.8
5	$H_2{}^{H}$**L2**	1/1/1/20	DCM	25	24	50	-	-
6	$H_2{}^{H}$**L1**	1/1/1/20	THF	25	24	4	NA	0.6
7	H_2-**salan**	1/1/1/20	DCM	25	24	0	-	-

Reaction conditions: $[LA]_0$ = 1 mol.L^{-1}; a) Determined by ^{1}H NMR by relative integration of signals at 5.06 ppm (monomer) and 5.20 ppm (polymer); b) Determined by SEC calibrated with polystyrene standards in THF and corrected (see ESI); c) Calculated using the conversion.

2.5 Conclusion

This chapter demonstrated the relative ease in which the catam pro-ligands $H_2{}^{H}$**L1** and $H_2{}^{H}$**L2** can be synthesised and modulated. The NH groups were found to be reactive enough to deuterate the pro-ligands to $D_2{}^{D}$**L1** and $D_2{}^{D}$**L2**. Furthermore, *N*-methylations could be performed *via* a one-step reaction to yield $H_2{}^{Me}$**L1** and $H_2{}^{Me}$**L2**.

The pro-ligands were successfully reacted with $Al(Et)_3$ and various alcohols to yield aluminium alkyl and alkoxide derivatives **1**-**11**. These were successfully characterised using methods such XRD as well as NMR and IR spectroscopy.

Application of the complexes in *rac*-LA polymerisation showed the ^{H}**L** complexes to be very active in polymerisation at room temperature yielding highly heterotactic and slightly isotactic PLA for **2** and **8c** respectively. The use of the deuterated ^{D}**L** complexes resulted in a decrease in activity indicating that the NH moieties play an important role in the polymerisation which was substantiated by DFT calculations. The substrate was found to bind onto the NH groups,

which suitably orients and withdraws electron density from the monomer prior to nucleophilic attack. The polymerisation was found to only occur at elevated temperatures upon use of the ^{Me}**L** complexes, further substantiating the claims.

Polymerisations carried out on a variety of monomers showed the protonated complexes to be active at room temperature in the polymerisation of *L*-LA, *meso*-LA, ε-CL, ε-DL, β-BL, and TMC. Despite the absence of stereoselectivities for *meso*-LA and β-BL, catam catalysts were found to be highly versatile toward lactone ROP. However, ROP of entropy-driven monomers such as PDL, EB, and *S*-PhDOX remains challenging.

The catam ligand is a promising ligand scaffold which affords highly active catalysts for lactone ROP. Owing to these positive results, the catam family was explored further in the subsequent chapters by modification of the scaffold.

2.6 References

1. IUPAC, *Compendium of Chemical Terminology*. Blackwell Scientific Publications: Oxford, 1997.
2. Smith, M. B.; March, J., Localized Chemical Bonding. In *March's Advanced Organic Chemistry*, 2006; pp 3-31.
3. Miessler, G. L., Tarr, D. A., *Inorganic Chemistry*. Upper Saddle River, N. J., 1999.
4. Pauling, L., *J. Am. Chem. Soc.* **1931,** *53*, 1367-1400.
5. Ouellette, R. J.; Rawn, J. D., 1 - Structure of Organic Compounds. In *Principles of Organic Chemistry*, Ouellette, R. J.; Rawn, J. D., Eds. Elsevier: Boston, 2015; pp 1-32.
6. Lide, D. R., *CRC Handbook of Chemistry and Physics*. CRC Press: 2010; Vol. 101st ed.
7. Waals, J. D. v. d. Over de continuiteit van den gas- en vloeistoftoestand. Leiden, 1873.
8. Černý, J.; Hobza, P., *Phys. Chem. Chem. Phys.* **2007,** *9*, 5291-5303.
9. Lodish, H.; Berk, A.; Zipursky, S.; Matsudaira, P.; Baltimore, D.; Darnell, J., Noncovalent Bonds. In *Molecular Cell Biology*, 4th Edition ed.; W. H. Freeman: New York, 2000.
10. Müller-Dethlefs, K.; Hobza, P., *Chem. Rev.* **2000,** *100*, 143-168.

11. Mahmudov, K. T.; Kopylovich, M. N.; Guedes da Silva, M. F. C.; Pombeiro, A. J. L., *Noncovalent Interactions in Catalysis*. RSC Publishing: 2019.
12. Neel, A. J.; Hilton, M. J.; Sigman, M. S.; Toste, F. D., *Nature* **2017,** *543*, 637-646.
13. Anjana, R.; Vaishnavi, M. K.; Sherlin, D.; Kumar, S. P.; Naveen, K.; Kanth, P. S.; Sekar, K., *Bioinformation* **2012,** *8*, 1220-1224.
14. Burley, S. K.; Petsko, G. A., *FEBS Lett.* **1986,** *203*, 139-143.
15. Purdue, U. o. Dipole-Dipole Forces. https://www.chem.purdue.edu/gchelp/liquids/dipdip.html (accessed 15/04/2020).
16. Chapter 4 - Biophysical Principles. In *Cell Biology (Third Edition)*, Pollard, T. D.; Earnshaw, W. C.; Lippincott-Schwartz, J.; Johnson, G. T., Eds. Elsevier: 2017; pp 53-62.
17. Frank, H. S.; Evans, M. W., *J. Chem. Phys.* **1945,** *13*, 507-532.
18. Meyer, E. E.; Rosenberg, K. J.; Israelachvili, J., *Proc. Natl. Acad. Sci. U. S. A.* **2006,** *103*, 15739-15746.
19. Scheiner, S., *J. Indian I. Sci.* **2020,** *100*, 61-76.
20. Szalewicz, K., Hydrogen Bond. In *Encyclopedia of Physical Science and Technology (Third Edition)*, Meyers, R. A., Ed. Academic Press: New York, 2003; pp 505-538.
21. Cavallo, G.; Metrangolo, P.; Milani, R.; Pilati, T.; Priimagi, A.; Resnati, G.; Terraneo, G., *Chem. Rev.* **2016,** *116*, 2478-2601.
22. Biswal, H. S.; Wategaonkar, S., *J. Phys. Chem. A* **2009,** *113*, 12774-12782.
23. Hansen, A. S.; Du, L.; Kjaergaard, H. G., *The Journal of Physical Chemistry Letters* **2014,** *5*, 4225-4231.
24. Schmidbaur, H., *Angew. Chem. Int. Edit.* **2019,** *58*, 5806-5809.
25. Warshel, A.; Sharma, P. K.; Kato, M.; Xiang, Y.; Liu, H.; Olsson, M. H. M., *Chem. Rev.* **2006,** *106*, 3210-3235.
26. Davis, H. J.; Phipps, R. J., *Chem. Sci.* **2017,** *8*, 864-877.
27. Knowles, R. R.; Jacobsen, E. N., *Proc. Natl. Acad. Sci. U. S. A.* **2010,** *107*, 20678-20685.
28. Hammes, G. G.; Benkovic, S. J.; Hammes-Schiffer, S., *Biochemistry* **2011,** *50*, 10422-10430.
29. Guo, H.; Salahub, D. R., *Angew. Chem. Int. Edit.* **1998,** *37*, 2985-2990.
30. Anderson, V., Ground State Destabilization. 2001.
31. Robinson, R., *PLOS Biol.* **2013,** *11*, e1001600.

32. Jindal, G.; Ramachandran, B.; Bora, R. P.; Warshel, A., *ACS Catal.* **2017,** *7*, 3301-3305.
33. *Nature* **1925,** *116*, 744-744.
34. Knowles, J. R., *Nature* **1991,** *350*, 121-124.
35. Bornscheuer, U. T.; Huisman, G. W.; Kazlauskas, R. J.; Lutz, S.; Moore, J. C.; Robins, K., *Nature* **2012,** *485*, 185-194.
36. Toste, F. D.; Sigman, M. S.; Miller, S. J., *Accounts Chem. Res.* **2017,** *50*, 609-615.
37. Richard, J. P., *J. Am. Chem. Soc.* **1984,** *106*, 4926-4936.
38. Mahmudov, K. T.; Gurbanov, A. V.; Guseinov, F. I.; Guedes da Silva, M. F. C., *Coord. Chem. Rev.* **2019,** *387*, 32-46.
39. Raynal, M.; Ballester, P.; Vidal-Ferran, A.; Van Leeuwen, P., W N M, *Chem. Soc. Rev.* **2014,** *43*, 1660-1733.
40. Grabowski, S. J., *Chem. Rev.* **2011,** *111*, 2597-2625.
41. Bickelhaupt, F. M.; Baerends, E. J., *Angew. Chem. Int. Edit.* **2003,** *42*, 4183-4188.
42. Weinhold, F., *Angew. Chem. Int. Edit.* **2003,** *42*, 4188-4194.
43. Matta, C. F.; Hernández-Trujillo, J.; Tang, T.-H.; Bader, R. F. W., *Chem. Eur. J.* **2003,** *9*, 1940-1951.
44. Riley, K. E.; Pitoňák, M.; Jurečka, P.; Hobza, P., *Chem. Rev.* **2010,** *110*, 5023-5063.
45. Johnson, E. R.; Keinan, S.; Mori-Sánchez, P.; Contreras-García, J.; Cohen, A. J.; Yang, W., *J. Am. Chem. Soc.* **2010,** *132*, 6498-6506.
46. Contreras-García, J.; Johnson, E. R.; Keinan, S.; Chaudret, R.; Piquemal, J.-P.; Beratan, D. N.; Yang, W., *J Chem Theory Comput* **2011,** *7*, 625-632.
47. Mati, I. K.; Cockroft, S. L., *Chem. Soc. Rev.* **2010,** *39*, 4195-4205.
48. Hunter, C. A., *Angew. Chem. Int. Edit.* **2004,** *43*, 5310-5324.
49. Peris, E.; Lee, J. C.; Rambo, J. R.; Eisenstein, O.; Crabtree, R. H., *J. Am. Chem. Soc.* **1995,** *117*, 3485-3491.
50. Wheeler, S. E.; Seguin, T. J.; Guan, Y.; Doney, A. C., *Accounts Chem. Res.* **2016,** *49*, 1061-1069.
51. Trouvé, J.; Gramage-Doria, R., *Chem. Soc. Rev.* **2021,** *50*, 3565-3584.
52. Breit, B.; Seiche, W., *J. Am. Chem. Soc.* **2003,** *125*, 6608-6609.
53. Park, J.; Lang, K.; Abboud, K. A.; Hong, S., *J. Am. Chem. Soc.* **2008,** *130*, 16484-16485.
54. Park, J.; Lang, K.; Abboud, K. A.; Hong, S., *Chem. Eur. J.* **2011,** *17*, 2236-2245.

55. Hashiguchi, S.; Fujii, A.; Takehara, J.; Ikariya, T.; Noyori, R., *J. Am. Chem. Soc.* **1995,** *117*, 7562-7563.
56. Ohkuma, T.; Ooka, H.; Hashiguchi, S.; Ikariya, T.; Noyori, R., *J. Am. Chem. Soc.* **1995,** *117*, 2675-2676.
57. Noyori, R.; Hashiguchi, S., *Accounts Chem. Res.* **1997,** *30*, 97-102.
58. Zhao, B.; Han, Z.; Ding, K., *Angew. Chem. Int. Edit.* **2013,** *52*, 4744-4788.
59. Ikariya, T.; Murata, K.; Noyori, R., *Org. Biomol. Chem.* **2006,** *4*, 393-406.
60. Clapham, S. E.; Hadzovic, A.; Morris, R. H., *Coord. Chem. Rev.* **2004,** *248*, 2201-2237.
61. Sigman, M. S.; Jacobsen, E. N., *J. Am. Chem. Soc.* **1998,** *120*, 4901-4902.
62. Zhang, Z.; Schreiner, P. R., *Chem. Soc. Rev.* **2009,** *38*, 1187-1198.
63. Takemoto, Y., *Chem. Pharm. Bull.* **2010,** *58*, 593-601.
64. Brière, J. F.; Oudeyer, S.; Dalla, V.; Levacher, V., *Chem. Soc. Rev.* **2012,** *41*, 1696-1707.
65. Brak, K.; Jacobsen, E. N., *Angew. Chem. Int. Edit.* **2013,** *52*, 534-561.
66. Serdyuk, O. V.; Heckel, C. M.; Tsogoeva, S. B., *Org. Biomol. Chem.* **2013,** *11*, 7051-7071.
67. Auvil, T. J.; Schafer, A. G.; Mattson, A. E., *Eur. J. Org. Chem.* **2014,** *2014*, 2633-2646.
68. Nishikawa, Y., *Tetrahedron Lett.* **2018,** *59*, 216-223.
69. Saito, J.; Mitani, M.; Mohri, J.-i.; Yoshida, Y.; Matsui, S.; Ishii, S.-i.; Kojoh, S.-i.; Kashiwa, N.; Fujita, T., *Angew. Chem. Int. Edit.* **2001,** *40*, 2918-2920.
70. Mitani, M.; Mohri, J.-i.; Yoshida, Y.; Saito, J.; Ishii, S.; Tsuru, K.; Matsui, S.; Furuyama, R.; Nakano, T.; Tanaka, H.; Kojoh, S.-i.; Matsugi, T.; Kashiwa, N.; Fujita, T., *J. Am. Chem. Soc.* **2002,** *124*, 3327-3336.
71. Suzuki, Y.; Tanaka, H.; Oshiki, T.; Takai, K.; Fujita, T., *Chem. Asian J.* **2006,** *1*, 878-887.
72. Saito, J.; Mitani, M.; Onda, M.; Mohri, J.-I.; Ishii, S.-I.; Yoshida, Y.; Nakano, T.; Tanaka, H.; Matsugi, T.; Kojoh, S.-I.; Kashiwa, N.; Fujita, T., *Macromol. Rapid. Comm.* **2001,** *22*, 1072-1075.
73. Tian, J.; Hustad, P. D.; Coates, G. W., *J. Am. Chem. Soc.* **2001,** *123*, 5134-5135.
74. Talarico, G.; Busico, V.; Cavallo, L., *Organometallics* **2004,** *23*, 5989-5993.

75. Matsui, S.; Mitani, M.; Saito, J.; Tohi, Y.; Makio, H.; Matsukawa, N.; Takagi, Y.; Tsuru, K.; Nitabaru, M.; Nakano, T.; Tanaka, H.; Kashiwa, N.; Fujita, T., *J. Am. Chem. Soc.* **2001,** *123*, 6847-6856.
76. Weberski, M. P.; Chen, C.; Delferro, M.; Zuccaccia, C.; Macchioni, A.; Marks, T. J., *Organometallics* **2012,** *31*, 3773-3789.
77. Zuideveld, M. A.; Wehrmann, P.; Röhr, C.; Mecking, S., *Angew. Chem. Int. Edit.* **2004,** *43*, 869-873.
78. Göttker-Schnetmann, I.; Wehrmann, P.; Röhr, C.; Mecking, S., *Organometallics* **2007,** *26*, 2348-2362.
79. Popeney, C. S.; Rheingold, A. L.; Guan, Z., *Organometallics* **2009,** *28*, 4452-4463.
80. Iwashita, A.; Chan, M. C. W.; Makio, H.; Fujita, T., *Catal. Sci. Technol.* **2014,** *4*, 599-610.
81. Busico, V., *MRS Bull.* **2013,** *38*, 224-228.
82. Chen, C., *Nat. Rev. Chem.* **2018,** *2*, 6-14.
83. Hormnirun, P.; Marshall, E. L.; Gibson, V. C.; White, A. J. P.; Williams, D. J., *J. Am. Chem. Soc.* **2004,** *126*, 2688-2689.
84. Marshall, E. L.; Gibson, V. C.; Rzepa, H. S., *J. Am. Chem. Soc.* **2005,** *127*, 6048-6051.
85. Amgoune, A.; Thomas, C. M.; Ilinca, S.; Roisnel, T.; Carpentier, J.-F., *Angew. Chem. Int. Edit.* **2006,** *45*, 2782-2784.
86. Amgoune, A.; Thomas, C. M.; Roisnel, T.; Carpentier, J.-F., *Chem. Eur. J.* **2006,** *12*, 169-179.
87. Amgoune, A.; Thomas, C. M.; Carpentier, J.-F., **2007,** *79*, 2013.
88. Bouyahyi, M.; Ajellal, N.; Kirillov, E.; Thomas, C. M.; Carpentier, J.-F., *Chem. Eur. J.* **2011,** *17*, 1872-1883.
89. Klitzke, J. S.; Roisnel, T.; Kirillov, E.; Casagrande, O. d. L.; Carpentier, J.-F., *Organometallics* **2014,** *33*, 5693-5707.
90. Klitzke, J. S.; Roisnel, T.; Kirillov, E.; Casagrande, O. d. L.; Carpentier, J.-F., *Organometallics* **2014,** *33*, 309-321.
91. Ligny, R.; Hänninen, M. M.; Guillaume, S. M.; Carpentier, J.-F., *Angew. Chem. Int. Edit.* **2017,** *56*, 10388-10393.
92. Ligny, R.; Hänninen, M. M.; Guillaume, S. M.; Carpentier, J.-F., *Chem. Comm.* **2018,** *54*, 8024-8031.

93. Sarazin, Y.; Liu, B.; Roisnel, T.; Maron, L.; Carpentier, J.-F., *J. Am. Chem. Soc.* **2011,** *133*, 9069-9087.
94. Liu, B.; Roisnel, T.; Sarazin, Y., *Inorg. Chim. Acta* **2012,** *380*, 2-13.
95. Liu, B.; Roisnel, T.; Maron, L.; Carpentier, J.-F.; Sarazin, Y., *Chem. Eur. J.* **2013,** *19*, 3986-3994.
96. Sarazin, Y.; Carpentier, J.-F., CHAPTER 4 Secondary (Agostic Si–H/Electrostatic C–F) Interactions in Alkaline Earth-based Catalysts. In *Noncovalent Interactions in Catalysis*, The Royal Society of Chemistry: 2019; pp 94-121.
97. Khusnutdinova, J. R.; Milstein, D., *Angew. Chem. Int. Edit.* **2015,** *54*, 12236-12273.
98. Benhamou, L.; Chardon, E.; Lavigne, G.; Bellemin-Laponnaz, S.; César, V., *Chem. Rev.* **2011,** *111*, 2705-2733.
99. Min, K. S.; Weyhermüller, T.; Bothe, E.; Wieghardt, K., *Inorg. Chem.* **2004,** *43*, 2922-2931.
100. Kragh, H., *arXiv* **2011**.
101. Meppelder, G.-J. M.; Fan, H.-T.; Spaniol, T. P.; Okuda, J., *Organometallics* **2009,** *28*, 5159-5165.
102. Addison, A. W.; Rao, T. N.; Reedijk, J.; van Rijn, J.; Verschoor, G. C., *J. Chem. Soc., Dalton Trans.* **1984**, 1349-1356.
103. Ian Storer, R.; Aciro, C.; Jones, L. H., *Chem. Soc. Rev.* **2011,** *40*, 2330-2346.
104. Quiñonero, D.; Prohens, R.; Garau, C.; Frontera, A.; Ballester, P.; Costa, A.; Deyà, P. M., *Chem. Phys. Lett.* **2002,** *351*, 115-120.
105. Quiñonero, D.; Frontera, A.; Suñer, G. A.; Morey, J.; Costa, A.; Ballester, P.; Deyà, P. M., *Chem. Phys. Lett.* **2000,** *326*, 247-254.
106. Jeffrey, G. A., *An Introduction to Hydrogen Bonding*. Oxford University Press: New York, 1997.
107. Dagorne, S.; Bellemin-Laponnaz, F., Coordination Chemistry and Applications of Salen, Salan and Salalen Metal Complexes. In *PATAI'S Chemistry of Functional Groups*.
108. Tang, Z.; Chen, X.; Pang, X.; Yang, Y.; Zhang, X.; Jing, X., *Biomacromolecules* **2004,** *5*, 965-970.
109. Nomura, N.; Ishii, R.; Yamamoto, Y.; Kondo, T., *Chem. Eur. J.* **2007,** *13*, 4433-4451.
110. Nomura, N.; Ishii, R.; Yamamoto, Y.; Kondo, T., *Chem. Eur. J.* **2007,** *13*, 4433-4451.

111. Hild, F.; Haquette, P.; Brelot, L.; Dagorne, S., *Dalton Trans.* **2010,** *39*, 533-540.
112. Robert, C.; Schmid, T. E.; Richard, V.; Haquette, P.; Raman, S. K.; Rager, M.-N.; Gauvin, R. M.; Morin, Y.; Trivelli, X.; Guérineau, V.; del Rosal, I.; Maron, L.; Thomas, C. M., *J. Am. Chem. Soc.* **2017,** *139*, 6217-6225.
113. Anker, M.; Balasanthiran, C.; Balasanthiran, V.; Chisholm, M. H.; Jayaraj, S.; Mathieu, K.; Piromjitpong, P.; Praban, S.; Raya, B.; Simonsick, W. J., *Dalton Trans.* **2017,** *46*, 5938-5945.
114. Praban, S.; Piromjitpong, P.; Balasanthiran, V.; Jayaraj, S.; Chisholm, M. H.; Tantirungrotechai, J.; Phomphrai, K., *Dalton Trans.* **2019,** *48*, 3223-3230.
115. Schnee, G.; Bolley, A.; Hild, F.; Specklin, D.; Dagorne, S., *Catal. Today* **2017,** *289*, 204-210.
116. Lee, C.-L.; Lin, Y.-F.; Jiang, M.-T.; Lu, W.-Y.; Vandavasi, J. K.; Wang, L.-F.; Lai, Y.-C.; Chiang, M. Y.; Chen, H.-Y., *Organometallics* **2017,** *36*, 1936-1945.
117. Platel, R. H.; Hodgson, L. M.; Williams, C. K., *Polym. Rev.* **2008,** *48*, 11-63.
118. Press, K.; Goldberg, I.; Kol, M., *Angew. Chem. Int. Edit.* **2015,** *54*, 14858-14861.
119. Nielsen, C. D. T.; Burés, J., *Chem. Sci.* **2019,** *10*, 348-353.
120. Burés, J., *Angew. Chem. Int. Edit.* **2016,** *55*, 2028-2031.
121. Chen, C.; Bai, Z.; Cui, Y.; Cong, Y.; Pan, X.; Wu, J., *Macromolecules* **2018,** *51*, 6800-6809.
122. Fieser, M. E.; Sanford, M. J.; Mitchell, L. A.; Dunbar, C. R.; Mandal, M.; Van Zee, N. J.; Urness, D. M.; Cramer, C. J.; Coates, G. W.; Tolman, W. B., *J. Am. Chem. Soc.* **2017**.
123. Schütze, M.; Dechert, S.; Meyer, F., *Chem. Eur. J.* **2017,** *23*, 16472-16475.
124. Abel, B. A.; Lidston, C. A. L.; Coates, G. W., *J. Am. Chem. Soc.* **2019,** *141*, 12760-12769.
125. Kamber, N. E.; Jeong, W.; Waymouth, R. M.; Pratt, R. C.; Lohmeijer, B. G. G.; Hedrick, J. L., *Chem. Rev.* **2007,** *107*, 5813-5840.
126. Thomas, C.; Bibal, B., *Green Chem.* **2014,** *16*, 1687-1699.
127. Coderre, D. N.; Fastnacht, K. V.; Wright, T. J.; Dharmaratne, N. U.; Kiesewetter, M. K., *Macromolecules* **2018,** *51*, 10121-10126.
128. Lin, B.; Waymouth, R. M., *Macromolecules* **2018,** *51*, 2932-2938.
129. McMurray, J.; Simanek, E., *Fundamentals of Organic Chemistry*. Thomson Brooks/Cole: Belmont, California, 2007.

130. Falivene, L.; Credendino, R.; Poater, A.; Petta, A.; Serra, L.; Oliva, R.; Scarano, V.; Cavallo, L., *Organometallics* **2016,** *35*, 2286-2293.
131. Falivene, L.; Cao, Z.; Petta, A.; Serra, L.; Poater, A.; Oliva, R.; Scarano, V.; Cavallo, L., *Nat. Chem.* **2019,** *11*, 872-879.
132. García-Valle, F. M.; Tabernero, V.; Cuenca, T.; Mosquera, M. E. G.; Cano, J.; Milione, S., *Organometallics* **2018,** *37*, 837-840.
133. Świderek, K.; Paneth, P., *Chem. Rev.* **2013,** *113*, 7851-7879.
134. Knowles, W. S., *Accounts Chem. Res.* **1983,** *16*, 106-112.
135. Gómez-Gallego, M.; Sierra, M. A., *Chem. Rev.* **2011,** *111*, 4857-4963.
136. McKeown, P.; Davidson, M. G.; Kociok-Kohn, G.; Jones, M. D., *Chem. Comm.* **2016,** *52*, 10431-10434.
137. Osten, K. M.; Aluthge, D. C.; Patrick, B. O.; Mehrkhodavandi, P., *Inorg. Chem.* **2014,** *53*, 9897-9906.
138. Stasiw, D. E.; Mandal, M.; Neisen, B. D.; Mitchell, L. A.; Cramer, C. J.; Tolman, W. B., *Inorg. Chem.* **2017,** *56*, 725-728.
139. Stasiw, D. E.; Luke, A. M.; Rosen, T.; League, A. B.; Mandal, M.; Neisen, B. D.; Cramer, C. J.; Kol, M.; Tolman, W. B., *Inorg. Chem.* **2017**.
140. Macaranas, J. A.; Luke, A. M.; Mandal, M.; Neisen, B. D.; Marell, D. J.; Cramer, C. J.; Tolman, W. B., *Inorg. Chem.* **2018**.
141. Miranda, M. O.; DePorre, Y.; Vazquez-Lima, H.; Johnson, M. A.; Marell, D. J.; Cramer, C. J.; Tolman, W. B., *Inorg. Chem.* **2013,** *52*, 13692-13701.
142. Mandal, M.; Luke, A. M.; Dereli, B.; Elwell, C. E.; Reineke, T. M.; Tolman, W. B.; Cramer, C. J., *ACS Catal.* **2019,** *9*, 885-889.
143. Herschlag, D.; Pinney, M. M., *Biochemistry* **2018,** *57*, 3338-3352.
144. Broekaert, J. A. C., *Anal. Bioanal. Chem.* **2015,** *407*, 8943-8944.
145. Ishii, R.; Nomura, N.; Kondo, T., *Polymer Journal* **2004,** *36*, 261-264.
146. Degée, P.; Dubois, P.; Jérôme, R., *Macromol. Chem. Phys.* **1997,** *198*, 1973-1984.
147. Kricheldorf, H. R.; Boettcher, C., *Makromolekul. Chem.* **1993,** *194*, 1653-1664.
148. Kricheldorf, H. R.; Boettcher, C.; Tönnes, K.-U., *Polymer* **1992,** *33*, 2817-2824.
149. Ovitt, T. M.; Coates, G. W., *J. Am. Chem. Soc.* **1999,** *121*, 4072-4073.
150. Du, H.; Velders, A. H.; Dijkstra, P. J.; Sun, J.; Zhong, Z.; Chen, X.; Feijen, J., *Chem. Eur. J.* **2009,** *15*, 9836-9845.
151. Du, H.; Velders, A. H.; Dijkstra, P. J.; Zhong, Z.; Chen, X.; Feijen, J., *Macromolecules* **2009,** *42*, 1058-1066.

152. Jitonnom, J.; Meelua, W., *Chem. Phys. Lett.* **2020,** *750*, 137482.
153. Martello, M. T.; Burns, A.; Hillmyer, M., *ACS Macro. Lett.* **2012,** *1*, 131-135.
154. Chuang, H.-J.; Chen, H.-L.; Huang, B.-H.; Tsai, T.-E.; Huang, P.-L.; Liao, T.-T.; Lin, C.-C., *J. Polym. Sci. Pol. Chem.* **2013,** *51*, 1185-1196.
155. Pitt, G. G.; Gratzl, M. M.; Kimmel, G. L.; Surles, J.; Sohindler, A., *Biomaterials* **1981,** *2*, 215-220.
156. Endrizzi, A.; Pagot, Y.; Clainche, A. L.; Nicaud, J.-M.; Belin, J.-M., *Crit. Rev. Biotechnol.* **1996,** *16*, 301-329.
157. Romero-Guido, C.; Belo, I.; Ta, T. M. N.; Cao-Hoang, L.; Alchihab, M.; Gomes, N.; Thonart, P.; Teixeira, J. A.; Destain, J.; Waché, Y., *Appl. Microbiol. Biot.* **2011,** *89*, 535-547.
158. Olsén, P.; Borke, T.; Odelius, K.; Albertsson, A.-C., *Biomacromolecules* **2013,** *14*, 2883-2890.
159. Schneiderman, D. K.; Hill, E. M.; Martello, M. T.; Hillmyer, M. A., *Polym. Chem.* **2015,** *6*, 3641-3651.
160. Cole-Hamilton, D. J., *Angew. Chem. Int. Edit.* **2010,** *49*, 8564-8566.
161. Pepels, M. P. F.; Hansen, M. R.; Goossens, H.; Duchateau, R., *Macromolecules* **2013,** *46*, 7668-7677.
162. van der Meulen, I.; Gubbels, E.; Huijser, S.; Sablong, R.; Koning, C. E.; Heise, A.; Duchateau, R., *Macromolecules* **2011,** *44*, 4301-4305.
163. Pepels, M. P. F. Exploring the potential of polymacrolactones as polyethylene-mimics. Technische Universiteit Eindhoven, Eindhoven, 2015.
164. Engelberg, I.; Kohn, J., *Biomaterials* **1991,** *12*, 292-304.
165. Nylund, A. M.; Chen, C.-Y.; Höglund, O. V.; Campbell, B. G.; Fransson, B. A., *Vet. Surg.* **2019,** *48*, 845-849.
166. Xu, Y.; Perry, M. R.; Cairns, S. A.; Shaver, M. P., *Polym. Chem.* **2019,** *10*, 3048-3054.
167. Cairns, S. A.; Schultheiss, A.; Shaver, M. P., *Polym. Chem.* **2017,** *8*, 2990-2996.
168. Cross, E. D.; Allan, L. E. N.; Decken, A.; Shaver, M. P., *J. Polym. Sci. Pol. Chem.* **2013,** *51*, 1137-1146.
169. MacDonald, J. P.; Parker, M. P.; Greenland, B. W.; Hermida-Merino, D.; Hamley, I. W.; Shaver, M. P., *Polym. Chem.* **2015,** *6*, 1445-1453.
170. García-Valle, F. M.; Cuenca, T.; Mosquera, M. E. G.; Milione, S.; Cano, J., *Eur. Polym. J.* **2020,** *125*, 109527.

171. Isnard, F.; Carratù, M.; Lamberti, M.; Venditto, V.; Mazzeo, M., *Catal. Sci. Technol.* **2018,** *8*, 5034-5043.
172. Fagerland, J.; Finne-Wistrand, A.; Pappalardo, D., *New J. Chem.* **2016,** *40*, 7671-7679.
173. Matsubara, K.; Eda, K.; Ikutake, Y.; Dan, M.; Tanizaki, N.; Koga, Y.; Yasuniwa, M., *J. Polym. Sci. Pol. Chem.* **2016,** *54*, 2536-2544.
174. Nomura, N.; Aoyama, T.; Ishii, R.; Kondo, T., *Macromolecules* **2005,** *38*, 5363-5366.
175. Iwasa, N.; Fujiki, M.; Nomura, K., *J. Mol. Catal. A Chem.* **2008,** *292*, 67-75.
176. Ajellal, N.; Carpentier, J.-F.; Guillaume, C.; Guillaume, S. M.; Helou, M.; Poirier, V.; Sarazin, Y.; Trifonov, A., *Dalton Trans.* **2010,** *39*, 8363-8376.
177. Yang, J.; Yu, Y.; Li, Q.; Li, Y.; Cao, A., *J. Polym. Sci. Pol. Chem.* **2005,** *43*, 373-384.
178. Darensbourg, D. J.; Ganguly, P.; Billodeaux, D., *Macromolecules* **2005,** *38*, 5406-5410.
179. Koller, J.; Bergman, R. G., *Organometallics* **2011,** *30*, 3217-3224.
180. Hild, F.; Brelot, L.; Dagorne, S., *Organometallics* **2011,** *30*, 5457-5462.
181. Wilson, J. A.; Ates, Z.; Pflughaupt, R. L.; Dove, A. P.; Heise, A., *Prog. Polym. Sci.* **2019,** *91*, 29-50.
182. Fernandez, J. E.; Butler, G. B., *J. Org. Chem.* **1963,** *28*, 3258-3259.
183. Wagner, E. C., *J. Org. Chem.* **1954,** *19*, 1862-1881.
184. Tsunetake, S.; Tetsuo, N.; Makoto, O., *Chem. Lett.* **2006,** *35*, 824-829.
185. Mlynarski, J., *Eur. J. Org. Chem.* **2006,** *2006*, 4779-4786.

Chapter 3

Synthesis and Characterisation of Aluminium Complexes Bearing Chiral Catam Ligands: Influence of Chirality on Aggregation

3.1 Introduction

As will be elucidated in this section, chiral metal complexes can be synthesised using chiral pro-ligands. Chirality transfer from a ligand onto a metal complex has been of interest in catalysis as enantiopure compounds are of importance across many fields in chemistry.[1-3] However, such a chirality transfer is not always straightforward and can result in multiple diastereomers being produced (see complexes **IV-a** to **-c** in this section). This introduction describes recent examples of chiral aluminium complexes in cyclic ester ROP. For the sake of brevity, only aluminium-based complexes will be discussed.

3.1.1 Pioneering Work on Chiral Aluminium Catalysts

As mentioned in Section 1.5.1, Spassky and co-workers were the first to employ salen metal complexes in the polymerisation of cyclic esters.[4, 5] Achiral aluminium methoxide complexes required high temperatures to proceed with the polymerisation of LA (70 - 100 °C), and generally offered poor control (Đ ~ 2 - 5). In 1996, Spassky and co-workers published a landmark paper in which they use a chiral aluminium SalBinap (salen ligand tethered by a Binap linker) methoxide complex (*R*-SalBINAP-Al-OMe) for the ROP of *rac*-LA (Chart 1, (*R*)-**I**).[6] The enantiopure complex, which consisted of the *(R)* enantiomer exclusively, still required elevated temperatures to proceed but was able to reach a 19 % conversion having polymerised mostly *D*-LA (P_m = 0.88). In fact, (*R*)-**I** polymerised *D*-LA 20 times faster than *L*-LA, meaning that polymerisations in *rac*-LA go through two distinct kinetic regimes:

- An initial fast regime in which (*R*)-**I** predominantly polymerises the *D*-LA molecules present in the substrate leading to highly isotactic PDLA.
- A slower regime after most of the *D*-LA in the substrate pool is consumed. This regime polymerises the *L*-LA left in the mixture at a slower rate (in this case 20-fold).

By allowing the polymerisation to go to completion (97.5 % conversion), the resulting polymer was found to form a stereoblock polymer (PDLA-*b*-PLLA) [M_n = 12.7 kg/mol, Đ = 1.3] exhibiting melting points higher than that of optically pure PLLA (187 °C *vs.* 175 °C for PDLA-*b*-PLLA *vs.* PLLA respectively), indicating the formation of a stereocomplex.[7] Ovitt and Coates found that (*R*)-**I** had a propensity to aggregate, which was hindered by substituting the methoxide ligand with the bulkier isopropoxide group (Chart 1, (*R*)-**II**).[8, 9] The stereoselectivity of the complex remained the same, showing that *rac*- and *meso*-LA can be polymerised to yield isotactic and syndiotactic PLA respectively regardless of the nuclearity of the complex.[7-9]

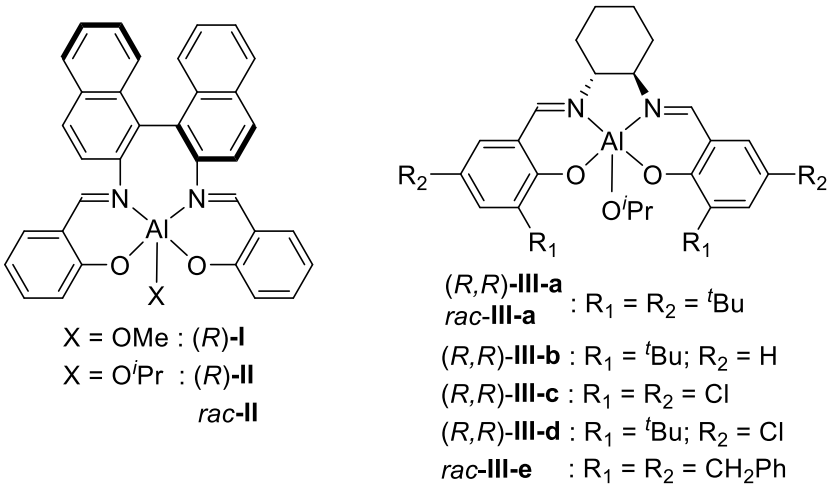


Chart 1. Salen complexes bearing BINAP and diaminocyclohexane linkers.

In 2000, Radano *et al.* extended this research by synthesising a racemic mixture of the complex (Chart 1, *rac*-**II**) and employing it in the polymerisation of *rac*-LA.[10] This should have ideally led to the parallel synthesis of PDLA and PLLA chains (and thus resulting in a stereocomplex) as each enantiomer of the catalyst preferentially polymerises an enantiomer of *rac*-LA.[11] Although the resulting polymer exhibited a higher melting point than optically pure PLLA, Coates and co-workers proved that PDLA-*b*-PLLA block polymers were formed instead of separate PLLA and PDLA chains.[7, 9] This was attributed to the fact that stereoerrors cause the polymer chain to exchange to a catalyst preferential to that error. This results in propagation of the stereoerror which is exhibited by the formation of isotactic regions in the chain. In 2004, Majerska and Duda took advantage of this mechanism to synthesise stereoblock polymers with a melting point of 210 °C *via* a chiral-ligand-exchange mechanism.[12] Therein, they allowed *S*-SalBINAP and Al(O^{i}Pr)$_3$ to react in THF for 24 hours prior to the addition of *rac*-LA. The polymerisation was then monitored until a conversion of 50 % was reached, upon which an equimolar amount of *R*-SalBINAP (relative to *S*-SalBINAP) was introduced. The polymerisation was allowed to continue until high conversions (> 90 %) were reached. A crystallinity of 70 % was observed in the polymer and the unusually high melting temperatures point towards the formation of a stereocomplex.

Overall, the SalBINAP system illuminated a grey area in LA polymerisation, allowing to finally make stereocomplex PLA from *rac*-LA and thus omitting the need of blending PLLA and PDLA. In 2002, Feijen and co-workers expanded on this research by studying aluminium isopropoxide complexes bearing the well-studied Jacobsen salen ligand.[13, 14] Extensively employed in asymmetric epoxidation,[15] the Jacobsen ligand is considerably more convenient

to synthesise than the SalBINAP ligand and bears two stereocentres on the cyclohexyl moiety. Thus, complexes (*R,R*)-**III-a** and *rac*-**III-a** (Chart 1) were prepared from the enantiopure (*R,R*) and a racemic mixture of the Jacobsen ligand respectively. (*R,R*)-**III-a** was found to have a strong preference for *L*-LA, polymerising the enantiomer 14 times faster than with *D*-LA (*c.f.* k_D / k_L = 20 for *R*-**I**).[16] The racemic complex *rac*-**III-a** catalysed the polymerisation of *rac*-LA to form a stereoblock PLA with a P_m of 0.93. The high isoselectivity was maintained in solvent free conditions (130 °C) which was at the time unprecedented. Furthermore, the polymer showed no signs of transesterification which was in sharp contrast to achiral aluminium salen methoxides.[17]

In 2015, Gao *et al.* extended Feijen's work to other aluminium complexes by changing the substituent of the aromatic backbone ((*R,R*)-**III-b** to (*R,R*)-**III-d**).[18] It was found that high isoselectivities were generally maintained with (*R,R*)-**III-b** and (*R,R*)-**III-d** (P_m > 0.85). However, the use of the chloro-substituted (*R,R*)-**III-c** resulted in a loss in selectivity (P_m = 0.57). Although Gao and co-workers attributed this behaviour to the loss of steric bulk on the aromatic substituents, it is important to note that Carpentier and co-workers observed C-H···Cl interactions between the chloro groups and the protons on the polymer chain when using a chloro-substituted yttrium complex (see Section 2.1.4.2). Furthermore Chen *et al.* synthesised a racemic analogue *rac*-**III-e** which bears the bulkier cumyl substituents instead and found a decrease in the isoselectivity of their complex (P_m = 0.76).[19] Thus the observed trend may not simply be reduced to steric bulk only. The electronic effects that come with the change in substituents may influence the complex and even lead to the formation of NCIs between the ligand and the polymer chain, affecting stereoselectivity.

3.1.2 Enantiotopic-Site Control *vs.* Chain-End Control Mechanism

As mentioned in Section 1.4.4, stereocontrol can mainly occur *via* two mechanisms:

- Chain-end control (CEC) in which the chirality of the chain-end bound to the catalyst determines the preference of the next monomer insertion.
- Enantiotopic-site control (ESC) in which the chirality of the catalyst dictates the preference for the enantiomer regardless of the chirality of the chain-end.

The above results indicate that stereocontrol can occur through an ESC mechanism as enantiopure forms of the described catalysts preferentially polymerise one LA enantiomer over the other when placed in *rac*-LA. This can be rationalised by the stereocentres imparting a

chirality on the catalytic pocket that favours a particular LA enantiomer.[20] However, mechanistic studies conducted by Chisholm *et al.* show that rationalising and segregating catalyst selectivities into ESC and CEC mechanisms is an inaccurate method.[21, 22] Furthermore, looking at Feijen's system specifically (**III**), it was postulated that the chiral centres on the catalyst, the chirality of the ultimate (as well as the penultimate) unit of the chain-end, the coordination mode of the ligand around the metal centre (Λ *vs.* Δ), and the solvent all affect stereoselectivity.

Thus, a chiral catalyst does not necessarily regulate stereoselectivity *via* an ESC mechanism only and can carry out both forms of stereocontrol simultaneously.

3.1.3 Elucidation of Selectivity in Chiral Catalysts

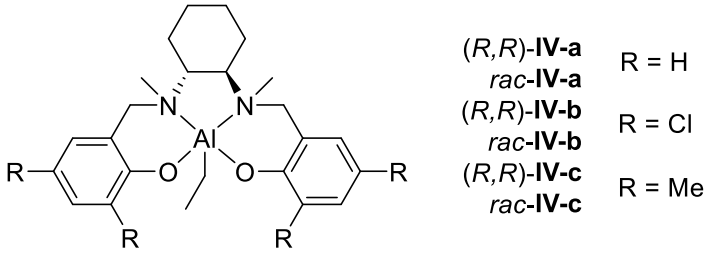


Chart 2. Salan analogues of Feijen's salen complex **III**.

In 2009, Feijen and co-workers extended their work to include chiral salan ligands.[23] Using their previous "Jacobsen motif", the group attempted to synthesise enantiopure and racemic versions of different chiral salan aluminium ethyl complexes (Chart 2). Interestingly, NMR studies have found that complexes (*R,R*)-**IV-a** to **-c** exist as two monomeric diastereomers in solution in which the *N*-Me groups are either *cis* or *trans* to one another. At room temperature, these exist in a *cis*:*trans* ratio of 10:4, 10:2.5, and 10:3 for (*R,R*)-**IV-a**, **-b**, and **-c** respectively. Despite the presence of multiple diastereomers in solution, **IV-a** to **-c** were tested in the polymerisation of *rac*-LA. The microstructure of the polymers ranged from slightly isotactic (P_m = 0.66) to moderately heterotactic (P_r = 0.73). Furthermore, the complexes bearing the (*R,R*) ligand showed a strong propensity to polymerise one enantiomer over the other, albeit to a lesser extent than **I** and **III-a**. For example, (*R,R*)-**IV-a** polymerises *L*-LA 10 times faster than *D*-LA but still only produces PLA with an isotactic bias (P_m = 0.66). While preferential polymerisation of one LA enantiomer over the other is indicative of an ESC mechanism, it is impossible for it to produce heterotactically biased PLA as was seen with complexes (*R,R*)-**IV-b** and **-c**. This indicates that the ESC and CEC mechanisms co-exist in these cases. It has been postulated that both mechanisms compete (leading to lower stereoselectivity) and that polymer

chain exchange occurs throughout polymerisation. However, given that diastereomers of the complexes were observed in solution, it is difficult to rationalise whether the competition between CEC and ESC mechanisms arises due to each diastereomer preferring one mechanism over the other, or whether both mechanisms are simultaneously carried out regardless of the diastereomer.

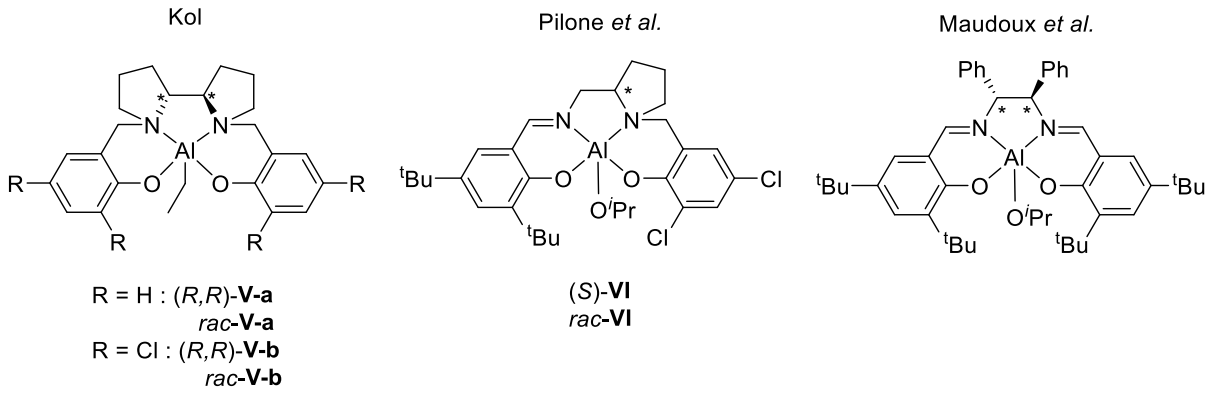
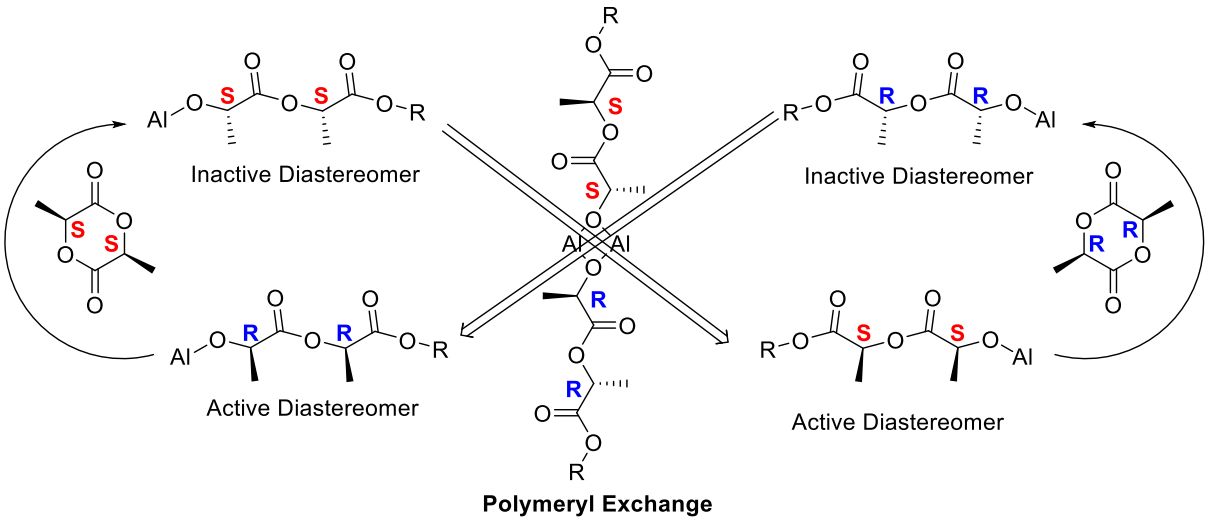


Chart 3. Chiral complexes synthesised by Kol and co-workers, Pilone *et al.*, and Maudoux *et al.*

The exchange of the propagating chain was later coherently incorporated into a mechanism by Kol and co-workers.[24] The group synthesised enantiopure and racemic versions of two complexes supported by a chiral 2,2'-bipyrrolidine salan ligands (Chart 3, left). The polymerisation of *rac*-LA by (*R,R*)-**V-a** resulted in PLA with moderate isotacticity (P_m = 0.72) while the use of the racemic catalyst *rac*-**V-a** led to a significantly lower isotacticity (P_m = 0.56). The use of (*R,R*)-**V-b** led to the formation of slightly heterotactic PLA (P_r = 0.64) while *rac*-**V-b** produced highly heterotactic PLA (P_r = 0.86). The drastic increase in heteroselectivity was explained with a mechanism in which the insertion of a given lactide enantiomer is only favoured for a specific chirality of the catalyst (Scheme 1). The resulting diastereomeric combination leads to an inactive species which undergoes polymeryl exchange with a catalyst of opposite chirality, leading to an active diastereomeric combination that can insert the next lactide unit and thus restart the cycle. This is conducive to a chain-end control mechanism in which the insertion of a monomer specifies the preference of the next monomer insertion.



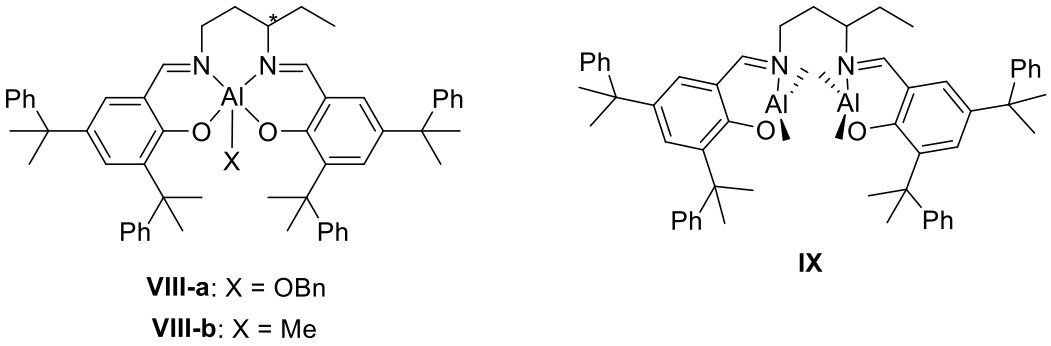
Scheme 1. Chain-end control mechanism proposed for the heteroselectivity of catalysts (Adapted from Kol and co-workers).[24]

An ESC mechanism is not imperative to the production of isotactically enriched PLA. For example, Pilone *et al.* reported chiral aluminium salalen catalysts that partly rely on a CEC mechanism for the isoselective polymerisation of *rac*-LA (Chart 3, centre).[25] (*S*)-**VI** was slightly slower than *rac*-**VI** (78 *vs.* 85 % conversion after 24 hours at 70 °C) but produced PLA that was more isotactic (P_m = 0.82 *vs*. 0.70). Analysis of aliquots taken periodically during polymerisation of *rac*-LA by (*S*)-**VI** found an ESC mechanism to be preferred at low conversions. However, the CEC mechanism becomes more dominant as conversion increases and was found to be the prevailing mechanism over the course of the polymerisation. Maudoux *et al.* have also described an enantiopure chiral aluminium salen catalyst (Chart 3, right) that generates highly isotactic PLA (P_m ~ 0.90) albeit with low activities (38 % after 144 hours at 90 °C).[26] Kinetic studies found no change in the kinetic regime as *rac*-LA was polymerised indicating that a CEC mechanism was dominant.

3.1.4 Other Chiral Aluminium Catalysts

Chen *et al.* found that a salen aluminium alkoxide complex tethered by a chiral 1,3-pentanediamine linker was highly isoselective (P_m = 0.97) at 70 °C, converting 57 % of *rac*-LA over 24 hours while retaining the living features of ROP (Chart 4, **VIII-a**).[19] Interestingly, its alkyl analogue (**VIII-b**) was found to be more active at the same conditions (with addition of BnOH), reaching conversions of 93 % after 18 hours albeit with lower selectivities (P_m = 0.60). Furthermore, the same ligand bearing two aluminium metals (Chart 4, **IX**) was found to be slower (73 % after 18 hours) but exhibited higher selectivities (P_m = 0.76).

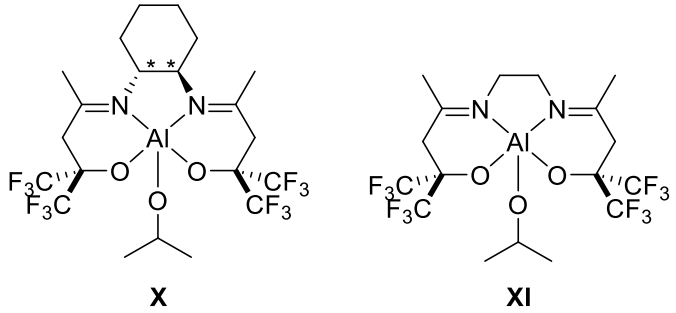
Zhao *et al.* synthesised several monomeric and dimeric chiral biaryl Schiff-base aluminium complexes tethered by BINAP-type linker. Interestingly, all polymerisations led to heterotactically-enriched PLA.[27-30]



VIII-a: X = OBn
VIII-b: X = Me

Chart 4. Chiral complexes synthesised by Chen *et al.*

Exploration of chiral aluminium catalysts was not only limited to salen/salan complexes. Carpentier and co-workers examined aluminium complexes of fluorinated dialkoxy-diimino salen-like ligands (Chart 5, **X**) showing that high isoselectivities can be maintained in solution and melt conditions (P_m = 0.77 – 0.81).[31] A conversion of 68 % was achieved after 24 hours at 70 °C while 88 % of monomer was converted after 72 hours in the melt (130 °C). However, the high isoselectivity was not exclusive to the chiral complexes but also exhibited by the more active achiral catalyst (Chart 5, **XI**), indicating that the chiral component of the catalyst may not be the reason for such selectivities.



X **XI**

Chart 5. Chiral and achiral dialkoxy-diimino salen-like complexes synthesised by Carpentier and co-workers.

It should become increasingly apparent that stereoselectivity is not inherently linked to chirality of a catalyst. In fact, a clear rationale is not present regarding the design of chiral catalysts as many different factors affect a catalyst's performance. For example, Okuda and co-workers synthesised complexes bearing O'S'S'O-donor ligands (Chart 6, *rac*-**XII** and *rac*-**XIII**).[32]

Complex *rac*-**XII** was a stable dimer. The crystal structure of *rac*-**XIII** showed a dimeric heterochiral structure, meaning that the *mers* correspond to a (*R,R*) and (*S,S*) component. However, the complex was found to be monomeric in solution. In polymerisation, complex *rac*-**XIII** was found to be 8 times more active than the dimeric *rac*-**XII**, reaching 91 % conversion after 6 hours at 70 °C. Complex *rac*-**XII** required a polymerisation time of 49 hours to reach the same conversion. It is thus apparent that nuclearity of the complexes makes a difference in *rac*-LA polymerisation. However, the PLA was found to be atactic in both cases, indicating that the proximity of the chiral centres to the metal centre may not always have an impact on stereoselectivity.

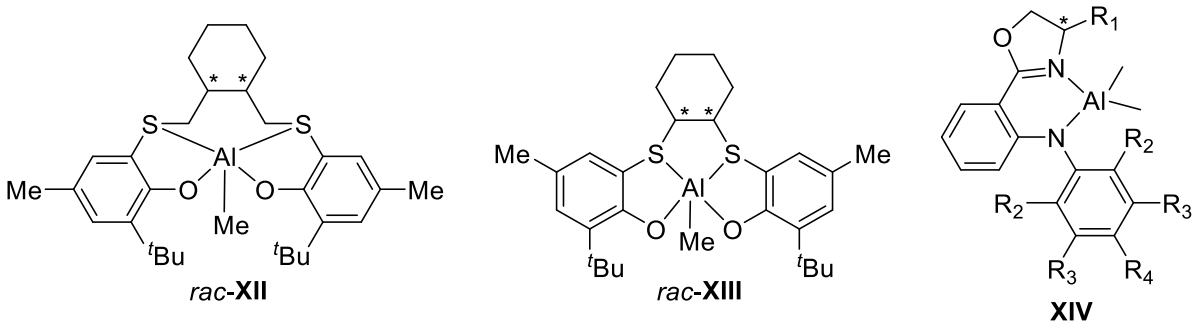


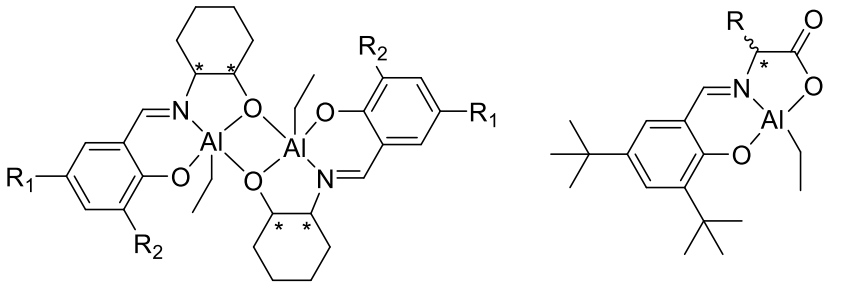
Chart 6. Complexes synthesised by the groups of Okuda (**XII** and **XIII**) and Du (**XIV**).

Du and co-workers synthesised a range of chiral aluminium anilido-oxazolinate complexes that feature a chiral centre on the fifth membered ring backbone (Chart 6, **XIV**, R_1 = (*S*)-^{i}Pr, (*R*)-Ph, (*R*)-^{t}Bu). The complexes polymerised *rac*-LA at 80 °C in a controlled fashion, reaching conversions of up to 98 % after 24 hours, with polymer microstructures ranging from slightly isotactic to moderately heterotactic (P_r = 0.4 – 0.74) . The authors attributed the observed trends to the other substituents on the ligands (R_2 - R_4), citing electronic and steric factors as the sole reason for the observed behaviour.[33]

Darensbourg and Karroonnirun reported chiral (and achiral) half-salen complexes (Chart 7). Complexes **XV-a** to **-d** were dinuclear aluminium complexes of which **XV-a** was the most active and isoselective (57 % conversion after 66 hours at 70 °C; P_m = 0.70). Interestingly, complex **XV-d** showed no activity at the same conditions. All complexes were found to epimerise *rac*-LA into *meso*-LA to some extent. Complexes **XVI-a** and **XVI-b** showed better activity, polymerising up to 36 and 42 % of *rac*-LA after 15 hours at the same conditions. Furthermore, stereoselectivity was found to be moderate (P_m = 0.74 and 0.72 for **XVI-a** and

XVI-b respectively). Although not discussed the mononuclearity of the complexes **XVI-a** and **-b** is likely the cause for the higher activity. Whether this contributed to the increased isoselectivity is unclear.

Darensbourg and Karroonnirun

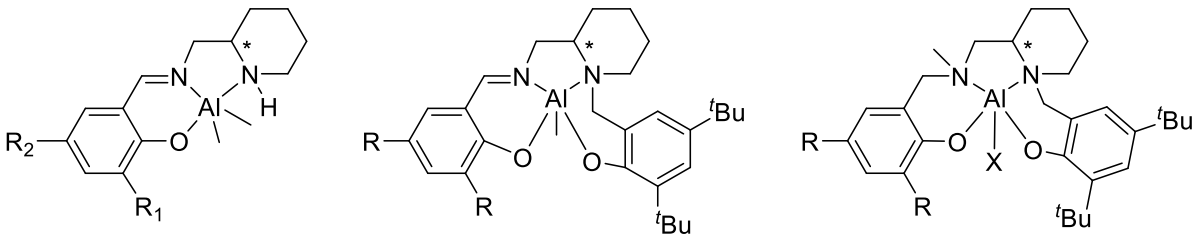


XV-a: $R_1 = R_2 = {}^t$Bu
XV-b: R_1 = H; R_2 = OMe
XV-c: R_1 = Me; $R_2 = SiPh_3$
XV-d: R_1 = Me; $R_2 = SiMe_2{}^t$Bu

XVI-a: R = 2-(methylthio)ethyl
XVI-b: R = benzyl

Chart 7. Chiral complexes synthesised by Darensbourg and Karroonnirun.

In the same vein, Jones and co-workers synthesised a variety of chiral aminopiperidine-based half-salalen ligands (Chart 8, **XVII-a** to **XVII-c**) and complexed them with $AlMe_3$ (amongst other metals). The complexes were active at 80 °C, polymerising between 72 – 96 % over 24 hours.[34] Complexes **XVII-a** and **-b** were moderately heteroselective (P_r = 0.69 and 0.68 respectively) while **XVII-c** was slightly isoselective (P_m = 0.61). They noted that the production of isotactic PLA for the adamantylated **XVII-c** was due to steric contributions. The group extended the research to salalen complexes bearing the same aromatic substitutions as with complexes **XVII** (**XVIII-a** to **-c**). These were considerably slower with complexes **XVIII-a** to **-c** taking 10 days at 80 °C to reach a conversion of 88, 88, and 89 % respectively. Furthermore, the molecular weights were much higher than anticipated (19.4 – 22.7 kg/mol *vs.* expected weights of ~12.7 kg/mol). This could be due to slow generation of an active species, resulting in only a fraction of the complexes carrying out the polymerisation. While **XVIII-a** exhibited a slight isotactic bias (P_m = 0.63), complexes **XVIII-b** and **-c** produced atactic (P_r = 0.56) and moderately heterotactic (P_r = 0.68) polymers respectively.



XVII-a: $R_1 = R_2 = {}^tBu$
XVII-b: $R_1 = R_2 = Me$
XVII-c: $R_1 = Me$; $R_2 = Ad$

XVIII-a: $R_1 = R_2 = {}^tBu$
XVIII-b: $R_1 = R_2 = Me$
XVIII-c: $R_1 = Me$; $R_2 = Ad$

XIX-a: $R_1 = R_2 = {}^tBu$
XIX-b: $R_1 = R_2 = Me$
XIX-c: $R_1 = Me$; $R_2 = Ad$

Chart 8. Chiral salan and salalen complexes synthesised by the Jones group.

Salan ligands bearing the same motif were also considered (**XIX-a** to -**c**) with complex **XIX-a** showing moderate isoselectivity (P_m = 0.75) and converting 65 % of *rac*-LA after 3 hours at 80 °C. Complexes **XIX-b** and **XIX-c** showed slight isoselectivities (P_m = 0.59 and 0.64).

3.1.5 Aims and Objectives

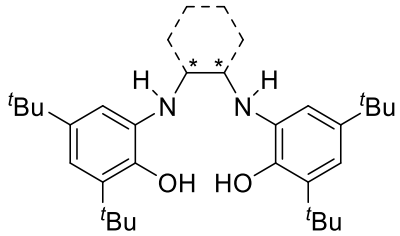


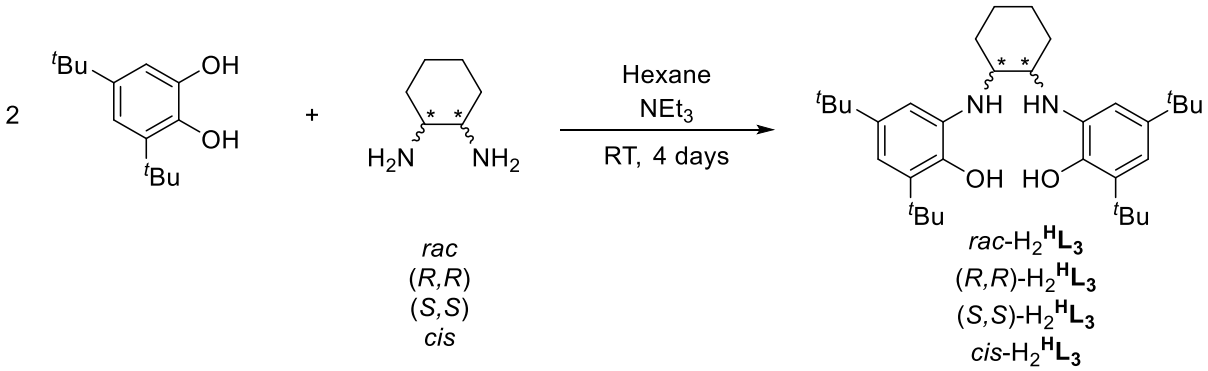
Figure 1. Structure of $H_2{}^{H}L_3$.

It is apparent that chiral components in a catalyst can lead to enhanced stereoselectivities, although the mechanism through which this occurs is not always clear. An ESC mechanism is not always a dominant one and the selectivity can end up being governed by the chirality of the chain-end instead (*via* CEC). Further to this, Gibson and co-workers previously showed how sensitive aluminium catalysts are to the nature of substituents on their ligand, meaning that a slight change in steric or electronic properties can nullify the advantageous effects that a chiral component may bring.[35] This is substantiated by the studies conducted by the groups of Darensbourg and Jones. There are numerous instances where highly isotactic PLA was achieved using achiral aluminium catalysts,[19, 36-39] which prompts the question as to why a chiral catalyst is necessary in the first place. Given the lack of understanding for structure-activity relationships with aluminium-based catalysts, the field of chiral catalysis was explored further by synthesising chiral catam ligands and examining their behaviour in cyclic ester ROP.

The previous chapter detailed how the $^{H}L_2$ ligand led to Al catalysts affording highly active polymerisation at room temperature and slightly isotactic PLA (P_m = 0.60). Given these promising results, chiral ligands were sought after to enhance stereoselectivity whilst keeping high activity. The ethylene linker was replaced by a *trans*-cyclohexane bridge (Figure 1, dotted line) to yield $H_2{}^{H}L_3$, which would increase the rigidity of the scaffold as well as introduce two chiral centres, both factors being beneficial to stereoselectivity. As the salen-analogue by Feijen was known to be highly stereoselective (**III-a**), this catam ligand was a good contender.

3.2 Pro-Ligand Synthesis and Complex Characterisation

3.2.1 Pro-Ligand Synthesis



Scheme 2. Synthesis of pro-ligands (*R,R*)-, (*S,S*)-, *rac*-, and *cis*-$H_2{}^{H}L_3$.

The synthesis of *rac*-$H_2{}^{H}L_3$ was initially attempted using the method previously reported by Wieghardt and co-workers in which the diamine and catechol reagents were refluxed in acetonitrile.[40] Although the procedure was successful for the synthesis of $H_2{}^{H}L_1$ and $H_2{}^{H}L_2$, no product precipitated out of solution. Instead, a modified literature procedure was employed, where 3,5-di-*tert*-butylcatechol and *rac-trans*-1,2-diaminocyclohexane were stirred in *n*-hexane with a catalytic amount of triethylamine over the course of 4 days at room temperature (Scheme 2).[41] This resulted in a precipitate, which was filtered and washed with *n*-hexane to afford the pro-ligand in good yield. Although the synthesis of this compound was never described academically, a patent that follows a similar synthetic procedure mentioned its use as a precursor for the synthesis of a *N*-heterocyclic carbene ligand.[42] The ^{1}H NMR spectrum ($CDCl_3$, 298 K) of *rac*-$H_2{}^{H}L_3$ exhibits a C_2-symmetric species in solution with two characteristic aromatic doublets (δ^1_H = 7.17 and 6.85 ppm) and ^{t}Bu peaks (δ^1_H = 1.45 and 1.36

ppm) (Figure A3). The protons on the cyclohexyl moiety appear to be non-equivalent, resulting in multiple downfield signals across the spectrum (1.26 < d < 2.40).

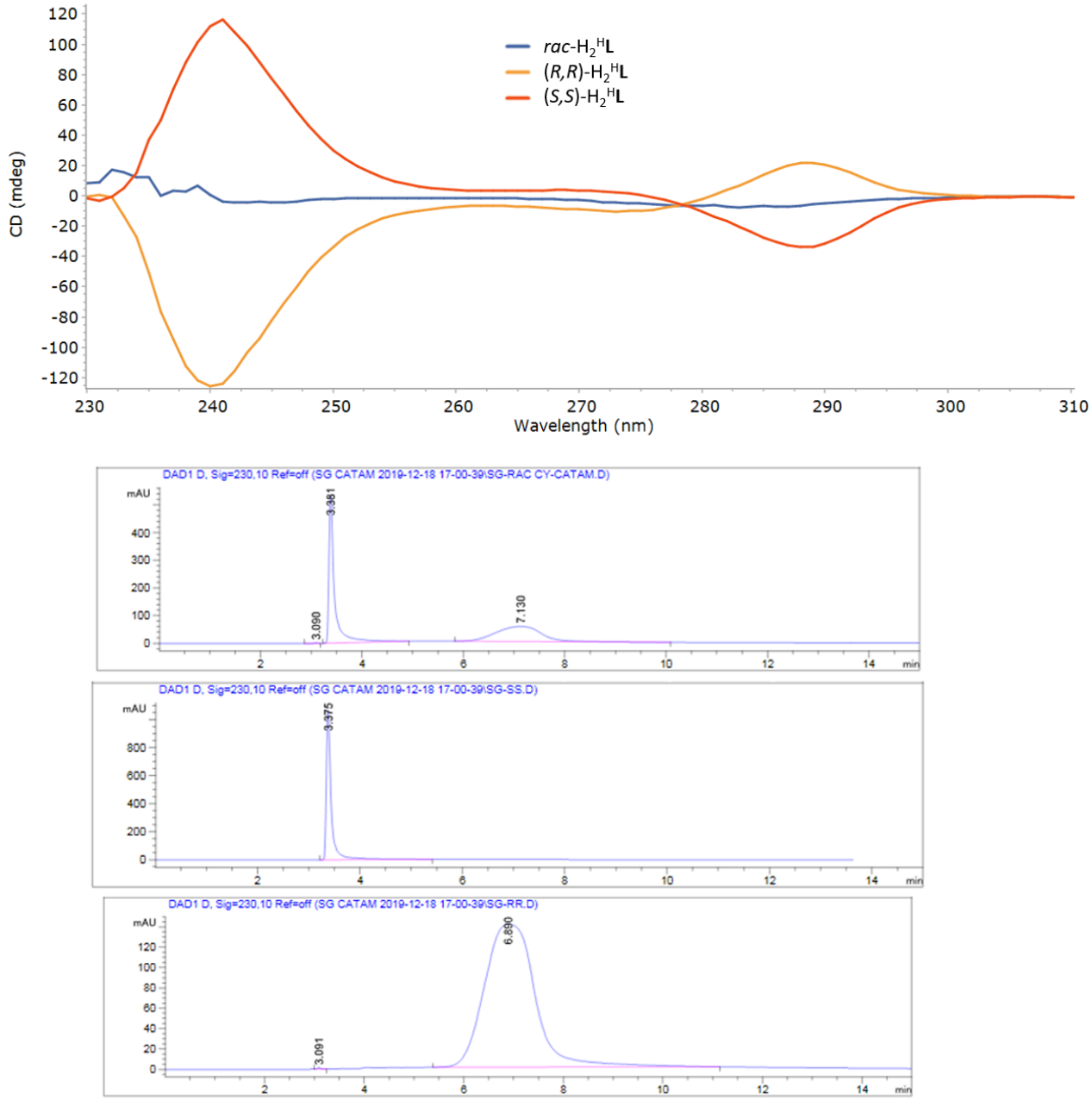


Figure 2. Top: CD spectra of ligands *rac*-H_2^H**L3** (blue), (*R,R*)-H_2^H**L3** (orange), (*S,S*)-H_2^H**L3** (red) in dichloromethane (c = 0.33 mM). Bottom: Chiral HPLC traces for *rac*-H_2^H**L3** (top), (*S,S*)-H_2^H**L3** (middle), and (*R,R*)-H_2^H**L3** (bottom) showing a high enantiomeric excess for the enantiopure ligands.

Given the success in the synthesis of *rac*-H_2^H**L3**, the scope was extended to the synthesis of enantiopure analogues (*R,R*)- and (*S,S*)-H_2^H**L3** using (*R,R*)- and (*S,S*)-*trans*-1,2-diaminocyclohexane respectively. The ^{1}H NMR spectra ($CDCl_3$, 298 K) of the enantiopure

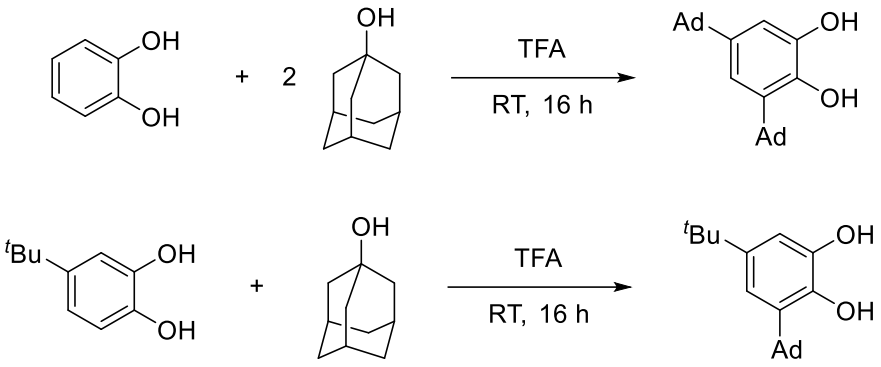
pro-ligands are identical to that of the racemic ligand, which was expected due to enantiomers exhibiting only a difference in optical properties as opposed to physical properties (Figure A4). However, this does not guarantee that the expected products were formed as the chirality of the reactants may not be retained throughout the reaction. Thus, the optical activity of the racemic and enantiopure ligands were analysed by circular dichroism (CD) (Figure 2, top). The overlay of the traces shows that the enantiopure ligands each absorb circular polarised light of one particular direction, resulting in traces that are opposites of each other. The racemic ligand however exhibits a trace that is relatively flat due to the absorptions of the enantiomers cancelling each other out. These results indicate that the enantiopure ligands are at an enantiomeric excess. The analysis was extended through the use of chiral HPLC which found that the enantiopure ligands had a high enantiomeric excess (%ee > 99 %) while the racemic ligand had a %ee of 0 (Figure 2, bottom). It can thus be said with certainty that the chiral centres of the diamines were retained throughout the ligand synthesis, resulting in a highly enantiopure ligand in the case of (*R,R*)- and (*S,S*)-H_2**^{H}L$_3$**, and a racemic ligand in the case of *rac*-H_2**^{H}L$_3$**.

Using the same synthetic procedure as for (*R,R*)-, (*S,S*)-, and *rac*-H_2**^{H}L$_3$**, the synthesis of *cis*-H_2**^{H}L$_3$** was attempted using *cis*-1,2-diaminocyclohexane (Scheme 2), which features two chiral carbon atoms of opposite absolute configuration. After 4 days, a precipitate had formed which was filtered and washed. The ^{1}H NMR spectrum ($CDCl_3$, 298 K) shows a C_2-symmetry in solution and exhibits a distinct set of broad peaks (Figure A5). This indicates that a slow exchange occurs as the peaks are not sharp and thus difficult to integrate. Three signals corresponding to the cyclohexyl CH_2 protons, integrating to a total of 6 protons, can be found at δ^1_H = 1.69 ppm. A fourth peak is present under the ^{t}Bu peak at δ^1_H = 1.41 ppm. The high-resolution mass spectrum (HRMS) confirmed the formation of the expected product *cis*-H_2**^{H}L$_3$**. Thus, the synthesis of (*R,R*)- and (*S,S*)- and *rac*- and *cis*-H_2**^{H}L$_3$** was carried out successfully through a modified literature procedure resulting in good yields (> 45 %).[41]

3.2.2 Modification of Aromatic Substituents

In order to increase the bulkiness around the metal, synthesis of the *rac*-H_2**^{H}L$_3$** analogue bearing adamantyl (Ad) instead of ^{t}Bu groups was undertaken. The synthesis of a partially and fully adamantylated ligand was targeted (Scheme 3). Although not expanded on in this thesis, this work seeks to demonstrate that aromatic modulation of the catam pro-ligand is possible.

The 3,5-*di*-adamantyl-catechol was synthesised following a well-established literature procedure in which 1 equivalent of catechol was stirred with 2 equivalents of 1-adamantol in trifluoroacetic acid (TFA) for 16 hours at room temperature (Scheme 3, top).[43] The protonation of the hydroxy group of 1-adamantol by TFA is favoured, which following a dehydration yields a stable tertiary cation that can undergo electrophilic substitution on the aromatic ring.



Scheme 3. Synthesis of 3,5-di-adamantyl catechol (top) and 3-tert-butyl-5-adamantyl catechol (bottom).

The partially adamantylated 3-*tert*-butyl-5-adamantyl-catechol was also synthesised in a similar fashion as per above using 1 equivalent of 4-*tert*-butylcatechol and 1 equivalent of 1-adamantol instead (Scheme 3, bottom). The ^{1}H NMR spectrum ($CDCl_3$, 298 K) shows the presence of one ^{t}Bu and one Ad group on the catechol (Figure A6). Further confirmation of the product was obtained *via* HRMS.

Two equivalents of the partially adamantylated 3-*tert*-butyl-5-adamantyl-catechol was reacted with one equivalent of *rac-trans*-1,2-diaminocyclohexane in hexane under the presence of a catalytic amount of triethylamine to yield *rac*-$H_2^{Ad}\mathbf{L_3}$ after 4 days. Interestingly, the ^{1}H NMR spectrum ($CDCl_3$, 298 K) showed the presence of two species in solution, making attribution to the peaks complicated. This likely arises from different forms of intramolecular H-bonding involving the NH and OH moieties, giving rise to species that are magnetically inequivalent. However, upon measuring the ^{1}H NMR spectrum in DMSO-d_6 (298 K), a single set of peaks was obtained (Figure 3). As DMSO can act as an H-bond acceptor, it would influence the intramolecular H-bonding to yield a single species in the ^{1}H NMR spectrum. The molecule exhibits a C_2-symmetric structure in solution with two peaks in the aromatic region (δ^{1}_{H} 6.91 and 6.81 ppm) as well as characteristic NH (δ^{1}_{H} 4.71 ppm), adamantyl (δ^{1}_{H} 2.09, 2.01, and 1.71 ppm), and ^{t}Bu (δ^{1}_{H} 1.21 ppm) signals. This confirms the successful synthesis of the *rac*-$H_2^{Ad}\mathbf{L_3}$.

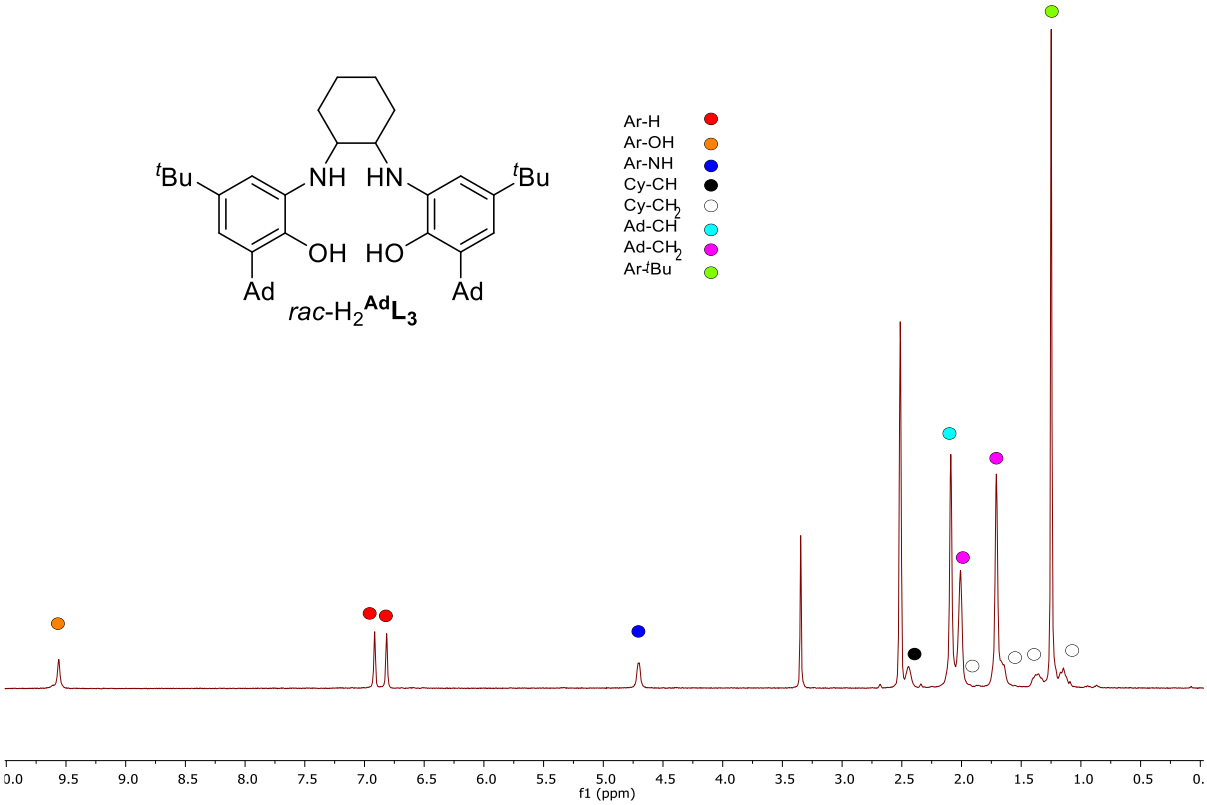
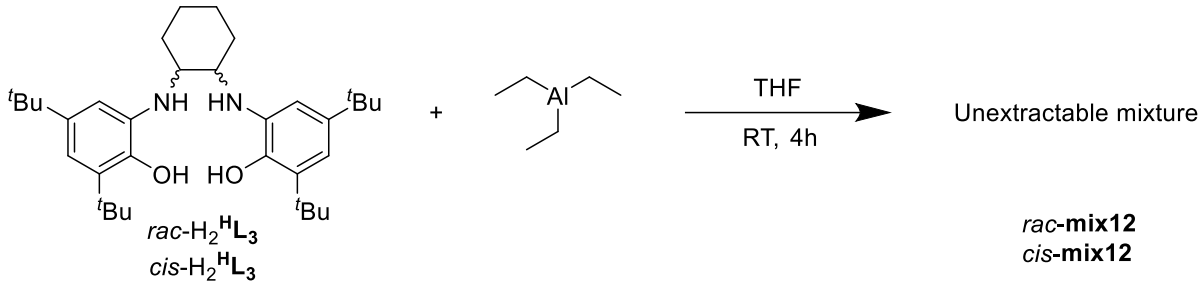


Figure 3. ^{1}H NMR spectrum (DMSO-d_6, 298 K) of rac-$H_2^{Ad}\mathbf{L_3}$.

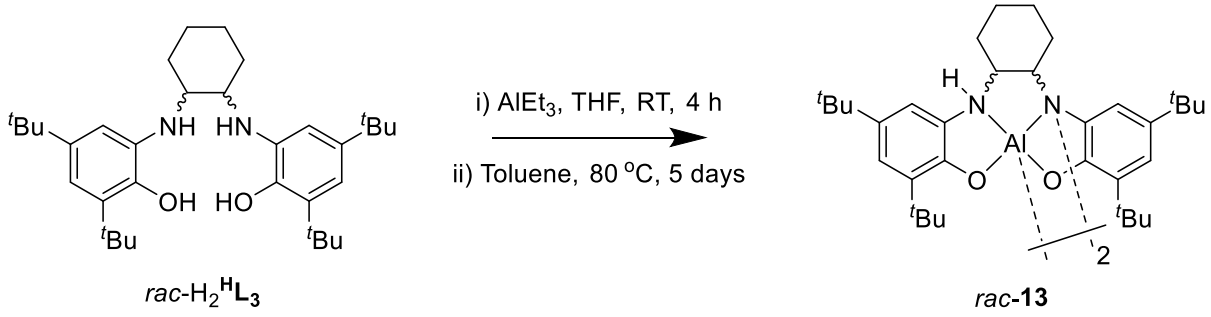
The synthesis of the fully adamantylated Cy-catam ligand (*rac*-$H_2^{Ad2}\mathbf{L_3}$) was then attempted with two equivalents of 3,5-*di*-adamantyl-catechol being reacted with one equivalent of *rac*-*trans*-1,2-diaminocyclohexane. The only successful route appeared to be the refluxing of the reagents in MeCN over 2 hours. The resulting product was poorly soluble in most common organic NMR solvents (*e.g.* $CDCl_3$, C_6D_6, DMSO-d_6, and THF-d_8) at room temperature, preventing characterisation of the substance. However, HRMS indicated the formation of the desired product. It appears that the substitution of all ^{t}Bu groups with adamantyl groups led to a worsening of solubility properties. Thus, *rac*-$H_2^{Ad2}\mathbf{L_3}$ was not employed any further. The increased solubility of 3-*tert*-butyl-5-adamantyl-catechol and the ligand *rac*-$H_2^{Ad}\mathbf{L_3}$ arises from the ^{t}Bu group at position 3. As this hydrophobic group is at the periphery of the ligand, it can interact better with organic solvent molecules, leading to better solubility properties. Keeping one ^{t}Bu group on the aromatic ring is thus beneficial as it allows for easier synthesis of pro-ligands and complexes, as well as facilitating their subsequent employment.

3.2.3 Attempted Synthesis of the Alkyl Complexes of *rac*- and *cis*-H_2**^{H}L$_3$**



Scheme 4. Attempted synthesis of alkyl complexes bearing *rac*- and *cis*-H_2**^{H}L$_3$** affording unextractable mixtures referred to as *rac*- and *cis*-**mix12** respectively.

The synthesis of Al complexes was initially explored using the pro-ligands *rac*- and *cis*-H_2**^{H}L$_3$** (Scheme 4). Their reaction with one equivalent of $AlEt_3$ in THF at room temperature afforded an unextractable mixture of products (*rac*-**mix12** and *cis*-**mix12** respectively) after purification in pentane (Figures A25 and A26). These were comprised of the desired aluminium ethyl complex as well as the NH-deprotonated complex, similar to what was observed with complex **7** (See Section 2.3.2.1). This was attributed to the cyclohexyl ligand backbone which is a C_2-linker (like the ethylene backbone in H_2**^{H}L$_2$**), leading to a geometry favouring the NH deprotonation. Stirring the crude product mixtures in pentane over 2 days did not change the composition of either *rac*- or *cis*-**mix12**, contrary to what was previously observed with complex **6**. Furthermore, heating an NMR sample (C_6D_6) of *cis*-**mix12** at 80 °C for 3 days did not resolve the spectrum (Figure A26, bottom).



Scheme 5. Synthesis of deprotonated complex *rac*-**13** from *rac*-H_2**^{H}L$_3$** involving a step in which the mixture was heated.

However, after dissolving *rac*-**mix12** in toluene and heating it at 80 °C over 5 days (Scheme 5), a single well-defined species was obtained as determined by ^{1}H NMR spectroscopy. The ^{1}H NMR spectrum (CD_2Cl_2, 298 K) exhibits a C_1-symmetric structure in solution (Figure 4) with four aromatic peaks (δ^1_H 7.07, 6.86, and 6.54 ppm), one NH peak (δ^1_H 2.65 ppm), and four

^{t}Bu peaks (δ^1_H 1.52, 1.48, 1.17, and 0.87 ppm). The absence of the alkyl chain indicates the formation of the deprotonated complex *rac*-**13**. However, high yielding purification of the complex was found to be difficult due to high solubility in all common solvents (such as THF, pentane, toluene, diethyl ether, and DCM) and no satisfactory EA was obtained.

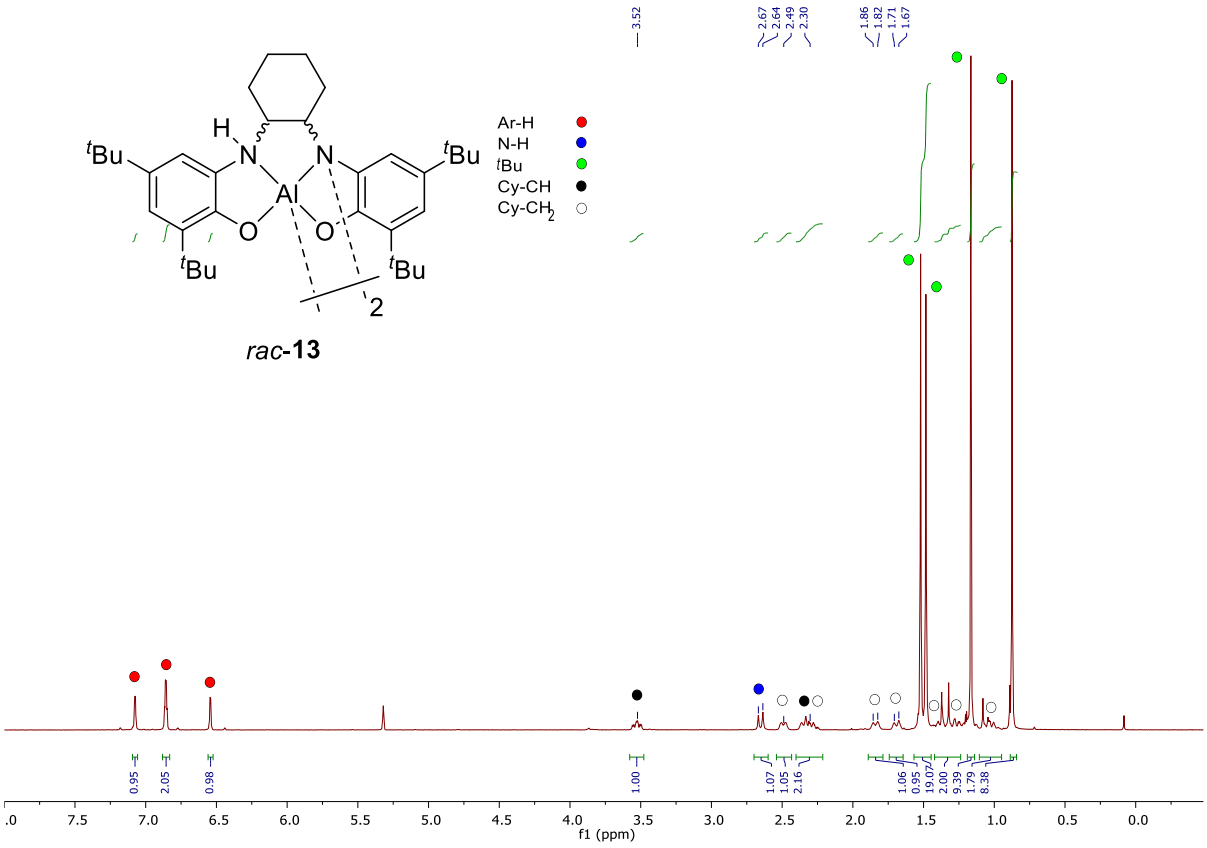


Figure 4. ^{1}H NMR spectrum (CD_2Cl_2, 298 K) of *rac*-**13** obtained from the deprotonation of *rac*-**mix12** through heating the mixture in toluene at 80 °C.

Single crystals of *rac*-**13** were grown by slow cooling of a warm solution in DCM and the molecular structure was determined using XRD (Figure 5). As with complex **6**, the crystal structure is a centrosymmetric dimer consisting of two units. The two aluminium centres are bridged by the deptrotonated μ-N atoms, forming an Al_2N_2 quadrangle with a centre of inversion sitting at the middle. Both aluminium centres are pentacoordinate, exhibiting a geometry intermediate between square pyramidal and trigonal bipyramidal (τ_5 = 0.53). This contrasts with complex **6**, in which each aluminium centre exhibits a near-perfect square pyramidal geometry due to meridional coordination of the ligand. This deviation can be traced back to the rigid nature of the cyclohexyl linker, which forces the O'N'N'O-donors to occupy equatorial and axial positions. The dimer consists of both a (*R,R*)- and a (*S,S*)-^{H}**L**$_3$ unit, resulting in the formation of a heterochiral dimer. As the ^{1}H NMR spectrum is in line with the formation

of a single species, this indicates that the heterochiral dimer (as observed by XRD analysis) is likely to be more stable than the corresponding homochiral dimers. Due to difficult high-yielding synthesis of pure *rac*-**12** and *rac*-**13**, the synthesis of alkoxide derivatives was investigated.

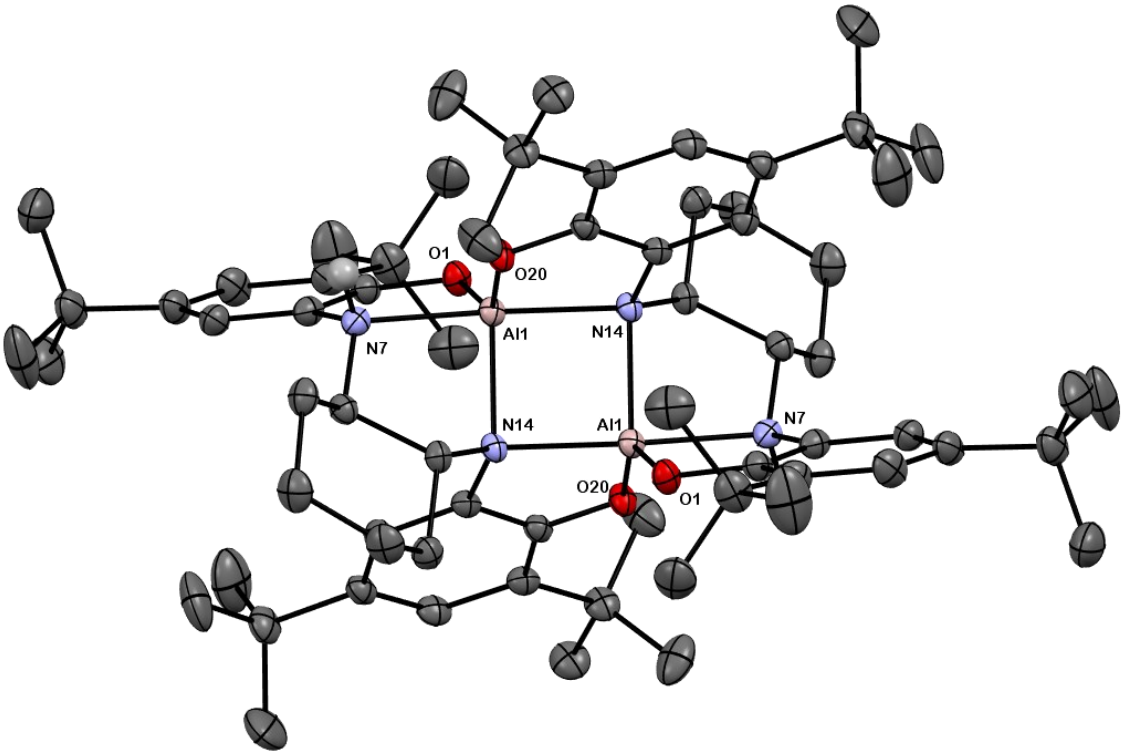
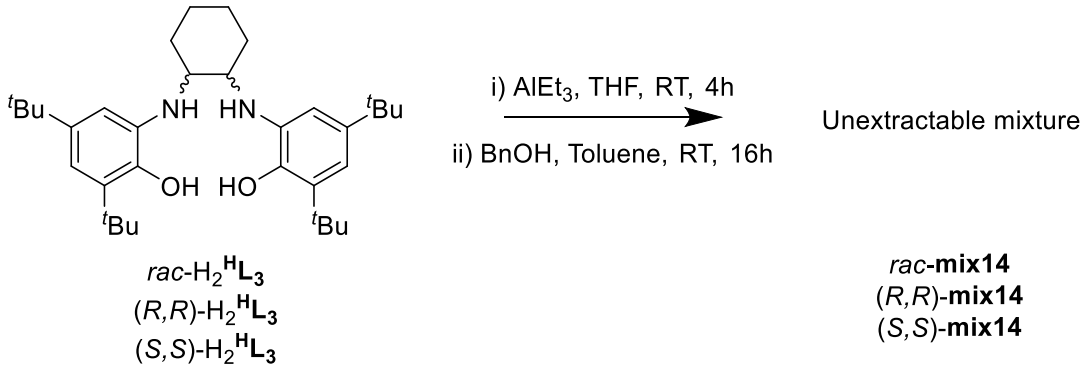


Figure 5. Crystal structure of *rac*-**13** (ellipsoid plot, 50% probability) showing a μ-N bridged dimeric structure as seen with complex **7** (Section 2.3.2.1).

3.2.4 Synthesis of the Benzyloxy Complexes of (*R*,*R*)-, (*S*,*S*)-, and *rac*-H_2^{H}**L**$_3$

3.2.4.1 Attempted Synthesis of (*R*,*R*)-, (*S*,*S*)-, and *rac*-**14**



Scheme 6. Attempted complexation of (*R*,*R*)-, (*S*,*S*)-, and *rac*-H_2^{H}**L**$_3$ and reaction with BnOH yielding unextractable mixtures referred to as (*R*,*R*)-, (*S*,*S*)-, and *rac*-**mix14** respectively

Given that a well-defined benzyloxy complex (**8c**) was synthesised through the addition of one equivalent of BnOH to the alkyl complex of H_2**^{H}L$_2$** (**6**), and that the cyclohexyl moiety of pro-ligand H_2**^{H}L$_3$** is a C_2-linker just like the ethylene moiety of H_2**^{H}L$_2$**, the synthesis of **^{H}L$_3$**Al(OBn) was attempted (Scheme 6). However, the reaction of (*R,R*)-, (*S,S*)-, and *rac*-H_2**^{H}L$_3$** with $AlEt_3$ and subsequent addition of BnOH led to unextractable mixtures referred to as (*R,R*)-, (*S,S*)-, and *rac*-**mix14**. The ^{1}H NMR spectra (C_6D_6, 298 K) of (*R,R*)- and (*S,S*)-**mix14** are identical (as expected using enantiomeric ligand precursors) but differ significantly from the spectrum of *rac*-**mix14** (Figure 6). As the EA suggests that the desired product was formed in all cases, it was thought that the spectra consist largely of a variety of aggregated species. This is favoured by the oxophilic nature of aluminium as well as the primary nature of the alkoxide co-ligand, allowing the species to aggregate in multiple ways, leading to a convoluted NMR spectrum. This was reinforced through DOSY analysis (C_6D_6, 298 K) on (*S,S*)-**mix14**, which shows that the relevant peaks adopt the same diffusion coefficient in line with a dinuclear structure (Figure A27).

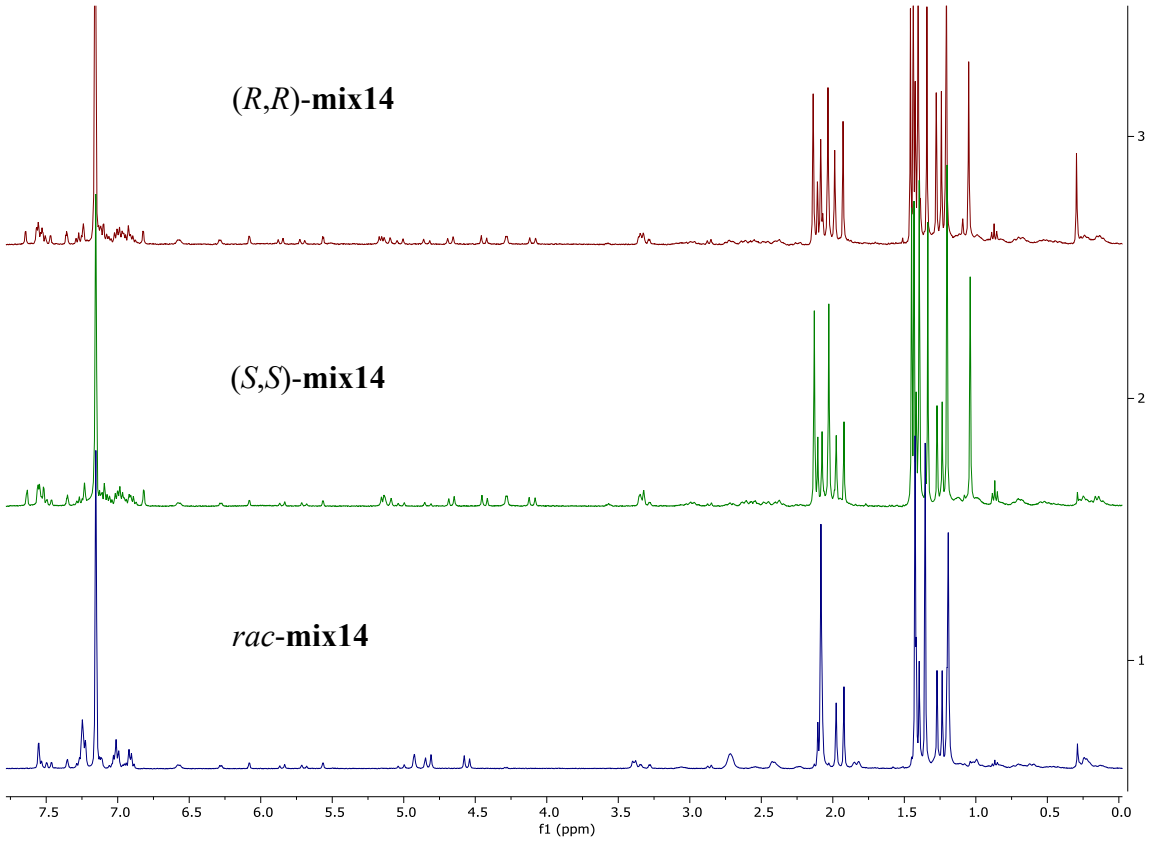


Figure 6: Stacked ^{1}H NMR spectra (C_6D_6, 298 K) of (*R,R*)-**mix14** (top), (*S,S*)-**mix14** (middle), and *rac*-**mix14** (bottom) obtained at room temperature by reaction of $AlEt_3$ and BnOH with *rac*-H_2**^{H}L$_3$**, (*S,S*)-H_2**^{H}L$_3$** and (*R,R*)-H_2**^{H}L$_3$** respectively.

The NMR samples of (*S,S*)-, and *rac*-**mix14** (C_6D_6, 298 K) were heated at 80 °C. For (*S,S*)-**mix14**, the ^{1}H NMR spectrum did not resolve after 16 hours (Figure A28). However, by either heating the solution of rac-**mix14** at 80 °C over 2 hours or allowing it to stand at room temperature overnight, the ^{1}H NMR spectrum became resolved and showed the formation of a single well-defined species termed *rac*-**14** (Figure 7).

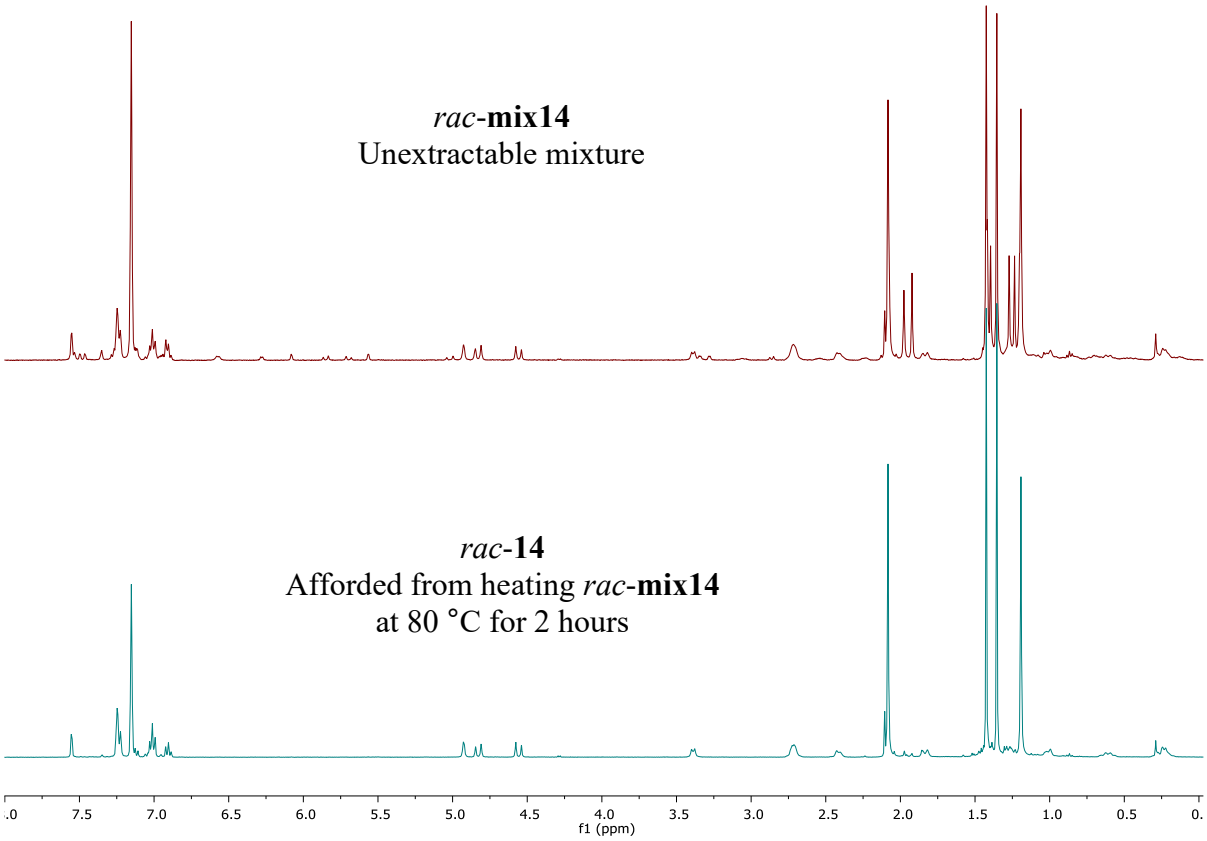


Figure 7. Stacked ^{1}H NMR spectra (C_6D_6, 298 K) showing the formation of the well-defined single species *rac*-**14** upon heating of *rac*-**mix14** at 80 °C for 2 hours.

Thus, assuming that the unextractable mixtures consist of multiple diastereomers, the above findings would suggest that a solution containing 50% of (*R,R*)-**mix14** and 50% of (*S,S*)-**mix14** would eventually lead to the formation of the well-defined *rac*-**14**. This was confirmed experimentally by preparing an NMR sample (C_6D_6) containing an even mixture of both enantiomers. Although initially convoluted (Figure 8, top), the ^{1}H NMR spectrum (C_6D_6, 298 K) eventually resolved itself into a single species upon heating the tube overnight at 80 °C (Figure 8, centre). The resulting spectrum is identical to that of *rac*-**14** (Figure 8, bottom), suggesting that the unextractable mixture formed consists of diastereomers.

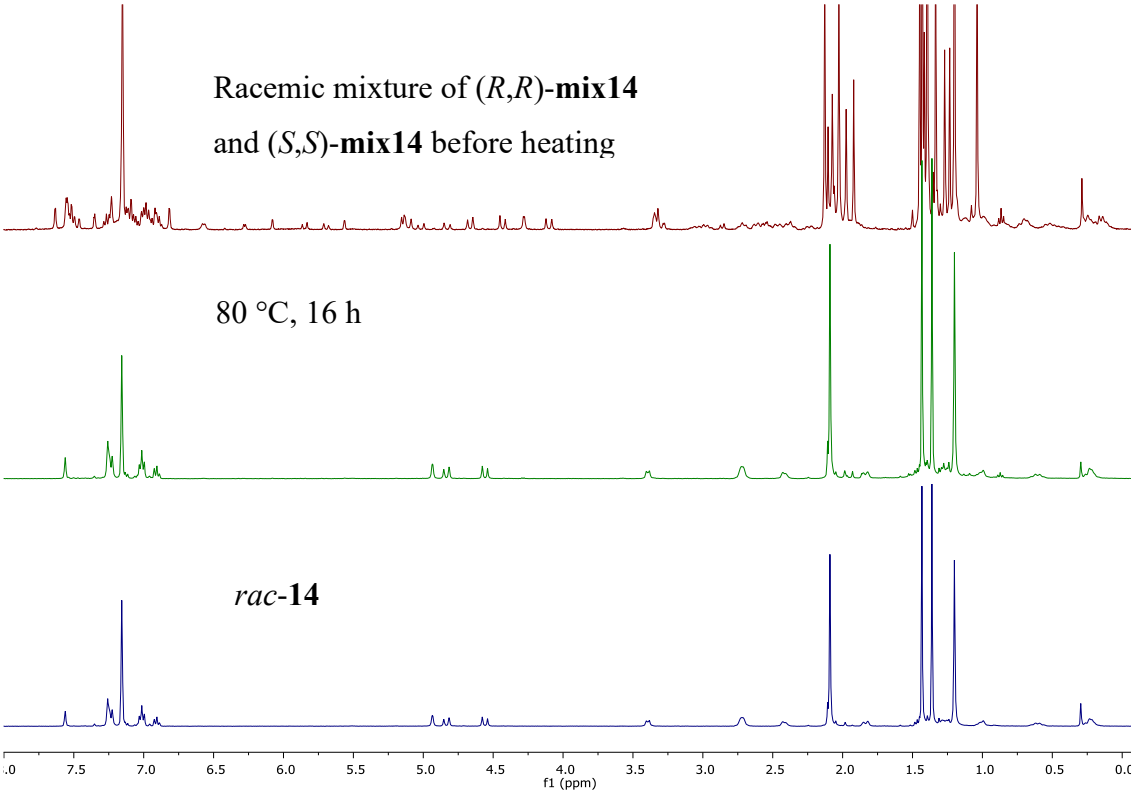


Figure 8: Stacked NMR spectra (C_6D_6, 298 K) of a 1 : 1 mixture of (*R,R*)-**mix14** : (*S,S*)-**mix14** at room temperature (top), after heating at 80°C overnight (middle), and *rac*-**14** synthesised from *rac*-H_2^{H}**L**$_3$ (bottom).

To investigate the unextractable mixtures, a single crystal of (*S,S*)-**mix14** was grown by slow diffusion of pentane into a concentrated C_6D_6 solution, and subsequently analysed by XRD. The crystal structure shows a dinuclear structure with two Al centres connected by two bridging μ-O atoms of a benzyloxy and hydroxy moiety (Figure 9). The hydroxide was likely introduced by the adventitious presence of water. Although not ideal, an interesting aspect of the structure is the absolute configuration of the stereocentres on one of the (*S,S*)-^{H}**L**$_3$ ligands. Instead of the N atoms adopting a *R*- and *S*- configuration as in the structure of *rac*-**14** (see next Section), the absolute configuration of one (*S,S*)-^{H}**L**$_3$ ligand is (*S*)-N(7), (*S*)-C(8), (*S*)-C(13), (*S*)-N(14), resulting in the NH moieties being *trans* to one another. The collection of the crystal XRD data was incomplete as the wrong unit cell was assumed after the pre-experiment. This means that the data is not of sufficient quality to be published. However, it can be used as a starting point for DFT optimisations, which were carried out to study the energetics of dimerisation of this complex family (Section 3.2.6).

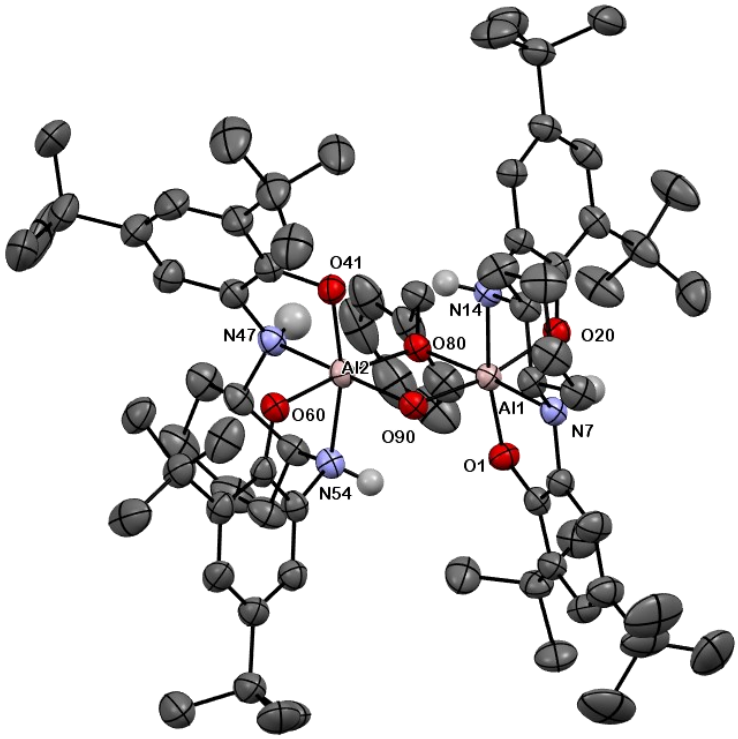
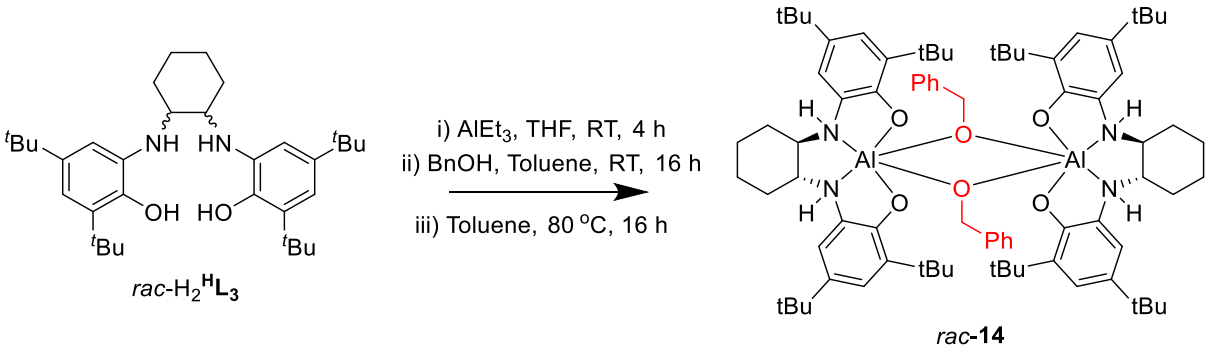


Figure 9. Crystal structure of a diastereomer of (*S,S*)-**mix14** (ellipsoid plot, 50% probability) showing a μ-O bridged dimeric structure with a set of NH moieties trans to one another.

3.2.4.2 Synthesis and Characterisation of *rac*-**14**



Scheme 7. Direct synthesis of *rac*-**14** from *rac*-$H_2^HL_3$ involving a step in which the mixture is heated overnight.

Knowing that the well-defined *rac*-**14** can be accessed through heating of *rac*-**mix14**, the synthesis of the complex was targetted. The unextractable mixture *rac*-**mix14** was initially synthesised. The crude product was then redissolved in toluene and heated for 16 hours at 80 °C which afforded *rac*-**14** in high yields (82 %) after removal of volatiles and purification in pentane (Scheme 7). The ^{1}H NMR spectrum (CD_2Cl_2, 298 K) of *rac*-**14** exhibits a C_1-symmetric structure in solution displaying (amongst others) two well-defined peaks (δ^1_H 4.63 and 3.24 ppm) attributed to the NH moieties as well as the aromatic proton peaks (δ^1_H 7.51,

7.49, and 7.23 ppm) attributed to the benzyloxy moiety (Figure A29). Interestingly, the hydrogens on the cyclohexyl backbone each experience their own environment and thus show up as separate peaks.

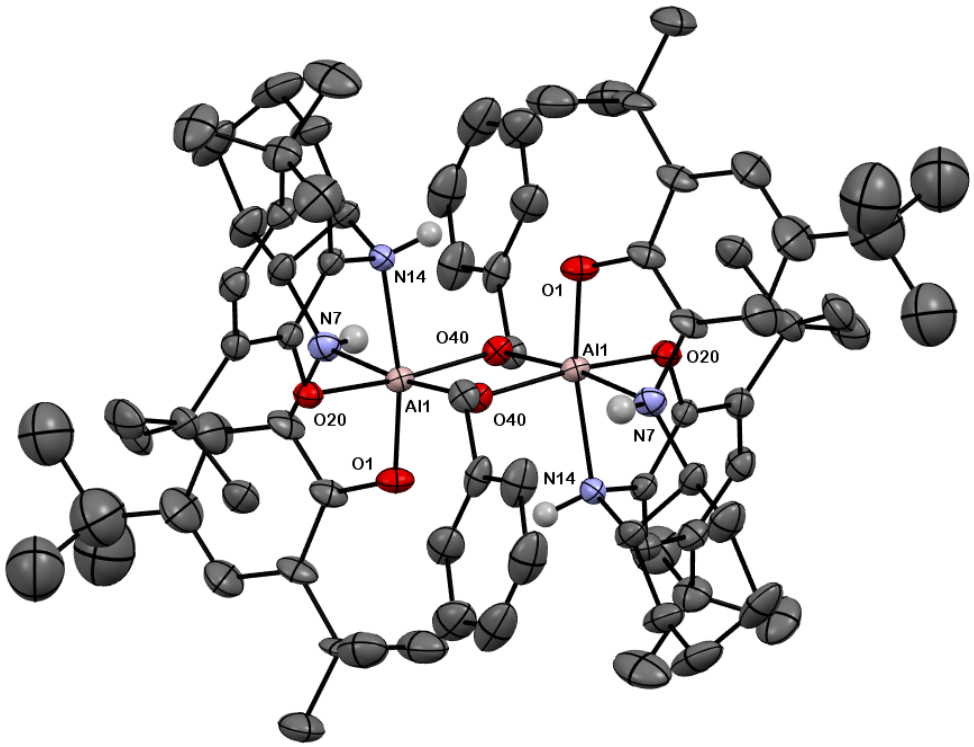


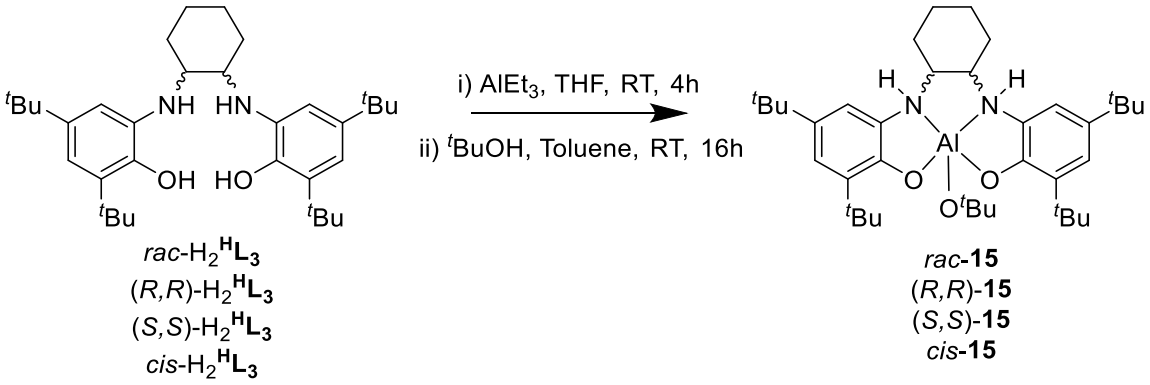
Figure 10. Crystal structure of *rac*-**14** (ellipsoid plot, 50% probability) showing a μ-O bridged dimeric structure as with **8c**.

A single crystal of *rac*-**14** was grown by slowly cooling a hot solution (in DCM), and the molecular structure was determined by XRD. The crystal structure shows a centro-symmetric dinuclear structure containing two Al centres connected to each other by two bridging μ-O atoms of two benzyloxy groups (Figure 10). The centre of inversion sits in the middle of the Al_2O_2 quadrangle and each hexacoordinated Al centre exhibits a distorted octahedral geometry. The wrapping of the tetradentate O'N'N'O-ligand yields a *cis*-β conformation with the μ-O atoms of the benzyloxy moieties occupying equatorial and axial positions, thus completing the coordination sphere. This crystal structure is very similar to that of the H_2**L**$_2$ analogue, **8c** (Section 2.3.2.1, Figure 18). The dimeric structure of *rac*-**14** is heterochiral, meaning that it includes both (*S*,*S*)-**L**$_3$ and (*R*,*R*)-**L**$_3$ ligands. These adopt *cis*-β wrappings that are in opposite direction to each other (*i.e.* Λ-*cis*-β and Δ-*cis*-β) which minimises steric repulsion and thus facilitates the dimerisation. Each ligand has four stereogenic centres (two C and two N atoms), exhibiting an absolute configuration of (*R*)-N(7), (*R*)-C(8), (*R*)-C(13), (*S*)-N(14) for (*R*,*R*)-**L**$_3$, and (*S*)-N(7), (*S*)-C(8), (*S*)-C(13), (*R*)-N(14) for (*S*,*S*)-**L**$_3$. The NH moieties on each ligand are

cis to each other and thus pointing towards the same general direction. Since the ^{1}H NMR spectrum shows only four signals for the *o*-aminophenolate moieties (δ^{1}_{H} = 7.15 ppm, 6.89ppm, 6.85 ppm, and 6.79 ppm) and four signals for the ^{t}Bu groups (δ^{1}_{H} = 1.75 ppm, 1.19 ppm, 1.15 ppm, and 0.82 ppm), the spectrum is in good agreement with a solid-state molecular structure that features an inversion centre (Figure A29).

Contrary to **8c**, which retains a dimeric structure in C_6D_6 but a monomeric structure in THF-d_8, the DOSY NMR of *rac*-**14** shows that the dimeric structure is retained in both solvents, suggesting that the dimer is too stable to be broken up by a coordinating solvent at room temperature (Figures A30 and A31).

3.2.5 Synthesis and Characterisation of (*R,R*)-, (*S,S*)-, *rac*-, and *cis*-**15**



rac-$H_2{}^{H}L_3$
(*R,R*)-$H_2{}^{H}L_3$
(*S,S*)-$H_2{}^{H}L_3$
cis-$H_2{}^{H}L_3$

rac-**15**
(*R,R*)-**15**
(*S,S*)-**15**
cis-**15**

Scheme 8. Complexation of (*R,R*)-, (*S,S*)-, *rac*-, and *cis*-$H_2{}^{H}L_3$ and reaction with ^{t}BuOH yielding (*R,R*)-, (*S,S*)-, *rac*-, and *cis*-**15** respectively.

It is becoming abundantly clear that the catalyst's propensity to dimerise and form multiple aggregated species increases the complexity of the system. Using a mixture of compounds as initiators can be detrimental to the polymerisation as different species may have different reactivities, leading to differences in the polymer chains formed. The lack of a single well-defined species can complicate analysis and thus the synthesis of a monomeric species was sought. Coates and co-workers previously reported that they changed their dimeric catalytic system into a monomeric one by substitution of the methoxide ligand by a bulkier isopropoxide group.[8, 9] The benzyloxy group on complex *rac*-**14** is a primary alcohol which may allow for the dimerisation to proceed. Thus, a synthesis was carried out in which a bulky tertiary alcohol (^{t}BuOH) was used (Scheme 8).

The pro-ligand *rac*-H_2**^{H}L$_3$** was reacted with one equivalent of $AlEt_3$ to yield *rac*-**mix12** (alkyl derivative and deprotonated species). The mixture was redissolved in toluene and reacted with one equivalent of ^{t}BuOH overnight at room temperature. Upon removal of the volatiles and purification with pentane, the complex *rac*-**15** was afforded (63 % yield). The ^{1}H NMR spectrum (C_6D_6, 298 K) shows a C_1-symmetric structure in solution with four signals in the aromatic region (δ^1_H = 7.52, 7.42, 6.81, and 6.66 ppm), 10 signals for the cyclohexyl moiety, and two distinct signals for the NH groups (δ^1_H = 3.69 and 2.65 ppm) (Figure A32). Amongst the four aromatic ^{t}Bu groups (δ^1_H = 1.89, 1.66, 1.38, and 1.32 ppm), another peak corresponding to the *tert*-butoxy group can be observed (δ^1_H = 1.62 ppm). DOSY NMR analysis (C_6D_6, 298 K) shows that the complex is monomeric in solution, confirming that the use of a bulky alkoxide hindered dimerisation (Figure A33).

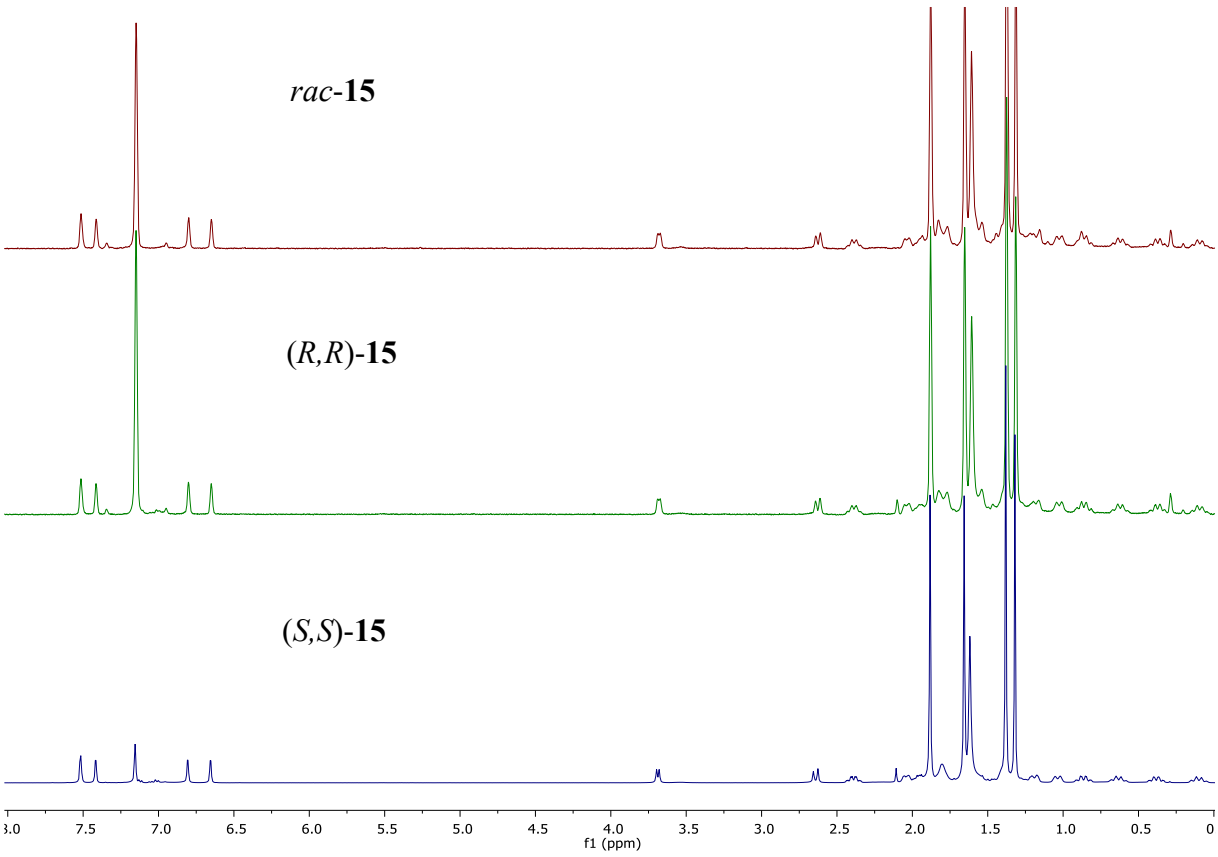


Figure 11. Stacked ^{1}H NMR spectra (C_6D_6, 298 K) of rac-**15** (top), (R,R)- **15** (middle), and (S,S)-**15** (bottom) showing identical spectra.

These results prompted the repetition of the synthesis using the enantiopure pro-ligands (*R,R*)- and (*S,S*)-H_2**^{H}L$_3$**. The resulting complexes (*R,R*)- and (*S,S*)-**15** were isolated in good yields (77% and 80% respectively). The ^{1}H NMR spectra (C_6D_6, 298 K) are identical to that of *rac*-**15** (Figure 11), showing that the complexes are optical isomers of each other and confirming

that no diastereomers are formed. This is remarkable as complexations with an enantiopure ligand do not always lead to enantiopure complexes. As detailed in the introduction (see Section 3.1.3), Feijen's enantiopure salan analogue of (*R,R*)-H_2**^{H}L$_3$** led to the formation of diastereomers when reacted with $Al(Et)_3$.[23] The fact that the ^{1}H NMR spectra of (*R,R*)- ,(*S,S*)-, and *rac*-**15** are identical, indicates that they are devoid of diastereomers and that successful chirality transfer from the ligand onto the complex occurred.

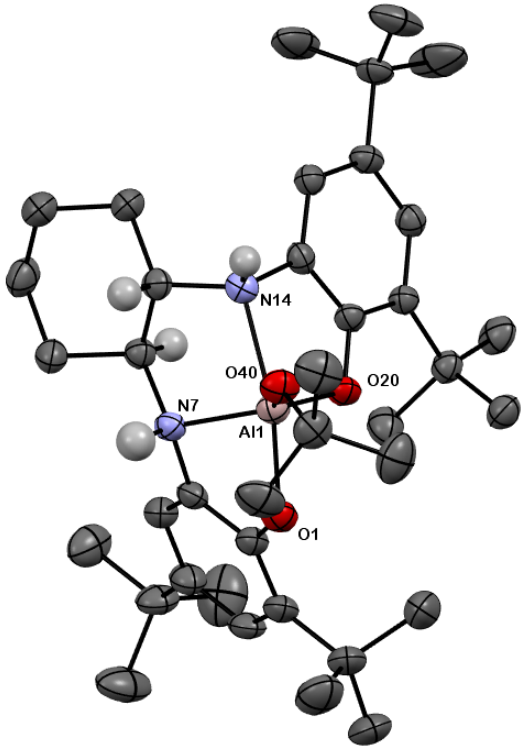


Figure 12. Crystal structure of (*S,S*)-**15** (ellipsoid plot, 50% probability) showing a monomeric trigonal bipyramidal structure.

Twinned crystals were grown by slow diffusion of pentane into a concentrated solution of *rac*-**15** in C_6D_6 and analysed by XRD. The crystal structure of (*S,S*)-**15** was obtained, which features a mononuclear molecular structure (Figure 12). The aluminium centre is pentacoordinate and adopts a distorted trigonal bipyramidal geometry (τ_5 = 0.59) in line with the results obtained by ^{1}H NMR and DOSY analysis. The tetradentate O'N'N'O-ligand coordinates around the metal centre in a folded fashion where three atoms (O, N and N) occupy equatorial positions while one O atom occupies an axial position. This is different from previously mentioned pentacoordinate aluminium catam complexes (**1** and **5**) which did not exhibit such a coordination. There are four stereogenic centres present on the ligand for which the absolute configuration is: (*S*)-N(7), (*S*)-C(8), (*S*)-C(13), (*R*)-N(14).

The same synthetic procedure as for (*R,R*)-, (*S,S*)-, and *rac*-**15** was employed for the meso *cis*-H_2**^{H}L$_3$** pro-ligand (Scheme 8) to yield *cis*-**15** in good yields (64 %). The ^{1}H NMR spectrum (C_6D_6, 298 K, Figure A34) of *cis*-**15** shows a single well-defined species as a C_2-symmetric structure in solution with two peaks in the aromatic region (δ_{1H} = 7.48 and 6.77 ppm) as well as a doublet corresponding to the NH groups (δ_{1H} = 3.26). The alkyl region features two singlets corresponding to the aromatic ^{t}Bu groups (δ_{1H} = 1.80 and 1.36 ppm) and a singlet corresponding to the *tert*-butoxy group (δ_{1H} = 1.65 ppm). This suggests that the desired complex *cis*-**15** was formed. The DOSY (C_6D_6, 298 K) confirms that the complex is monomeric in solution, suggesting that *cis*-**15** has similar aggregation properties (or lack thereof) as the *trans*-**15** complexes (Figure A35).

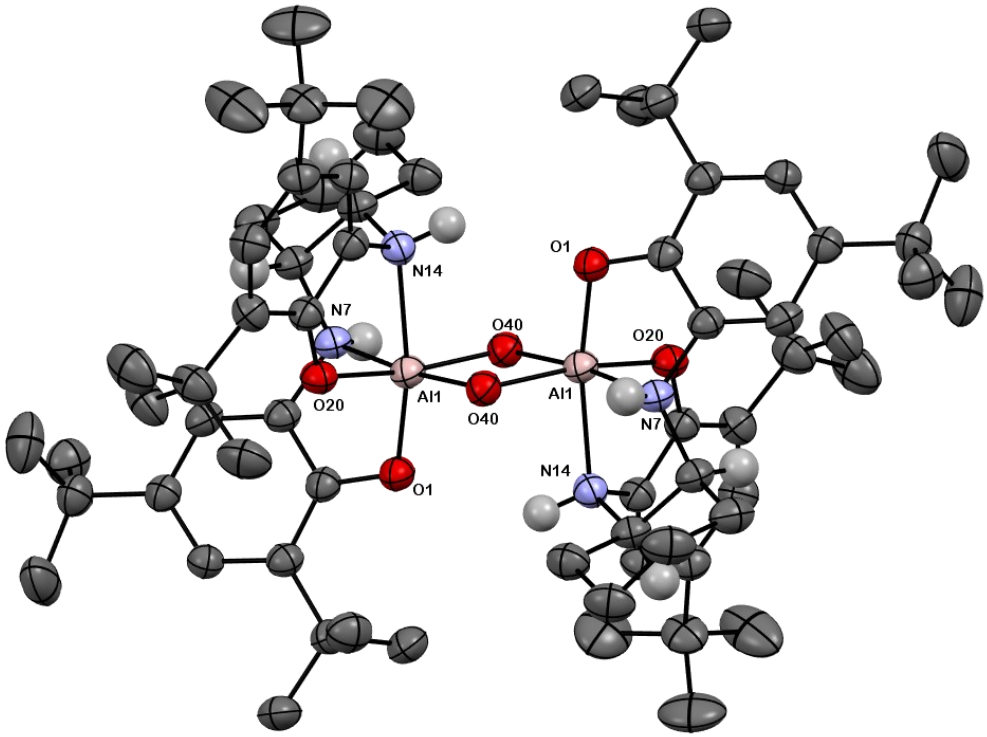


Figure 13. Crystal structure of a diastereomer of *cis*-**15** (ellipsoid plot, 50% probability) showing a μ-O bridged dimeric structure obtained from the adventitious presence of water.

Single crystals were grown out of a concentrated solution of *cis*-**15** in C_6D_6 (obtained *via* vapor diffusion method using pentane as precipitant) and analysed by XRD. The crystal structure of *cis*-**15** was found to be a dimeric hydroxo complex, likely due to the adventitious presence of water (Figure 13). It features a centrosymmetric dinuclear structure containing two Al centres connected to each other by two bridging μ-O atoms of two hydroxy groups. There is a centre of symmetry sitting in the middle of the Al_2O_2 quadrangle with each hexacoordinated Al centre

exhibiting a distorted octahedral geometry. As seen with the structure of **8c** (Section 2.3.2.1, Figure 18) and *rac*-**14** (Section 3.2.4.2, Figure 10), the ligands wrap around the metal centre to yield a *cis*-β conformation where the μ-O atoms occupy an axial and equatorial position. The nature of the *cis* linker appears to allow the ligand to adopt *cis*-β wrappings that are in opposite direction of one another (*i.e.* Λ-*cis*-β and Δ-*cis*-β). The absolute configuration of each ligand was found to be (*S*)-N(7), (*S*)-C(8), (*R*)-C(13), (*R*)-N(14) and (*R*)-N(7), (*R*)-C(8), (*S*)-C(13), (*S*)-N(14).

3.2.6 Preliminary DFT Calculations on the Stability of Dimers

As highlighted by the previous reactivity studies, the attempted synthesis of enantiopure and racemic benzyloxy complexes initially led to the formation of various aggregated species (Section 3.2.4.1). However, if a racemic mixture of these species were heated, the formation of a single well-defined species (*rac*-**14**) was observed. Clearly, the chirality of the backbone plays a role in directing aggregation and the dimerisation behaviour was elucidated using DFT. The dinuclear molecular structures obtained from *rac*-**14**, (*S*,*S*)-**mix14**, and *cis*-**15** were used as a starting point for the DFT calculations (details in the ESI). The bridging -OBn and -OH groups were replaced by -OMe groups for computational efficiency. The geometries were then optimised in the gas-phase at the M06-2X level using the split-valence double-zeta basis set 6-31G(d,p). It is clear that the heterochiral dimer (*rac*-**II**) is favoured over the homochiral dimers (*S*,*S*-**II** and *S*,*S*-**II'**) by at least 3.6 kcal/mol (Figure 14). This explains why *rac*-**mix14** eventually leads to the formation of *rac*-**14**; the stability drove the transformation. It also explains why an even mixture of (*R,R*)-**mix14** and (*S,S*)-**mix14** was found to form *rac*-**14** when heated.

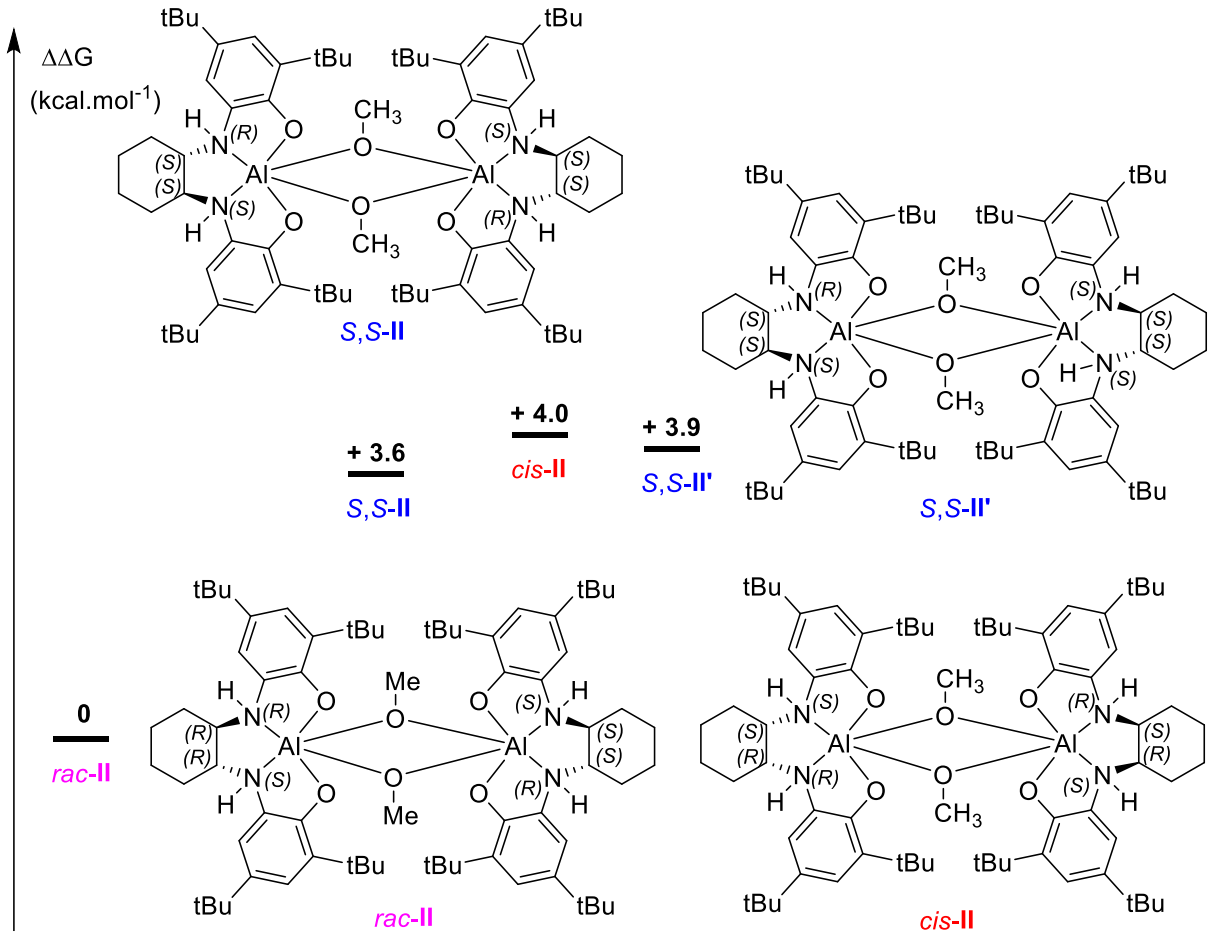


Figure 14. Graphical representation of the energies of the dimeric structures *rac*-**II**, *S,S*-**II**, *S,S*-**II'**, and *cis*-**II** showing a stabilisation of at least 3.6 kcal/mol for the heterochiral dimer *rac*-**II**.

The structure *cis*-**II** was found to be 4 kcal/mol higher in energy than the heterochiral dimer *rac*-**II**. Furthermore, the structure was similar in energy to the homochiral dimers *S,S*-**II** and *S,S*-**II'** (3.6 and 3.9 kcal/mol respectively). This indicates that the nature of the *cis*-^{H}**L**$_3$ ligand would not favour a dimeric structure in solution. As seen in the previous section, this is in line with the measured DOSY NMR spectrum (C_6D_6, 298 K) which shows a monomeric structure of *cis*-**15** in solution (Figure A35).

3.3 Polymerisation Results and Discussion

As mentioned in the introduction, the chiral nature of the complexes makes them good candidates for the stereoselective ROP of cyclic esters. The *trans* complexes (*R,R*)-, (*S,S*)-, and *rac*-**15** will be discussed first, followed by the *meso* complex *cis*-**15**. For the *trans* complexes, the studied monomers are examined by increasing order of "complexity" starting from the achiral ε-CL and then moving onto the enantiopure *L*-LA, followed by *meso*-LA, and finally *rac*-LA. Other monomers such as β-BL, ε-DL, TMC, and PDL were briefly examined and are discussed towards the end. When appropriate, the mechanism of the polymerisation was elucidated using DFT calculations, normalised time scale methods (as seen in the previous chapter), and kinetic models.

3.3.1 Polymerisations with Enantiopure [(*R,R*)-**15** and (*S,S*)-**15**] and Racemic Catalysts (*rac*-**15**)

3.3.1.1 Polymerisation of an Achiral Monomer (ε-CL)

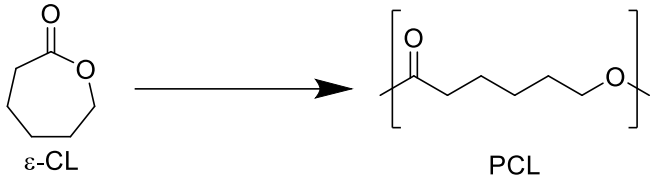


Table 1. ε-CL polymerisations using complexes (*R,R*)-, (*S,S*)-, and *rac*-**15**, (**8c** added for comparison).

Entry	Catalyst	ε-CL (equiv.)	Time (h)	Conv.[a] (%)	$M_{n(SEC)}$ (Đ)[b] (kg/mol)	$M_{n(calc.)}$[c] (kg/mol)	Initial rate[d] (M s^{-1})	TOF (h^{-1})
1	(*R,R*)-**15**	100	19.25	87	11.1 (1.9)	9.9	2.79×10^{-5}	5
2	(*S,S*)-**15**	100	19.25	82	10.5 (2.0)	9.4	2.79×10^{-5}	4
3	*rac*-**15**	100	19.25	55	7.1 (1.8)	6.3	9.31×10^{-6}	3
4	**8c**	100	21	60	10.8 (1.3)	6.9	NA	3

Reaction conditions: $[\varepsilon\text{-CL}]_0 = 1$ mol.L^{-1}, THF, 25 °C; a) Determined by ^{1}H NMR by relative integration of monomer and polymer signals (see ESI); b) Determined by SEC calibrated with polystyrene standards in THF and corrected (see ESI); c) Calculated using the conversion; d) Determined assuming a zero order in monomer

The complexes were found to work for the room-temperature ROP of ε-CL (Table 1). The polymerisations were well-controlled, exhibiting a linear increase of molecular weight with conversion (Figures B41 and B42) but resulted in larger dispersities (Đ = 1.8 – 2.0) than what was previously observed with complexes **2** and **8c** in Chapter 2 (Đ = 1.3 – 1.4). Using two different initial concentrations of ε-CL ($[\varepsilon\text{-CL}]_0 = 1.0$ and 1.5 M), a partial positive order (*i.e.*

between 0 and 1) in monomer was observed for both the enantiopure and racemic complexes (Figures B109 and B110). This signifies that k_{app} cannot be calculated using pseudo-first order plots as these are meant for reactions following a first order in monomer. In most literature, a first order dependency in ε-CL is reported. However, zero or partial positive orders have been reported in some instances, which was explained by "saturation kinetics" arising from reversible catalyst-monomer binding equilibria.[44-48] These stem from Michaelis-Menten kinetics which relate the concentration of the substrate to the rate of reaction. DFT calculations of the ε-CL coordination on the monomeric and dimeric aluminium complexes were carried out and support a favourable interaction between the substrate and the catalyst, showing a stabilisation of 6.9 and 19.0 kcal/mol for the monomeric and dimeric aluminium catalysts respectively (Figure E6). This is not surprising as complexes **2** and **8c** were found to interact favourably with LA through the formation of hydrogen bonds *via* the NH moieties. It is important to note that a partial positive order does not necessarily exclude the coordination-insertion mechanism from being considered. To the knowledge of the author, the ROP still occurs *via* this mechanism.

The kinetic profiles of ε-CL ROP were superimposed and are shown in Figure 15 the enantiopure catalysts (*R,R*)- and (*S,S*)-**15** appear to have similar activities while *rac*-**15** was slower throughout the reaction. As the order in monomer is close to zero towards the beginning of the polymerisation, the k_{app} of the polymerisations were calculated using initial rates that assume a zero order rate law. As only the first three data points are used, the method can lend itself to inaccuracy and the extracted values should only be used to gauge the polymerisation behaviour. With that in mind, the initial rate of (*R,R*)- and (*S,S*)-**15** was 2.79×10^{-5} M s^{-1} (Table 1, Entries 1 and 2). However, *rac*-**15** was more than 2.9 times slower ($k_{app} = 9.31 \times 10^{-6}$ M s^{-1}), confirming the trend observed on the kinetic profiles (Table 1, Entry 3). This would suggest that different catalytic species arise from the employment of *rac*-**15** which ultimately slow down the reaction. The activity of *rac*-**15** is comparable to that of the achiral derivative **8c** bearing the $^{H}\mathbf{L}_2$ ligand (Table 1, Entry 4), showing that the enantiopure catalysts can outperform racemic as well as achiral derivatives in the ROP of an achiral monomer.

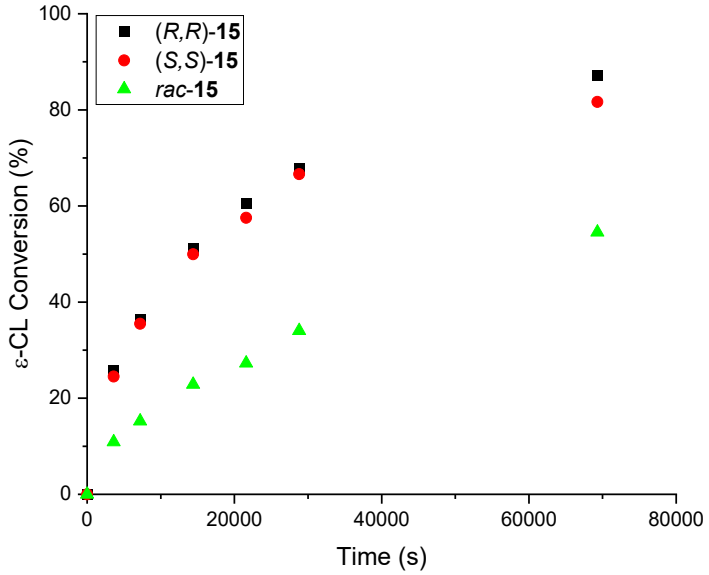


Figure 15. Superimposition of kinetic profiles showcasing the higher activity (*R,R*)- and (*S,S*)-**15** (black and red) over that of *rac*-**15** (green) in ε-CL polymerisation.

Apart from a paper published by Kong *et al.* in which an enantiopure *nacnac* aluminium complex was found to be faster than its racemic counter-part,[49] very little is known on the effect of catalyst chirality on the rate of ε-CL ROP. Given the results and the fact that DFT studies conducted in Section 3.2.6 suggested that heterochiral dimers are thermodynamically favoured, the lower activity of *rac*-**15** was rationalised by its propensity to form heterodimers that lead to a lower overall activity. As (*R,R*)- and (*S,S*)-**15** formed less favourable homodimers, they were able to polymerise ε-CL at higher rates.

An additional experiment was carried out in which scalemic mixtures of complex **15** were prepared and subsequently employed in ε-CL ROP. The initial rates can then give a picture of how the rate varies with respect to $\%ee_{cat} = ([(R,R)\text{-}\mathbf{15}] - [(S,S)\text{-}\mathbf{15}]) / ([(R,R)\text{-}\mathbf{15}] + [(S,S)\text{-}\mathbf{15}])$. Starting from pure samples of (*R,R*)-**15**, complex (*S,S*)-**15** was added to make scalemic mixtures of $\%ee_{cat}$ = 80, 60, 40, 20, and 0. The ε-CL ROP was then carried out for each mixture and initial rates were measured (Figure B43). A plot of the rates as a function of $\%ee_{cat}$ is shown in Figure 16 below. Starting from the slower racemic catalyst ($\%ee_{cat}$ = 0; *rac*-**15**), the rate increases in a linear fashion as the enantiopurity of the catalyst mixture increases. The addition of an enantiomeric impurity to an enantiopure catalyst thus hampers the rate of reaction as $\%ee_{cat}$ decreases, which further confirms the DFT results. The lower the $\%ee_{cat}$, the higher the propensity of the catalyst mixture to form the less active heterodimers. The mechanism through which this occurs will be elucidated in the following section.

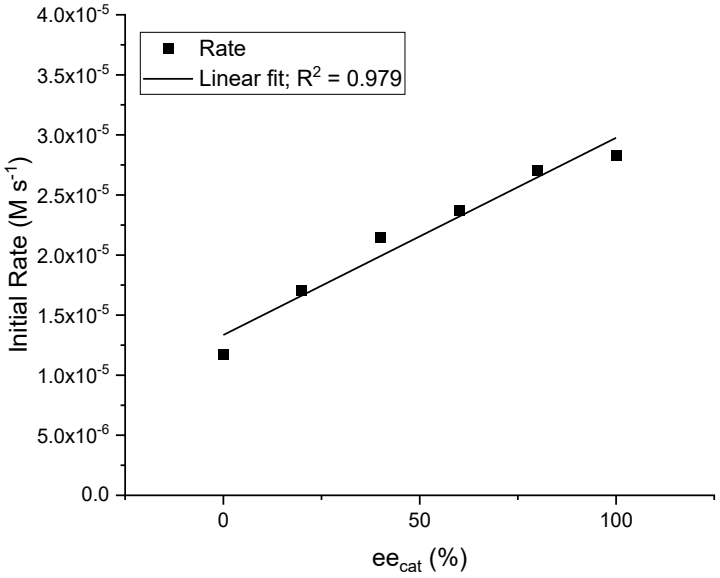


Figure 16. Plot of initial rates as a function of %ee$_{cat}$ [(*R,R*)-**15** = 100 and *rac*-**15** = 0] for the polymerisation of ε-CL. The trend was modelled using a linear fit and appears to exhibit a linear relationship.

3.3.1.2 Kinetic Analysis of ε-CL ROP

Using the VTNA method previously described in Chapter 2, the order in catalyst for (*R,R*)- and *rac*-**15** was investigated (see details in Appendix B).[50, 51] Whereas a catalyst order close to one (~ 0.8) was determined for (*R,R*)-**15** (Figure B97), an order between 0.5 and 0.6 (Figure B98) was observed for *rac*-**15**.

While the former is in line with a well-controlled polymerisation occurring *via* a coordination-insertion mechanism involving a mononuclear active species,[52] the order of 0.5 for *rac*-**15** suggests the formation of a dimeric species that is not part of the catalytic cycle.[53] Such an order has been previously observed in the context of cyclic ester ROP which was attributed to the formation of an inactive dimer.[54, 55] The formation of the heterodimeric benzyloxy complex *rac*-**14**, as well as the DFT calculations carried out in Section 3.2.6 are in agreement with the formation of higher order species when using *rac*-**15** in ε-CL ROP. The ring-opening of ε-CL leads to the formation of a primary alkoxide species which would favour aggregation, yielding dimeric species of lower activity due to presence of a racemic mixture of ligands. It is important to note that predicting catalyst nuclearity in ROP is not straightforward. A dinuclear species in the solid state can easily dissociate into a mononuclear species in solution, and vice-versa. Furthermore, the nuclearity of a complex is not necessarily conducive to its activity, as a dimer can also be active due to a cooperative mechanism arising from the proximity of two metal

centres. Mehrkhodavandi and co-workers details this in a review on dinuclear catalysts for LA ROP,[56] and active as well as inactive bimetallic species have been previously reported in literature.[57-61]

To gain an understanding of catalyst speciation and their relative activity, further kinetic analysis was carried out by the Bures group at the University of Manchester. As this was done externally by collaborators, the kinetic theory behind the procedure will not be discussed at length. The reader is advised to refer to the published joint paper which gives a detailed treatment of the kinetic analysis.[62] Given that ROP mechanisms involving monomeric and dimeric species have been deduced, a general mechanism in which both species can be active was investigated. Assuming that:

- The monomeric and dimeric species are in a thermodynamic equilibrium.
- ε-CL can reversibly bind onto the species.
- Both species can propagate the reaction.

It was found that the rate of polymerisation of the enantiopure catalysts was over twice as fast for the monomeric species than its dimeric counterpart for catalyst orders of 0.8. This was attributed to the formation of tightly bound dimers which make the approach, coordination, and insertion of the monomer less favourable. The speciation and relative activity was illustrated with a plot of the fraction of starting material consumed by the monomeric species (Y_{mono}) as a function of the fraction of the catalyst existing in its monomeric form (f_{mono})

$$Y_{mono} = 2 - 2\,\varepsilon^{r\text{enant}}_{[cat]_T} + \varepsilon^{r\text{enant}}_{[cat]_T}\, f_{mono}$$

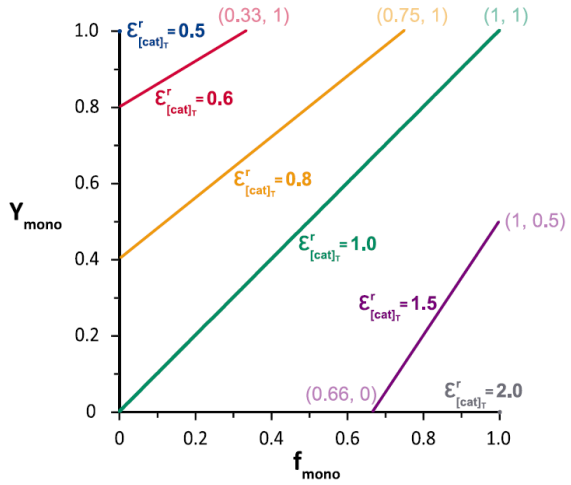


Figure 17. Possible fractions of catalyst as a monomeric species (f_{mono}) and fraction of starting material consumed by the monomeric species (Y_{mono}) for different catalyst orders $\varepsilon^r_{[cat]_T}$.

The graph does not only help the visualisation of fringe cases [*e.g.* where an order of 0.5 leads to no consumption of the monomer by the dimeric species ($Y_{mono} = 1$; $f_{mono} = 0$)] but gives an idea of the polymerisation behaviour involving intermediate orders between 0.5 and 2.0. Thus, an order of 0.8 leads to the conclusion that:

- At least 25 % of the catalyst is present as a dinuclear species.
- At least 40 % of ε-CL is consumed by the mononuclear species.

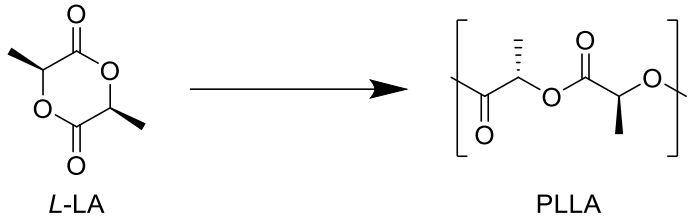
Therefore, a small amount of the catalyst will be present in its dimeric form, which can still be active in polymerisation as it can consume up to 60 % of the ε-CL.

The mechanism for polymerisation carried out by a racemic mixture of catalysts also considers the formation of monomeric and dimeric species. However, the presence of both catalyst enantiomers allows for the formation of homodimers and heterodimers. Referring to Figure 17, a catalyst order of 0.6 thus signifies that the monomeric species is not the most abundant one in solution, representing less than 33 % of the total amount of catalyst. This confirms the hypothesis that the employment of a racemic mixture of catalyst favours the formation of dimeric species, as confirmed by previously discussed DFT calculations. Furthermore, the monomeric species has the highest activity, and accounts for the polymerisation of at least 80 % of ε-CL, in line with the interpretation that a catalyst order of 0.5 indicates the formation of "inactive" dimers that are not part of the productive catalytic cycle. Furthermore, knowing that the enantiopure catalysts are 2.9 times faster than the racemic one, the formation of the heterodimeric species has an equilibrium constant that is 44 times larger than the formation of homodimeric species. From those observations, one can conclude that:

- The homodimeric species makes up less than 4 % of the total catalyst in solution.
- The heterodimeric species is the most abundant one, making up over 66 % of the total catalyst in solution.

Further calculations indicate that the homodimeric and heterodimeric species consume less than 5 % and 17 % of ε-CL respectively, making them the least productive species. This fortifies the claim that a racemic mixture of chiral catalysts favours aggregation which ultimately affects the polymerisation rate as the species are less productive than their monomeric counterparts. The use of an enantiopure catalyst can thus disfavour these processes, leading to a higher overall activity. Given these results, catalysts (*R,R*)-, (*S,S*)-, and *rac*-**15** were investigated with enantiopure substrates (*i.e. D*- and *L*-LA).

3.3.1.3 Polymerisation of an Enantiopure Monomer (*D*- and *L*-LA)



L-LA PLLA

Table 2. L-LA and D-LA polymerisations using complexes (*R,R*)-, (*S,S*)-, and *rac*-**15**, (**8c** added for comparison).

Entry	Catalyst	Monomer (equiv.)	Time (min)	Conv.[a] (%)	$M_{n(SEC)}$ (Đ)[b] (kg/mol)	$M_{n(calc.)}$[c] (kg/mol)	k_{app}[d] (s^{-1})	TOF (h^{-1})
1	(*R,R*)-**15**	*L*-LA (100)	180	64	10.5 (1.1)	9.2	9.20×10^{-5}	21
2	(*S,S*)-**15**	*L*-LA (100)	6	83	13.7 (1.1)	12.0	4.53×10^{-3}	830
3	*rac*-**15**	*L*-LA (100)	20	93	14.3 (1.2)	13.4	2.33×10^{-3}	282
4	(*R,R*)-**15**	*D*-LA (100)	8	87	15.6 (1.1)	12.6	4.50×10^{-3}	670
5	**8c**	*L*-LA (100)	60	96	17.5 (1.1)	13.8	9.17×10^{-4}	96
6[e]	(*S,S*)-**15**	*L*-LA (1,000)	60	66	12.4 (1.1)	9.5	-	660
7[f]	(*S,S*)-**15**	*L*-LA (10,000)	4.5	92	14.1 (1.3)	13.2	-	122,667

Reaction conditions: $[LA]_0 = 1$ mol.L^{-1}, THF, 25 °C; a) Determined by ^{1}H NMR by relative integration of monomer and polymer signals (see ESI); b) Determined by SEC calibrated with polystyrene standards in THF and corrected (see ESI); c) Calculated using the conversion; d) Determined assuming a pseudo-first order; e) Immortal conditions (9 equiv. of ^{i}PrOH added); f) Carried out without solvent at 150 °C

Complexes (*R,R*)- (*S,S*)- and *rac*-**15** were tested for the polymerisation of *L*-LA at room temperature in THF (Table 2, Entries 1-3). In every case, living characteristics were exhibited throughout polymerisation (Figures B44-49). MALDI-ToF analysis of the polymers indicates the presence of *tert*-butoxide end-groups, as is expected from a coordination-insertion mechanism (Figure D3). However, peaks that were spaced apart by 72 a.u. were found, suggesting a small extent of transesterification occurring throughout polymerisation. Analysis of catalyst activities (extracted assuming a pseudo-first order rate law) clearly shows that each catalyst enantiomer has a strong preference for one lactide enantiomer. (*S,S*)-**15** requires only 6 minutes to convert 83 % of *L*-LA while (*R,R*)-**15** requires 3 hours to reach a conversion of 64 %. When comparing the k_{app} values, this makes (*S,S*)-**15** about 50 times faster than (*R,R*)-**15** (k_{SS} / k_{RR} ~ 49). Conversely, (*R,R*)-**15** was employed with *D*-LA ROP (Table 2, Entry 4) and as expected, the resulting rate constant was nearly identical to that of (*S,S*)-**15** for *L*-LA ROP (4.50×10^{-3} *vs*. 4.53×10^{-3} s^{-1}). These findings are in line with the fundamentals of kinetic resolution where one catalyst enantiomer reacts favourably with one given enantiomer of the substrate.[61, 63] When *rac*-**15** was employed in *L*-LA ROP, the resulting rate was an average of

that of (*S,S*)-**15** and (*R,R*)-**15** ((k_{SS} + k_{RR}) / 2 = 2.31 × 10^{-3} s^{-1}; *rac*-**15** = 2.33 × 10^{-3} s^{-1}), which initially hinted at a linear relationship between the $\%ee_{cat}$ and the rate constant.

The activity of (*S,S*)-**15** in the polymerisation of *L*-LA is unprecedented. Not only is it ~4.9 times faster than its achiral counterpart **8c** (Table 2, Entry 5), but it outperforms every aluminium-based catalyst that has been published to date.[64] The catalyst is also active at low loadings and immortal conditions (0.1 mol%; 9 equiv. of ^{i}PrOH), polymerising 66 % of 1000 equivalents of *L*-LA in 1 hour while maintaining good control (Đ = 1.1) (Table 2, Entry 6). (*S,S*)-**15** was also tested in industrially relevant conditions and showed very high activity, 10,000 equivalents of L-LA (and 99 equiv. of ^{i}PrOH) at 150 °C, reaching 92 % conversion in 4.5 minutes with only a slight increase in dispersity (Đ = 1.3) (Table 2, Entry 7). This is in stark contrast to other aluminium complexes employed at similar conditions, of which the fastest requires 18 minutes to polymerise 50 % of 900 equivalents.[65] The results highlight the advantage that a matching enantiopure catalyst can bring to the polymerisation of enantiopure monomers.

To gain an understanding of how the activity varies with catalyst enantiopurity, the testing of scalemic mixtures of catalysts with *L*-LA was undertaken (Figures B52 and B53).

Following a similar procedure as previously described, the k_{app} was determined (assuming a first order in monomer) for different scalemic mixtures of catalysts and plotted as a function of $\%ee_{cat}$. In this case, $\%ee_{cat}$ values of -100, 0, and +100 corresponded to (*R,R*)-, *rac*-, and (*S,S*)-**15** respectively. The corresponding graph suggests that the rates are distributed along an "S-shaped" curve rather than a linear trend (Figure 18, a sigmoid and linear trend were plotted for information). Starting from a racemic mixture of the catalyst (ee_{cat} = 0), a small impurity of the "match" catalyst leads to a k_{app} significantly higher than that of an expected linear trend ("rate amplification"). Here, this will be referred as "Non-Linear Kinetic Effect" (NLKE) which describes a rate amplification without an asymmetric amplification. Thus, the graph indicates a positive NLKE for $\%ee_{cat}$ = 0 - 100. Conversely, a small impurity of the "mismatch" catalyst leads to a k_{app} lower than that of an expected linear trend ("rate suppression", negative NLKE for $\%ee_{cat}$ = -100 - 0). However, starting from an enantiopure catalyst (ee_{cat} = -100 or +100), a small impurity initially only has a small effect on the k_{app}, which becomes more apparent as the fraction of chiral impurity increases. This is favourable as it means that one does not require a 100 % enantiopure catalyst of which its resolution may not be industrially feasible.

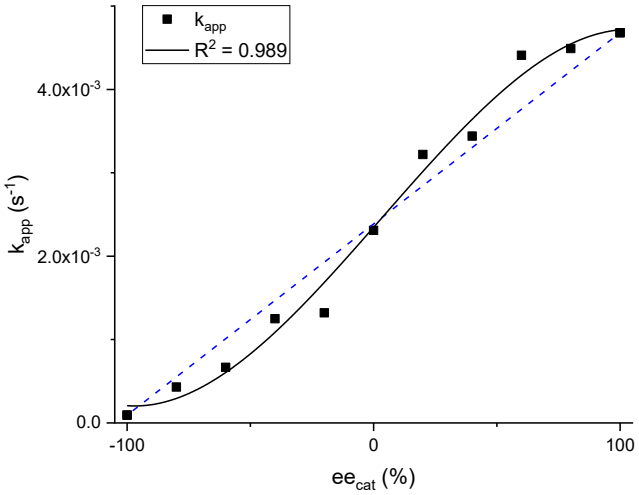


Figure 18. Plot of k_{app} as a function of $\%ee_{cat}$ [(*R,R*)-**15** = -100 and (*S,S*)-**15** = +100] for the polymerisation of L-LA. The trend was modelled using a sigmoid fit and appears to exhibit a NLKE.

Pioneered by Kagan, the field of non-linear effects (NLE) has cemented itself as a powerful tool that allows for elucidation reaction mechanisms in asymmetric catalysis, and thus improve catalyst design.[66, 67] By looking at the product *ee* as a function of catalyst *ee*, NLE studies allow for the creation of models which explain the relationship of both variables.[68-70] These usually imply the formation of dimeric or even polymeric species (*e.g.* ML_n model and reservoir model).[71, 72] Noyori and co-workers extensively studied NLEs in the enantioselective addition of dialkylzincs to alcohols, which validated many of the proposed models.[73, 74] To date, a variety of reactions were found to exhibit an NLE, though studies in the context of polymerisation catalysis remain scarce. Nozaki and co-workers observed an asymmetric amplification in the asymmetric alternating copolymerisation of CHO and CO_2 using chiral zinc complexes (prepared from diethylzinc and chiral alcohols).[75] Horeglad and co-workers reported the effect of Lewis bases on the formation of homochiral dimeric Ga and In alkoxides and their stereoselectivity in *rac*-LA polymerisation. They observed an NLE between heteroselectivity and the fraction of homochiral complexes.[76] The chiral bipyrrolidine scaffold by Kol and co-workers (See Section 3.1.3) also led to the postulation that an NLE may exist within that system as they suggested that enantiomeric impurities may increase the stereoselectivity of their system.[24, 77] In 2012, the Mehrkhodavandi group observed that the k_{app} of a chiral dinuclear indium catalyst decreases in a non-linear fashion as its enantiopurity is increased starting from a racemic mixture of catalyst in *rac*-LA ROP.[61] The stereoselectivity decreases in a similar fashion from P_m = 0.6 to 0.5. However, these relationships were never considered for aluminium-based catalysts. In most cases, NLEs were related to asymmetric

amplification and how the enantiomeric excess of the catalyst species influences the enantiomeric outcome of the reaction.

To complement these results, an experiment was conducted in which the enantiopurity of the monomer was varied from *D*- to *L*-LA with scalemic mixtures (%ee$_{LA}$ = -100 or +100) whilst the enantiopurity of the catalyst remained the same (in this case (*S,S*)-**15** was used, Figures B54 and B55). %ee$_{LA}$ values of -100, 0, and +100 correspond to *L*-, *rac*-, and *D*-LA respectively. The k_{app} were measured assuming a pseudo-first order rate law in monomer. The resulting plot shows an obvious non-linear dependence of k_{app} on the enantiopurity of the monomer (Figure 19). When using (*S,S*)-**15**, a small quantity of chiral impurity in the monomer (%ee$_{LA}$ > -100) leads to a significant decrease of the reaction rate. This rate of change decreases rapidly and plateaus the closer the monomer is to pure *D*-LA (%ee$_{LA}$ > 0). It appears that the 'mismatch' monomer, *D*-LA, acts as a poison to (*S,S*)-**15** and thus decreases the k_{app}. The catalyst poisoning pictured in Figure 19 likely arises from fractional deactivation by forming an inactive diastereomeric catalyst-substrate complex. The chirality of the chain-end appears to play an important role in governing the stability of these species, and further studies were eventually conducted on more complicated systems involving *meso*- and *rac*-LA.

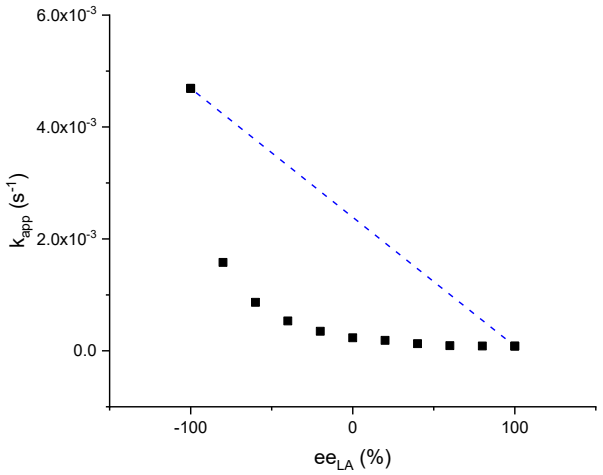


Figure 19. Plot of k_{app} as a function of %ee$_{LA}$ [*L*-LA = -100 and *D*-LA = +100] for the polymerisation of LA by (*S,S*)-**15**.

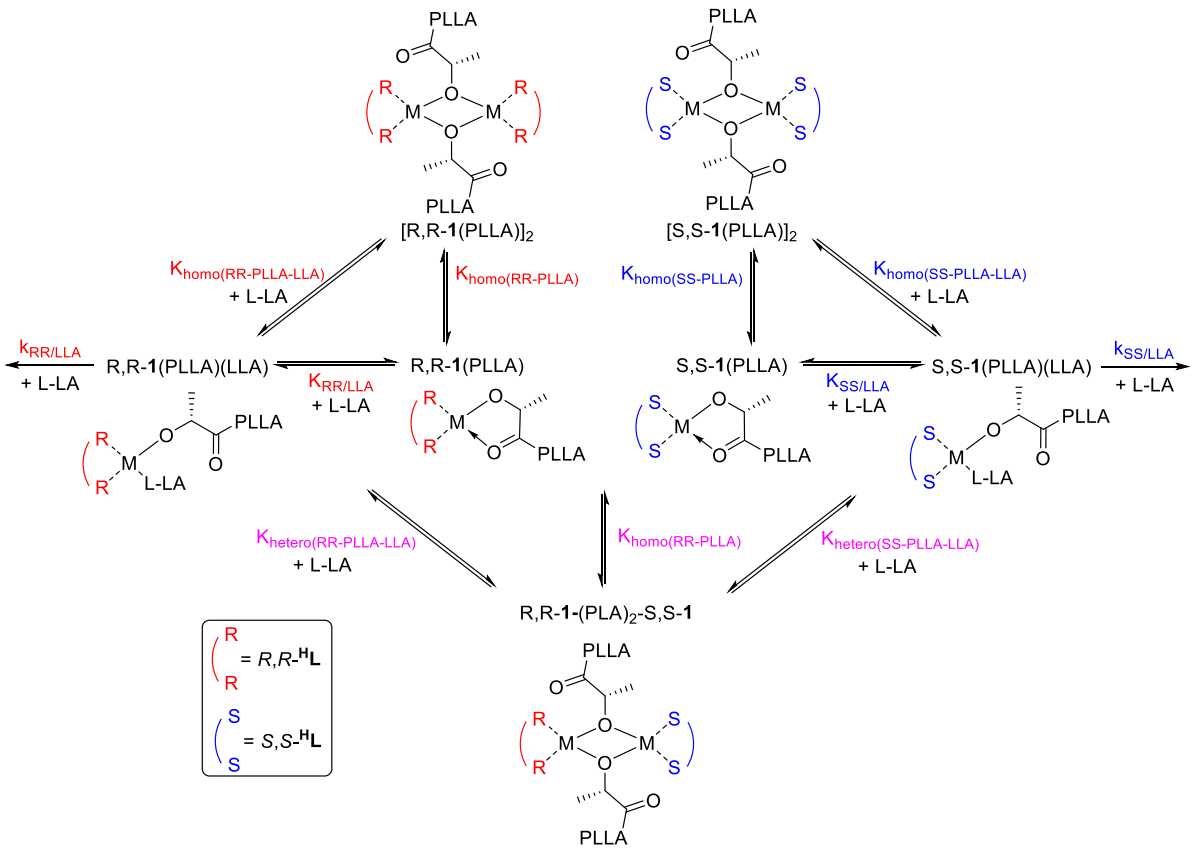
3.3.1.4 Kinetic Analysis of *L*-LA ROP

Having elucidated the mechanism of polymerisation of an achiral monomer, the understanding of a more complex system was sought. (*S,S*)-**15** preferentially polymerises *L*-LA over *D*-LA by a factor of 49. Varying the enantiomeric excess of the catalyst (%ee$_{cat}$) from -100 to 100 whilst using *L*-LA resulted in it having a sigmoidal relationship with k_{app} (Figure 18). Varying

the enantiomeric excess of LA ($\%ee_{LA}$) from -100 to 100 whilst using (*S,S*)-**15** resulted in poisoning of the catalyst as more of the mismatch substrate (*D*-LA) was added (Figure 19).
To gain a further understanding of the system, the catalyst order for (*S,S*)-, (*R,R*)-, and *rac*-**15** with *L*-LA was determined (Figures B104, B106, and B108). A first order was observed for complex (*S,S*)-**15** which indicates that the polymerisation occurs solely through either a mononuclear of dinuclear active species. However, (*R,R*)-**15** exhibited an order of 1.5 which suggests that a dimeric species can be part of the catalytic cycle and involved in an elementary step of the mechanism. This contrasts with the catalyst order of 0.6 for *rac*-**15** in the ROP of ε-CL where the dimeric species is not involved in the polymerisation mechanism ("in-cycle" *vs.* "off-cycle"). A catalyst order that is greater than 1 is not unheard of in LA ROP. Kol and co-workers reported that polymeryl exchange *via* a dimeric species can lead to catalyst orders that are greater than 1.[24] The supposedly dimeric elementary step in the mechanism of (*R,R*)-**15** can have a higher activation energy than the mononuclear mechanism of (*S,S*)-**15**, which results in the polymerisation having a lower overall activity.

Somewhat expectedly, the order of *rac*-**15** in *L*-LA ROP is 1.25, an average of the order of (*S,S*)-**15** (1.0) and (*R,R*)-**15** (1.5). This trend is analogous to the rate constants observed where that of *rac*-**15** (2.33×10^{-3} s^{-1}) is an average of that of (*S,S*)-**15** (4.53×10^{-3} s^{-1}) and (*R,R*)-**15** (9.20×10^{-5} s^{-1}). Whether this order arises from the mechanisms of (*R,R*)- and (*S,S*)-**15** occurring simultaneously, or from a new mechanism altogether, remains unclear.

The dimerisation mechanism for ε-CL ROP can be extended to the sigmoidal trend observed when scalemic mixtures of the catalysts were tested with *L*-LA (Figure 18). It was found that a positive NLKE (rate amplification) occurred for scalemic mixtures of $\%ee_{cat} > 0$. In those cases, part of the slower species, (*R,R*)-**15**, is consumed to form a heterochiral species which suppresses the formation of the "slower" homochiral dimer of (*R,R*)-**15**. The negative NLKE (rate suppression) was observed for scalemic mixtures of $\%ee_{cat} < 0$. There, the faster species (*S,S*)-**15** is incorporated into the heterochiral species and thus into a mechanism that is thought to be slower than that of the monomeric (*S,S*)-**15**. The mechanism is summarised in Scheme 9.



Scheme 9. Proposed mechanism of the ROP of *L*-LA via scalemic mixtures of (*R,R*)- and (*S,S*)-**15** which may form heterochiral species that affect the overall rate, yielding a NLKE.

3.3.1.5 Polymerisation of *meso*-LA

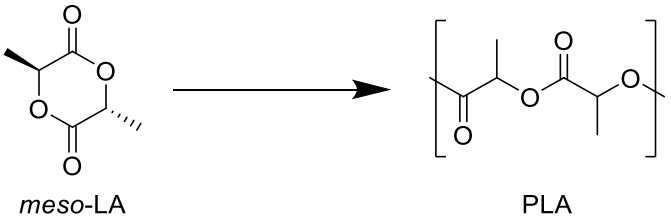


Table 3. meso-LA polymerisations using complexes (*R,R*)-, (*S,S*)-, and *rac*-**15**, (**8c** added for comparison).

Entry	Catalyst	*meso*-LA (equiv.)	Time (min)	Conv.[a] (%)	$M_{n(SEC)}$ (Đ)[b] (kg/mol)	$M_{n(calc.)}$[c] (kg/mol)	P_m[d]	k_{app}[e] (s^{-1})	TOF (h^{-1})
1	(*R,R*)-**15**	100	30	90	-	-	0.38	1.04×10^{-3}	180
2	(*S,S*)-**15**	100	30	96	-	-	0.40	1.34×10^{-3}	192
3	*rac*-**15**	100	6	96	8.9 (1.2)	13.9	0.76	6.69×10^{-3}	960
4	**8c**	100	40	99	11.3 (1.1)	14.2	0.54	1.98×10^{-3}	149

Reaction conditions: $[LA]_0 = 1$ mol.L^{-1}, THF, 25 °C; a) Determined by ^{1}H NMR by relative integration of monomer and polymer signals (see ESI); Determined by SEC calibrated with polystyrene standards in THF and corrected (see ESI); c) Calculated using the conversion; d) Probability of *meso* linkage determined by ^{1}H NMR spectroscopy (see ESI); e) Determined assuming a pseudo-first order

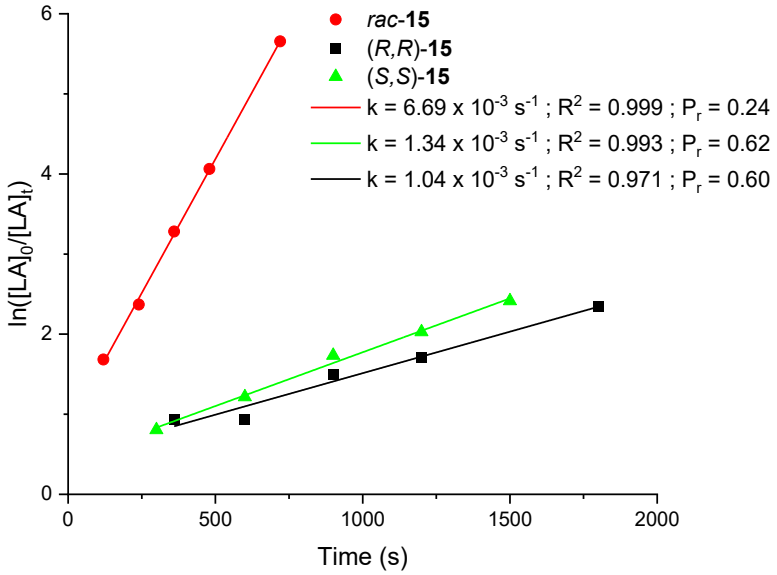


Figure 20. Superimposition of log plots showcasing the higher activity of rac-**15** (red) over that of (R,R)- and (S,S)-**15** (black and green) in meso-LA polymerisation.

Polymerisations carried out with *meso*-LA showed that the monomer was polymerised readily which is not usually seen with aluminium-based catalysts (See Section 2.4.2).[8, 23, 78-81] The complex *rac*-**15** was found to outperform the enantiopure catalysts by a factor of ~ 6 (Figure 20). The conversion of 96 % of monomer within 6 minutes makes the ROP of *meso*-LA by *rac*-**15** the fastest polymerisation so far achieved with catam catalysts at standard conditions (Table 3 Entry 3). Interestingly, (*R,R*)- and (*S,S*)-**15** led to the formation of syndiotactic PLA (P_m ~ 0.4) while *rac*-**15** produced predominantly heterotactic PLA (P_m = 0.76) (Table 3, Entries 1 and 2). GPC analysis was carried out on the polymers of *rac*-LA. The measured molecular weight was significantly lower than expected (8.9 *vs.* 13.9 kg/mol) although dispersities remained low (Đ = 1.2). The molecular weights were found to increase linearly with conversion, indicating that the polymerisation displayed living characteristics (Figure B56). Given that a change in catalyst resulted in a change in activity as well as a change in stereochemical outcome, scalemic mixtures of the catalysts with *meso*-LA were tested to study the variation of k_{app} as a function of $\%ee_{cat}$ (Figure B57). Starting from the enantiopure catalyst (*S,S*)-**15** ($\%ee_{cat}$ = 100 %), the k_{app} increases the closer one gets to a racemic mixture ($\%ee_{cat}$ = 0 %). The trend itself is non-linear (Figure 21) which is expected given previous results with chiral monomers (*L*-LA). This is a positive NLKE as a small amount of (*R,R*)-**15** added to (*S,S*)-**15** increases the k_{app} more than is expected (blue dotted line). A particularly interesting feature of the graph is how the stereoregularity changes with $\%ee_{cat}$. Whilst the enantiopure

catalyst (%ee_{cat} = 100 %) produces slightly syndiotactic PLA (P_m = 0.35), a small presence of chiral impurity (%ee_{cat} = 80 %) shifts the stereoselectivity drastically towards heterotactic PLA (P_m = 0.58). The heteroselectivity then increases linearly up to a P_m of 0.70. This is the first occurrence of an NLE concerning the stereoselectivity in this thesis.

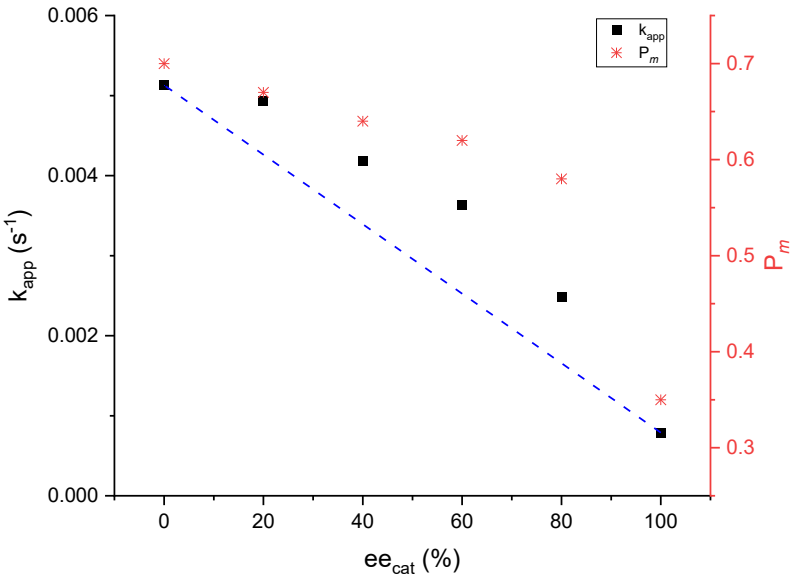
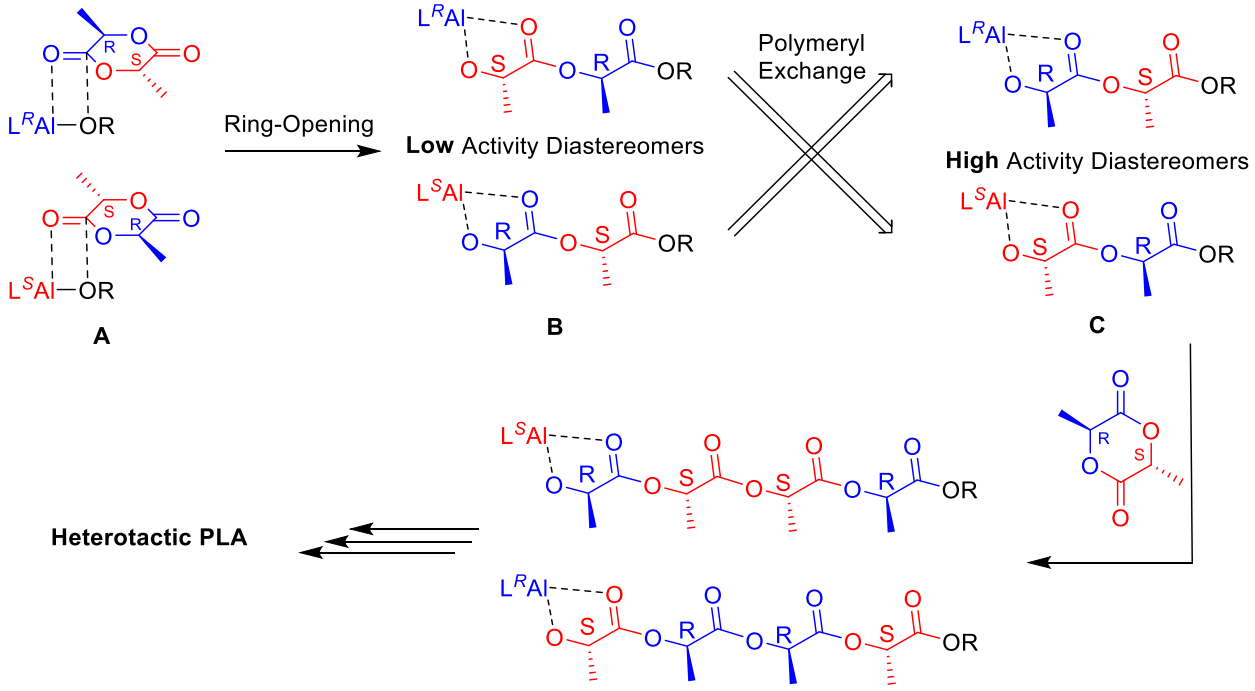


Figure 21. Plot of k_{app} as a function of %ee_{cat} [*rac*-**15** = 0 and (*S,S*)-**15** = +100] for the polymerisation of *meso*-LA, exhibiting a NLKE. The polymer became more heterotactic as %ee_{cat} approached 0.

This trend is not the first of its kind: Ovitt and Coates have reported a similar behaviour when employing racemic and enantiopure aluminium SalBINAP complexes.[9] The enantiopure complex produced highly syndiotactic PLA while the racemic counterpart produced heterotactic PLA (P_m = 0.80). To account for this, the group has proposed a mechanism that considers polymeryl exchange and absolute stereoconfiguration upon opening and is conceptually related to an ancillary ligand exchange mechanism proposed by Brookhart and Wagner in 1996.[82] Together with mechanisms published by Kol and co-workers,[24, 77] the insights were adapted to fit with the ^{H}**L**$_3$ catalytic systems (Scheme 10).

It was assumed that (*R,R*)- and (*S,S*)-**15** open *meso*-LA at the *R* and *S* stereocentre respectively (**A**). Whilst the proximal stereocentre is involved in the reaction, it is the distal stereocentre that forms the chain-end upon opening. This signifies that (*R,R*)- and (*S,S*)-**15** will bear a chain end with a *S* and *R* configuration respectively (**B**). In a racemic mixture of the catalyst, these diastereomers are then present in equal quantities but will undergo polymeryl exchange through

a μ-alkoxide species to yield (*R,R*)- and (*S,S*)-**15** with a *R* and *S* configuration respectively (**C**). These species then insert another *meso*-LA unit and steps **B** and **C** are repeated, ultimately yielding heterotactic PLA. We postulate that the diasteromeric species in **B** have a low activity, mainly due to the fact that these are the species predominantly present when the enantiopure catalysts are employed. These are lower in activity than *rac*-**15** by a factor of 6 and continue inserting *meso*-LA without polymeryl exchange, leading to syndiotactic PLA. The polymeryl exchange step itself is fast and favourable, as evidenced by the fact that a small chiral impurity in the enantiopure catalyst ($\%ee_{cat} = 80\ \%$) leads to a large increase in activity and an immediate shift to heterotactic PLA being produced (Figure 21).



Scheme 10. Proposed mechanism for the formation of heterotactic PLA when *rac*-**15** was employed with *meso*-LA. Fast polymeryl exchange is thought to be the source of the selectivity.

3.3.1.6 Polymerisation of a Racemic Monomer (*rac*-LA)

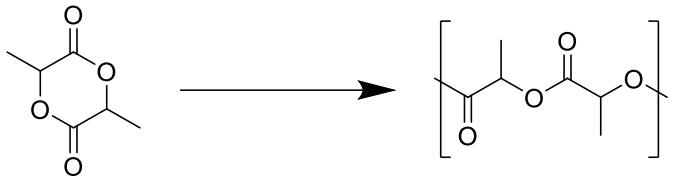


Table 4. *rac*-LA polymerisations using complexes (*R,R*)-, (*S,S*)-, and *rac*-**15**, (**8c** added for comparison).

Entry	Catalyst	*rac*-LA (equiv.)	Time (min)	Conv.[a] (%)	$M_{n(SEC)}$ (Đ)[b] (kg/mol)	$M_{n(calc.)}$[c] (kg/mol)	P_m[d]	k_{app}[e] (s^{-1})	TOF (h^{-1})
1	(*R,R*)-**15**	100	50	59	10.1 (1.2)	8.6	0.50	2.86×10^{-4}	71
2	(*S,S*)-**15**	100	50	51	11.0 (1.2)	7.3	0.50	2.32×10^{-4}	61
3	*rac*-**15**	100	40	94	15.9 (1.2)	13.6	0.50	1.23×10^{-3}	141
4	**8c**	100	90	96	14.3 (1.2)	13.8	0.60	5.47×10^{-4}	64
5[f]	*rac*-**15** + **8c**	100	60	95	17.3 (1.1)	13.8	0.50	-	95
6	*rac*-**15**	1000	13 * 60	93	77.0 (1.2)	134.0	0.52	-	71
7	*rac*-**14**	100	21 * 60	44	21.2 (1.1)	6.4	0.50	-	2

Reaction conditions: $[LA]_0 = 1$ mol.L^{-1}, THF, 25 °C; a) Determined by ^{1}H NMR by relative integration of monomer and polymer signals (see ESI); b) Determined by SEC calibrated with polystyrene standards in THF and corrected (see ESI); c) Calculated using the conversion; d) Probability of *meso* linkage determined by ^{1}H NMR spectroscopy (see ESI); e) Determined assuming a pseudo-first order; f) Equimolar amount of *rac*-**15** and **8c** were used

Given that an NLE was observed in *meso*-LA ROP, the complexes were tested for the polymerisation of *rac*-LA in THF at room temperature. For each of the three catalysts, the polymerisation proceeded in a controlled fashion, displaying the usual characteristics of a living polymerisation (Figures B58-B63) including a pseudo-first order in monomer and a linear increase in molecular weight *vs.* conversion. It was found that *rac*-**15** polymerised *rac*-LA considerably faster than the enantiopure complexes with $k_{rac}/k_{RR} \sim k_{rac}/k_{SS} \sim 4.5$, as depicted in Figure 22 (data in Table 4, entry 1-3).

Complex *rac*-**15** is so far the fastest catalyst in the catam-series for *rac*-LA polymerisation. Due to *rac*-**15** being composed of an equimolar amount of (*R,R*)- and (*S,S*)-**15**, this initially led to the conclusion that the increased activity was due to each of the catalyst enantiomers preferring the insertion of a single LA enantiomer (as per an ESC mechanism). This would also explain the lower activities of the enantiopure complexes as only one of the LA enantiomers is considered a "match" (Table 4, Entries 1 and 2). However, decoupled ^{1}H NMR analysis showed all polymers to be atactic ($P_m = 0.50$) (See Appendix C). This is in contrast to the achiral **8c** which exhibited an isotactic bias, albeit with lower activities (Table 4, Entry 4). Thus, the

incorporation of a chiral component within the catalyst framework as well as the use of enantiopure catalysts did not result in an improvement in tacticity control (compared to the achiral analogue). At first glance, the results appear to be antithetical to those obtained with *L*-LA where a given catalyst enantiomer prefers to polymerise a given LA enantiomer by a factor of 49. However, the use of a racemic monomer mixture can cause the preferred mechanism of polymerisation to change. The quasi-random insertions of LA enantiomers are thought to arise from CEC and ESC mechanisms competing with one another, leading to an atactic polymer.

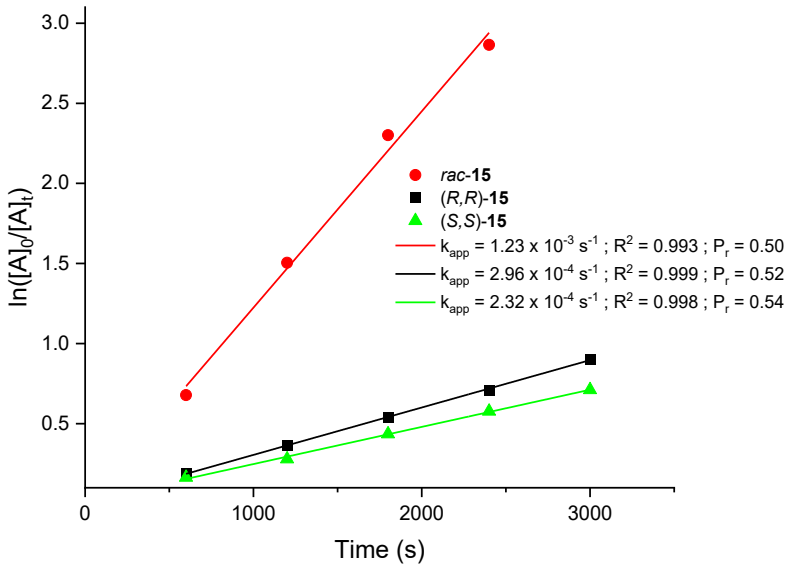


Figure 22. Superimposition of log plots showcasing the higher activity of *rac*-**15** (red) over that of (*R,R*)- and (*S,S*)-**15** (black and green) in *rac*-LA polymerisation.

As seen with *meso*-LA, an NLE was observed in the activity and stereoselectivity when scalemic mixtures were employed (Figure 21). In the hopes of gaining an understanding of the underlying mechanism of *rac*-LA polymerisation, scalemic mixtures of complex **15** were prepared (%ee$_{cat}$ = 0 – 100 %) and employed in *rac*-LA ROP. For each reaction, k_{app} values were measured, assuming a first order in monomer (Figure B64). These were then plotted on a graph as a function of %ee$_{cat}$ (Figure 23). As with *meso*-LA, the graph shows a non-linear dependence between %ee$_{cat}$ and k_{app} with a large deviation from an expected linear trend (blue dotted line). Adding a small chiral impurity [(*R,R*)-**15** to (*S,S*)-**15**] resulted in a tripling of the rate constant which slowly tapers off as a racemic catalyst mixture (%ee$_{cat}$ = 0) is approached. An interesting point to make is that none of the polymerisations resulted in an enhancement of the tacticity, shown by the P_r values being around 0.50 in every case. This differs from the ROP

of *meso*-LA as well as from NLEs usually reported in asymmetric catalysis where asymmetry enhancement is usually associated with a rate decrease (or vice-versa).[69]

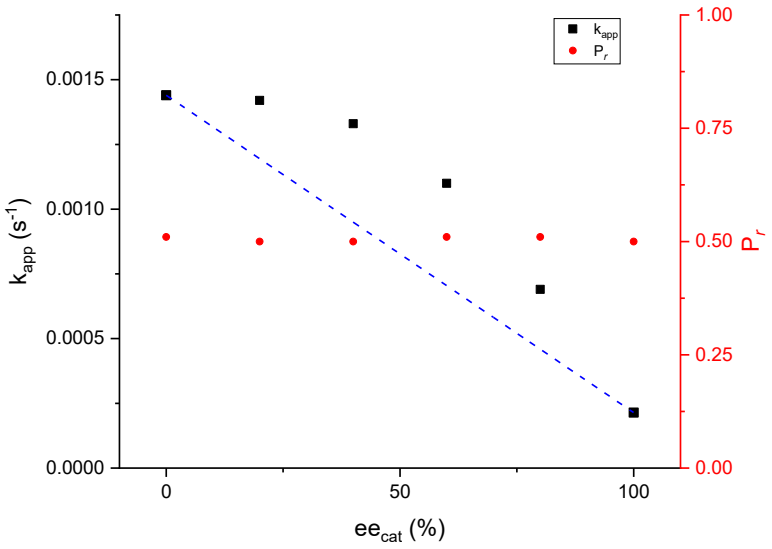


Figure 23. Plot of k_{app} as a function of $\%ee_{cat}$ [*rac*-**15** = 0 and (*S,S*)-**15** = 100] for the polymerisation of *rac*-LA, exhibiting an NLKE. The tacticity of the polymer did not vary throughout.

Many factors such as catalyst deactivation, dimerisation, and polymeryl exchange could be occurring, which ultimately affects the reaction rate. It was demonstrated in Section 3.2.4.1 that the chiral complexes can form multiple species with varying degrees of stability. Whilst the *trans*-**15** complexes are monomeric, the addition of a polymer chain (2° alkoxide) can result in a decrease in steric bulk and give the active species a propensity to dimerise throughout the reaction. Coupled with the fact that the chirality of the catalyst and chirality of the lactide can lead to multiple combinations, the problem increases in complexity.

To evaluate whether polymeryl exchange occurs, *rac*-**15** was employed along with **8c** in a 1:1 ratio (Table 1, Entry 5) as carried out by Lamberti and co-workers to highlight the prevalence of polymeryl exchange in their ROP mechanism.[25] As these complexes differ significantly in activity ($k_{app} = 1.23 \times 10^{-3}$ s^{-1} *vs.* 5.47×10^{-4} s^{-1}), a lack of polymeryl exchange should result in a bimodal distribution of polymer molecular weights on the GPC trace. However, the polymer was found to be exhibit a narrow monomodal distribution, meaning that the polymer chains are continuously exchanged between the complexes. Thus, to minimise polymeryl exchange, *rac*-**15** was employed at high dilution which would shift its equilibrium towards a monomeric species (Table 1, Entry 6). This would ideally lead to a higher stereoregularity of the polymer.

However, results show that despite the dilution, the resulting polymer is atactic. The confirmation of polymeryl exchange also affirms the proposed mechanism for heteroselectivity of *rac*-**15** in *meso*-LA ROP (Scheme 10).

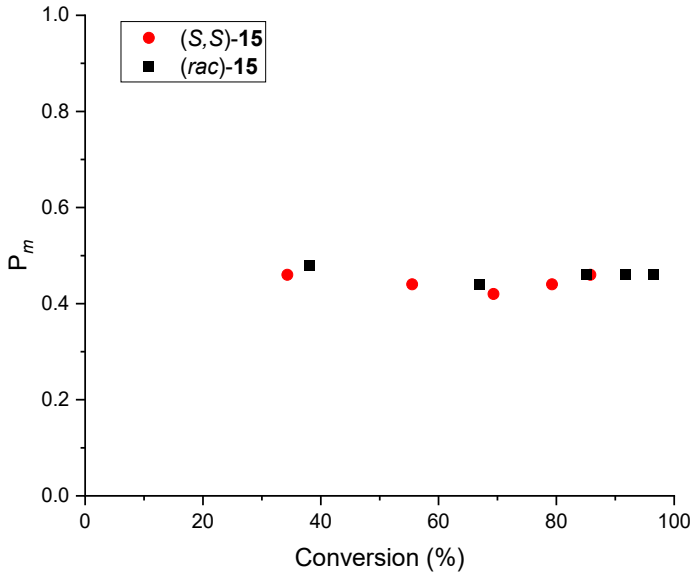


Figure 24. Plot of P_m as a function of conversion for *rac*-LA ROP by (*S,S*)-**15** and *rac*-**15**, showing atactic PLA being regardless of conversion.

The change in tacticity with conversion was also evaluated. Lamberti and co-workers have found that their catalyst initially polymerised *rac*-LA *via* an ESC mechanism. However, as the monomer was consumed, a predominantly CEC mechanism was observed. Thus, polymerisations were carried out in which aliquots were periodically taken and the stereoregularity of the polymer examined (Figure 24). It was found that at all conversions for (*S,S*)- and *rac*-**15**, the polymer was atactic (P_m = 0.42 – 0.50). This signifies that a CEC mechanism is dominant throughout polymerisation.

The dimeric complex *rac*-**14** was employed to evaluate whether polymerisation can be initiated by a dimeric Al complex (Table 1, Entry 7). A conversion of 44 % was achieved after 21 hours at room temperature, with the polymer having a molecular weight more than 3 times larger than expected (assuming that one Al centre initiates one polymer chain). The fact that the dispersity is surprisingly low (Đ = 1.1) indicates that the amount of active species remains constant during the reaction as newly generated active species would initiate much later, resulting in shorter chains that affect dispersity. This is dependent on the nature of the monomer-dimer equilibrium and solely a thermodynamic phenomenon. Assuming that the

polymerisation is carried out by a single active species, the discrepancy between the expected and measured molecular weight (6.4 *vs.* 21.2 kg/mol) indicates that only 30 % of the Al is present in its active form.

The order in catalyst was determined for *rac*-LA ROP by (*R,R*)-, (*S,S*)-, and *rac*-**15**. For the enantiopure catalysts (*R,R*)- and (*S,S*)-**15**, an order in catalyst of 1.2 was obtained (Figure B105). The racemic analogue *rac*-**15** exhibited a slightly lower order of 1.1 (Figure B107). In either case, a multinuclear species is part of the mechanism and plays an active role in the activity. This dimerisation, which is not part of the traditional coordination-insertion mechanism, is thought to be the cause of the observed lack of stereoselectivity. In this context, the dimerisation can take the form of a polymeryl exchange intermediate which could be a source for the quasi-random insertions. The other possibility is that the dimerisation yields a stable and thus inactive dimer that reduces the number of certain reactive species in solution. Unfortunately, a coherent mechanism cannot be drawn based on this kinetic data alone. DFT studies were thus conducted to further elucidate the mechanism of polymerisation.

3.3.1.7 Computational Studies on LA ROP

As was the case in the previous chapter, the calculations were carried out on an ωB97xD level of theory using a split valence double zeta 6-31G(d,p) basis set and implicit modelling of THF (cpcm) (details in the Appendix E). The crystal structure of (*S,S*)-**15** was used as a starting point and the *tert*-butoxide group replaced with methoxide for computational efficiency. This yielded the structure (*S,S*)-**I**. A standard mononuclear coordination-insertion mechanism was initially envisaged for the polymerisation of LA.

For the initiation step, multiple approaches of *D*- and *L*-LA were considered of which the most favourable one was displayed in Figure 25. In both cases, the rate-determining step was found to be the nucleophilic attack. However, (*S,S*)-**I** preferentially inserted *L*-LA with an activation energy of $\Delta\Delta G_{298}$ = 5.6 kcal/mol (*vs.* 11.0 kcal/mol for *D*-LA). Compared to the DFT calculations involving the initiation of LA by complexes **2** ($\Delta\Delta G_{298}$ = 11.8 kcal/mol) and **8c** ($\Delta\Delta G_{298}$ = kcal/mol), the activation energy is much lower, in line with the observed trend where the polymerisation of *L*-LA by (*S,S*)-**15** ($k_{app} = 4.53 \times 10^{-3}$ s^{-1}) is much faster than the polymerisation of *rac*-LA by **2** ($k_{app} = 4.75 \times 10^{-4}$ s^{-1}) as well as the polymerisation of *L*-LA by

8c (k_{app} = 5.47 × 10^{-4} s^{-1}). Interestingly, the insertion of a *D*-LA unit only required an activation energy of $\Delta\Delta G_{298}$ = 11.0 kcal/mol, making it significantly disfavoured to the *L*-LA.

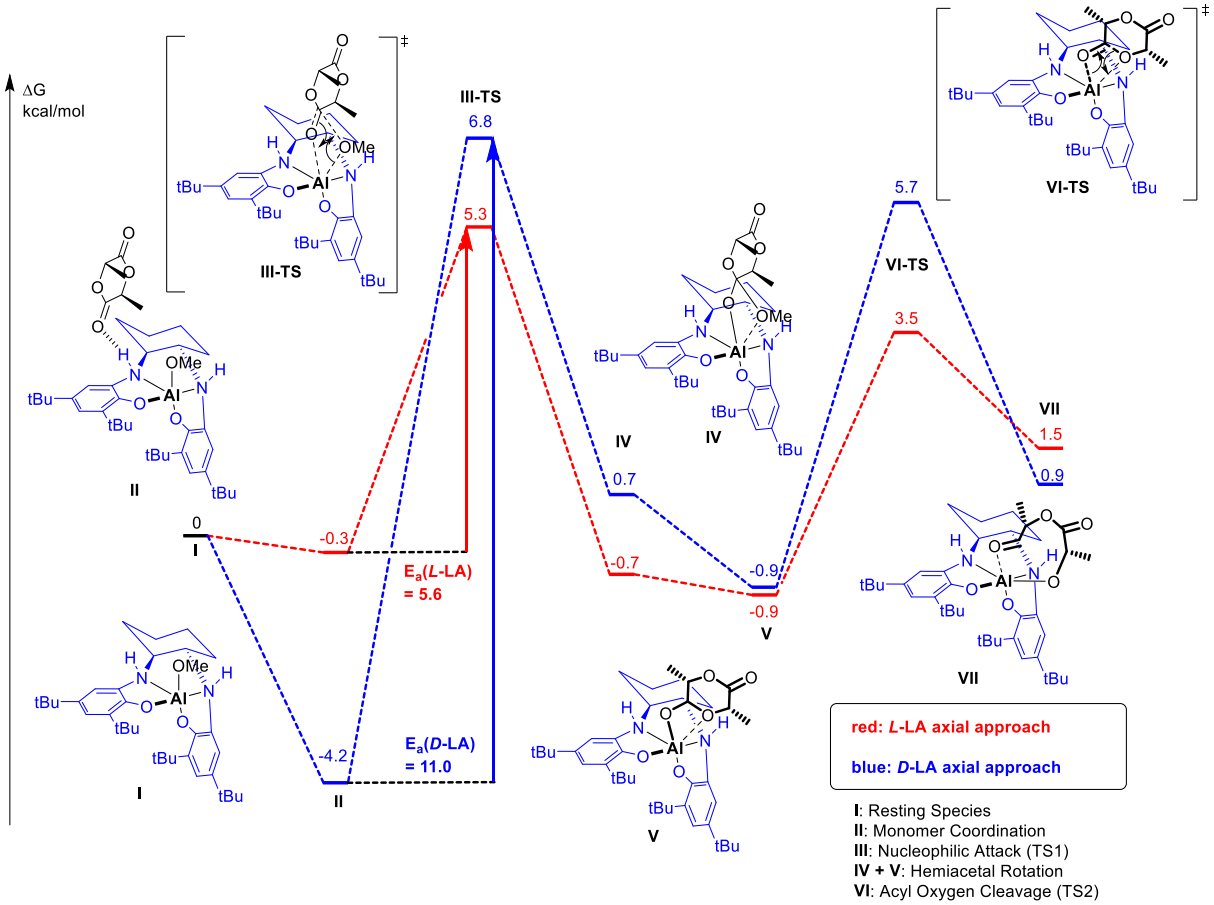


Figure 25. PES showing first insertion of a LA monomer into (S,S)-**15** (**I**). DFT protocol: # ωB97xD/6-31g(d,p) scrf=(cpcm, solvent = THF) nosymm integral=grid=ultrafine.

Previous DFT studies on the complexes **2** and **8c** highlighted the importance of NCIs in the room-temperature active ROP of *rac*-LA. Not surprisingly, such interactions were also present in this family of catalysts where favourable H-bonding occurred between the ester carbonyl of the monomer and the NH moieties of (*S,S*)-**I**. This was mainly observed in the coordination step and thought to withdraw electron density from the carbonyl to facilitate the subsequent nucleophilic attack (Figure 26). The framework distortion energy (FDE) was calculated and found to be 5.7 kcal/mol. This is considerably lower than that of complex **2** (*c.f.* 8.0 kcal/mol) and was attributed to the trigonal bipyramidal geometry of the complex being closer in shape to the octahedral transition states of the polymerisation, reminiscent of Hammond's postulate.

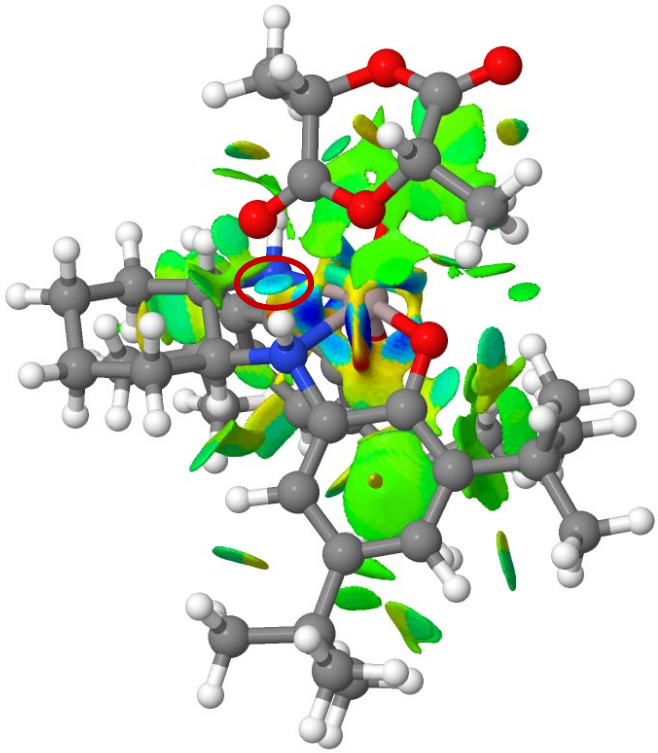


Figure 26. NCI surface of the monomer coordination step (**II**) featuring a hydrogen bond between the NH moiety and LA carbonyl (blue disc).

The propagation step was calculated for two pathways (Figure E7). Given the atactic nature of the polymers produced in *rac*-LA ROP, the propagation after the insertion of *L*-LA (the preferred initiation) as well as *D*-LA was considered. This is meant to emulate the different chiralities of the chain end while maximising computational efficiency. It was hoped that an insight is gained into the activity and selectivity of the diastereomers [(*S,S*)-**I**-PLLA] and [(*S,S*)-**I**-PDLA]. After initiation *via* the opening of a *L*-LA monomer, it was found that the catalyst hardly exhibits a preference. The second insertion of *L*-LA requires an activation energy of $\Delta\Delta G_{298}$ = 17.4 kcal/mol which is 0.7 kcal/mol lower than the insertion of *D*-LA ($\Delta\Delta G_{298}$ = 18.1 kcal/mol). Both insertions are still conducive to a room temperature active polymerisation as observed. However, while the difference between both insertions is rather small, an isoselective bias in the *rac*-LA polymerisations should still be observed. Since the occurrence of dimerisation and polymeryl exchange mechanisms during polymerisation was suggested, the reactivity of (*S,S*)-**15** with a *D*-LA chain-end was studied. In this case, the active species clearly prefers the insertion of *L*-LA at an activation energy of $\Delta\Delta G_{298}$ = 10.2 kcal/mol. The insertion of a second *D*-LA molecule is disfavoured by 3.9 kcal/mol ($\Delta\Delta G_{298}$ = 14.1 kcal/mol). Given the current data, a completely mononuclear reaction mechanism devoid of dimerisation and

polymeryl exchange would still lead to an isotactically biased polymer. Thus, polymeryl exchange appears to be an integral part in the mechanism of *rac*-LA polymerisation and likely one of the leading causes for the lack of stereoselectivity observed.

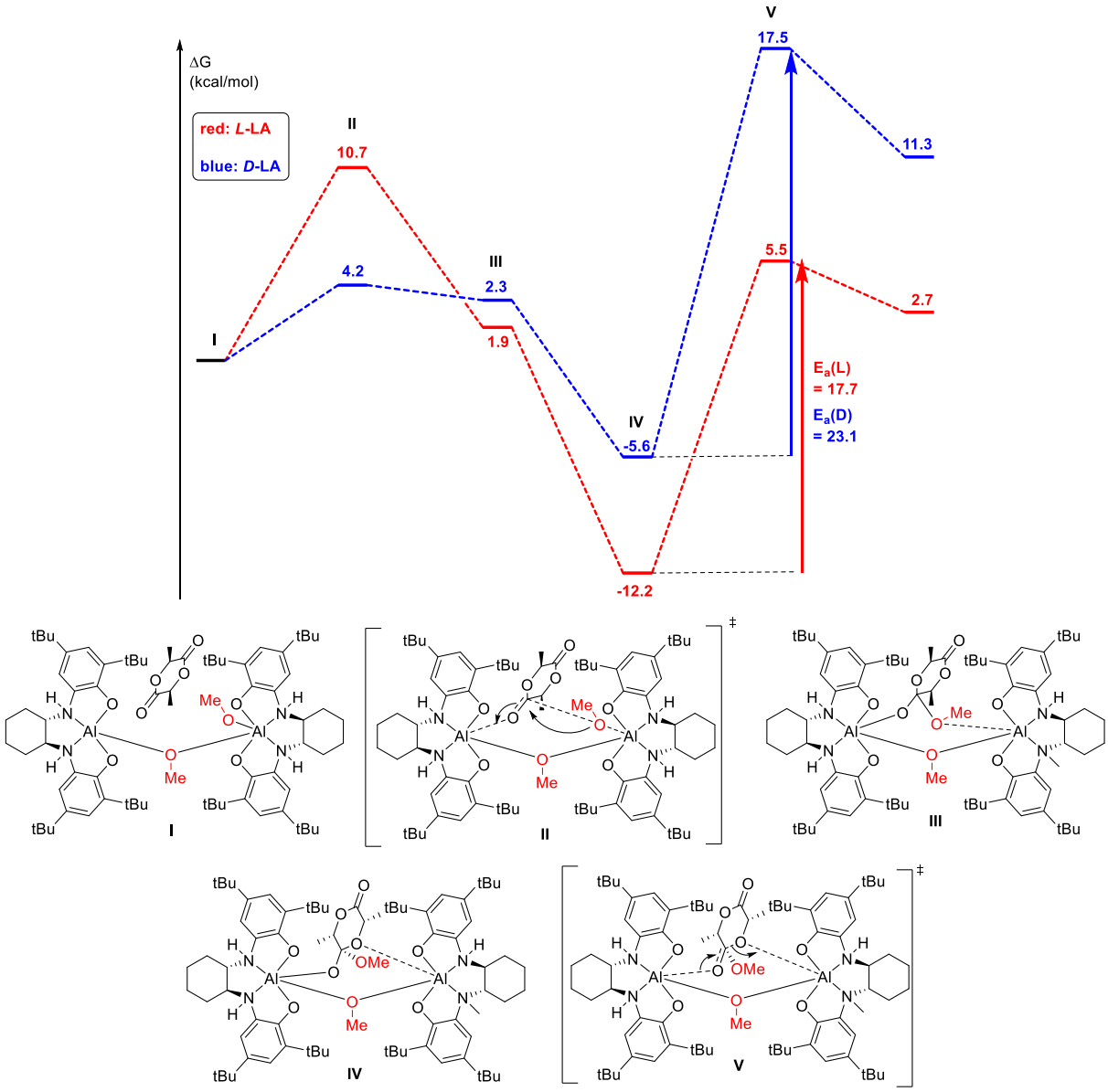


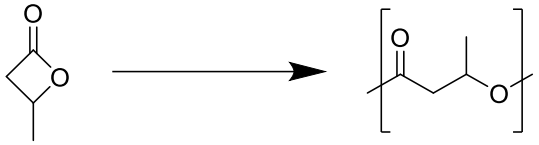
Figure 27. PES showing first insertion of a LA monomer into the dimeric (S,S)-**II**. DFT protocol: # ωB97xD/6-31g(d,p) scrf=(cpcm, solvent = THF) nosymm integral=grid=ultrafine.

As a final step a dimeric mechanism was calculated to gauge its plausibility. So far, it was assumed that the dimerisation of the active species leads to inactivity and must thus be suppressed. Using the optimised dimeric structure of *S,S*-**II** from Figure 14 in Section 3.2.6, evaluated the opening of a *D*- and *L*-LA molecule was evaluated (Figure 27). Interestingly, it was found that the polymerisation of *L*-LA can occur at room temperature in a dimeric state,

requiring an activation energy of $\Delta\Delta G_{298}$ = 17.7 kcal/mol. This is only 0.3 kcal/mol higher than the propagation step of a mononuclear active species ($\Delta\Delta G_{298}$ = 17.4 kcal/mol), suggesting that either one of the pathways is favourable. However, the opening of *D*-LA requires an activation energy of $\Delta\Delta G_{298}$ = 23.1 kcal/mol which is not conducive to a room temperature active polymerisation. This means that while *S,S*-**II** can readily polymerise *L*-LA whilst in a dinuclear state, it cannot do so with *D*-LA and thus has to break apart into its mononuclear constituents to carry out the polymerisation. This is reflected in the catalyst orders calculated for the polymerisation of *L*-LA by (*R,R*)-**15** and (*S,S*)-**15**. The respective orders of 1.5 and 1.0 show that (*R,R*)-**15** undergoes a multinuclear intermediate in the rate-determining step.

To summarise, the DFT calculations show that for a given catalyst enantiomer (*e.g.* (*S,S*)-**15**), its mononuclear polymerisation mechanism prefers the opening of its corresponding match monomer (*L*-LA). In the case of *rac*-LA ROP one would expect an isotactic instead of an atactic polymer. This indicates that additional processes beyond the classical coordination-insertion mechanism are occurring, which result in a lack of stereoregularity. The fact that the order of the enantiopure and racemic catalysts in *rac*-LA ROP is 1.2 and 1.1 respectively, indicates that dimerisation and polymeryl exchange may occur during polymerisation.
The DFT calculations also support the trends observed in *L*-LA ROP: (*S,S*)-**15** generally prefers *L*-LA and any stereoerror caused by the insertion of the mismatch enantiomer (*D*-LA) finds itself corrected. The data involving dinuclear polymerisation clearly shows that *L*-LA can be polymerised at room temperature while *D*-LA cannot. This is also reflected in the catalyst orders where the polymerisation of *L*-LA by (*S,S*)-**15** and (*R,R*)-**15** exhibited a catalyst order of 1.0 and 1.5 respectively.
The notion that a dimeric species cannot proceed with polymerisation was dispelled. Although a higher activation energy was observed, a dimeric analogue of (*S*,*S*)-**15** can polymerise LA at room temperature.

3.3.1.8 Polymerisation of β-BL



β-BL PHB

Table 5. β-BL polymerisations using complexes (*R,R*)-, (*S,S*)-, and *rac*-**15**, (**8c** added for comparison).

Entry	Catalyst	β-BL (equiv.)	Time (min)	Conv.[a] (%)	$M_{n(SEC)}$ (Đ)[b] (kg/mol)	$M_{n(calc.)}$[c] (kg/mol)	P_m[d]	k_{app}[e] (s^{-1})	TOF (h^{-1})
1	(*R,R*)-**15**	100	50	70	5.3 (1.1)	6.0	0.55	3.88×10^{-4}	84
2	(*S,S*)-**15**	100	50	68	5.5 (1.1)	5.8	0.55	3.70×10^{-4}	82
3	*rac*-**15**	100	50	71	5.3 (1.1)	6.1	0.55	4.07×10^{-4}	85
4	**8c**	100	240	57	4.1 (1.1)	5.8	0.43	7.32×10^{-5}	14
5	(*S,S*)-**15**	1000	120	36	17.5 (1.2)	31.0	0.56	-	180
6	*rac*-**15**	1000	120	25	15.5 (1.2)	21.1	0.54	-	125

Reaction conditions: $[\beta\text{-BL}]_0 = 1$ mol.L^{-1}, THF, 25 °C; a) Determined by ^{1}H NMR by relative integration of monomer and polymer signals (see ESI); b) Determined by SEC calibrated with polystyrene standards in THF and corrected (see ESI); c) Calculated using the conversion; d) Probability of *meso* linkage determined by ^{1}H NMR spectroscopy (see ESI); e) Determined assuming a pseudo-first order

As previously mentioned, synthesis of P3HB through ROP would allow for control of polymer properties *via* molecular weight and stereoregularity,[83, 84] but aluminium-based catalysts exhibit low activities and selectivities.[85] Complexes (*R,R*)-, (*S,S*)-, and *rac*-**15** polymerised β-BL much faster than their achiral derivative **8c** ($k_{app} = 7.32 \times 10^{-5}$ s^{-1}), reaching 70 % conversion in 50 minutes at room temperature (Table 5, Entries 1 – 4). Unlike with the previous monomers, the activity of the *trans*-**15** complexes did not differ from each other, reflected by the similar k_{app} values (Figure 28). Whilst the polymerisations were very controlled (Figures B65 – B70), none exhibited any notable stereoselectivity. The groups of Carpentier and Rieger synthesised yttrium and lanthanide complexes which exhibited characteristically high activity (TOF = 4800 and 6900 h^{-1} respectively at room temperature) and stereoselectivity ($P_r > 0.80$).[86, 87] Although the synthesis of an aluminium catalyst of this activity is unprecedented, the lack of stereoselectivity is a major flaw.

Polymerisations were conducted in bulk at room temperature to gauge whether the change in solvent would influence the stereoregularity of the polymers produced (Table 5, Entries 5 and 6). In either case, atactic P3HB was produced with no significant change in tacticity.

Furthermore, the molecular weights of the resulting polymers differed from the expected values, likely due to the reaction mixture increasing in viscosity and hindering mass transport.

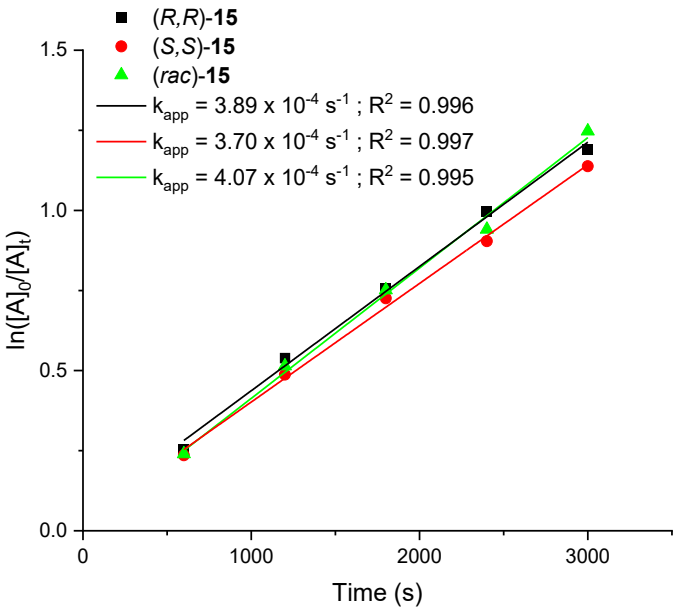


Figure 28. Superimposition of log plots showcasing the similar activity between (*R,R*)-, (*S,S*)-, and *rac*-**15** (black, red, and green respectively) in β-BL polymerisation.

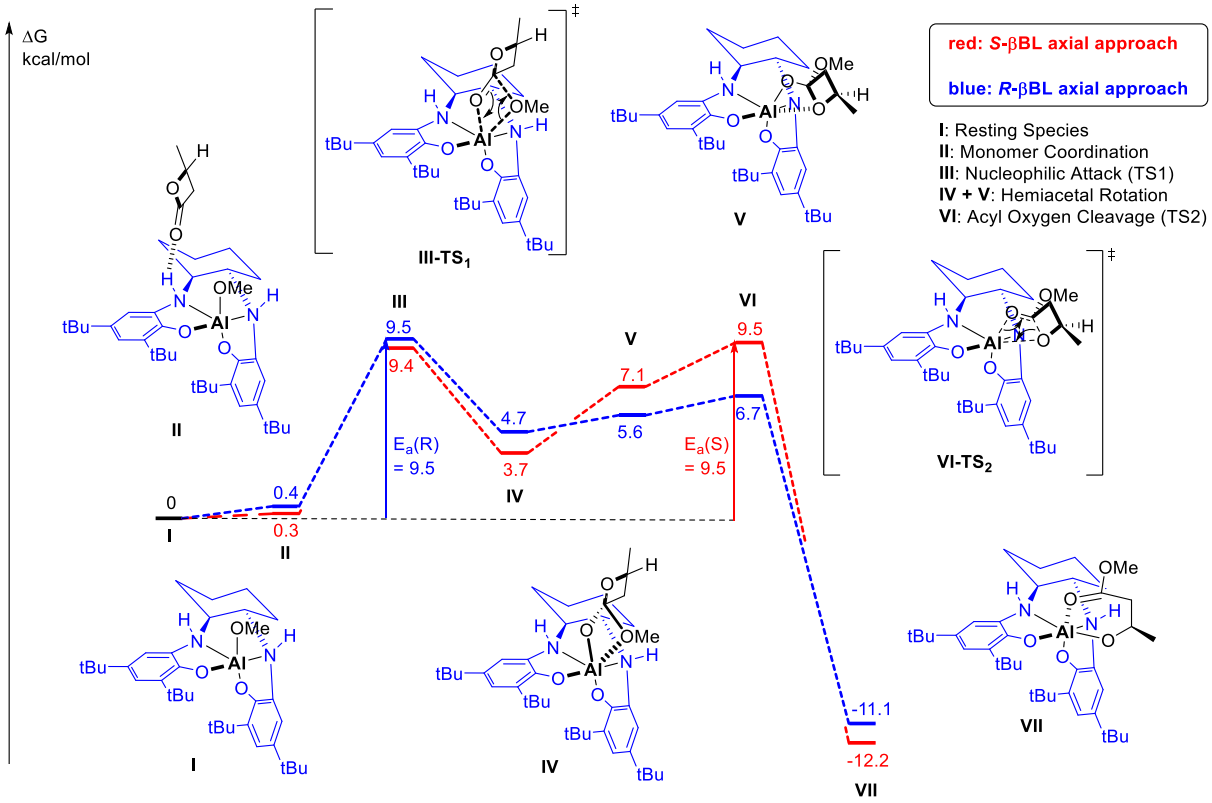


Figure 29. PES showing first insertion of a β-BL monomer into (*S,S*)-**15** (**I**). DFT protocol: # ωB97xD/6-31g(d,p) scrf=(cpcm, solvent = THF) nosymm integral=grid=ultrafine.

To gain a better understanding, DFT calculations were carried out on an ωB97xD level of theory using a split valence double zeta 6-31G(d,p) basis set (details in the ESI). The crystal structure of (*S,S*)-**15** was used as a starting point and the *tert*-butoxide group replaced with a methoxide for computational efficiency. A standard mononuclear coordination-insertion mechanism was envisaged for the polymerisation of β-BL. The initiation step was considered with multiple approaches of the *R* and *S* monomers. Each enantiomer led to an activation energy of $\Delta\Delta G_{298K}$ = 9.5 kcal/mol, in line with a room-temperature active polymerisation (Figure 29). The same activation energy for both enantiomers reflects the experimental data which shows the polymers to be atactic regardless of the catalyst employed. Furthermore, the k_{app} is the same overall which further indicates a lack of discrimination of monomer enantiomers by the catalysts.

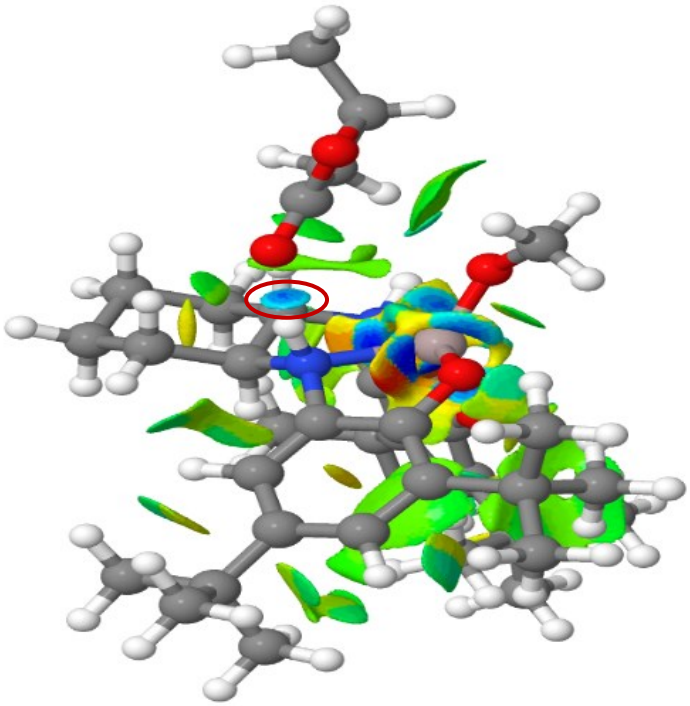


Figure 30. NCI surface of the monomer coordination step (**II**) featuring a hydrogen bond between the NH moiety and β-BL carbonyl (blue disc).

Inspecting the NCI surfaces of the various polymerisation intermediates, multiple favourable interactions between the carbonyl of the monomer and NH moieties of (*S,S*)-**15** can be discerned during the coordination step (Figure 30), as was the case with the polymerisation of *rac*-LA. Furthermore, such interactions were also present in certain transition states which would have a stabilising effect and thus decrease the activation energy of the ROP (Figure E9).

These results further highlight the importance of NCIs in the ROP activity of the catam family and demonstrate how these interactions are not only important to LA, but also to other cyclic esters.

3.3.1.9 Polymerisation of Other Monomers

Table 6. Polymerisation of ε-DL, TMC, and PDL using complexes (*R,R*)-, (*S,S*)-, and *rac*-**15** (**8c** added for comparison).

Entry	Catalyst	Monomer (equiv.)	T (°C)	Time (min)	Conv.[a] (%)	$M_{n(SEC)}$ (Đ)[b] (kg/mol)	$M_{n(calc.)}$[c] (kg/mol)	k_{app}[d] (s^{-1})	TOF (h^{-1})
1	(*R,R*)-**15**/(*S,S*)-**15**			7 * 60	79	21.5 (1.2)	12.2	7.21×10^{-5}	11
2	*rac*-**15**	ε-DL (100)	25	7 * 60	91	27.1 (1.2)	15.5	1.04×10^{-4}	13
3	**8c**			11 * 60	89	28.4 (1.2)	15.1	6.16×10^{-5}	8
4	(*R,R*)-**15**/(*S,S*)-**15**			4 * 60	63	18.6 (2.0)	6.4	5.42×10^{-5}	16
5	*rac*-**15**	TMC (100)	25	25 * 60	75	-	-	1.39×10^{-5}	3
6	**8c**			23 * 60	74	22.3 (1.4)	7.5	1.63×10^{-5}	3
7[e]	(*R,R*)-**15**/(*S,S*)-**15**				8	10.5 (1.4)	1.9	-	1.3
8[e]	*rac*-**15**	PDL (100)	100	6 * 60	6	11.9 (1.5)	1.4	-	1
9[e]	**8c**				6	5.2 (1.6)	1.4	-	1

Reaction conditions: $[M]_0$ = 1 mol.L^{-1}, THF, 25 °C; a) Determined by ^{1}H NMR by relative integration of monomer and polymer signals (see ESI); b) Determined by SEC calibrated with polystyrene standards in THF c) Calculated using the conversion; d) Determined assuming a pseudo-first order; e) Carried out in toluene

For the sake of comparison, further polymerisations were carried out with other monomers previously screened (Table 6). As discussed in Section 3.3.1.1, the polymerisation of ε-CL was faster using enantiopure catalysts, which was attributed to the differing dimerisation behaviour of both catalysts. Interestingly, whilst ε-DL is also a seven-membered ring, its polymerisation was much faster than that of ε-CL (at least 3 times as fast). Furthermore, the polymerisation of ε-DL was 40 % faster when mediated by the racemic complex (Table 6, Entry 2) instead of the enantiopure complexes (Table 6, Entry 1). The polymerisations by the *trans*-**15** complexes were faster than their achiral analogue **8c** (Table 6, Entry 3). Whilst the achiral nature of ε-CL brought the dimerisation behaviour of the complexes to the forefront, the chiral nature of ε-DL had two distinct effects:

- The ring-opening of ε-DL results in the formation of a secondary alcohol which may suppress dimerisation as it increases steric bulk around the metal centre. This has already been postulated for **8c** (Section 2.4.3).

- Each catalyst enantiomer will have a 'match' chirality of the ε-DL. This has the effect that the individual components of *rac*-**15** are more likely to encounter a 'match' monomer, thus increasing the overall rate.

This is contrasted by using TMC as a monomer, which is achiral and forms a primary alcohol upon opening. In this case, the dimerisation behaviour of the catalyst dominates again which results in the enantiopure complexes outperforming the racemic complex by a factor of ~ 3.9 (Table 6, Entries 4 and 5). The dispersity of the polymer is high (2.0) which further indicates the formation of inactive species that may result in a broadening of the molecular weight distribution. An interesting aspect is the fact that the enantiopure complexes were much faster than *rac*-**15** and their achiral analogue **8c** (Table 6, Entry 6). Given previous results with complexes **2** and **8c** deactivation *via* dimerisation is a plausible mechanism that would explain the ROP of TMC. The use of enantiopure complexes thus may again help the ROP of achiral monomers by disfavouring dimerisation.

The polymerisation of PDL proceeded sluggishly for both enantiopure and racemic complexes at 100 °C (≤ 8 % after 6 h, Table 6, Entries 7 and 8). The activity is comparable to that of the achiral complex **8c** (Table 6, Entry 9). Whilst dimerisation and subsequent deactivation *via* a primary alcohol is plausible, the observed activities are generally low which indicates that the coordination-insertion mechanism itself is slow.

3.3.2 Polymerisations with *cis*-**15**

Having extensively studied the polymerisation behaviour of chiral catalysts bearing a *trans*-diaminocyclohexane core, the focus was shifted onto *cis*-**15** which is tethered by the *meso* analogue. This complex still bears chiral centres, although it cannot be separated into individual components as it only forms one distinct species. The crystal structure shows the cyclohexane core to crowd the catalytic pocket unilaterally (Figure 13), which was hoped to impart stereoselectivity onto the catalyst.

3.3.2.1 Polymerisation of *rac*-LA, *L*-LA, *meso*-LA and ε-CL

Table 7. Polymerisation of *rac*-LA, *L*-LA, *meso*-LA, and ε-CL using complex *cis*-**15**.

Entry	Monomer (equiv.)	Time (min)	Conv.[a] (%)	$M_{n(SEC)}$ (Đ)[b] (kg/mol)	$M_{n(calc.)}$[c] (kg/mol)	P_m[d]	k_{app}[e] (s^{-1})	TOF (h^{-1})
1	*rac*-LA (100)	75	85	12.8 (1.1)	12.2	0.54	4.29×10^{-4}	68
2	*L*-LA (100)	40	83	14.9 (1.0)	11.9	-	7.85×10^{-4}	125
3	*meso*-LA (100)	20	89	10.7 (1.1)	12.8	0.54	1.85×10^{-3}	267
4	ε-CL	10	67	32.9 (1.5)	9.7	-	2.17×10^{-3}	402

Reaction conditions: $[M]_0$ = 1 mol.L^{-1}, THF, 25 °C; a) Determined by ^{1}H NMR by relative integration of monomer and polymer signals (see ESI); b) Determined by SEC calibrated with polystyrene standards in THF and corrected (see ESI); c) Calculated using the conversion; d) Probability of *meso* linkage determined by ^{1}H NMR spectroscopy (see ESI); e) Determined assuming a pseudo-first order

The ROP of *rac*-LA showed good activity comparable to that of complexes **2** and **8c** (Table 7, Entry 1). Furthermore, *cis*-**15** was twice as fast as (*R,R*)-/(*S,S*)-**15** but much slower than *rac*-**15**. The polymerisation itself was very controlled, following a linear relationship between molecular weight and conversion (Figure B77 and B78) with narrow dispersities (Đ = 1.1). Unfortunately, despite the constrained shape of the active site, *cis*-**15** afforded atactic PLA (P_m = 0.54). Whether this arises from a lack of selectivity or polymeryl exchange is unclear. The fact that the ROP of *L*-LA was ~1.8 faster indicates that the catalyst is slightly isoselective (Table 7, Entry 2). The crystal structure of *cis*-**15** as well as DFT calculations indicated that the mononuclear catalyst can adopt both Λ and Δ wrappings at identical energies. Given the isoselectivity of the catalyst, one can presume that each of these wrappings prefers a specific LA enantiomer. Given that the crystal structure of *cis*-**15** is dimeric, it is safe to assume that polymeryl exchange could occur through a μ-alkoxo species. This exchange must be favourable as the polymer appears to bear quasi-random insertions that lead to the low stereoregularity. The lack of stereoregularity in the *rac*-LA polymer thus implies that the polymer chains undergo exchange between the catalysts. The polymerisation of *L*-LA was itself very controlled (Figures B79 and B80).

The polymerisation of *meso*-LA was again faster than that of *rac*-LA (Table 7, Entry 3) and proceeded in a controlled fashion (Figure B81 and B82). The polymer did not exhibit stereoregularity (P_m = 0.54).

Rather surprisingly, the ROP of ε-CL by *cis*-**15** exhibited unprecedented activities when compared to the other complexes in the catam family (Table 7, Entry 4). The polymerisation

showed living properties as evidenced by Figures B83 and B84. A conversion of 67 % was achieved after 10 minutes only, yielding a k_{app} of 2.17×10^{-3} s^{-1}. In comparison, the enantiopure complexes (*R,R*)-/(*S,S*)-**15** were previously the fastest complexes and required 8 hours to reach similar conversions ($k_{app} \approx 3.20 \times 10^{-5}$ s^{-1}). Further studies were conducted in the next section to elucidate this drastic increase in activity.

The polymerisation mediated by *cis*-**15** exhibited a pronounced lag time for *L*-LA, *meso*-LA, and ε-CL, as evidenced by the linear fit of the log plots not intercepting the origin (Figures B79, B81, and B83). The catalyst can have a slow initiation but a fast propagation due to factors such as bulkiness and inaccessible active site.

3.3.2.2 Mechanistic Insight into ε-CL ROP by *cis*-**15**

It was established in Section 3.3.1.2 that for the ROP of ε-CL, (*R,R*)-/(*S,S*)-**Z** and *rac*-**15** exhibited an order in catalyst of 1.0 and 0.5 respectively. For comparison, the order of *cis*-**15** was determined to be 0.65 (Figure B99), in line with the partial formation of inactive off-cycle species. Given that the activity of *cis*-**15** is exceptionally high, this may seem counter-intuitive and implies that the active monomeric species (despite not being the major species) have a high activity. Further insight was sought *via* DFT calculations and multiple approaches of the ε-CL molecule were considered (Figure E8). The most favourable approach was again axial and had an overall activation energy of ΔG_{298K} = 8.7 kcal/mol, in line with a room temperature active polymerisation. Considering the bulkiness of the *cis*-diaminocyclohexane core, this activation energy is surprisingly low. Indeed, the TSM of the mononuclear *cis*-**15** complex shows the active site to be crowded by the linker, resulting in the NH moieties being buried (Figure 31, left). This initially gave the impression that NCIs would not be formed and the polymerisation thus disfavoured.

However, beneficial H-bonds between the ε-CL carbonyl and NH were observed in the coordination step, despite the bulky nature of the *cis*-diaminocyclohexane core (Figure 31, right). The ligand framework undergoes a distortion to accommodate the incoming monomer. The FDE was thus calculated to gauge the extent of the changes the ligand undergoes. The FDE for the polymerisation of ε-CL by *cis*-**15** was found to be 9.7 kcal/mol, much higher than that of (*S,S*)-**15** for *L*-LA ROP (*c.f.* 5.7 kcal/mol). This shows that bonding and NCIs offer a strong stabilisation energy throughout the polymerisation of ε-CL by *cis*-**15** indicating that the beneficial effects of NCIs can also in some cases be extended to ε-CL polymerisation.

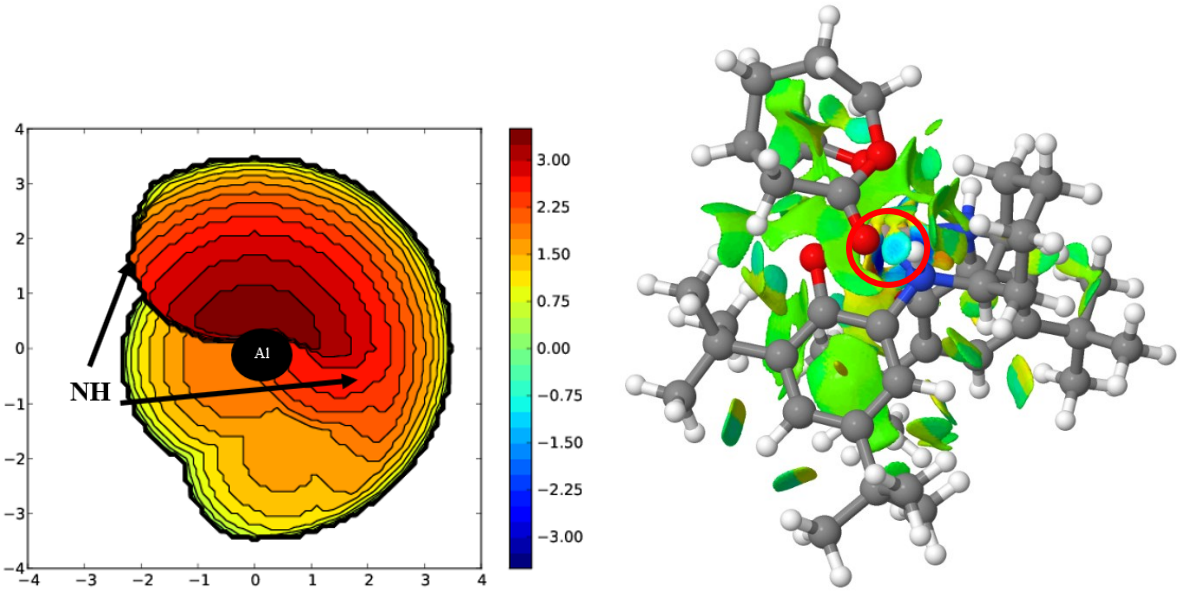


Figure 31. Left: TSM of the monomeric *cis*-**15** showcasing a crowded active centre due to the unusual coordination of the *cis*-diamnicyclohexane linker. The NH groups are buried within the coordination sphere. Right: NCI surface of the monomer coordination step (**II**) featuring a hydrogen bond between the NH moiety and ε-CL carbonyl (blue disc).

3.3.2.3 Polymerisation of Other Monomers

Table 8. Polymerisation of β-BL, ε-DL, TMC, and PDL using complex *cis*-**15**.

Entry	Monomer (equiv.)	T (°C)	Time (min)	Conv.[a] (%)	$M_{n(SEC)}$ (Đ)[b] (kg/mol)	$M_{n(calc.)}$[c] (kg/mol)	P_m[d]	k_{app}[e] (s^{-1})	TOF (h^{-1})
1	β-BL (100)	25	7 * 60	92	6.1 (1.1)	7.9	0.53	1.05×10^{-4}	13
2	ε-DL (100)	25	10 * 60	84	24.9 (1.3)	12.0	-	5.31×10^{-5}	8
3	TMC (100)	25	90	85	-	-	-	4.19×10^{-4}	57
4[f]	PDL (100)	100	105	69	48.4 (2.4)	16.6	-	-	39

Reaction conditions: $[M]_0 = 1$ mol.L^{-1}, THF; a) Determined by ^{1}H NMR by relative integration of monomer and polymer signals (see ESI); b) Determined by SEC calibrated with polystyrene standards in THF and corrected (see ESI); c) Calculated using the conversion; d) Probability of *meso* linkage determined by ^{1}H NMR spectroscopy (see ESI); e) Determined assuming a pseudo-first order; f) Carried out in toluene

Although the polymerisation of β-BL yielded predictable molar masses with low dispersities (Figures B85 and B86), it proceeded nearly four-fold slower than that mediated by the *trans*-**15** complexes (Table 8, Entry 1 *vs.* Table 5, Entries 1-3). Further to that, the P3HB was atactic ($P_m = 0.53$). A similar trend was observed with ε-DL where a conversion of 84 % was achieved after 10 hours, as opposed to the 7 hours needed for the *trans*-**15** complexes to achieve similar values (Table 8, Entry 2). Interestingly, the polymerisation of TMC proceeded exceptionally

fast, with a k_{app} of 4.19×10^{-4} s^{-1} (Table 8, Entry 3), similar to that of the polymerisation of *rac*-LA ($k_{app} = 4.29 \times 10^{-4}$ s^{-1}). The fastest TMC ROP thus far was that mediated by complex **2** which exhibited a k_{app} of 1.03×10^{-4} s^{-1}, more than fourfold slower than that of *cis*-**15**. A similar behaviour is exhibited with the polymerisation of the macrolactone PDL (Table 8, Entry 4), where 69 % conversion was achieved after 105 minutes at 100 °C (*c.f.* ~7 % after 6 hours for *trans*-**15** complexes). As a comparison, Wang and Kunioka achieved a conversion of 49 % after 6 hours using $Al(OTf)_3$ at similar conditions.[88] The polymerisation suffered through the dispersity, which was much higher than is expected from a controlled ROP (Đ = 2.4). The molecular weight itself is not accurate as no correction factor exists.

It is certain that *cis*-**15** exhibited unprecedented activities for the polymerisations of ε-CL, TMC and PDL. Polymerisations of these monomers by previously described complexes (**2**, **8c**, and *trans*-**15**) were much slower. It is important to note that the ring-opening of these monomers leads to the formation of a primary alkoxide which is thought to facilitate dimerisation and thus deactivation with the previous complexes. In the case of *cis*-**15**, the dimerisation is either disfavoured, or the polymerisations can proceed much faster when the catalyst is in a dinuclear state.

3.4 Conclusion

This chapter demonstrated how chiral pro-ligands (*R,R*)-, (*S,S*)-, *rac*-, and *cis*-H_2**^{H}L$_3$** can be synthesised *via* the use of chiral diamine precursors. Furthermore, modification of aromatic substituents was found feasible if the modification is carried out on the catechol precursor prior to pro-ligand synthesis.

Reaction of *rac*-H_2**^{H}L$_3$** and *cis*-H_2**^{H}L$_3$** with $AlEt_3$ resulted in the formation of unextractable mixtures *rac*-**mix12** and *cis*-**mix12** respectively, presumed to be composed of the alkyl and deprotonated complex. It was found that heating *rac*-**mix12** resulted in the full formation of the deprotonated derivative *rac*-**13**, adopting a similar solid-state structure to the **^{H}L$_2$** analogue (**7**).

Synthesising the benzyloxy complexes of (*R,R*)-, (*S,S*)-, and *rac*-H_2**^{H}L$_3$** also resulted in the formation of unextractable mixtures termed (*R,R*)-, (*S,S*)-, and *rac*-**mix14** respectively. Heating of *rac*-**mix14** formed a single well-defined complex *rac*-**14**, which was not the case for the

enantiopure counterparts. The stability of *rac*-**14** was traced to the formation of heterodimers which allow the constituents of the dimer to adopt favourable *cis*-β wrapping.

The use of a bulky tertiary alcohol (^{t}BuOH) with (*R,R*)-, (*S,S*)-, *rac*-, and *cis*-H_2**^{H}L$_3$** led to the formation of single well-defined species (*R,R*)-, (*S,S*)-, *rac*-, and *cis*-**15** respectively. The fact that (*R,R*)-, (*S,S*)-, and *rac*-**15** exhibited an identical NMR spectrum demonstrates successful chirality transfer from the pro-ligand onto the metal complex.

Enantiopure complexes outperformed the racemic complex in the ROP of the achiral ε-CL monomer. The propensity of *rac*-**15** to form the less-active heterodimers was found to be the leading cause of this trend. The activity of (*R,R*)- and (*S,S*)-**15** was higher than that of complex **8c**, showing that enantiopure complexes can lead to higher activities than their racemic and achiral counterparts.

Complex (*S,S*)-**15** was found to exhibit unprecedented activities in *L*-LA ROP but was considerably slower in polymerising *D*-LA. The enantiopure complexes thus demonstrated a monomer preference which indicates the presence of an ESC mechanism.

However, in *rac*-LA ROP, the preference desisted, evident by the resulting PLA being atactic. Further experiments confirmed that polymeryl exchange between the catalytic species can occur which was used to explain the quasi-random insertions of LA. Furthermore, depending on the chiral nature of the chain-end, the catalyst had different preferences for the next insertion, all of which were favourable at room temperature.

The *trans*-**15** complexes also exhibited unprecedented activities in the polymerisation of β-BL, ε-DL, and *meso*-LA.

Complex *cis*-**15** was found to be very active in ε-CL ROP, requiring 10 minutes to polymerise 67 % of monomer. Furthermore, the polymerisation of PDL was considerably quicker compared to that of previously described catam complexes. The strained configuration of the cyclohexyl moiety was thought to be the source of this trend.

Computational studies highlighted the importance of NCIs. The NH moieties take an active part in the polymerisation as was shown in chapter 2. Thus, ligand modulation was successfully carried out without losing the beneficial properties of the catam ligand.

3.5 References

1. Knof, U.; von Zelewsky, A., *Angew. Chem. Int. Edit.* **1999,** *38*, 302-322.

2. Crassous, J., *Chem. Soc. Rev.* **2009,** *38*, 830-845.
3. Crassous, J., *Chem. Comm.* **2012,** *48*, 9687-9695.
4. Le Borgne, A.; Vincens, V.; Jouglard, M.; Spassky, N., *Makromol. Chem. M. Symp.* **1993,** *73*, 37-46.
5. Vincens, V.; Le Borgne, A.; Spassky, N., *Makromol. Chem. M. Symp.* **1991,** *47*, 285-291.
6. Spassky, N.; Wisniewski, M.; Pluta, C.; Borgne, A. L., *Macromol. Chem. Phys.* **1996,** *197*, 2627-2637.
7. Ovitt, T. M.; Coates, G., *J. Polym. Sci. Pol. Chem.* **2000,** *38*, 4686-4692.
8. Ovitt, T. M.; Coates, G. W., *J. Am. Chem. Soc.* **1999,** *121*, 4072-4073.
9. Ovitt, T. M.; Coates, G. W., *J. Am. Chem. Soc.* **2002,** *124*, 1316-1326.
10. Radano, C. P.; Baker, G. L.; Smith, M. R., *J. Am. Chem. Soc.* **2000,** *122*, 1552-1553.
11. Che, C.-M.; Huang, J.-S., *Coord. Chem. Rev.* **2003,** *242*, 97-113.
12. Majerska, K.; Duda, A., *J. Am. Chem. Soc.* **2004,** *126*, 1026-1027.
13. Zhong, Z.; Dijkstra, P. J.; Feijen, J., *Angew. Chem. Int. Edit.* **2002,** *41*, 4510-4513.
14. Zhong, Z.; Dijkstra, P. J.; Feijen, J., *J. Am. Chem. Soc.* **2003,** *125*, 11291-11298.
15. Jacobsen, E. N., *Accounts Chem. Res.* **2000,** *33*, 421-431.
16. Dijkstra, P. J.; Du, H.; Feijen, J., *Polym. Chem.* **2011,** *2*, 520-527.
17. Montaudo, G.; Montaudo, M. S.; Puglisi, C.; Samperi, F.; Spassky, N.; LeBorgne, A.; Wisniewski, M., *Macromolecules* **1996,** *29*, 6461-6465.
18. Gao, B.; Li, D.; Li, Y.; Duan, Q.; Duan, R.; Pang, X., *New J. Chem.* **2015,** *39*, 4670-4675.
19. Chen, H.-L.; Dutta, S.; Huang, P.-Y.; Lin, C.-C., *Organometallics* **2012,** *31*, 2016-2025.
20. Zhong, Z.; Dijkstra, P. J.; Feijen, J., *Macromolecules* **2003,** *36*, 8198-8200.
21. Chisholm, M. H.; Patmore, N. J.; Zhou, Z., *Chem. Comm.* **2005**, 127-129.
22. Chisholm, M. H.; Gallucci, J. C.; Quisenberry, K. T.; Zhou, Z., *Inorg. Chem.* **2008,** *47*, 2613-2624.
23. Du, H.; Velders, A. H.; Dijkstra, P. J.; Sun, J.; Zhong, Z.; Chen, X.; Feijen, J., *Chem. Eur. J.* **2009,** *15*, 9836-9845.
24. Press, K.; Goldberg, I.; Kol, M., *Angew. Chem. Int. Edit.* **2015,** *54*, 14858-14861.
25. Pilone, A.; Press, K.; Goldberg, I.; Kol, M.; Mazzeo, M.; Lamberti, M., *J. Am. Chem. Soc.* **2014,** *136*, 2940-2943.

26. Maudoux, N.; Roisnel, T.; Dorcet, V.; Carpentier, J. F.; Sarazin, Y., *Chemistry A European Journal* **2014,** *20*, 6131-6147.
27. Zhao, N.; Wang, Q.; Hou, G.; Song, H.; Zi, G., *Inorg. Chim. Acta* **2014,** *413*, 128-135.
28. Zhao, N.; Wang, Q.; Hou, G.; Song, H.; Zi, G., *Inorg. Chem. Commun.* **2014,** *44*, 86-90.
29. Zhao, N.; Wang, Q.; Hou, G.; Song, H.; Zi, G., *J. Organomet. Chem.* **2014,** *754*, 51-58.
30. Zhao, N.; Wang, Q.; Hou, G.; Song, H.; Zi, G., *Inorg. Chem. Commun.* **2014,** *41*, 6-10.
31. Bouyahyi, M.; Grunova, E.; Marquet, N.; Kirillov, E.; Thomas, C. M.; Roisnel, T.; Carpentier, J.-F., *Organometallics* **2008,** *27*, 5815-5825.
32. Lian, B.; Ma, H.; Spaniol, T. P.; Okuda, J., *Dalton Trans.* **2009**, 9033-9042.
33. Bian, S.; Abbina, S.; Lu, Z.; Kolodka, E.; Du, G., *Organometallics* **2014,** *33*, 2489-2495.
34. McKeown, P.; Davidson, M. G.; Lowe, J. P.; Mahon, M. F.; Thomas, L. H.; Woodman, T. J.; Jones, M. D., *Dalton Trans.* **2016,** *45*, 5374-5387.
35. Hormnirun, P.; Marshall, E. L.; Gibson, V. C.; Pugh, R. I.; White, A. J. P., *Proc. Natl. Acad. Sci. U. S. A.* **2006,** *103*, 15343-15348.
36. Jhurry, D.; Bhaw-Luximon, A.; Spassky, N., *Macromol. Symp.* **2001,** *175*, 67-80.
37. Nomura, N.; Ishii, R.; Akakura, M.; Aoi, K., *J. Am. Chem. Soc.* **2002,** *124*, 5938-5939.
38. Tang, Z.; Chen, X.; Pang, X.; Yang, Y.; Zhang, X.; Jing, X., *Biomacromolecules* **2004,** *5*, 965-970.
39. Tang, Z.; Chen, X.; Yang, Y.; Pang, X.; Sun, J.; Zhang, X.; Jing, X., *J. Polym. Sci. Pol. Chem.* **2004,** *42*, 5974-5982.
40. Min, K. S.; Weyhermüller, T.; Bothe, E.; Wieghardt, K., *Inorg. Chem.* **2004,** *43*, 2922-2931.
41. Chaudhuri, P.; Hess, M.; Müller, J.; Hildenbrand, K.; Bill, E.; Weyhermüller, T.; Wieghardt, K., *J. Am. Chem. Soc.* **1999,** *121*, 9599-9610.
42. Steffanut, P. Romain, C.; Dagorne, S.; Bellemin-Laponnaz, S. N-heterocyclic carbene based zirconium complexes for use in lactones ring opening polymerisation. WO2012076140A1. 2012.

43. Sokolenko, V. A.; Svirskaya, N. M.; Kogai, T. I.; Karpova, M. S.; Pavlenko, N. I., *Russ. J. Appl. Chem.* **2008,** *81*, 509-510.
44. Ding, K.; Miranda, M. O.; Moscato-Goodpaster, B.; Ajellal, N.; Breyfogle, L. E.; Hermes, E. D.; Schaller, C. P.; Roe, S. E.; Cramer, C. J.; Hillmyer, M. A.; Tolman, W. B., *Macromolecules* **2012,** *45*, 5387-5396.
45. Huang, Y.; Wang, W.; Lin, C.-C.; Blake, M. P.; Clark, L.; Schwarz, A. D.; Mountford, P., *Dalton Trans.* **2013,** *42*, 9313-9324.
46. Miranda, M. O.; DePorre, Y.; Vazquez-Lima, H.; Johnson, M. A.; Marell, D. J.; Cramer, C. J.; Tolman, W. B., *Inorg. Chem.* **2013,** *52*, 13692-13701.
47. Normand, M.; Dorcet, V.; Kirillov, E.; Carpentier, J.-F., *Organometallics* **2013,** *32*, 1694-1709.
48. Oishi, M.; Ichinose, Y.; Iwata, N.; Nomura, N., *Organometallics* **2019,** *38*, 4233-4243.
49. Kong, D.; Peng, Y.; Li, D.; Li, Y.; Chen, P.; Qu, J., *Inorg. Chem. Commun.* **2012,** *22*, 158-161.
50. Nielsen, C. D. T.; Burés, J., *Chem. Sci.* **2019,** *10*, 348-353.
51. Burés, J., *Angew. Chem. Int. Edit.* **2016,** *55*, 2028-2031.
52. Wang, L.; Bochmann, M.; Cannon, R. D.; Carpentier, J.-F.; Roisnel, T.; Sarazin, Y., *Eur. J. Inorg. Chem.* **2013,** *2013*, 5896-5905.
53. Blackmond, D. G., *J. Am. Chem. Soc.* **2015,** *137*, 10852-10866.
54. O'Keefe, B. J.; Breyfogle, L. E.; Hillmyer, M. A.; Tolman, W. B., *J. Am. Chem. Soc.* **2002,** *124*, 4384-4393.
55. Forder, T. R.; Mahon, M. F.; Davidson, M. G.; Woodman, T.; Jones, M. D., *Dalton Trans.* **2014,** *43*, 12095-12099.
56. Kremer, A. B.; Mehrkhodavandi, P., *Coord. Chem. Rev.* **2019,** *380*, 35-57.
57. Osten, K. M.; Mehrkhodavandi, P., *Accounts Chem. Res.* **2017,** *50*, 2861-2869.
58. Aluthge, D. C.; Ahn, J. M.; Mehrkhodavandi, P., *Chem. Sci.* **2015,** *6*, 5284-5292.
59. Hu, J.; Kan, C.; Wang, H.; Ma, H., *Macromolecules* **2018,** *51*, 5304-5312.
60. Cols, J.-M. E. P.; Hill, V. G.; Williams, S. K.; McIntosh, R. D., *Dalton Trans.* **2018,** *47*, 10626-10635.
61. Yu, I.; Acosta-Ramírez, A.; Mehrkhodavandi, P., *J. Am. Chem. Soc.* **2012,** *134*, 12758-12773.
62. Gesslbauer, S.; Hutchinson, G.; White, A. J. P.; Burés, J.; Romain, C., *ACS Catal.* **2021**, 4084-4093.

63. Blackmond, D. G., *J. Am. Chem. Soc.* **2001,** *123*, 545-553.
64. Gao, J.; Zhu, D.; Zhang, W.; Solan, G. A.; Ma, Y.; Sun, W.-H., *Inorg. Chem. Front.* **2019,** *6*, 2619-2652.
65. McKeown, P.; Davidson, M. G.; Kociok-Kohn, G.; Jones, M. D., *Chem. Comm.* **2016,** *52*, 10431-10434.
66. B., K. H., *Oil Gas Sci. Technol.* **2007,** *62*, 731-738.
67. Satyanarayana, T.; Abraham, S.; Kagan, H. B., *Angew. Chem. Int. Edit.* **2009,** *48*, 456-494.
68. Blackmond, D. G., *J. Am. Chem. Soc.* **1997,** *119*, 12934-12939.
69. Blackmond, D. G., *J. Am. Chem. Soc.* **1998,** *120*, 13349-13353.
70. Blackmond, D. G.; Rosner, T.; Neugebauer, T.; Reetz, M. T., *Angew. Chem. Int. Edit.* **1999,** *38*, 2196-2199.
71. Blackmond, D. G., *Accounts Chem. Res.* **2000,** *33*, 402-411.
72. Noble-Terán, M. E.; Buhse, T.; Cruz, J.-M.; Coudret, C.; Micheau, J.-C., *ChemCatChem* **2016,** *8*, 1836-1845.
73. Kitamura, M.; Okada, S.; Suga, S.; Noyori, R., *J. Am. Chem. Soc.* **1989,** *111*, 4028-4036.
74. Kitamura, M.; Suga, S.; Oka, H.; Noyori, R., *J. Am. Chem. Soc.* **1998,** *120*, 9800-9809.
75. Nakano, K.; Hiyama, T.; Nozaki, K., *Chem. Comm.* **2005**, 1871-1873.
76. Horeglad, P.; Cybularczyk, M.; Litwińska, A.; Dąbrowska, A. M.; Dranka, M.; Żukowska, G. Z.; Urbańczyk, M.; Michalak, M., *Polym. Chem.* **2016,** *7*, 2022-2036.
77. Hador, R.; Botta, A.; Venditto, V.; Lipstman, S.; Goldberg, I.; Kol, M., *Angew. Chem. Int. Edit.* **2019,** *58*, 14679-14685.
78. Kricheldorf, H. R.; Boettcher, C., *Makromolekul. Chem.* **1993,** *194*, 1653-1664.
79. Kricheldorf, H. R.; Boettcher, C.; Tönnes, K.-U., *Polymer* **1992,** *33*, 2817-2824.
80. Du, H.; Velders, A. H.; Dijkstra, P. J.; Zhong, Z.; Chen, X.; Feijen, J., *Macromolecules* **2009,** *42*, 1058-1066.
81. Jitonnom, J.; Meelua, W., *Chem. Phys. Lett.* **2020,** *750*, 137482.
82. Brookhart, M.; Wagner, M. I., *J. Am. Chem. Soc.* **1996,** *118*, 7219-7220.
83. Hong, M.; Chen, E. Y. X., *Nat Chem* **2016,** *8*, 42-49.
84. Thomas, C. M., *Chem. Soc. Rev.* **2010,** *39*, 165-173.
85. García-Valle, F. M.; Tabernero, V.; Cuenca, T.; Mosquera, M. E. G.; Cano, J.; Milione, S., *Organometallics* **2018,** *37*, 837-840.

86. Altenbuchner, P. T.; Kronast, A.; Kissling, S.; Vagin, S. I.; Herdtweck, E.; Pöthig, A.; Deglmann, P.; Loos, R.; Rieger, B., *Chem. Eur. J.* **2015,** *21*, 13609-13617.
87. Amgoune, A.; Thomas, C. M.; Ilinca, S.; Roisnel, T.; Carpentier, J.-F., *Angew. Chem. Int. Edit.* **2006,** *45*, 2782-2784.
88. Wang, Y.; Kunioka, M., *Macromol. Symp.* **2005,** *224*, 193-206.

Chapter 4

Synthesis and Characterisation of Aluminium Complexes Bearing an Aromatic Catam Ligand: Artificial Switchable Catalysis *via* Redox Control

4.1 Introduction

4.1.1 Artificial Switchable Catalysis

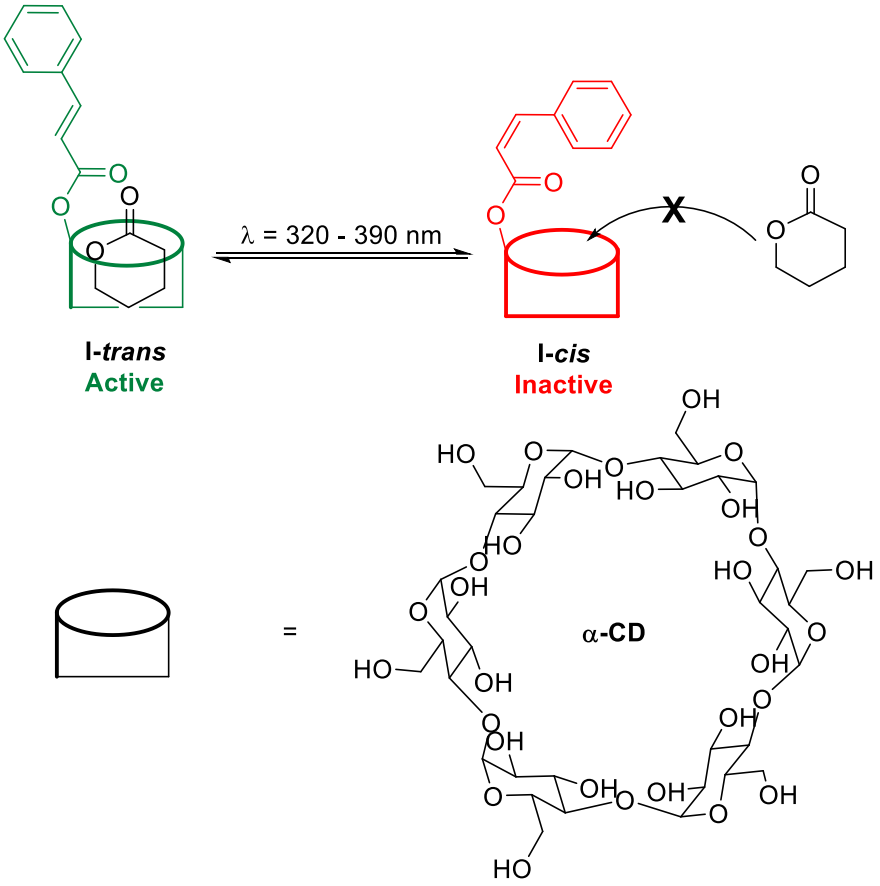
"Artificial switchable catalysis" has become increasingly relevant in recent years as there is an interest of having more control over a catalyst's output. This control can come in the form of modulating reaction rate or chemo-/regio-/stereo-selectivity. Furthermore, the exploitation of tandem or orthogonal reactivity as well as bi-/multi-functionality comprises another subset of switchable catalysis.[1]

The 'switch' of the catalyst manifests itself as a structural feature which responds reversibly to an external stimulus. Most commonly light, redox, pH, metal-ion coordination, and electrochemistry are utilised as a means to trigger a catalyst's "switch".[2] However, Johnson and co-workers have demonstrated that systems which respond to multiple stimuli can be designed.[3] Specifically, their system was found to respond to heat and light, forming a "logic-gated" catalyst that only performs radical polymerisation if the temperature is "low" AND the light is "on".

The most primitive form of achieving control is through the regulation of the reaction rate by switching the catalyst between an 'on'-state (upregulation) and an 'off'-state (downregulation) *via* the application of an external stimulus.[4] As a result, most switchable catalysts reported in literature focus on the control of the reaction rate. However, as these types of systems become more common, there is a greater drive to search for more sophisticated systems that offer advanced control over the reactions. In the context of cyclic ester polymerisation, modulation of the stereoselectivity of a catalyst can allow for the synthesis of polymers with fine-tuned properties (though this has yet to be achieved). Furthermore, establishing orthogonality between two monomers where a given catalyst can selectivity polymerise one monomer over the other (depending on the state) can pave the way for the formation of multi-block co-from a monomer mixture, thus eliminating the need of sequential monomer addition.[5] To gain an understanding of the current art, this introduction will feature examples of artificial switchable catalysts for cyclic ester ROP, with an emphasis on redox controlled 'switches'. A more detailed outline of artificial switchable catalysis can be found in recent reviews,[1, 2, 4, 6-10] some of which emphasise polymerisation catalysis.[5, 11-15]

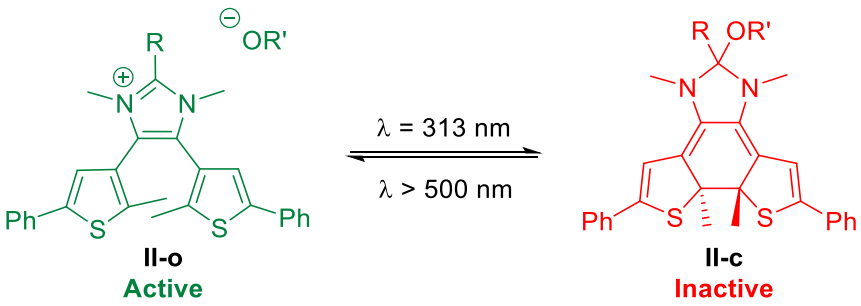
4.1.2 Photochemical-Controlled Switching

Light is an ideal external stimulus as it is non-invasive, "clean", chromophore selective, and provides temporal control.[10] This is in contrast with other stimuli which require additional substances to be added to solution, thus complicating the system. Photochemical switching is frequently employed in photo-initiating polymerisation processes and small-molecule organic transformations. Examples of photochemical control in cyclic ester ROP are scarce and are not metal-mediated. Both instances use a photoswitchable organocatalyst.



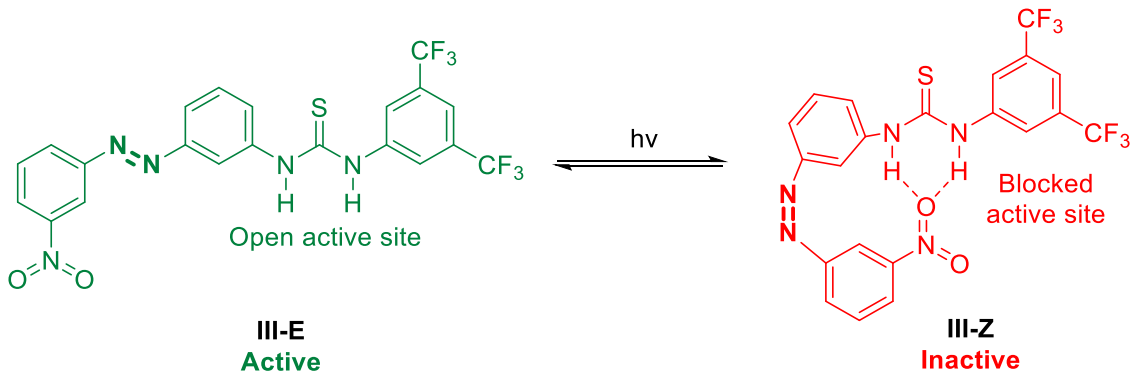
Scheme 1. Photoswitchable catalyst **I** based on a cinnamoyl functionalised α-CD

The first instance of such a catalyst was reported in 2009 by Harada and co-workers which used an α-cyclodextrin (α-CD) molecule functionalised with a cinnamoyl group (Scheme 1).[16] The latter can isomerise between *cis*/*trans* forms upon irradiation with light. The *trans*-form (**I-trans**) can polymerise δ-valerolactone (δ-VL) at 100 °C. Upon UV radiation of the reaction mixture, the catalyst is transformed into its *cis*-form (**I-cis**) which increases the steric bulk around the catalytic cavity and thus hinders subsequent polymerisation.



Scheme 2. Photoswitchable dithienylethene functionalised imidazolium (**II**) by Neilson and Bielawski

A faster catalyst was reported by Neilson and Bielawski in 2013, and comprises a system consisting of an imidazolium ring annulated to the photochromic dithienylethene (Scheme 2).[17, 18] Upon UV irradiation, the photoswitchable moiety undergoes cyclisation (**II-c**) which reverses to the open form (**II-o**) under exposure to visible light. **II-o** is generated into the corresponding carbene with one equivalent of potassium hexamehyldisilazide (KHMDS) and can catalyse the ROP of ε-CL at room temperature, converting 95 % of the starting material in one hour. The closed form **II-c** is inactive towards ε-CL ROP (less than 5 % in 1 hour) which was explained by the reduced electron density on the carbenoic centre. A similar behaviour was observed for the ROP of δ-VL. Thus, the authors demonstrated that system **II** can be reversibly switched between fast and slow states through the use of visible and UV light. This switch mechanism was later adapted by Hecht and co-workers which exploited cyclisation and keto-enol tautomerism to achieve switchable co-polymerisation.[19]



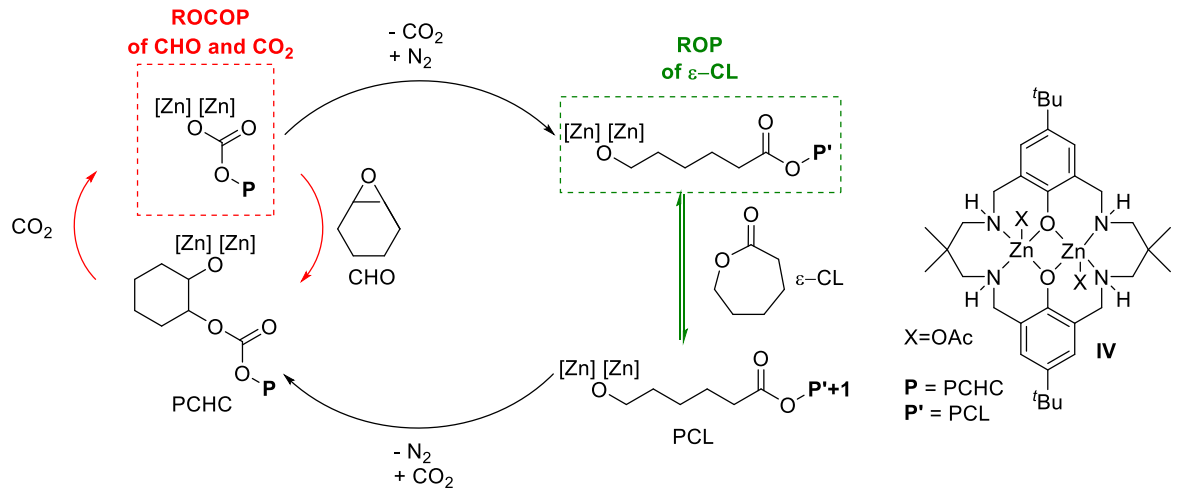
Scheme 3. Photoswitchable azobenzene functionalised thiourea (**III**) by Wu and co-workers

In 2016, Wu and co-workers reported an azobenzene-based thiourea catalyst (Scheme 3).[20] The azo group can undergo *E/Z* photo-isomerisation upon irradiation with light which changes the availability of the active site. The *Z*-isomer (**III-Z**) is generated with UV light and was found to be inactive as it blocked the catalytic site of the thiourea *via* intramolecular (NO_2-HN) hydrogen bonding. Exposure of the system to visible light generated the *E*-isomer (**III-E**)

which freed the catalytic site and made the species active towards LA ROP. The use of azobenzenes was extended to Zn-centred catalyst by Changle Chen and co-workers where they used the isomerisation properties to alternate the availability of two different active sites.[21] Jones and co-workers have also applied azobenzene-containing ligands to aluminium and zinc and were able to regulate the polymerisation of ε-CL.[22]

4.1.3 Chemical-Controlled Switching

Changes in a catalyst's properties can be induced through the addition or removal of chemicals which may induce changes in its structure amongst others. An interesting form of switching was reported by Williams and Romain in which CO_2 was used as both a chemical switch and a reagent (Scheme 4).[23] When the dizinc complex (**IV**) was employed in a mixture of ε-CL and CHO, only PCL was formed whilst the CHO was "ignored". However, upon addition of CO_2 into the system at a pressure as low as 1 bar, **IV** catalysed the ring-opening co-polymerisation (ROCOP) of CHO and CO_2, forming polycyclohexene carbonate whilst "ignoring" ε-CL. This is due to the formation of a zinc carbonate species which prefers the opening of CHO over ε-CL. The selectivity for ε-CL was restored by replacing the CO_2 with N_2, reverting to a zinc alkoxide species which prefers the opening of ε-CL over CHO.



Scheme 4. Romain and Williams' dizinc catalyst (**IV**) which changes substrate specificity upon addition/removal of CO_2 into the system.

Gases as switch mediators are attractive as they are theoretically reversible due to their ease of introduction and removal from a system. Another use for CO_2 was discovered by Coulembier and Dubois in which they were able to upregulate and downregulate the activity of a system consisting of triazabicyclodecene (TBD) and diazabicyclo[5.4.0]undec-7-ene (DBU).[24] The

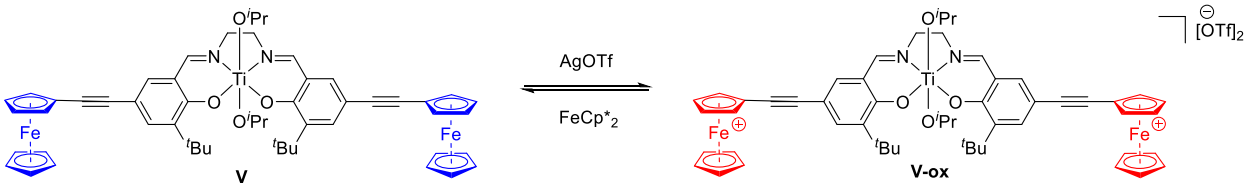
introduction of CO_2 stopped the ROP of ε-CL which was reversed through the replacement of the gas with N_2.

Mirkin and co-workers reported an allosteric supramolecular structure in which the active site is buried between two layers.[25] This methodology, termed the "weak-link approach" (WLA) allows the structure to be modulated between "open" and "closed" states through reversible binding events of chloride anions.[26] In such a way, the activity of the catalyst was modulated through changing the availability of the active site. This allosteric switch demonstrates an interesting approach to controlling catalyst properties.

4.1.4 Redox-Controlled Switching

Redox events are another popular type of external stimuli and are often used in reactions catalysed by transition metals. These use a redox-active ligand – often times bearing a ferrocene or cobaltocene group – which aids in constructing a redox-active catalyst.[2, 14] The oxidation/reduction of these metallocenes is reversible and allows for the effortless generation of electronically poor/rich catalytic species which have differing rates for particular reactions. This modulation of electron density can be utilised for up/down-regulation, or to achieve on-command substrate selectivity.[27] The field of switchable polymerisation has been meticulously discussed in a recent review by Doerr *et al.* and selected examples for cyclic ester ROP are summarised below.[12]

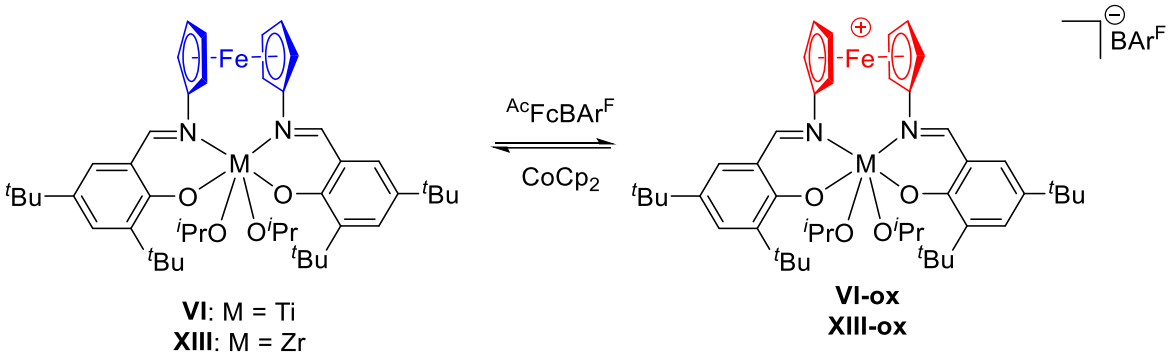
4.1.4.1 Ferrocenyl-mediated redox catalysis



Scheme 5. Redox-switchable ferrocenyl functionalised titanium complex (**V**) by Gibson and Long. Addition of AgOTf results in the oxidised species (**V-ox**)

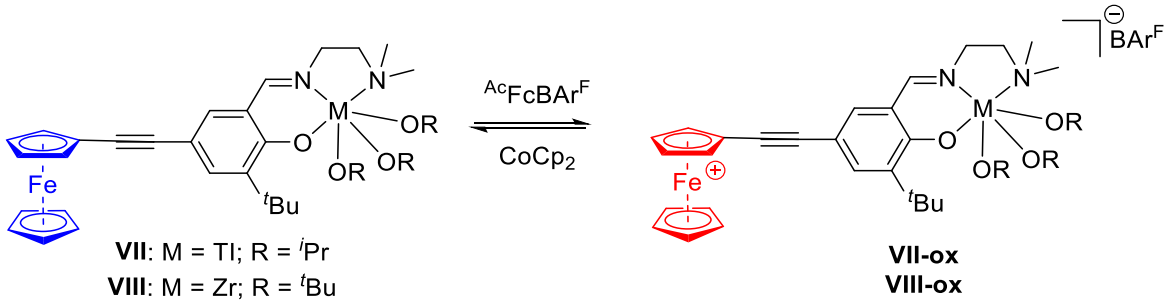
The first instance of a redox-switchable catalyst was reported in 2006 by Gibson, N. Long, and co-workers, wherein they functionalised a titanium salen complex with a conjugated ferrocenyl moiety on each of the two aromatic groups (**V**).[28] The complex was oxidised and reduced with two equivalents of silver triflate (AgOTf) and decamethyl ferrocene (FeCp*$_2$) respectively. At 70 °C, the reduced form (**V**) was found to be 30 times faster in *rac*-LA ROP than the oxidised

form (**V-ox**) of the catalyst. The catalyst could readily be switched from one state to another with no apparent loss in activity upon switching back (k_{app} = 4.98 x 10^{-6} s^{-1} *vs.* 4.73 x 10^{-6} s^{-1}). The molecular weights of the polymers were well controlled (Đ = 1.20) but neither **V** nor **V-ox** exhibited stereocontrol. The difference in activity was attributed to the change of electron density on the metal centre. It appears that despite the remote location of the ferrocenyl units relative to the metal centre, the modulation of their oxidation state has a profound impact on the rate of reaction.



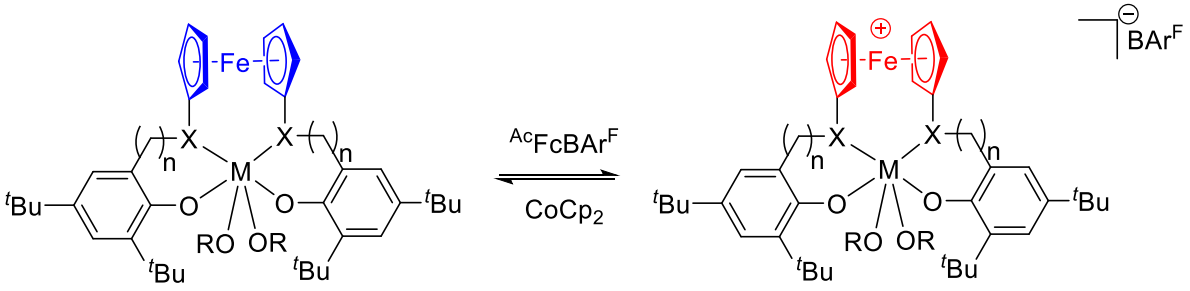
Scheme 6. Ferrocenyl-tethered Ti (**VI**) and Zr (**XIII**) complexes by B. Long and co-workers. Addition of $^{Ac}FcBAr^{F}$ results in the oxidised species (**VI-ox** and **XIII-ox**)

Given the instrumentality of the ferrocenyl units, the importance of their proximity to the metal centre eventually comes into question. B. Long and co-workers reported an analogue of **V** in which the ferrocene unit is used as a tether to the aromatic groups (**VI**).[29] Using acetylferrocenium (3,5-bis(trifluoromethyl)phenyl)-borate ($^{Ac}FcBAr^{F}$) as an oxidant and cobaltocene ($CoCp_2$) as a reductant, the polymerisation of *L*-LA was investigated. Interestingly, the activity of the oxidised species (**VI-ox**) depended on whether it was generated in the presence of monomer or not. If **VI-ox** was generated prior to the addition of *L*-LA, the species exhibited faster activities than its reduced form (**VI**). However, if the switching was carried out in the presence of monomer, **VI** exhibited much higher activities while **VI-ox** was completely inactive. Further studies proposed that the generation of **VI-ox** in the presence of *L*-LA changes the geometry of the complex from the *cis*-β form to either the *trans* or the *cis*-α form which results in a loss of activity. The results are in contrast with **V** where the oxidised and reduced form still exhibit activity. It appears that the proximity of the ferrocenyl unit does play a critical role in affecting the catalytic activity. Thus, to maximise redox-switchability, one should place the redox-active moiety as close to the metal centre as possible.



Scheme 7. Ferrocenyl-functionalised half-salen complexes (**VII** and **VIII**) by B. Long and co-workers. Addition of $^{Ac}FcBAr^{F}$ results in the oxidised species (**VII-ox** and **VIII-ox**)

The group of B. Long also investigated the tridentate half-salen **VII** and **VIII** which bear a titanium and zirconium metal centre respectively.[30] In both cases, a single ferrocenyl unit was placed on the aromatic ring as was done by Gibson and N. Long for **V**. Complexes **VII** and **VIII** were oxidised with silver tetrakis(3,5-bis(trifluoromethyl)phenyl)borate ($AgBAr^{F}$) to yield **VII-ox** and **VIII-ox** respectively. For the polymerisation of *L*-LA, **VII** and **VIII** were found to be faster than their oxidised form by a factor of 44 and 82 respectively. Whilst both catalysts were slower than **V**, the relative rates of polymerisation between reduced and oxidised form was similar for all three cases. This indicates that the switching behaviour is not affected by the number of ferrocenyl units in a given complex. However, the activity may be affected by the identity of the metal centre.



Scheme 8. Ferrocenyl-tethered Ti and Zr complexes by Diaconescu and co-workers (**IX-XII**). Addition of $^{Ac}FcBAr^{F}$ results in the oxidised species (**IX-ox**, **X-ox**, **XI-ox**, and **XII-ox**)

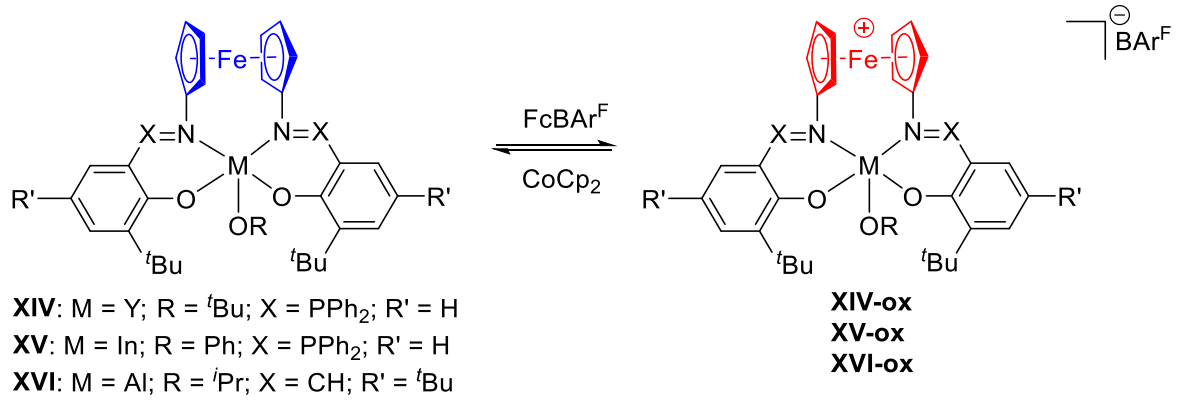
Despite the valuable insight gained through the studying of complex **VI**, Diaconescu and co-workers were in fact the first to use a ferrocenyl unit as a linker. A series of ferrocenyl-tethered Group IV complexes with different bridging heteroatoms were synthesised by the group in

2014 and employed in the ROP of *L*-LA and ε-CL (**IX-XI**).[31] Each catalyst was found to exhibit higher rates in the polymerisation of *L*-LA (at T ≥ 80 °C) in the reduced state. However, for ε-CL ROP, **IX** and **XI** were much slower in their reduced state than in their respective oxidised state (**IX-ox** and **XI-ox**) at room temperature. The experimentally observed orthogonality between the monomers led to the first one-pot synthesis of block copolymers without the need of sequential monomer addition. However, this was only achieved with **XI** as the *in-situ* oxidation of **IX** led to an inactive species, arising from to the strong coordination of *L*-LA to the metal centre of **IX-ox** which prevents coordination of the ε-CL monomer.

The monomer scope of **IX** was expanded to include β-BL, propylene oxide, oxetane, cyclohexene oxide (CHO), and styrene oxide.[32] Particularly striking orthogonality was exhibited between *L*-LA and CHO. DFT studies have shown that the polymerisation of CHO was mediated by coordination-insertion mechanism instead of an anionic/cationic mechanism more commonly observed for cyclic ether polymerisation.[33]

When the monomer scope of **XI** was expanded, it was found that only *L*-LA was polymerised with ease in its native form.[34] However, besides ε-CL, **XI-ox** was found to polymerise δ-VL, β-BL, oxetane, TMC, and CHO. The zirconium analogue (**XII**) was found to not exhibit any orthogonality between monomers, which was substantiated with DFT studies.[35] This is further proof of the importance of the metal centre and the ligand in the switch properties of a catalyst. The group of Diaconescu expanded their ligand library to include a salen analogue of **IX** which is fully conjugated (Scheme 6, **XIII**).[36] Orthogonality between *L*-LA and CHO was quickly established and **XIII** was found to polymerise *L*-LA faster than **IX** but exhibited slower activities for CHO.

So far, these studies show how sensitive artificial switchable catalysts are to structural modulation. The number of ferrocenyl units, their relative proximity to the metal centre, the degree of conjugation of the ligand, the nature of the bridging heteroatom, and the nature of the metal centre all play an important role in determining the properties of a system. If designed correctly, these systems have the potential of establishing a variety of monomer orthogonalities which can produce sophisticated multi-block co-polymers without the need of sequential monomer addition.[37]

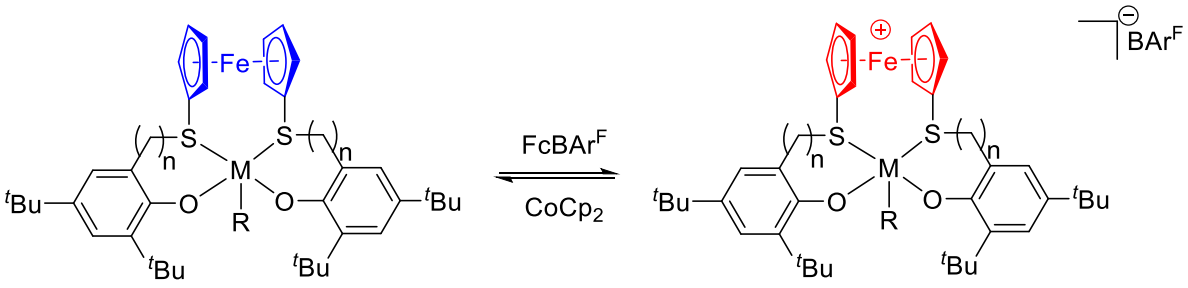


XIV: M = Y; R = ^{t}Bu; X = PPh_2; R' = H
XV: M = In; R = Ph; X = PPh_2; R' = H
XVI: M = Al; R = ^{i}Pr; X = CH; R' = ^{t}Bu

XIV-ox
XV-ox
XVI-ox

Scheme 9. Ferrocenyl tethered Y and In complexes by Diaconescu and co-workers (XIV-XVI). Addition of $FcBAr^F$ results in the oxidised species (**XIV-ox**, **XV-ox**, **XVI-ox**)

Moving beyond Group IV metals, phosphasalen complexes around a yttrium (**XIV**) and an indium (**XV**) metal centre were synthesised by the Diaconescu group.[38] Both complexes showed good switchability in *L*-LA ROP with **XIV** resuming polymerisation at similar rates once returned to the 'on' state (k_{app} = 0.3424 h^{-1} *vs.* 0.3733 h^{-1}). Interestingly for the ROP of TMC, the native **XIV** was active while **XIV-ox** was not. However, complex **XV** showed an inverse trend where **XV-ox** was active in TMC ROP while the native species was not. The fact that the switch mechanism can be implemented with Group III and Group XIII metals shows that if the metal centre is active in ROP, a well-designed ligand can in turn make the complex act as a switch. This is substantiated further by incorporating aluminium into a ferrocenyl containing salen scaffold (**XVI**).[39] The native species showed good activity for *L*-LA, β-BL, and TMC ROP whereas **XVI-ox** was only active for CHO ROP.



XVII: M = La; n = 1; R = O^{i}Pr
XVIII: M = La; n = 1; R = BH_4
XIX: M = Al; n = 0; R = O^{t}Bu

XVII-ox
XVIII-ox
XIX-ox

Scheme 10. Ferrocenyl-tethered La (**XVII** and **XVIII**) and Al (**XIX**) by the groups of Okuda and Diaconescu. Addition of $FcBAr^F$ results in the oxidised species (**XVII-ox**, **XVIII-ox**, **XIX-ox**)

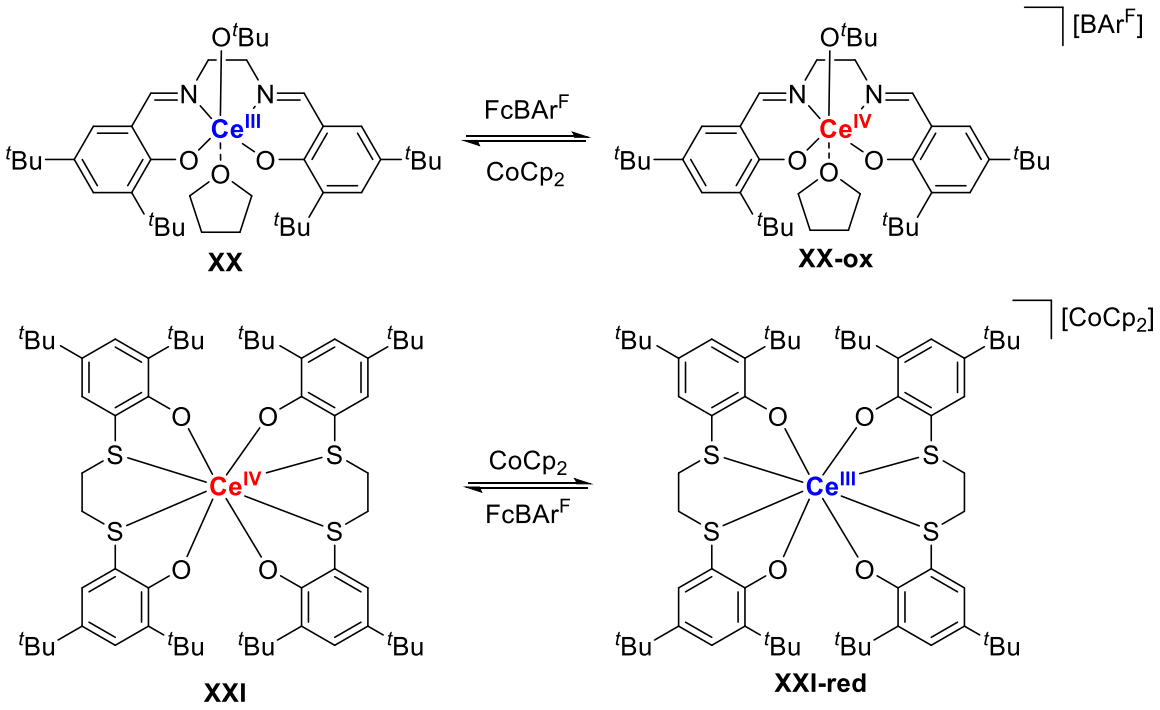
Okuda and co-workers used Diaconescu's ligand motif to synthesise salan ligands bearing sulfur heteroatoms. These were coordinated around a lanthanum metal centre with different co-ligands to yield **XVII** and **XVIII**.[40] These were highly active compared to previous complexes, owing to the Lewis acidic metal centre. Particularly **XVII** polymerised 94 % of monomer over the course of 80 minutes at room temperature. Both complexes however lost their activity upon oxidation. The nature of the co-ligand thus does not affect the switchability of a catalyst. A modified ligand scaffold was employed by Diaconescu and co-workers when synthesising an aluminium-centred complex (**XIX**).[41] Although employed in the ROP of a variety cyclic esters, the orthogonality between *L*-LA and CHO was the most synergistic. A particularly interesting aspect is the fact that the polymerisation of *L*-LA by **XIX** required 24 hours at 70 °C to reach a conversion of 88 %. However, the polymerisation of CHO by the oxidised **XIX-ox** converted 90 % of monomer in 20 minutes at ambient conditions. The native species was inactive in CHO ROP. The group studied these trends through DFT and found that changes in the electronic properties brought forth by the oxidation or reduction of the species did not only affect the individual catalytic steps. During propagation, the polymer chain can form five-membered chelate intermediates, their stability depending on the oxidation state of the catalyst. The energy barrier of a polymerisation thus does not only depend on initiation, but also on the strength of polymer chain chelation during the propagation steps.

4.1.4.2 Metal-mediated redox catalysis

The prior section demonstrated that the inclusion of a ferrocenyl unit into the ligand has enabled the oxidation and reduction of complexes that would in most cases be redox non-innocent. Through this, switch mechanisms were implemented that led to primitive 'on'/'off' switches as well as to more sophisticated substrate-selective switches. However, synthesising a ferrocenyl-containing ligand is not always straightforward.[26] Furthermore, using such ligands with redox active metals can lead to problematic interference. Redox-active catalysts relying on the metal centre are a solution as they simplify the system greatly. Matyjaszewski and co-workers have demonstrated that atom transfer radical polymerisation can be controlled using a metal-based redox switch.[42]

As early as 2011, Diaconescu and co-workers synthesised a salen-based cerium catalyst (**XX**) which can be oxidised from its native Ce(III) form to its Ce(IV) form (**XX-ox**).[43] The native complex **XX** was active in *L*-LA polymerisation at room temperature but stopped when $FcBAr^F$ was added to form **XX-ox**. Regeneration of the native species with $CoCp_2$ resumed the

polymerisation with no apparent loss in activity. This demonstrated that redox-switchable catalysis can be carried out without ligand assistance.

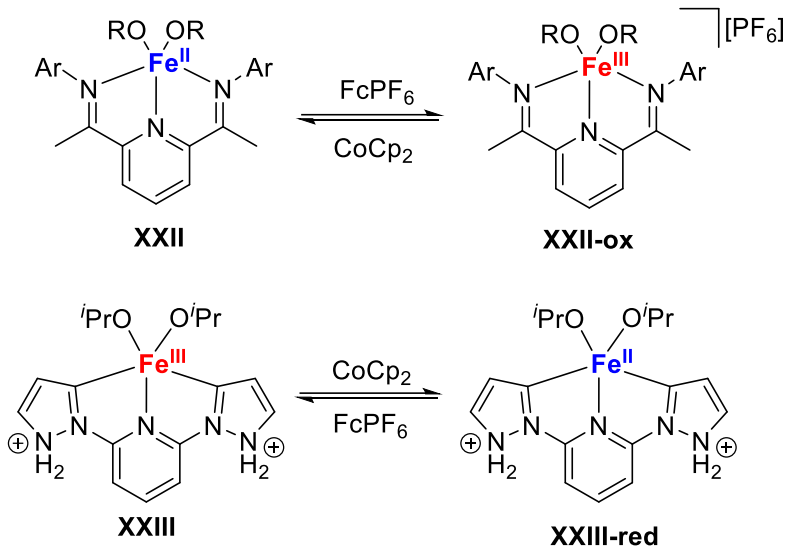


Scheme 11. Top: Ce(III) complex by Diaconescu and co-workers (**XX**) which forms the oxidised **XX-ox** upon addition of $FcBAr^F$. Bottom: Ce(IV) complex by Okuda and co-workers (**XXI**) which forms the reduced **XXI-red** upon addition of $CoCp_2$

Two years later in 2013, Okuda and co-workers synthesised a cerium based system containing two units of a tetradentate [OSSO]-donor ligand (**XXI**).[44] In this case, the native species is the oxidised Ce(IV) which can be reduced with $CoCp_2$ to generate the reduced Ce(III) (**XXI-red**). Complex **XXI-red** was found to polymerise *meso*-LA approximately 60 times faster than **XXI**, reaching a conversion of 78 % in 7 h at 40 °C. Furthermore, the complex can be switched between 'on' and 'off' states multiple times before experiencing a loss of activity.

In the same year, Byers and co-workers developed an iron catalyst supported by a bis(imino)pyridine ligand (**XXII**).[45] The Fe(II) pincer complex showed good activity in *rac*-LA ROP at ambient temperatures, albeit slower than **XX**. Complex **XXII** can be oxidised with an equivalent of ferrocenium hexafluorophosphate ($FcPF_6$) to yield the oxidised Fe(III) species **XXII-ox**, leading to inactivity. Further studies indicated that the complex can be switched back and forth multiple times without significantly affecting the activity or polymer properties. The complex was later demonstrated to act as an orthogonal mediator between *rac*-LA and CHO.[46]

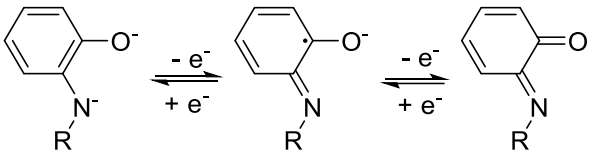
XXII-ox showed excellent activity for the ROP of CHO. Thus, through multiple experiments, the complex was shown to be able to effortlessly generate PLA-*b*-PCHO as well as PCHO-*b*-PLA block co-polymers.



Scheme 12. Top: Fe(II) complex by Byers and co-workers (**XXII**) which forms the oxidised **XXII-ox** upon addition of $FcPF_6$. Bottom: Fe(III) complex by Lang and co-workers (**XXIII**) which forms the reduced **XXIII-red** upon addition of $CoCp_2$.

Lang and co-workers also synthesised a Fe(III) complex supported by a di(1*H*-pyrazol-3-yl)pyridine pincer ligand (**XXIII**) and employed it in the ROP of ε-CL.[47] **XXIII** polymerised 65 % of starting material at 100 °C after 16 h. Upon reduction to **XXIII-red** with $CoCp_2$, the polymerisation stopped.

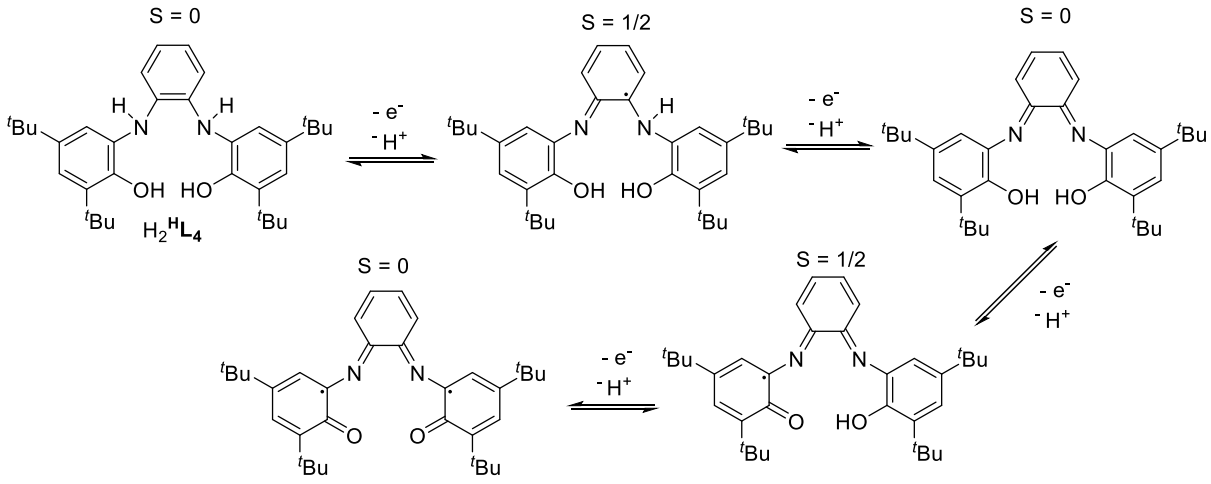
4.1.5 The Ph-Catam Ligand



Scheme 13. General structure of an ortho-aminophenolate (left) as well as its corresponding semiquinonato (middle) and quinone (right) form upon oxidation.

Ortho-aminophenols have been studied extensively for their redox properties and found to be redox non-innocent.[48] Their oxidation and reductions are more energetically accessible than redox-inactive ligands.[49] Thus, the ligand can change oxidation state without affecting that of

the metal, resulting in a change in the overall charge of the complex. Such a ligand would be termed an "actor" ligand as it takes an active part in a particular reaction. A simple *ortho*-aminophenol ligand can already be oxidised into semiquinonato and quinone form (Scheme 13), which has been exploited by Wieghardt and co-workers in 1999, who synthesised a catam ligand tethered by a *o*-phenylenediamine moiety (Scheme 14, H_2**^{H}L$_4$**).[50] The redox properties of the *o*-aminophenols as well as the conjugated nature of the ligand, allows H_2**^{H}L$_4$** to exist in five different oxidation states (Scheme 14). From this ligand, copper and zinc complexes were synthesised and found to stoichiometrically oxidise primary alcohols such as methanol and ethanol.



Scheme 14. Structure of the phenylene-tethered catam ligand H_2**^{H}L$_4$** (top-left) and the different oxidation states that can be achieved.

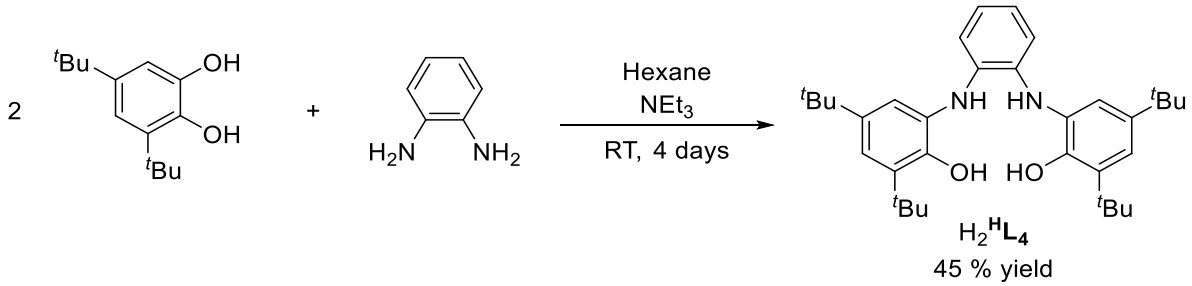
The interesting properties of the ligand were largely ignored until 2008 where it was revived by Heyduk and co-workers. They reported a zirconium-centred complex of H_2**^{H}L$_4$** which catalysed the two-electron disproportionated of 1,2-diphenylhydrazine into azobenzene.[51] The valence changes occurred at the redox-active ligand instead of the metal centre, demonstrating the ability of the H_2**^{H}L$_4$** to act as an actor-ligand in catalytic processes.[52] Since then, the ligand was discovered to act as an electron reservoir,[53] assist the catalysis of 1-hexene oligomerisation,[54] or exhibit interesting properties with tin,[55] molybdenum,[56, 57] cobalt,[58] and tungsten, [59]

H_2**^{H}L$_4$** was employed in cyclic ester ROP by Kol, Coates, and co-workers.[60] The titanium and zirconium alkoxides were found to exhibit unusually high activity in the ROP of *rac*-LA (full conversion after 1 h at 75 °C in toluene; 300:1 LA:cat), yielding heterotactic PLA (P_r up to 0.87).

4.1.6 Aim and Objectives

The aim of this project was to implement a redox-switchable aluminium catalyst using H_2**^{H}L$_4$** as a ligand. Whilst aluminium is not a redox-active metal centre, the employment of a redox non-innocent ligand was thought to overcome this limitation, as any change of the oxidation state would be occurring on the ligand instead. Contrary to the systems outlined in Section 4.1.4, this complex possesses neither a redox-active metal centre, nor a ferrocenyl-functionalised ligand, making this an unprecedented complex (if it were to work). Thus, the synthesis of the complex was carried out and tested in multiple switch experiments. The goal was to implement a switch that would at least upregulate and downregulate a rate of reaction. Furthermore, finding orthogonality between two monomers would allow for the synthesis of block co-polymers from a substrate mixture.

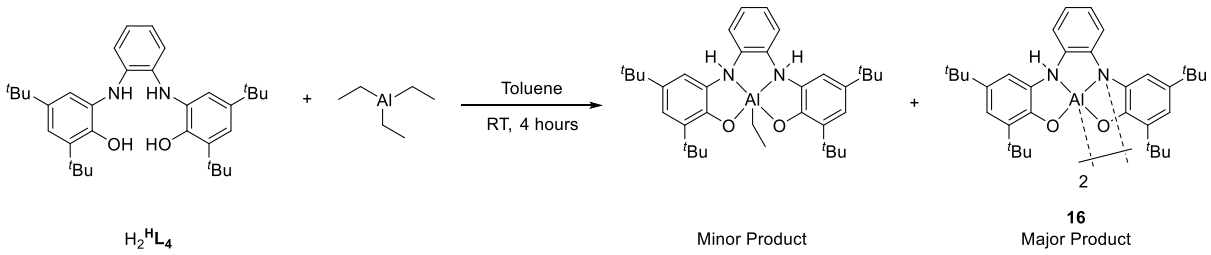
4.2 Pro-Ligand Synthesis and Complex Characterisation



Scheme 15. Synthesis of pro-ligand H_2**^{H}L$_4$**.

The synthesis of pro-ligand H_2**^{H}L$_4$** was carried out according to a modified literature procedure by Heyduk and co-workers in which two equivalents of 3,5-di-*tert*-butylcatechol was stirred with one equivalent of *ortho*-phenylenediamine in *n*-hexane with a catalytic amount of triethylamine over the course of 4 days at room temperature (Scheme 15).[50, 52] This resulted in a precipitate which was filtered to yield the crude product. The solid was re-dissolved in diethyl ether and filtered through a plug of silica. Evaporation of volatiles and subsequent washing with cold hexane yielded pure H_2**^{H}L$_4$** (45 % yield).

4.2.1 Synthesis of the alkyl complex of $H_2^{H}L_4$ and deprotonation behaviour



$H_2^{H}L_4$

Scheme 16. Complexation of $H_2^{H}L_4$ with $AlEt_3$ to produce the corresponding alkyl and deprotonated complex (**16**).

The synthesis of the alkyl complex of $H_2^{H}L_4$ was initially attempted as per scheme 16. Performing the synthesis in THF resulted in the formation of a THF adduct, conducive to three coordinated THF molecules. These were impossible to remove under vacuum or usual purification methods (*i.e.* washing with pentane, recrystallisation), which was attributed to the electron-withdrawing phenylene linker imparting the NH moieties with better hydrogen-bond donor properties as they become more acidic. The H-bonds formed with the oxygen atoms of the THF molecules were thus exceptionally strong. To overcome this, the synthesis was instead carried out in a non-coordinating solvent (Scheme 16). After 4 hours, the crude product was found to be a mixture of products as per the ^{1}H NMR spectrum (C_6D_6, 298 K, Figure A36). The products were suspected to be the alkyl complex (Scheme 16, minor product) and its corresponding deprotonated complex (major product, **16**). The deprotonation of the NH moiety by the alkyl chain is thus very favourable at room temperature for C_2-linkers (as seen in the synthesis of the alkyl complex of $H_2^{H}L_2$ and $H_2^{H}L_3$ in Sections 2.3.2.1 and 3.2.3). Again, this was attributed to the electronegative phenylene moiety making the proton of the NH moiety more acidic. This in turn facilitates the deprotonation of the NH by the anionic alkyl chain. As the synthesis of the alkyl complex was not as straightforward as envisaged, the direct synthesis of the deprotonated complex **16** was targeted by carrying out the reaction in toluene and increasing the reaction time to 16 hours. Removal of the volatiles yielded a single well-defined species as per the ^{1}H NMR spectrum (C_6D_6, 298 K, Figure 1). The spectrum features a species with a C_1-symmetric structure in solution with the peaks in the aromatic region corresponding to a total of eight aromatic protons, a NH peak corresponding to one proton (δ^1_H 5.00 ppm), and four ^{t}Bu peaks corresponding to 9 protons each (δ^1_H 1.61, 1.51, 1.20, and 1.10 ppm).

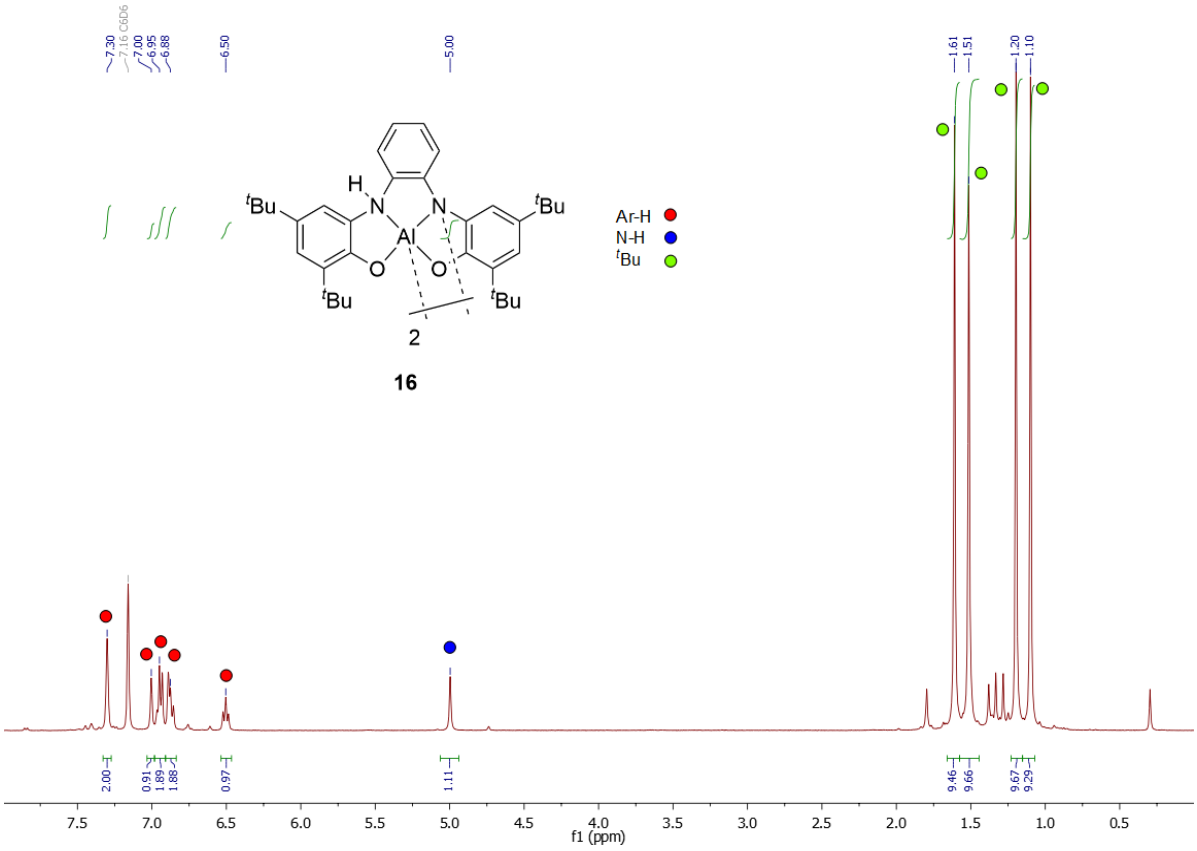
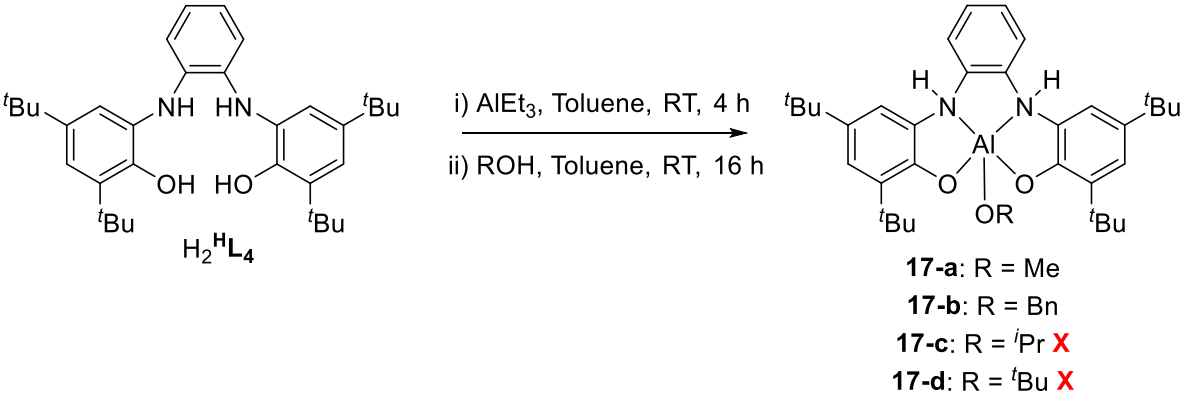


Figure 1. ^{1}H NMR spectrum (C_6D_6, 298 K) of complex **16**.

Purification of **16** proved to be problematic as it dissolved in all common solvents at room temperature and -40 °C. The best attempt at purification yielded an identical spectrum to Figure 1. Elemental analysis of **16** only deviated 3 % from the expected carbon values. Whilst not entirely pure, the complex has been deemed characterised and was used in subsequent experiments.

4.2.2 Synthesis of alkoxide complexes **17-a** to **17-b**



Scheme 17. Complexation of $H_2^{H}L_4$ and reaction with MeOH or BnOH to yield **17-a** and **17-b** respectively. Use of ^{i}PrOH and ^{t}BuOH did not yield a single well-defined species.

The synthesis of an alkoxide species was then targeted by reacting complex **16** (*in-situ* generated) with a variety of alcohols (Scheme 17). These include: MeOH, BnOH, ^{i}PrOH, and ^{t}BuOH.

The addition of one equivalent of either MeOH or BnOH resulted in the formation of a single species as per the ^{1}H NMR spectrum (C_6D_6, 298 K, Figures A37 and A38). This prompted the direct synthesis of the methoxy and benzyloxy complexes (Scheme 17, **17-a** and **17-b**), each of which yielding a well-defined product as per the ^{1}H NMR spectra (C_6D_6, 298 K, Figures 2 and A39). The acquisition of a ^{13}C NMR proved to be difficult as the complexes were poorly soluble in all common NMR solvents. Given the primary nature of the alkoxide of complexes **17-a** and **17-b**, they likely form dimers in solution. Furthermore, the ligand ^{H}**L**$_{4}$ is has strong electron-withdrawing properties. Coordination of such a ligand onto aluminium results in the metal centre being more electropositive which increases the complex's propensity to dimerise. Thus, despite the difficulty in obtaining a ^{13}C NMR spectrum, complexes **17-a** and **17-b** were deemed successfully synthesised based on the ^{1}H NMR spectra and the results of the elemental analysis (see Experimental for details).

Addition of one equivalent of the secondary alcohol ^{i}PrOH to complex **16** in THF resulted in the formation of multiple species as per the ^{1}H NMR spectrum (C_6D_6, 298 K, Figure 3). The multiple species (**17-c**) can arise from a monomer-dimer equilibrium, disorder in the coordination of the isopropoxy unit, as well as the coordination of THF onto the metal and NH moieties of the complex, all of which resulting in the many species found in the NMR spectrum. The direct synthesis **17-c** was subsequently attempted in toluene, removing the presence of THF from the reaction mixture. The resulting ^{1}H NMR spectrum (Figure A40, C_6D_6, 298 K) still showed a large degree of convolution. As the reaction did not form a single-well defined species, the targeting of **17-c** was ceased.

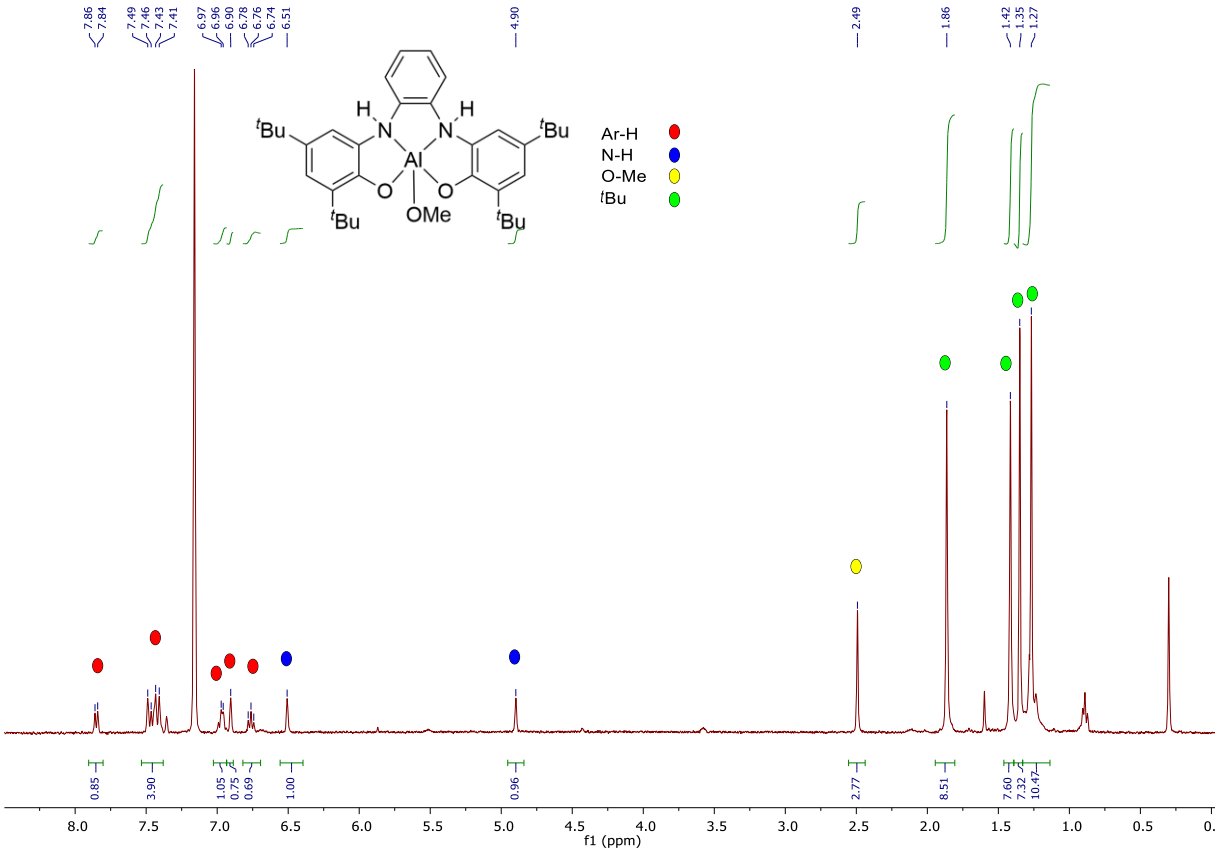


Figure 2. ^{1}H NMR spectrum (C_6D_6, 298 K) of **17-a**

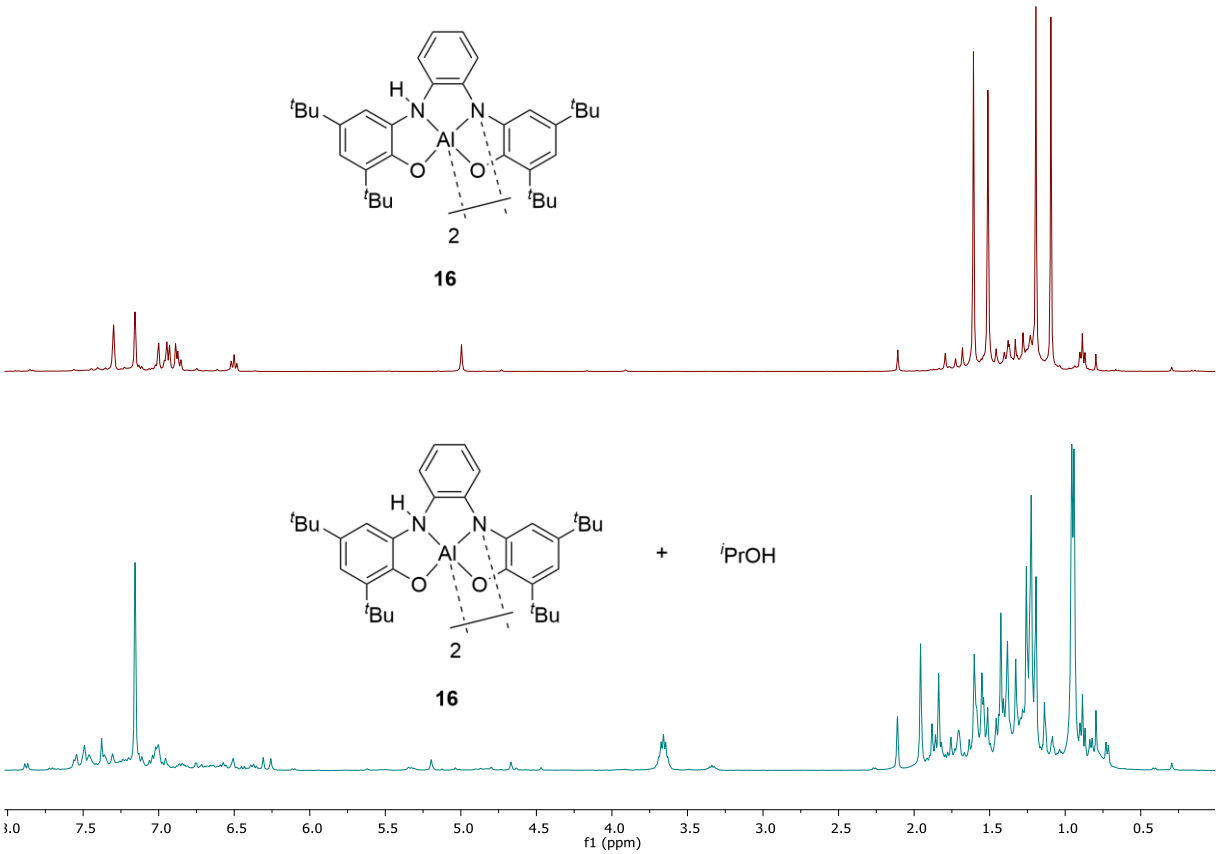


Figure 3. ^{1}H NMR spectrum (C_6D_6, 298 K) of **16** (top) and **16** + ^{i}PrOH showing a transformation taking place, yielding multiple species in solution.

Given that the synthesis of the *tert*-butoxy complexes of *(R,R)*-, *(S,S)*-, *rac*-, and *cis*-H_2**^{H}L$_3$** resulted in the formation of a single monomeric species, the synthesis of a *tert*-butoxy complex bearing the H_2**^{H}L$_4$** pro-ligand was also attempted (**17-d**). However, the addition of one equivalent of ^{t}BuOH to **16** did not result in a change in the ^{1}H NMR spectrum (C_6D_6, 298 K) after reacting at room temperature over 3 days or heating it at 80 °C overnight (Figure 4). Even the direct synthesis of **17-d** only resulted in the formation of the deprotonated complex **16**, which indicates that **16** is not reactive towards tertiary alcohols. A final attempt was made in which the chloro complex **18** (see next section) was reacted with one equivalent of KO^{t}Bu in C_6D_6. The aim of this salt metathesis was to exchange the chloride ligand with with a *tert*-butoxy group which should be thermodynamically driven by the formation of a salt (KCl) and the formation of a strong Al-O bond. Interestingly, as per the ^{1}H NMR spectrum, the reaction led to the formation of a new product (Figure A41, C_6D_6, 298 K). Although it appears that a single well-defined species was formed, the reaction never went to completion despite further additions of KO^{t}Bu to the reaction mixture. Given the difficulty in separating the multiple products of the reaction mixture, any further attempt in synthesising complex **17-d** was ceased.

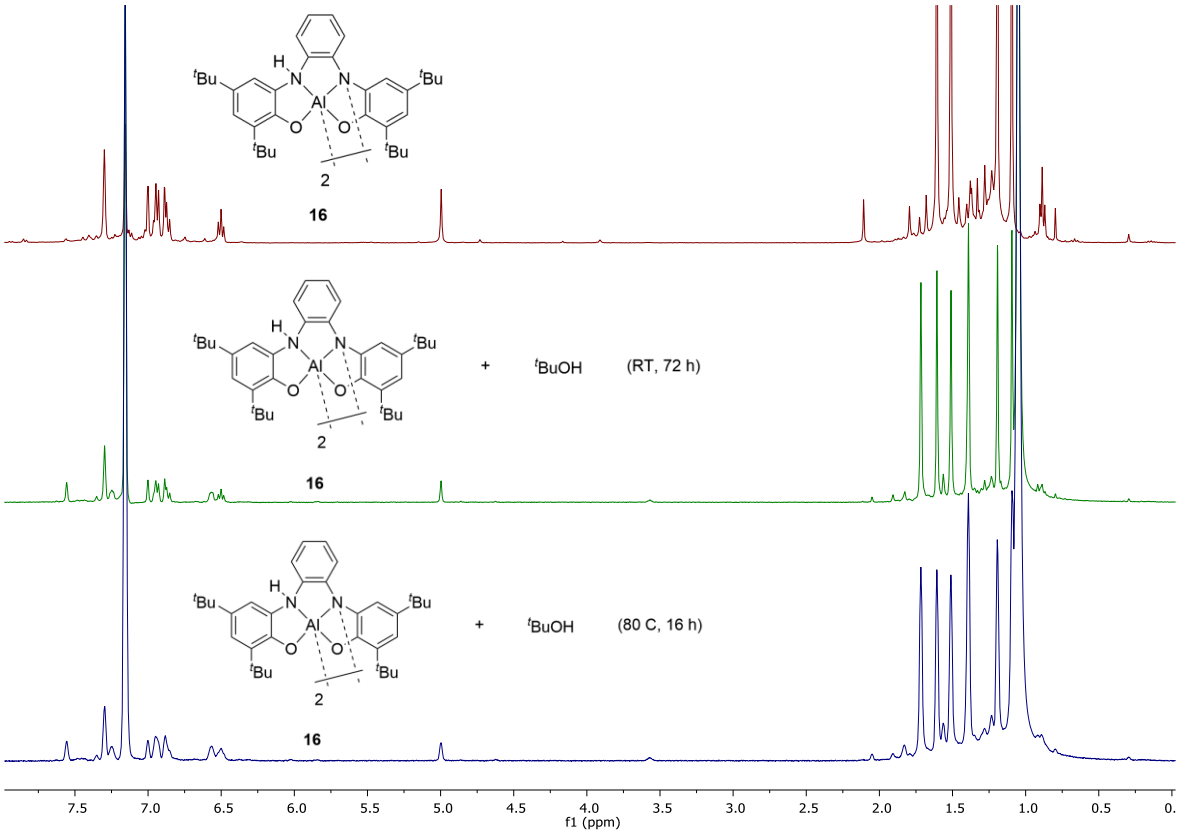
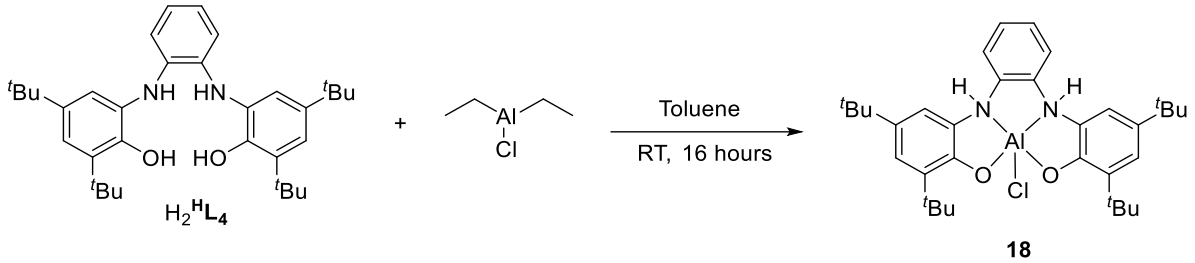


Figure 4. ^{1}H NMR spectrum (C_6D_6, 298 K) of **16** (top) and **16** + ^{t}BuOH after 72 hours at RT (middle) and 16 hours at 80°C (bottom) showing no transformation taking place.

To conclude, alkoxide derivatives **17-a** and **17-b** were successfully synthesised, isolated, and characterised using MeOH and BnOH. Although the addition of ^{i}PrOH to **16** led to the formation of new products, the direct synthesis attempts did not yield a single well-defined species. Complex **16** was found to be unreactive towards ^{t}BuOH.

4.2.3 Synthesis and Characterisation of the chloro complex (**18**)



Scheme 18. Complexation of H_2**^{H}L$_4$** with $AlEt_2Cl$ to produce the corresponding chloro complex **18**

Given the solubility issues experienced with **17-a** and **17-b**, the chloro complex **18** was targeted through the reaction of one equivalent of H_2**^{H}L$_4$** with one equivalent of diethylaluminium chloride ($AlEt_2Cl$). The pro-ligand and aluminium precursor were separately dissolved in toluene and cooled to -40 °C. The solutions were then mixed and allowed to stir at room temperature overnight, upon which a precipitate was formed. Filtration and subsequent washings with pentane yielded the pure complex **18** (77 % yield).

The NMR spectrum (CD_2Cl_2, 298 K) of **18** agrees with a C_s-symmetric structure in solution with four peaks in the aromatic region corresponding to the protons on the *ortho*-aminophenol (δ^1_H 7.44 and 7.38 ppm) and phenylene (δ^1_H 7.40 and 7.35 ppm) moieties (Figure 5). The single NH peak at δ^1_H 5.50 ppm, and the two ^{t}Bu peaks (δ^1_H 1.41 and 1.40 ppm) confirm the formation of a single, well-defined species.

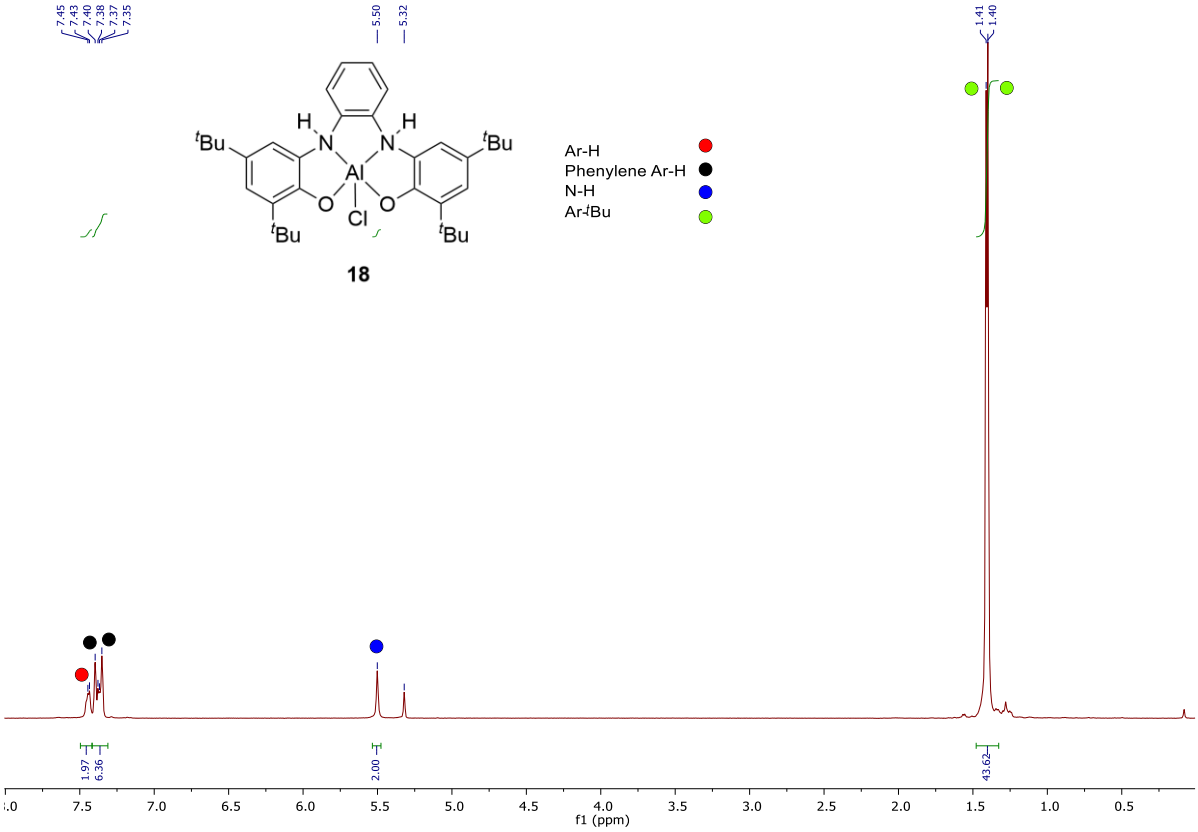


Figure 5. ^{1}H NMR spectrum (CD_2Cl_2, 298 K) of **18**.

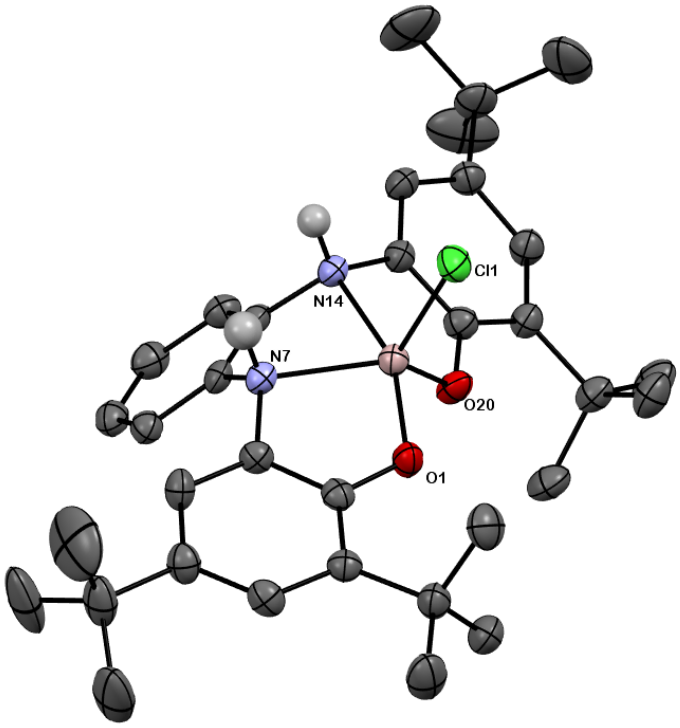


Figure 6. Crystal structure of **18** (ellipsoid plot, 50% probability) showing a monomeric structure in the solid state.

A single crystal was grown *via* vapour-diffusion of pentane into a concentrated solution of **18** in DCM and subsequently analysed by XRD. The crystal structure of **18** was obtained which features a mononuclear molecular structure (Figure 6). The aluminium centre is pentacoordinate and adopts a distorted square pyramidal structure (τ_5 = 0.44).[61] The tetradentate O'N'N'O-ligands coordinates around the metal centre in a pseudo-meridional fashion with the chloride ligand sitting at the apical position. An interesting feature is the arrangement of the phenylene moiety which sits below the average plane of the molecule and exposes the NH groups. This would likely allow the monomer units to coordinate much easier from a "top-down" approach, maximising the possible NCIs. The distance between the NH moieties is 2.702 Å, which is smaller than what was measured for complex **1** (2.789 Å, Section 2.3.1.1). This can be attributed to **18** bearing a C_2 linker as opposed to a C_3 linker. The distances are reminiscient of the previously discussed squaramides which have an average distance of 2.80 Å between the NH moieties.

4.3.4 Electrochemical behaviour of **18** and oxidant choice

The ^{H}**L**$_4$ ligand has already been subject to multiple redox studies when coordinated to Co,[53] W,[59] Mo,[56] Sn,[55] Ti,[52] as well as Cu and Zn.[50] The majority of complexes studied featured transition metals, and resulted in reversible multi-electron oxidations of the metal centres. However, the Sn complex studied by Cherkasov *et al.* found the complex to undergo a reversible one-electron oxidation which was postulated to occur on the ligand.[55] Given the favourable redox properties of the ligand, a cyclic voltammogram (CV) was performed on the THF adduct of **18** (Figure 7, see details in Experimental) by Lucy Wilson from the Long group. If **18** can be reversibly oxidised, it would signify that there is a good possibility to perform redox-switchable catalysis as detailed in the introduction. The CV featured a quasi-reversible redox event that corresponds to an oxidation of **18** to **[18]**$^+$. An additional redox reaction can be found further along the voltammogram corresponding to the conversion of **[18]**$^+$ to **[18]**$^{2+}$. However, the redox event appears to be irreversible, suggesting that the oxidised species **[18]**$^{2+}$ undergoes a process (*e.g.* degradation or ligand loss) which is not reversible.[62] Lucy Wilson also carried out a CV on an aluminium catam complex tethered by a piperazine linker (synthesised by Floriana Moruzzi within the group). The voltammogram (Figure A42) shows that the complex is indeed redox-active. However, the redox events appear to be irreversible, showing that the aromatic properties of the ^{H}**L**$_4$ ligand can impart complex **18** with favourable redox properties.

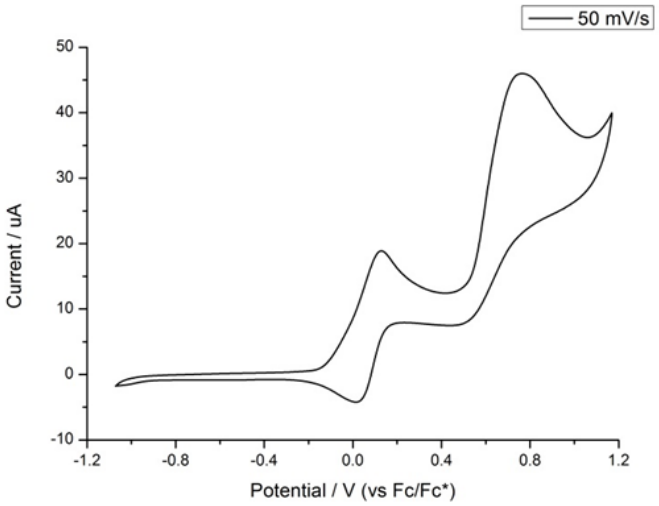


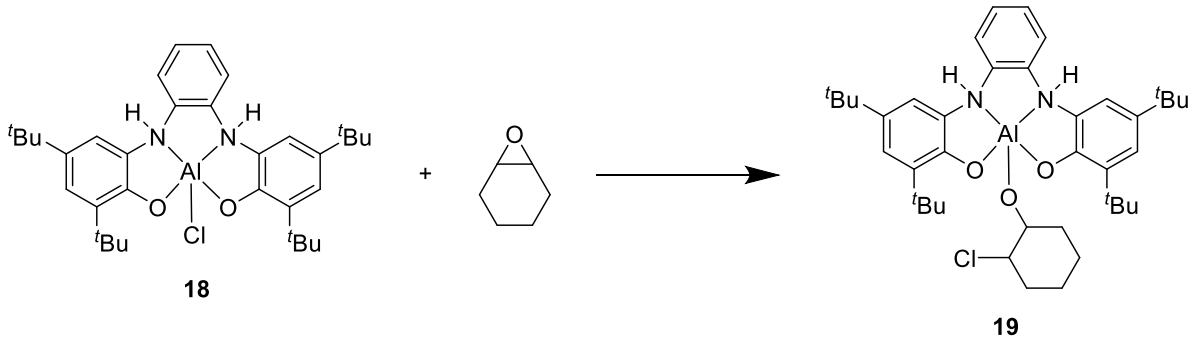
Figure 7. CV Trace of the first two oxidations of the THF adduct of **18** showing a reversible 1st oxidation followed by an irreversible 2nd oxidation.

This confirms that complex **18** can be oxidised at least once to form **18-ox**. The positive charge is likely distributed across the redox non-innocent ^{H}**L4** ligand instead of the metal centre. Tthe oxidation of **18** to **18-ox** occurs close to the redox potential of ferrocene (+ 0.1 V *vs.* Fc/Fc^{+}) suggesting that ferrocenium salts may be suitable oxidants as previously reported by others. Oxidant with higher redox potential may be favourable, such as AgOTf. However, it is important to note that these results concerns the monomeric aluminium chloride complex. The active species formed during polymerisation is an alkoxide which could result in a different redox potential. Given the promising CV results, investigating the switchability of **18** was considered.

As outlined in Section 4.1.4, a variety of oxidising salts were employed in literature for the purposes of artificial switchable catalysis. This includes silver salts (*e.g.* AgOTf and $AgBAr^{F}$) as well as ferrocenium salts (*e.g.* $FcPF_6$ and $FcBAr^{F}$). Silver salts were not considered at this stage as the chloro ligand of **18** can react with silver to form the insoluble AgCl. Instead, the decision was made to initially use $FcBAr^{F}$ because of its high solubility in organic solvents and the weak-coordinating properties of the $[BAr^{F}]^{-}$ counter-anion.

4.3 Reactivity of Complexes and Preliminary Polymerisation Studies

4.3.1 Reaction of 18 with CHO



Scheme 19. Envisioned reaction pathway between **18** and CHO producing the suspected 2-chlorocyclohexano derivative **19**.

The chloride anion is not nucleophilic enough to initiate the polymerisation of *rac*-LA. The groups of Thomas and Maron overcame this hurdle by pre-activating their aluminium chloride complex with an epoxide overnight.[63, 64] The pre-activation pathway consists of the opening of the epoxide *via* nucleophilic attack by the chloride, resulting in an aluminium alkoxide species being generated. This newly formed complex can then initiate LA ROP. The reactivity of the chloro complex **18** was thus tested with cyclohexene oxide (CHO) to gauge whether a transformation from complex **18** to **19** is also possible (Scheme 19).

Addition of one equivalent of CHO to **18** in CD_2Cl_2 turned the colourless solution into a red colour almost immediately and ^1H NMR spectrum shows the formation of new species (CD_2Cl_2, 298 K, Figure 8). It is clear that a transformation takes place under these conditions as the starting material does not appear in the product spectrum. Due to a convoluted spectrum, likely arising from the presence of multiple species, determination of the product proved to be rather difficult. To shed more light onto the mechanism of action, the reaction between **18** and CHO was carried out in diethyl ether instead of DCM, in the hopes of forming a precipitate and isolate well-defined species. A solid was observed after 2 hours which was filtered and analysed by NMR spectroscopy. The ^1H NMR spectrum (CD_2Cl_2, 298 K) also exhibits a convoluted spectrum, showing the same mixture of compounds being afforded as the chloroalkoxo species generated from the *in-situ* addition of CHO to **18** (Figure A43). More information was obtained when a single colourless crystal of the solid compound was grown

out of the NMR solution *via* layering with pentane, which was subsequently analysed by XRD (Figure 9).

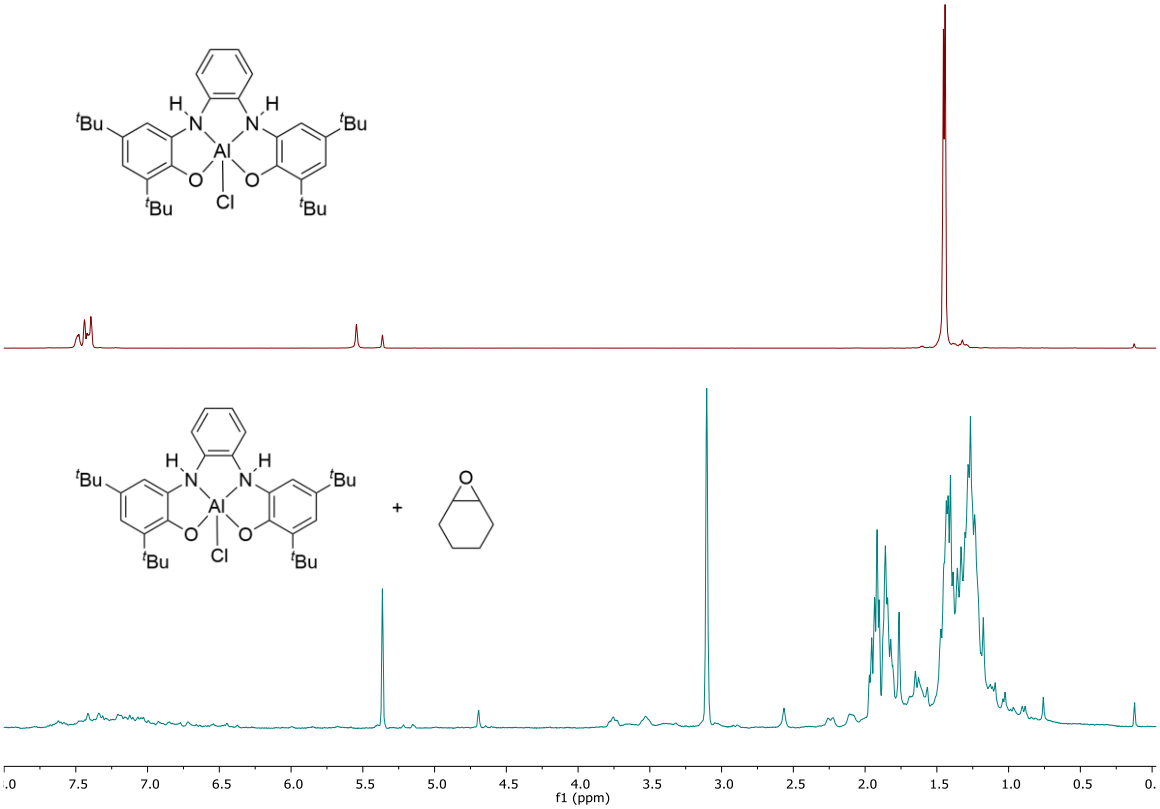


Figure 8. ^{1}H NMR spectrum (CD_2Cl_2, 298 K) of **18** (top) and **18** + CHO (bottom) showing a transformation taking place and multiple species being formed in solution.

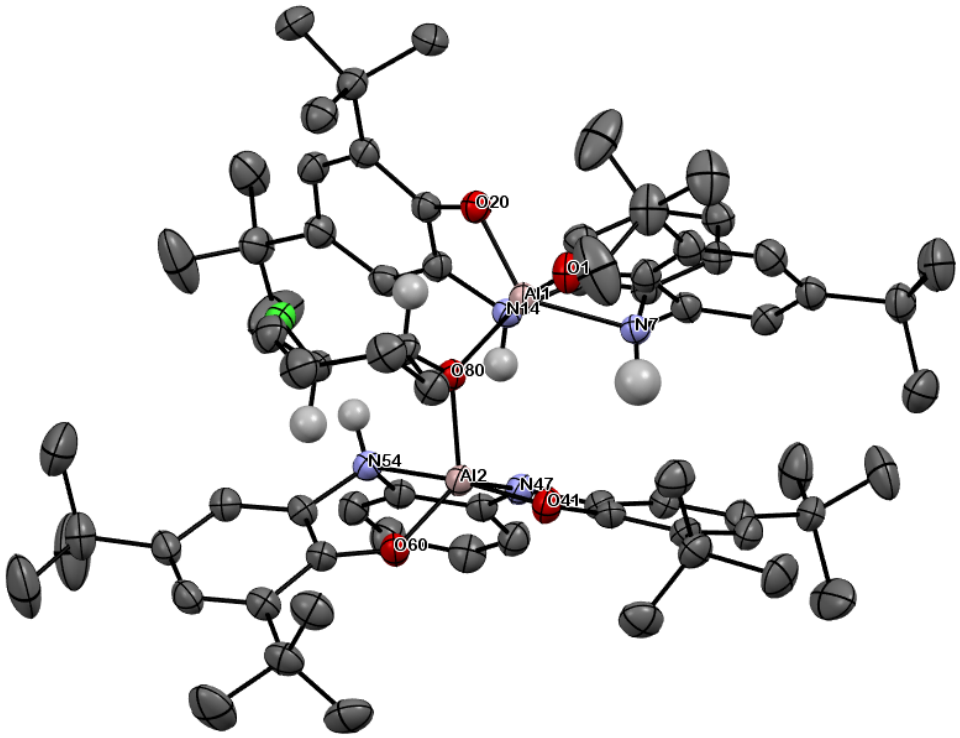
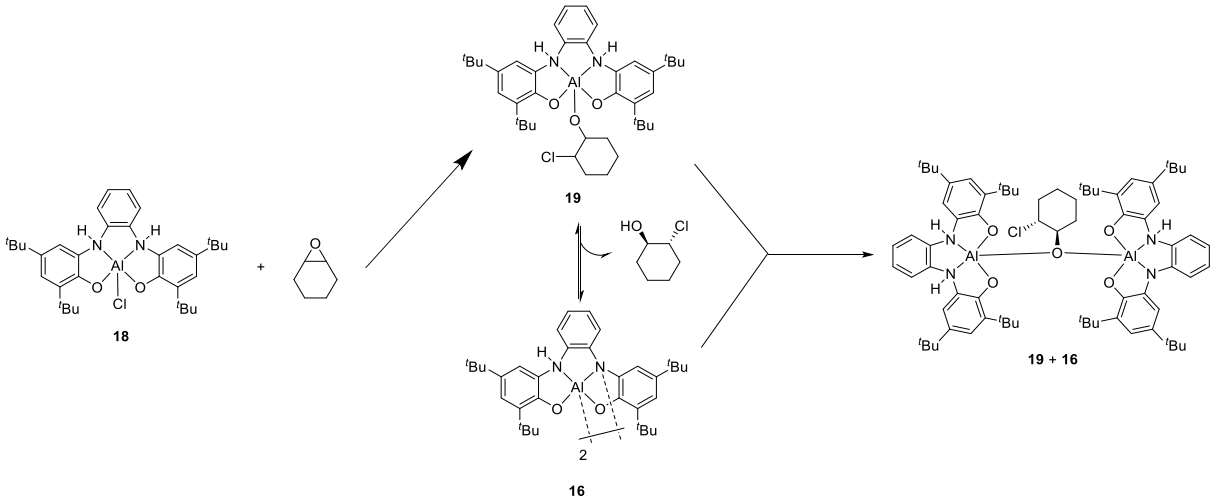


Figure 9. Crystal structure of the species produced from the addition of CHO to **18** in diethyl ether (ellipsoid plot, 50% probability). The structure consists of complexes **19** and **16**, bridged by the 2-chlorocyclohexano ligand.

The crystal structure consists of an adduct of the deprotonated complex (**16**) and the 2-chlorocyclohexanoxy complex **19**. These are connected by the μ-O bridging atom of the 2-chlorocyclohexano co-ligand at a bond angle (Al1-O80-Al2) of 123.96°. Looking at the components of adduct, complex **19** adopts a conformation that is biased towards a trigonal bipyramidal geometry (τ_5 = 0.57).[61] The geometry of the deprotonated complex **16** has a stronger trigonal bipyramidal character (τ_5 = 0.64). The chloride and oxygen atoms on the bridging unit are *trans* to one another and occupy equatorial positions. Judging from the crystal structure one can suggest the following:

- The CHO molecule is opened *via* an SN_2 mechanism in which the nucleophile (Cl^-) performs a backside attack to yield the *trans*-2-chlorocyclohexano product.
- The 2-chlorocyclohexano ligand can readily deprotonate the NH moiety of **19** to form the deprotonated **16** and 2-chlorocyclohexanol. This likely arises from the increased acidity of the NH moieties relative to other catam complexes.
- The products appear to exhibit a propensity to dimerise and precipitate over time which provides the necessary thermodynamic driving force for this transformation to occur.

Indeed, DOSY experiments (C_6D_6 and THF-d_8, 298 K) show that the "isolated" complex is dimeric when dissolved in C_6D_6 (Figure A46). However, when the experiment is carried out in THF-d_8, the complex reverts to a monomeric state likely due to the coordinating properties of THF (Figure A47).



Scheme 20. Proposed mechanism for the reaction between **18** and CHO in which **19** is formed and can be deprotonated to form **16** which leads to the aggregate **19** + **16**.

The mechanism is summarised in Scheme 20. Addition of CHO to **18** leads to the formation of the 2-chlorocyclohexano complex **19**. Deprotonation of the NH moieties by the 2-chlorocyclohexano ligand can occur to yield the corresponding alcohol and deprotonated

complex **16**. Complexes **19** and **16** can then combine to form the species observed in the crystal structure.

A route was attempted in which the monomeric alkoxide **19** was synthesised from the deprotonated complex **16** *via* the addition of 2-chlorocyclohexanol. The *trans*-2-chlorohexanol was synthesised from a literature procedure in which HCl was added to CHO.[65] The addition of 2-chlorocyclohexanol to **16** was then studied on an NMR scale to gauge the effectiveness of the method (Figure 10). The ^{1}H NMR spectrum shows a strong similarity to the **19** + **16** dimer (CD_2Cl_2, 298 K), meaning that the monomeric complex **19** cannot be generated from **16**.

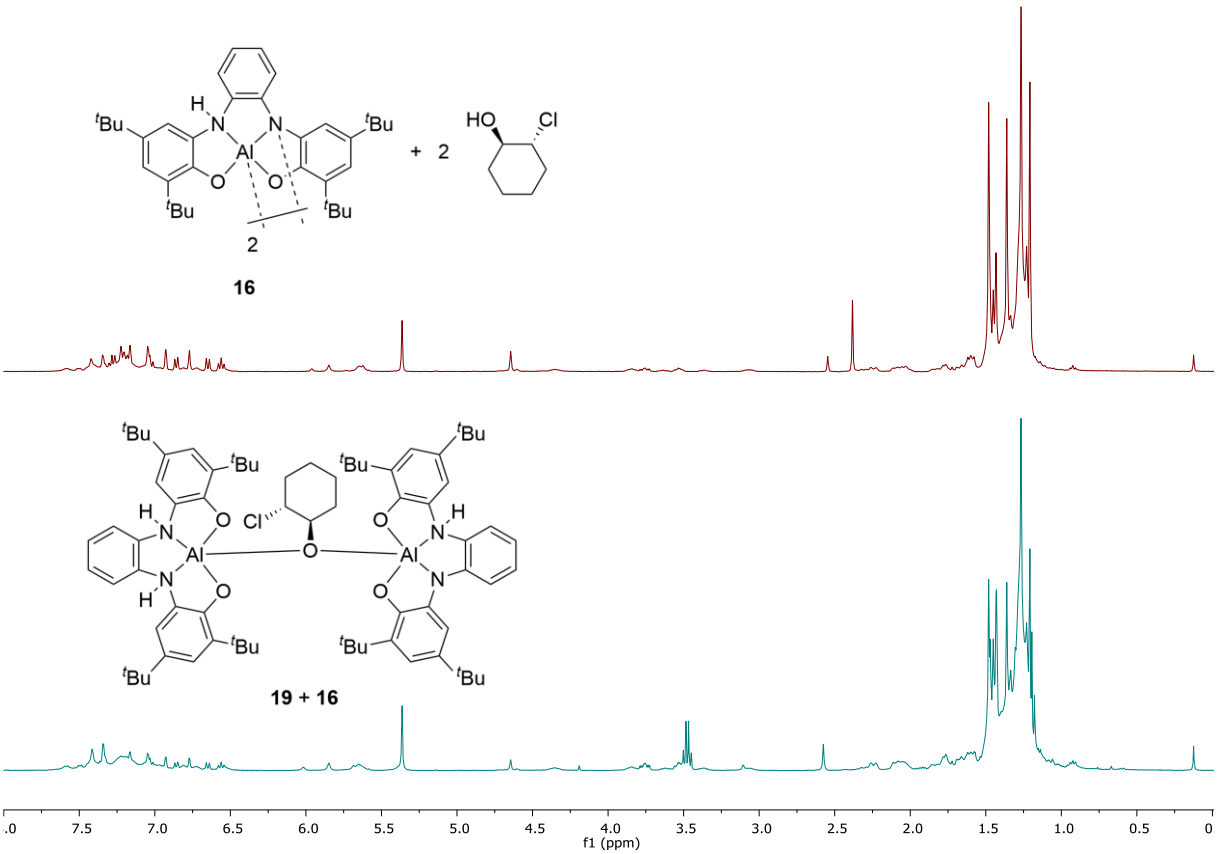


Figure 10. ^{1}H NMR spectrum (CD_2Cl_2, 298 K) of **16** + 2-chlorocyclohexanol (top) and **19** + **16** (bottom) showing similarities between both spectra.

The reactivity of **18** towards CHO is not as straightforward as envisaged in Scheme 19 and was corrected in Scheme 20. There are multiple products formed upon addition of CHO to **18** and a single well-defined species could not be isolated. However, the reaction occurred almost immediately compared to the salen-Al chloro complex reported by Thomas and co-workers which required a lengthy pre-activation period.[64] Similar complexes by the Garden group were

more reactive to epoxides and could be activated relatively quickly.[66] However, their reactions were carried out at 120 °C which accelerated the conversion of the chloro complex to the active species. Thus, the quick transformation of **18** by the addition of CHO at room temperature demonstrates its high reactivity. To gain an understanding of the mechanism of action, DFT studies were conducted on the reaction between **18** and CHO.

4.3.2 DFT calculations on the reaction of **18** with CHO

Initially a monomeric mechanism was envisaged wherein the CHO molecule coordinates axially to the metal centre and subsequently undergoes a nucleophilic attack by the chloride ligand to yield the opened 2-chlorocyclohexano ligand (Figure 11). The coordination of the CHO (**II**) lead to minor energy penalty of $\Delta\Delta G_{298} =$ 1.3 kcal/mol. The nucleophilic attack (**III-TS**) appeared to proceed in a single step with an activation energy of $\Delta\Delta G_{298} =$ 35.7 kcal/mol. This value is too high to be conducive to a room temperature active reaction as observed experimentally. Furthermore, the 2-chlorocyclohexano product has the chloride and alkoxide substituents *cis* to one another, which is not consistent with the *trans* configuration observed in the crystal structure. More approaches were thus considered which all led to higher activation energies. None were found to produce the desired *trans*-2-chlorocyclohexano product which prompted the investigation of an alternative mechanism.

A dimeric mechanism was considered in which a molecule of CHO initially coordinates onto **18** (Figure 12, $\mathbf{X_1}$, **II**). This was followed by the approach of a second molecule of **18** ($\mathbf{X_2}$) yielding an aggregate that is stabilised $\Delta\Delta G_{298} =$ - 5.7 kcal/mol (**III**). The chloride ligand of the $\mathbf{X_2}$ then performs a backside attack on the CHO molecule while the chloride ligand of $\mathbf{X_1}$ migrates onto $\mathbf{X_2}$. This preserves one molecule of **18** while yielding one molecule of the 2-chlorocyclohexano derivative (**V-di-ax**, $\Delta G_{298} =$ -6.8 kcal/mol). The activation energy of this reaction is $\Delta\Delta G_{298} =$ 23.8 kcal/mol, which is significantly more favoured than the monomeric mechanism. Furthermore, the 2-chlorocyclohexano molecule formed has a di-axial *trans* conformation which can undergo a chair flip to yield the di-equatorial molecule observed (**V-di-eq**, $\Delta G_{298} =$ -13.0 kcal/mol), resulting in a stabilisation of the system by $\Delta\Delta G_{298} =$ 6.2 kcal/mol.

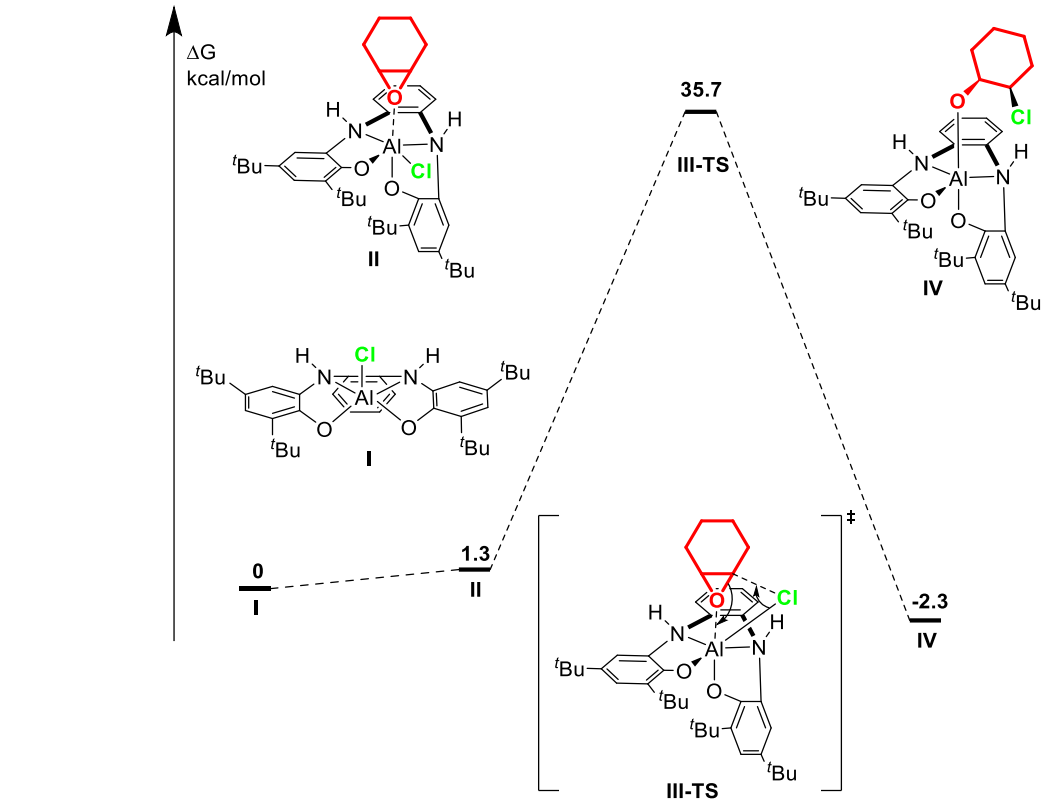


Figure 11. PES showing the reaction between **18** and CHO as per a monomeric mechanism. DFT protocol: # m062x/6-31g(d,p) scrf=(cpcm, solvent = DCM) nosymm integral=grid=ultrafine.

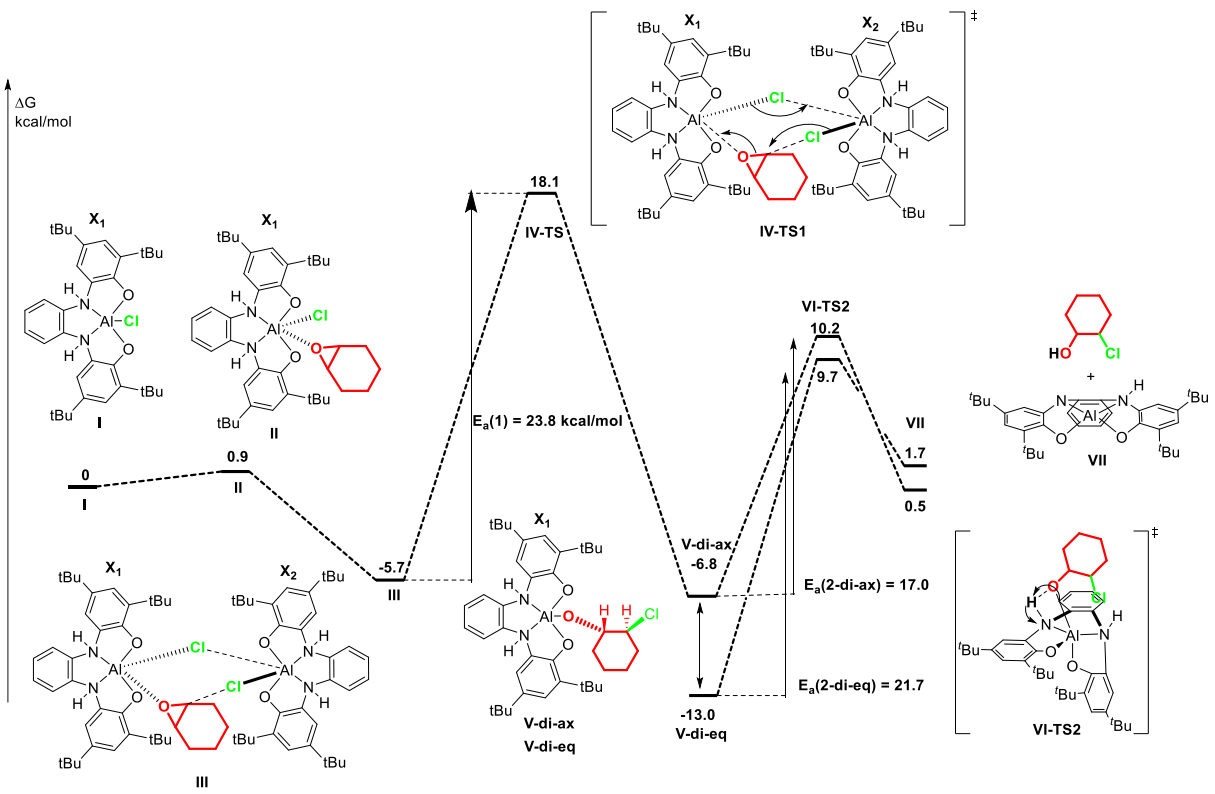
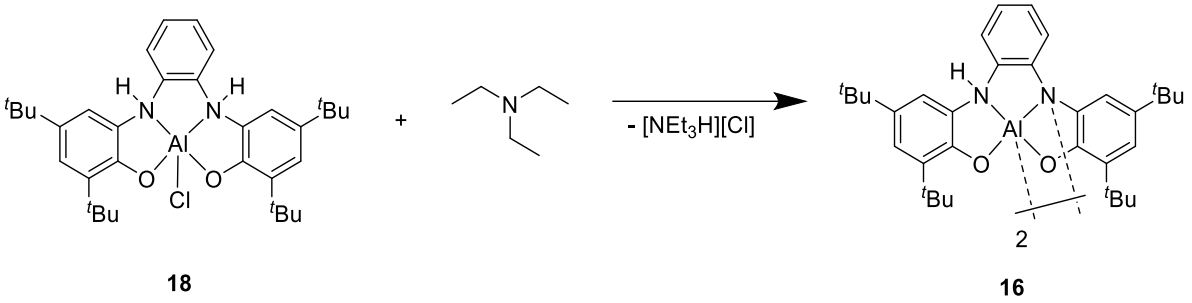


Figure 12. PES showing the reaction between **18** and CHO as per a dimeric mechanism. DFT protocol: # m062x/6-31g(d,p) nosymm integral=grid=ultrafine.

The subsequent deprotonation was studied for **V-di-ax** and **V-di-eq**. The deprotonation of the NH moiety was favourable at room temperature for both species. However, the activation energy was significantly lower for **V-di-ax** ($\Delta\Delta G_{298}$ = 17.0 kcal/mol). DFT calculations confirm the favourable formation of complex **19** and its deprotonation ($\Delta\Delta G_{298}$ = 17.0 kcal/mol) to afford **16**. These results help to rationalise the crystal structure previously discussed (Figure 9). Thus, the opening of CHO by **18** is mediated *via* a dimeric mechanism in which the product can easily interconvert between a di-axial and di-equatorial species, of which **V-di-ax** readily undergoes deprotonation of the NH moiety.

4.3.3 Other reactions of **18**



18 **16**

Scheme 21. Reaction between **18** and NEt_3 producing the deprotonated **16** along with one equivalent of triethylammonium chloride.

It appears that the chloride group of **18** is particularly reactive, allowing for multiple transformations to take place. It was discovered that complex **16** can be synthesised from **18** by adding one equivalent of a weak base to the solution (Scheme 21). The base, in this case triethylamine (pK_a = 10.8), deprotonates the NH moiety and abstracts the chloride group to form **16** and the salt triethylammonium chloride. This was carried out in an NMR experiment using triethylamine with the transformation taking place cleanly as per the ^{1}H NMR spectrum (C_6D_6, 298 K, Figure 13). This reaction takes place readily at room temperature and is thermodynamically driven by the formation of a salt.

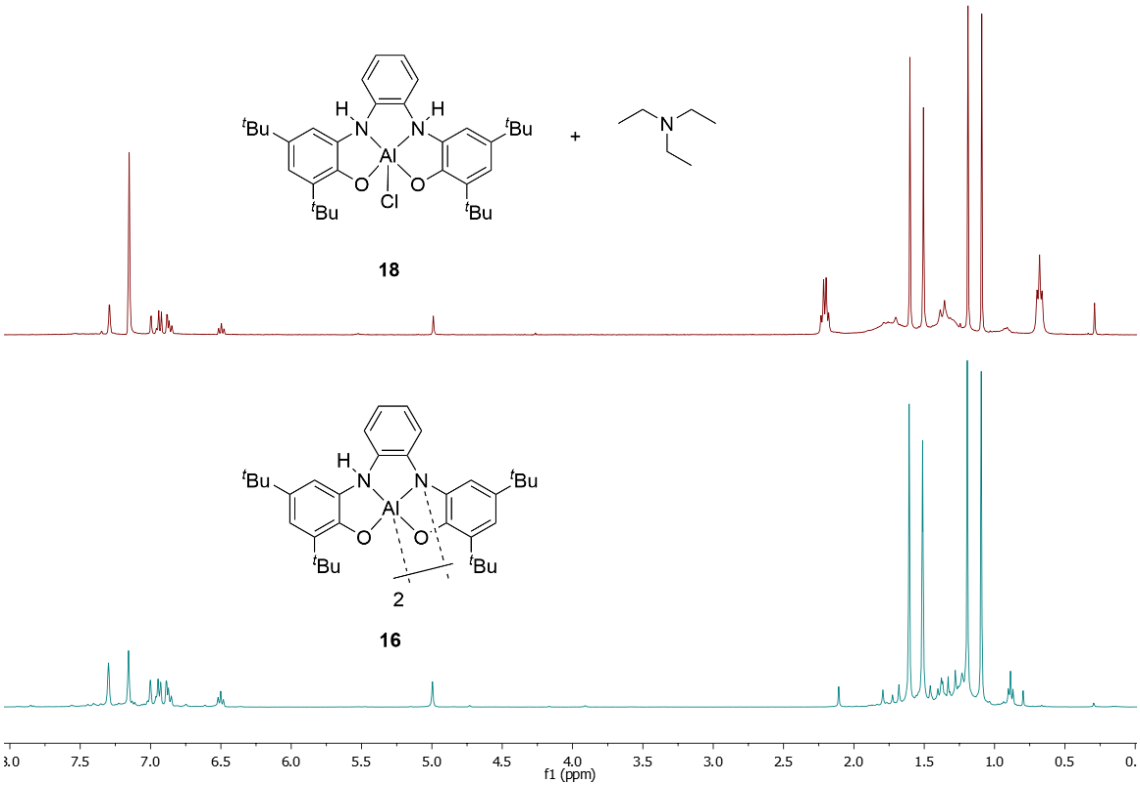
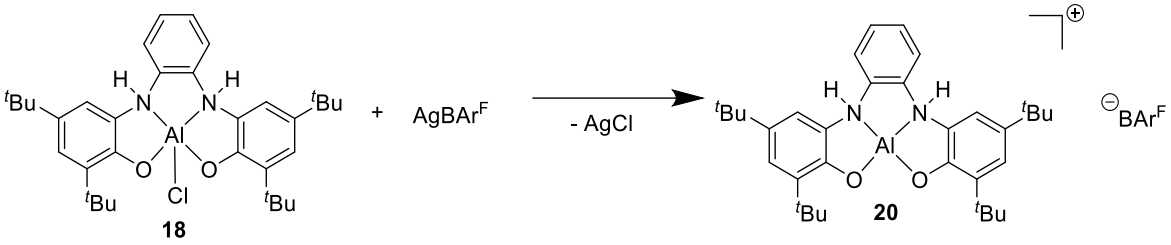


Figure 13. ^{1}H NMR spectrum (C_6D_6, 298 K) of the product of **18** + NEt_3 (top) and **16** (bottom) showing that the base abstracts the chloride and deprotonates one NH moiety to form **16** upon addition to **18**.



Scheme 22. Reaction between **18** and AgBAr^F yielding the cationic complex **20** and one equivalent of AgCl.

The abstraction of the chloride was studied further by attempting to form a cationic aluminium species from **18** *via* the addition of a silver salt. The salt metathesis would form the insoluble silver chloride which provides the necessary thermodynamic driving force for this reaction to occur (Scheme 22). Initial reactions between **18** and one equivalent of silver tetrafluoroborate ($AgBF_4$) showed a transformation taking place but does not appear to form a well-defined species as per the ^{1}H NMR spectrum (CD_2Cl_2, 298 K, Figure A44). This was attributed to the $^{-}BF_4$ counter-ion exhibiting some coordinating properties which would result in different species being shown to the spectrum. An attempt to rectify this was made by synthesising a silver BAr^F salt , as the anion is regarded as "non-coordinating". Following a well-established

literature procedure,[67-69] a solution of $NaBAr^F$ in diethyl ether was vigorously shaken with a solution of $AgNO_3$ in water. Isolating the organic layer and removing the volatiles yielded $AgBAr^F$ as a white solid which was stored in the dark at -40 °C. Addition of one equivalent of $AgBAr^F$ to **18** in diethyl ether resulted in the formation of a precipitate suspected to be AgCl. This was removed using a syringe filter and the filtrate was evaporated off affording a dark red solid in quantitative yields. Analysis of the product *via* ^1H NMR spectroscopy (CD_2Cl_2, 298 K) shows a single well-defined species, suspected to be the cationic **20** (Figure 14). The integration of the peaks suggests that the charge is countered with one equivalent of the $^-BAr^F$ anion, as expected. Further to that a coordinated diethyl ether molecule was observed. Elemental analysis performed on **20** confirms the formation of the proposed species. Unfortunately, no single crystals suitable for analysis by X-Ray diffraction have been obtained.

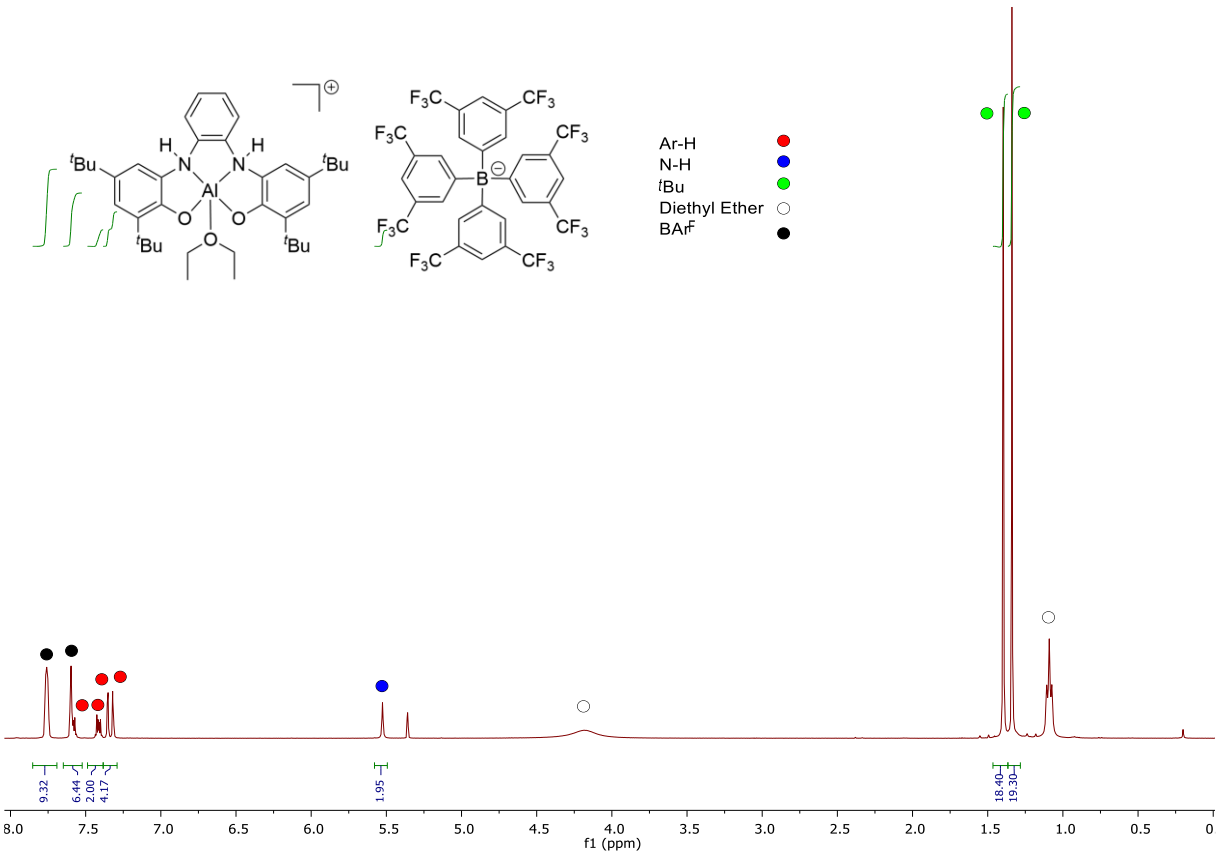


Figure 14. ^1H NMR spectrum (CD_2Cl_2, 298 K) of **20**.

4.3.4 Preliminary polymerisation studies

Given that the alkoxide complexes **17-a** and **17-b** were successfully synthesised, and that **16** can afford alkoxide complexes upon addition of an alcohol, they were tested in the ROP of *rac*-LA (Table 1). Given that some complexes exhibited solubility issues, DCM was primarily used

to maximise dissolution and thus activity. This screening was conducted to identify the best candidate for *rac*-LA ROP. For more detailed studies, the reader is referred to the next section.

Table 1. Preliminary polymerisations of rac-LA using complexes **17-a** and **17-b** as well as **16** in conjunction with ^{i}PrOH or 2-chlorocyclohexanol.

Entry	Complex	co-catalyst	Monomer (equiv.)	Solvent	Temperature (°C)	Time (h)	Conv.[a] (%)
1a	**17-a**	-	*rac*-LA (100)	DCM	25	1.5	< 5
1b				THF	60	16	89
2	**17-b**	-	*rac*-LA (100)	DCM	25	2	14
3	**16**	^{i}PrOH	*rac*-LA (100)	DCM	25	1	12
4	**16**	2-chlorocyclohexanol	*rac*-LA (100)	DCM	25	1	< 5

Reaction conditions: $[LA]_0$ = 1 mol.L^{-1}; a) Determined by ^{1}H NMR by relative integration of monomer and polymer signals (see ESI)

The methoxy complex **17-a** was found to exhibit minimal conversion of the monomer in DCM after 90 minutes at room temperature (Table 1, Entry 1a). The complex fared even worse in THF at room temperature and afforded no polymer according to the ^{1}H NMR spectrum (likely due to inhibition *via* the coordination of the solvent). Only upon heating the reaction mixture overnight at 60 °C, a conversion of 89 % was observed (Table 1, Entry 1b). Moving on to the benzyloxy complex **17-b**, the polymerisation at room temperature in DCM showed a conversion of 14 % after 2 hours (Table 1, Entry 2). This is marginally better than **17-a** and was attributed to an easier breakdown of the dimer.

The polymerisation using the deprotonated complex **16** was attempted as well as this class of complexes was found to be a good precursor to the active species. Employing **16** alongside an equivalent of ^{i}PrOH in DCM led to 12 % of *rac*-LA being converted after 1 hour (Table 1, Entry 3). This is twice as fast as **17-b** and demonstrates that active species can indeed be in-situ generated from **16**. However, despite the improvement, the activity is still significantly slower than the aluminium catam complexes detailed in Chapter 2 and 3.

The activity showed no improvement and even worsened when 2-chlorocyclohexanol was used instead of ^{i}PrOH (Table 1, Entry 4). This means that although a transformation takes place, the resulting species aggregates quickly, hindering polymerisation activity. In all cases, dimerisation appears to be the main reason for the low polymerisation activity of the alkoxide complexes, which can only be overcome by heating.

Table 2. Preliminary polymerisations of CHO and *rac*-LA using different complexes and different solvents.

Entry	Complex	Monomer (equiv.)	Solvent	Temperature (°C)	Time (h)	Conv.[a] (%)
1a	**18**	CHO (100)	DCM	25	16	< 5
1b			THF	60	4	
1c			Toluene	90	4	
2a	**18**	*rac*-LA (100)	THF	25	16	0
2b			DCM		1.5	
3	**18** + CHO	*rac*-LA (100)	THF	25	72	54
			DCM		4	86
4	**19 + 16**	*rac*-LA (100)	DCM	25	16	< 5
5	**20**	CHO (100)	CD_2Cl_2	25	0.17	100
6	**20**	*rac*-LA (100)	CD_2Cl_2	25	16	0

Reaction conditions: $[M]_0$ = 1 mol.L^{-1}; a) Determined by ^{1}H NMR by relative integration of monomer and polymer signals (see ESI)

Given that the alkoxo complexes did not achieve a satisfactory activity, the chloro complex **18** was tested. Even though the reaction of **18** with CHO forms a product mixture at room temperature, it is not conducive to its ability to polymerise CHO. Attempted polymerisations of CHO by **18** at different temperatures and solvents did not result in a significant polymer after multiple hours (Table 2, Entry 1a-1c). **18** likely reacts with one equivalent of CHO *in-situ* to form the chlorocyclohexano derivative **19** along with other products as evidenced in Section 4.3.1. However, the nature of the secondary alkoxide, along with the insufficient Lewis acidity of the aluminium metal centre, prevents any further ring openings to be carried out by the complex.

The ability of **18** to polymerise *rac*-LA "on its own" has also been investigated. As previously mentioned, the chloro ligand is not nucleophilic enough to initiate polymerisation. Furthermore, the opening of a molecule of LA by a chloride anion would result in the formation of highly reactive acyl. In the interest of due diligence, an attempted polymerisation of *rac*-LA in THF was carried out which yielded no polymer after 16 hours at room temperature (Table 2, Entry 2a and 2b). The repetition of the polymerisation in DCM did not show any form of improvement, which shows that the chloride group of **18** will not initiate the polymerisation at room temperature regardless of the circumstances.

Given that the groups of Thomas, Maron, Taton, and Garden showed that an active species can be obtained *via* the reaction of an aluminium chloro complex with an epoxide, the

polymerisation of *rac*-LA by **18** was finally studied in conjunction with CHO (Table 2, Entry 3). Complex **18** was pre-activated with 5 equivalents of CHO in THF for 5 minutes to generate complex **19** *in-situ* prior to addition of *rac*-LA. The subsequent polymerisation proceeded slowly with only 54 % of the monomer being converted after 3 days at room temperature. As mentioned, it was suspected that the coordination properties of the solvent may impair the active species from carrying out the polymerisation efficiently, which prompted the use of the non-coordinating DCM instead. Indeed, the coordination of THF did impair the activity as the polymerisation in DCM reached a conversion of 86 % after only 4 hours. Thus, the pre-activation of **18** prior to polymerisation is imperative to ensure that *rac*-LA is polymerised with good activities.

Given this success, the investigation of **19** + **16** as an initiator was carried out. As mentioned in Section 4.3.1, the reaction of **18** with CHO in diethyl ether yielded a solid which was not well-defined and assumed to be primarily composed of an aggregate between the desired chlorocyclohexano species (**19**) and the deprotonated complex (**16**). One may logically infer that starting with the 2-chlorocyclohexano derivative may yield similar results found in Entry 3. However, reacting **19** + **16** with *rac*-LA in DCM overnight only yielded minimal conversions (Table 2, Entry 4). A look at the crystal structure of **19** + **16** (Figure 9) and associated DOSY analysis (Figures A46 and A47) sheds some light on the issue. The species is likely an aggregate in DCM that hinders the approach and opening of the monomer. The sole reason as to why the *in-situ* pre-activation of **18** leads to an active species, is the fact that the reaction forms a monomeric alkoxide species *in-situ* which immediately initiates ROP (before slowly converting to an aggregated state). The attempted direct synthesis and purification of **19** encourages aggregation into higher order structures which are unable to polymerise the substrate. Although DOSY analysis has shown the complex to be monomeric in THF, the polymerisations cannot be carried out in a coordinating solvent as these were clearly shown to inhibit the activity.

It therefore appears that the only reliable way to effectively carry out polymerisations with the chloro complex **18** is *via* the *in-situ* pre-activation prior to the addition of the substrate. This method will be employed in the later sections of this chapter.

To conclude the preliminary polymerisation tests, the reactivity of **20** towards CHO and *rac*-LA was tested. The cationic nature of **20** proves to be valuable in polymerising CHO (Table 2, Entry 5), converting 100 equivalents at room temperature in the span of 10 minutes on a NMR

scale (Figure A45). This result suggests that the generation of a cationic species or more electron deficient species can be beneficial to CHO ROP and the switch polymerisation. The polymerisation of *rac*-LA by **20** (Table 2, Entry 6) was found to be inactive after 16 hours even with the presence of a co-initiator (^{i}PrOH).

The polymerisation tests provided valuable insights into the polymerisation behaviour of **18** and its derivatives. It was found that its pre-activation results in an active species that can proceed with *rac*-LA polymerisation, provided it is carried out in a non-coordinating solvent such as DCM. Further tests have shown that **19** cannot be isolated for its use as an initiator as the direct synthesis results in the formation of aggregates that hinder the approach and opening of the monomer.

4.4 Polymerisation Studies

4.4.1 Polymerisation of *rac*-LA

Table 3. Polymerisations of *rac*-LA using the pre-activated **18** in conjunction with various co-catalysts.

Entry	cat/CHO/LA (eq.)	co-cat (eq.)	Time (min)	Conv.[a] (%)	$M_{n(SEC)}$(Đ)[b] (kg/mol)	$M_{n(calc.)}$[c] (kg/mol)
1	1/10/100	-	90	91	10.3 (1.3)	13.1
2	1/10/1000	^{i}PrOH (9)	300	61	8.0 (1.1)	8.8
3a	1/10/100	-	30	49	4.3 (1.1)	7.0
3b		+ $FcBAr^{F}$	20	48	4.3 (1.1)	6.8
4a	1/10/100	$FcBAr^{F}$	30	0	-	-
4b		+ $CoCp_2$	90	34	4.0 (1.3)	4.9
5a	1/10/100	-	30	49	-	-
5b		+ $FcBAr^{F}$	30	50		
5c		+ $CoCp_2$	50	74		
6a	1/10/100	-	30	35	5.7 (1.2)	5.0
6b		+ AgOTf	20	35	5.7 (1.3)	5.1
6c		+ $CoCp_2$	20	89	11.1 (1.1)	12.8

Reaction conditions: $[LA]_0$ = 1 mol.L^{-1}, DCM, 25 °C; Pre-activation carried out by stirring catalyst and CHO in DCM for 10 minutes prior to the addition of monomer (see ESI); a) Determined by ^{1}H NMR by relative integration of monomer and polymer signals (see ESI); b) Determined by SEC calibrated with polystyrene standards in THF and corrected (see ESI); c) Calculated using the conversion

Whilst optimising the conditions of the pre-activation period of **18**, it was found that the resulting activity was highly dependent on the CHO loading as well as the pre-activation time. To standardise subsequent polymerisations and ensure consistency, the pre-activation procedure was established to be a 10-minute period in which 10 equivalents of CHO were stirred with **18** prior to the addition of the desired monomers and co-catalysts.
Under these conditions the polymerisation of *rac*-LA was carried out at room temperature over the course of 90 minutes resulting in a conversion of 91 % (Table 3, Entry 1). Despite the less conventional pre-activation, the polymerisation retained its living features:

1. A pseudo-first order rate law with a k_{app} of 4.61×10^{-4} s^{-1} (Figure B90)
2. A linear increase of polymer molar mass with conversion (Figure B91)
3. Low dispersities in the polymer (Đ = 1.3)

The polymer was found to be moderately heterotactic ($P_r = 0.70$) putting **18** on a similar level to **2** regarding activity and selectivity. MALDI-ToF analysis was carried out on the polymer, exhibiting metal ion peaks ($M + K^+$) that are equally spaced by 144 atomic units (Figure D4). The exact masses indicate that the PLA is linear, having a chlorocyclohexanoxide initiating group consistent with the proposed CHO opening by the chloride group and a coordination-insertion mechanism. There are no peaks that indicate transesterification or backbiting reactions which explains the low dispersity of the polymer (Đ = 1.3). Complex **18** was also stable to immortal polymerisation conditions (up to 10 equiv. of ^{i}PrOH) and was able to proceed without any apparent deactivation, resulting in molecular weights that were close to what was expected (Table 3, Entry 2).

Having established good polymerisation behaviour for **18**, its switchability was explored. Initially, the ability for **18** to be switched off *via* the addition of $FcBAr^F$ was investigated (Table 3, Entry 3). **18** was allowed to polymerise *rac*-LA at standard conditions for 30 minutes, resulting in a conversion of 49 % (Table 3, Entry 3a). The complex was then oxidised to **18-ox** with one equivalent of $FcBAr^F$. After 20 more minutes, the conversion remained unchanged, indicating that the activity of **18** can be successfully switched off (Table 3, Entry 3b). Whilst dispersities remained low (Đ = 1.1), the molecular weights were much lower than expected. This signifies that there are more active species than expected which could be traced back to insufficiently pure CHO containing protic sources that can act as chain-transfer agents. The conversion plot shows a steady increase in conversion up until the oxidation of **18** to **18-ox**, stopping the polymerisation (Figure 15).

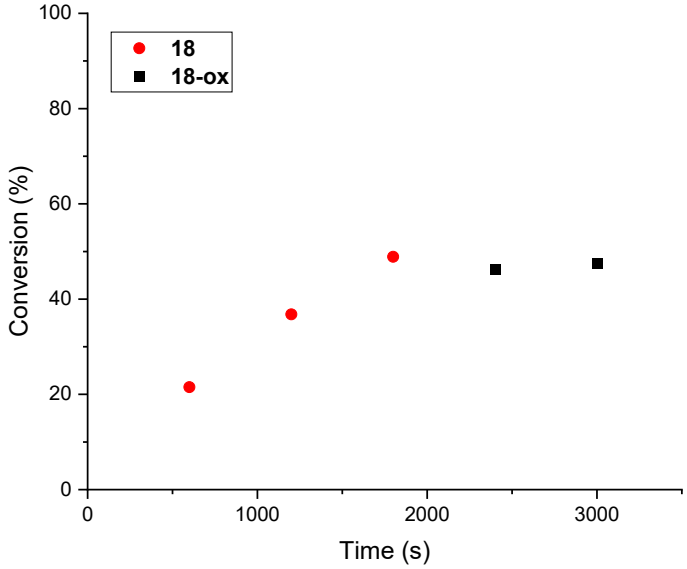


Figure 15. Conversion *vs.* time plot for *rac*-LA ROP initiated by **18** as per conditions in Table 3, Entry 3. Upon addition of one equivalent of $FcBAr^F$, the polymerisation stops which indicates successful switching of **18** to the inactive **18-ox**.

Having successfully switched off *rac*-LA ROP using $FcBAr^F$, it was investigated whether the polymerisation can be resumed *via* the addition of a reducing agent ($CoCp_2$) (Table 3, Entry 4). Starting from the oxidised species **18-ox** (generated by reaction of $FcBAr^F$ to pre-activated complex **18** for 5 minutes) the complex was allowed to react with *rac*-LA for 30 minutes which resulted in no conversion (Table 3, Entry 4a). Addition of $CoCp_2$ to the reaction mixture appeared to reduce **18-ox** to **18** which was active in *rac*-LA ROP, converting 34 % in the subsequent 90 minutes (Table 3, Entry 4b). Although the conversion plot shows a steady increase in conversion upon reduction of **18-ox** to **18** (Figure 16), the polymerisation was slower when compared to the benchmark polymerisation (Table 3, Entry 1). This can stem from either incomplete reduction of **18-ox** to **18**, or from **18-ox** reacting with itself (or the monomers) to irreversibly form an inactive species. Furthermore, **18-ox** could be less stable than **18** and decompose over time, yielding fewer active species upon reduction to **18**. However, the polymerisation was still controlled, and the polymer exhibited the expected molecular weights along with narrow dispersities (Figure B92).

As mentioned in Section 4.1.5, the $^{H}\mathbf{L_4}$ ligand is redox active and likely stabilises the positive charge generated by the oxidation of **18**, causing the aluminium centre to be more electron deficient. The deactivation could arise from the generation of a stable chelate between the polymer chain and the metal centre, hindering the approach of the next monomer. Alternatively, the positive charge would make the NH moieties more acidic, allowing the

alkoxide group of the polymer chain to deprotonate the NH group, leading to an inactive species. Depending on the species, the chelate is either broken upon reduction, or the deprotonated complex regeneration by reaction with the free polymer. The true nature of the mechanism is still not known and investigations are currently underway to explain the observed effect.

Despite the lower activity, the selective switching between 'on' and 'off' states is a remarkable feat as complex **18** does not contain a redox-active metal.

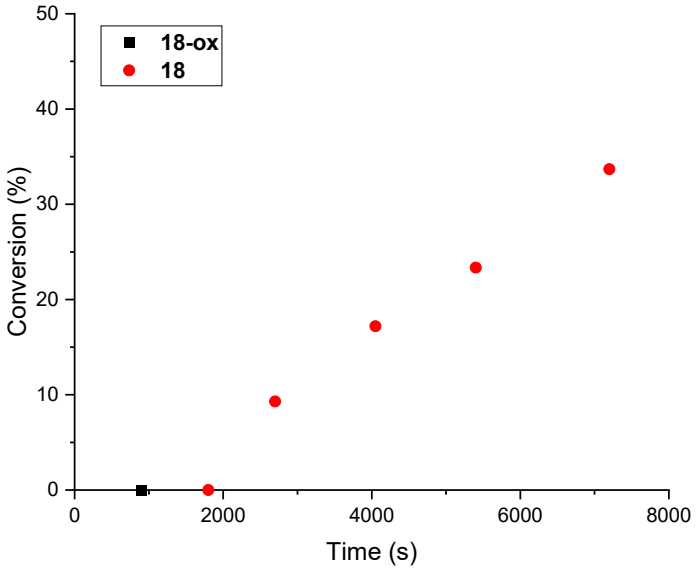


Figure 16. Conversion *vs.* time plot for *rac*-LA ROP initiated by **18-ox** as per conditions in Table 3, Entry 4. Upon addition of one equivalent of $CoCp_2$, the polymerisation resumes which indicates successful switching of **18-ox** to the active **18**.

Knowing that one can readily interconvert between **18** and **18-ox** (and hence 'on' and 'off' states), a polymerisation was carried out in which the polymerisation was turned off and resumed in the same pot (Table 3, Entry 5). Complex **18** was oxidised with $FcBAr^F$ after 30 minutes of polymerisation (49 % conversion, Table 3, Entry 5a) and **18-ox** was allowed to stir for a further 30 minutes. No further reaction appeared to have occurred (50 % conversion, Table 3, Entry 5b) upon which **18-ox** was reduced to **18** with $CoCp_2$ to resume polymerisation. After 50 minutes, a conversion of 74 % shows that the reaction continued (Table 3, Entry 5c). The conversion plot shows a clear halting of polymerisation upon oxidation to **18-ox**, and the increase in conversion resumed upon reduction to **18** (Figure 17). However, as was seen in Figure 16, the activity appeared to be lower upon switching from **18-ox** to **18**. However, to the knowledge of the author, this is the first instance in which a complex without a redox-active

metal was able to be selectively switched between 'off' and 'on' states using oxidising and reducing agents.

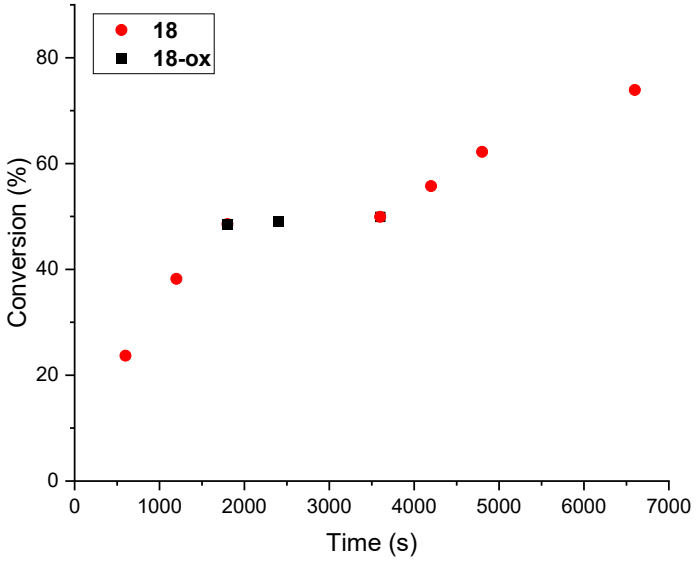


Figure 17. Conversion *vs.* time plot for *rac*-LA ROP initiated by **18** as per conditions in Table 3, Entry 5. Upon addition of one equivalent of $FcBAr^F$, the polymerisation stops until resumed with the addition of one equivalent of $CoCp_2$ showing that **18** can be switched to **18-ox** and back.

Despite the positive results, the lower activity upon switching **18-ox** to **18** is an undesired trait that makes the system unreliable. Incomplete regeneration of **18** from **18-ox** decreases the practicality of the complex as deactivation may have a detrimental effect molecular weight control. The use of alternative oxidising agents was thus investigated. Long, Gibson, and co-workers demonstrated that AgOTf can be successfully used in conjunction with $CoCp_2$.[28] Given that AgOTf has a higher redox potential than ferrocenium salts, its employment with **18** was investigated (Table 3, Entry 6). A standard polymerisation was carried out for 30 minutes yielding a conversion of 35 % (Table 3, Entry 6a). Addition of one equivalent of AgOTf halted the polymerisation and led to no apparent increase in conversion after 20 minutes (Table 3, Entry 6b). Addition of one equivalent of $CoCp_2$ resumed the polymerisation which led to a total conversion of 89 % after 20 minutes (Table 3, Entry 6c). The conversion plot shows the polymerisation to halt upon oxidation to **18-ox** and resumes upon reduction to **18** (Figure 18). However, the activity of **18** upon reduction from **18-ox** appears to be much higher than the initial activity of **18**. This increase in activity could stem from the reduction of **18-ox** generating an active species different to **18**, which can polymerise *rac*-LA at much faster rates. The molecular weights show good agreement with the expected values and increased linearly with

conversion (Figure B93) at low dispersities (Đ = 1.1). Despite the discrepancy in activities, the polymerisation was successfully switched between 'on' and 'off' states without sacrificing molecular weight control.

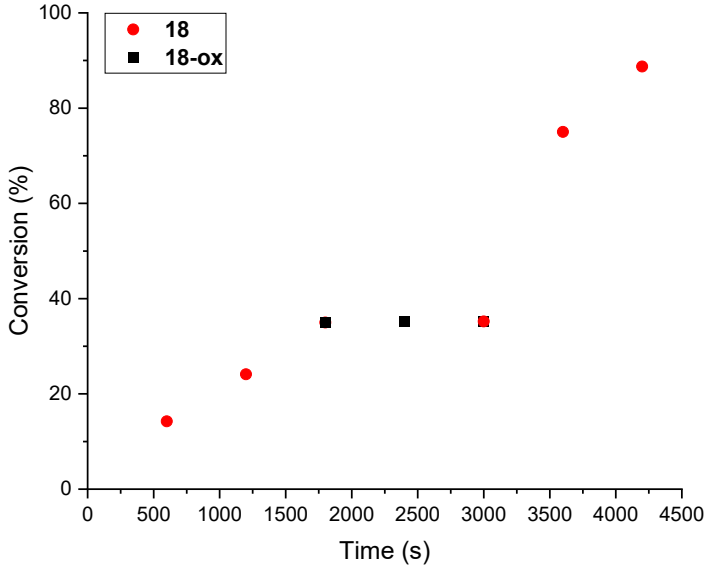


Figure 18. First-order plot (linear fit) for *rac*-LA ROP initiated by **18** as per conditions in Table 3, Entry 6. Upon addition of one equivalent of AgOTf, the polymerisation stops until resumed with the addition of one equivalent of $CoCp_2$ showing that **18** can be switched to **18-ox** and back using other oxidising agents.

The experiments on *rac*-LA have demonstrated that it is possible to switch complex **18** between 'off' and 'on' states using $FcBAr^F$ (or AgOTf) and $CoCp_2$. Although there appeared to be inconsistencies in activity when either $FcBAr^F$ or AgOTf were employed, the fact that redox-controlled switching can be carried out on aluminium complexes supported by redox non-innocent ligands shows remarkable potential in the field of artificial switchable catalysis. As mentioned in Section 4.1.4, the most common orthogonality in ROP switch catalysis is that between LA and CHO. Thus, the ability of **18** and **18-ox** to polymerise CHO was investigated.

4.4.2 Polymerisation of CHO

Table 4. Polymerisations of CHO using the pre-activated **18** in conjunction with various co-catalysts.

Entry	cat/CHO (eq.)	co-cat (eq.)	[CHO] (M)	Time (min)	Conv.[a] (%)	$M_{n(SEC)}$(Đ)[b] (kg/mol)	$M_{n(calc.)}$[c] (kg/mol)	TOF (h^{-1})
1	1/100	-	1	16 x 60	< 5	-	-	-
2	1/100	$FcBAr^F$ (1)	1	1	100	39.2 (2.4)	9.8	6000
3	1/10000	$FcBAr^F$ (1)	0.25	6	77	68.8 (1.8)	755.7	77000
4	1/10000	$FcBAr^F$ (1) ^{i}PrOH (99)	0.25	7	34	31.7 (2.2)	3.4	29142
5a	1/10000	$FcBAr^F$	0.25	3	23	-	-	46000
5b		+ $CoCp_2$		2	23			0
5c		+ $FcBAr^F$		3	38			30000
6	1/100	AgOTf	1	240	29	3.9 (1.6)	2.8	7

Reaction conditions: DCM, 25 °C; Pre-activation carried out by stirring catalyst and CHO in DCM for 10 minutes prior to oxidation (see ESI); a) Determined by ^{1}H NMR by relative integration of monomer and polymer signals (see ESI); b) Determined by SEC calibrated with polystyrene standards in THF and corrected (see ESI); c) Calculated using the conversion

Complex **18** on its own does not appear to polymerise CHO to a significant extent after 16 hours at room temperature (Table 4, Entry 1). However, generating **18-ox** *via* the addition of $FcBAr^F$ produces an active species that reacts with CHO almost instantaneously and polymerises 100 equivalents in one minute (Table 4, Entry 2). The reaction seems to proceed very quickly, generating a lot of heat (due to the exothermicity of the CHO opening) which has an auto-catalytic effect on the reaction. The result is an uncontrolled polymerisation which is evidenced by the disparity between expected and measured molecular weights (9.8 *vs.* 39.2 kg/mol) as well as a high dispersity (Đ = 2.4).

The polymerisation of CHO by **18-ox** is promising and thus it was sought to achieve control over the highly active reaction. The loading was changed, increasing the ratio of CHO to **18** from 100 to 10,000. Furthermore, to mitigate the exothermicity, the initial concentration of CHO was decreased from 1 M to 0.25 M (Table 4, Entry 3). A conversion of 77 % was achieved in 6 minutes corresponding to a TOF of 77,000 h^{-1}. The polymerisation follows a pseudo-first order rate law yielding a rate constant of 3.90 x 10^{-3} s^{-1} (Figure B94). However, the disparity between calculated and measured molecular weight still exists (755.7 *vs.* 68.8 kg/mol) and the plot of conversion *vs.* M_n shows no clear relationship (Figure 19).

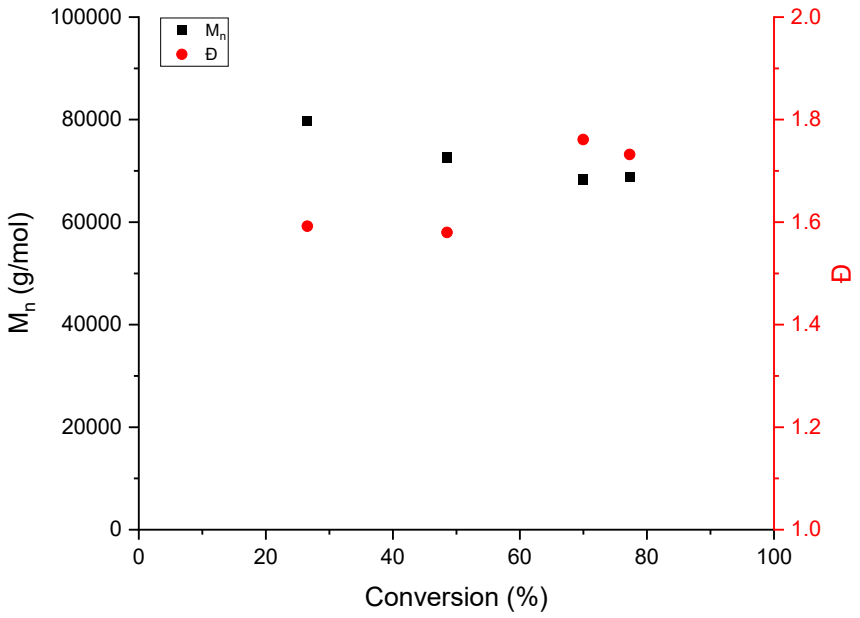


Figure 19. Plot of M_n vs CHO conversion for CHO ROP as initiated by **18-ox**, as per conditions in Table 4, Entry 3. There appears to be no correlation between conversion and molecular weight.

The expected molecular weights are well within the upper bound of the GPC instrument's measuring capabilities (1,000 kg/mol). Furthermore, similar values for the molecular weights were measured using a different instrument in a different solvent (THF). This seems to suggest that there is a process inherent to the polymerisation methodology that results in this large molecular weight disparity (*e.g.* pre-activation, work-up, etc.). Brief experiments indicated $FcBAr^F$ to be active in polymerising CHO. However, at the high loading and low monomer concentration employed in Entry 3, no conversion seemed to occur over several hours.

In the hopes of getting better control of the molar masses, an immortal polymerisation was carried out in which CHO was reacted in the presence of ^{i}PrOH (Table 4, Entry 4). The molecular weight of the polymer was measured to be 10 times higher than what was expected (31.7 *vs.* 3.4 kg/mol) showing no clear improvement.

Putting the lack of molecular weight control aside, it was tested whether the polymerisation of CHO by **18-ox** can be switched off on command (Table 4, Entry 5). A conversion of 23 % was initially achieved after 3 minutes (Table 4, Entry 5a) upon which one equivalent of $CoCp_2$ was added which halted the polymerisation for 2 minutes (Table 4, Entry 5b). Addition of one equivalent of $FcBAr^F$ resumed the polymerisation leading to 38 % conversion after a further 3 minutes (Table 4, Entry 5c). The conversion plot shows a clear halting of the polymerisation

upon reduction of **18-ox** to **18** (Figure 20). Resuming the reaction resulted in an activity similar to the initial rate which indicates that the same active species is regenerated once re-oxidised. Thus, it appears that the polymerisation of CHO can be reliably stopped and resumed using $CoCp_2$ and $FcBAr^F$.

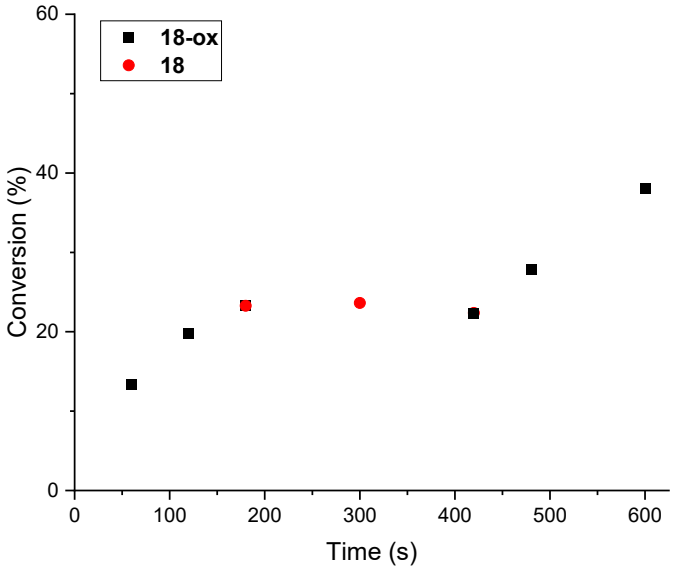


Figure 20. Conversion *vs.* time plot for CHO ROP initiated by **18-ox** as per conditions in Table 4, Entry 5. Upon addition of one equivalent of $CoCp_2$, the polymerisation stops until resumed with the addition of one equivalent of $FcBAr^F$ showing that **18-ox** can be switched back from **18**.

Given the positive results in Section 4.4.1, the use of AgOTf to generate the active **18-ox** was also briefly investigated (Table 4, Entry 6). At a loading of 100 equivalents of CHO, the conversion was found to be 29 % after 4 hours, much lower than what was observed with $FcBAr^F$. In this case however, the measured molecular weight shows good agreement with what was calculated, indicating a controlled polymerisation (3.9 *vs.* 2.8 kg/mol for calculated and measured molecular weights respectively). The strong disparity between the observed activities of AgOTf and $FcBAr^F$ suggest that these oxidising agents produce different species when reacted with **18**. Further studies will be conducted to elucidate the mechanism of oxidation and how different oxidising agents affect the outcome of a reaction.

The fact that the **18-ox** does not polymerise LA but readily reacts with CHO is particularly interesting. A reason for the inactivity towards LA can be the fact that, once oxidised, the aluminium centre becomes too Lewis acidic, which ultimately stops the polymerisation. Dagorne and co-workers have demonstrated that some cationic Al species cannot proceed with ROP as they form a stable species with the monomer after nucleophilic attack.[70] However, **18-**

ox can in turn readily polymerise CHO. It has been shown in Section 4.3.4 that a cationic aluminium complex **20** can initiate CHO ROP in the presence of an alcohol. Upon reduction of **18-ox** to **18**, the neutral species is regenerated which can polymerise LA but not CHO. Thus, the switching between both species can lead to the formation of block co-polymers which was investigated in the next section.

4.4.3 Synthesis of block co-polymers

Having shown that **18** and **18-ox** can polymerise *rac*-LA and CHO respectively and exclusively, the synthesis of block co-polymers was investigated. The main concern for such a reaction is that despite the fact that polymers of LA and CHO can be generated *via* switching of **18** to **18-ox** and *vice-versa*, there is no guarantee that the generated polymers are connected. In simpler terms, homopolymers may be generated instead of the desired block co-polymers. Thus, a polymerisation was carried out at monomer loadings of 100 equivalents for both *rac*-LA and CHO in which **18** was allowed to polymerise all of the *rac*-LA prior to being switched to **18-ox** with $FcBAr^F$ for the complete polymerisation of the CHO.

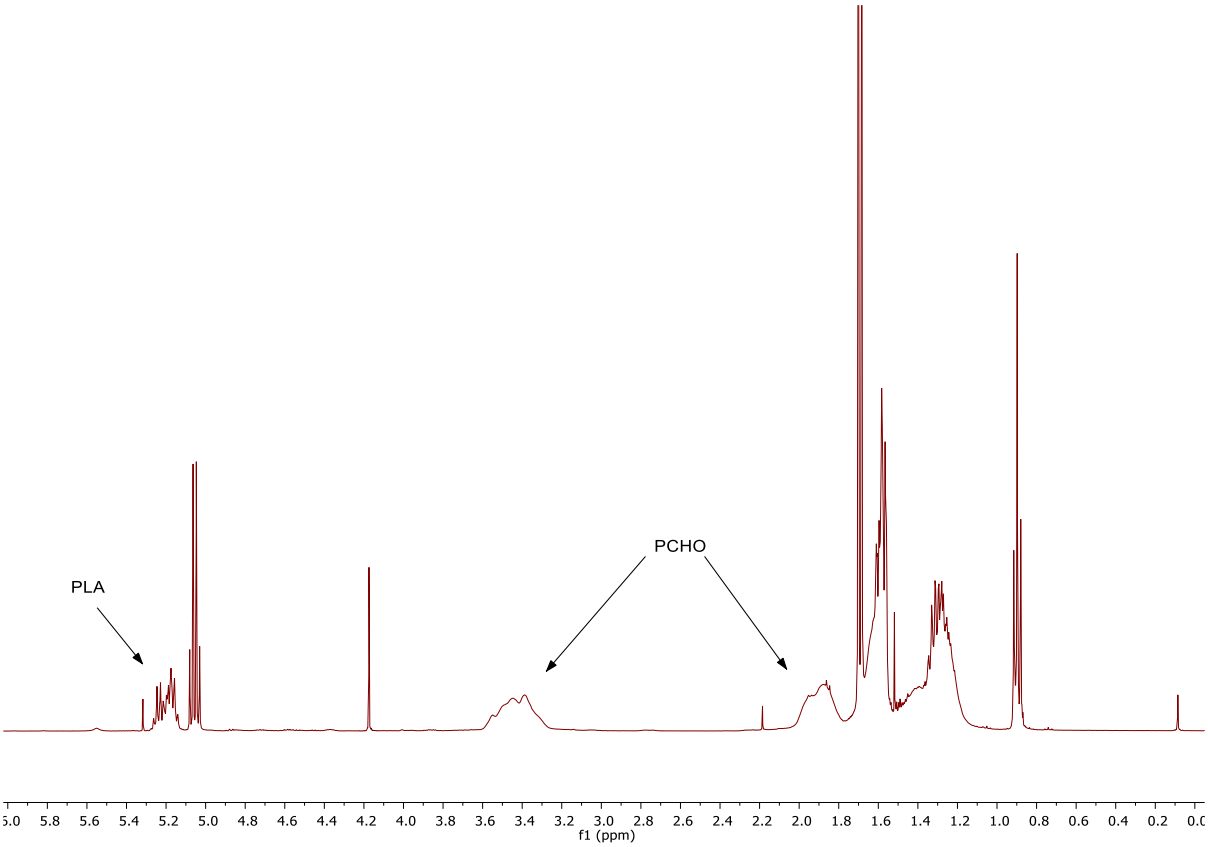


Figure 21. ^1H NMR spectrum ($CDCl_3$, 298 K) of the polymer of a switch polymerisation of 100 equivalents of *rac*-LA and CHO showing that both PLA and PCHO were produced.

The ^{1}H NMR spectrum ($CDCl_3$, 298 K) of the polymer shows the presence of PLA and PCHO (Figure 21), indicating successful synthesis of both polymers in one pot. Furthermore, the DOSY NMR spectrum ($CDCl_3$, 298 K) show that the PLA and PCHO peaks have the same diffusion constant, which indicates that they are situated on the same polymer chain (Figure A48). However, as *rac*-LA and CHO have very similar molecular weights (144.13 *vs.* 98.14 g/mol respectively), there is a possibility that homo-polymers were generated which appear to be on the same chain as each other due to similarities in the diffusion constant. Thus, a polymerisation was carried out in which *rac*-LA and CHO were polymerised at 100 and 1000 equivalents respectively. The DOSY NMR spectrum ($CDCl_3$, 298 K) shows the polymer peaks to have the same diffusion constant, indicating that the polymers generated are in fact block co-polymers (Figure 22).

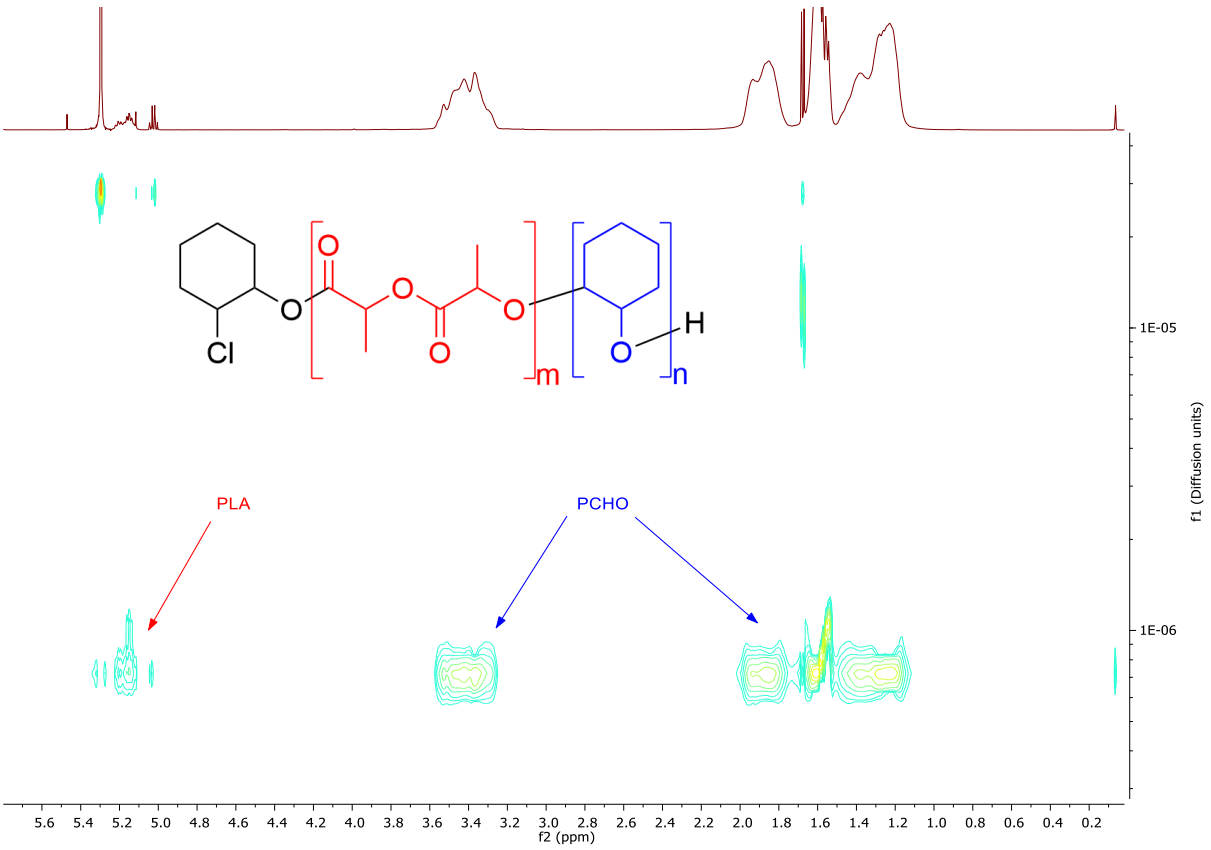


Figure 22. DOSY NMR ($CDCl_3$, 298 K) of a block co-polymer generated from 100 equivalents of *rac*-LA and 1000 equivalents of CHO indicating that the polymer blocks are situated on the same chain.

4.4.4 Polymerisation of other monomers by **18** and **18-ox**

Table 5. Polymerisations of various monomers using the pre-activated **18** as well as the oxidised **18-ox**.

Entry	Complex	Monomer	Time (min)	Conv. (%)[a]	TOF (h^{-1})
1	**18**	*meso*-LA	90	89	59
2	**18-ox**		120	< 5	-
3	**18**	ε-CL	120	< 5	-
4	**18-ox**		120	0	-
5	**18**	β-BL	120	< 5	-
6	**18-ox**		120	< 5	-
7	**18**	ε-DL	120	0	-
8	**18-ox**		120	< 5	-
9	**18**	TMC	120	14	7
10	**18-ox**		120	< 5	-

Reaction conditions: $[M]_0$ = 1 mol.L^{-1}, DCM, 25 °C; Pre-activation carried out by stirring catalyst and 10 eq. of CHO in DCM for 10 minutes prior to the addition of monomer a) Determined by ^{1}H NMR by relative integration of monomer and polymer signals (see ESI)

To gauge the presence of other reaction orthogonalities, the polymerisation of various monomers was conducted with **18** and **18-ox** (Table 5). Complex **18** was able to polymerise *meso*-LA efficiently, converting 89 % of the monomer in 90 minutes (Table 5, Entry 1). The pseudo-first order log-plot shows a strong hyperactivity at the beginning of the polymerisation which stabilises at a k_{app} of 2.61 x 10^{-4} s^{-1} after 60 % conversion (Figure B95). The molecular weight was found to increase linearly with conversion while maintaining a low dispersity (Đ = 1.2) indicating good control (Figure B96). The polymer itself was found to exhibit slight heteroselectivity (P_m = 0.60). As was observed with *rac*-LA, the oxidised form did not polymerise *meso*-LA at a significant rate, signifying that the polymerisation of *meso*-LA can be selectively switched off and on (Table 5, Entry 2).

Polymerisations of ε-CL, β-BL, and ε-DL were also carried out using **18** and **18-ox** (Table 5, Entries 3-8). However, neither one of the complexes were able to polymerise the monomer to a significant extent after 2 hours at room temperature. However, a slightly better activity was achieved when TMC was polymerised using **18** (Table 5, Entry 9), in which 14 % of monomer was converted after 2 hours. However, the oxidised form **18-ox** did not yield a meaningful conversion (Table 5, Entry 10).

The results outlined it Table 5 show that the monomer scope of **18** and **18-ox** is surprisingly small. While **18** was able to polymerise dilactones such as *rac*- and *meso*-LA, neither **18** nor **18-ox** exhibited remarkable activities in the polymerisation of lactones or cyclic carbonates. The decreased reactivity can be traced back to stronger chelates being formed by the opened lactones. These would hinder subsequent approach of a new monomer and slow down polymerisation drastically.

4.5 Conclusion

This chapter detailed the synthesis of complexes bearing the aromatic $^{H}L_4$ ligand. Particularly the chloro complex **18** was found to be of interest as it was able to react readily with CHO to form a variety of new species. Amongst others, a 2-chlorocyclohexano alkoxide species was formed which was demonstrated to initiate the ROP of *rac*-LA. DFT studies highlighted how the CHO opening by the chloride co-ligand underwent a dinuclear mechanism and it was found that the alkoxide species readily underwent deprotonation of the NH moiety to yield the deprotonated complex **16**. Complex **18** was also found to be redox active, showing a quasi-reversible one-electron oxidation close to the oxidation potential of ferrocene. Polymerisation studies showed that pre-activation of **18** *via* stirring with CHO for 10 minutes resulted in a sufficiently active species, with polymerisation rates comparable to other catam complexes **2** and **8c**. Remarkably, the activity of the complex can be intentionally switched 'off' and 'on' *via* oxidation with $FcBAr^F$ (or AgOTf) to **18-ox** and reduction of that species to **18** with $CoCp_2$. Despite the introduction of co-catalysts, the molecular weights were found to be controlled. However, some cases indicated that the switching led to some deactivation of the catalyst as the polymerisation rates did not appear to recover to previous activities upon reduction of **18-ox**. It was found that the oxidised species **18-ox** was able to polymerise CHO at very high activities, needing less than 10 minutes to polymerise 10,000 equivalents. The molecular weights of the polymers did not match with the expected masses which was attributed to possible errors in the methodology.

The fact that one can selectively switch between the polymerisation of two monomers is a discovery that has already been detailed extensively in academic literature. However, the fact that an aluminium metal centre supported by an organic ligand was able to mediate such polymerisation is highly remarkable and underlines the versatility of the catam ligand.

One-pot polymerisations were carried out in which block-polymers of PLA and PCHO were synthesised. DOSY analysis showed that the polymer blocks were situated on the same chain, showing that the polymer was indeed a block-copolymer instead two sets of homo-polymers. The attempted expansion of the monomer scope was fruitless as either **18** or **18-ox** were unable to polymerise lactones (*i.e.* β-BL, ε-CL, ε-DL) or carbonates (TMC) at sufficiently high rates. Only other dilactones (*L*- and *meso*-LA) were found to be active which was traced back to possible chelation events occurring upon opening of the lactones which hindered subsequent approach of a new monomer.

This proof of concept was thus successful, demonstrating just how versatile the catam ligand is. To gain an understanding of the polymerisation mechanism of **18** and **18-ox** with LA and CHO, further studies will have to be conducted.

4.6 References

1. Choudhury, J., *Tetrahedron Lett.* **2018,** *59*, 487-495.
2. Blanco, V.; Leigh, D. A.; Marcos, V., *Chem. Soc. Rev.* **2015,** *44*, 5341-5370.
3. Chen, M.; Deng, S.; Gu, Y.; Lin, J.; MacLeod, M. J.; Johnson, J. A., *J. Am. Chem. Soc.* **2017,** *139*, 2257-2266.
4. Choudhury, J.; Semwal, S., *Synlett* **2018,** *29*, 141-147.
5. Guillaume, S. M.; Kirillov, E.; Sarazin, Y.; Carpentier, J.-F., *Chem. Eur. J.* **2015,** *21*, 7988-8003.
6. Lüning, U., *Angew. Chem. Int. Edit.* **2012,** *51*, 8163-8165.
7. Göstl, R.; Senf, A.; Hecht, S., *Chem. Soc. Rev.* **2014,** *43*, 1982-1996.
8. Lifschitz, A. M.; Rosen, M. S.; McGuirk, C. M.; Mirkin, C. A., *J. Am. Chem. Soc.* **2015,** *137*, 7252-7261.
9. Romanazzi, G.; Degennaro, L.; Mastrorilli, P.; Luisi, R., *ACS Catal.* **2017,** *7*, 4100-4114.
10. Neilson, B. M.; Bielawski, C. W., *ACS Catal.* **2013,** *3*, 1874-1885.
11. Walsh, D. J.; Hyatt, M. G.; Miller, S. A.; Guironnet, D., *ACS Catal.* **2019,** *9*, 11153-11188.
12. Doerr, A. M.; Burroughs, J. M.; Gitter, S. R.; Yang, X.; Boydston, A. J.; Long, B. K., *ACS Catal.* **2020**, 14457-14515.

13. Leibfarth, F. A.; Mattson, K. M.; Fors, B. P.; Collins, H. A.; Hawker, C. J., *Angew. Chem. Int. Edit.* **2013,** *52*, 199-210.
14. Teator, A. J.; Lastovickova, D. N.; Bielawski, C. W., *Chem. Rev.* **2016,** *116*, 1969-1992.
15. Teator, A. J.; Bielawski, C. W., *J. Polym. Sci. Pol. Chem.* **2017,** *55*, 2949-2960.
16. Osaki, M.; Takashima, Y.; Yamaguchi, H.; Harada, A., *Org. Biomol. Chem.* **2009,** *7*, 1646-1651.
17. Neilson, B. M.; Bielawski, C. W., *Chem. Comm.* **2013,** *49*, 5453-5455.
18. Neilson, B. M.; Bielawski, C. W., *J. Am. Chem. Soc.* **2012,** *134*, 12693-12699.
19. Eisenreich, F.; Kathan, M.; Dallmann, A.; Ihrig, S. P.; Schwaar, T.; Schmidt, B. M.; Hecht, S., *Nat. Catal.* **2018,** *1*, 516-522.
20. Dai, Z.; Cui, Y.; Chen, C.; Wu, J., *Chem. Comm.* **2016,** *52*, 8826-8829.
21. Li, M.; Zhang, P.; Chen, C., *Macromolecules* **2019,** *52*, 5646-5651.
22. Kaler, S.; McKeown, P.; Ward, B. D.; Jones, M. D., *Inorg. Chem. Front.* **2020**.
23. Romain, C.; Williams, C. K., *Angew. Chem. Int. Edit.* **2014,** *53*, 1607-1610.
24. Coulembier, O.; Moins, S.; Todd, R.; Dubois, P., *Macromolecules* **2014,** *47*, 486-491.
25. Yoon, H. J.; Kuwabara, J.; Kim, J.-H.; Mirkin, C. A., *Science* **2010,** *330*, 66-69.
26. Allgeier, A. M.; Mirkin, C. A., *Angew. Chem. Int. Edit.* **1998,** *37*, 894-908.
27. Lastovickova, D. N.; Shao, H.; Lu, G.; Liu, P.; Bielawski, C. W., *Chem. Eur. J.* **2017,** *23*, 5994-6000.
28. Gregson, C. K. A.; Gibson, V. C.; Long, N. J.; Marshall, E. L.; Oxford, P. J.; White, A. J. P., *J. Am. Chem. Soc.* **2006,** *128*, 7410-7411.
29. Brown, L. A.; Rhinehart, J. L.; Long, B. K., *ACS Catal.* **2015,** *5*, 6057-6060.
30. Doerr, A. M.; Burroughs, J. M.; Legaux, N. M.; Long, B. K., *Catal. Sci. Technol.* **2020,** *10*, 6501-6510.
31. Wang, X.; Thevenon, A.; Brosmer, J. L.; Yu, I.; Khan, S. I.; Mehrkhodavandi, P.; Diaconescu, P. L., *J. Am. Chem. Soc.* **2014,** *136*, 11264-11267.
32. Quan, S. M.; Wang, X.; Zhang, R.; Diaconescu, P. L., *Macromolecules* **2016,** *49*, 6768-6778.
33. Quan, S. M.; Wei, J.; Diaconescu, P. L., *Organometallics* **2017**.
34. Lowe, M. Y.; Shu, S.; Quan, S. M.; Diaconescu, P. L., *Inorg. Chem. Front.* **2017,** *4*, 1798-1805.

35. Xu, X.; Luo, G.; Hou, Z.; Diaconescu, P. L.; Luo, Y., *Inorg. Chem. Front.* **2020,** *7*, 961-971.
36. Dai, R.; Diaconescu, P. L., *Dalton Trans.* **2019,** *48*, 2996-3002.
37. Wei, J.; Diaconescu, P. L., *Accounts Chem. Res.* **2019,** *52*, 415-424.
38. Broderick, E. M.; Guo, N.; Vogel, C. S.; Xu, C.; Sutter, J.; Miller, J. T.; Meyer, K.; Mehrkhodavandi, P.; Diaconescu, P. L., *J. Am. Chem. Soc.* **2011,** *133*, 9278-9281.
39. Lai, A.; Hern, Z. C.; Diaconescu, P. L., *ChemCatChem* **2019,** *11*, 4210-4218.
40. Hermans, C.; Rong, W.; Spaniol, T. P.; Okuda, J., *Dalton Trans.* **2016,** *45*, 8127-8133.
41. Wei, J.; Riffel, M. N.; Diaconescu, P. L., *Macromolecules* **2017,** *50*, 1847-1861.
42. Magenau, A. J. D.; Strandwitz, N. C.; Gennaro, A.; Matyjaszewski, K., *Science* **2011,** *332*, 81-84.
43. Broderick, E. M.; Guo, N.; Wu, T.; Vogel, C. S.; Xu, C.; Sutter, J.; Miller, J. T.; Meyer, K.; Cantat, T.; Diaconescu, P. L., *Chem. Comm.* **2011,** *47*, 9897-9899.
44. Sauer, A.; Buffet, J.-C.; Spaniol, T. P.; Nagae, H.; Mashima, K.; Okuda, J., *ChemCatChem* **2013,** *5*, 1088-1091.
45. Biernesser, A. B.; Li, B.; Byers, J. A., *J. Am. Chem. Soc.* **2013,** *135*, 16553-16560.
46. Biernesser, A. B.; Delle Chiaie, K. R.; Curley, J. B.; Byers, J. A., *Angew. Chem. Int. Edit.* **2016,** *55*, 5251-5254.
47. Fang, Y.-Y.; Gong, W.-J.; Shang, X.-J.; Li, H.-X.; Gao, J.; Lang, J.-P., *Dalton Trans.* **2014,** *43*, 8282-8289.
48. Broere, D. L. J.; Plessius, R.; van der Vlugt, J. I., *Chem. Soc. Rev.* **2015,** *44*, 6886-6915.
49. Chirik, P. J.; Wieghardt, K., *Science* **2010,** *327*, 794-5.
50. Chaudhuri, P.; Hess, M.; Müller, J.; Hildenbrand, K.; Bill, E.; Weyhermüller, T.; Wieghardt, K., *J. Am. Chem. Soc.* **1999,** *121*, 9599-9610.
51. Blackmore, K. J.; Lal, N.; Ziller, J. W.; Heyduk, A. F., *J. Am. Chem. Soc.* **2008,** *130*, 2728-2729.
52. Blackmore, K. J.; Lal, N.; Ziller, J. W.; Heyduk, A. F., *Eur. J. Inorg. Chem.* **2009,** *2009*, 735-743.
53. Lesh, F. D.; Lord, R. L.; Heeg, M. J.; Schlegel, H. B.; Verani, C. N., *Eur. J. Inorg. Chem.* **2012,** *2012*, 463-466.

54. Despagnet-Ayoub, E.; Henling, L. M.; Labinger, J. A.; Bercaw, J. E., *Dalton Trans.* **2013,** *42*, 15544-15547.
55. Cherkasov, V. K.; Piskunov, A. V.; Trofimova, O. Y.; Smolyaninov, I. V.; Fukin, G. K., *Dokl. Chem.* **2013,** *448*, 61-65.
56. Hänninen, M. M.; Paturi, P.; Tuononen, H. M.; Sillanpää, R.; Lehtonen, A., *Inorg. Chem.* **2013,** *52*, 5714-5721.
57. Baltrun, M.; Watt, F. A.; Schoch, R.; Hohloch, S., *Organometallics* **2019,** *38*, 3719-3729.
58. Harris, C. F.; Bayless, M. B.; van Leest, N. P.; Bruch, Q. J.; Livesay, B. N.; Bacsa, J.; Hardcastle, K. I.; Shores, M. P.; de Bruin, B.; Soper, J. D., *Inorg. Chem.* **2017,** *56*, 12421-12435.
59. Hossain, M. K.; Haukka, M.; Hänninen, M. M.; Lisensky, G. C.; Paturi, P.; Nordlander, E.; Lehtonen, A., *Inorg. Chem. Commun.* **2018,** *93*, 149-152.
60. Zelikoff, A. L.; Kopilov, J.; Goldberg, I.; Coates, G. W.; Kol, M., *Chem. Comm.* **2009**, 6804-6806.
61. Addison, A. W.; Rao, T. N.; Reedijk, J.; van Rijn, J.; Verschoor, G. C., *J. Chem. Soc., Dalton Trans.* **1984**, 1349-1356.
62. Elgrishi, N.; Rountree, K. J.; McCarthy, B. D.; Rountree, E. S.; Eisenhart, T. T.; Dempsey, J. L., *J. Chem. Educ.* **2018,** *95*, 197-206.
63. Bender, M. L., *Chem. Rev.* **1960,** *60*, 53-113.
64. Robert, C.; Schmid, T. E.; Richard, V.; Haquette, P.; Raman, S. K.; Rager, M.-N.; Gauvin, R. M.; Morin, Y.; Trivelli, X.; Guérineau, V.; del Rosal, I.; Maron, L.; Thomas, C. M., *J. Am. Chem. Soc.* **2017,** *139*, 6217-6225.
65. Kassai, C.; Juvancz, Z.; Bálint, J.; Fogassy, E.; Kozma, D., *Tetrahedron* **2000,** *56*, 8355-8359.
66. Rae, A.; Gaston, A. J.; Greindl, Z.; Garden, J. A., *Eur. Polym. J.* **2020,** *138*, 109917.
67. Zeng, J.; Wang, R.; Zhang, S.; Fang, J.; Liu, S.; Sun, G.; Xu, B.; Xiao, Y.; Fu, D.; Zhang, W.; Hu, Y.; Wan, Q., *J. Am. Chem. Soc.* **2019,** *141*, 8509-8515.
68. Hayashi, Y.; Rohde, J. J.; Corey, E. J., *J. Am. Chem. Soc.* **1996,** *118*, 5502-5503.
69. Shyshov, O.; Brachvogel, R.-C.; Bachmann, T.; Srikantharajah, R.; Segets, D.; Hampel, F.; Puchta, R.; von Delius, M., *Angew. Chem. Int. Edit.* **2017,** *56*, 776-781.
70. Dagorne, S.; Le Bideau, F.; Welter, R.; Bellemin-Laponnaz, S.; Maisse-François, A., *Chem. Eur. J.* **2007,** *13*, 3202-3217.

Chapter 5

Conclusions and Future Work

This thesis described the synthesis and characterization of a variety of aluminium complexes bearing catam ligands. These were then employed in cyclic esters ROP, with a particular focus on *rac*-LA monomer. The main modulation carried out across the ligands was through the substitution of the diamine linker between the *o*-aminophenolate moieties. In certain cases, deuteration and *N*-methylation of the NH moieties was carried out to gain insight into the polymerisation mechanism of certain catalysts. The pro-ligands and complexes were fully characterised using a range of techniques, including NMR spectroscopy (^{1}H and ^{13}C), IR spectroscopy, high-resolution mass spectrometry, elemental analysis, and XRD. For each ligand family, the most promising candidates were tested in cyclic esters ROP, including *rac*-LA, *L*-LA, *meso*-LA, ε-CL, ε-DL, β-BL, TMC, and ω-PDL. The catalysts' performances were evaluated considering activity, polymer molar mass control (*i.e.* polymerisation "livingness") and polymer tacticity control. To gain a mechanistic insight on the observed trends, further studies predominantly including DFT calculations, were carried out. Additionally, the order in catalyst was also measured to support the proposed mechanisms.

All aluminium catam complexes were found to be active in *rac*-LA ROP, often proceeding with high activities at room temperature. This is remarkable as aluminium catalysts are usually slow, requiring high temperatures and high loadings to adequately proceed with ROP.

The first complexes in the catam series that exhibited high activities at room temperature were 2,2-dimethyl-1,3-propanediamine and 1,2-ethanediamine tethered catam alkoxide complexes [^{H}**L**$_1$Al(O^{i}Pr) (**2**) and ^{H}**L**$_2$Al(OBn) (**8c**) respectively]. These were investigated in detail in Chapter 2. Complex **2** was found to be highly hetereoselective (P_r = 0.90), making it the first aluminium complex to afford heterotactic PLA at room-temperature. DFT studies highlighted the formation of H-bonds between the NH moieties and the carbonyl of the LA monomer near the catalytic pocket. The deuterated analogue of **2** bearing ND moieties (complex **4**) was employed in the same polymerisation conditions and found to be significantly slower ($k_H/k_D \approx$ 1.9), confirming that the NH moieties are important to the activity of the catalyst. This KIE value is conducive to an equilibrium or binding isotope effect. Complex **8c** exhibited similar activities to **2** but afforded slightly isotactic PLA (P_m = 0.60). Whilst DFT studies showed similar NCIs between the substrate and the NH moieties, the KIE value was negligible (k_H/k_D ≈ 1.06). The NH moieties thus do not appear to be as impactful as for complex **2**. DFT calculations showed that the LA monomer can also approach equatorially without having to interact with the NH moieties, which can be a reason for the lack of a KIE. Synthesis and employment of the *N*-methylated analogues of **2** and **8c** (**5** and **11** respectively) highlight the

importance of the NH moieties. Neither **5** or **11** was active at room temperature and required heat to proceed with the polymerisation.

Complexes **2** and **8c** were found to be stable at high temperatures and in the presence of CTAs. Both were able to carry out immortal polymerisation at temperatures up to 90 °C. Furthermore, the complexes were able to polymerise *rac*-LA in the melt at 130 °C.

The complexes were found to be active in the polymerisation of other cyclic esters at room temperature. The polymerisation of *meso*-LA proceeded at unprecedented rates (for aluminium complexes), but the polymers exhibited no significant stereoregularity. The polymerisation of ε-CL was particularly sluggish which was attributed to the formation of a primary alkoxide upon opening of the monomer, which allowed for aggregation of the active species to a less active form. Polymerisation of ε-DL was significantly faster as its opening resulted in the formation of a bulkier secondary alkoxide. The propensity of the complexes to aggregate was eventually found in many of the other catam complexes studied in this thesis (Chapter 3). Unprecedented activities were also observed in the polymerisation of β-BL, making **2** and **8c** the first aluminium complexes able to afford P3HB at room temperature. The ROP of TMC proceeded much slower for **8c**, further highlighting the complex's tendency to aggregate. For entropy-driven polymerisations of ω-PDL, the catalysts required elevated temperatures (100 °C) to proceed with ROP.

Chapter 3 investigated the synthesis of chiral (and enantiopure) Al catam catalysts. Using the chiral (*R,R*)-, (*S,S*)-, *rac*-, and *cis*-1,2-diaminocyclohexane, the pro-ligands (*R,R*)-, (*S,S*)-, *rac*-, and *cis*-H_2**^{H}L$_3$** were synthesised. During the synthesis of the alkoxide complexes, it was found that the nature of the alkoxide co-ligand is important in determining catalyst nuclearity. Attempted synthesis of the benzyloxide complexes of (*R,R*)-, (*S,S*)-, and *rac*-H_2**^{H}L$_3$** resulted in the formation of unextractable mixtures (*R,R*)-, (*S,S*)-, *rac*-**mix14** consisting of mononuclear and dinuclear diastereomers. It was found that heating *rac*-**mix14** resulted in the formation of a single well-defined dimer *rac*-**14** which consisted of a (*R,R*)- and a (*S,S*)-**^{H}L$_3$**Al(OBn) unit. DFT studies indicated that a heterochiral dimer is more stable than a homochiral one. The aggregation tendencies were overcome through the employment of a tertiary alkoxide co-ligand (-O^{t}Bu) to yield (*R,R*)-, (*S,S*)-, *rac*-, and *cis*-**15** which yielded a single well-defined species in each case and demonstrated successful chirality transfer. Employment of the catalysts in the ROP of an achiral monomer (ε-CL) showed that the enantiopure species (*R,R*)- and (*S,S*)-**15** were much faster than *rac*-**15**, which was traced back to the racemic complex having a

propensity to form heterochiral dimers which lower overall activity. This was substantiated using kinetic studies and shows how an enantiopure catalyst can be employed to boost activities in the ROP of an achiral monomer. Interestingly, the polymerisation of ε-CL by *cis*-**15** was found to proceed particularly quickly, resulting in a conversion of 67 % in 10 minutes at room-temperature.

Unprecedented activities were achieved in the ROP of *L*-LA when (*S,S*)-**15** was employed, achieving a conversion of 83 % after 6 minutes at room-temperature. Conversely, (*R,R*)-**15** required 3 hours to polymerise 64 % which shows that the chiral catalysts obey the fundamental law of kinetic resolution and initially hinted at the occurrence of an ESC mechanism. Employing scalemic mixtures of the catalyst shows that the rate constant varies in a non-linear fashion which indicates the presence of an NLKE. In *rac*-LA ROP, the kinetic resolution appeared to subside as the polymers produced by either (*R,R*)-, (*S,S*)-, and *rac*-**15** were atactic. The use of scalemic mixtures again hinted at an NLKE taking place. DFT studies showed that (*S,S*)-**15** prefers the insertion of *L*-LA, and NCIs between the NH moiety and monomer were also present which demonstrates that the findings in Chapter 2 can be applied across different catam ligands.

The *trans*-**15** complexes exhibited unprecedented activities for other monomers, including β-BL, *meso*-LA, and ε-DL. The use of chiral complexes can thus be beneficial for a range of monomers.

The versatility of the catam ligand has been demonstrated further in Chapter 4, where an *o*-phenylenediamine tethered catam pro-ligand (H_2**^{H}L$_4$**) was employed. Due to difficulties in synthesising an alkoxide complex, the chloro complex **18** was the focus of that project. The complex was found to be redox active, undergoing a reversible first oxidation and an irreversible second oxidation. Complex **18** reacts with CHO to form a variety of species, one of which being the 2-chlorocyclohexano derivative **19**, which can carry out ROP of *rac*-LA. DFT studies highlight that opening of the CHO occurs *via* a backside S_N2 reaction. The alkoxide can readily deprotonate the NH moiety to form the deprotonated complex **16**, which can aggregate with **19** as seen on the crystal structure. The formation of an alkoxide *via* addition of CHO was then exploited in the ROP of *rac*-LA. The activated complex **18** afforded heterotactic PLA with good activities at room-temperature. Treatment of the active species with one equivalent of either $FcBAr^F$ or AgOTf resulted in oxidation of the species into the inactive **18-ox**. The polymerisation stopped but was able to be resumed *via* addition of one

equivalent of $CoCp_2$, after which the reaction resumed with expected increases in the molecular weight of the polymer. It was thought that the oxidation of **18** to **18-ox** results in an increased Lewis acidity of the metal centre, which prefers the formation of a stable chelate over the propagation of the polymerisation.

The polymerisation of CHO by **18** was inactive towards CHO but proceeded with high activities upon oxidation of **18** to **18-ox**. The inactivity was restored through the reduction of **18-ox** to **18** *via* addition of one equivalent of $CoCp_2$. The polymers generated did not fit the expected weights which indicates an uncontrolled system or an error in methodology. The activity of **18-ox** towards CHO ROP can be traced back to the increased Lewis acidity of the metal centre, which activates the monomer sufficiently for attack by the alkoxide group.

It was found that this orthogonality can be exploited to form block co-polymers in "one pot" where one can selectively switch between the polymerisation of one monomer over the other (*rac*-LA *vs.* CHO). DOSY analysis indicated that both PLA and PCHO blocks were on the same chain and excludes the formation of homo-polymers.

The viability and versatility of aluminium catam complexes in cyclic ester ROP was thus demonstrated in this doctoral thesis. Highly active aluminium-based catalysts were synthesised, with one of them being the most active aluminium catalyst for *L*-LA ROP to date. The NCIs between the substrate and complex was ubiquitous across all catam complexes, showing that intermolecular bonding can be exploited effectively for the purposes of cyclic ester ROP. Furthermore, the inclusion of stereocentres in the ligand scaffold can lead to increased activities in the ROP of achiral (ε-CL) and chiral (LA) monomers by influencing catalyst aggregation. Additionally, using a redox active catam-analogue, a complex was synthesised that was reactive towards oxidising and reducing agents despite the redox inactive nature of aluminium. This was effectively demonstrated by selectively switching between the polymerisation of one monomer over the other.

The results herein only scratch the surface of the potential within the catam ligand class. As the tuneability of the ligand allows for further modifications, it is only a matter of time until more applications are discovered.

Increasing activity and selectivity

Given that the use of catam ligands $^{H}L_1$, $^{H}L_2$, $^{H}L_3$, and $^{H}L_4$ has led to improved activities in the aluminium-mediated ROP of cyclic esters, obvious modulations would include the exploration of the different metal centres. Kol and co-workers have already shown that using $^{H}L_4$ on titanium resulted in a highly active complex for the polymerisation of *rac*-LA in melt conditions, yielding heterotactically enriched polymers.[1]

Building off the work in this thesis, one may consider other metals in Group 13. Using indium as a metal centre would be of particular interest, as it is considerably less studied when compared to aluminium. The groups of Mehrkhodavandi, Okuda, Arnold, and Carpentier have already indicated that indium complexes appear to be more reactive while still carrying the potential of exhibiting high stereoselectivity.[2-4] This was attributed to the higher Lewis acidity and the larger atomic radius of the metal centre. This, however, is a double-edged sword as the same properties are what drives aggregation, which often results in dinuclear indium complexes being formed.[5, 6] Whilst multiple highly active and selective dinuclear indium complexes were reported,[7] aggregation can result in less clarity regarding a catalyst's speciation and reactivity, which may contribute to a decrease in polymerisation control. Despite these potential drawbacks, investigating indium catam complexes may yield interesting results regarding activity and stereoselectivity (Figure 1).

Group 3 metals [*e.g.* Y(III)] and lanthanides [*e.g.* Ce(III)] may also form beneficial catalysts upon complexation with the catam ligands. These metals are particularly reactive at room temperature which may be exacerbated when the NCI-forming properties of the catam ligand are brought into play.[8, 9]

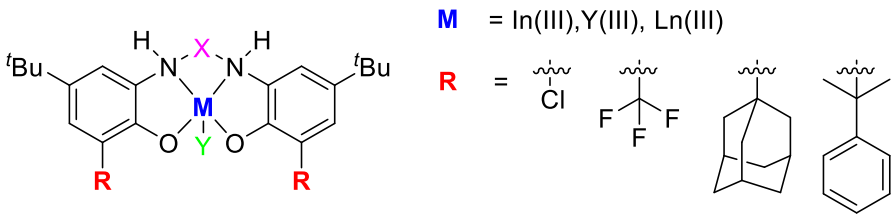


Figure 1. Modification of the metal centre and aromatic substituents

The modulation of the aromatic backbone has not received much attention in this thesis. Although not explored in this work, it is a simple way of changing the electronic and steric properties of a ligand and is amongst the most common modulation carried out on salen

ligands.[10] In Section 3.2.2, it was found that the replacement of the ^{t}Bu groups in the catam backbone led to a drastic worsening in the ligand's solubility properties. Due to the polymerisation reactions being carried out at room temperature, the resulting complexes would scarcely go into solution. However, keeping one ^{t}Bu group on the 3-position of the aromatic backbone was found the maintain the high solubility of the ligand in organic solvents. The ^{t}Bu group on the 5-position could therefore be replaced. Methyl groups could be used to decrease the steric bulk around the metal centre while cumyl and adamantyl groups could increase it. Especially the latter two would create a steric environment that may increase stereoselectivity. Furthermore, the tendency of some catam complexes to aggregate could be reduced.

A change in electronic environment can be induced by replacement of the ^{t}Bu group with electron-withdrawing groups. It has been previously shown by Gibson and co-workers that a chloride group decreases the electron density around the metal centre and thus increases activity.[10] Furthermore, Carpentier and co-workers have found C-H···Cl interactions in between the aromatic chloride groups and the methylene group of the growing polymer chain (see Section 2.1.4.2).[11]

Expansion of the chiral catalyst scope

The chiral catalysts synthesised in chapter 3 showed strong improvements in the polymerisation of enantiopure monomers (*i.e. D*- and *L*-LA). However, the polymerisation of *rac*-LA resulted in atactic polymers which was attributed to polymeryl exchange as well as competition between ESC and CEC mechanisms. Although not ideal, chiral catam catalysts should be explored further by using different chiral linkers.

Spassky found that salen ligands containing a chiral BINAP linker were able to polymerise *rac*-LA to yield highly isotactic PLA.[12] An ESC mechanism was found to be dominant. Employing this linker could result in similar behaviour in catam complexes (Figure 2). The diphenyl ethylene diamine linker employed by Maudoux *et al*. also resulted in isotactic PLA but was mediated *via* a CEC mechanism.[13]

To address the dimerisation behaviour, adamantyl and cumyl substituents on the aromatic backbone could lessen the complex's tendency to aggregate and thus result in only one catalytic species being present in solution.

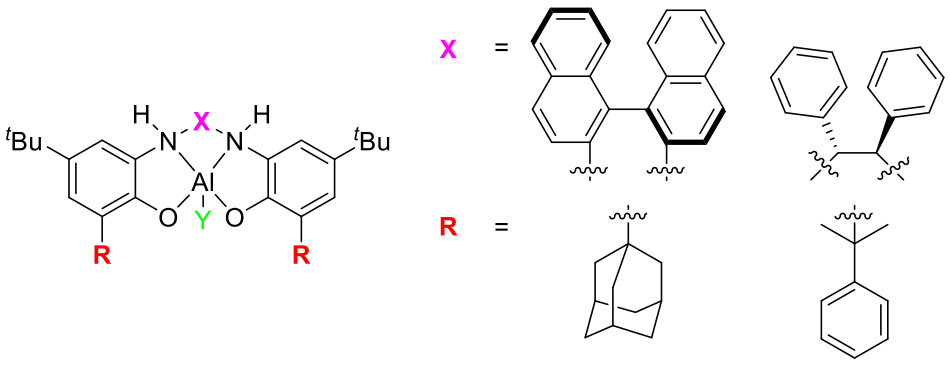


Figure 2. Modification of the chiral linker and aromatic substituents for improved stereoselectivity

Redox active aluminium complexes

The testing of a redox active aluminium complex bearing the $^{H}L_3$ ligand yielded promising results which will be expanded on in the future. To form a clearer picture of the behaviour of these complexes, the aromatic linker may be changed to different substituents (Figure 3). These either change the steric environment near the metal centre, or increase the distance between the NH moieties, resulting in a looser N_2Al chelate.

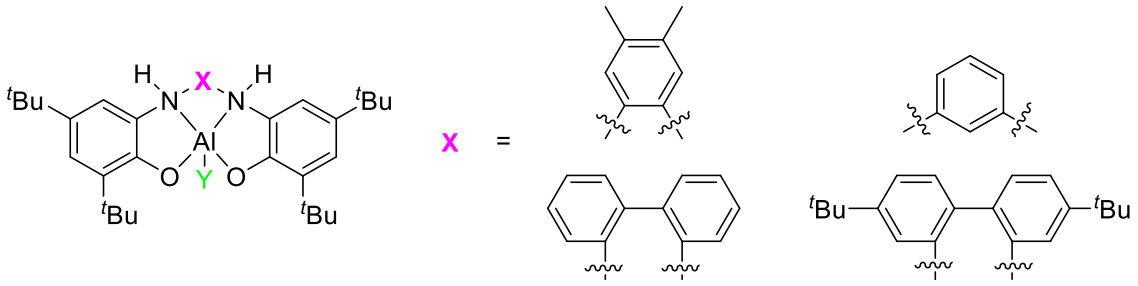


Figure 3. Modification of the aromatic substituents for improved redox properties

The Diaconescu group focussed on implementing redox activity in salen complexes *via* the use of a ferrocenyl linker. Interestingly the Brown group synthesised a catam pro-ligand with a 1,1'-ferrocene-bis(*para*-phenylene) tether.[14] Although electrochemical measurements found the interactions between the ferrocenyl and *ortho*-aminophenol units to be minimal, synthesising its aluminium complex may lead to some interesting behaviour when used with oxidising and reducing agents.

1. Zelikoff, A. L.; Kopilov, J.; Goldberg, I.; Coates, G. W.; Kol, M., *Chem. Comm.* **2009**, 6804-6806.
2. Aluthge, D. C.; Patrick, B. O.; Mehrkhodavandi, P., *Chem. Comm.* **2013,** *49*, 4295-4297.
3. Buffet, J.-C.; Okuda, J.; Arnold, P. L., *Inorg. Chem.* **2010,** *49*, 419-426.
4. Normand, M.; Kirillov, E.; Roisnel, T.; Carpentier, J.-F., *Organometallics* **2012,** *31*, 1448-1457.
5. Aluthge, D. C.; Ahn, J. M.; Mehrkhodavandi, P., *Chem. Sci.* **2015,** *6*, 5284-5292.
6. Aluthge, D. C.; Yan, E. X.; Ahn, J. M.; Mehrkhodavandi, P., *Inorg. Chem.* **2014,** *53*, 6828-6836.
7. Kremer, A. B.; Mehrkhodavandi, P., *Coord. Chem. Rev.* **2019,** *380*, 35-57.
8. Kerr, R. W. F.; Ewing, P. M. D. A.; Raman, S. K.; Smith, A. D.; Williams, C. K.; Arnold, P. L., *ACS Catal.* **2021,** *11*, 1563-1569.
9. Amgoune, A.; Thomas, C. M.; Carpentier, J. F., *Macromol. Rapid. Comm.* **2007,** *28*, 693-697.
10. Hormnirun, P.; Marshall, E. L.; Gibson, V. C.; Pugh, R. I.; White, A. J. P., *Proc. Natl. Acad. Sci. U. S. A.* **2006,** *103*, 15343-15348.
11. Ligny, R.; Hänninen, M. M.; Guillaume, S. M.; Carpentier, J.-F., *Chem. Comm.* **2018,** *54*, 8024-8031.
12. Spassky, N.; Wisniewski, M.; Pluta, C.; Borgne, A. L., *Macromol. Chem. Phys.* **1996,** *197*, 2627-2637.
13. Maudoux, N.; Roisnel, T.; Dorcet, V.; Carpentier, J. F.; Sarazin, Y., *Chemistry A European Journal* **2014,** *20*, 6131-6147.
14. Swanson, D. D.; Conner, K. M.; Brown, S. N., *Dalton Trans.* **2017,** *46*, 9049-9057.

Chapter 6

Experimental

6.1 General Considerations

Unless stated otherwise, all manipulations for complex synthesis and polymerisation reactions were performed under nitrogen using Schlenk techniques or using an MBraun glovebox. THF was dried over sodium / benzophenone and stored under nitrogen over activated molecular sieve (3 Å) in a glove box. Pentane, DCM, diethyl ether, and toluene were obtained from a solvent purification system and stored under nitrogen over activated molecular sieve (3 Å) in a glove box.

NMR spectra were recorded on Bruker AVIII-400 and AVIII-500 spectrometers. All chemicals shifts were determined using residual signals of the deuterated solvents and were calibrated *vs.* SiMe4.

Elemental analysis was carried out by Stephen Boyer at London Metropolitan University.

IR spectra were recorded using a using a Perkin and Elmer Spectrum 100 FT-IR spectrometer.

MALDI-ToF spectrometry measurements were performed on Waters/Micromass MALDI micro MX spectrometer using positive ionisation. Polymers were dissolved in THF at a concentration of 10 mg/mL. Dithranol was used as matrix (10 mg/mL in THF).Potassium trifluoroacetate (KTFA) was used as cationizing agent (10 mg/mL in THF). The solutions of polymer, matrix and salt were mixed in a ratio of 1/1/1 (v/v/v), respectively. The mixed solution was spotted on a stainless steel MALDI plate and left to dry for a couple of hours. The spectra were recorded using reflectron mode.

Size Exclusion Chromatography measurements were performed on a Waters 1515 equipped with a set of Styragel® HR 5E columns (one 4.6 × 30mm guard column and two 4.6 × 300mm columns) using GPC grade THF (Fischer) as eluent at 1mL/min and 40 °C. RID detection was used using an external Waters 2414 RID at 40 °C. Polystyrene standards (Agilent) were used for calibration.
If possible, the following correction factors were applied:[1]
PLA: 0.58
PCL: 0.56
P3HB: 0.54

Circular Dichroism (CD) spectra were recorded on a JASCO J-810 CD spectrophotometer. A 1 cm quartz cuvette was used and a temperature of 25 °C was maintained using a Peltier module. Spectra were recorded from 200 to 800 nm with a scanning speed of 100 nm min^{-1} and a band width of 2.0 nm. A blank run of DCM was used as baseline correction.
Solutions of the ligands were prepared in DCM to a concentration of 0.33 mM and the CD spectra recorded.

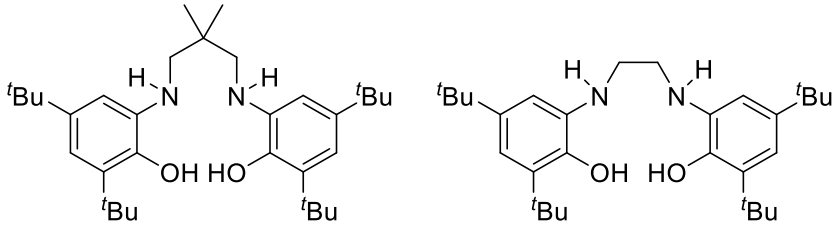
Chiral HPLC analysis were carried out on an Agilent 1260 Infinity Series system using a Daicel Chiracel IA 3-column. A 1:99 *i*-PrOH:*n*-hexane mixture was used as an eluent at a flow rate of 1 $mL.min^{-1}$. For the UV detection, a wavelength of 230 nm was used. Samples were prepared in neat *i*-PrOH at a concentration of 1 $mg.ml^{-1}$ and passed through a 0.2 μm PTFE syringe filter prior to injection.
The order in catalyst for various polymerizations was determined through visual kinetic analysis. Orders were considered in increments of 0.1. The order yielding the best overlap of traces was deemed the correct catalyst order.

Cyclic Voltammetry was conducted using a 3-electrode setup where a glassy carbon rod was employed as a working electrode and two Pt wires were used as a reference and counter electrode. The electrodes were suspended in 5 mL of MeCN containing $^{n}Bu_4NPF_6$ (0.1 M) and **18** (5 mg, 8.7 µmol). To minimise decomposition of **18** in air, the sample was weighed out inside a glovebox and placed in the electrochemical cell under nitrogen. The CV was measured between -1.1 and +1.1 V at a scan rate of 50 mV/s.

6.2 Synthesis of Pro-Ligands

6.2.1 Chapter 2

H_2**^{H}L$_1$** and H_2**^{H}L$_2$**



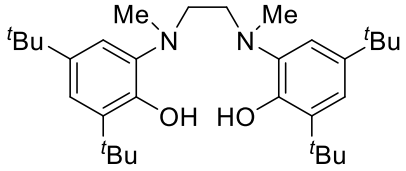
$H_2{}^{H}L_1$

$H_2{}^{H}L_2$

Pro-ligands $H_2{}^{H}L_1$ and $H_2{}^{H}L_2$ were synthesised according to the literature procedure using 3,5-di-*tert*-butylcatechol and 2,2-dimethyl-1,3-propanediamine or 1,2-ethanediamine respectively.[2]

$H_2{}^{H}L_1$ (55 % yield). ^{1}H NMR (400 MHz, $CDCl_3$) δ_{1H} (ppm): 6.97 (s, 2H, Ar-H), 6.84 (s, 2H, Ar-H), 2.98 (s, 4H, CH_2), 1.40 (s, 18H, ^{t}Bu), 1.30 (s, 18H, ^{t}Bu), 1.14 (s, 6H, CH_3)
$H_2{}^{H}L_2$ (35 % yield) ^{1}H NMR (400 MHz, $CDCl_3$) δ_{1H} (ppm): 7.01 (s, 2H, Ar-H), 6.88 (s, 2H, Ar-H), 3.24 (s, 4H, CH_2), 1.41 (s, 18H, ^{t}Bu), 1.29 (s, 18H, ^{t}Bu)

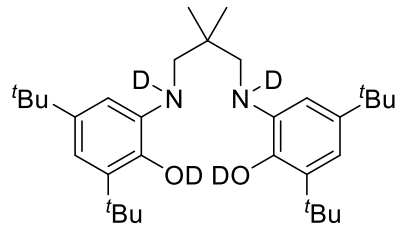
$H_2{}^{Me}L_2$



$H_2{}^{Me}L_2$

$H_2{}^{Me}L_2$ was synthesised according to an established literature procedure.[3]
(68 % yield) ^{1}H NMR (400 MHz, $CDCl_3$) δ_{1H} (ppm): 8.42 (b, 2H, OH), 7.13 (d, 2H, Ar-H), 7.07 (d, 2H, Ar-H), 2.87 (s, 4H, CH_2), 2.73 (s, 6H, N-CH_3), 1.41 (s, 18H, ^{t}Bu), 1.29 (s, 18H, ^{t}Bu)

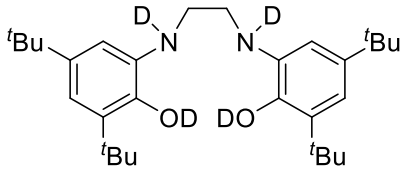
$D_2{}^{D}L_1$



$D_2{}^{D}L_1$

Under nitrogen, $H_2^{H}\mathbf{L_1}$ (200 mg, 0.39 mmol) was dissolved in 5 mL of CD_3Cl then 5 mL of CD_3OD was added leading to formation of a white precipitate. The mixture was heated to dissolve the ligand and allowed to reflux under nitrogen overnight. After cooling to room temperature, a white precipitate was observed. Subsequent filtration and drying under vacuum afforded pure $D_2^{D}\mathbf{L_1}$ (114 mg, 56 % yield) as a white powder. ^{1}H NMR (400 MHz, $CDCl_3$) δ_{1H} (ppm): 6.53 (s, 4H, Ar-H), 2.97 (s, 4H, N-CH_2), 1.33 (s, 18H, ^{t}Bu), 1.20 (s, 18H, ^{t}Bu), 1.09 (s, 6H, CH_3), no signals for OH or NH were observed.

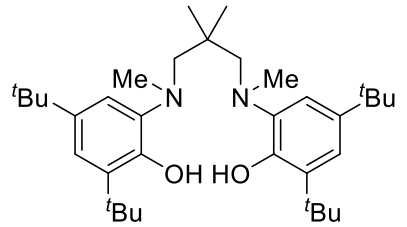
$D_2^{D}\mathbf{L_2}$



$D_2^{D}\mathbf{L_2}$

Under nitrogen, $H_2^{H}\mathbf{L_2}$ (0.5 g, 2.1 mmol) was dissolved in $CDCl_3$ (5cm^3). CD_3OD (5 cm^3) was added and the mixture heated at 50 °C under nitrogen atmosphere overnight. The volatiles were removed *in vacuo* to yield a white powder quantitatively.
^{1}H NMR (400 MHz, C_6D_6) δ_{1H} (ppm): 7.11 (d, 2H, Ar-H), 6.55 (s, 2H, Ar-H), 2.02 (s, 4H, CH_2), 1.62 (s, 18H, ^{t}Bu), 1.34 (s, 18H, ^{t}Bu)

$H_2^{Me}\mathbf{L_1}$

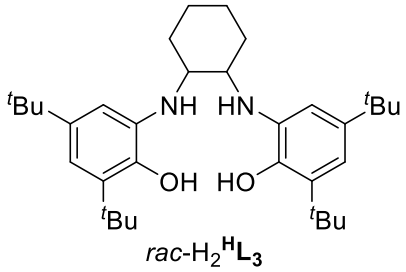


$H_2^{Me}\mathbf{L_1}$

Using a modified procedure from literature.[3] To a cooled solution (- 78 °C) of $H_2^{H}\mathbf{L_1}$ (1.5 g, 2.94 mmol) in THF (30 mL) was slowly added 2.6 mL (6.46 mmol) of a 2.5M ^{n}BuLi solution in hexane leading to a yellow solution. The solution was stirred for 15 minutes at – 78 °C and allowed to react for 2 hours at room temperature. MeI (0.4 mL, 6.46 mmol) was then slowly added and the solution was stirred overnight at room temperature. The solution was finally heated at reflux for 6 hours before evaporation of the volatiles. 25mL of water was added, and the product was extracted with 50 mL (2 × 25 ml) of DCM. The organic phases weres collected and dried over Na_2SO_4. Evaporation of the volatiles affords a yellow oil. ^{1}H NMR spectroscopy analysis shows the presence of the expected di-methyl compound $H_2^{Me}\mathbf{L_1}$ along with starting material and presumably some mono methylated compound. Unreacted starting materials was removed by recrystallisation from methanol. Further purifications by flash chromatography using neutral alumina (0.5:99.5, Ethyl acetate: hexane) afforded pure $H_2^{Me}\mathbf{L_1}$ (first fraction, 452 mg, 28.6% yield) as deduced from the ^{1}H NMR spectrum (total yield: 931 mg, 58.7% yield). F1 was used without further purification. ^{1}H NMR (400 MHz, $CDCl_3$) δ_{1H} (ppm): 7.11 (d, $^4J_{HH}$ = *2.3 Hz*, 2H, Ar-H), 7.09 (d, $^4J_{HH}$ = *2.3 Hz*, 2H, Ar-H), 2.83 (s br, 2H, N-CH_2), 2.41 (s, 6H, N-CH_3), 1.41 (s, 18H, ^{t}Bu), 1.30 (s, 18H, ^{t}Bu), 0.70 (s, 6H, CH_3); ^{13}C NMR (100 MHz, $CDCl_3$) δ_{13C} (ppm): 148.3 (C_{quat}, Ar), 141.4 (C_{quat}, Ar), 140.6 (C_{quat}, Ar), 134.1 (C_{quat}, Ar), 120.5 (CH, Ar-H), 116.9 (CH, Ar-H), 65.8 (CH2, N-*C*H_2), 48.3 (CH_3, N-CH_3), 37.9 (C_{quat}), 35.0 (C_{quat}), 34.7 (C_{quat}), 31.8 (CH_3, ^{t}Bu), 29.6 (CH_3, ^{t}Bu), 25.3 (CH_3, Me); HRMS *m/z* $[M + H]^+$ calcd. for $C_{35}H_{59}N_2O_2$ 539.4577, found: 539.4577.

6.2.2 Chapter 3

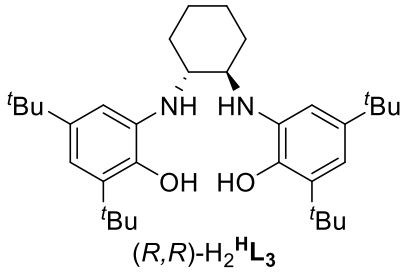
rac-H_2**^{H}L$_3$**



rac-H_2**^{H}L$_3$**

To a suspension of 3,5-di-*tert*-butylcatechol (3 g, 13.5 mmol) in hexane (30 mL), the *rac-trans*-1,2-diaminocyclohexane (0.77 g, 6.75 mmol) and a catalytic amount of triethylamine were added. The mixture was left to stir at room temperature under air for 4 days. The precipitate was then filtered, washed with methanol, and dried under vacuum yielding a white solid (2.1 g, 4.0 mmol, 59% yield).
^{1}H NMR (400 MHz, $CDCl_3$) δ_{1H} (ppm): 9.32 (s broad, 2H, O-H), 7.17 (s, $^4J_{HH}$ *= 2.4 Hz,* 2H, Ar-H), 6.85 (d, $^4J_{HH}$ *= 2.4 Hz,* 2H, Ar-H), 2.82 (s broad, 2H, N-H), 2.56 (s, 2H, Cy-CH), 2.39 (d, 2H, Cy-CH_aH-), 1.80 (d, 2H, Cy-CH_cH-), 1.45 (s, 18H, ^{t}Bu), 1.36 (s, 18H, ^{t}Bu), 1.27 (m, 2H, 1 × Cy-CH_bH- + 1 × Cy-CH_dH)
^{13}C NMR (100 MHz, $CDCl_3$) δ_{13C} (ppm): 147.5 (C_{quat}, Ar), 140.5 (C_{quat}, Ar), 136.3 (C_{quat}, Ar), 133.2 (C_{quat}, Ar), 120.3 (CH, Ar), 119.0 (CH, Ar), 65.3 (CH, Cy), 35.3 (C_{quat}, ^{t}Bu), 34.3 (C_{quat}, ^{t}Bu), 33.5 (CH_2, Cy), 31.9 (CH_3, ^{t}Bu), 29.9 (CH_3, ^{t}Bu), 25.4 (CH_2, Cy)
HRMS m/z $[M + H]^+$ calcd. for $C_{34}H_{55}N_2O_2$ 523.4264, found: 523.4255.

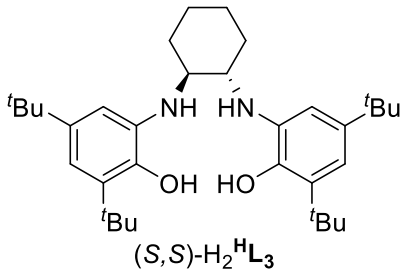
(*R,R*)-H_2**^{H}L$_3$**



(*R,R*)-H_2**^{H}L$_3$**

Same procedure as per *rac*-H_2**^{H}L$_3$** but using (*R,R*)-1,2-diaminocyclohexane instead of *trans*-1,2-diaminocyclohexane. Same ^{1}H and ^{13}C NMR spectra as per *rac*-H_2**^{H}L$_3$** (1.9 g, 3.6 mmol, 53%).
HRMS m/z $[M + H]^+$ calcd. for $C_{34}H_{55}N_2O_2$ 523.4264, found: 523.4248.

(*S,S*)-H_2**^{H}L$_3$**

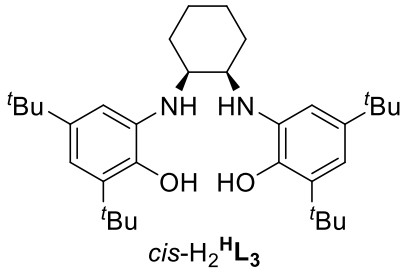


(*S,S*)-H_2**^{H}L$_3$**

Same procedure as per *rac*-H_2**^{H}L$_3$** but using (S,S)-1,2-diaminocyclohexane instead of *trans*-1,2-diaminocyclohexane. Same ^{1}H and ^{13}C NMR spectra as per *rac*-H_2**^{H}L$_3$** (1.8 g, 3.4 mmol, 51%).
HRMS m/z $[M + H]^+$ calcd. for $C_{34}H_{55}N_2O_2$ 523.4264, found: 523.4265.

---

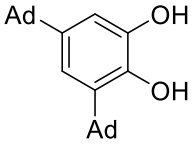
cis-H_2**L_3**



cis-H_2**L_3**

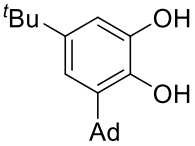
Same procedure as per *rac*-H_2**L_3** but using *cis*-1,2-diaminocyclohexane instead of *trans*-1,2-diaminocyclohexane. (1.6 g, 3.0 mmol, 45%)
^{1}H NMR (400 MHz, $CDCl_3$) δ_{1H} (ppm): 7.02 (b, 2H, Ar-H), 6.78 (b, 2H, Ar-H), 3.31 (b, 2H, Cy-CH), 1.73 (b, 4H, Cy-CH_2), 1.64 (b, 2H, Cy-CH_2), 1.41 (m, 20H, Cy-CH_2 + ^{t}Bu), 1.27 (s, 18H, ^{t}Bu)
^{13}C NMR (100 MHz, $CDCl_3$) δ_{13C} (ppm): 146.78 (C_{quat}, Ar), 141.70 (C_{quat}, Ar), 135.35 (C_{quat}, Ar), 133.70 (C_{quat}, Ar), 118.70 (CH, Ar-H), 117.51 (CH, Ar-H), 57.50 (CH, Cy), 34.99 (C_{quat}, ^{t}Bu), 34.43 (C_{quat}, ^{t}Bu), 31.82 (CH_3, ^{t}Bu), 29.92 (CH_3, ^{t}Bu), 28.20 (CH_2, Cy) , 22.33 (CH_2, Cy)
HRMS m/z $[M + H]^+$ calcd. for $C_{34}H_{55}N_2O_2$ 523.4264, found: 523.4271

3,5-adamantylcatechol



Synthesised according to a literature procedure.[4]
(74% yield) ^{1}H NMR (400 MHz, $CDCl_3$) δ_{1H} (ppm): 6.82 (d, 1H, Ar-H), 6.73 (d, 1H, Ar-H), 2.13 (m, 6H, 3 × Ad-CH_2), 2.08 (b, 6H, 6 × Ad-CH), 1.86 (m, 6H, 3 × Ad-CH_2), 1.78 (m, 6H, 3 × Ad-CH_2), 1.76 (m, 6H, 3 × Ad-CH_2)

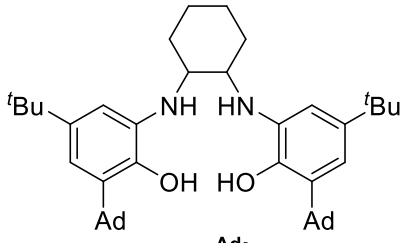
3-*tert*-butyl-5-adamantylcatechol



To a suspension of 4-*tert*-butylcatechol (3 g, 18.1 mmol) in trifluoroacetic acid (36 mL), 1-adamantol (2.75 g, 18.1 mmol) was added. The mixture was allowed to stir at room temperature for 16 h upon which a precipitate is formed. The solid was filtered and recrystallised from a mixture of toluene and hexane to yield a white powder in good yields (4.1 g, 13.6 mmol, 75 % yield).
^{1}H NMR (400 MHz, $CDCl_3$) δ_{1H} (ppm): 6.84 (d, $^4J_{HH}$ = *2.4 Hz*, 1 H, Ar-H), 6.76 (d, $^4J_{HH}$ = *2.4 Hz*, 1 H, Ar-H), 5.46 (s, 1H, OH), 4.79 (s, 1H, OH), 2.13 (s, 6 H, 3 × Ad-CH_2), 2.08 (s, 3 H, 3 × Ad-CH), 1.78 (s, 6 H, 3 × Ad-CH_2), 1.27 (s, 9H, ^{t}Bu)
^{13}C NMR (100 MHz, $CDCl_3$) δ_{13C} (ppm): 142.4 (C_{quat}, Ar), 142.3 (C_{quat}, Ar), 141.1 (C_{quat}, Ar), 136.1 (C_{quat}, Ar), 116.1 (CH, Ar), 110.4 (CH, Ar), 40.8 (CH_2, Ad), 37.2 (CH_2, Ad), 37.2 (C_{quat}, Ad), 34.6 (C_{quat}, ^{t}Bu), 31.7 (CH3, ^{t}Bu), 29.2 (CH, Ad)
HRMS m/z $[M + H]^+$ calcd. for $C_{20}H_{27}O_2$ 299.2011, found: 299.2023

---

rac-$H_2^{Ad}L_3$

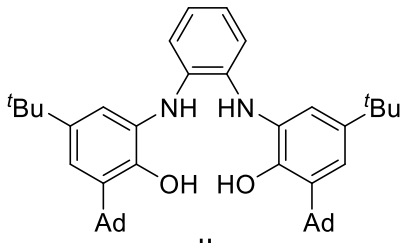


rac-$H_2^{Ad}L_3$

To a suspension of 3-*tert*-butyl-5-adamantyl-catechol (1 g, 3.3 mmol) in hexane (10 mL), the *rac*-*trans*-1,2-diaminocyclohexane (0.2 mL, 1.6 mmol) and a catalytic amount of triethylamine were added. The mixture was left to stir at room temperature for four days, resulting in a precipitate which was filtered, washed with methanol, and dried *in vacuo* to yield a white solid (0.78 g, 1.1 mmol, 72 % yield).
^{1}H NMR (400 MHz, DMSO-d_6) δ_{1H} (ppm): 9.56 (s, 2H, OH), 6.91 (s, 2 H, Ar-H), 6.81 (s, 2 H, Ar-H), 4.71 (s, 2H, NH), 2.44 (s, 2H, Cy-CH), 2.09 (s, 12 H, 6 × Ad-CH_2), 2.05 (m, 2H, Cy-CH_2), 2.01 (s, 6 H, 6 × Ad-CH), 1.71 (s, 12 H, 6 × Ad-CH_2), 1.67 (m, 2H, Cy-CH_2), 1.36 (m, 2H, Cy-CH_2), 1.25 (s, 18H, ^{t}Bu) 1.15 (s, 2H,Cy-CH_2)
HRMS m/z $[M + H]^+$ calcd. for $C_{46}H_{67}N_2O_2$ 679.5203, found: 679.5204

6.2.3 Chapter 4

$H_2^{H}L_4$



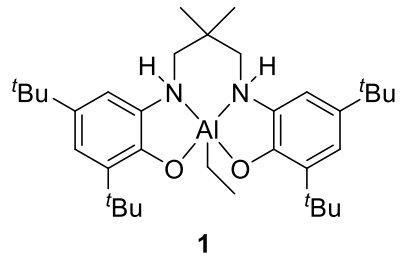
$H_2^{H}L_4$

Pro-ligand $H_2^{H}L_4$ was synthesised according to a literature procedure using 3,5-di-*tert*-butylcatechol and 1,2-phenylenediamine.[5]
^{1}H NMR (400 MHz, $CDCl_3$) δ_{1H} (ppm): 7.15 (d, 2H, Ar-H), 6.90 (m, 4H, Ar-H + Phenylene), 6.66 (m, 2H, Phenylene), 5.89 (b, 2H), 5.13 (b, 2H), 1.44 (s, 18H, ^{t}Bu), 1.27 (s, 18H, ^{t}Bu)

6.3 Synthesis of Complexes

6.3.1 Chapter 2

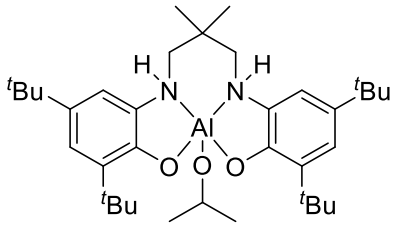
^{H}**L**$_1$Al(Et) (Complex **1**)



1

A pre-cooled solution (-40 °C) of $AlEt_3$ (44.7 mg, 0.39 mmol) in THF (2 mL) was added to a pre-cooled solution (-40 °C) of $H_2{}^{H}\mathbf{L_1}$ (200.0 mg, 0.39 mmol) in THF (5 mL). The solution was allowed to warm to room temperature and subsequently stirred for 4 hours. Evaporation of the volatiles and subsequent precipitation from a THF/pentane mixture afforded pure $^{H}\mathbf{L_1}$Al(Et) as deduced from ^{1}H NMR spectroscopy (125.9 mg, 56% yield). ^{1}H NMR (500 MHz, C_6D_6) δ_{1H} (ppm): 7.54 (d, ^4J = *2.3Hz*, 2H, Ar-*H*), 6.93 (d, ^4J = *2.3Hz*, 2H, Ar-*H*), 2.98 (dd, $^3J_{H\text{-}Ha}$ = *12.6 Hz*, $^3J_{H\text{-}Ha'}$ = *3.6 Hz*, 1H, N-*H*), 2.39 (dd, $^3J_{Ha\text{-}H}$ = *12.6 Hz*, $^2J_{Ha\text{-}Ha'}$ = *12.6 Hz*, 2H, CH_aH$_{a'}$), 2.34 (dd, $^2J_{Ha'\text{-}Ha}$ = *12.6 Hz*, $^3J_{Ha'\text{-}H}$ = *3.6 Hz*, 2H, C$H_{a'}$H$_a$), 1.86 (s, 18H, ^{t}Bu), 1.39 (s, 18H, ^{t}Bu), 1.19(t, ^3J = *8.2 Hz*, 3H, Al-CH$_2$-CH_3), 0.38 (s, 3H, CH_3), 0.05 (s, 3H, CH_3), - 0.05 (q, ^3J = *8.2 Hz*, 2H, Al-CH_2); ^{13}C NMR (125 MHz, C_6D_6) δ_{13C}: 155.4 (C_{quat}, Ar), 138.6 (C_{quat}, Ar), 137.9 (C_{quat}, Ar), 131.5 (C_{quat}, Ar), 123.4 (CH, *Ar*-H), 116.3 (CH, *Ar*-H), 63.0 (CH2, N-*C*H$_2$), 35.8 (C_{quat}, ^{t}Bu), 34.5 (C_{quat}, ^{t}Bu), 32.6 (C_{quat}, (CH$_2$)$_2$-*C*-(CH$_3$)$_2$), 32.2 (CH$_3$, ^{t}Bu), 29.8 (CH$_3$, ^{t}Bu), 26.2 (CH$_3$, Me), 20.4 (CH$_3$, Me), 11.0 (CH$_3$, Al-*Et*), 0.07 (CH$_2$, Al-*Et*); Found: C, 74.46; H, 10.47; N, 5.01, Calc. for C37H61AlN2O2: C, 74.43; H, 10.17; N, 4.78).

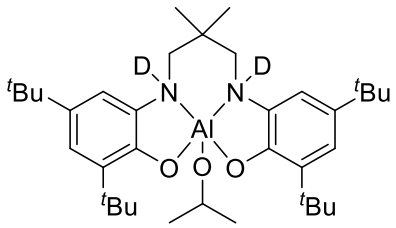
$^{H}\mathbf{L}$Al(O^{i}Pr) (Complex **2**)



2

A pre-cooled solution (-40 °C) of $AlEt_3$ (55. mg, 0.49 mmol) in THF (2 mL) wa added to a pre-cooled solution (-40 °C) of $H_2{}^{H}\mathbf{L_1}$ (250.0 mg, 0.49 mmol) in THF (5 mL). The solution was allowed to warm to room temperature and subsequently stirred for 4 hours. A solution of ^{i}PrOH (37 µl, 0.49 mmol) in THF (1mL) was then added to the solution and allowed to stir overnight. Evaporation of the volatiles and subsequent washing with pentane afforded $^{H}\mathbf{L_1}$Al(O^{i}Pr) as a white powder (108.4 mg, 36.8 % yield). ^{1}H NMR (400 MHz, THF-d_8) δ_{1H} (ppm): 7.10 (d, ^4J = *2.3Hz*, 2H, Ar-*H*), 7.03 (d, ^4J = *2.3Hz*, 2H, Ar-*H*), 5.02 (dd, $^3J_{H\text{-}Ha}$ = *12.6 Hz*, $^3J_{H\text{-}Ha'}$ = *2.4 Hz*, 1H, N-*H*), 3.91 (s br, 1H, O^{i}Pr), 3.06 (dd, $^2J_{Ha'\text{-}Ha}$ = *12.6 Hz*, $^3J_{Ha'\text{-}H}$ = *2.4 Hz*, 1H, CH_aH$_{a'}$), 2.93 (dd, $^3J_{Ha\text{-}H}$ = *12.6 Hz*, $^2J_{Ha\text{-}Ha'}$ = *12.6 Hz*, 1H, CH_aH$_{a'}$), 1.46 (s, 3H, CH3), 1.45 (s, 18H, ^{t}Bu), 1.00 (s, 6H, CH_3), 0.82 (d, 6H, $^3J_{HH}$ = *5.5 Hz*, O^{i}Pr); ^{13}C NMR (100 MHz, THF-d_8) δ_{13C} : 155.6 (C_{quat}, Ar), 137.0 (C_{quat}, Ar), 136.8 (C_{quat}, Ar), 133.0 (C_{quat}, Ar), 122.0 (CH, *Ar*-H), 117.1 (CH, *Ar*-H), 63.5 (CH, O^{i}Pr), 63.3 (CH$_2$, N-*C*H$_2$), 35.5 (C_{quat}, ^{t}Bu), 34.7 (C_{quat}, ^{t}Bu), 34.2 (C_{quat}, (CH$_2$)$_2$-*C*-(CH$_3$)$_2$), 32.1 (CH$_3$, ^{t}Bu), 29.7 (CH$_3$, ^{t}Bu), 28.0 (CH, O^{i}Pr), 27.1 (CH$_3$), 22.3 (CH$_3$); Found: C, 72.59; H, 9.99; N, 4.69, Calc. for C36H59AlN2O3: C, 72.69; H, 10.00; N, 4.71).

$^{D}\mathbf{L_1}$Al(O^{i}Pr) (Complex **4**)



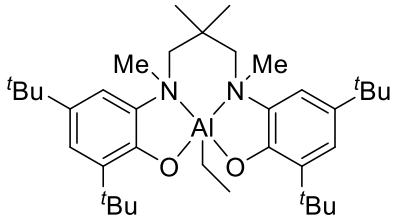
4

Analogous to the synthesis of complex **1** and **2** using $\mathbf{D_2}{}^{D}\mathbf{L}^1$ instead. Yield: 46%.
^{1}H NMR (500 MHz, THF-d_8) δ_{1H} (ppm) for the main product: 7.10 (br, 2H, Ar-H), 7.03 (br, 2H, Ar-H), 3.98 (sept, ^3J = *6.0 Hz*, 1H, CH, O^{i}Pr), 3.05 (d, ^2J = *12 Hz*, 2H, C*H*H), 2.86 (d, ^2J = *12 Hz*, 2H, CH*H*), 1.47 (br, CH_3, 3H), 1.45 (br, 18H, ^{t}Bu), 1.28 (br, 18H, ^{t}Bu), 0.95 (s, 3H, CH_3), 0.78 (d, ^3J = *6.0 Hz*, CH_3, O^{i}Pr).
^{13}C NMR (125 MHz, THF-d_8) δ_{13C}: 155.6 (C_{quat}, Ar), 137.0 (C_{quat}, Ar), 136.8 (C_{quat}, Ar), 132.9 (C_{quat}, Ar), 122.0 (CH, *Ar*-H), 117.1 (CH, *Ar*-H), 63.4 (CH, O^{i}Pr), 63.1 (CH$_2$, N-*C*H$_2$), 35.5 (C_{quat}, ^{t}Bu), 34.7

(C_{quat}, ^{t}Bu), 34.1 (C_{quat}, $(CH_2)_2$-*C*-$(CH_3)_2$), 32.1 (CH_3, ^{t}Bu), 29.7 (CH_3, ^{t}Bu), 28.1 (CH, O^{i}Pr), 27.1 (CH_3), 22.3 (CH_3); Found: C, 71.9; H, 10.65; N, 4.55, Calc. for $C_{36}H_{57}D_2AlN_2O_3$: C, 72.4; H, 10.3; N, 4.7).

---

^{Me}**L$_1$**Al(Et) (Complex **5**)

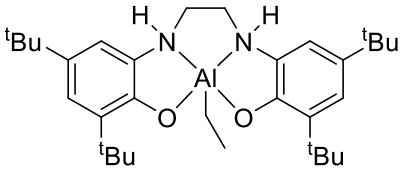


5

A pre-cooled solution (-40 °C) of $AlEt_3$ (50.9 mg, 0.45 mmol.) in THF (2 mL) was added to a pre-cooled solution (-40 °C) of H_2^{Me}**L$_1$** (240.5 mg, 0.45 mmol.) in THF (5 mL). The solution was allowed to warm to room temperature and subsequently stirred overnight. Evaporation of the volatiles and a recrystallisation in pentane afforded pure ^{Me}**L$_1$**Al(Et) as a white powder. The complex was further purified by dissolving it in a minimal amount of pentane and then filtering it to remove any inorganic salts formed during the ligand synthesis (42.0 mg, 16% yield). ^{1}H NMR (400 MHz, C_6D_6) δ_{1H} (ppm): 7.42 (d, ^4J = *2.3Hz*, 2H, Ar-*H*), 6.80 (d, ^4J = *2.3Hz*, 2H, Ar-*H*), 2.99 (d, $^2J_{H-H'}$ = *2.8 Hz, 2*H, N-C*H*$_2$), 2.58 (s, 6H, N-C*H*$_3$), 1.96 (d, $^2J_{H'-H}$ = *2.8 Hz, 2*H, N-C*H*$_2$), 1.71 (s, 18H, ^{t}Bu), 1.63 (t, ^3J = *8.0 Hz*, 3H, Al-CH$_2$-C*H*$_3$), 1.37 (s, 18H, ^{t}Bu), 0.75-0.56 (m, 2H, Al-C*H*$_2$), 0.00 (s, 3H, CH_3); ^{13}C NMR (100 MHz, C_6D_6) δ_{13C}: 156.1 (C_{quat}, Ar), 137.1 (C_{quat}, Ar), 136.7 (C_{quat}, Ar), 135.1 (C_{quat}, Ar), 122.6 (CH, *Ar*-H), 115.1 (CH, *Ar*-H), 66.7 (CH2, N-*C*H$_2$), 46.8 (CH_3, N-CH_3), 35.5 (C_{quat}), 35.0 (C_{quat}), 34.5 (C_{quat}), 32.1 (CH_3, ^{t}Bu), 30.6 (CH_3, Me), 29.9 (CH_3, ^{t}Bu), 12.0 (CH_3, Al-ethyl), 2.8 (CH_2, Al-ethyl); Found: C, 74.81; H, 10.50; N, 4.89, Calc. for C37H61AlN2O2: C, 74.96; H, 10.37; N, 4.73).

---

^{H}**L$_2$**Al(Et) (Complex **6**)



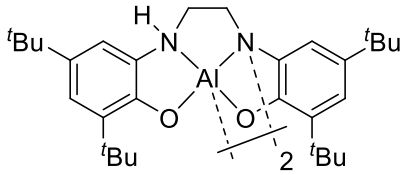
6

A pre-cooled solution (-40 °C) of $AlEt_3$ (61 mg; 0.53 mmol) in THF (2 mL) was added to a pre-cooled solution (-40 °C) of H_2^{H}**L$_2$** (250 mg; 0.53 mmol) in THF (5 mL). The solution was allowed to warm to room temperature and stirred for 4 hours. The solvent was evaporated off to yield the crude compound ^{H}**L$_2$**Al(Et) (quantitative yield) as determined by NMR spectroscopy (see below). All attempts to purify the complex using pentane or mixtures pentane/THF at different temperatures (-40 °C and r.t.) led to formation of complex **7**.

^{1}H NMR (500 MHz, C_6D_6) δ_{1H} (ppm): 7.41 (d, ^4J = *2.3 Hz*, 2H, Ar-H), 6.61 (d, ^4J = *2.3 Hz*, 2H, Ar-H), 2.36 (m, 2H, N-H), 2.00 (m, ^3J = *5.02 Hz*, 2H, -CH_2-), 1.84 (m, 2H, -CH_2-), 1.69 (s, 18H, ^{t}Bu), 1.48 (t, ^3J = *8.0 Hz*, 3H, Al-CH_2-CH_3), 1.39 (s, 18H, ^{t}Bu), 0.24 (q, ^3J = *8.0 Hz*, 2H, Al-CH_2).

^{13}C NMR (125 MHz, C_6D_6) δ_{13C} (ppm): 156.7 (C_{quat}, Ar), 137.7 (C_{quat}, Ar), 137.0 (C_{quat}, Ar), 129.4 (C_{quat}, Ar), 122.6 (CH, Ar-H), 116.6 (CH, Ar-H), 46.6 (CH_2, N-CH_2), 35.2 (C_{quat}, ^{t}Bu), 34.1 (C_{quat}, ^{t}Bu), 31.8 (CH_3, ^{t}Bu), 29.3 (CH_3, ^{t}Bu), 10.4 (CH_3, Al-CH_2-CH_3), 1.1 (CH_2, Al-CH_2). EA attempted but a low carbon content was found, possibly due to the air- and moisture-sensitivity of **6** as well as the presence of residual aluminium contaminants.

$^{H}\mathbf{L_2}$Al (Complex **7**)



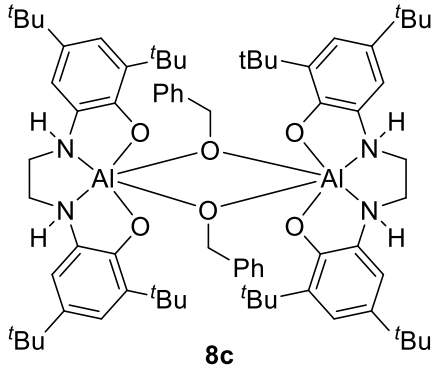
7

Complex **6** (277 mg; 0.53 mmol) was stirred in pentane overnight to lead to formation of a white precipitate. Subsequent filtration and washing with pentane afford **7** as a white powder (198 mg, 76% yield).

^{1}H NMR (500 MHz, C_6D_6) δ_{1H} (ppm): 7.30 (d, $^{4}J = 2.0$ *Hz*, 1H, Ar-H), 7.09 (d, $^{4}J = 2.0$ *Hz*, 1H, Ar-H), 7.01 (d, $^{4}J = 2.0$ *Hz*, 1H, Ar-H), 6.48 (d, $^{4}J = 2.0$ *Hz*, 1H, Ar-H), 3.89 (td, 1H, N-CH_aH), 3.31 (dd, 1H, N-H), 2.92 (dd, 1H, N-CH_bH), 2.28 (m, 1H, N-CH_cH), 1.82 (s, 9H, ^{t}Bu), 1.72 (s, 9H, ^{t}Bu), 1.22 (s, 9H, ^{t}Bu), 1.19 (s, 9H, ^{t}Bu).

^{13}C NMR (125 MHz, C_6D_6) δ_{13C}: 154.9 (C_{quat}, Ar), 151.6 (C_{quat}, Ar), 140.8 (C_{quat}, ^{t}Bu), 138.4 (C_{quat}, ^{t}Bu), 136.9 (C_{quat}, ^{t}Bu), 135.6 (C_{quat}, ^{t}Bu), 122.8 (CH, Ar-H), 118.7 (CH, Ar-H), 117.0 (CH, Ar-H), 116.8 (CH, Ar-H), 49.5 (CH_2, N-CH_2), 48.7 (CH_2, N-CH_2), 31.9 (CH_3, ^{t}Bu), 31.8 (CH_3, ^{t}Bu), 29.8 (CH_3, ^{t}Bu). EA: Found: C, 72.97; H, 9.35; N, 5.59, Calc. for $C_{30}H_{45}AlN_2O_2$: C, 73.14; H, 9.21; N, 5.69.

$^{H}\mathbf{L_2}$Al(OBn) (Complex **8c**)



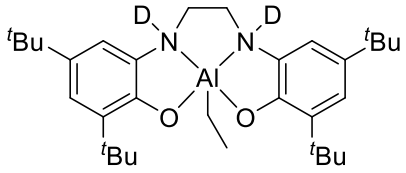
8c

To a solution of complex **7** (153 mg, 0.31 mmol) in toluene (3 mL) was added 1 equivalent of BnOH (33.8 mg, 32.4 µL, 0.31 mmol). The mixture was allowed to stir at room temperature overnight. Evaporation of the volatile and subsequent washing with pentane afford pure **8c** as a white powder (148 mg, 79 % yield).

^{1}H NMR (400 MHz, C_6D_6) δ_{1H} (ppm): 7.53 (d, $^{4}J = 2.3$ *Hz*, 1H, Ar-H), 7.26 (d, 2H, Benzyloxy Ar-H) 7.22 (d, $^{4}J = 2.3$ *Hz*, 1H, Ar-H), 7.07 (m, 3H, Ar-H + 2 × Benzyloxy Ar-H), 6.94 (t, 1H, Benzyloxy Ar-H), 6.65 (d, $^{4}J = 2.3$ *Hz*, 1H, Ar-H), 4.83 (m, 2H, N-H + Benzyloxy CH_2), 4.55 (d, 1H, Benzyloxy CH_2), 3.49 (dd, $^{3}J = 11.2$ *Hz, 5.1 Hz*, 1H, N-H), 2.40 (m, 1H, N-CH_aH-), 2.26 (m, 2H, N-CH_bH- + N-CH_cH-), 2.09 (s, 10H, N-CH_dH- + 9 × ^{t}Bu), 1.39 (s, 9H, ^{t}Bu), 1.31 (s, 9H, ^{t}Bu), 1.20 (s, 9H, ^{t}Bu).

^{13}C NMR (125 MHz, C_6D_6) δ_{13C}: 158.1 (C_{quat}, Ar), 157.7 (C_{quat}, Ar), 142.3 (C_{quat}, BnO- Ar), 137.5 (C_{quat}, Ar), 136.9 (C_{quat}, Ar), 136.4 (C_{quat}, Ar), 136.3 (C_{quat}, Ar), 132.7 (C_{quat}, Ar), 131.9 (C_{quat}, Ar), 128.8 (CH, BnO- Ar-H), 127.4 (CH, BnO- Ar-H), 127.3 (CH, BnO- Ar-H), 122.5 (CH, Ar-H), 121.8 (CH, Ar-H), 117.7 (CH, Ar-H), 115.6 (CH, Ar-H), 65.1 (CH_2, BnO- Ar-CH_2-), 51.8 (CH_2, N-CH_2), 42.2 (CH_2, N-CH_2), 35.7 (C_{quat}, ^{t}Bu), 35.0 (C_{quat}, ^{t}Bu), 34.5 (C_{quat}, ^{t}Bu), 34.4 (C_{quat}, ^{t}Bu), 32.1 (CH3, ^{t}Bu), 32.1 (CH_3, ^{t}Bu), 30.6 (CH_3, ^{t}Bu), 29.3 (CH_3, ^{t}Bu). EA: Found: C, 73.84; H, 9.02; N, 4.56, Calc. for $C_{37}H_{53}AlN_2O_3$: C, 73.97; H, 8.89; N, 4.66.

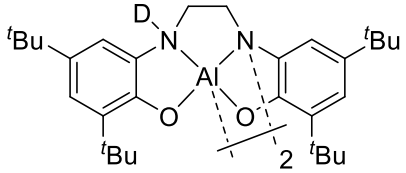
$^{D}L_2$Al(Et) (Complex **9**)



9

Analogous to the synthesis of **6** using $D_2{}^{D}L_2$ instead (quantitative yield due to difficulties in purification). ^{1}H NMR (500 MHz, C_6D_6) δ_{1H} (ppm): 7.43 (d, ^4J = *2.2 Hz*, 2H, Ar-H), 6.62z (d, ^4J = *2.2 Hz*, 2H, Ar-H), 1.98 (m, i2H, -CH_2-), 1.79 (m, 2H, -CH_2-), 1.71 (s, 18H, ^{t}Bu), 1.5 (t, ^3J = *8.2 Hz*, 3H, Al-CH_2-CH_3), 1.40 (s, 18H, ^{t}Bu), 0.24 (q, ^3J = *8.2 Hz*, 2H, Al-CH_2). No signals for NH were observed. EA attempted but a low carbon content was found, possibly due to the air- and moisture-sensitivity of **9** as well as the presence of residual aluminium contaminants.

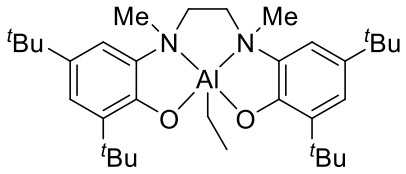
$^{D}L_2$Al (Complex **10**)



10

Analogous to the synthesis of **7** using **9** instead (72% yield).
^{1}H NMR (500 MHz, C_6D_6) δ_{1H} (ppm): 7.29 (d, 1H, Ar-H), 7.08 (d, 1H, Ar-H), 7.01 (d, 1H, Ar-H), 6.48 (d, 1H, Ar-H), 3.88 (td, 1H, N-CH_aH), 2.91 (dd, 1H, N-CH_bH), 2.27 (dd, 1H, N-CH_cH), 1.82 (s, 9H, ^{t}Bu), 1.72 (s, 9H, ^{t}Bu), 1.22 (s, 9H, ^{t}Bu), 1.18 (s, 9H, ^{t}Bu). No signal for NH was observed.
EA: Found: C, 72.98; H, 9.32; N, 5.65, Calc. for $C_{30}H_{44}DAlN_2O_2$: C, 72.99; H, 9.39; N, 5.67.

$^{Me}L_2$Al(Et) (Complex **11**)



11

A pre-cooled solution (-40 °C) of $AlEt_3$ (23 mg; 0.2 mmol) in toluene (2 mL) is added to a pre-cooled solution (-40 °C) of $H_2{}^{Me}L_2$ (100 mg; 0.2 mmol) in toluene (5 mL). The solution was allowed to warm to room temperature and stirred for 4 hours. The solvent was evaporated off to yield a mixture of compounds which was recrystallised in pentane to yield clean **11** as determined by NMR spectroscopy (57 mg, 0.1 mmol, 52% yield).
^{1}H NMR (500 MHz, C_6D_6) δ^1H (ppm): 7.35 (d, ^{4}J = 2.0 Hz, 2H, Ar-H), 7.04 (d, ^{4}J = 2.0 Hz, 2H, Ar-H), 3.98 (s broad, 2H, N-CH_aH-), 3.22 (s broad, 2H, N-CH_bH-), 2.76 (s, 6H, N-CH_3), 1.41 (s, 18H, ^{t}Bu), 1.34 (s, 18H, ^{t}Bu), 0.85 (t, 3H, Al-CH_2-CH_3), -0.15 (tq, 2H, Al-CH_2-).
^{13}C NMR (125 MHz, C_6D_6) δ^{13}C (ppm): 151.9* (C_{quat}, Ar), 152.0* (C_{quat}, Ar), 138.4* (C_{quat}, Ar), 136.8* (C_{quat}, Ar), 122.9 (CH, Ar-H), 113.1 (CH, Ar-H), 40.8* (CH_3, N-CH_3), 34.6* (C_{quat}, ^{t}Bu), 34.3* (C_{quat}, ^{t}Bu), 32.1 (CH_3, ^{t}Bu), 30.0 (CH_3, ^{t}Bu), 10.8 (CH_3, Al-Et), -2.4 (CH_2, Al-Et)
*Determined by HSQC/HMBC NMR experiments

6.3.2 Chapter 3

rac-^{H}**L**$_3$Al(Et) / *rac*-^{H}**L**$_3$Al (*rac*-**mix12**)

A pre-cooled solution (-40 °C) of $AlEt_3$ (54.6 mg; 0.48 mmol) in THF (2 mL) was added to a pre-cooled solution (-40 °C) of *rac*-$H_2{}^{H}$**L**$_3$ (250 mg; 0.48 mmol) in THF (5 mL). The solution was allowed to warm to room temperature and stirred for 4 hours. The solvent was evaporated off to yield a mixture of products as determined by NMR spectroscopy.

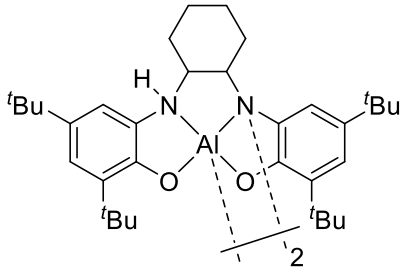
---

cis-^{H}**L**$_3$Al(Et) / *cis*-^{H}**L**$_3$Al (*cis*-**mix12**)

A pre-cooled solution (-40 °C) of $AlEt_3$ (54.6 mg; 0.48 mmol) in THF (2 mL) was added to a pre-cooled solution (-40 °C) of *cis*-$H_2{}^{H}$**L**$_3$ (250 mg; 0.48 mmol) in THF (5 mL). The solution was allowed to warm to room temperature and stirred for 4 hours. The solvent was evaporated off to yield a mixture of products as determined by NMR spectroscopy.

---

rac-^{H}**L**$_3$Al (Complex *rac*-**13**)



rac-**13**

In a vial, *rac*-**mix12** (277 mg, 0.48 mmol) was dissolved in toluene. The vial was sealed, and the contents heated at 80 °C for 4 days. The solvent was removed *in vacuo* and the resulting solid recrystallised in pentane to yield a fine white powder (101 mg, 0.26 mmol, 38% yield).

^{1}H NMR (400 MHz, CD_2Cl_2) δ_{1H} (ppm): 7.07 (d, 1H, aromatic), 6.86 (m, 2H, aromatic), 6.54 (d, 1H, aromatic), 3.53 (td, 1H, Cy-CH), 2.65 (d, 1H, N-H), 2.49 (dd, 1H, Cy- CH_2), 2.30 (m, 2H, 1 × Cy-CH_2 + 1 × Cy-CH), 1.84 (d, 1H, Cy- CH_2), 1.69 (d, 1H, Cy- CH_2), 1.52 (s, 10H, 9 × ^{t}Bu + 1 × Cy-CH_2), 1.48 (s, 9H, ^{t}Bu), 1.39* (m, 1H, Cy-CH_2), 1,26 (m, 1H, Cy-CH_2), 1.17 (s, 10H, 9 × ^{t}Bu + 1 × N-H), 1.03 (td, 1H, Cy-CH_2) 0.87 (s, 9H, ^{t}Bu).

^{13}C NMR (125 MHz, CD_2Cl_2) δ_{13C} (ppm): 155.63 (C_{quat}, Ar), 153.93 (C_{quat}, Ar), 138.57 (C_{quat}, Ar), 137.34 (C_{quat}, Ar), 136.76 (C_{quat}, Ar), 135.77 (C_{quat}, Ar), 134.05 (C_{quat}, Ar), 127.50 (C_{quat}, Ar) 123.44 (CH, Ar), 123.00 (CH, Ar), 119.92 (CH, Ar), 119.71 (CH, Ar), 65.88 (CH, -Cy-), 62.53 (CH, -Cy-), 35.61 (C_{quat}, ^{t}Bu), 35.42 (C_{quat}, ^{t}Bu), 34.43 (C_{quat}, ^{t}Bu), 34.30 (C_{quat}, ^{t}Bu), 32.92 (CH_2, -Cy-), 31.92 (CH_3, ^{t}Bu), 31.86 (CH_2, -Cy-) 31.77 (CH_3, ^{t}Bu), 29.88 (CH_3, ^{t}Bu), 29.68 (CH_3, ^{t}Bu), 26.10 (CH_2, -Cy), 24.76 (CH_2, -Cy)

---

rac-**mix14**

A pre-cooled solution (-40 °C) of $AlEt_3$ (54.6 mg, 0.48 mmol.) in THF (2 mL) was added to a pre-cooled solution (-40 °C) of *rac*-$H_2{}^{H}$**L**$_3$ (250 mg, 0.48 mmol.) in THF (5 mL). The mixture was allowed to warm to room temperature and then stirred for 4 hours. The solvent was removed *in vacuo*, and the crude product re-dissolved in toluene (5 mL) to which benzyl alcohol (49.7 µL, 51.9 mg, 0.48 mmol) was added. The solution was then stirred for 16 hours after which the solvent was removed *in vacuo*. The crude product was purified by stirring it in pentane (5 mL) for 2 hours and subsequently filtering the mixture with copious washings of pentane, affording a white solid (239 mg, 0.36 mmol, 75% yield).
EA: Found: C, 75.41; H, 9.23; N, 3.98, Calc. for $C_{38}H_{61}AlN_2O_3$: C, 75.19; H, 9.08; N, 4.28.

(*R,R*)-**mix14**

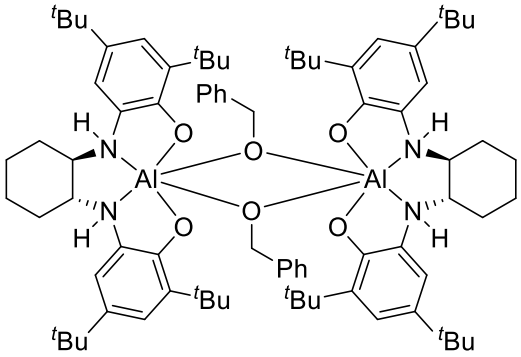
Same procedure as per *rac*-**mix14** but using (*R*,*R*)-H_2**^{H}L$_3$** instead of *rac*-H_2**^{H}L$_3$**. Yield: 109 mg (0.16 mmol, 33% yield).
EA: Found: C, 75.32; H, 8.96; N, 4.19, Calc. for $C_{38}H_{61}AlN_2O_3$: C, 75.19; H, 9.08; N, 4.28.

(*S,S*)-**mix14**

Same procedure as per *rac*-**mix14** but using (*S*,*S*)-H_2**^{H}L$_3$** instead of *rac*-H_2**^{H}L$_3$**. Yield: 79 mg (0.12 mmol, 25% yield);
EA: Found: C, 75.20; H, 9.27; N, 4.18, Calc. for $C_{38}H_{61}AlN_2O_3$: C, 75.19; H, 9.08; N, 4.28.

---

rac-**^{H}L$_3$**Al(OBn) (Complex *rac*-**14**)

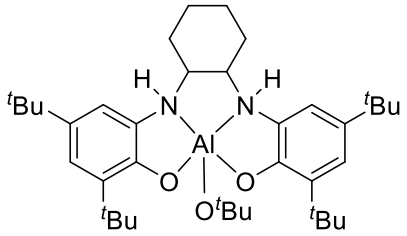


rac-**14**

A pre-cooled solution (-40 °C) of $AlEt_3$ (54.6 mg, 0.48 mmol.) in THF (2 mL) was added to a pre-cooled solution (-40 °C) of *rac*-H_2**^{H}L$_3$** (250 mg, 0.48 mmol.) in THF (5 mL). The mixture was allowed to warm to room temperature and then stirred for 4 hours. The solvent was removed *in vacuo*, and the crude product re-dissolved in toluene (5 mL) to which benzyl alcohol (49.7 μL, 51.9 mg, 0.48 mmol) was added. The solution was heated at 100 °C for 16h. Subsequent evaporation of the volatiles affords pure *rac*-**14** (259 mg, .40 mmol, 82 % yield),
^{1}H NMR (400 MHz, CD_2Cl_2) δ_{1H} (ppm): 7.51 (s, 1H, BnO- aromatic), 7.49 (s, 1H, BnO- aromatic), 7.23 (m, 3H, BnO- aromatic), 7.15 (m, 1H, aromatic), 6.89 (d, 1H, aromatic), 6.85 (d, 1H, aromatic), 6.79 (d, 1H, aromatic), 4.63 (d, 1H, N-H), 4.47 (q, 2H, BnO- CH_2), 3.24 (d, 1H, N-H), 2.61 (m, 1H, Cy-CH), 2.39 (m, 2H, 1 × Cy-CH_2 + 1 × Cy-CH), 1.75 (s, 10H, 9 × ^{t}Bu, 1 × Cy-CH_2), 1.57 (dd, 1H, Cy-CH_2), 1.38 (dd?, 1H, Cy-CH_2), 1.19 (s, 9H, ^{t}Bu), 1.15 (s, 10H, 9 × ^{t}Bu, 1 × Cy-CH_2), 0.89 (m, 1H, Cy-CH_2) 0.82 (s, 9H, ^{t}Bu), 0.72 (m, 1H, Cy-CH_2), 0.29 (m, 1H, Cy-CH_2)
^{13}C NMR (125 MHz, CD_2Cl_2) δ_{13C} (ppm): 158.4 (C_{quat}, Ar), 157.9 (C_{quat}, Ar), 136.52 (C_{quat}, Ar), 136.07 (C_{quat}, Ar), 136.01 (C_{quat}, Ar), 135.15 (C_{quat}, Ar), 128.92 (CH, BnO- Ar), 128.36 (CH, BnO- Ar), 127.99 (CH, BnO- Ar), 126.9 (C_{quat}, BnO- Ar), 115.69 (CH, Ar), 122.37 (CH, Ar), 121.47 (CH, Ar), 121.37 (CH, Ar), 65.29 (CH_2, BnO-), 61.42 (CH, -Cy-), 56.22 (CH, -Cy-), 35.70 (CH_2, -Cy-), 34.92 (C_{quat}, ^{t}Bu), 34.86 (CH_2, -Cy-), 34.56 (C_{quat}, ^{t}Bu), 34.24 (C_{quat}, ^{t}Bu), 32.07 (CH_3, ^{t}Bu), 31.97 (CH_3, ^{t}Bu), 30.89 (C_{quat}, ^{t}Bu), 30.58 (CH_3, ^{t}Bu), 29.41 (CH_3, ^{t}Bu), 24.88 (CH_2, -Cy-), 24.67 (CH_2, -Cy)
EA: Found: C, 75.06; H, 9.16; N, 4.40, Calc. for $C_{38}H_{61}AlN_2O_3$: C, 75.19; H, 9.08; N, 4.28.

---

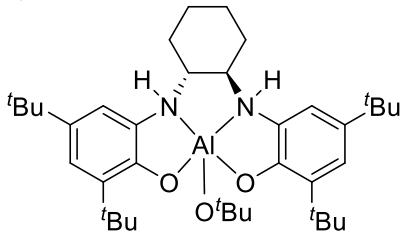
rac-**^{H}L$_3$**Al(O^{t}Bu) (Complex *rac*-**15**)



rac-**15**

A pre-cooled solution (-40 °C) of $AlEt_3$ (54.6 mg, 0.48 mmol.) in THF (2 mL) was added to a pre-cooled solution (-40 °C) of *rac*-H_2**^{H}L$_3$** (250 mg, 0.48 mmol.) in THF (5 mL). The mixture was allowed to warm to room temperature and then stirred for 4 hours. The solvent was removed *in vacuo*, and the crude product re-dissolved in toluene (5 mL) to which was added *tert*-butanol (45.7 µL, 35.4 mg, 0.48 mmol). The solution was then stirred for 16 hours after which the solvent was removed *in vacuo*. The crude product was purified by stirring it in pentane (5 mL) for 2 hours and subsequently filtering the mixture with copious washings of pentane, affording a flaky white solid (189.0 mg, 0.30 mmol, 63% yield).
^{1}H NMR (400 MHz, C_6D_6) δ_{1H} (ppm): 7.52 (s, 1H, *Ar*-H), 7.42 (s, 1H, *Ar*-H), 6.81 (s, 1H, *Ar*-H), 6.66 (s, 1H, *Ar*-H), 3.69 (d, *J* = 6.8 Hz, 1H, NH), 2.65 (d, *J* = 11.9 Hz, 1H, NH), 2.40 (qd, *J* =11.3, 4.0 Hz, 1H, Cy-CH), 2.05 (m, 1H, Cy-CH_2), 1.96 (m, 1H, Cy-CH), 1.89 (s, 9H, ^{t}Bu), 1.66 (s, 9H, ^{t}Bu), 1.62 (s, 9H, O-^{t}Bu), 1.45 (m, 1H, Cy-CH_2), 1.38 (s, 9H, ^{t}Bu), 1.32 (s, 9H, ^{t}Bu), 1.20 (m, 1H, Cy-CH_2), 1.04 (d, *J* = 13.9 Hz, 1H, Cy-CH_2), 0.88 (m, 1H, Cy-CH_2), 0.63 (m, 1H, Cy-CH_2), 0.39 (m, 1H, Cy-CH_2), 0.11 (d, *J* = 13.4 Hz, 1H, Cy-CH_2)
^{13}C NMR (100 MHz, C_6D_6) δ_{13C} (ppm): 157.5 (C_{quat}, *Ar*), 157.0 (C_{quat}, *Ar*), 138.0 (C_{quat}, *Ar*), 137.9 (C_{quat}, *Ar*), 136.7 (C_{quat}, *Ar*), 136.0 (C_{quat}, *Ar*), 127.4 (C_{quat}, *Ar*), 126.3 (C_{quat}, *Ar*), 123.2 (CH, *Ar*-H), 123.1 (CH, *Ar*-H), 122.1 (CH, *Ar*-H), 118.4 (CH, *Ar*-H), 68.3 (C_{quat}, O-^{t}Bu), 61.7 (CH, -Cy-), 59.7 (CH, -Cy-), 35.7 (C_{quat}, ^{t}Bu), 35.6 (C_{quat}, ^{t}Bu), 34.4 (C_{quat}, ^{t}Bu), 34.2 (C_{quat}, ^{t}Bu), 33.9 (CH_3, O-^{t}Bu), 33.2 (CH_2, -Cy-), 32.1 (CH_3, ^{t}Bu) , 32.1 (CH_3, ^{t}Bu), 30.3 (CH_2, -Cy-), 29.9 (CH_3, ^{t}Bu), 29.7 (CH_3, ^{t}Bu), 24.9 (CH_2, -Cy-), 23.5 (CH_2, -Cy-), EA: Found: C, 73.38; H, 9.99; N, 4.46, Calc. for $C_{38}H_{61}AlN_2O_3$: C, 73.51; H, 9.90; N, 4.51.

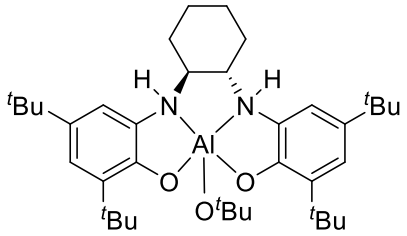
(*R,R*)-**^{H}L$_3$**Al(O^{t}Bu) [Complex (*R,R*)-**15**]



(*R,R*)-**15**

same procedure as per *rac*-**15** but using (*R*,*R*)-H_2**^{H}L$_3$** instead of *rac*-H_2**^{H}L$_3$**. Same ^{1}H and ^{13}C NMR spectra as per *rac*-**15**. Yield: 230 mg (0.37 mmol, 77% yield).
EA: Found: C, 73.39; H, 10.07; N, 4.41, Calc. for $C_{38}H_{61}AlN_2O_3$: C, 73.51; H, 9.90; N, 4.51.

(*S,S*)-**^{H}L$_3$**Al(O^{t}Bu) [Complex (*S,S*)-**15**]

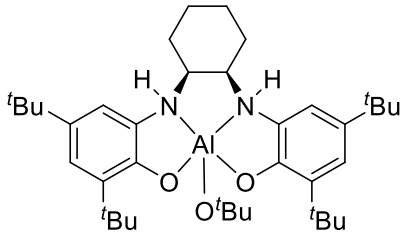


(*S,S*)-**15**

same procedure as per *rac*-**15** but using (S,S)-H_2**^{H}L$_3$** instead of *rac*-H_2**^{H}L$_3$**. Same ^{1}H and ^{13}C NMR spectra as per *rac*-**15**. Yield: 237 mg (0.38 mmol, 80% yield).
EA: Found: C, 73.52; H, 9.99; N, 4.46, Calc. for $C_{38}H_{61}AlN_2O_3$: C, 73.51; H, 9.90; N, 4.51.

---

cis-^{H}**L$_3$**Al(Et) (Complex *cis*-**15**)

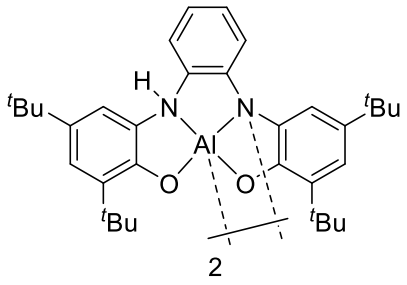


***cis*-15**

A pre-cooled solution (-40 °C) of $AlEt_3$ (54.6 mg; 0.48 mmol) in THF (2 mL) is added to a pre-cooled solution (-40 °C) of *cis*-$H_2{}^{H}$**L$_3$** (250 mg; 0.48 mmol) in THF (5 mL). The solution was allowed to warm to room temperature and stirred for 4 hours. The solvent was evaporated off to yield a mixture of products, with the major product suspected of being *cis*-**15** as determined by NMR spectroscopy.
Synthesis of cis-^{H}***L$_3$***Al(O^{t}Bu) *(Complex cis-**15**)*: same procedure as per *rac*-**15** but using *cis*-$H_2{}^{H}$**L$_3$** instead of *rac*-$H_2{}^{H}$**L$_3$**. ^{1}H NMR (400 MHz,C_6D_6) δ_{1H} (ppm): 7.48 (m, 2H, Ar-H), 6.77 (s, 2H, Ar-H), 3.26 (d, 2H, NH), 2.59 (s, 2H, Cy-CH), 1.80 (s, 18H, ^{t}Bu), 1.65 (s, 9H, O^{t}Bu), 1.36 (s, 20H, 18 × ^{t}Bu + 2 × Cy-CH_2), 0.75 (m, 6H, Cy-CH_2), ^{13}C NMR (100 MHz, C_6D_6) δ_{13C} (ppm): 156.5 (C_{quat}, Ar), 137.9 (C_{quat}, Ar), 137.2 (C_{quat}, Ar), 129.1 (C_{quat}, Ar), 123.0 (CH, Ar-H), 117.4 (CH, Ar-H), 68.5 (C_{quat}, O^{t}Bu), 57.6 (CH, Cy), 35.7 (C_{quat}, ^{t}Bu), 34.4 (C_{quat}, ^{t}Bu), 34.1 (CH_3, O^{t}Bu), 32.1 (CH_3, ^{t}Bu), 29.8 (CH_3, ^{t}Bu), 26.8 (CH_2, Cy), 20.6 (CH_2, Cy); EA: Found: C, 73.44; H, 10.2; N, 4.50, Calc. for $C_{38}H_{61}AlN_2O_3$: C, 73.51; H, 9.90; N, 4.51.

6.3.3 Chapter 4

^{H}**L$_4$**Al (Complex **16**)

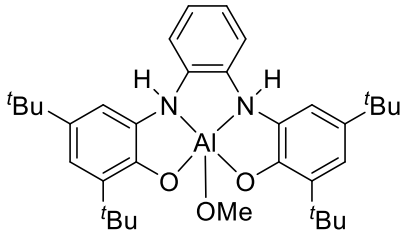


16

A pre-cooled solution (-40 °C) of $AlEt_3$ (55.2 mg, 0.48 mmol.) in toluene (2 mL) was added to a pre-cooled solution (-40 °C) of $H_2{}^{H}$**L$_4$** (250 mg, 0.48 mmol.) in toluene (7 mL). The mixture was allowed to warm to room temperature and then stirred for 16 hours. Removal of volatiles afforded complex **16** in quantitative yields.
^{1}H NMR (400 MHz, C_6D_6) δ_{1H} (ppm): 7.30 (s, 2H, Ar-H), 7.00 (s, 1H, Ar-H), 6.95 (m, 2H, Ar-H), 6.88 (m, 2H, Ar-H), 6.50 (t, 1H, ^{4}J = 8.3 Hz, Ar-H), 5.00 (s, 1H, NH), 1.61 (s, 9H, ^{t}Bu), 1.51 (s, 9H, ^{t}Bu), 1.20 (s, 9H, ^{t}Bu), 1.10 (s, 9H, ^{t}Bu)
^{13}C NMR (100 MHz, C_6D_6) δ_{13C} (ppm): 153.6 (C_{quat}, *Ar*), 146.6 (C_{quat}, *Ar*), 144.0 (C_{quat}, *Ar*), 141.7 (C_{quat}, *Ar*), 140.6 (C_{quat}, *Ar*), 139.9 (C_{quat}, *Ar*), 139.3 (C_{quat}, *Ar*), 136.8 (C_{quat}, *Ar*), 132.5 (C_{quat}, *Ar*), 129.5 (C_{quat}, *Ar*), 128.7 (CH, *Ar*-H), 124.1 (CH, *Ar*-H), 124.1 (CH, *Ar*-H), 118.3 (CH, *Ar*-H), 116.6 (CH, *Ar*-H), 114.0 (CH, *Ar*-H), 113.0 (CH, *Ar*-H), 110.1 (CH, *Ar*-H), 35.7 (C_{quat}, ^{t}Bu), 35.6 (C_{quat}, ^{t}Bu), 34.9 (C_{quat}, ^{t}Bu), 34.4 (C_{quat}, ^{t}Bu), 31.8 (CH_3, ^{t}Bu), 31.6 (CH_3, ^{t}Bu), 31.0 (CH_3, ^{t}Bu), 29.6 (CH_3, ^{t}Bu)
EA: Found: C, 73.26; H, 8.52; N, 4.96, Calc. for $C_{34}H_{45}AlN_2O_2$: C, 75.52; H, 8.39; N, 5.18.

---

^{H}**L**$_4$Al(OMe) (Complex **17-a**)

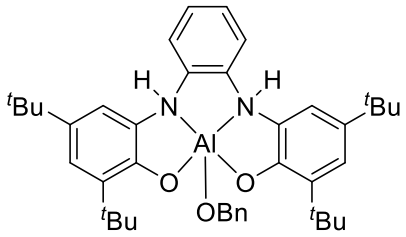


17-a

A pre-cooled solution (-40 °C) of $AlEt_3$ (55.2 mg, 0.48 mmol.) in toluene (2 mL) was added to a pre-cooled solution (-40 °C) of H_2^{H}**L**$_4$ (250 mg, 0.48 mmol.) in toluene (7 mL). The mixture was allowed to warm to room temperature and then stirred for 4 hours upon which MeOH (19.4 µL, 0.48 mmol.) was added. A precipitate was observed after a further 16 hours of stirring which was filtered, washed with pentane, and dried to yield a white free-flowing powder (184 mg, 0.32 mmol, 67 % yield).
^{1}H NMR (400 MHz, C_6D_6) δ_{1H} (ppm): 7.85 (d, 1H, Ar-H), 7.45 (m, 4H, Ar-H), 6.97 (d, 1H, Ar-H), 6.90 (s, 1H, Ar-H), 6.76 (t, 1H, Ar-H), 6.51 (s, 1H, NH), 4.90 (s, 1H, NH), 2.49 (s, 3H, -OMe), 1.86 (s, 9H, ^{t}Bu), 1.42 (s, 9H, ^{t}Bu), 1.35 (s, 9H, ^{t}Bu), 1.27 (s, 9H, ^{t}Bu)
EA: Found: C, 73.23; H, 8.61; N, 4.83, Calc. for $C_{35}H_{49}AlN_2O_3$: C, 73.40; H, 8.62; N, 4.89

---

^{H}**L**$_4$Al(OBn) (Complex **17-b**)

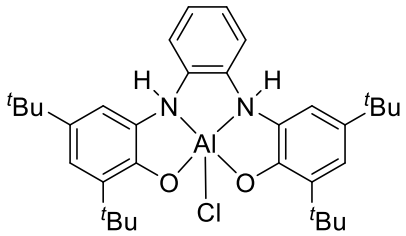


17-b

Same as the synthesis of **17-a** but using BnOH (49.7 µL, 0.48 mmol) instead of MeOH. Yield: 142 mg (0.22 mmol, 45 % yield).
^{1}H NMR (400 MHz, C_6D_6) δ_{1H} (ppm): 7.61 (d, 1H, Ar-H), 7.58 (d, 1H, Ar-H), 7.47 (d, 1H, Ar-H), 7.32 (d, 1H, Ar-H), 6.94 (d, 1H, Ar-H), 6.88 (s, 3H, Ar-H), 6.72 (s, 1H, Ar-H), 6.53 (t, 1H, Ar-H), 6.33 (t, 1H, Ar-H), 4.95 (s, 1H, NH), 4.60 (d, 1H, -OBn CH_2, 4.29 (d, 1H, NH), 4.11 (d, 1H, -OBn CH_2), 2.06 (s, 9H, ^{t}Bu), 1.36 (s, 9H, ^{t}Bu), 1.22 (s, 9H, ^{t}Bu), 0.99 (s, 9H, ^{t}Bu)
EA: Found: C, 75.93; H, 8.45; N, 4.16, Calc. for $C_{41}H_{53}AlN_2O_3$: C, 75.89; H, 8.23; N, 4.32

---

^{H}**L**$_4$Al(Cl) (Complex **18**)

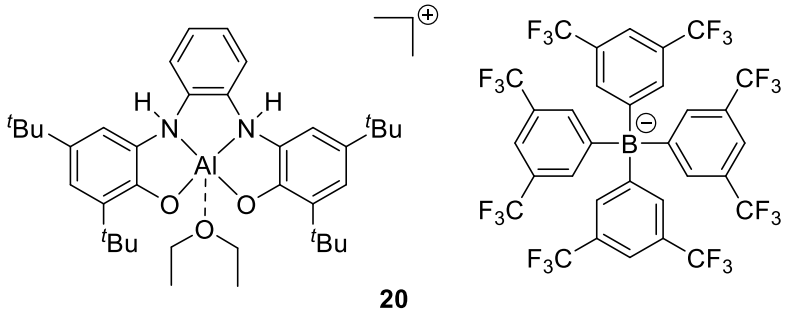


18

A pre-cooled solution (-40 °C) of $AlEt_2Cl$ (58.3 mg, 0.48 mmol.) in toluene (2 mL) was added to a pre-cooled solution (-40 °C) of H_2^{H}**L**$_4$ (250 mg, 0.48 mmol.) in toluene (7 mL). The mixture was allowed to warm to room temperature and then stirred for 16 hours upon which a precipitate can be observed. The slurry was cooled (-40 °C) and then filtered and washed with pentane. After drying, a fluffy white powder was obtained (214 mg, .37 mmol, 77 % yield).

^{1}H NMR (400 MHz, CD_2Cl_2) δ_{1H} (ppm): 7.44 (d, 2H, Ar-H), 7.40 (s, 2H, Phenylene Ar-H), 7.38 (d, 2H, Ar-H), 7.35 (s, 2H, Phenylene Ar-H), 5.50 (s, 2H, NH_2), 1.41 (s, 18H, ^{t}Bu), 1.40 (s, 18H, ^{t}Bu)
^{13}C NMR (125 MHz, CD_2Cl_2) δ_{13C} (ppm): 154.2 (C_{quat}, Phenylene Ar), 139.7 (C_{quat}, Ar), 139.1 (C_{quat}, Ar), 136.3 (C_{quat}, Ar), 129.5 (CH, Ar), 126.8 (C_{quat}, Ar), 124.8 (CH, Phenylene Ar), 123.9 (CH, Ar), 120.9 (CH, Phenylene Ar), 35.7 (C_{quat}, ^{t}Bu), 34.8 (C_{quat}, ^{t}Bu), 32.0 (CH_3, ^{t}Bu), 29.5 (CH_3, ^{t}Bu)
EA: Found: C, 70.60; H, 8.14; N, 4.75, Calc. for $C_{34}H_{46}AlClN_2O_2$: C, 70.75; H, 8.03; N, 4.85.

[^{H}**L**$_4$Al][BAr^F] (Complex **20**)



20

To a solution of **18** (10 mg, 0.017 mmol) in diethyl ether (2 mL) was added AgBAr^F (16.8 mg, 0.017 mmol). After 30 minutes of stirring at room temperature, the precipitated AgCl was removed using a syringe filter. The filtrate was dried *in vacuo* to yield **20** (with a coordinated diethyl ether molecule) in quantitative yields.
^{1}H NMR (400 MHz, $CDCl_3$) δ_{1H} (ppm): 7.72 (t broad, 8H, $^{-}$BAr^F), 7.54 (m, 6H, 4 × $^{-}$BAr^F + 2 × Phenylene), 7.38 (dq, 2H, Phenylene), 7.32 (d, $^{4}J_{HH}$ *= 2.3 Hz,* 2H, Ar-H), 7.28 (d, $^{4}J_{HH}$ *= 2.3 Hz,* 2H, Ar-H), 5.49 (s, 2H, N-H), 4.14 (s broad, 4H, Et-O-Et CH_2), 1.36 (s, 18H, ^{t}Bu), 1.30 (s, 18H, ^{t}Bu), 1.05 (t, $^{3}J_{HH}$ *= 6.8 Hz*, 6H, Et-O-Et CH_3*)*
^{13}C NMR (100 MHz, $CDCl_3$) δ_{13C} (ppm): 152.6 (C_{quat}, Ar), 141.8 (C_{quat}, Ar), 138.1 (C_{quat}, Ar), 135.4 (CH, BAr^F), 132.4 (C_{quat}, Ar), 130.8 (CH, Phenylene), 129.6 (C_{quat}, Ar), 129.2 (C_{quat}, Ar), 127.7 (CH, Phenylene), 126.5 (C_{quat}, Ar), 125.3 (CH, Ar), 123.8 (C_{quat}, Ar), 118.0 (CH, BAr^F), 117.4 (CH, Ar), 65.7 (CH_2, Et-O-Et) , 35.5 (C_{quat}, ^{t}Bu), 34.9 (C_{quat}, ^{t}Bu), 31.8 (CH_3, ^{t}Bu), 29.9 (CH_3, ^{t}Bu), 13.1 (CH_3, Et-O-Et)
EA: Found: C, 57.02; H, 5.04; N, 1.97, Calc. for $C_{70}H_{68}AlBF_{24}N_2O_3$: C, 56.84; H, 4.63; N, 1.89

6.4 General Procedure for Polymerisation Reactions

Reaction in solvent: In a glovebox, the desired amount of catalyst (~ 10 mg) was weighed out in a vial containing a stirrer bar. In a separate vial, the desired amount of monomer, co-catalyst, and solvent (to reach $[M]_0$ = 1 M) were dissolved. The resulting solution is added to the catalyst and the time was started. For high temperature polymerisations, the time is started when the vial is transferred to the hot plate. For kinetic studies, aliquots (0.1 mL) were periodically taken for analysis and quenched in *n*-pentane to stop any further reaction. If the monomer is a liquid, the aliquot is quenched in wet $CDCl_3$ and analysed directly to prevent evaporation. Samples were analysed by ^{1}H NMR spectroscopy to determine conversion by relative integration of the monomer and polymer signals.

Reaction in bulk: In a glovebox, the desired amount of LA is added to a vial equipped with an air-tight PTFE lid and containing the desired amount of catalyst (~ 10 mg). The vial is heated at the desired temperature in a silicone oil bath and the time recorded. The polymerisation is stopped once the mixture becomes too viscous to stir, upon which a sample is taken and quenched in pentane.

Polymerisation reactions with in-situ generation of the initiator: A solution of $Al(Et)_3$ in THF (1 mL, 0.017 M) was added to vial containing either H_2^{H}**L**$_1$ or H_2^{H}**L**$_2$ (0.017 mmol) and allowed to stir at room

temperature for 15 minutes. In a separate vial, *rac*-LA (250 mg; 1.7 mmol) was dissolved in THF (0.77 mL) to form a 2.2 M solution, to which ^{i}PA (1.3 µL; 0.017 mmol) was added using a Gilson pipette. Both vials were combined to start the polymerisation, which was run for a total of 4 hours. Aliquots were taken at 1 hour intervals and analysed by ^{1}H NMR spectroscopy and GPC.

Organocatalytic polymerisation reactions: In a glovebox, the desired catalyst (1 equiv.), (-)-sparteine (1 equiv.), and IPA (1 equiv.) were dissolved in DCM or THF to reach $[LA]_0$ = 1 M. The resulting solution was then added to *rac*-LA (20 equiv.) which was pre-weighed in a vial. An aliquot was taken after 24 hours and quenched in *n*-pentane to stop the reaction. Samples were analysed by ^{1}H NMR spectroscopy to determine conversion by relative integration of signals at 5.06 ppm (monomer) and 5.20 ppm (polymer).

Polymerisation reactions using scalemic mixtures of catalysts: Two solutions containing (*R,R*)-**15** and (*S,S*)-**15** were made up to a molarity of 10 mM. The appropriate amount of each was added to a vial containing a stirrer bar. To this 232 mg of LA (or 179 µL of ε-CL) was added and the time was started. Aliquots (0.1 mL) were periodically taken and quenched in *n*-pentane to stop any further reaction. In the case of ε-CL polymerisations, the aliquot was quenched in wet $CDCl_3$ and analysed directly to prevent evaporation. Samples were analysed by ^{1}H NMR spectroscopy to determine conversion by relative integration of the monomer and polymer signals.

Polymerisation reactions using complex **18**: To a vial containing a stirrer bar, the desired amount of **18** was weighed out and dissolved in the appropriate amount of DCM. 10 equivalents of CHO was added and the mixture was allowed to stir for 10 minutes. If the addition of a co-catalyst was required (*e.g.* $FcBAr^{F}$ or AgOTf), it was added after the 10 minute period and allowed to react with the activated complex for a further 5 minutes. Once the pre-activation was carried out, the desired amount of monomer was added and the time started. Aliquots were periodically taken and quenched in either *n*-pentane (for solid monomers) or wet $CDCl_3$ (for liquid monomers). These were analysed by ^{1}H NMR spectroscopy to determine conversion by relative integration of the monomer and polymer signals. If required, co-catalysts were added at the appropriate time points as solids.

Table 1. Regions for the monomer and polymer peaks in ^{1}H NMR spectroscopy ($CDCl_3$, 298 K)

Monomer	Monomer peak (ppm)	Polymer peak (ppm)
LA	5.02	5.15-5.30
β-BL	4.55	5.05-5.15
ε-CL	4.23	4.03-4.09
ε-DL	4.21	4.75-4.85
TMC	4.43	4.19-4.24
PDL	4.02-4.10	4.13-4.18

1. Save, M.; Schappacher, M.; Soum, A., *Macromol. Chem. Phys.* **2002,** *203*, 889-899.
2. Min, K. S.; Weyhermüller, T.; Bothe, E.; Wieghardt, K., *Inorg. Chem.* **2004,** *43*, 2922-2931.
3. Meppelder, G.-J. M.; Fan, H.-T.; Spaniol, T. P.; Okuda, J., *Organometallics* **2009,** *28*, 5159-5165.
4. Sokolenko, V. A.; Svirskaya, N. M.; Kogai, T. I.; Karpova, M. S.; Pavlenko, N. I., *Russ. J. Appl. Chem.* **2008,** *81*, 509-510.
5. Blackmore, K. J.; Lal, N.; Ziller, J. W.; Heyduk, A. F., *Eur. J. Inorg. Chem.* **2009,** *2009*, 735-743.

Appendices

Appendix A: NMR Data

A.1 Characterisation of Pro-Ligands

A.1.1 Chapter 2

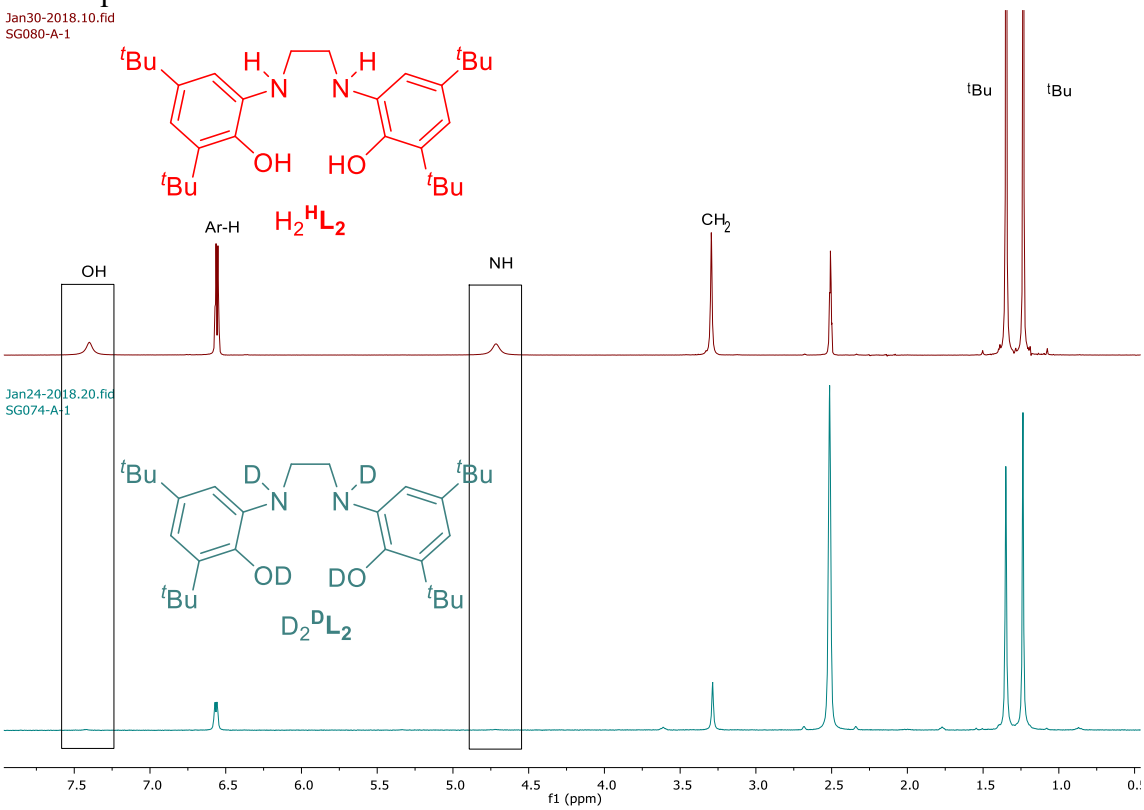


Figure A1. Stacked ^{1}H NMR spectra (DMSO-d$_6$, 24 °C) of $\mathbf{H_2^HL_2}$ (top) and $\mathbf{D_2^DL_2}$ (bottom) showing disappearance of the N-H and O-H signals upon deuteration of the pro-ligand.

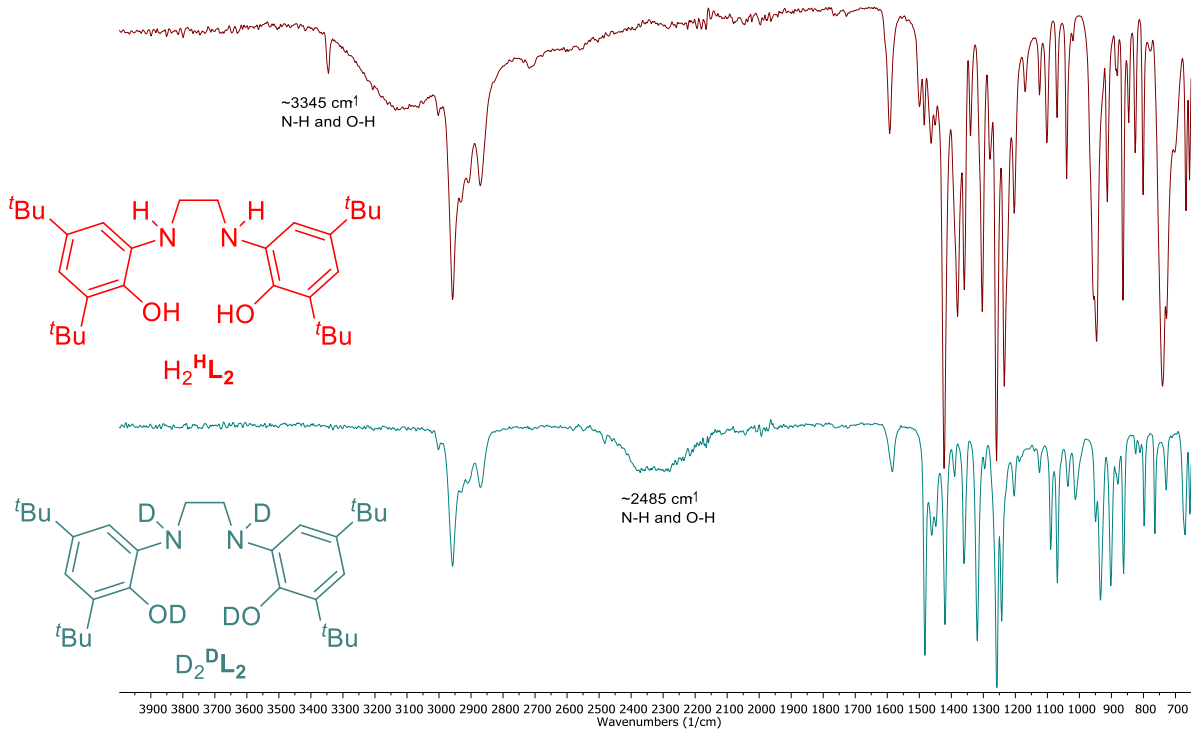


Figure A2. Stacked IR spectra of $\mathbf{H_2^HL_2}$ (top) and $\mathbf{D_2^DL_2}$ (bottom) showing a shift in the O-H and N-H stretching signals upon deuteration of the pro-ligand.

A.1.2 Chapter 3

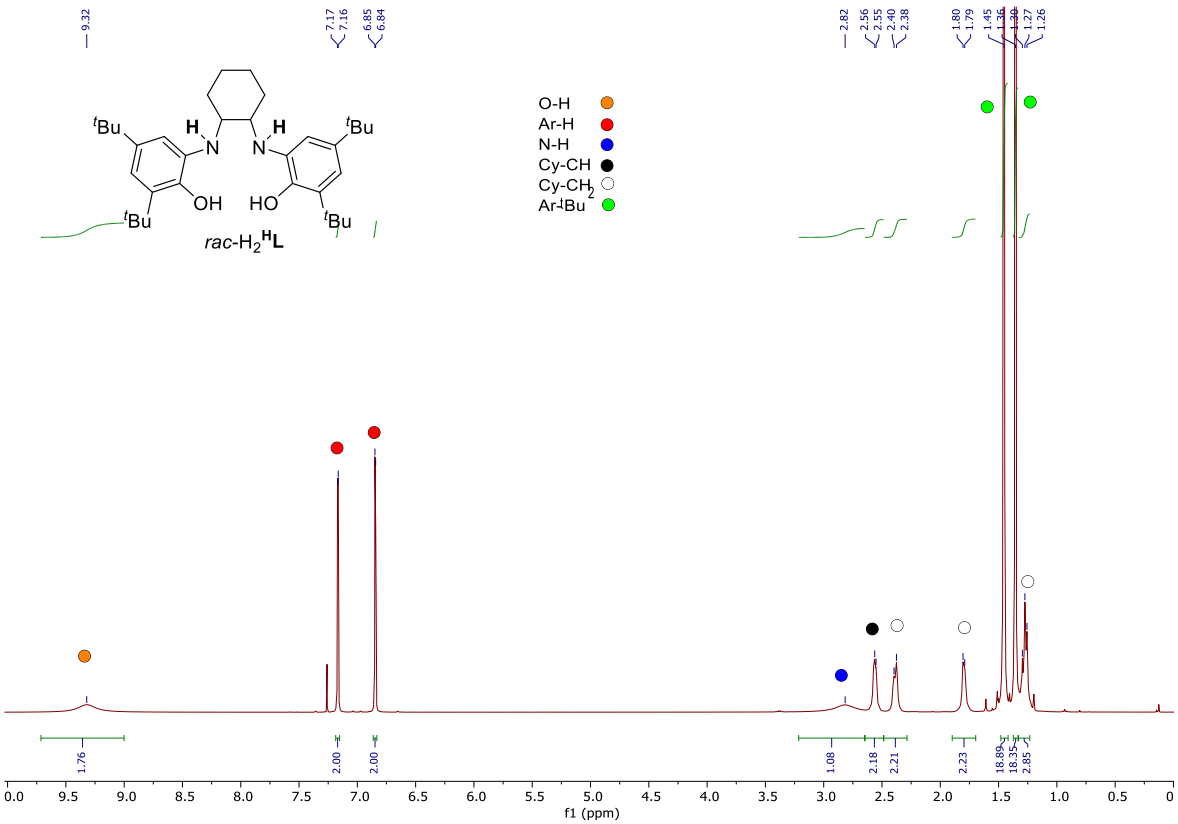


Figure A3. ^{1}H NMR spectrum ($CDCl_3$, 298 K) of *rac*-H_2**^{H}L$_3$**.

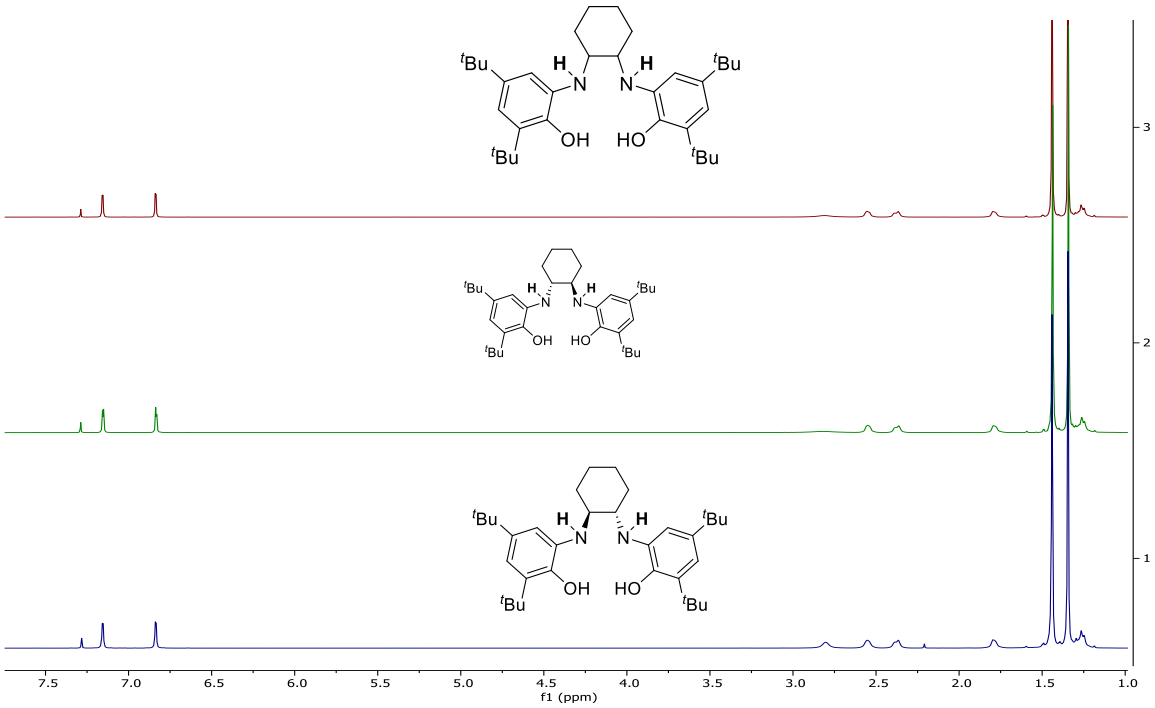


Figure A4. Stacked ^{1}H NMR spectra ($CDCl_3$, 298 K) of *rac*-H_2**^{H}L$_3$** (top), (*R,R*)- H_2**^{H}L$_3$** (middle), and (*S,S*)- H_2**^{H}L$_3$** (bottom) showing identical traces.

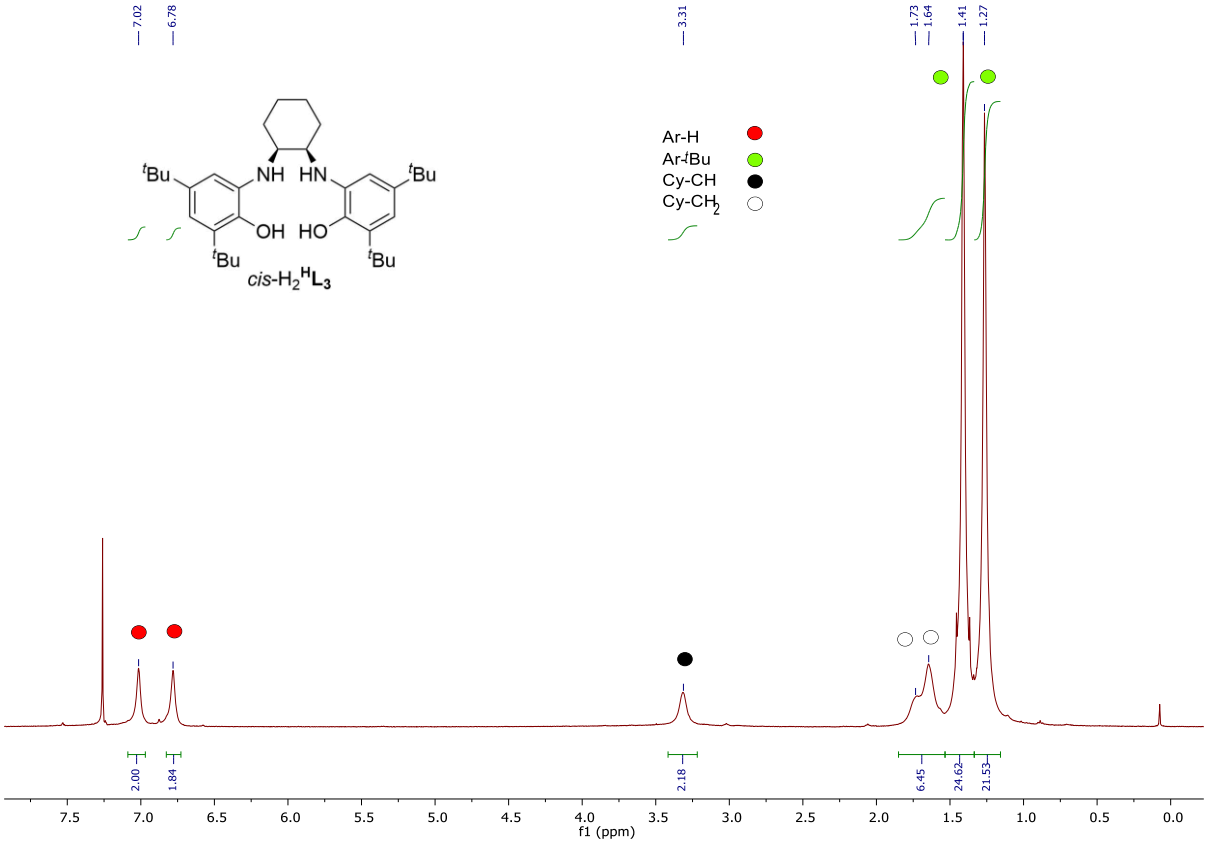


Figure A5. ^{1}H NMR spectrum ($CDCl_3$, 298 K) of *cis*-H_2**^{H}L$_3$**.

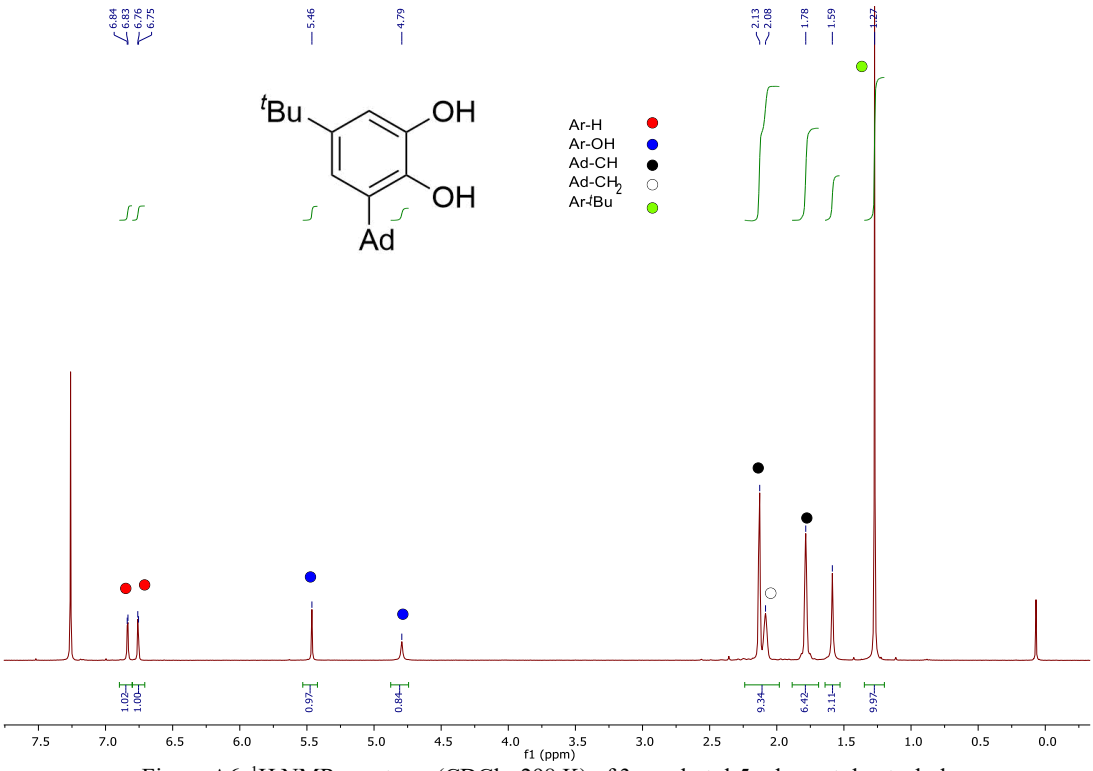


Figure A6. ^{1}H NMR spectrum ($CDCl_3$, 298 K) of 3-*tert*-butyl-5-adamantyl-catechol.

A.2 Characterisation of Complexes and Reactivity

A.2.1 Chapter 2

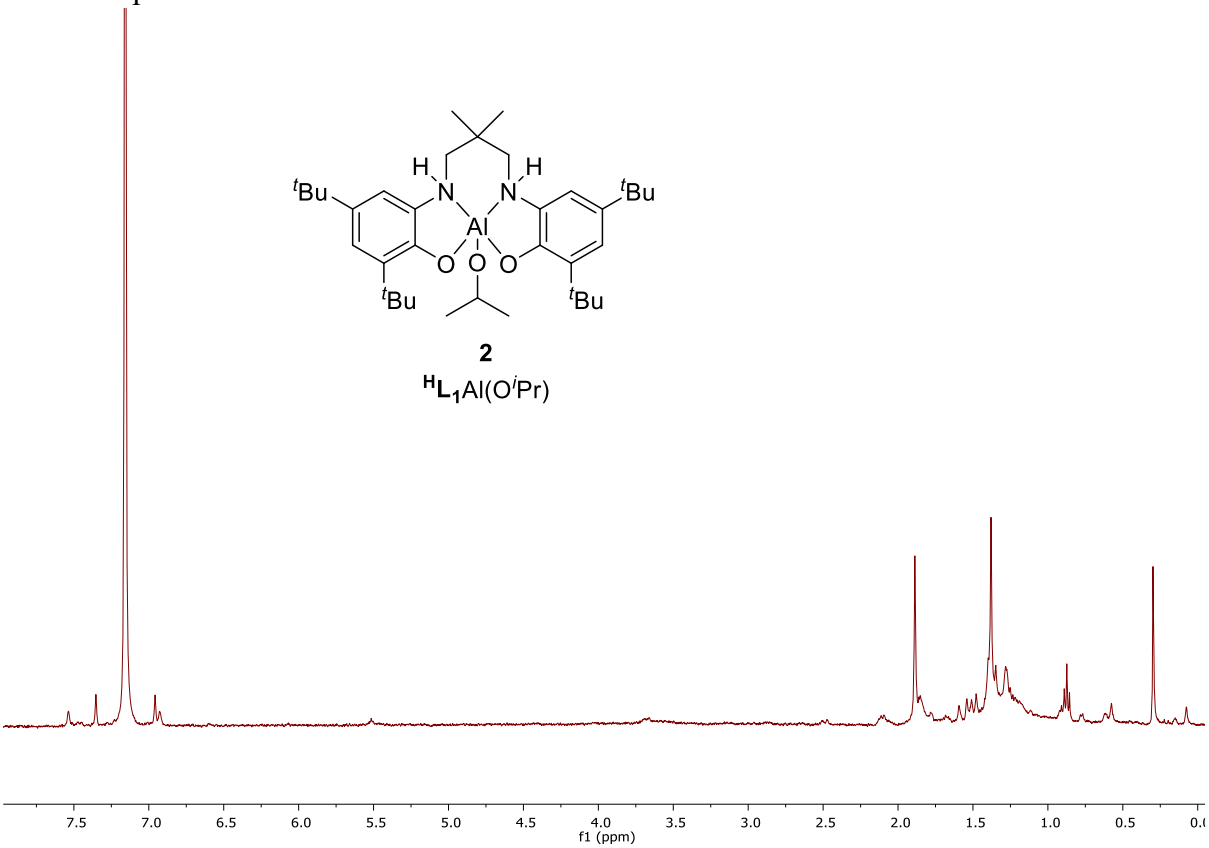


Figure A7. ^{1}H NMR spectrum (C_6D_6, 24 °C) of $\mathbf{L_1}^{\mathbf{H}}$Al(O^{i}Pr) (**2**).

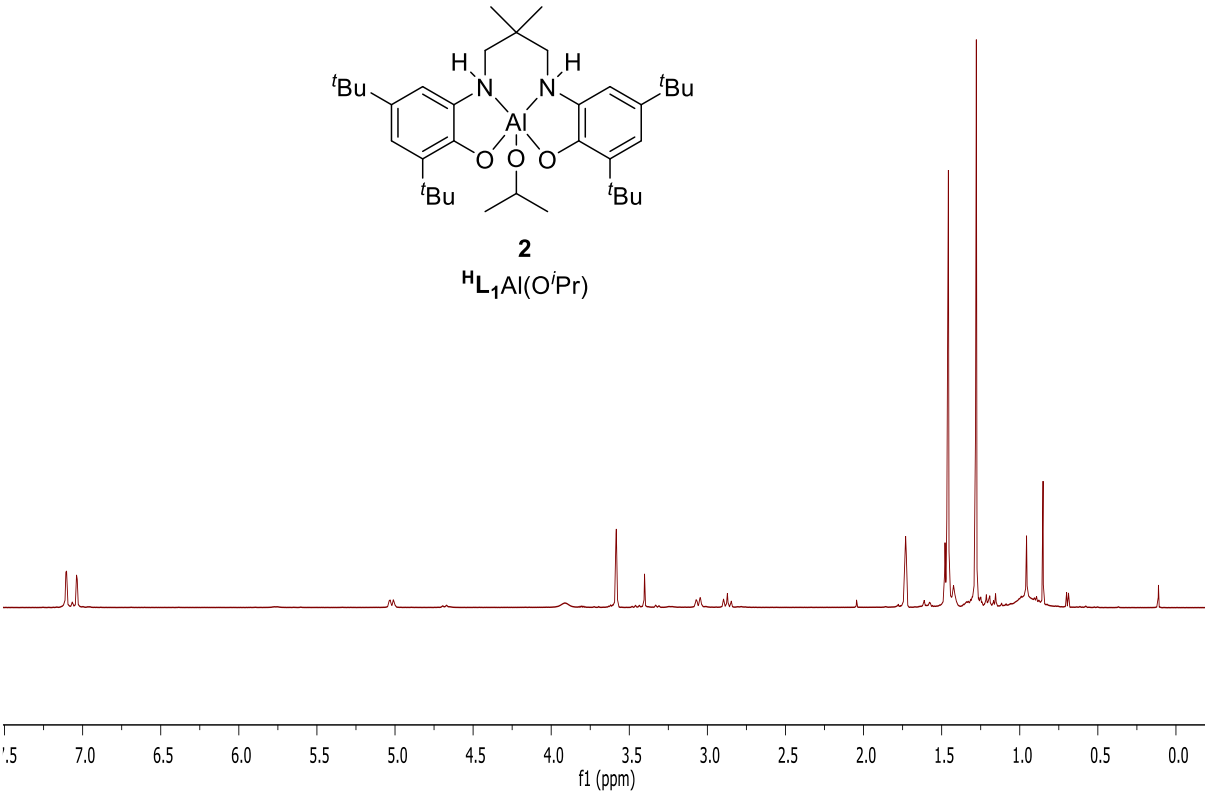


Figure A8: ^{1}H NMR spectrum (THF-d_8, 24 °C) of $^{\mathbf{H}}$LAl(O^{i}Pr) (**2**).

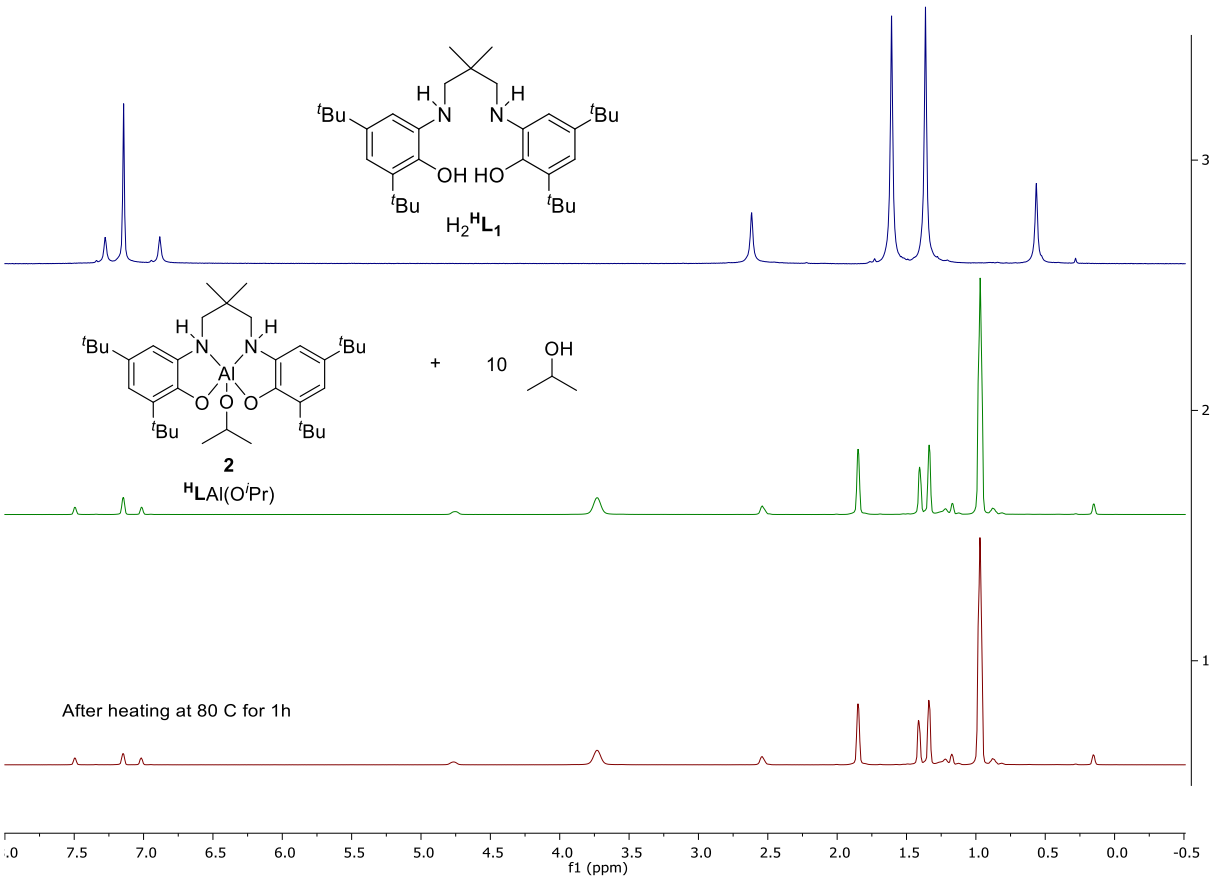


Figure A9. Stacked ^{1}H NMR spectra (C6D6, 24 °C) of $H_2{}^{H}L_1$ (top), $^{H}L_1Al(O^iPr)$ with 10 eq. of ^{i}PA (middle) and after heating at 80 °C for 1 hour (bottom) showing stability of the complex in "immortal" polymerisation.

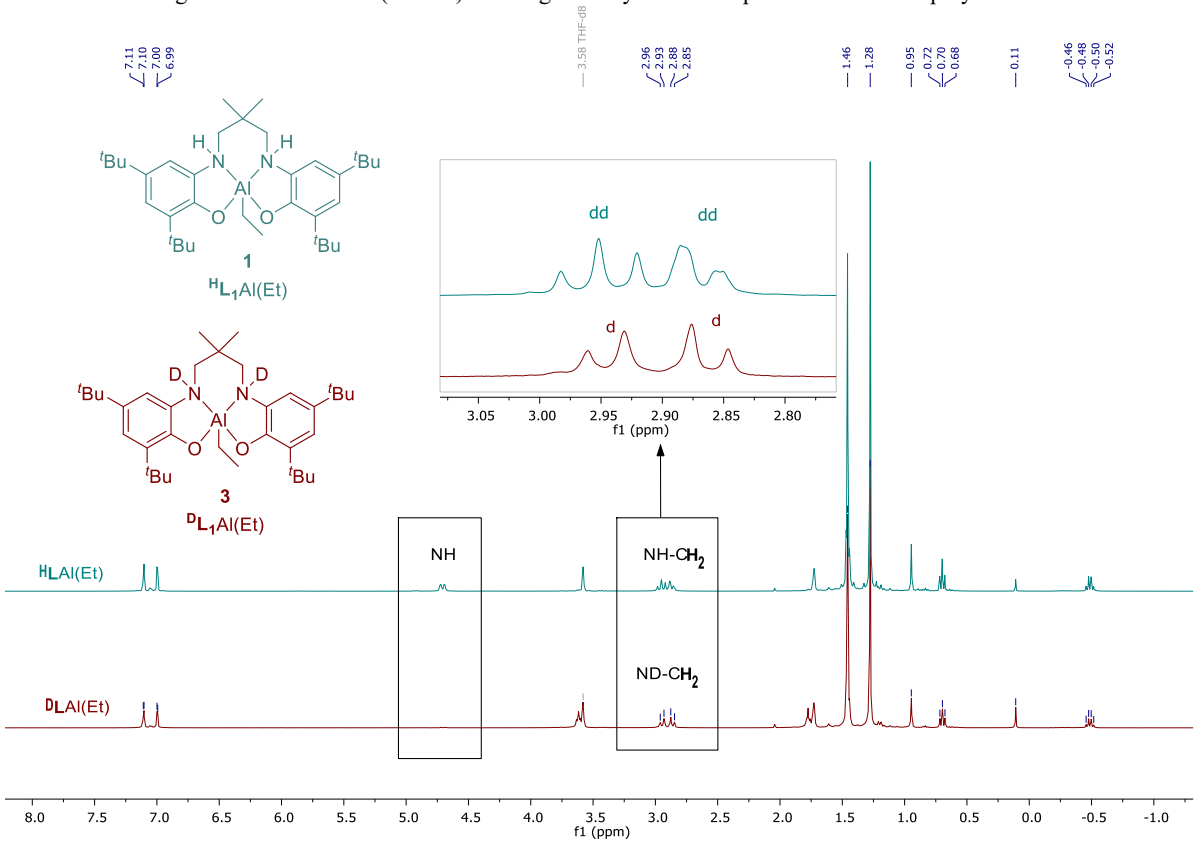


Figure A10: Stacked ^{1}H NMR spectra (THF_d8, 24 °C) of $^{H}L_1Al(Et)$ (**1**) and $^{D}L_1Al(Et)$ (**3**) showing the absence of NH signals and ^{3}J couplings for methylene signals (2.80 - 3.00ppm) in the $^{D}l_1Al(Et)$ (**3**) ^{1}H NMR spectrum.

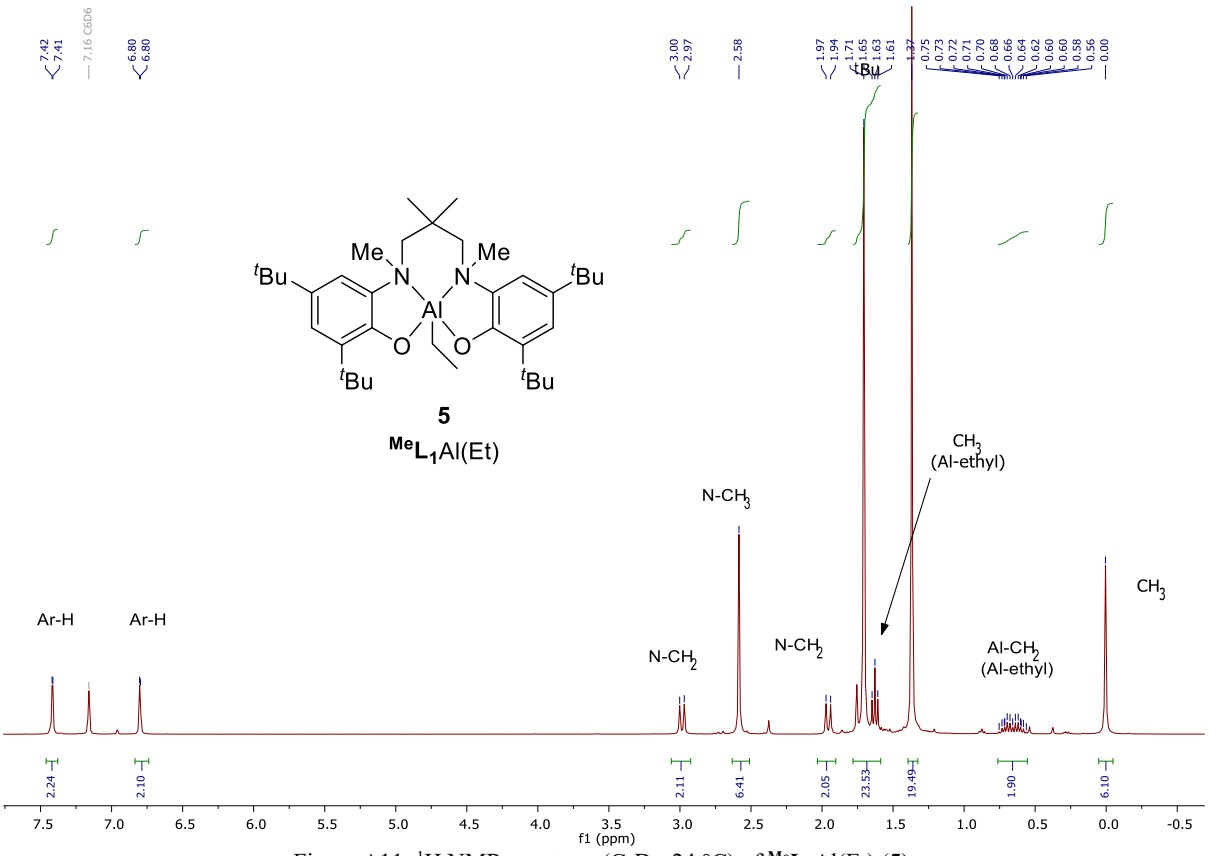


Figure A11: ^{1}H NMR spectrum (C_6D_6, 24 °C) of ^{Me}**L**$_1$Al(Et) (**5**).

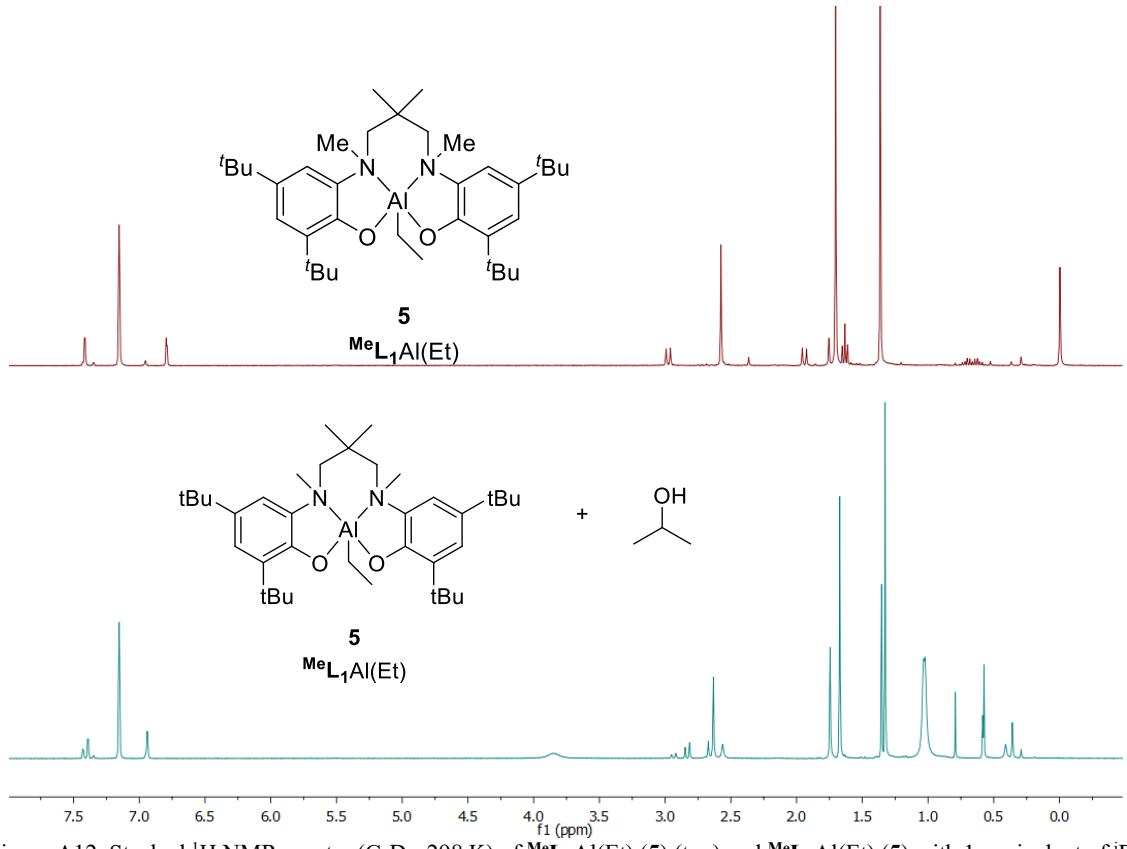


Figure A12. Stacked ^{1}H NMR spectra (C_6D_6, 298 K) of ^{Me}**L**$_1$Al(Et) (**5**) (top) and ^{Me}**L**$_1$Al(Et) (**5**) with 1 equivalent of ^{i}PA showing a transformation of the complex upon addition of the alcohol.

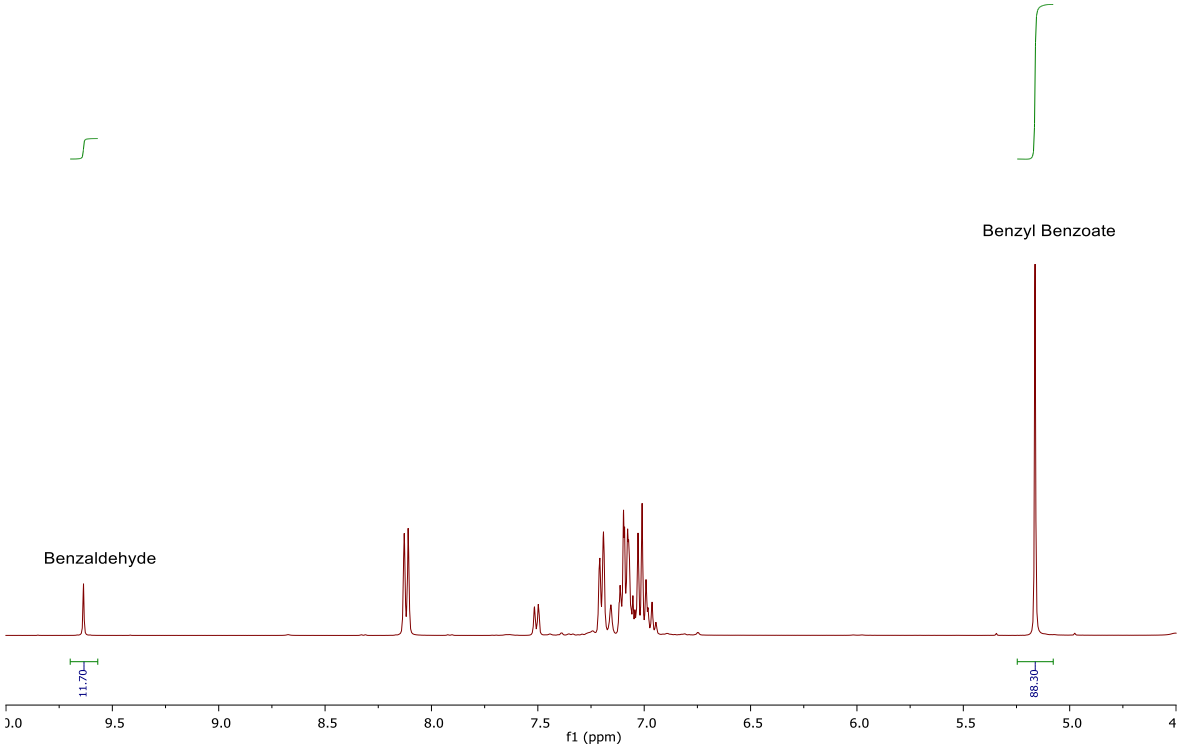


Figure A13. ^{1}H NMR spectrum showing the conversion of benzaldehyde to benzyl benzoate by **11** through the Tishchenko reaction.

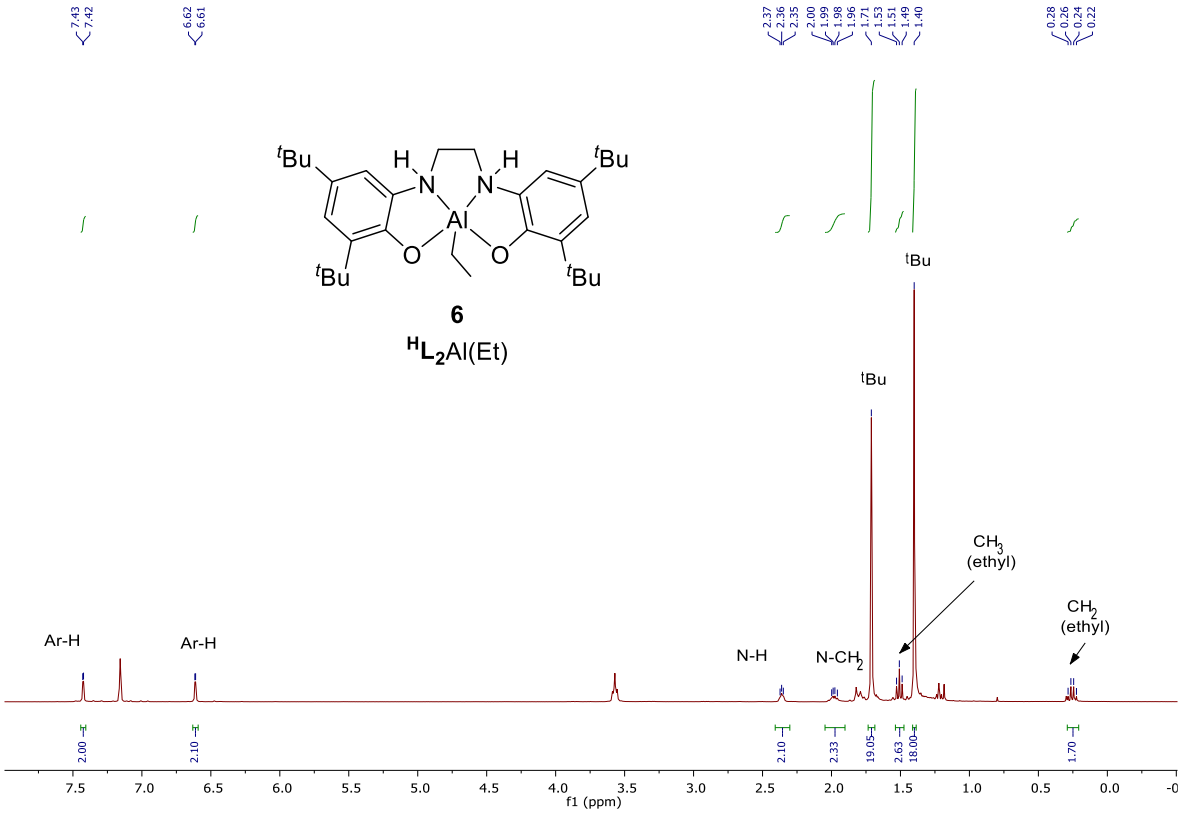


Figure A14. ^{1}H NMR spectrum (C_6D_6, 24 °C) of ^{H}**L**$_2$Al(Et) (**6**).

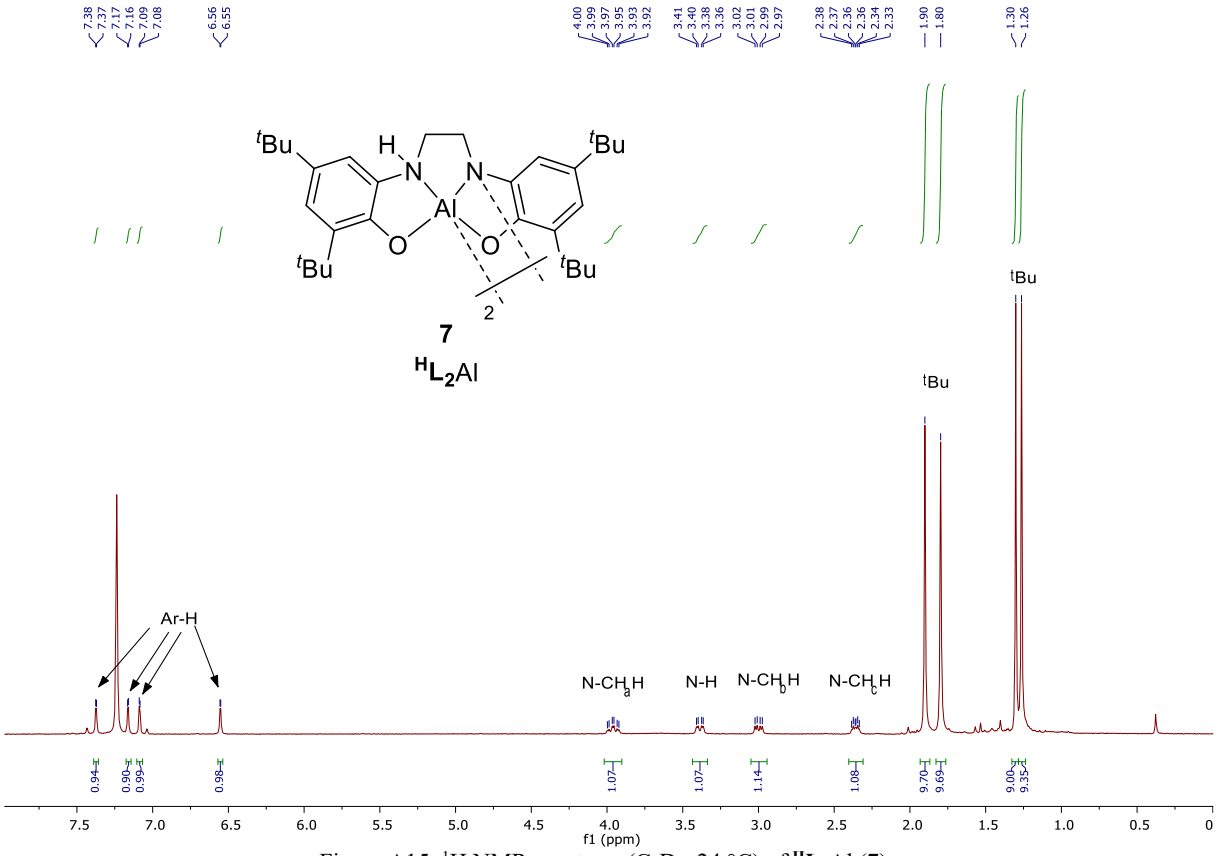


Figure A15. ^{1}H NMR spectrum (C_6D_6, 24 °C) of ^{H}**L**$_2$Al (**7**).

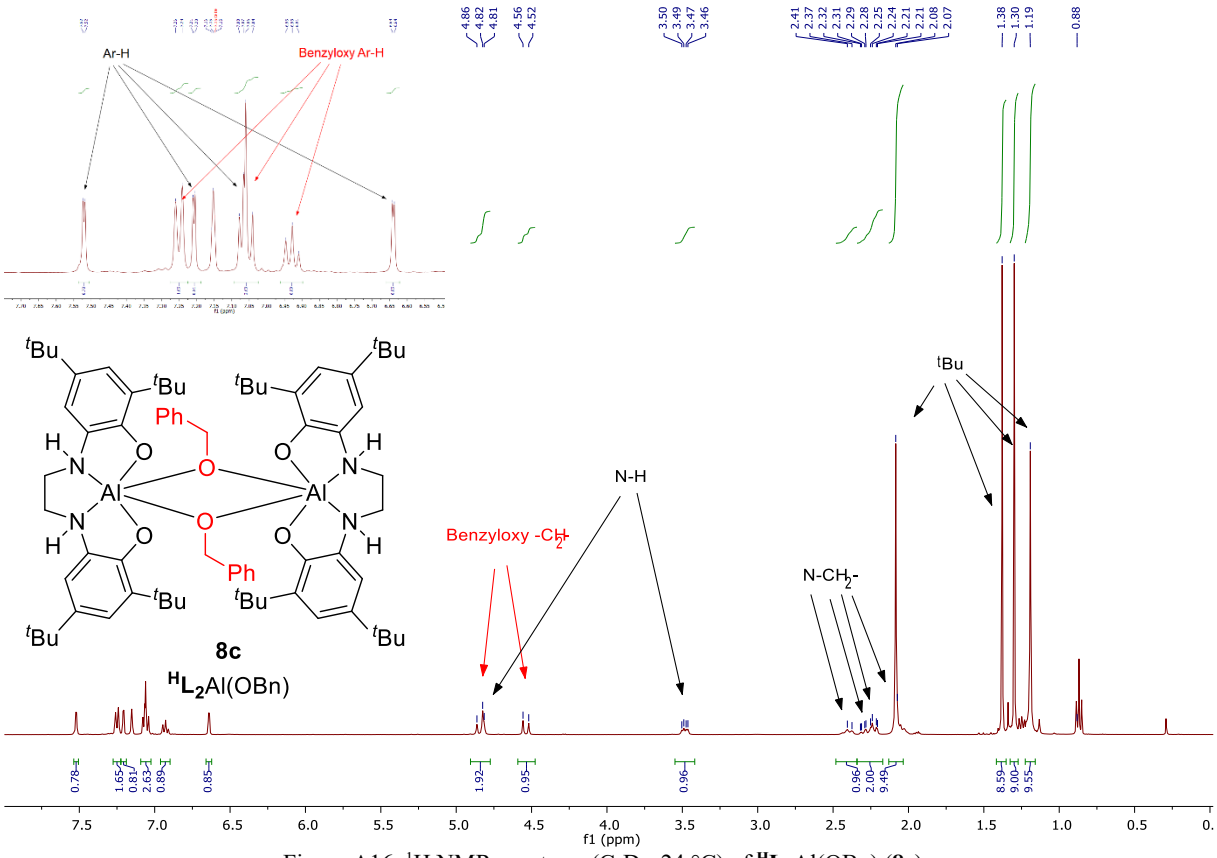


Figure A16. ^{1}H NMR spectrum (C_6D_6, 24 °C) of ^{H}**L**$_2$Al(OBn) (**8c**).

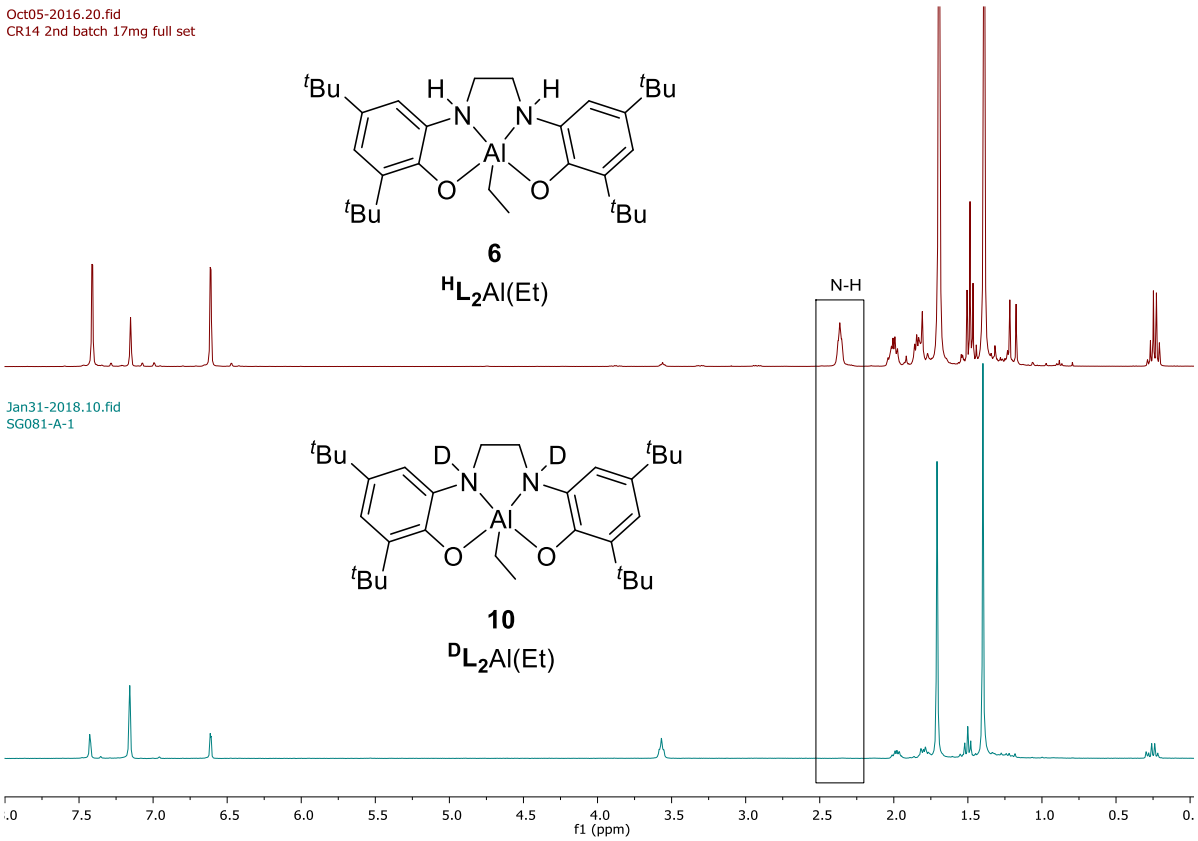


Figure A17. Stacked ^{1}H NMR spectra (C_6D_6, 298 K) of ^{H}**L**$_2$Al(Et) (**6**) and ^{D}**L**$_2$Al(Et) (**10**) showing the absence of NH signals in the ^{D}**L**$_2$Al(Et) (**10**) ^{1}H NMR spectrum.

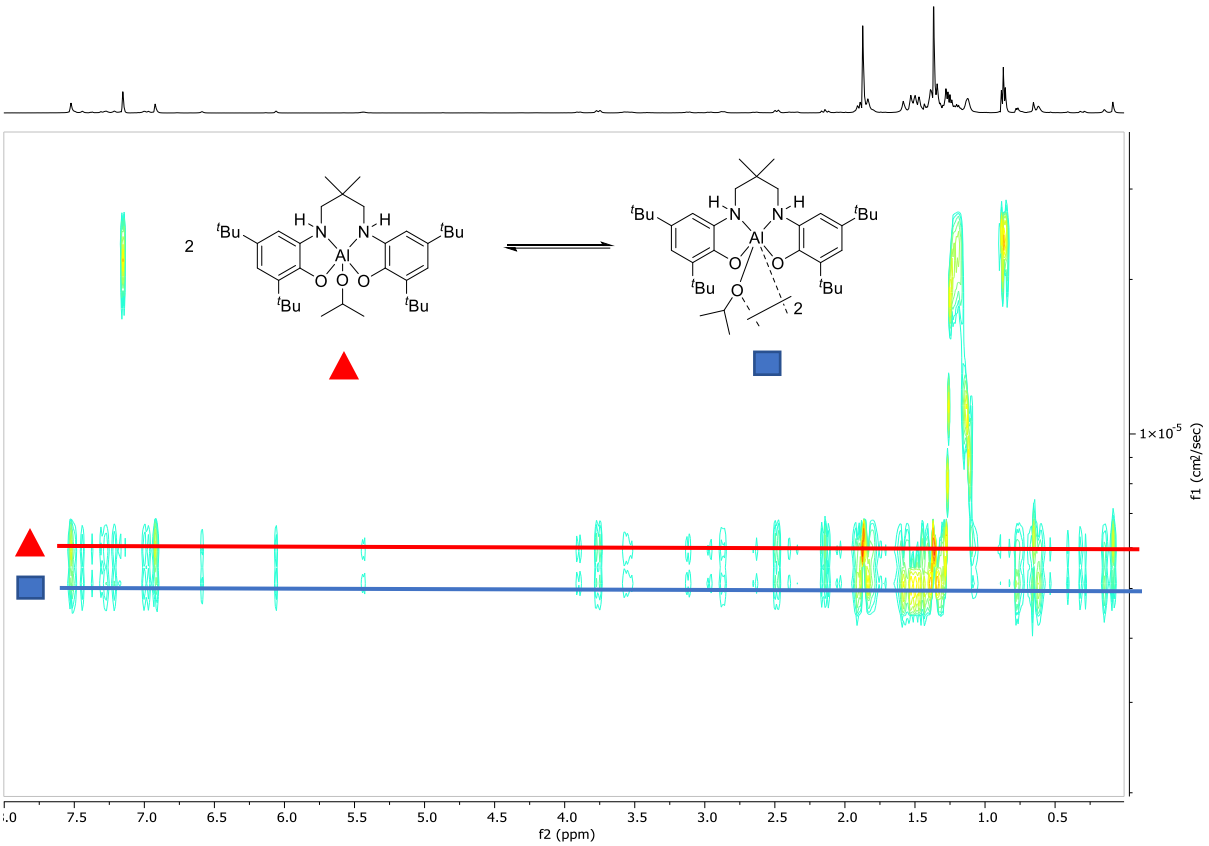


Figure A18. DOSY NMR spectrum (C_6D_6, 298 K) of ^{H}**L**$_1$Al(O^{i}Pr) (**2**) showing a monomer-dimer exchange in solution (as determined using in-house external calibration).

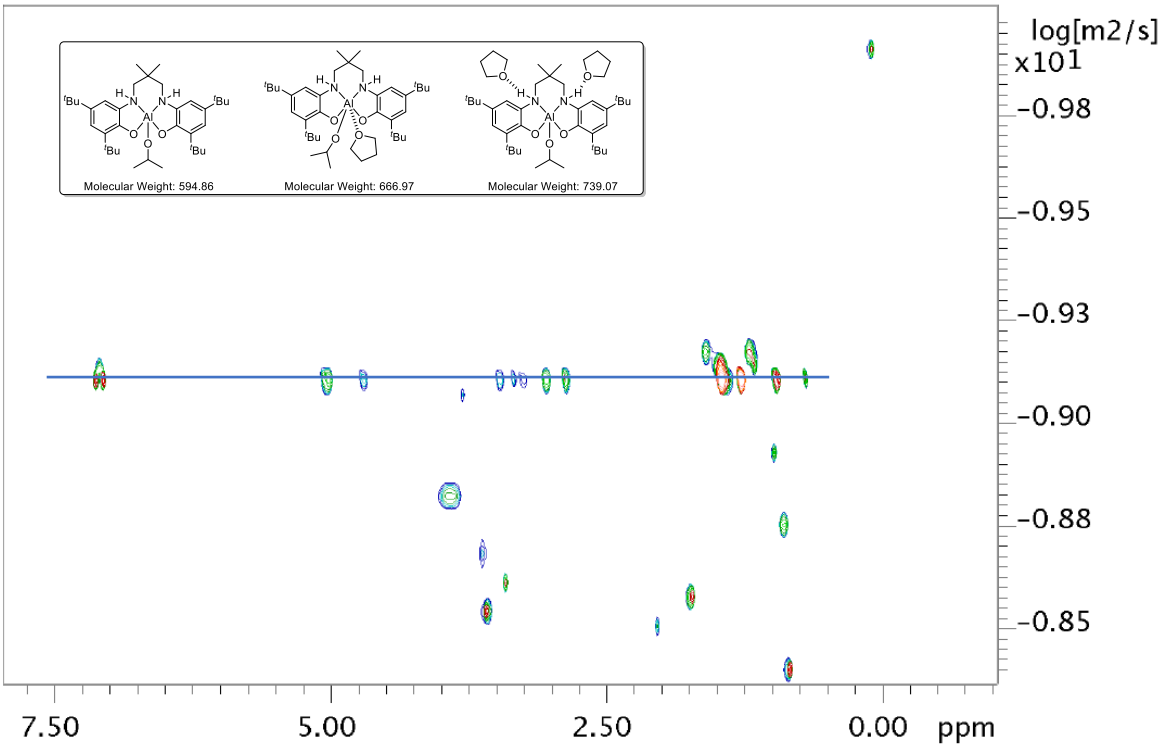


Figure A19: DOSY NMR spectrum (THF-d_8, 298 K) of ^{H}**L**Al(O^{i}Pr) (**2**) showing a monomeric structure in solution (with potential coordination of THF molecules as per insert) using an in-house external calibration The insert describes the different possible coordination of THF on complex **2** along with the corresponding molecular weight in line with the DOSY results.[1]

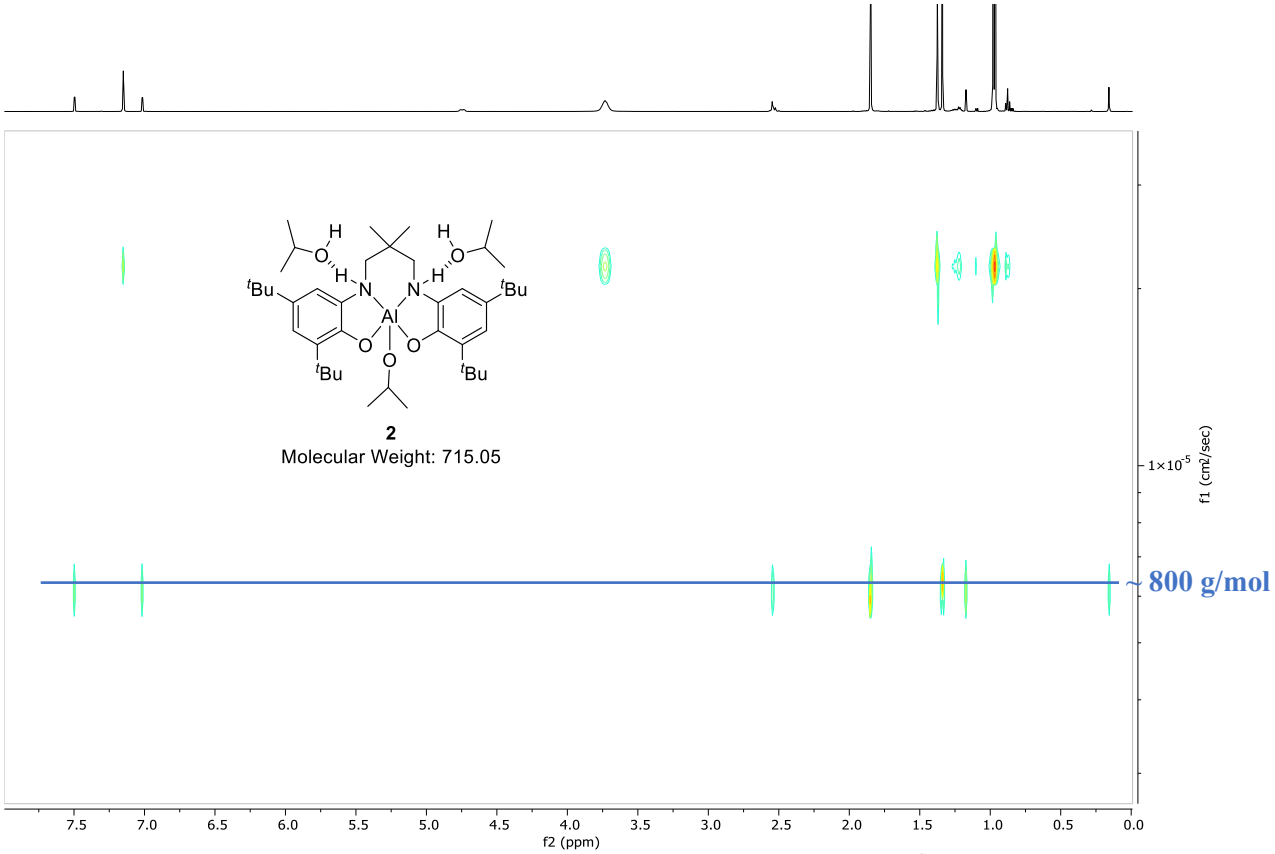


Figure A20. DOSY NMR spectrum (C_6D_6, 298 K) of ^{H}**L**$_1$Al(O^{i}Pr) (**2**) with 10 equivalents of ^{i}PA showing a mononuclear structure in solution under immortal conditions (as determined using in-house external calibration).

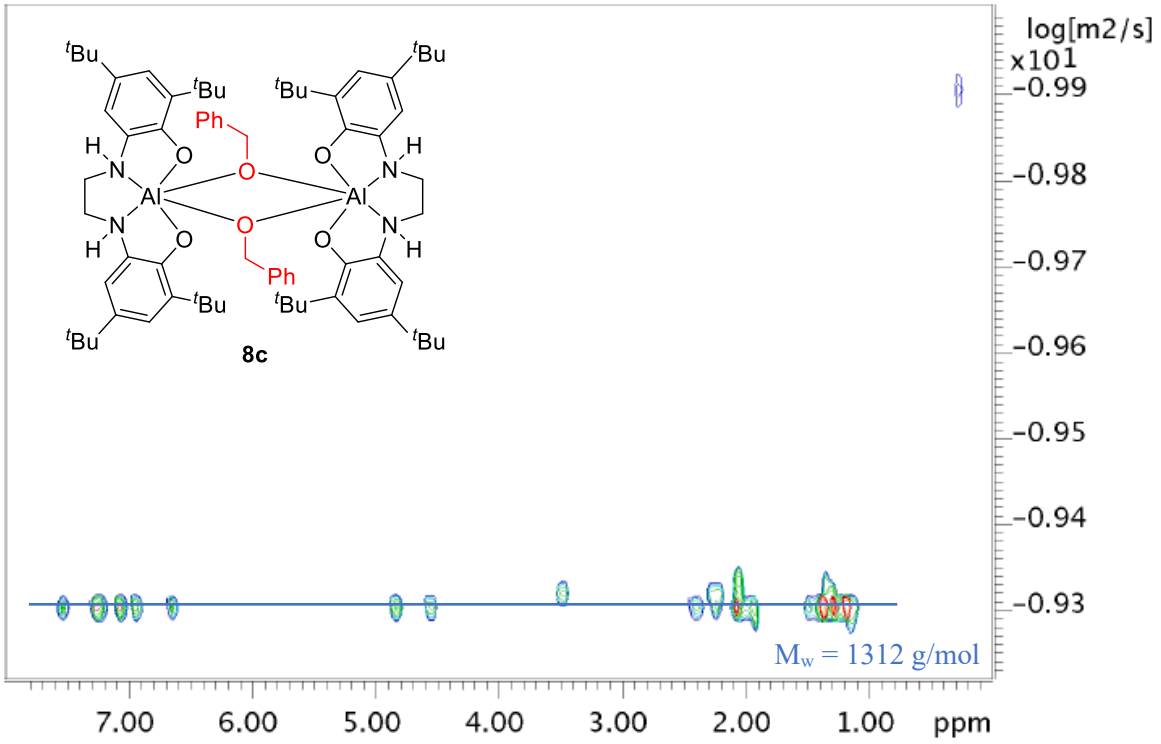


Figure A21. DOSY NMR spectrum (C_6D_6, 298 K) of $^{H}L_2Al(OBn)$ (**8c**) showing a dinuclear structure in solution (as determined using in-house external calibration).

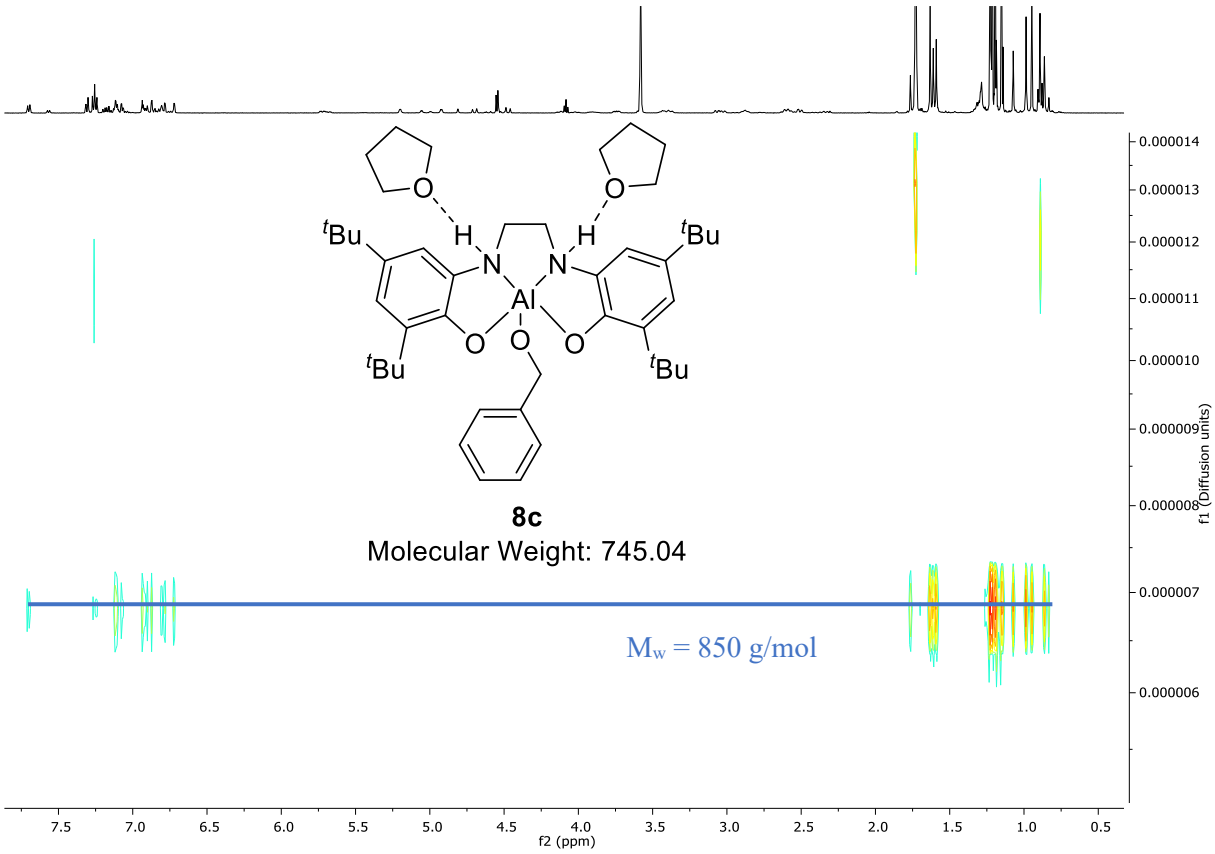


Figure A22. DOSY NMR spectrum (THF-d_8, 298 K) of $^{H}L_2Al(OBn)$ (**8c**) showing a mononuclear structure in solution (as determined using in-house external calibration).

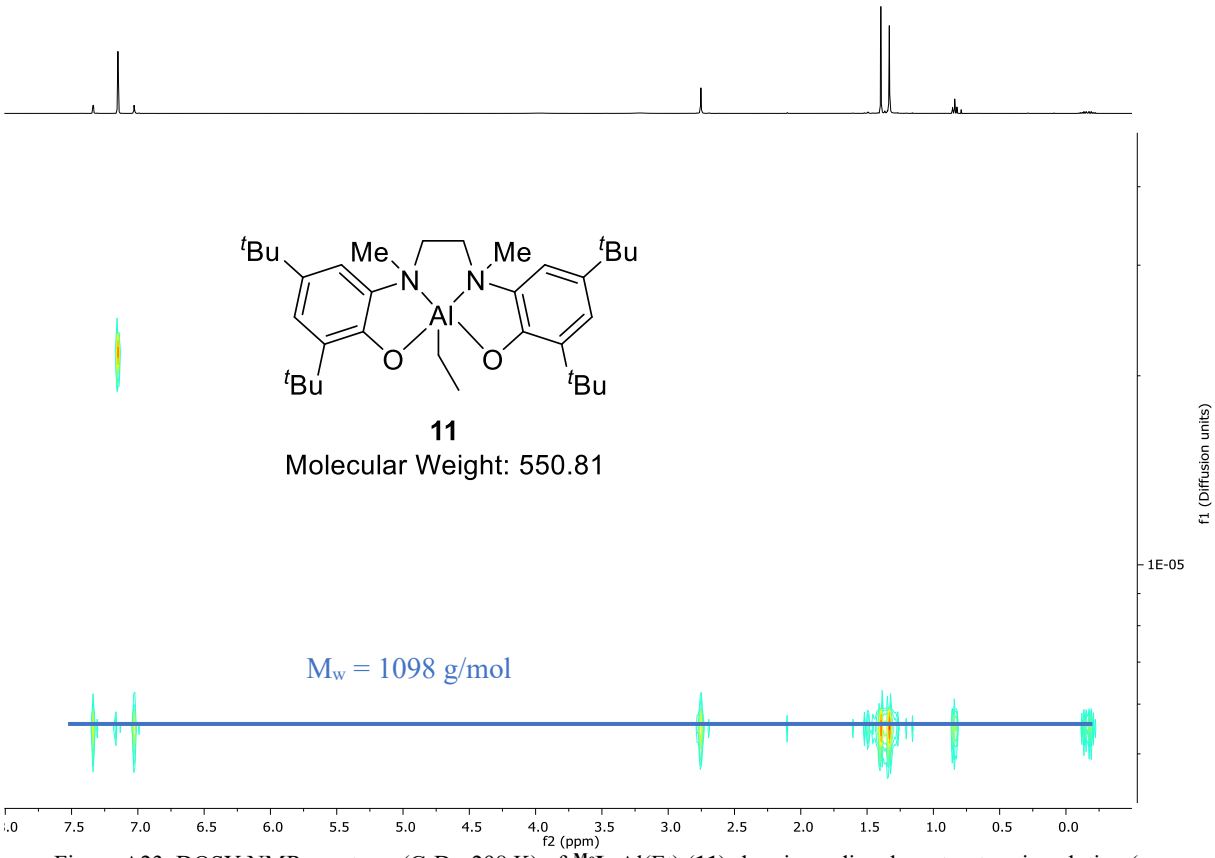


Figure A23. DOSY NMR spectrum (C_6D_6, 298 K) of ^{Me}**L**$_2$Al(Et) (**11**) showing a dinuclear structure in solution (as determined using in-house external calibration).

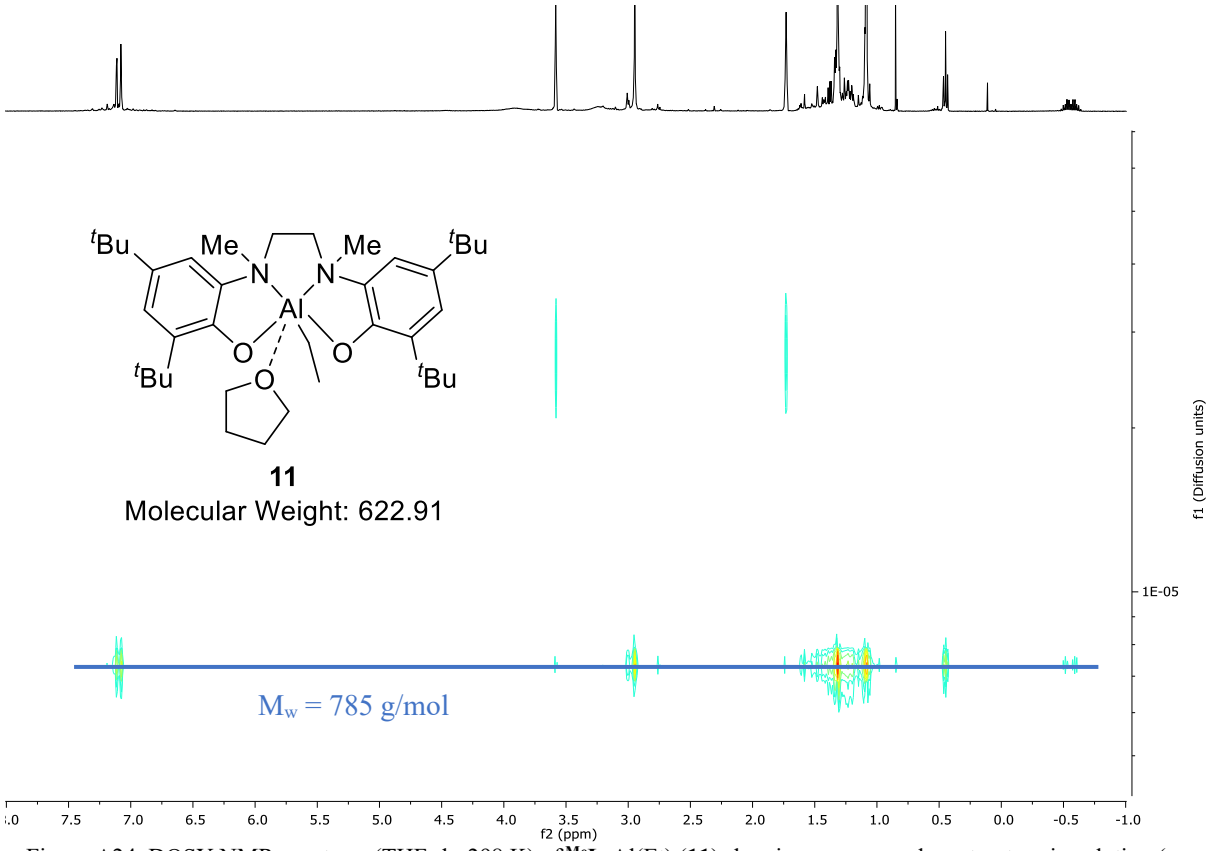


Figure A24. DOSY NMR spectrum (THF-d_8, 298 K) of ^{Me}**L**$_2$Al(Et) (**11**) showing a mononuclear structure in solution (as determined using in-house external calibration).

A.2.2 Chapter 3

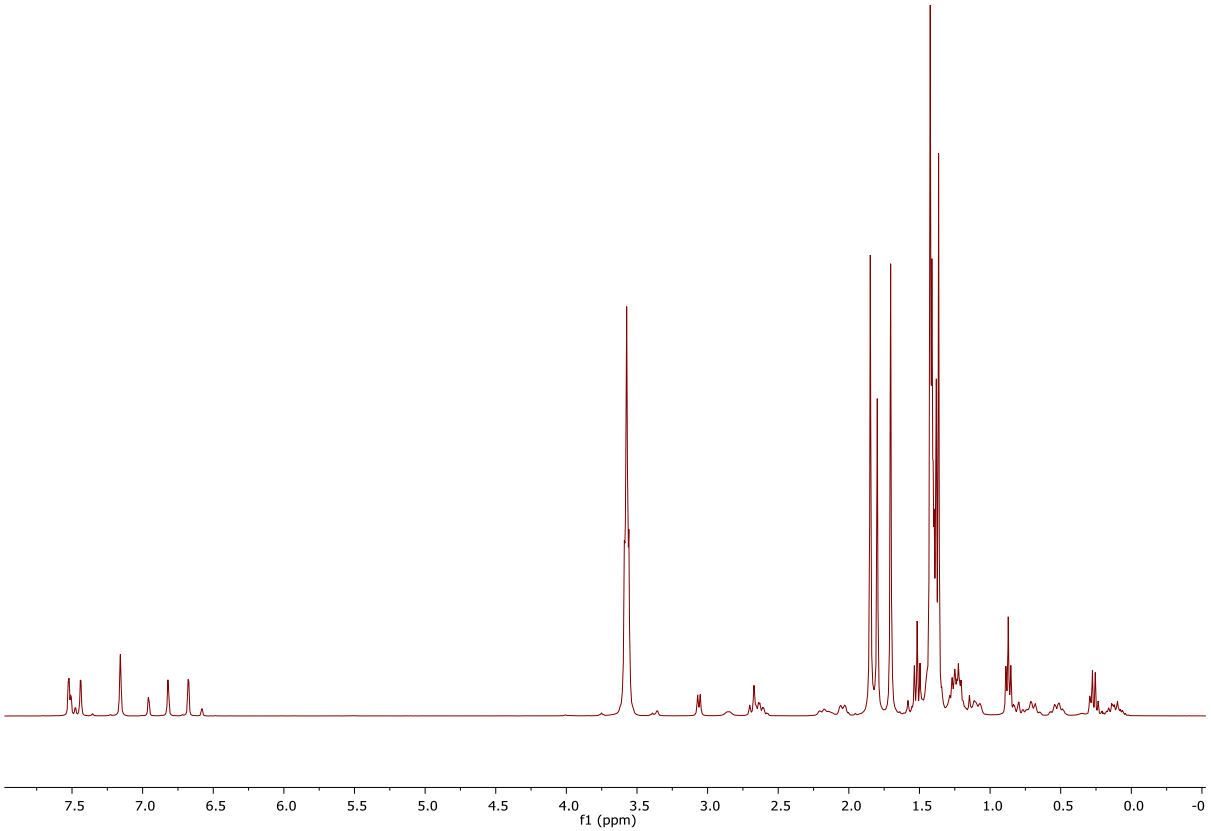


Figure A25. ^{1}H NMR spectrum (C_6D_6, 298 K) of *rac*-**mix12** showing a mixture of products formed.

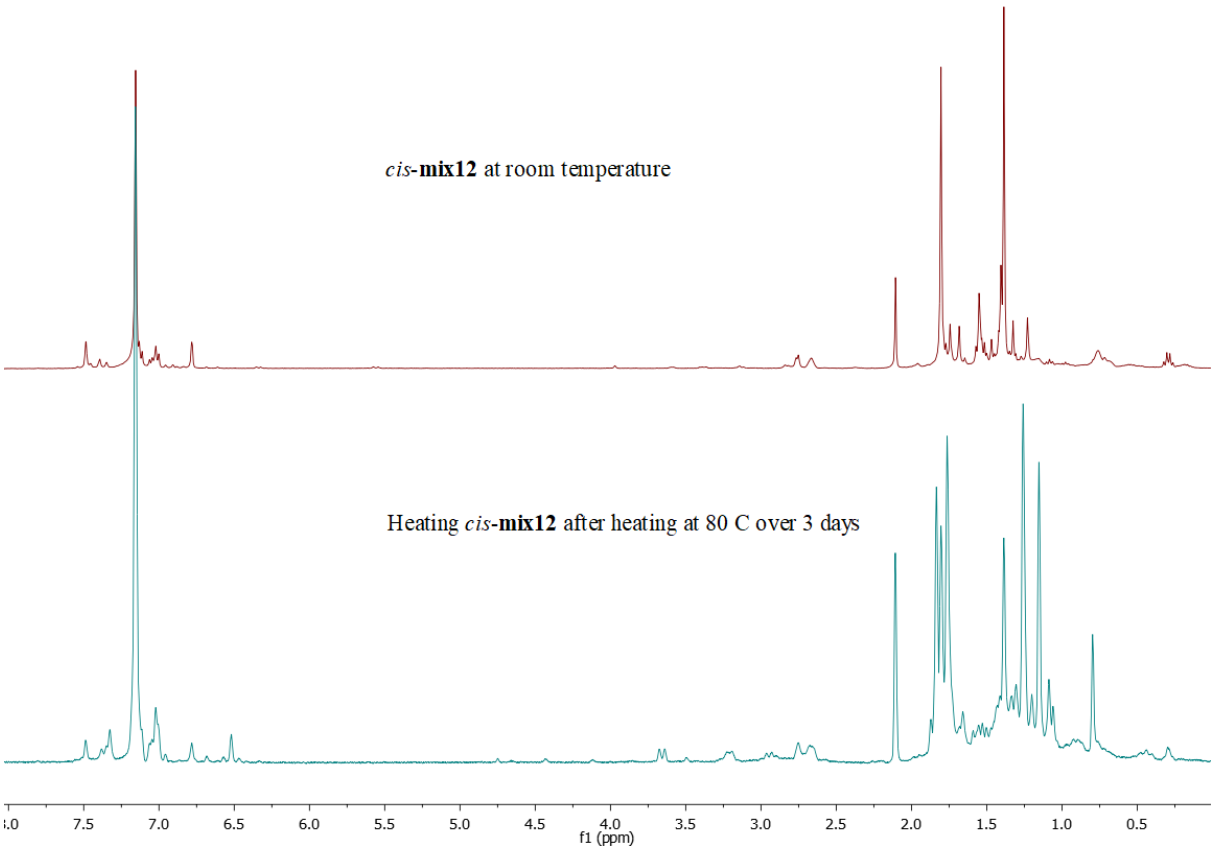


Figure A26. Stacked ^{1}H NMR spectra (C_6D_6, 298 K) showing *cis*-**mix12** (top) and its product after heating it at 80 °C over 3 days (bottom).

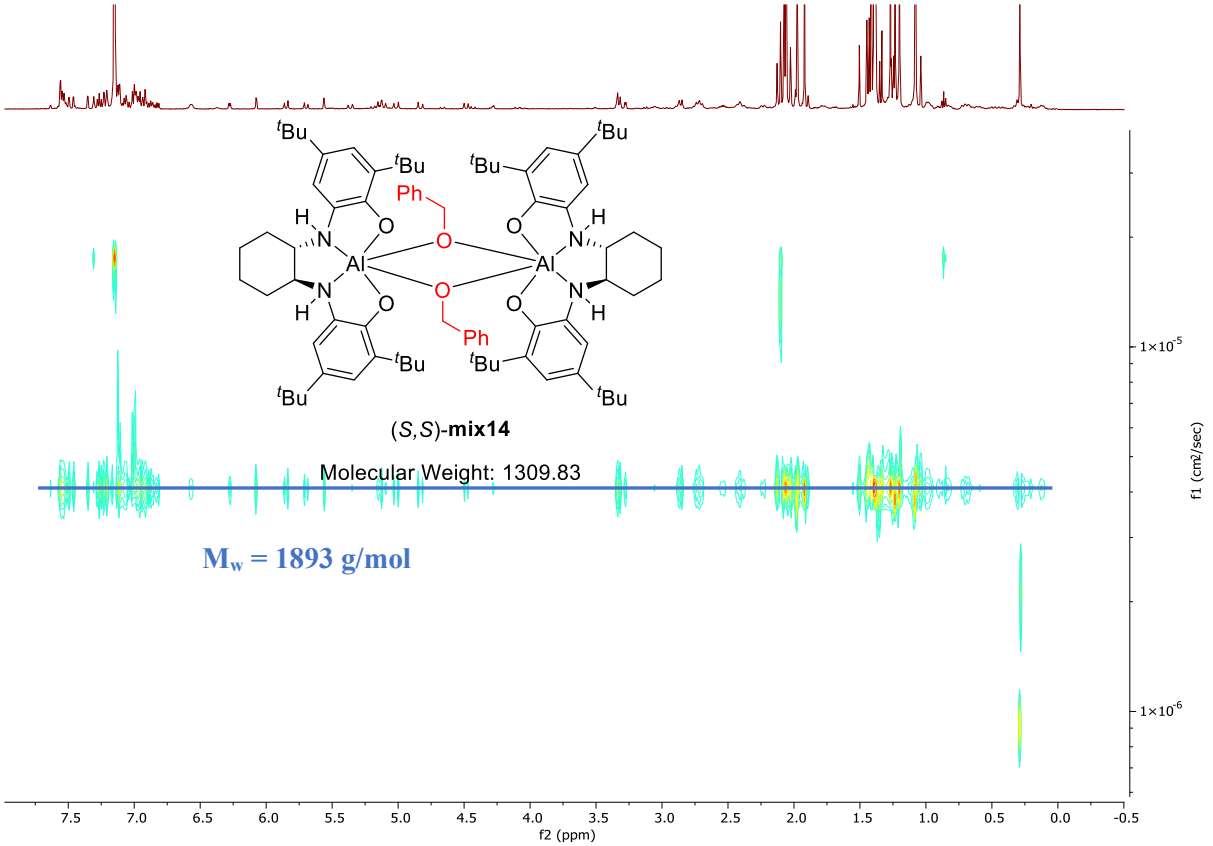


Figure A27. DOSY NMR (C_6D_6, 298 K) of (*S,S*)-**mix14** showing dimeric structures in solution.

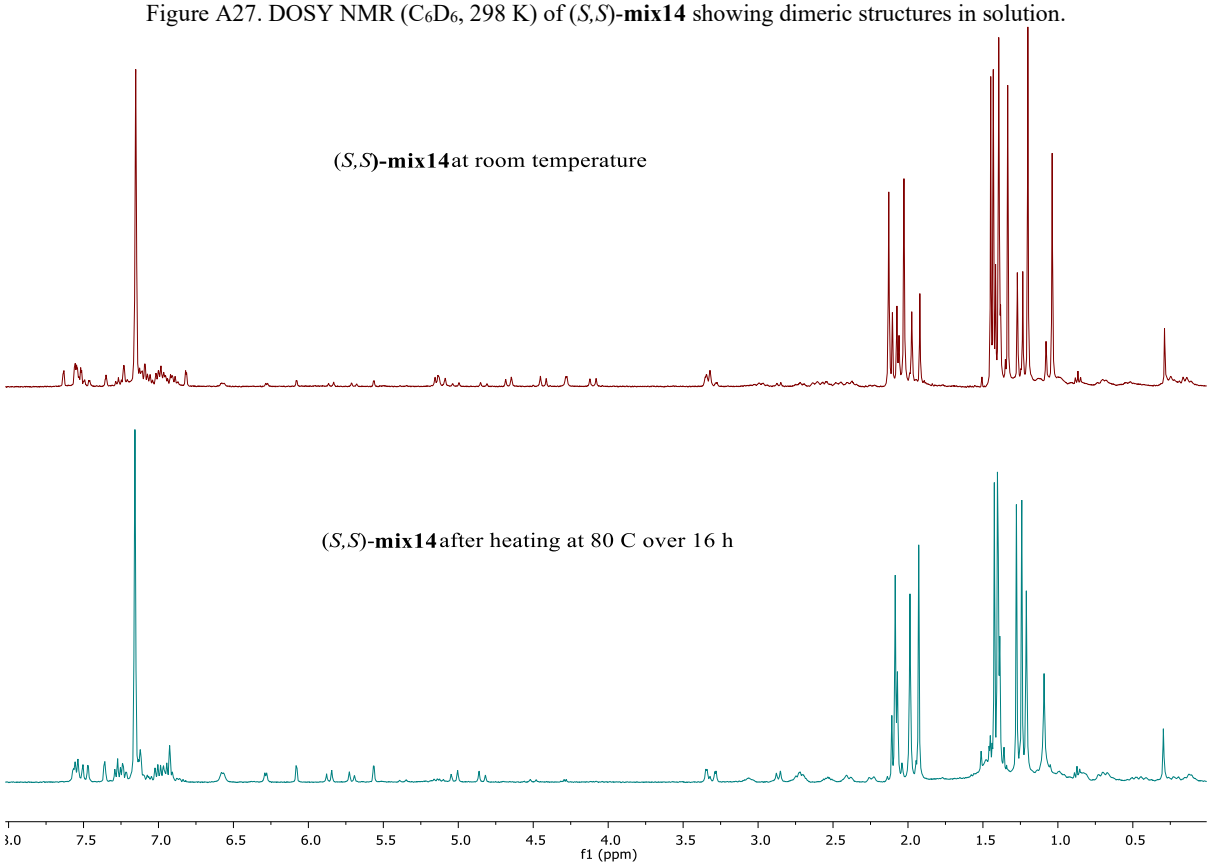


Figure A28. Stacked ^{1}H NMR spectra (C_6D_6, 298 K) of (*S,S*)-**mix14** at room temperature (top) and after heating at 80 °C overnight (bottom) showing no resolution.

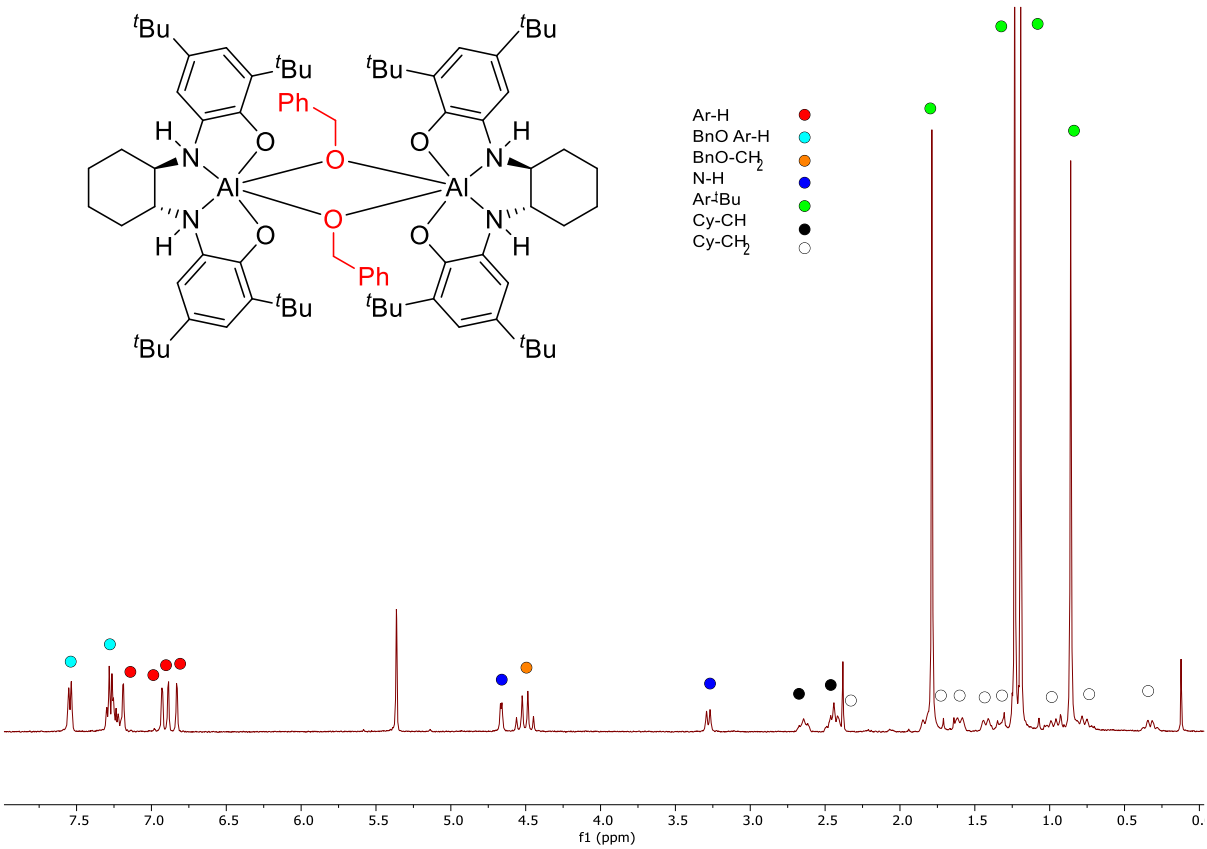


Figure A29. ^{1}H NMR spectrum (CD_2Cl_2, 298 K) of *rac*-**14**.

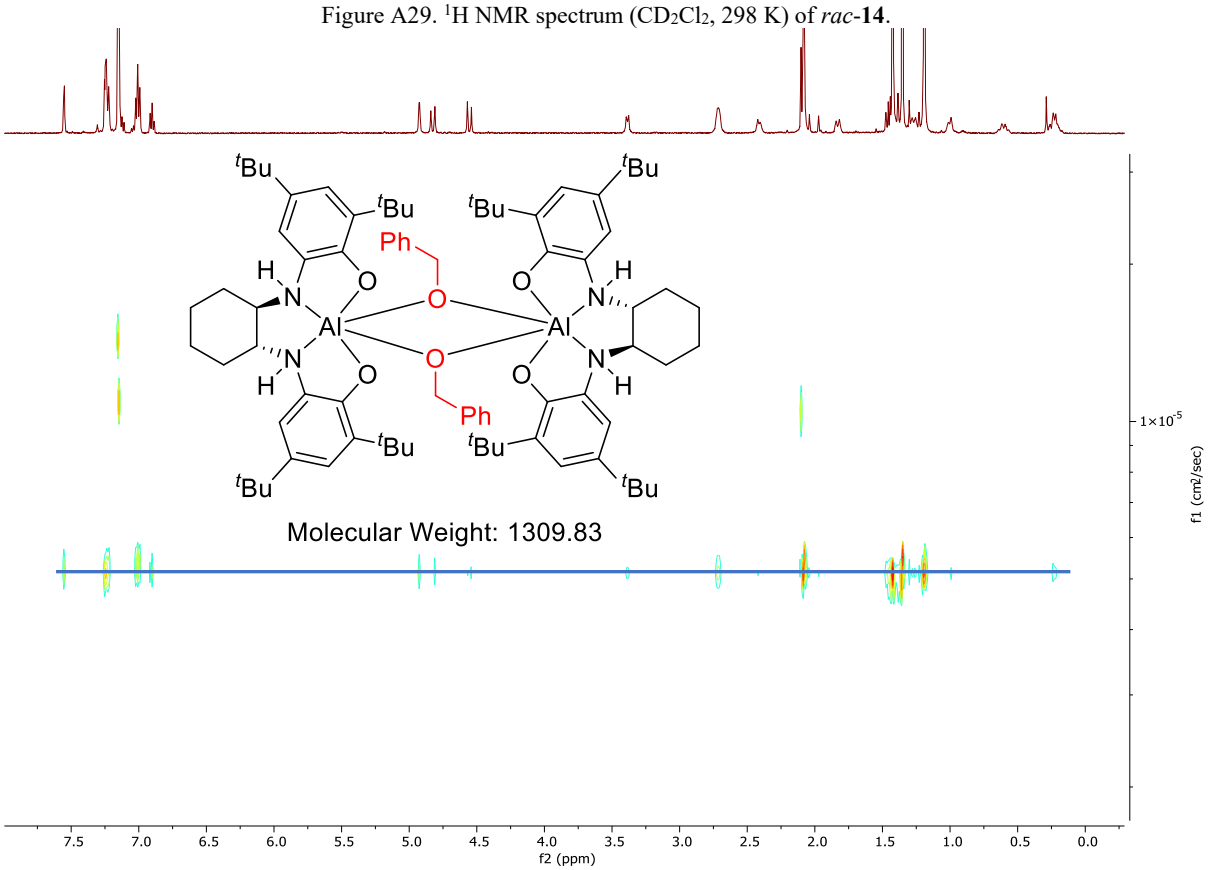


Figure A30: DOSY NMR (C_6D_6, 298 K) of *rac*-**14** showing a dimeric structure in solution.

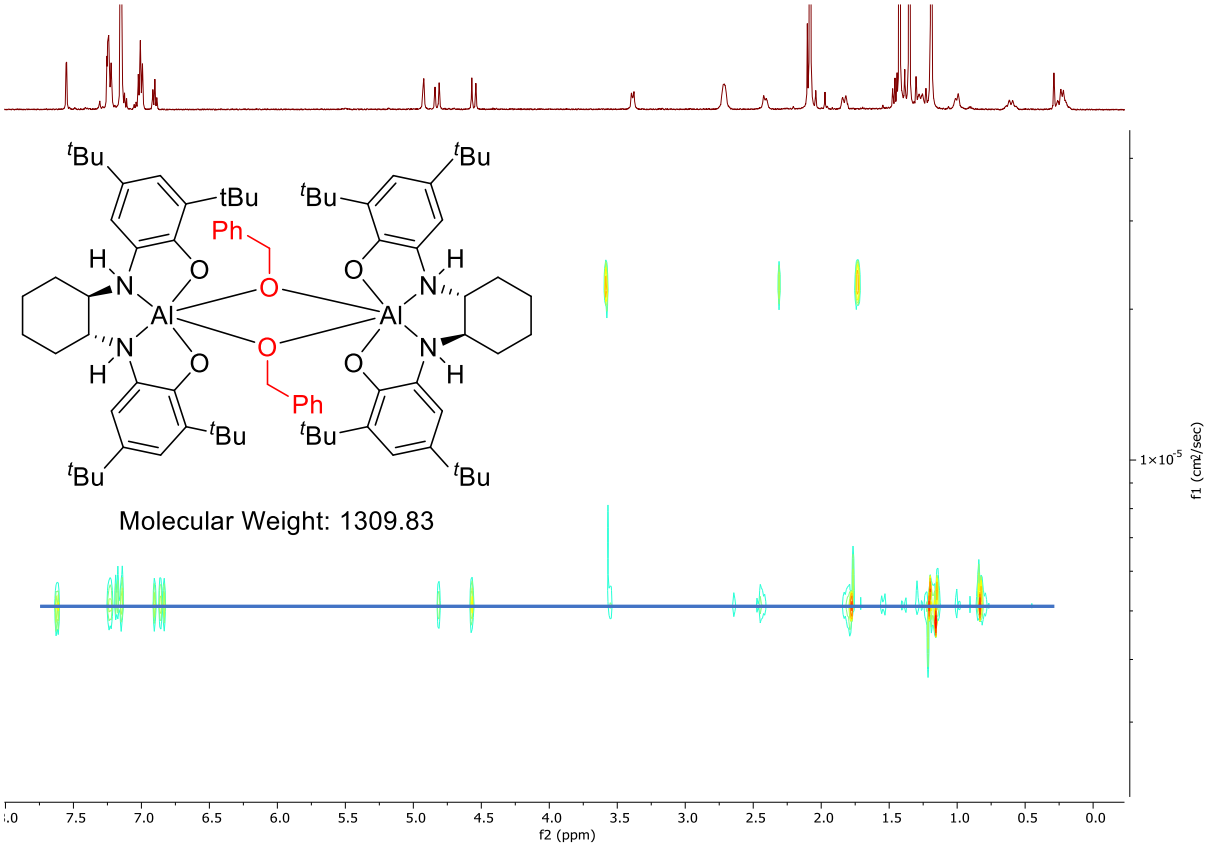


Figure A31: DOSY NMR (THF-d_8, 298 K) of *rac*-**14** showing a dimeric structure in solution.

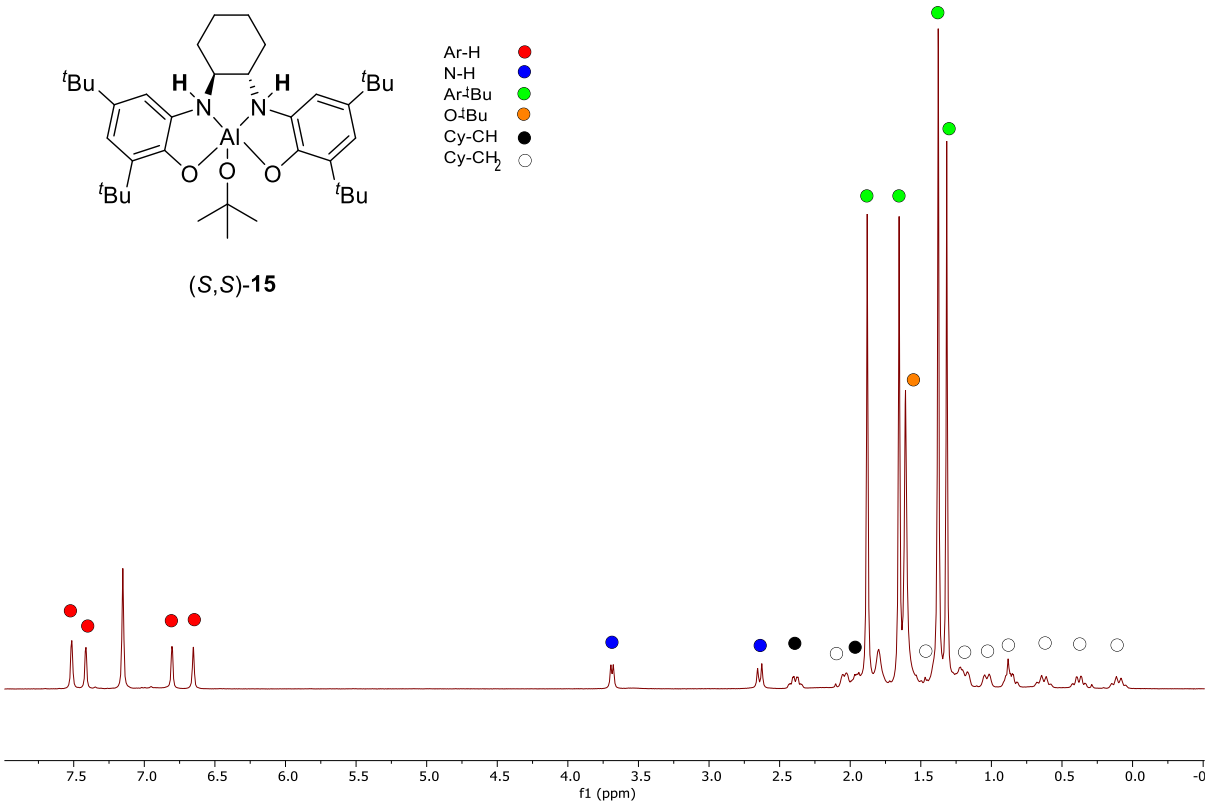


Figure A32: ^{1}H NMR spectrum (C_6D_6, 298 K) of (*S*,*S*)-**15**.

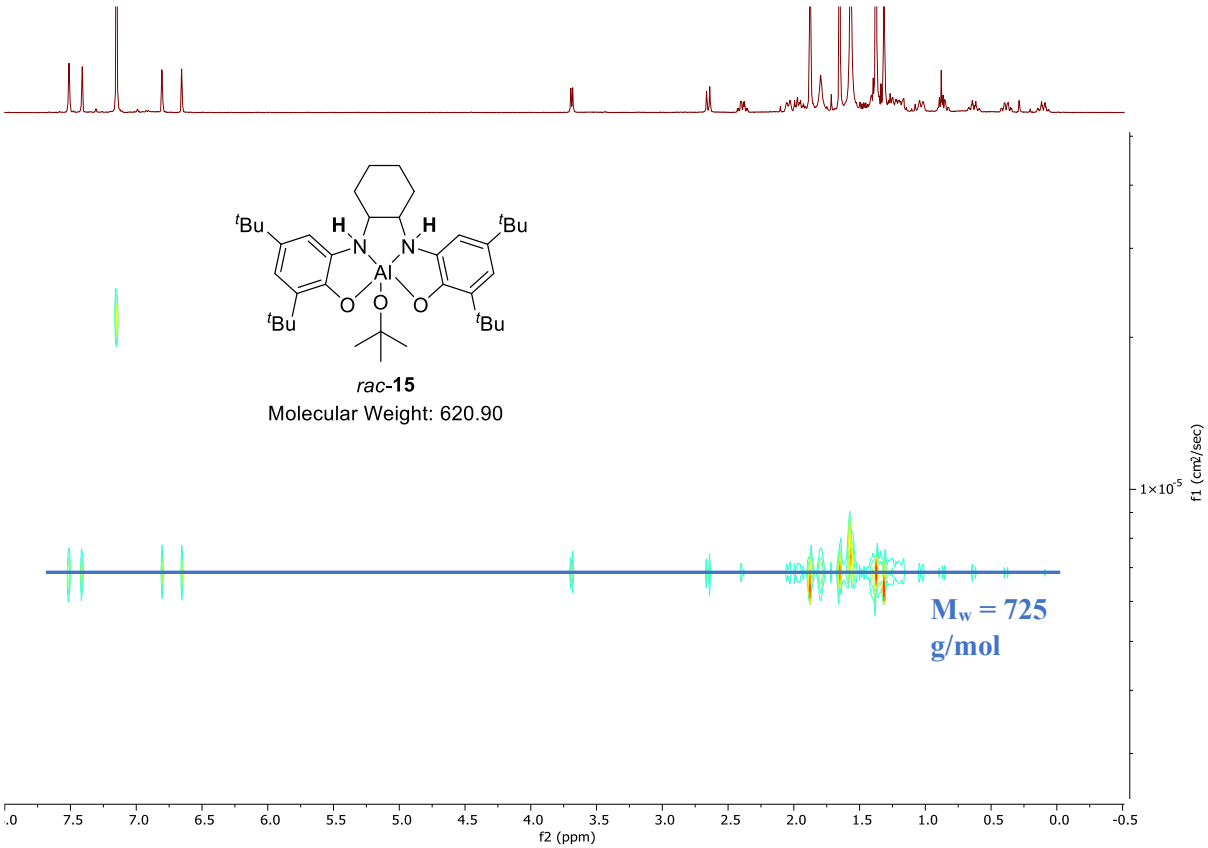


Figure A33: DOSY NMR (C_6D_6, 298 K) of *rac*-**15** showing a monomeric structure in solution.

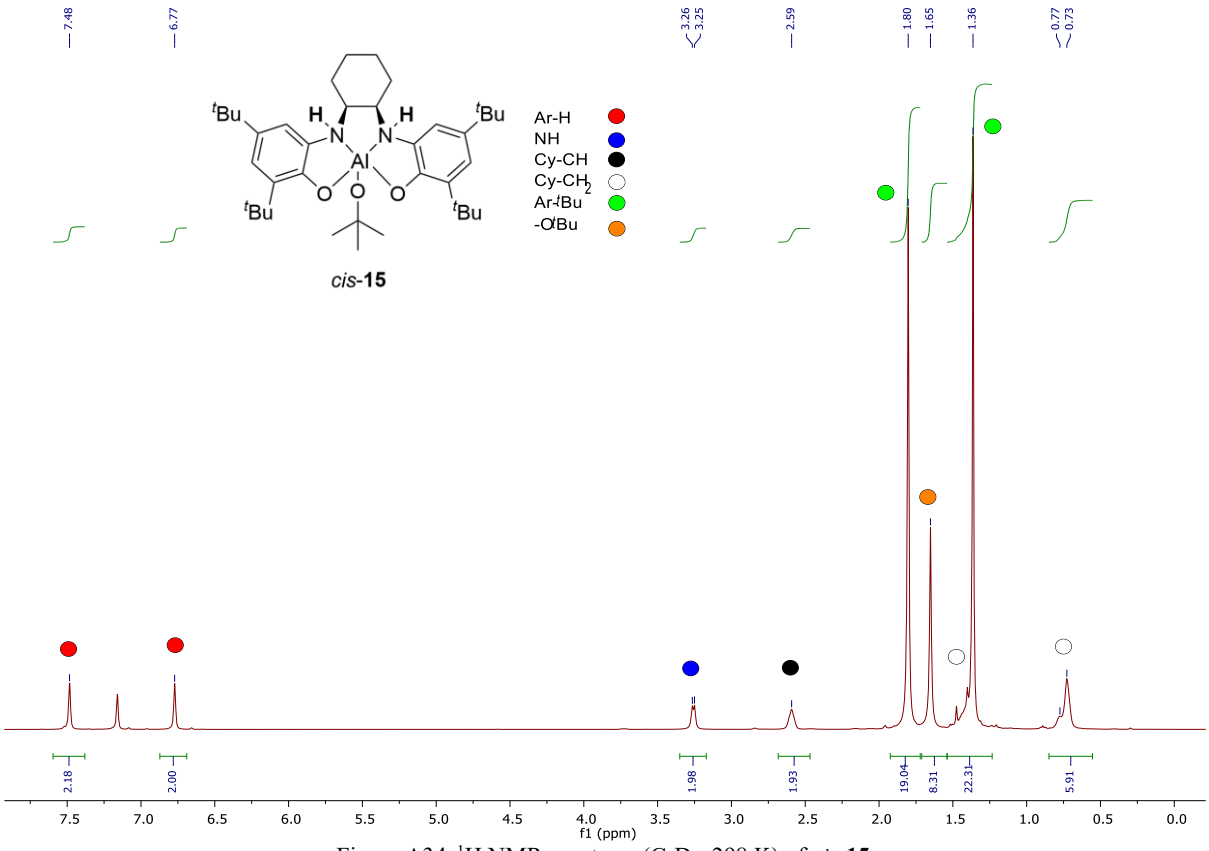


Figure A34. ^{1}H NMR spectrum (C_6D_6, 298 K) of *cis*-**15**.

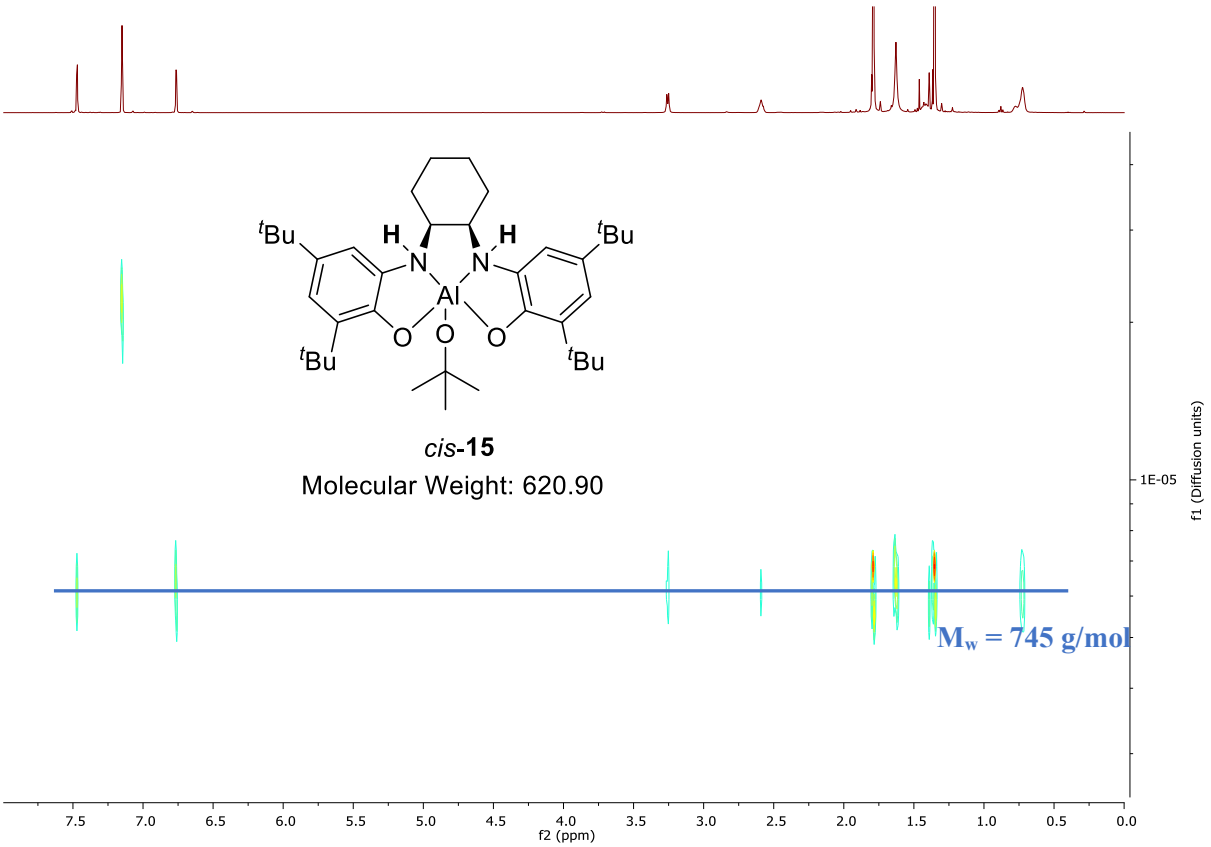


Figure A35. DOSY NMR (C_6D_6, 298 K) of *cis*-**15** showing a monomeric structure in solution.

A.2.3 Chapter 4

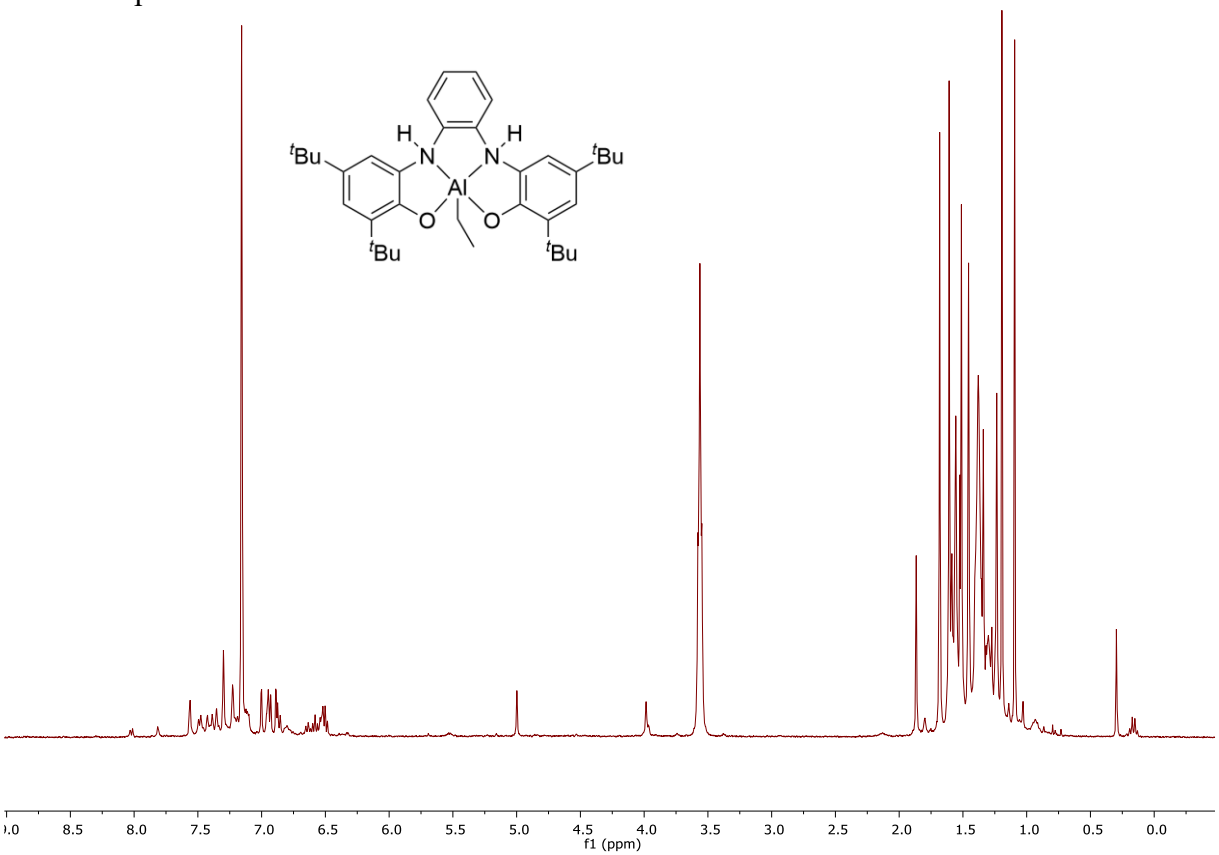


Figure A36. ^{1}H NMR spectrum (C_6D_6, 298 K) of the crude product of the attempted ^{H}**L**$_4$Al-Et synthesis showing a mixture of products formed.

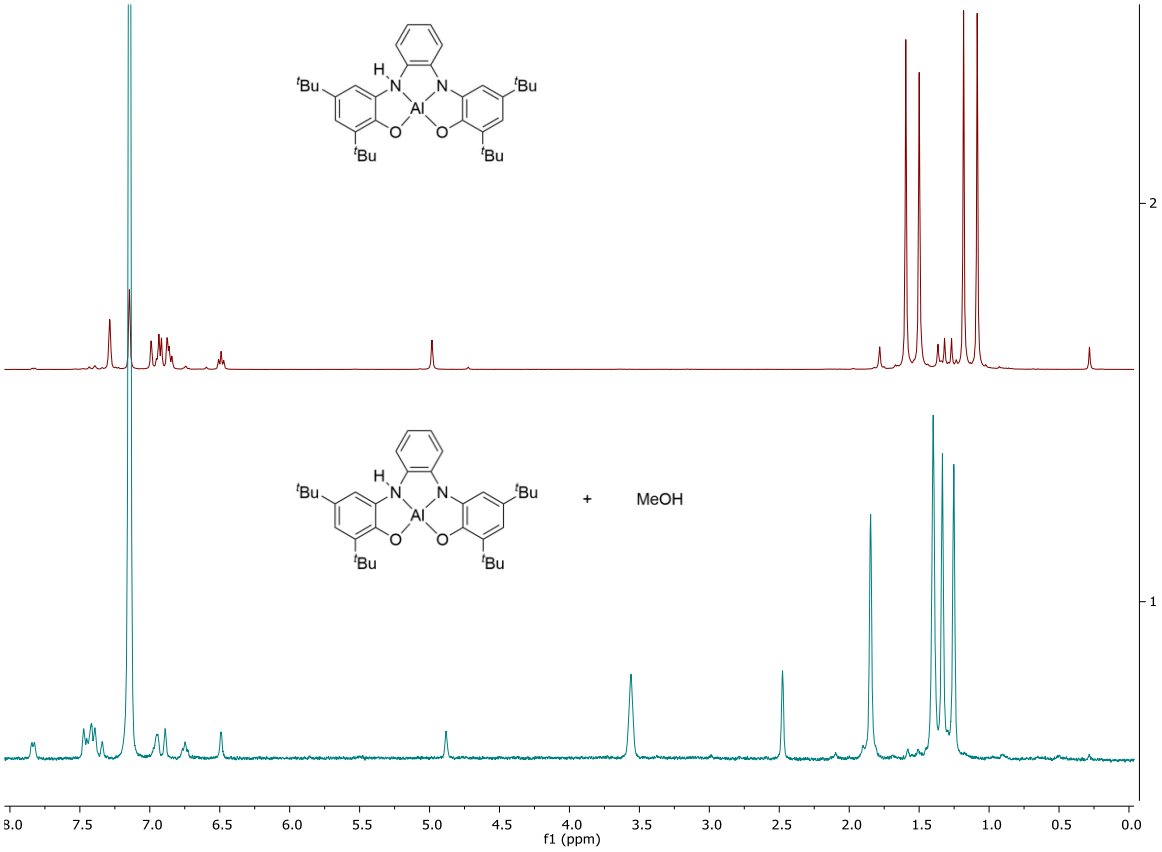


Figure A37. ^{1}H NMR spectrum (C_6D_6, 298 K) of **16** (top) and **16** + MeOH (bottom) showing a transformation taking place upon addition of one equivalent of MeOH.

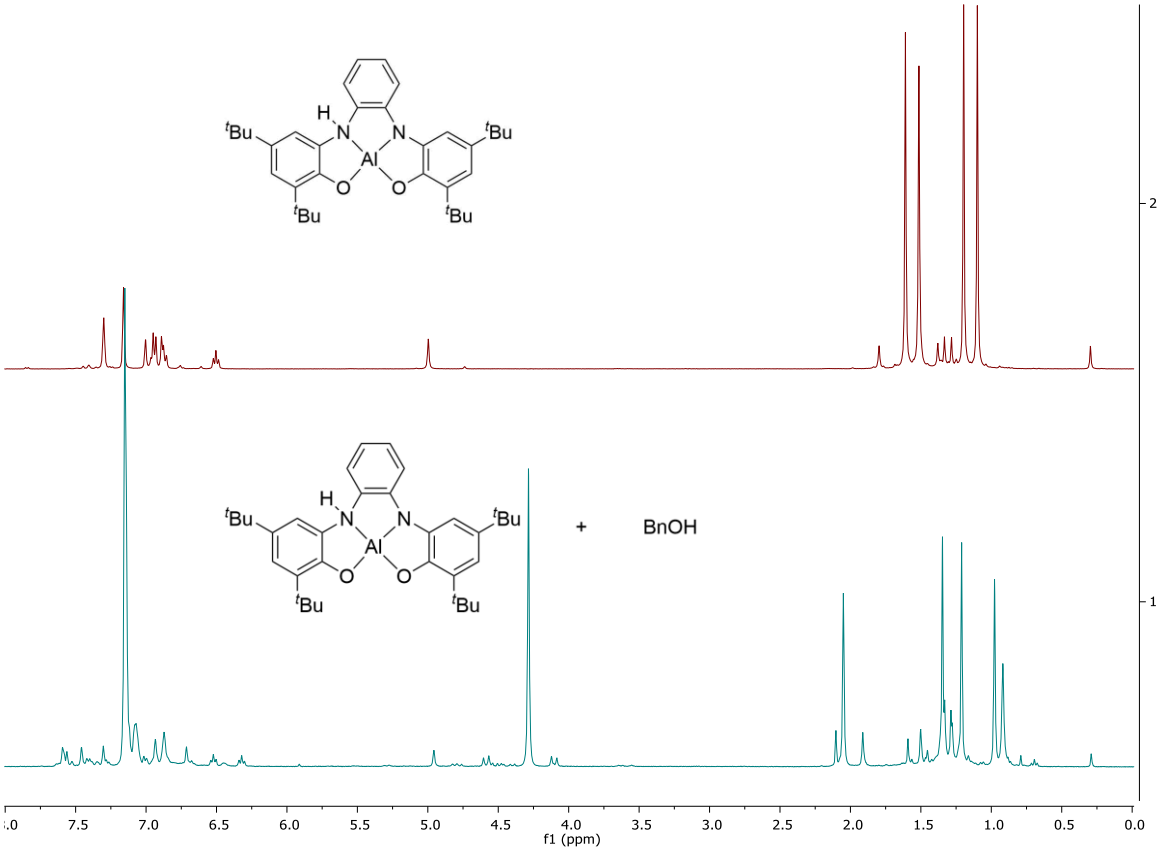


Figure A38. ^{1}H NMR spectrum (C_6D_6, 298 K) of **16** (top) and **16** +BnOH (bottom) showing a transformation taking place upon addition of one equivalent of BnOH.

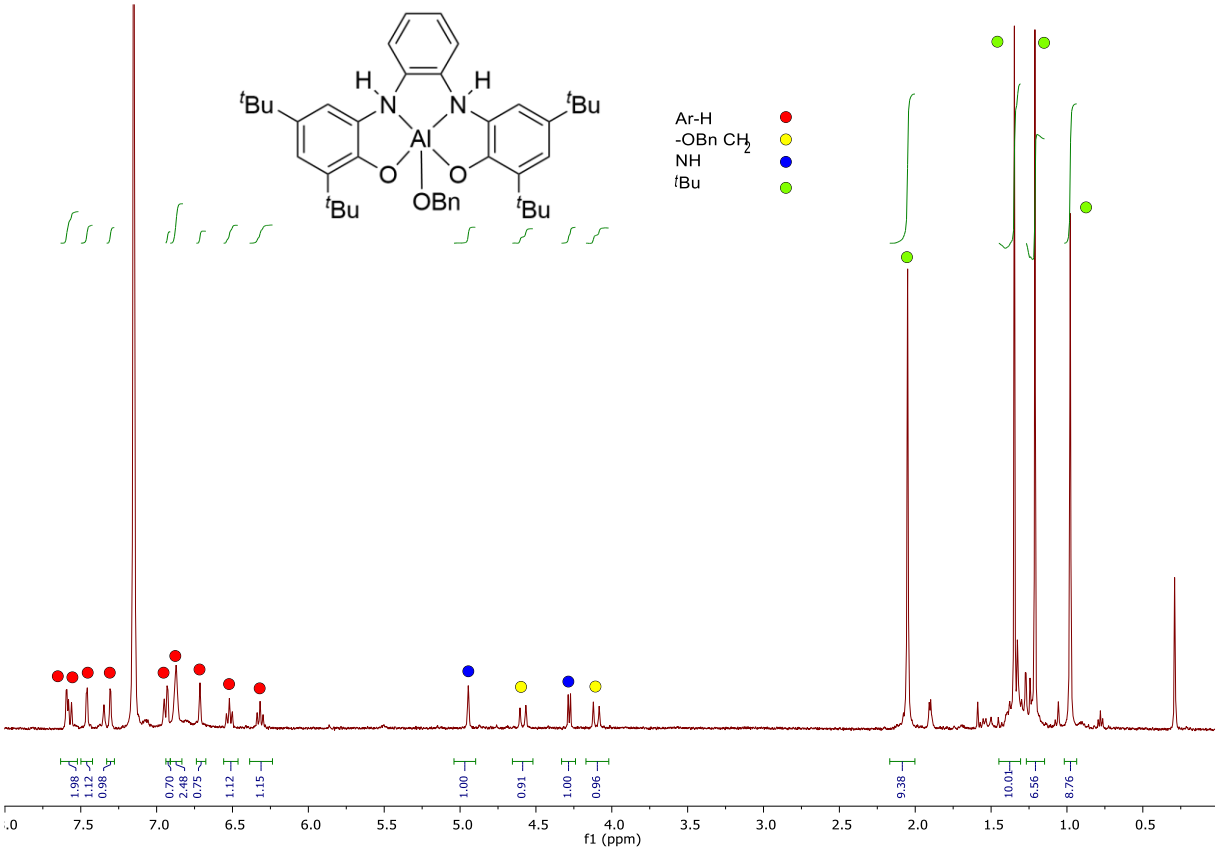


Figure A39. ^{1}H NMR spectrum (C_6D_6, 298 K) of ^{H}**L**$_4$Al(OBn) (**17-b**).

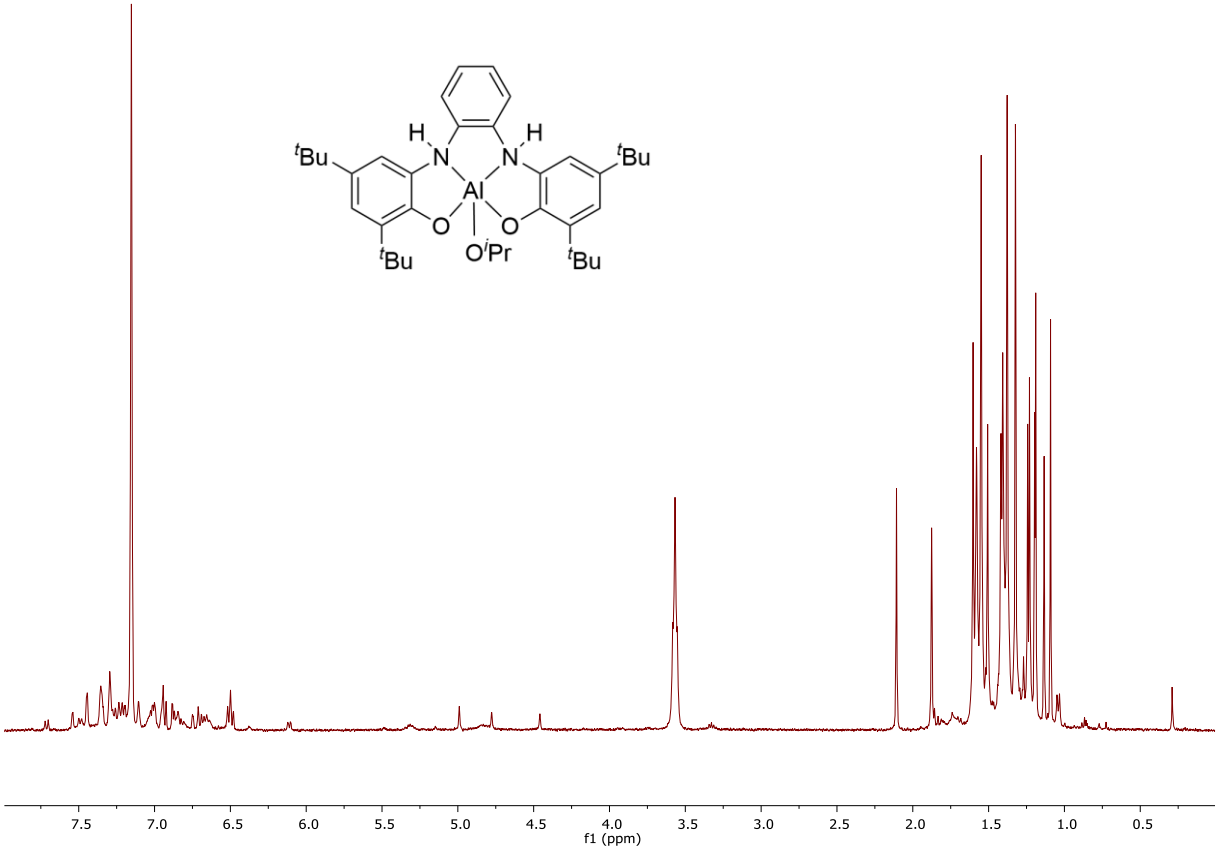


Figure A40. ^{1}H NMR spectrum of ^{H}**L**$_4$Al(O^{i}Pr) (**17-c**).

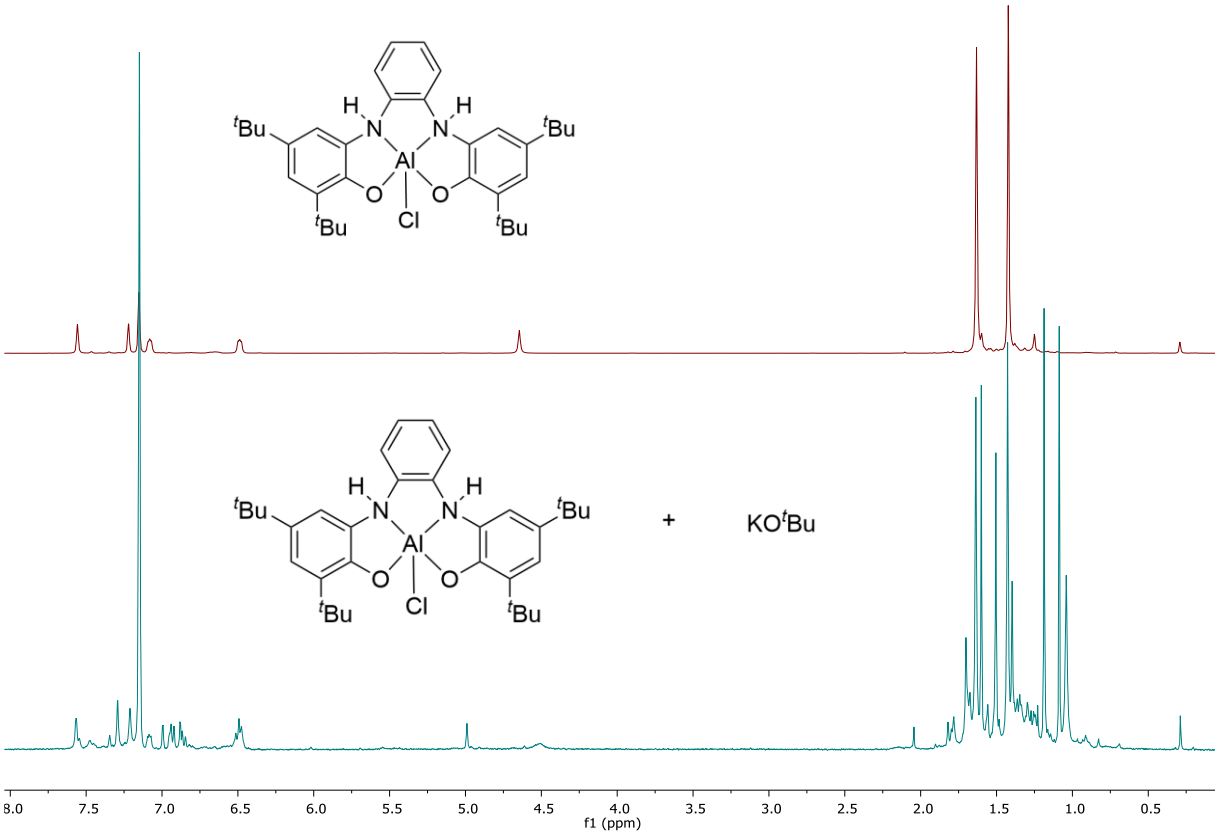


Figure A41. ^{1}H NMR spectrum (C_6D_6, 298 K) of **18** (top) and **18** + KO^{t}Bu (bottom) showing a transformation taking place upon addition of one equivalent of KO^{t}Bu.

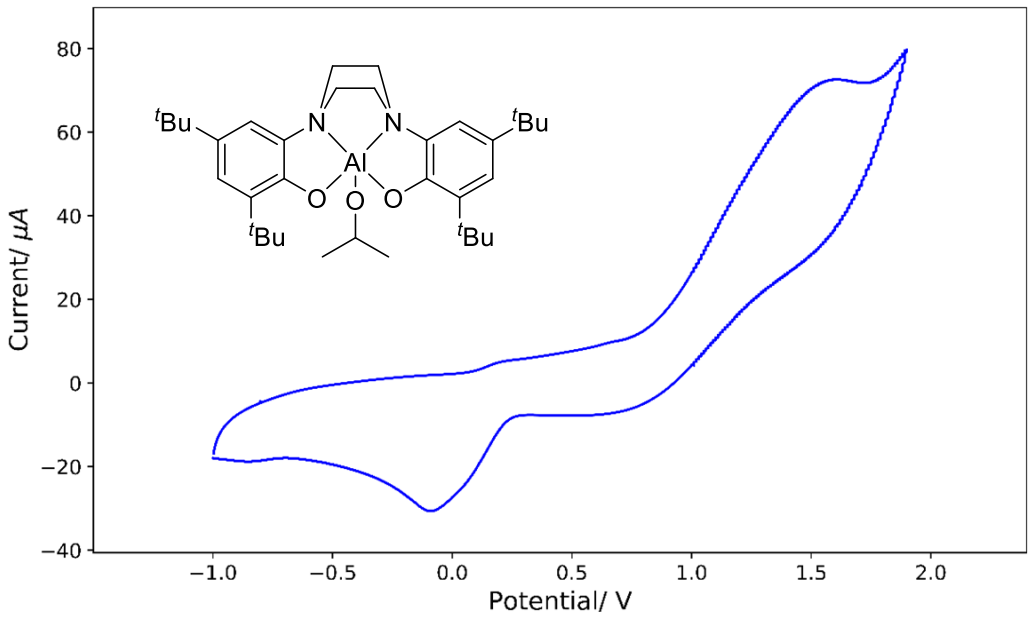


Figure A42. CV of piperazine-tethered aluminium complex showing irreversible redox-events.

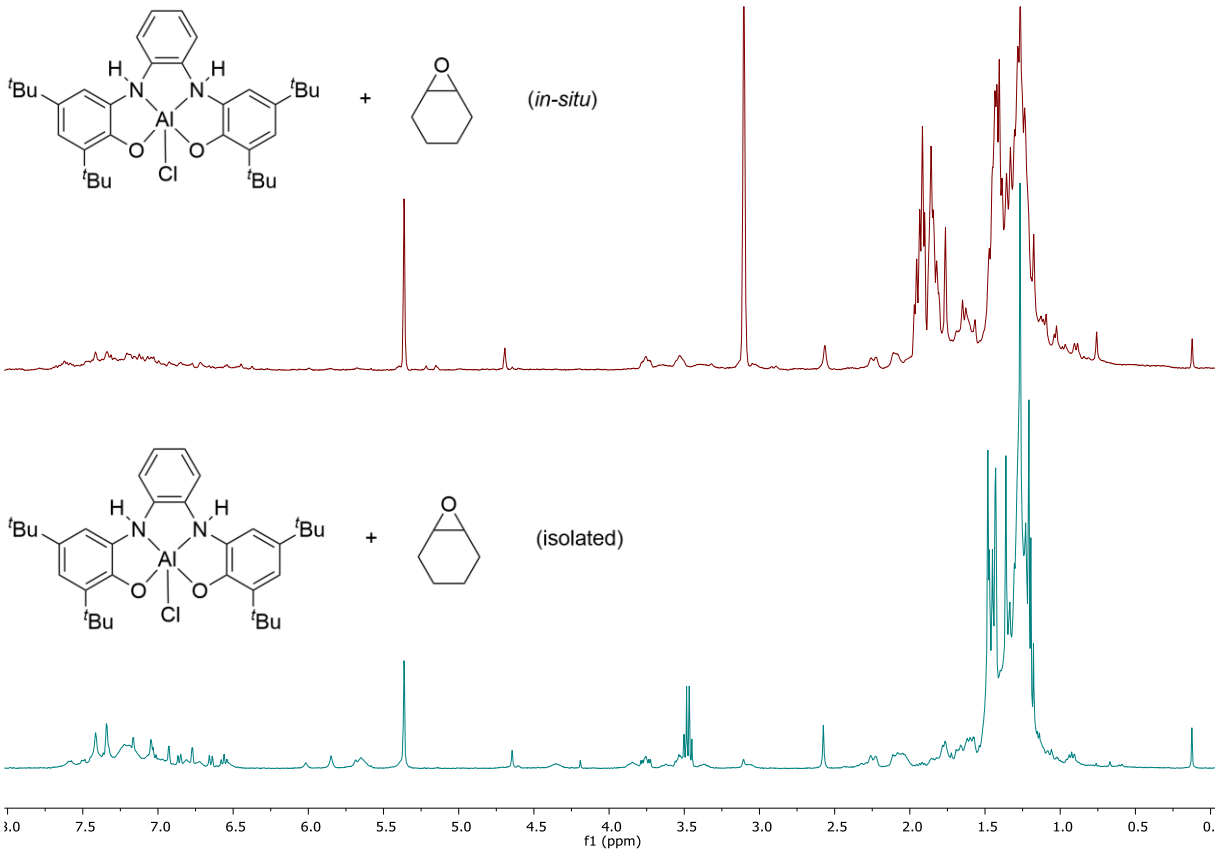


Figure A43. ^{1}H NMR spectrum (CD_2Cl_2 , 298 K) of the addition of CHO to **18** in-situ (top) and the isolated product of the reaction in diethyl ether (bottom).

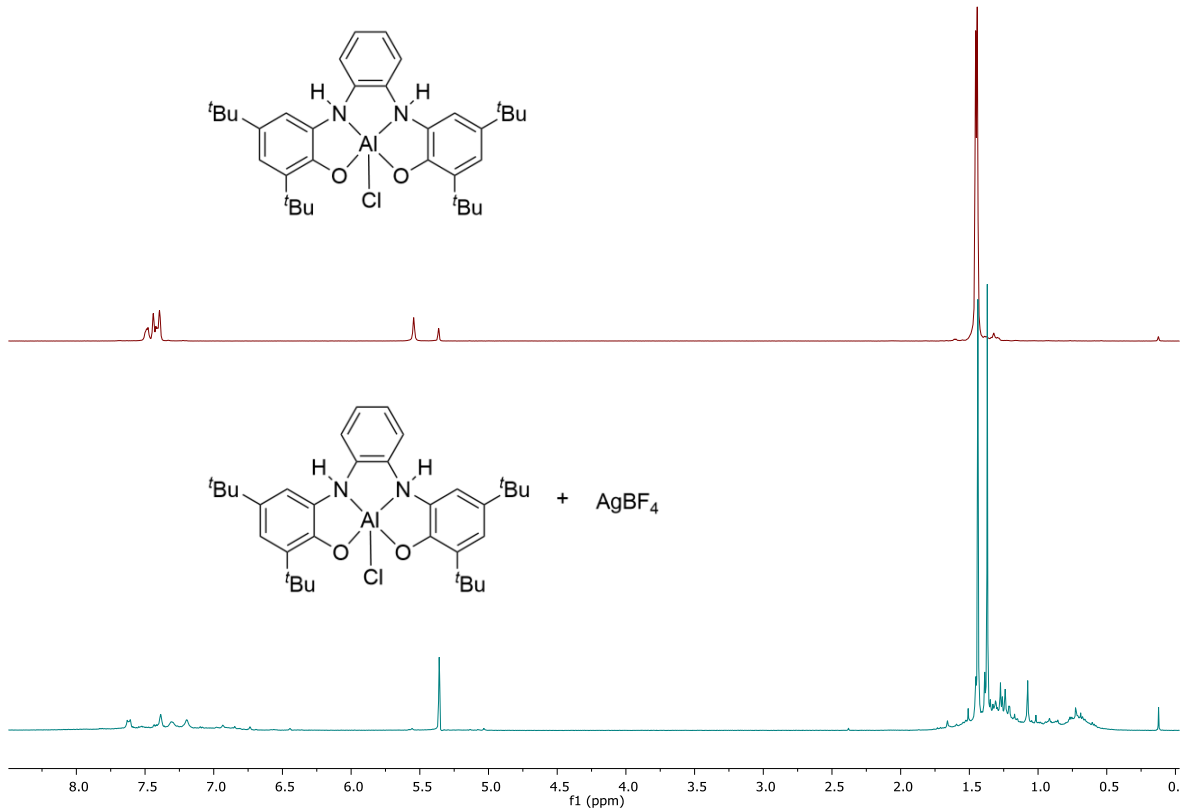


Figure A44. ^{1}H NMR spectrum (CD_2Cl_2, 298 K) of **18** (top) and the transformation taking place upon addition of one equivalent of $AgBF_4$ (bottom).

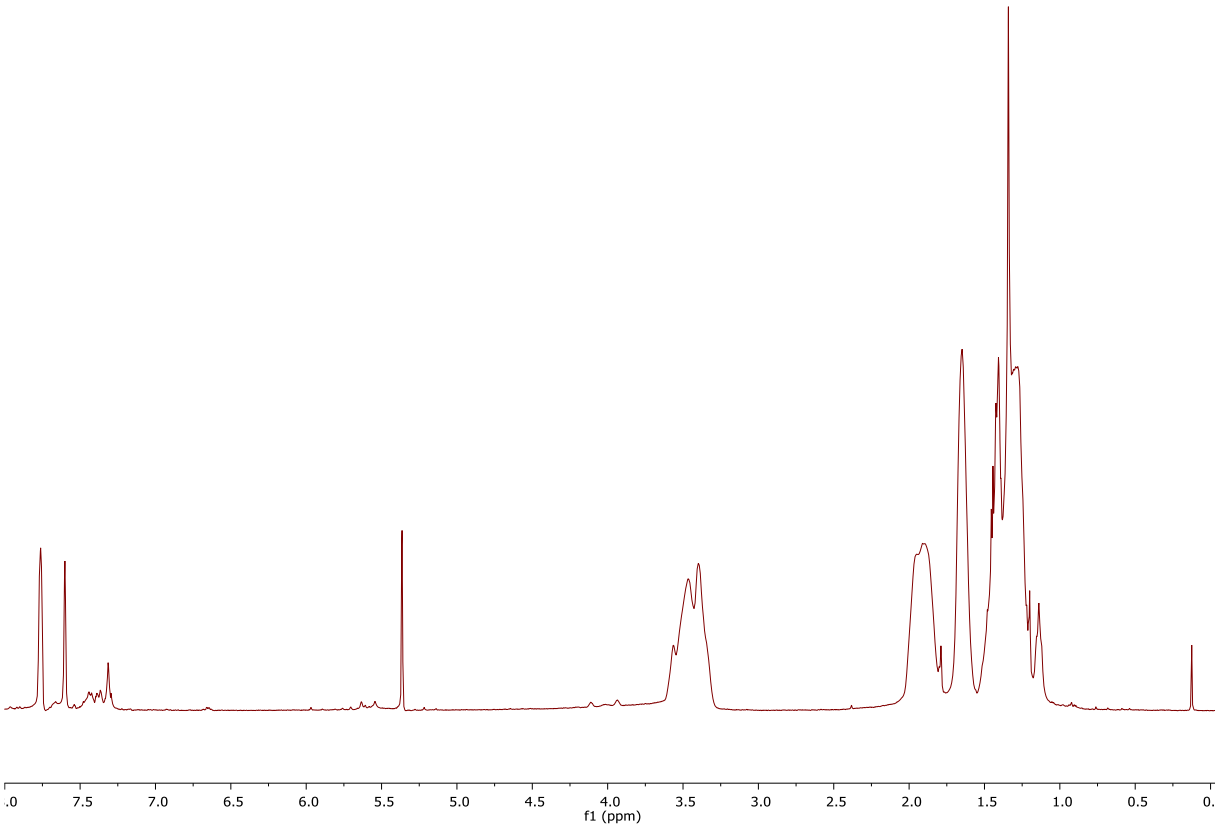


Figure A45. ^{1}H NMR spectrum (CD_2Cl_2, 298 K) of the reaction of **20** with 100 equivalents of CHO after 10 minutes at room temperature showing complete conversion of the monomer to PCHO.

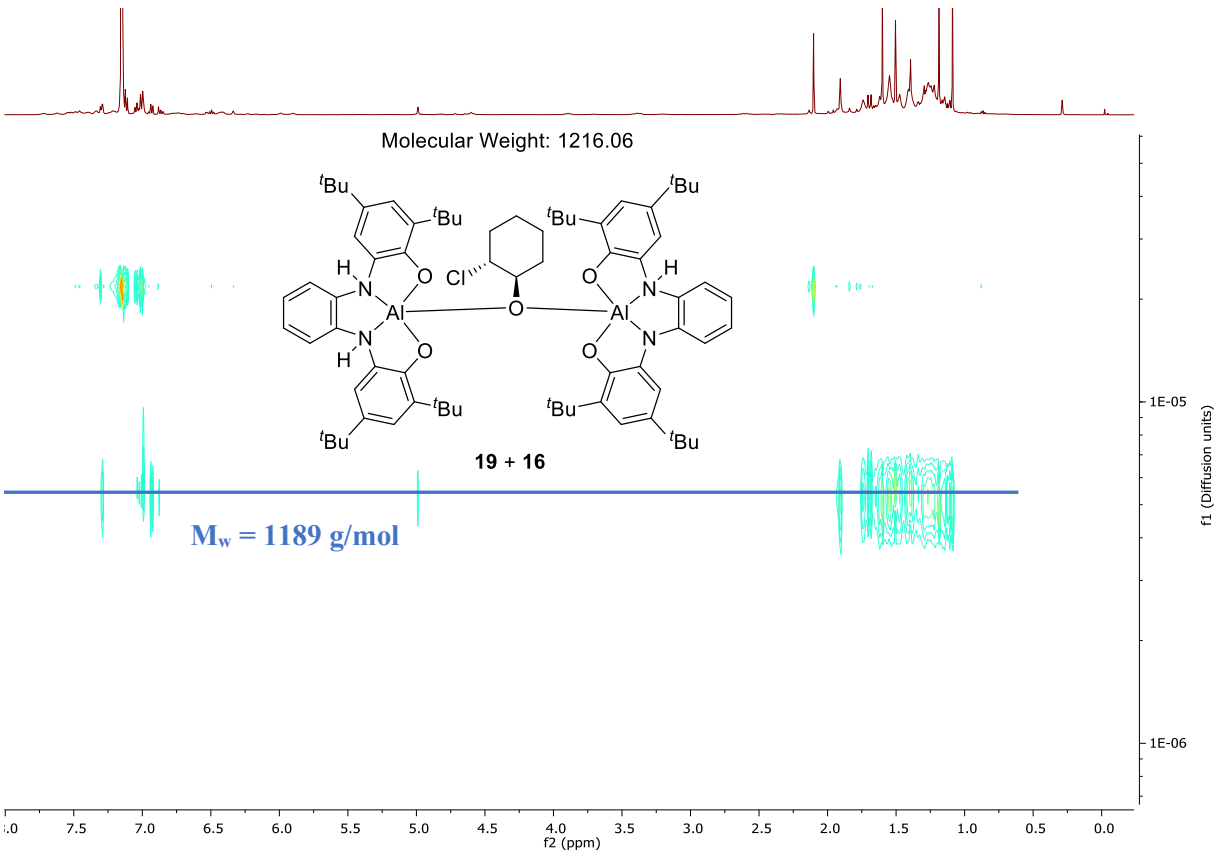


Figure A46. DOSY NMR (C_6D_6, 298 K) of **19** + **16** showing a dimeric structure in solution.

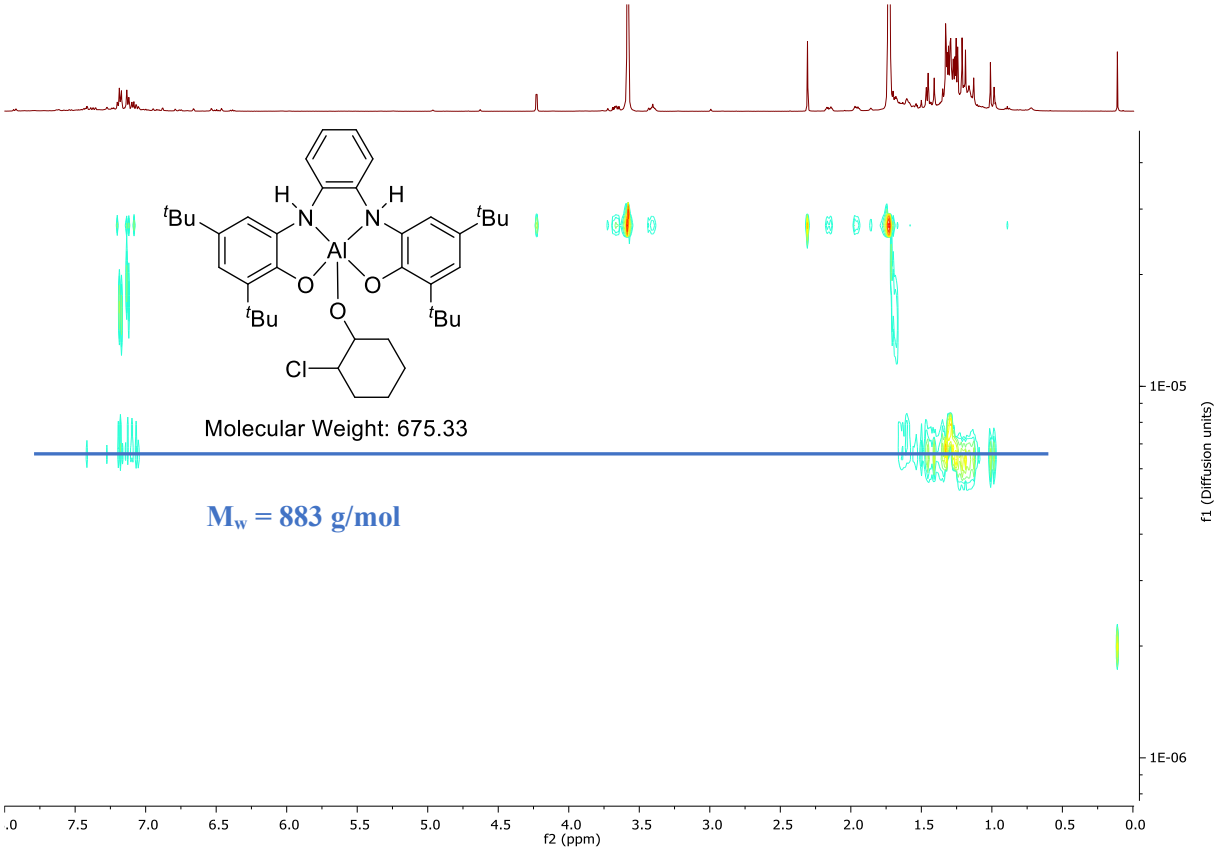


Figure A47. DOSY NMR (THF-d_8, 298 K) of **19** showing a monomeric structure in solution.

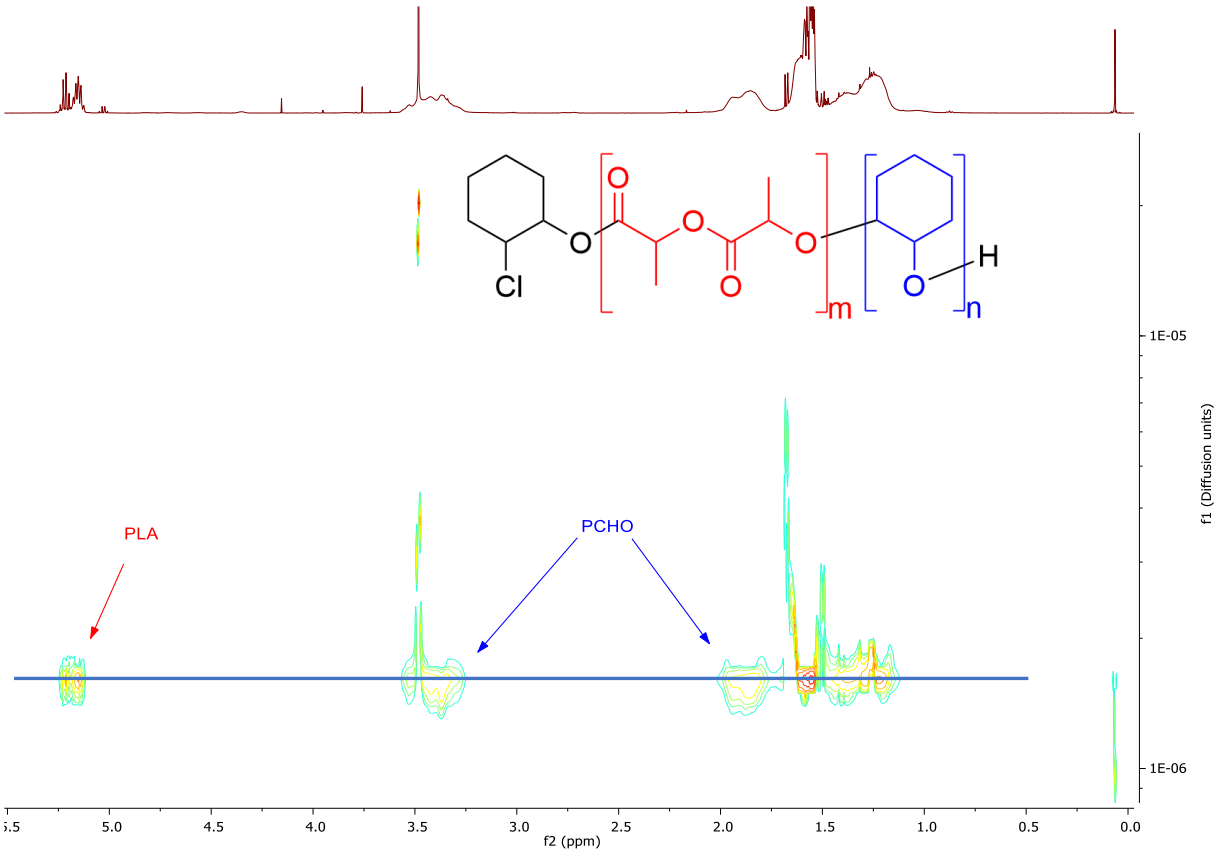


Figure A48. DOSY NMR ($CDCl_3$, 298 K) of a block co-polymer generated from 100 equivalents of *rac*-LA and CHO indicating that the polymer blocks are situated on the same chain.

1. Garden, J. A.; Saini, P. K.; Williams, C. K., *J. Am. Chem. Soc.* **2015,** *137*, 15078-15081.

Appendix B: Kinetic and Molecular Weight Data Plots

B.1 Kinetic and Molecular Weight Data Plots

B.1.1 Chapter 2

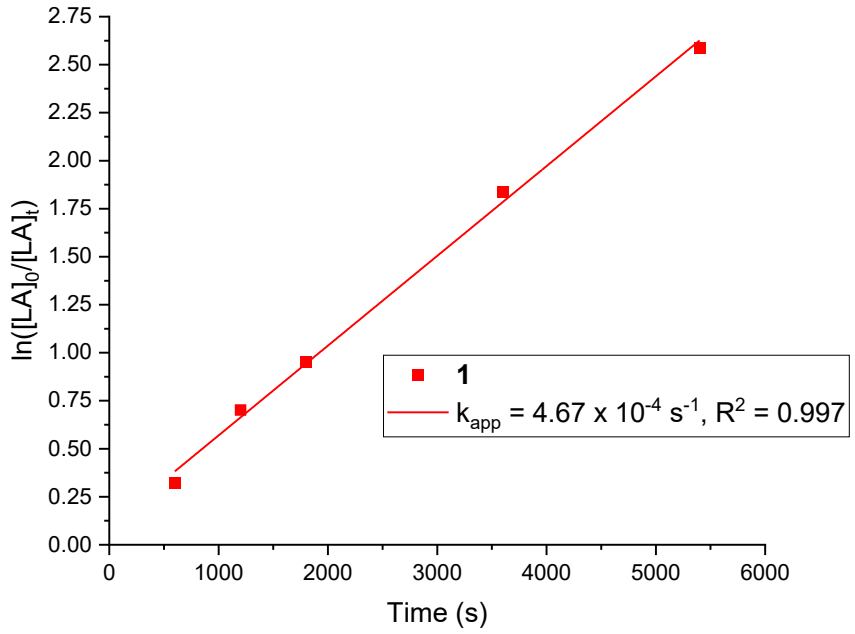


Figure B1: First-order plot (linear fit) for *rac*-LA ROP initiated by **1** as per conditions in Table 1, Entry 1.

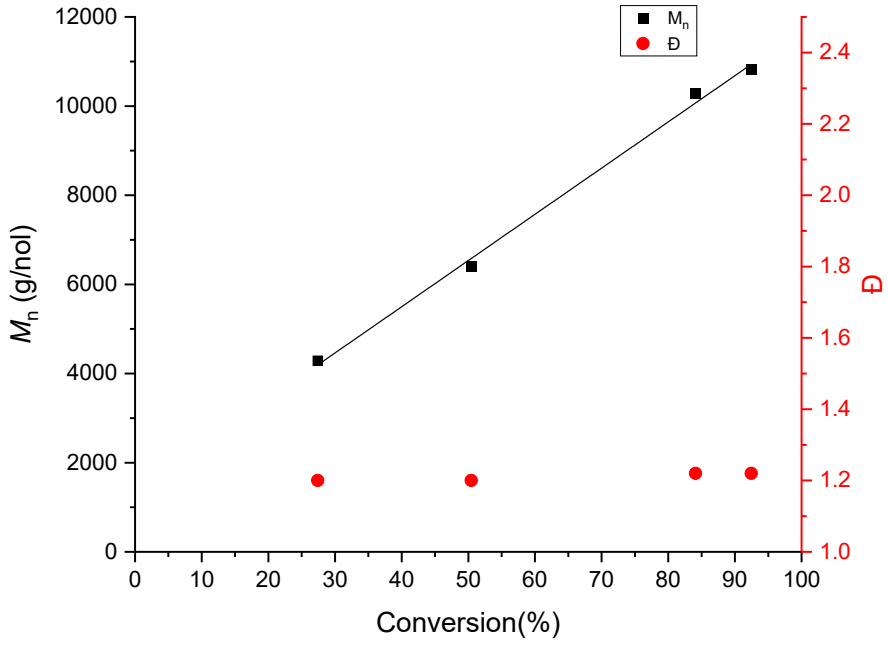


Figure B2: Plot of PLA M_n *vs. rac*-LA conversion for *rac*-LA ROP initiated by **1** as per conditions in Table 1, Entry 1.

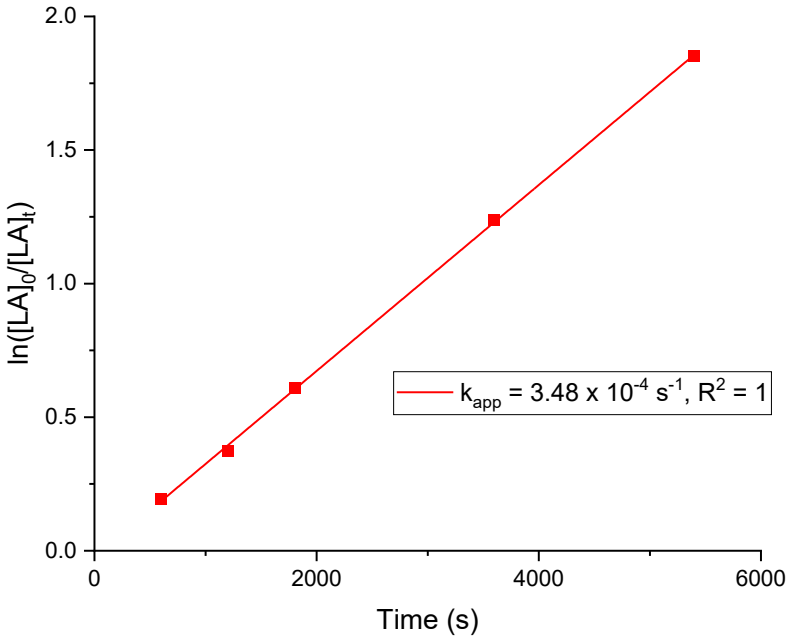


Figure B3. First-order plot (linear fit) for *rac*-LA ROP initiated by **1** as per conditions in Table 1, Entry 2.

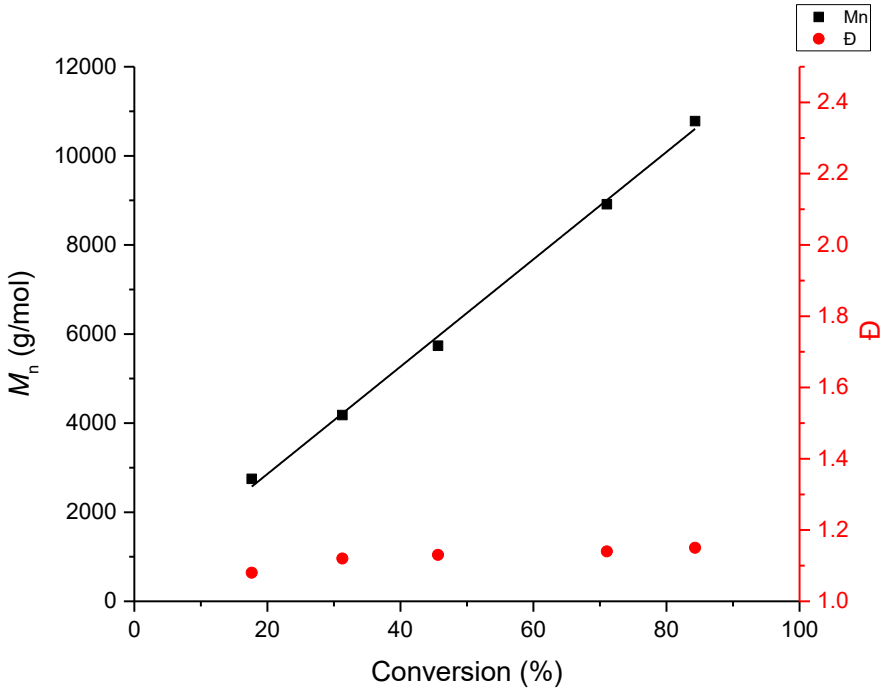
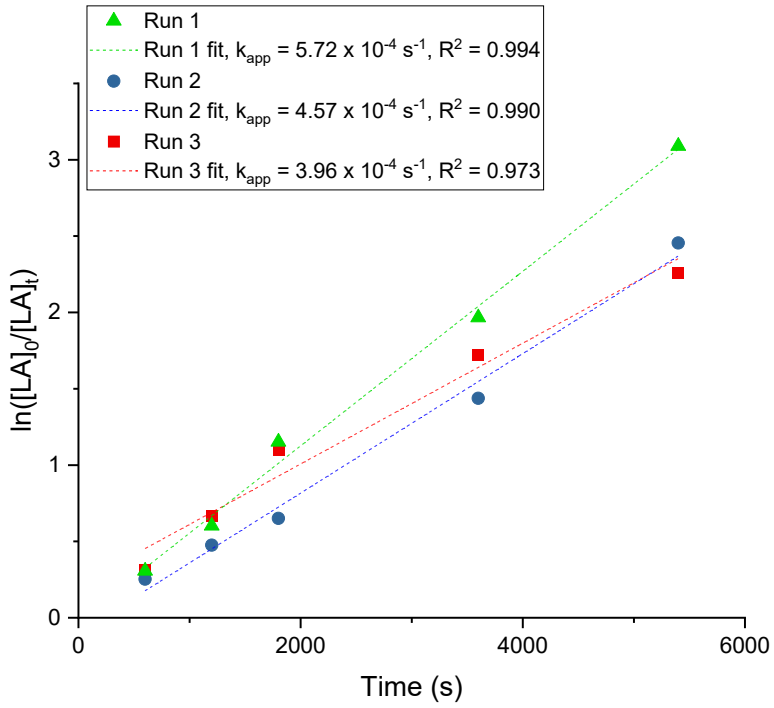


Figure B4. Plot of M_n *vs. rac*-LA conversion for *rac*-LA ROP initiated by **1** as per conditions in Table 1, Entry 2.



k_{app}(1)	k_{app}(2)	k_{app}(3)	k_{app}(average)	Population standard deviation
5.72E-04	4.57E-04	3.96E-04	4.75E-04	7.29E-05

Figure B5: Overlay of first-order plots (linear fit) for three repeated *rac*-LA ROP (dash lines) initiated by **2** as per conditions in Table 1, Entry 3.

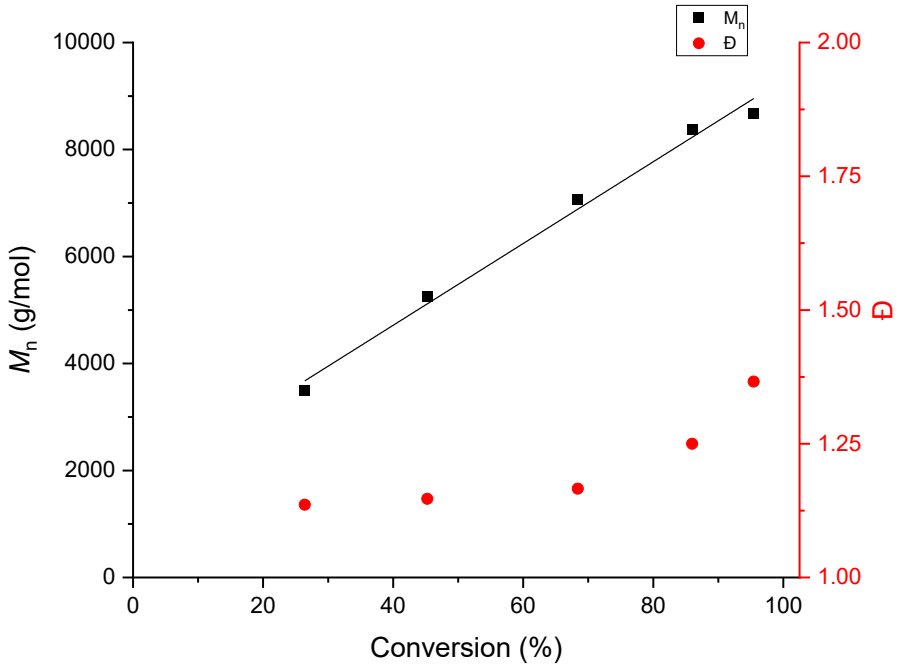


Figure B6: Plot of M_n vs rac-lactide conversion for rac-La ROP initiated by **2** as per conditions in Table 1, Entry 3.

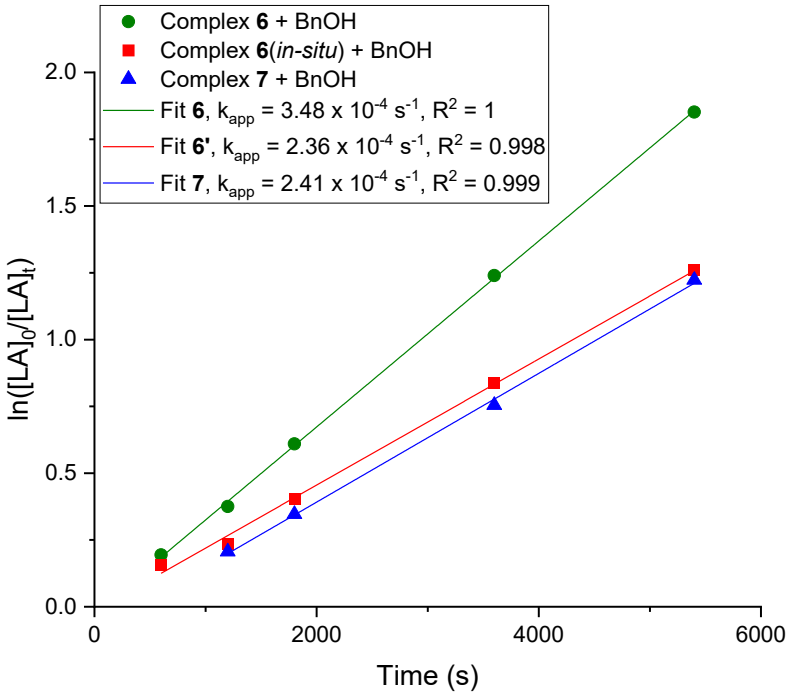


Figure B7: Overlay showing similar activities of complexes **6** and **7** in *rac*-LA ROP when reacted with BnOH, as per Table 1, Entries 4-6.

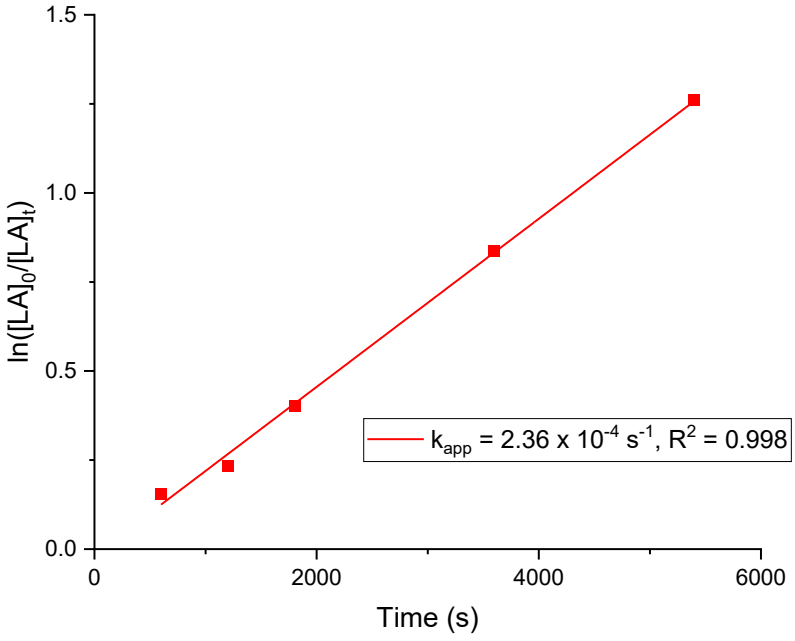


Figure B8. First-order plot (linear fit) for *rac*-LA ROP initiated by **6** as per conditions in Table 1, Entry 5.

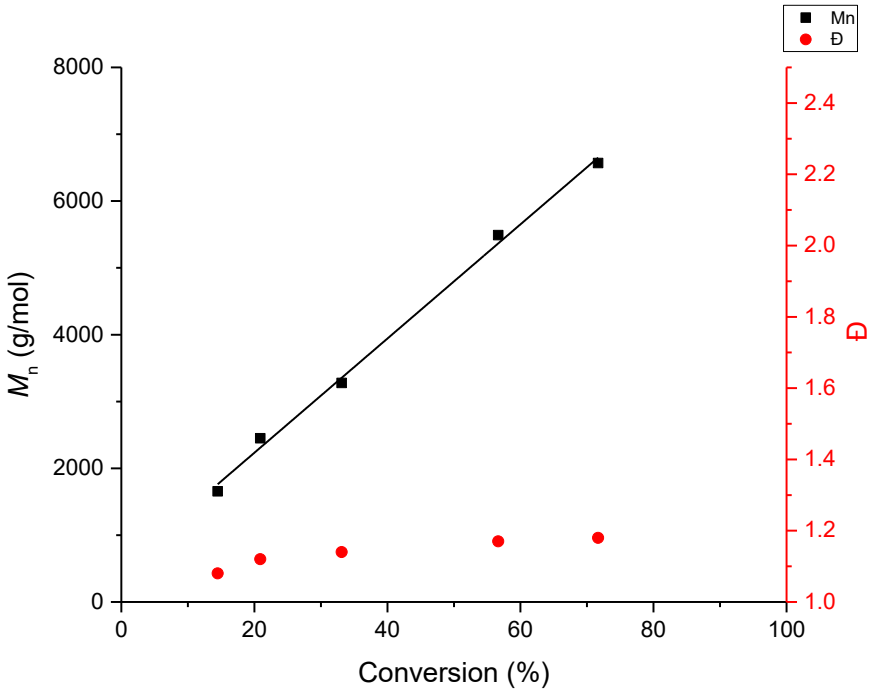


Figure B9. Plot of M_n *vs.* *rac*-LA conversion for *rac*-LA ROP initiated by **6** as per conditions in Table 1, Entry 5.

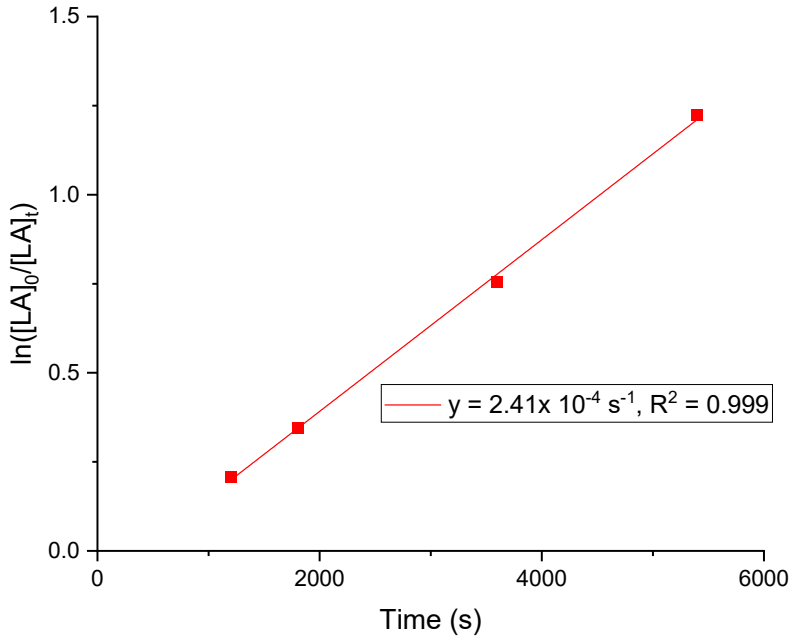


Figure B10. First-order plot (linear fit) for *rac*-LA ROP initiated by **7** as per conditions in Table 1, Entry 6.

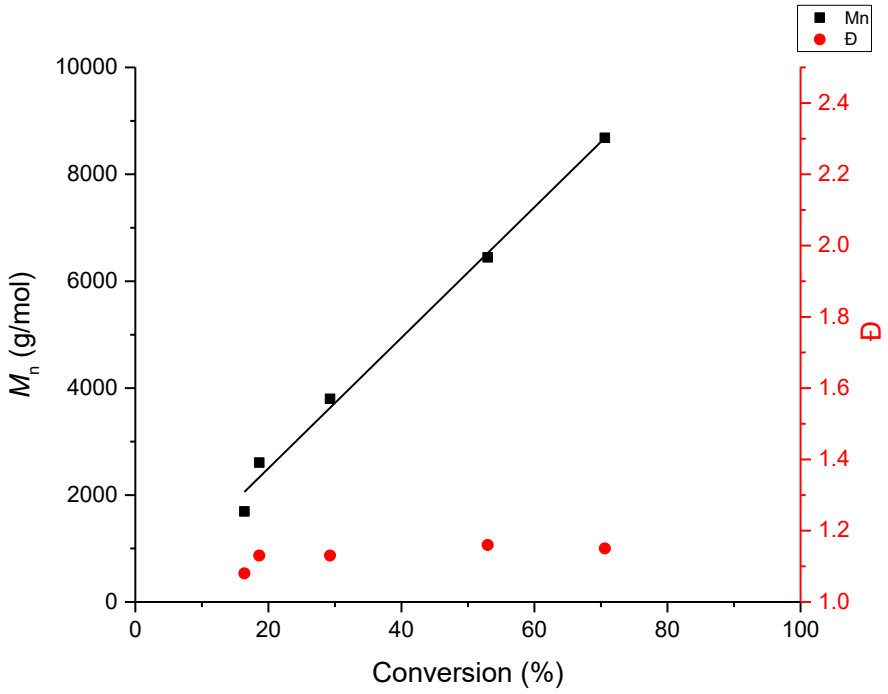


Figure B11. Plot of M_n *vs. rac*-LA conversion for *rac*-LA ROP initiated by **7** as per conditions in Table 1, Entry 6.

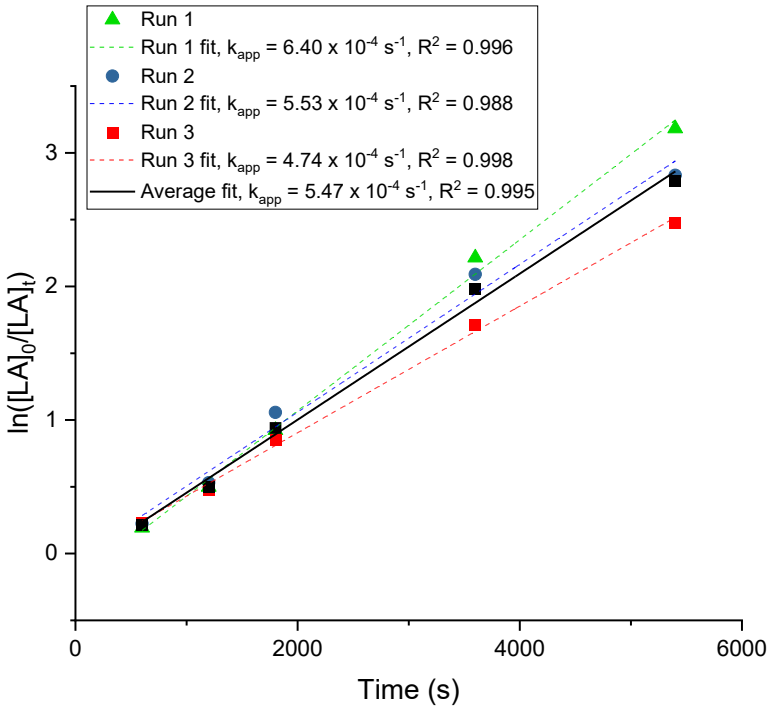


Figure B12. Overlay of first-order plots (linear fit) for three repeated *rac*-LA ROP (dash lines) initiated by **8c** as per conditions in Table 1, Entry 7 (black squares/plain line = average from the three values).

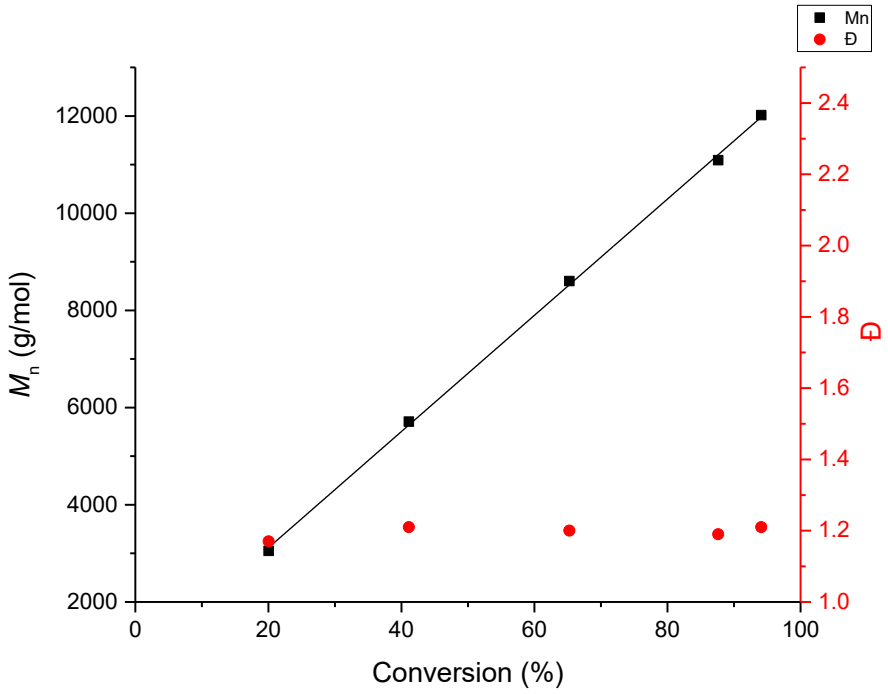
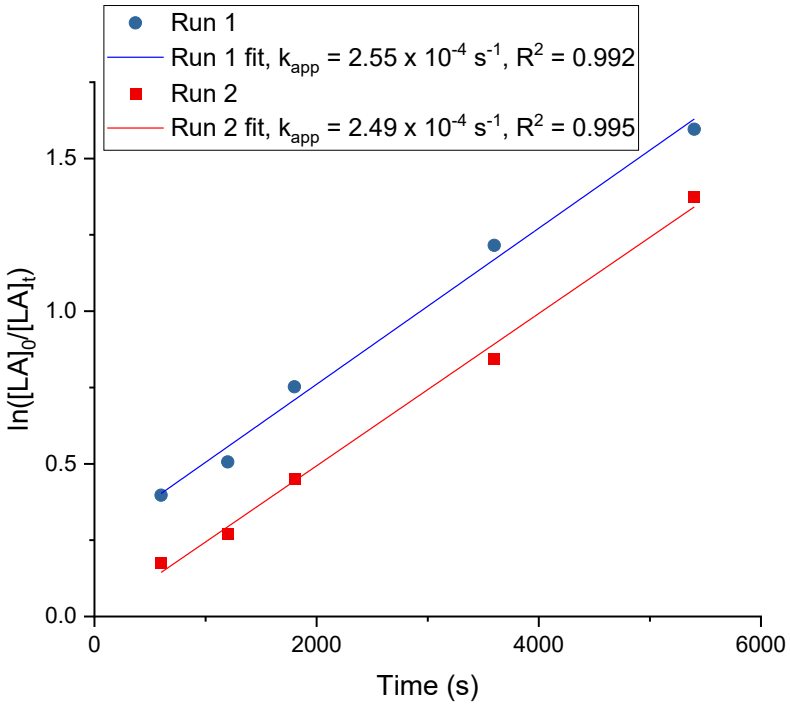
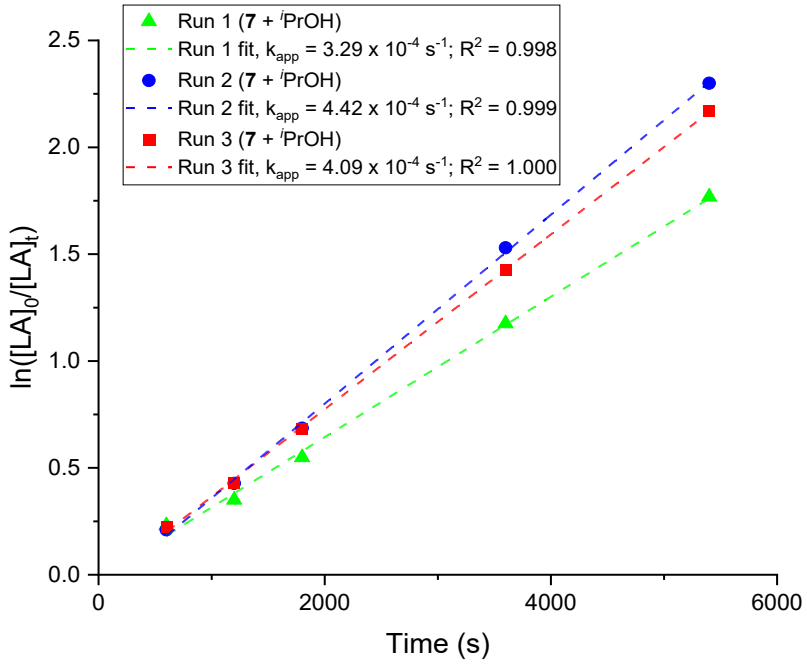


Figure B13. Plot of M_n *vs. rac*-LA conversion for *rac*-LA ROP initiated by **8c** as per conditions in Table 1, Entry 7.



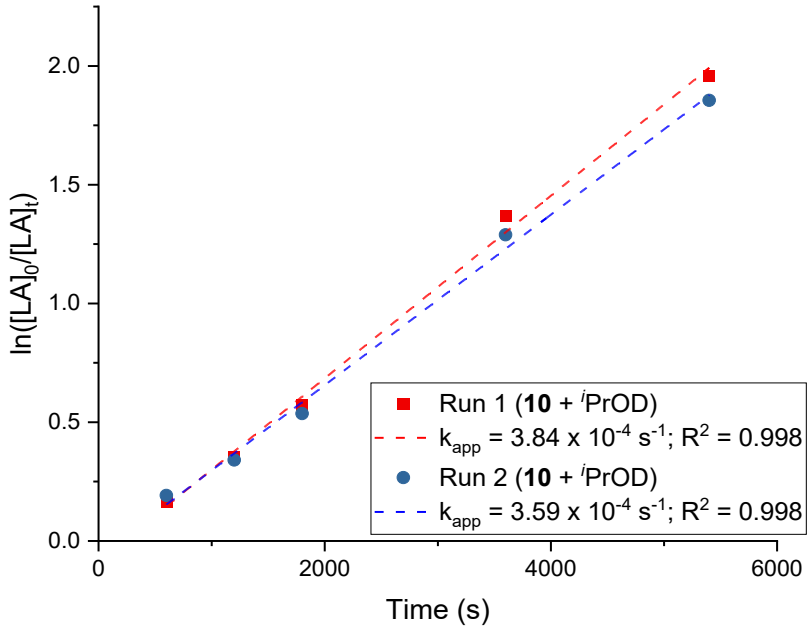
k_{app}(1)	k_{app}(2)	k_{app}(average)
2.55E-04	2.49E-04	2.52E-04

Figure B14: First-order plots (average of 2 repeated experiment) for *rac*-LA ROP initiated by **4** as per conditions in Table 3, Entry 2.



k_{app}(1)	k_{app}(2)	k_{app}(3)	k_{app}(average)	Population standard deviation
3.29E-04	4.42E-04	4.09E-04	3.93E-04	4.74E-05

Figure B15. First-order plot (average of 3 repeated experiment) for *rac*-LA ROP initiated by **7** + ^{i}PrOH as per conditions in Table 3, Entry 3.



k_{app}(1)	k_{app}(2)	k_{app}(average)
3.84E-04	3.59E-04	3.72E-04

Figure B16. First-order plot (average of 2 repeated experiment) for *rac*-LA ROP initiated by **10** + ^{i}PrOD as per conditions in Table 3, Entry 4.

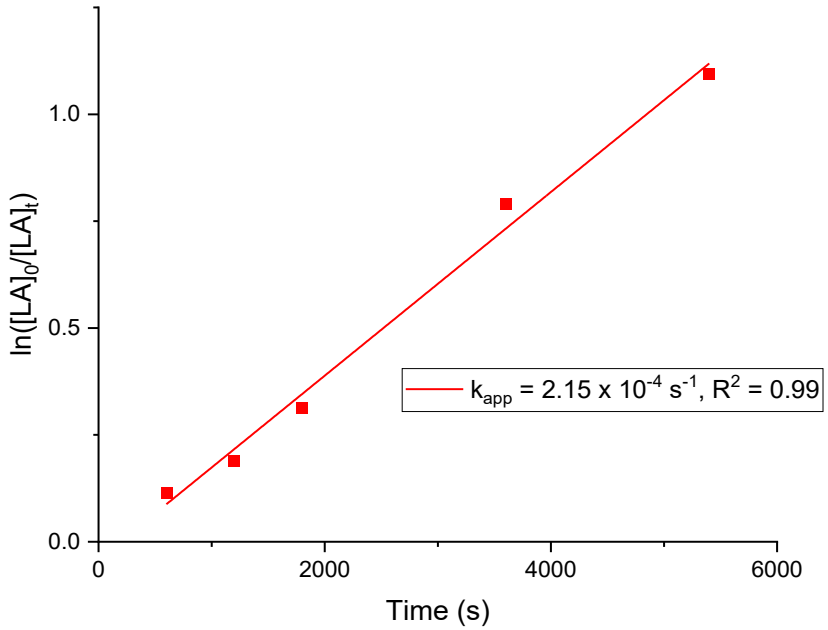


Figure B17. First-order plot (linear fit) for *rac*-LA ROP initiated by **2** as per conditions in Table 5, Entry 3.

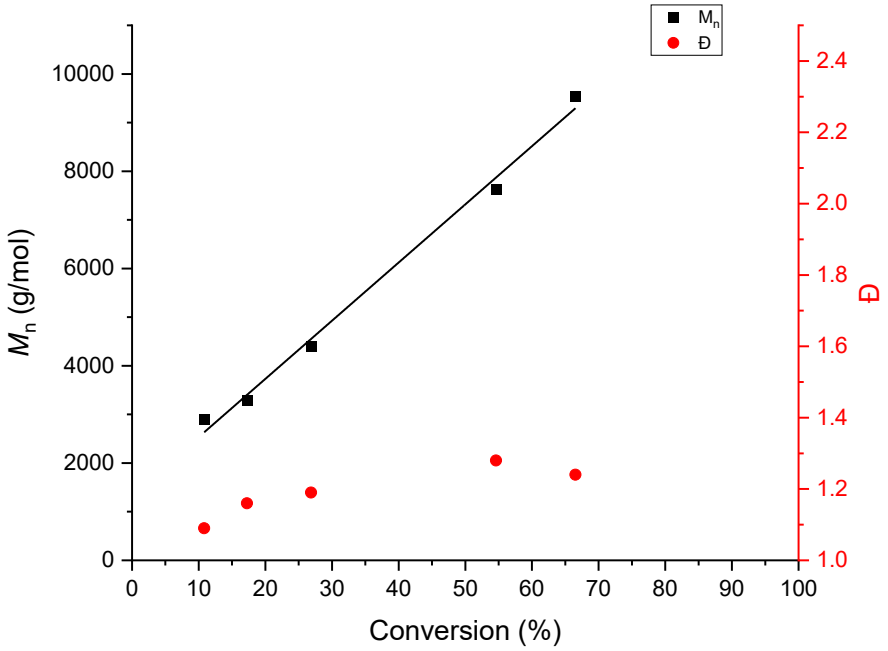


Figure B18. Plot of PLA M_n *vs. rac*-LA conversion for *rac*-LA ROP initiated by **2** as per conditions in Table 5, Entry 3.

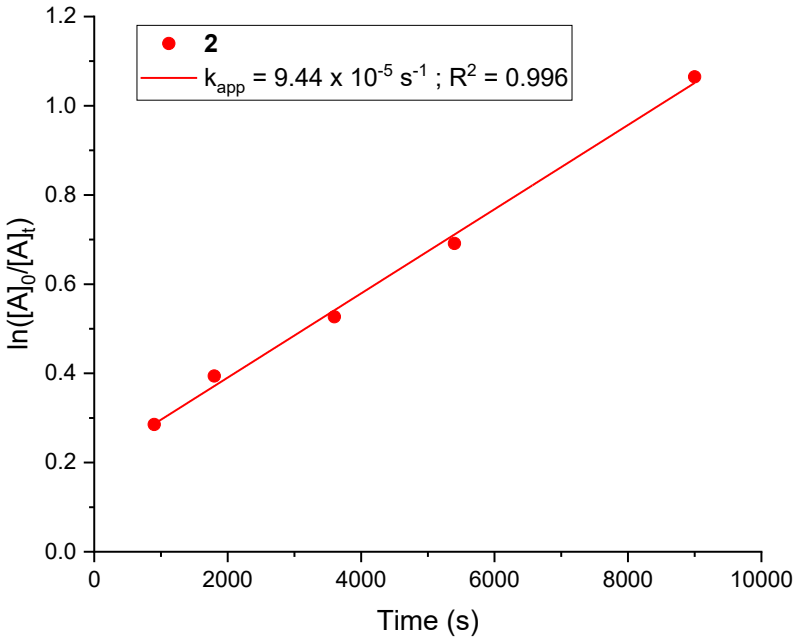


Figure B19. First-order plot (linear fit) for *L*-LA ROP initiated by **2** as per conditions in Table 7, Entry 1.

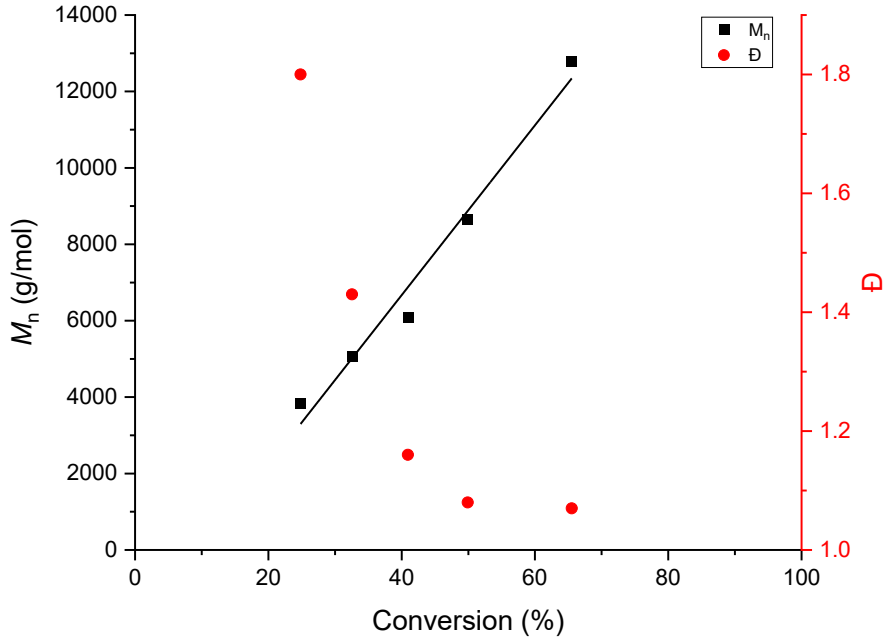


Figure B20. Plot of PLLA M_n *vs*. *L*-LA conversion for *L*-LA ROP initiated by **2** as per conditions in Table 7, Entry 1.

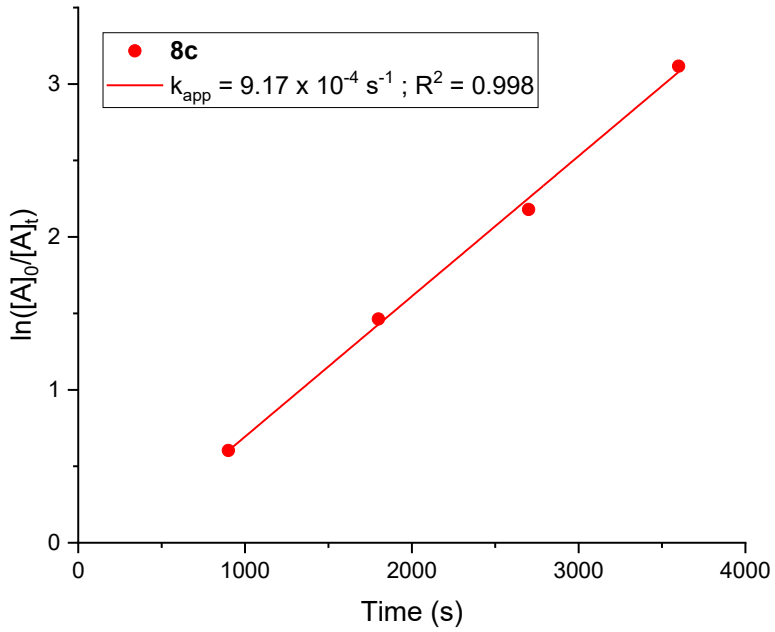


Figure B21. First-order plot (linear fit) for *L*-LA ROP initiated by **8c** as per conditions in Table 7, Entry 2.

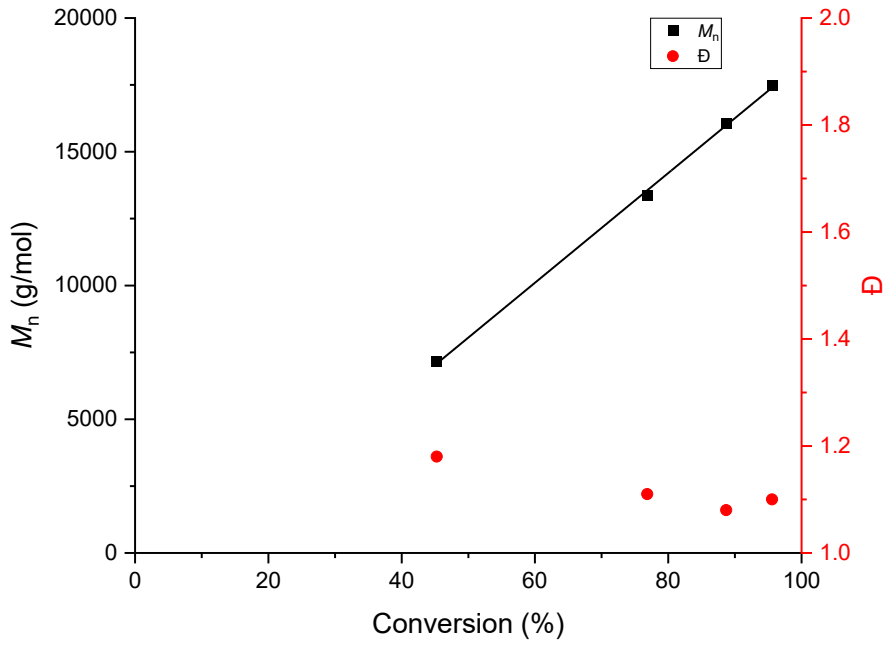


Figure B22. Plot of PLLA M_n *vs.* *L*-LA conversion for *L*-LA ROP initiated by **8c** as per conditions in Table 7, Entry 2.

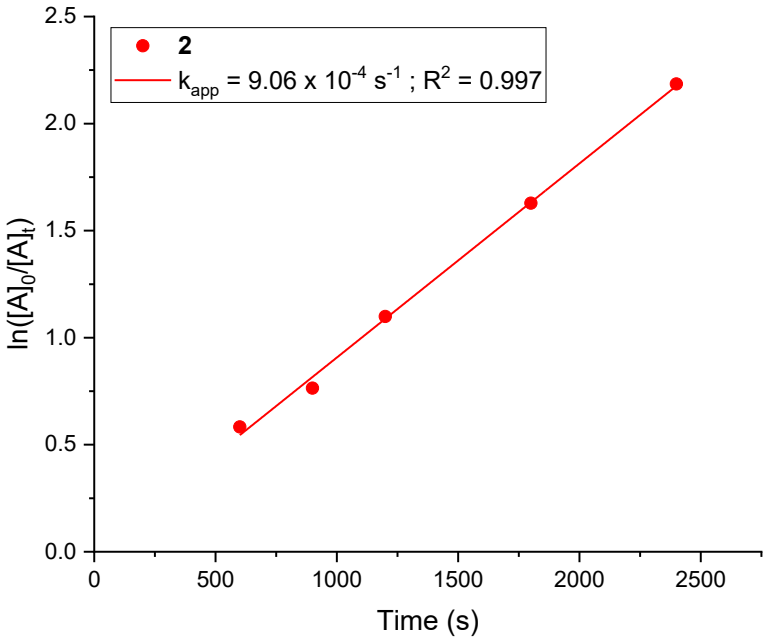


Figure B23. First-order plot (linear fit) for *meso*-LA ROP initiated by **2** as per conditions in Table 7, Entry 3.

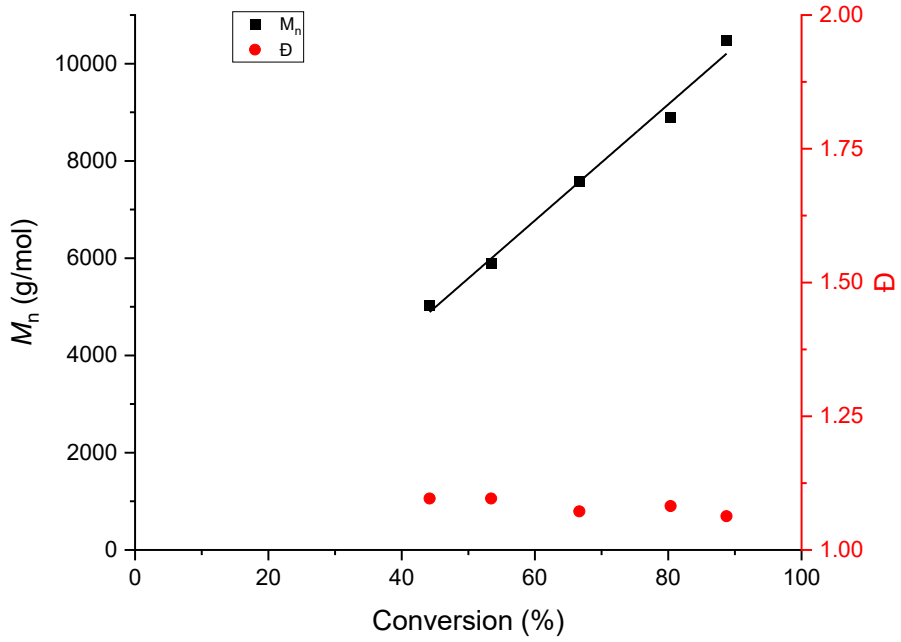


Figure B24. Plot of PLA M_n *vs*. *meso*-LA conversion for *meso*-LA ROP initiated by **2** as per conditions in Table 7, Entry 3.

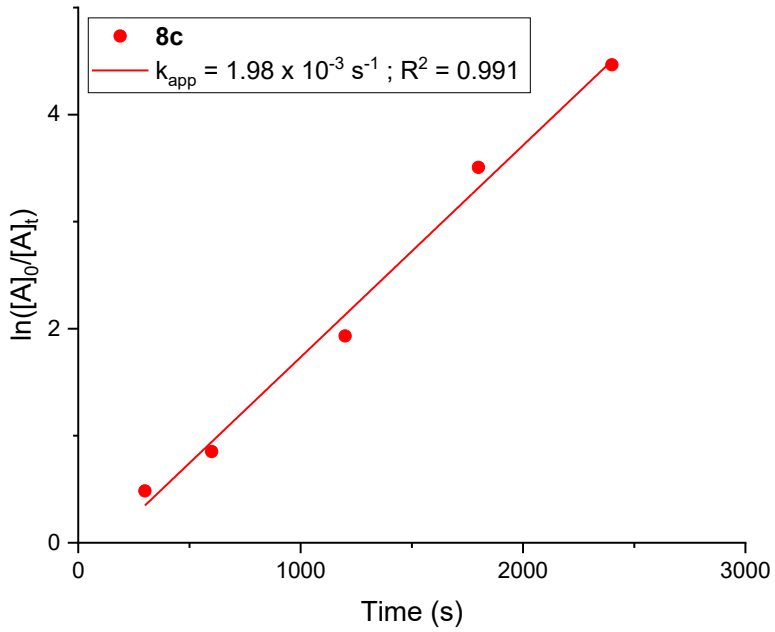


Figure B25. First-order plot (linear fit) for *meso*-LA ROP initiated by **8c** as per conditions in Table 7, Entry 4.

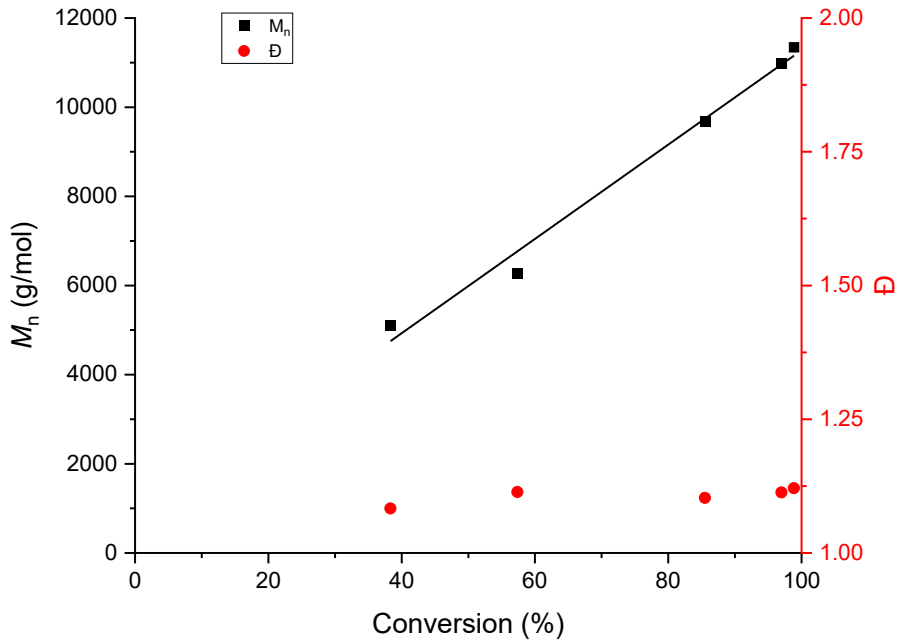


Figure B26. Plot of PLA M_n *vs. meso*-LA conversion for *meso*-LA ROP initiated by **8c** as per conditions in Table 7, Entry 4.

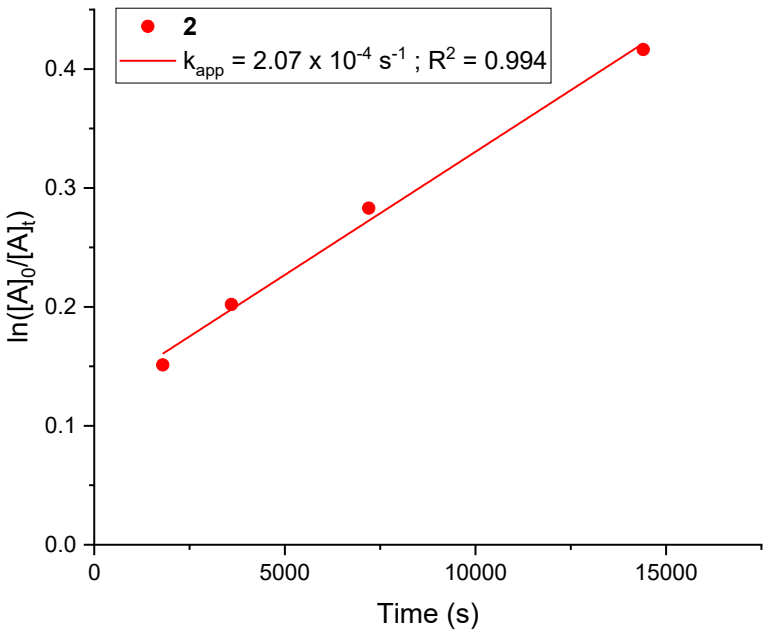


Figure B27. First-order plot (linear fit) for ε-CL ROP initiated by **2** as per conditions in Table 8, Entry 1.

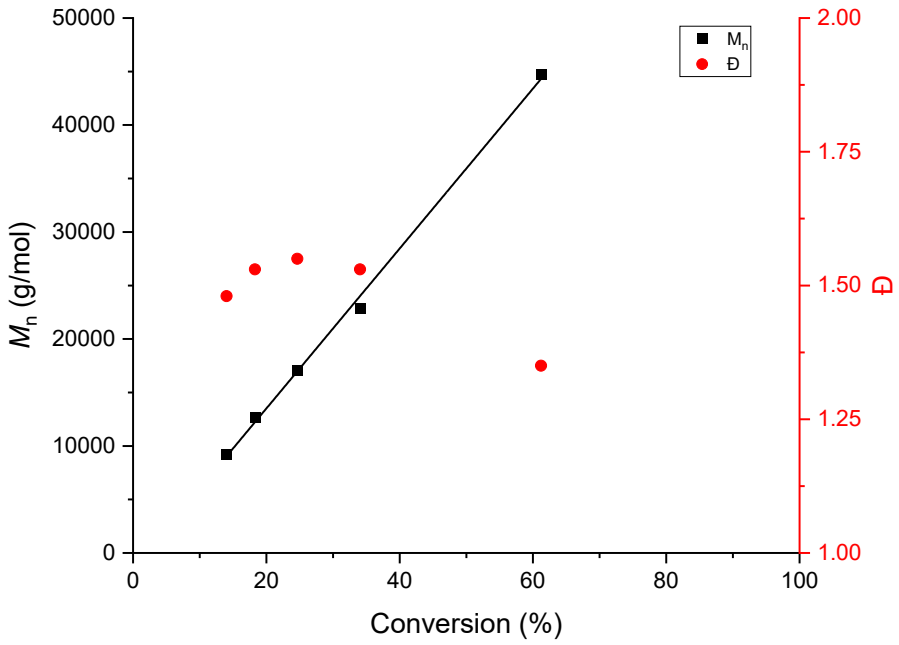


Figure B28. Plot of PCL M_n *vs*. ε-CL conversion for ε-CL ROP initiated by **2** as per conditions in Table 8, Entry 1.

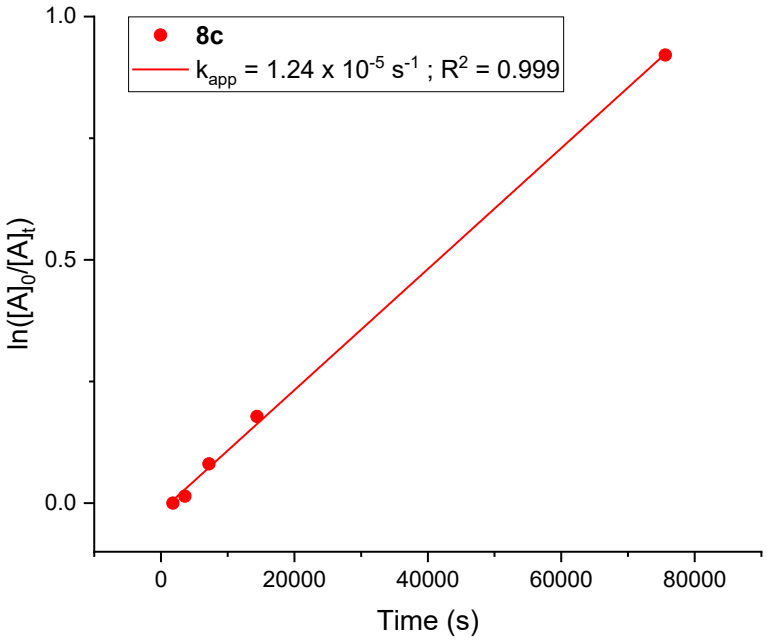


Figure B29. First-order plot (linear fit) for ε-CL ROP initiated by **8c** as per conditions in Table 8, Entry 2.

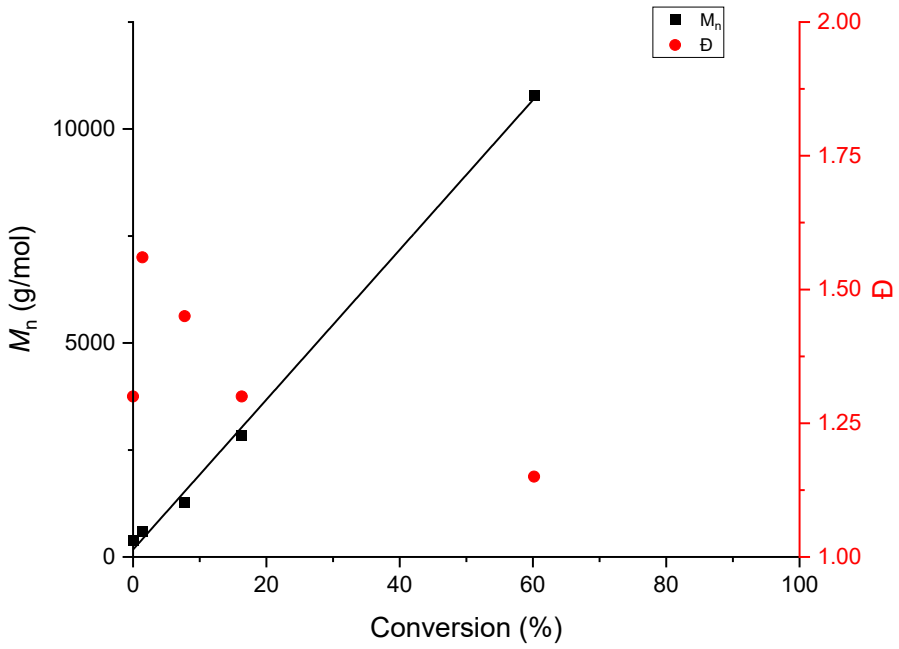


Figure B30. Plot of PCL M_n *vs*. ε-CL conversion for ε-CL ROP initiated by **8c** as per conditions in Table 8, Entry 2.

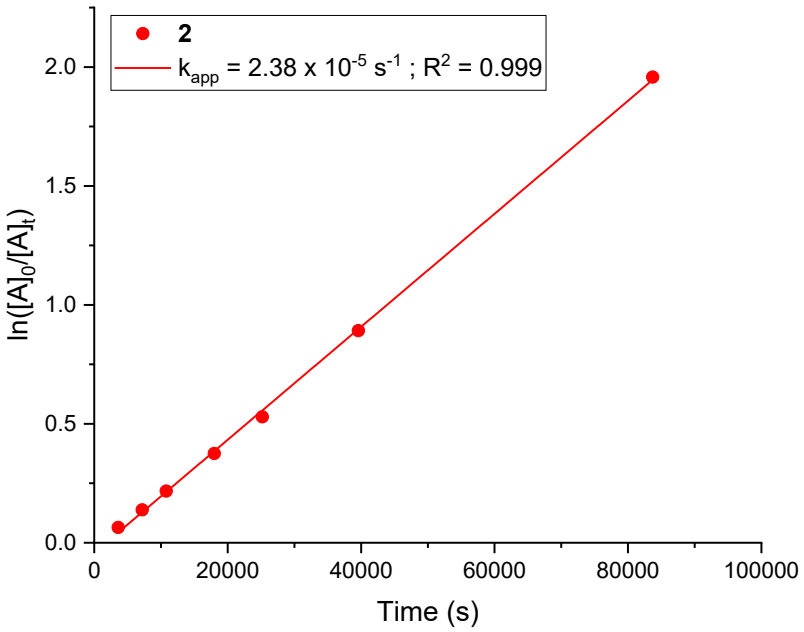


Figure B31. First-order plot (linear fit) for ε-DL ROP initiated by **2** as per conditions in Table 8, Entry 3.

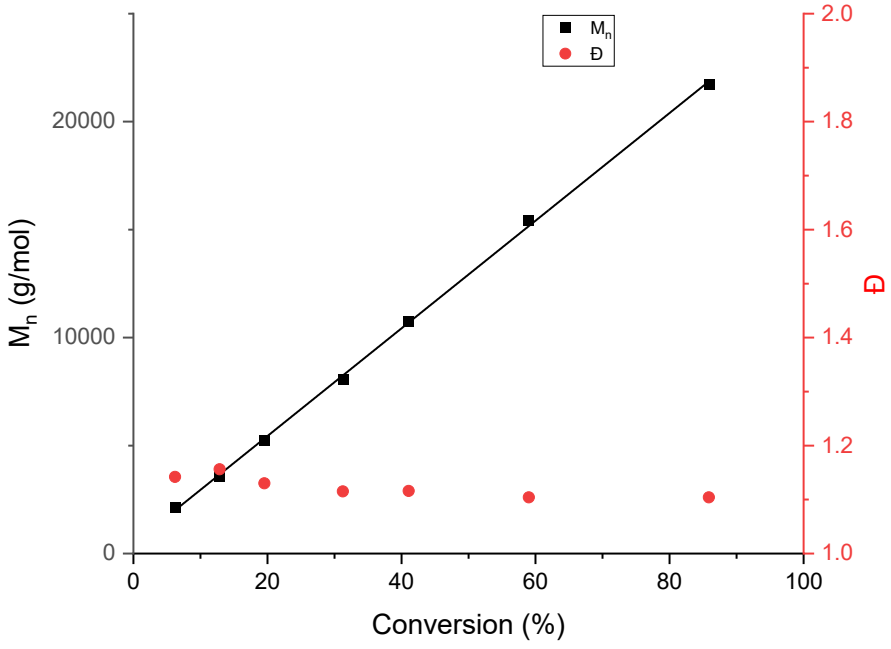


Figure B32. Plot of PDL M_n *vs.* ε-DL conversion for ε-DL ROP initiated by **2** as per conditions in Table 8, Entry 3.

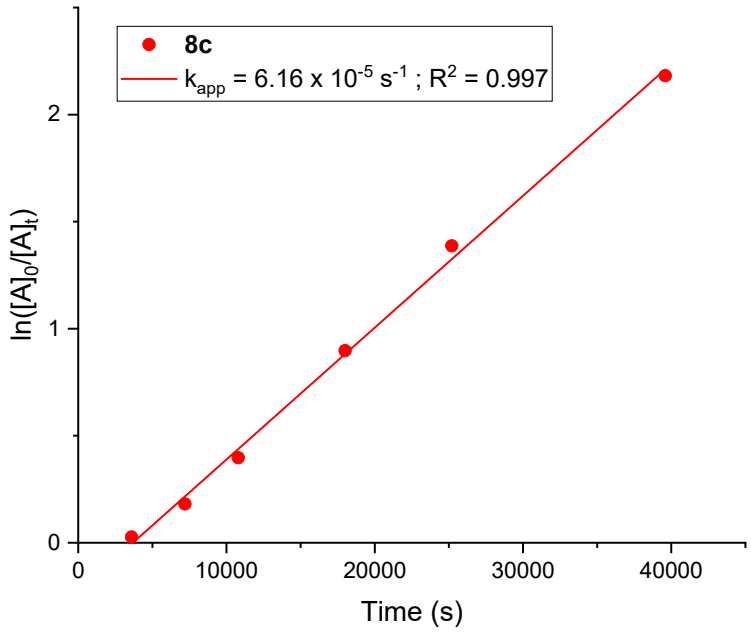


Figure B33. First-order plot (linear fit) for ε-DL ROP initiated by **8c** as per conditions in Table 8, Entry 4.

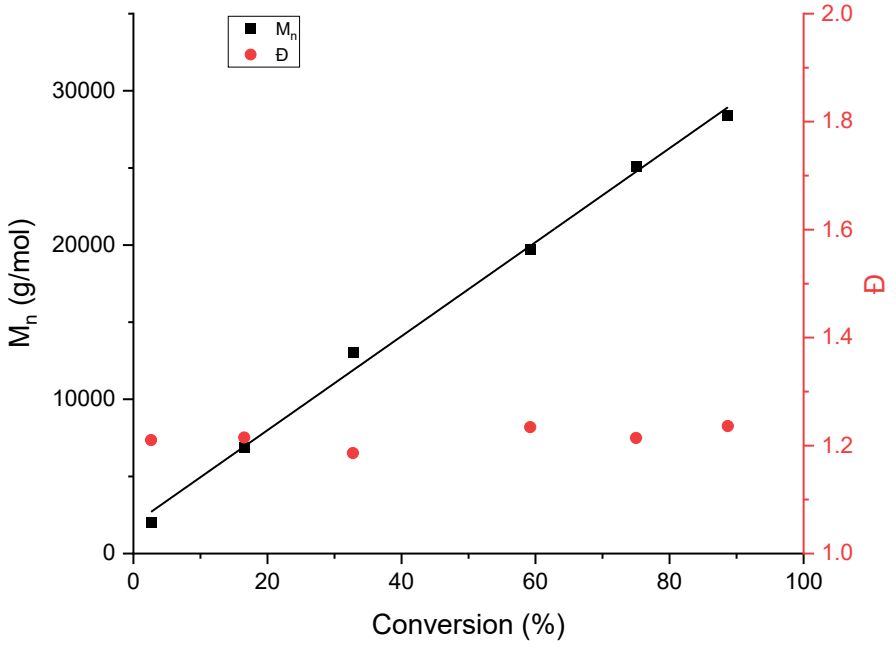


Figure B34. Plot of PDL M_n *vs*. ε-DL conversion for ε-DL ROP initiated by **8c** as per conditions in Table 8, Entry 4.

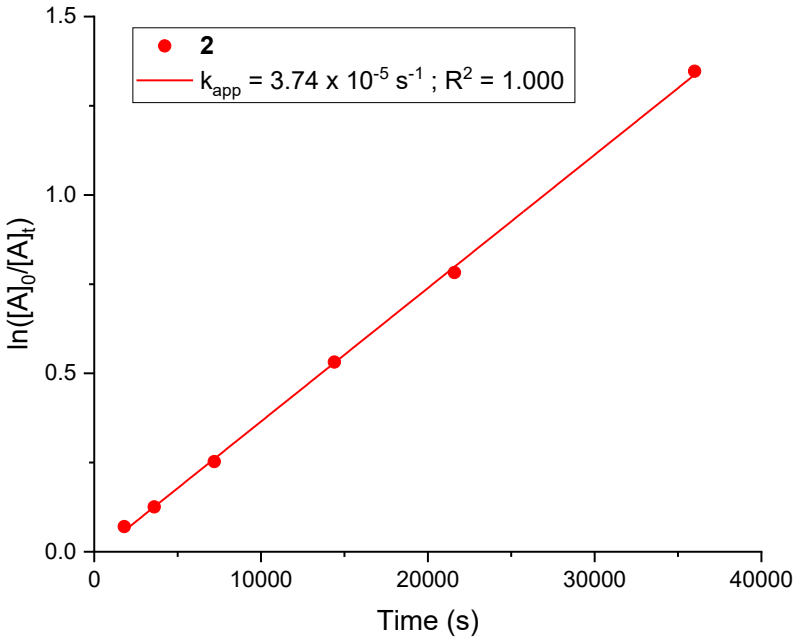


Figure B35. First-order plot (linear fit) for β-BL ROP initiated by **2** as per conditions in Table 9, Entry 1.

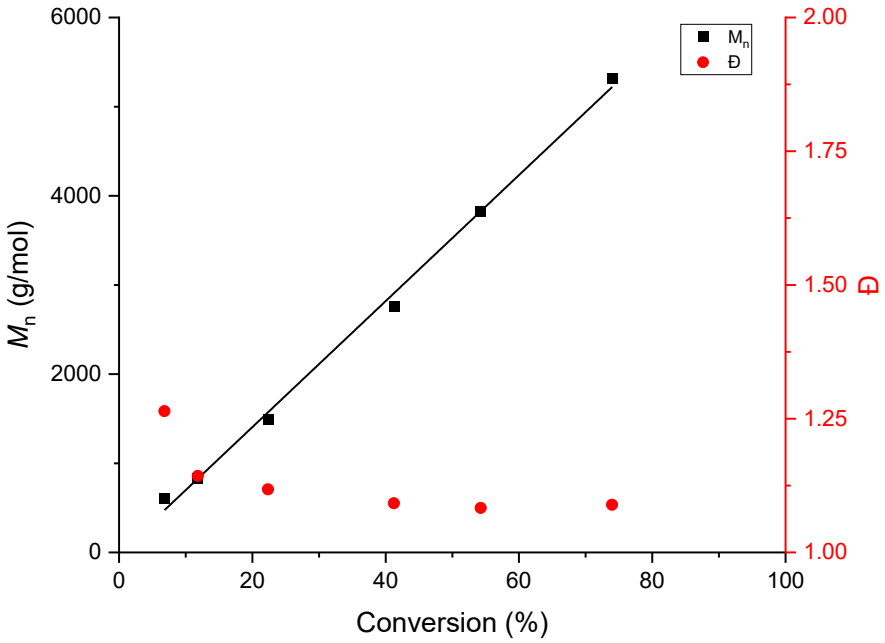


Figure B36. Plot of PHB M_n *vs*. β-BL conversion for β-BL ROP initiated by **2** as per conditions in Table 9, Entry 1.

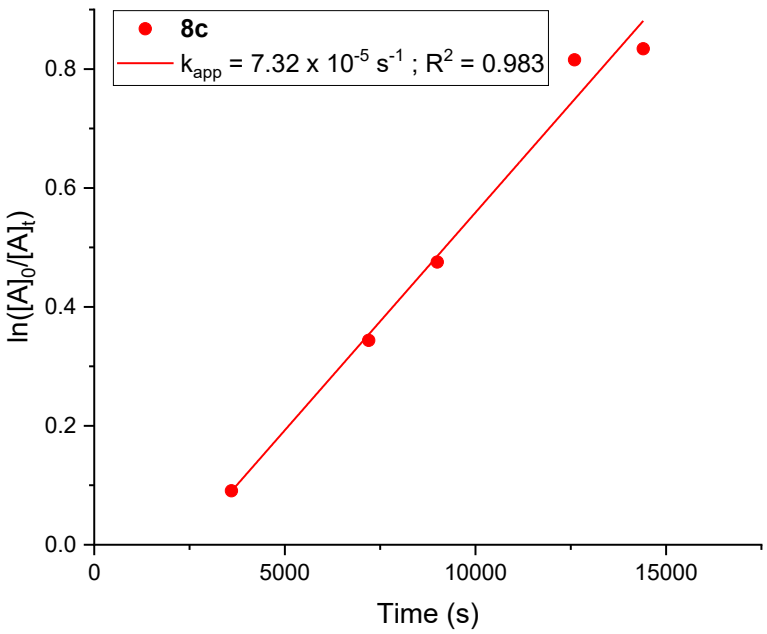


Figure B37. First-order plot (linear fit) for β-BL ROP initiated by **8c** as per conditions in Table 9, Entry 2.

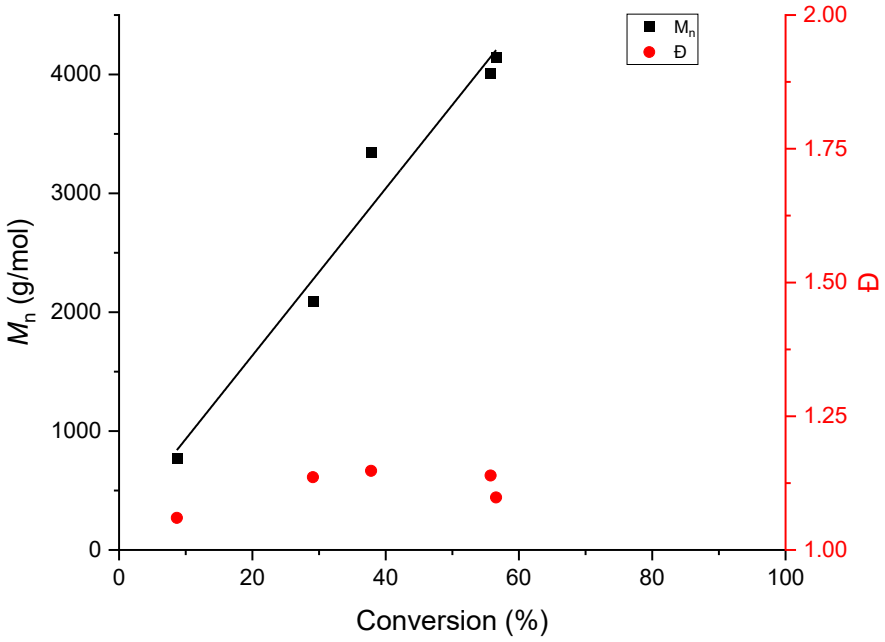


Figure B38. Plot of PHB M_n *vs*. β-BL conversion for β-BL ROP initiated by **8c** as per conditions in Table 9, Entry 2.

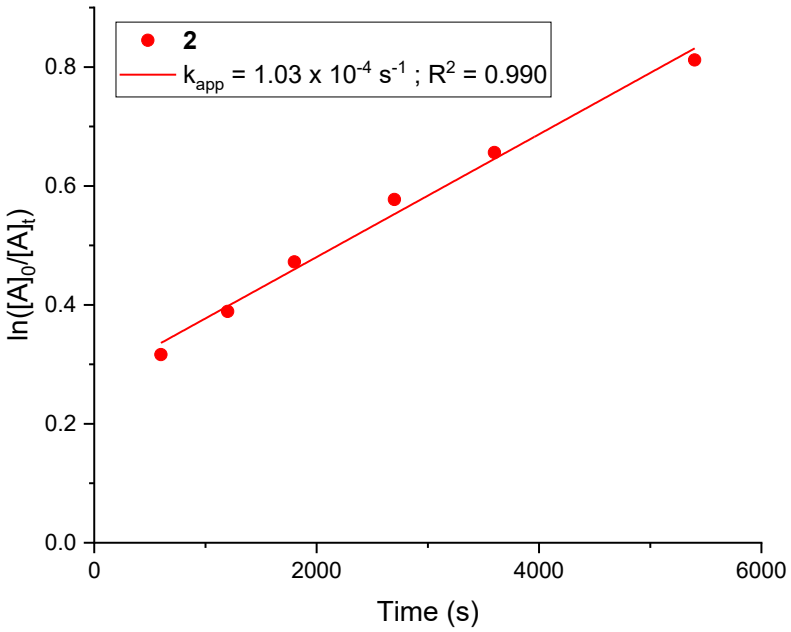


Figure B39. First-order plot (linear fit) for TMC ROP initiated by **2** as per conditions in Table 9, Entry 3.

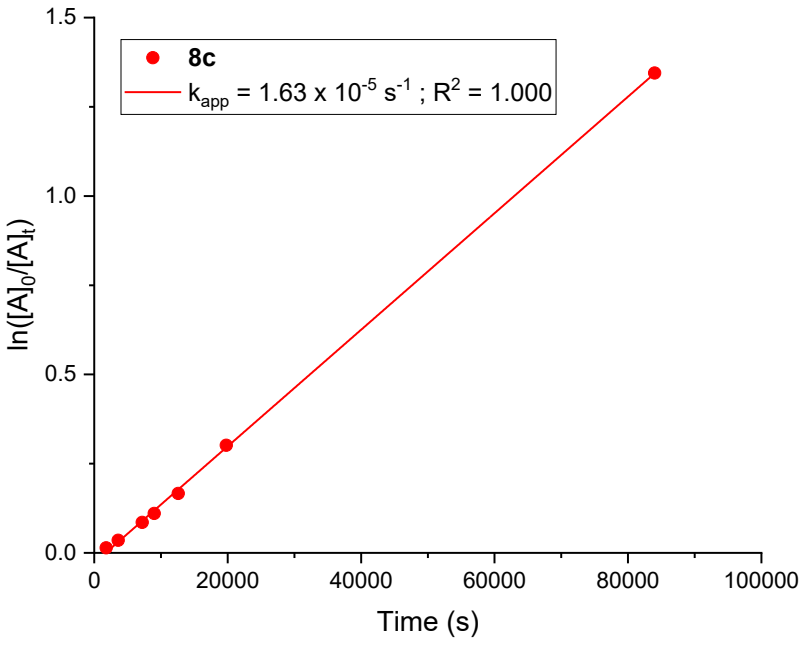


Figure B40. First-order plot (linear fit) for TMC ROP initiated by **8c** as per conditions in Table 9, Entry 4.

6.7.2 Chapter 3

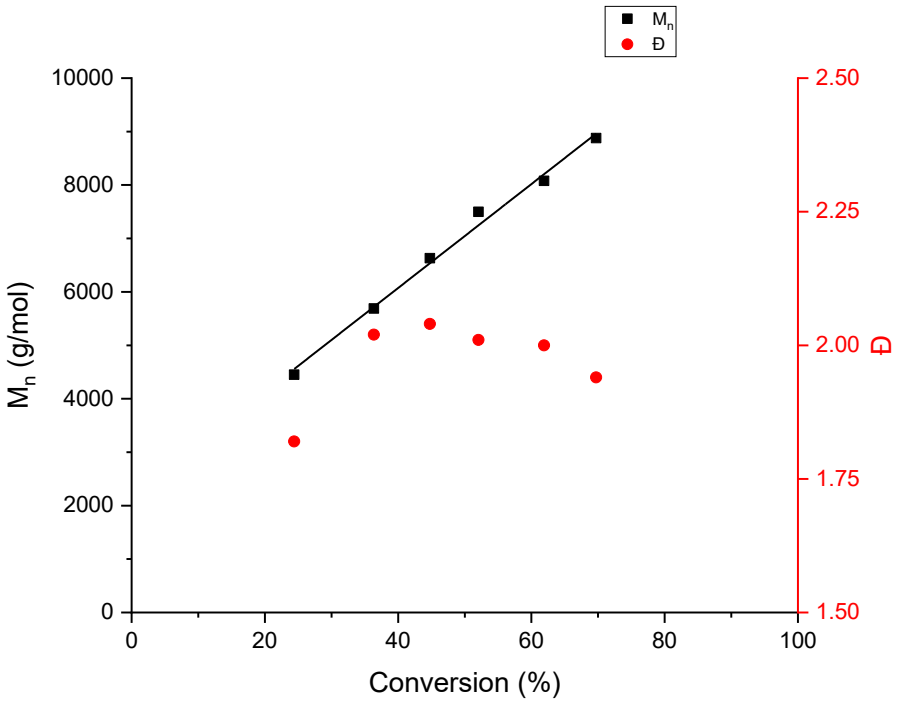


Figure B41: Plot of M_n *vs.* ε-CL conversion for ε-CL ROP as initiated by (*R,R*)-**15** as per conditions in Table 1, Entry 1.

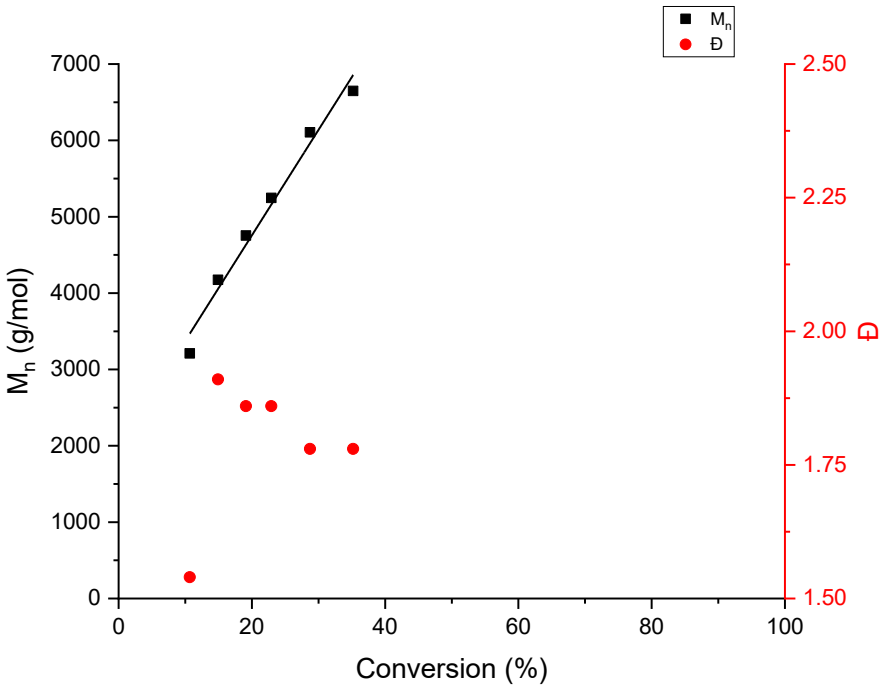


Figure B42: Plot of M_n *vs.* ε-CL conversion for ε-CL ROP as initiated by *rac*-**15** as per conditions in Table 1, Entry 3.

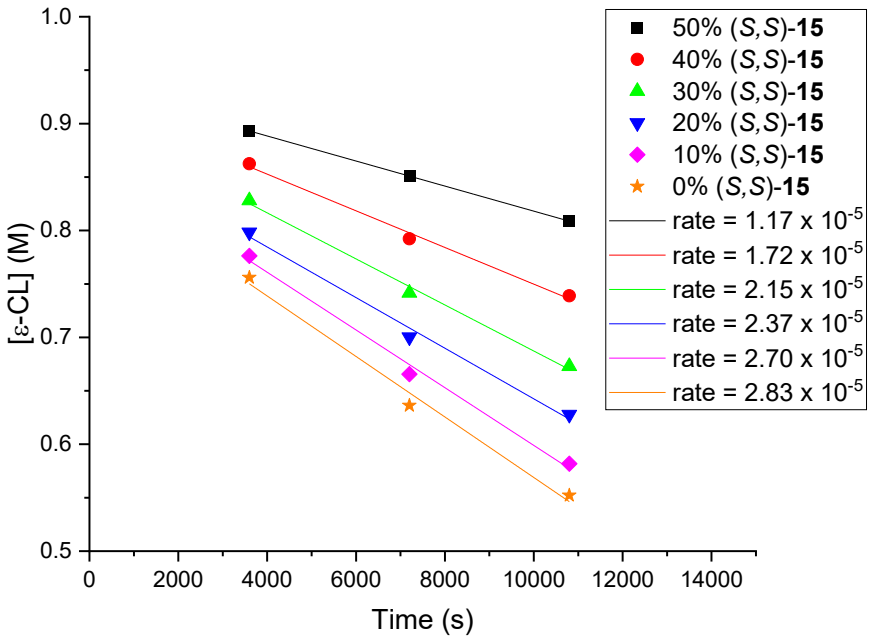


Figure B43. Superimposition of initial rate plots at various %ee$_{cat}$ (0-100 %) and their corresponding initial rate for ε-CL ROP.

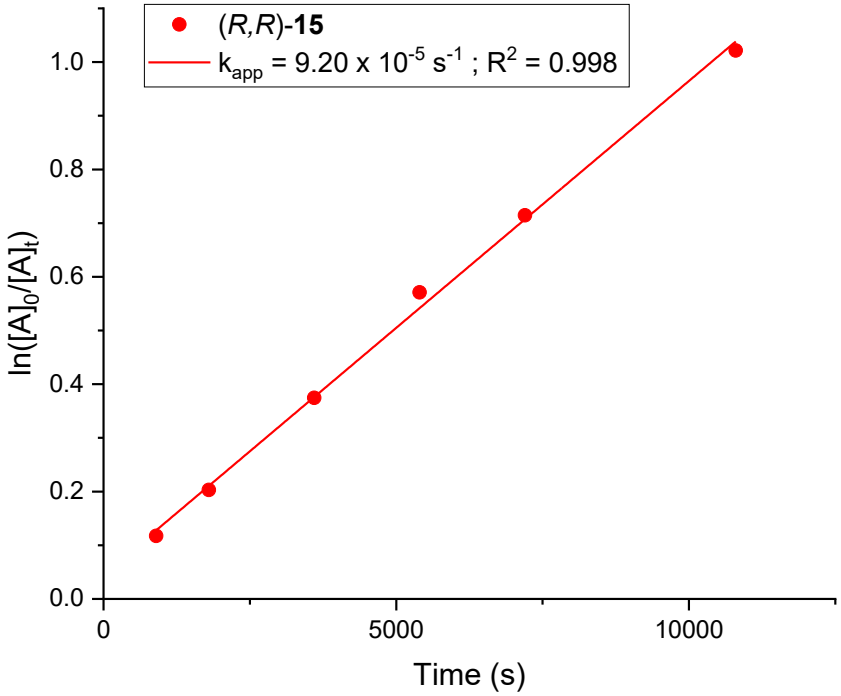


Figure B44. First-order plot (linear fit) for *L*-LA ROP initiated by (*R,R*)-**15** as per conditions in Table 2, Entry 1.

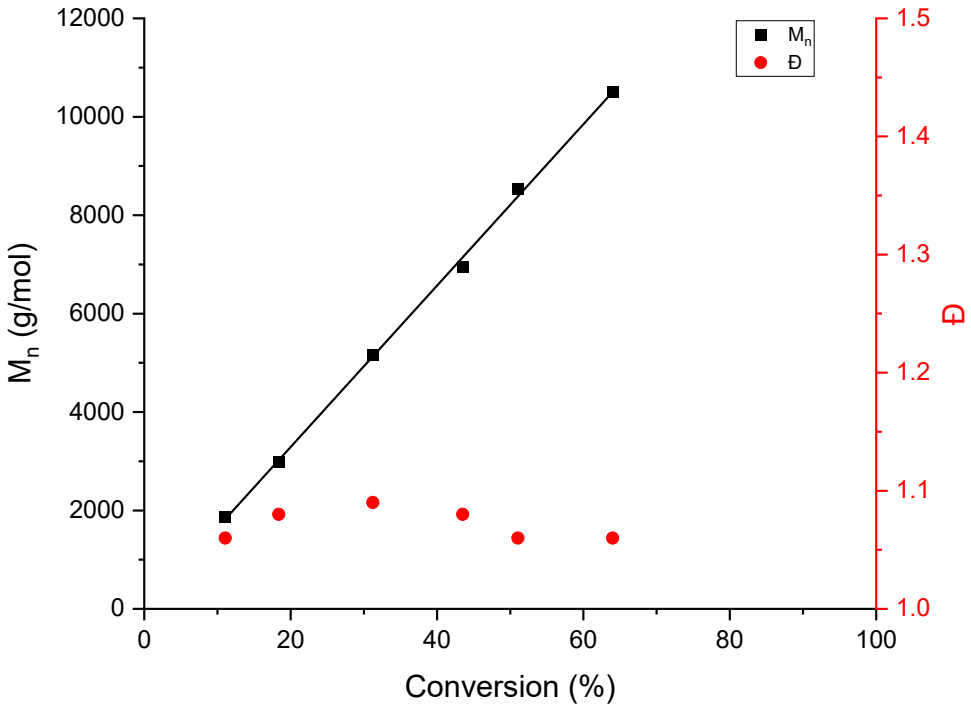


Figure B45. Plot of M_n vs *L*-LA conversion for *L*-LA ROP as initiated by (*R,R*)-**15** as per conditions in Table 2, Entry 1.

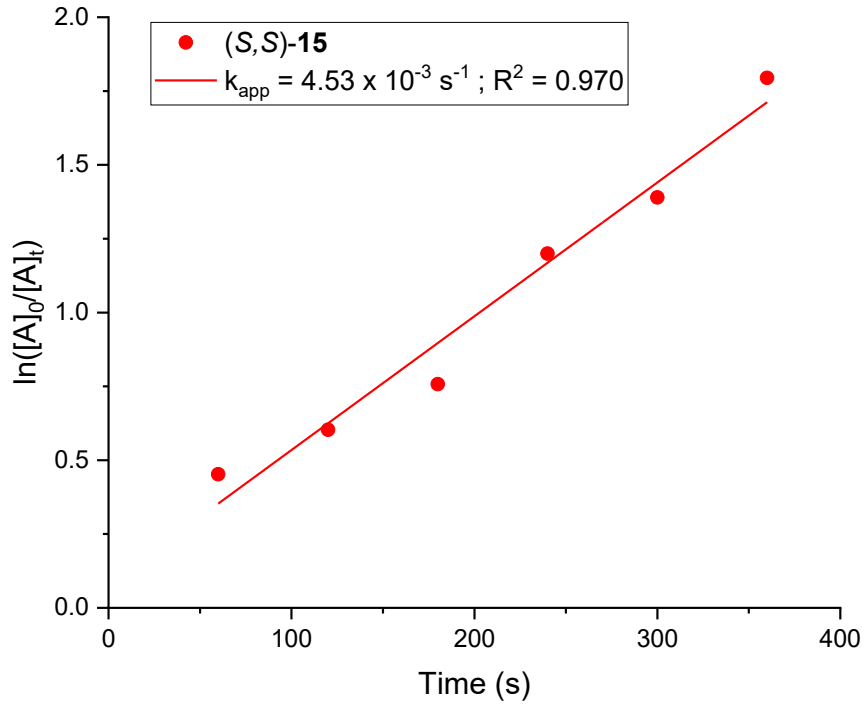


Figure B46. First-order plot (linear fit) for *L*-LA ROP initiated by (*S,S*)-**15** as per conditions in Table 2, Entry 2.

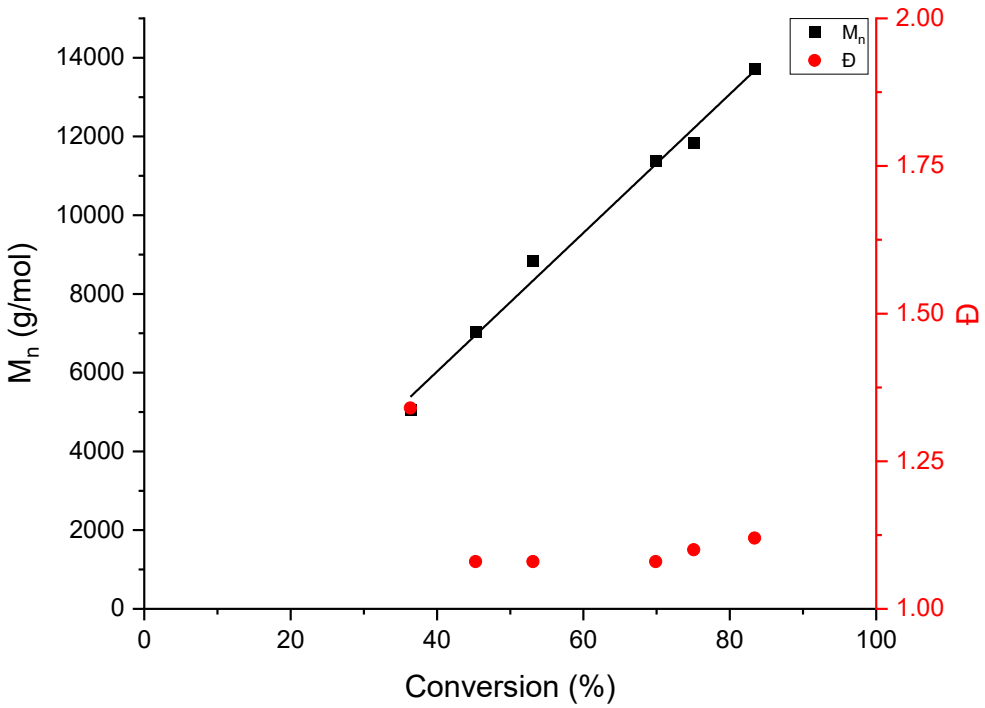


Figure B47. Plot of M_n *vs*. *L*-LA conversion for *L*-LA ROP as initiated by (*S*,*S*)-**15** as per conditions in Table 2, Entry 2.

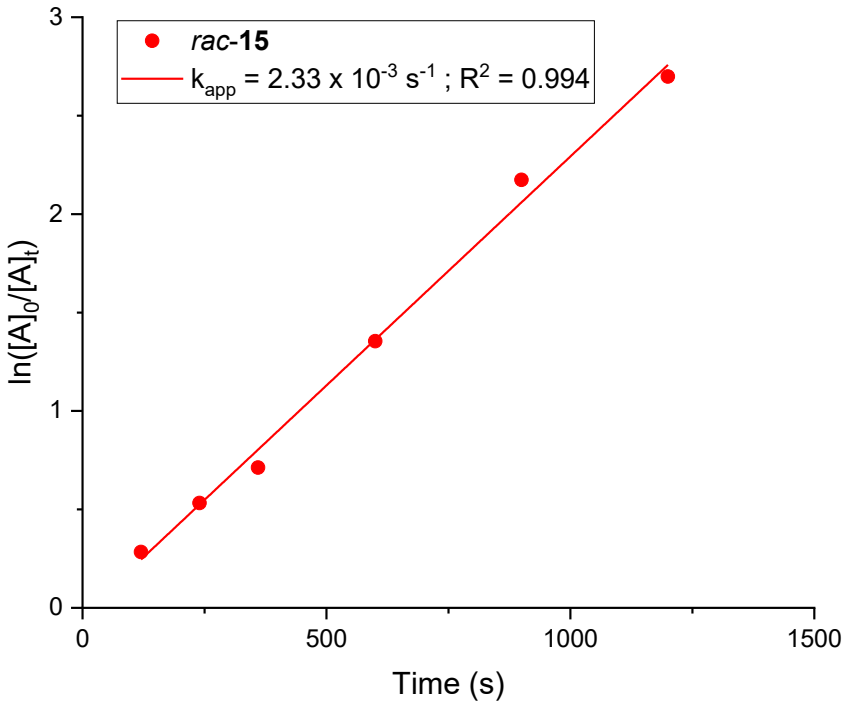


Figure B48. First-order plot (linear fit) for *L*-LA ROP initiated by *rac*-**15** as per conditions in Table 2, Entry 3.

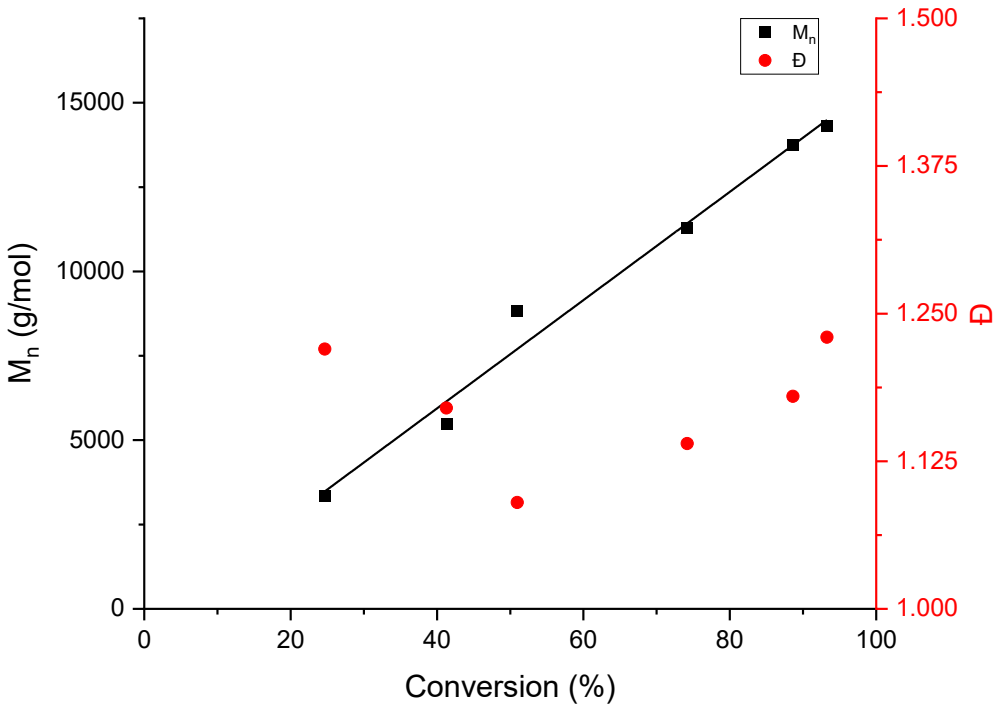


Figure B49. Plot of M_n *vs.* *L*-LA conversion for *L*-LA ROP as initiated by *rac*-**15** as per conditions in Table 2, Entry 3.

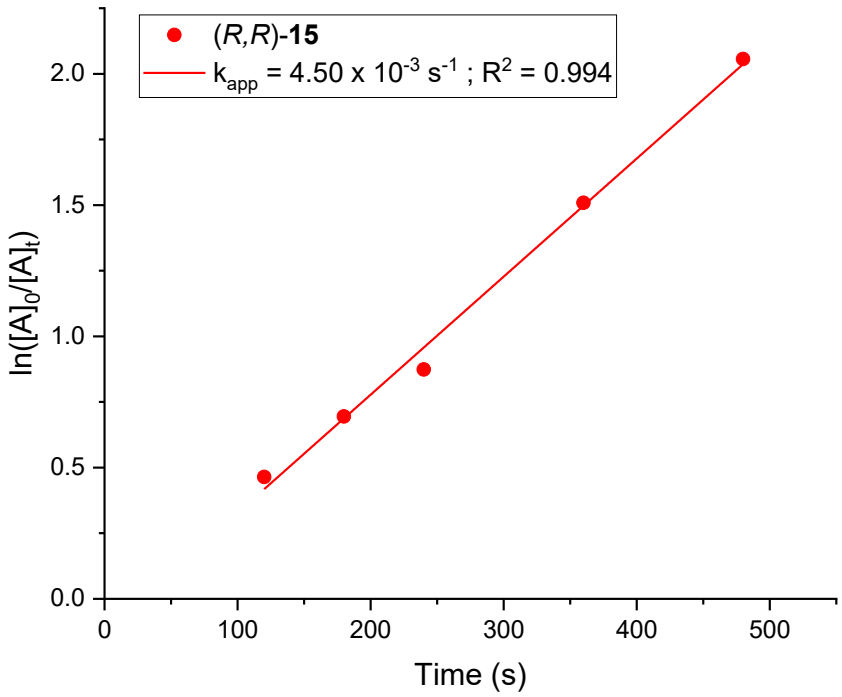


Figure B50. First-order plot (linear fit) for *D*-LA ROP initiated by (*R,R*)-**15** as per conditions in Table 2, Entry 4.

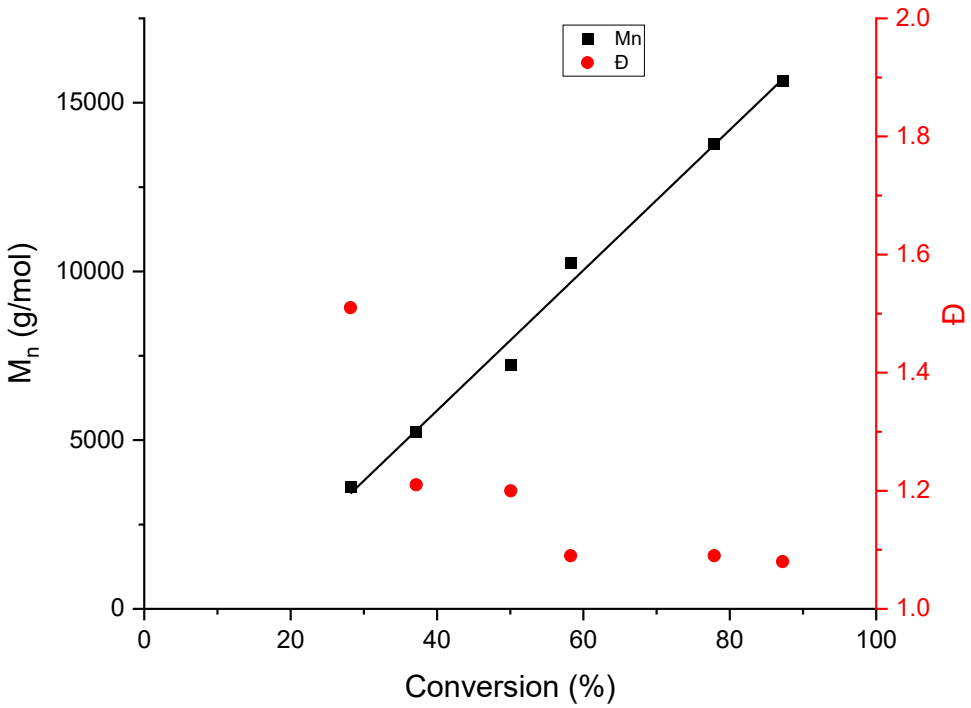


Figure B51. Plot of M_n *vs.* *D*-LA conversion for *D*-LA ROP as initiated by (*R*,*R*)-**15** as per conditions in Table 2, Entry 4.

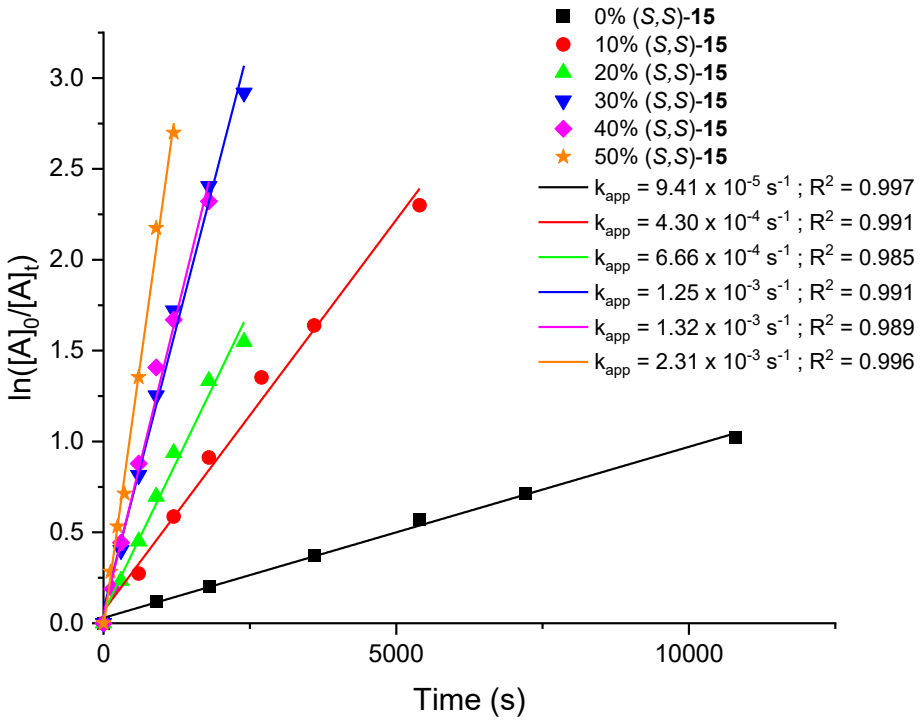


Figure B52. Superimposition of first-order log plots at various %ee_{cat} (-100-0 %) and their corresponding k_{app} for *L*-LA ROP.

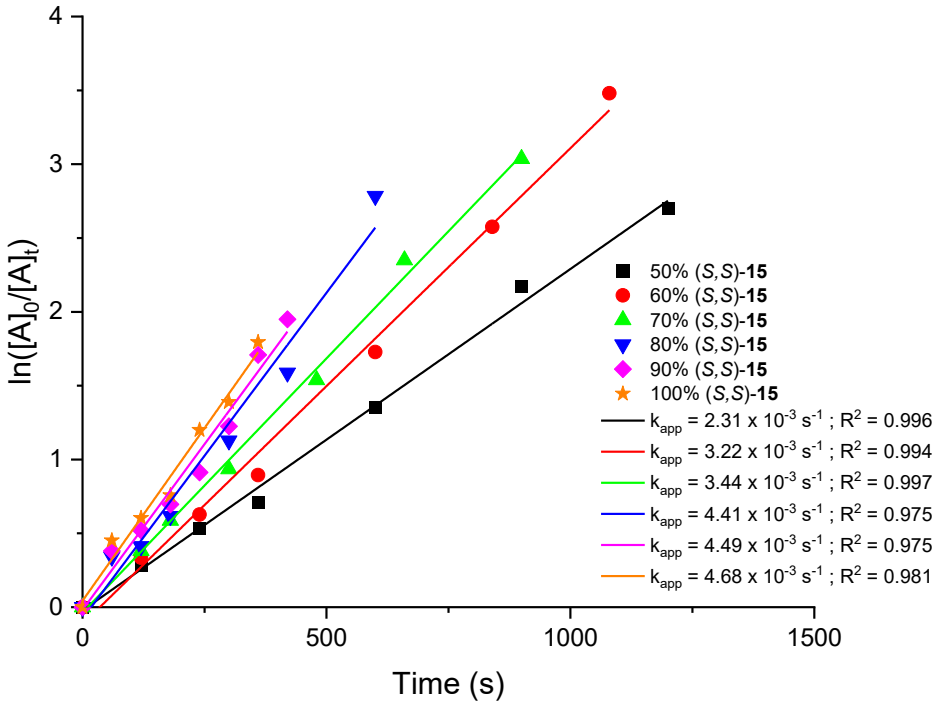


Figure B53. Superimposition of first-order log plots at various $\%ee_{cat}$ (0-100 %) and their corresponding k_{app} for *L*-LA ROP.

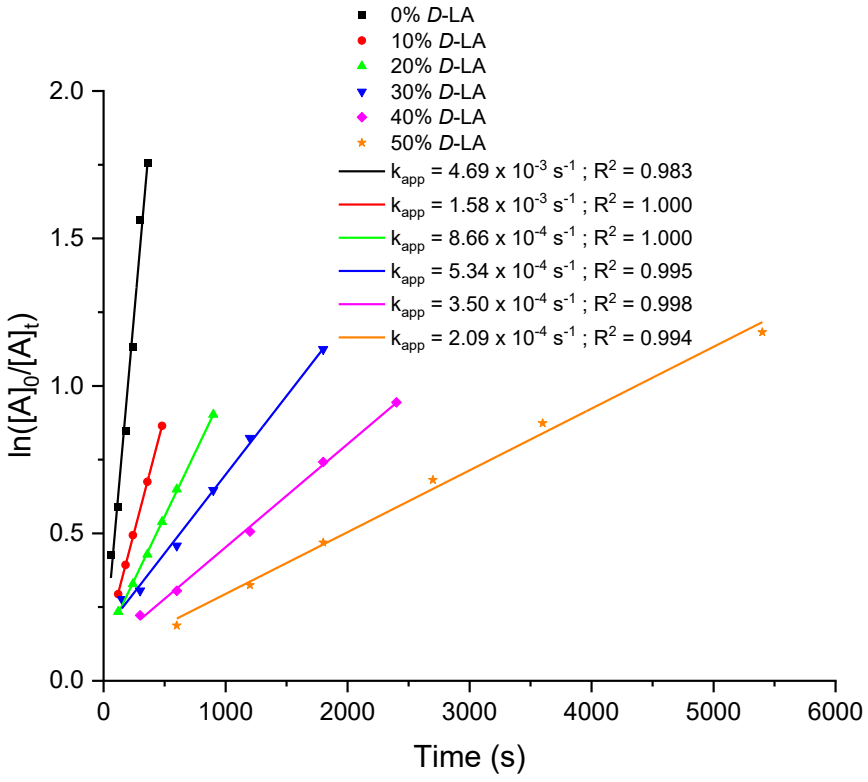


Figure B54. Superimposition of first-order log plots at various $\%ee_{LA}$ (-100-0 %) and their corresponding k_{app} for LA ROP mediated by (*S,S*)-**15**.

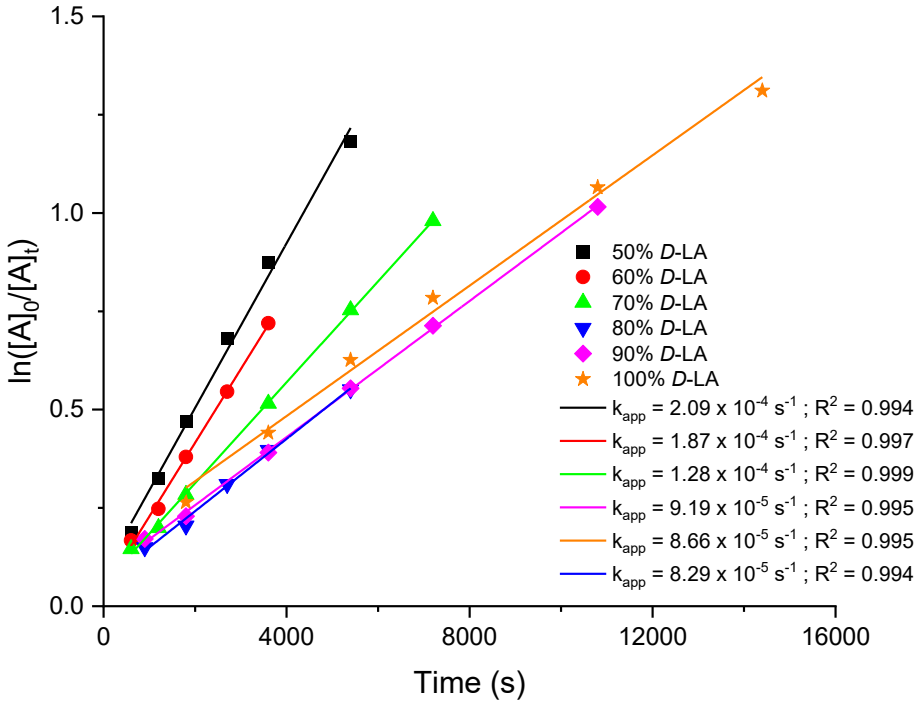


Figure B55. Superimposition of first-order log plots at various %ee$_{LA}$ (0-100 %) and their corresponding k_{app} for LA ROP mediated by (*S,S*)-**15**.

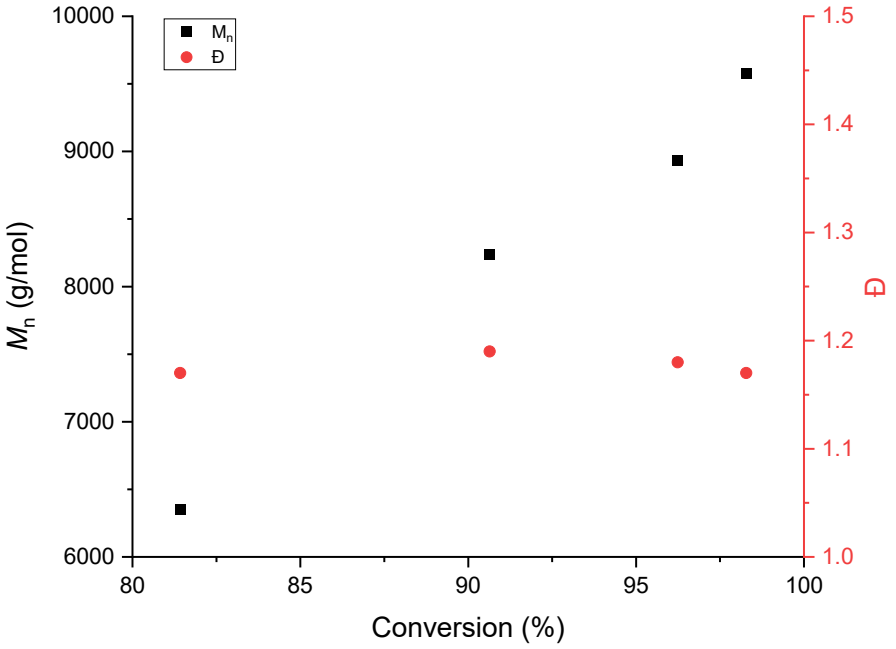


Figure B56. Plot of M_n *vs. meso*-LA conversion for *meso*-LA ROP as initiated by *rac*-**15** as per conditions in Table 3, Entry 3.

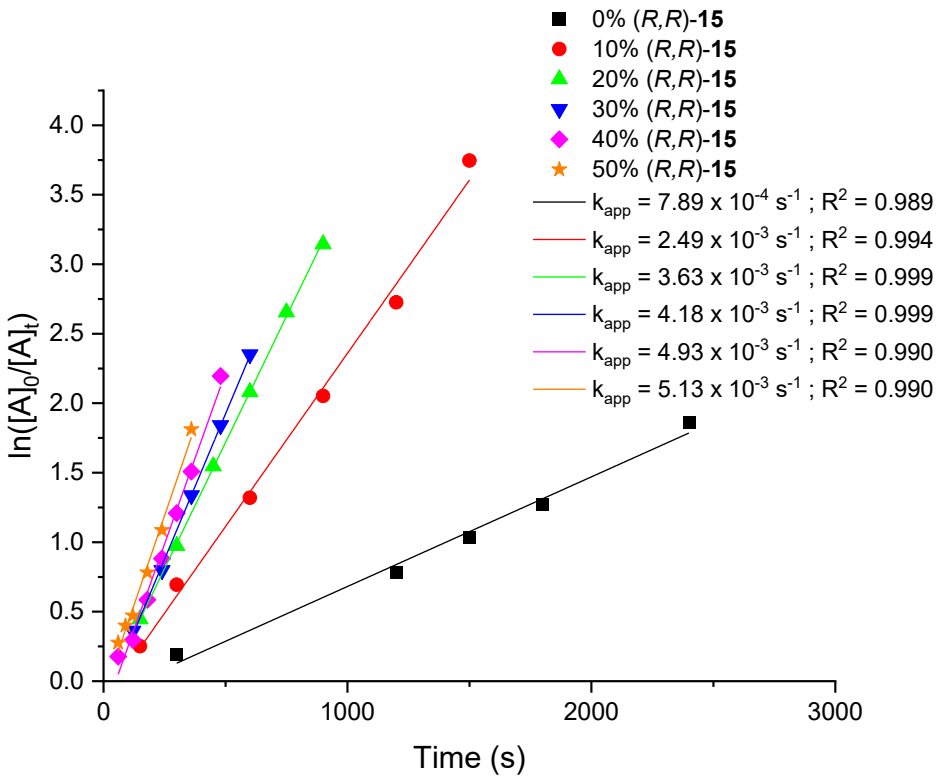


Figure B57. Superimposition of first-order log plots at various %ee$_{cat}$ (0-100 %) and their corresponding k_{app} for *meso*-LA ROP.

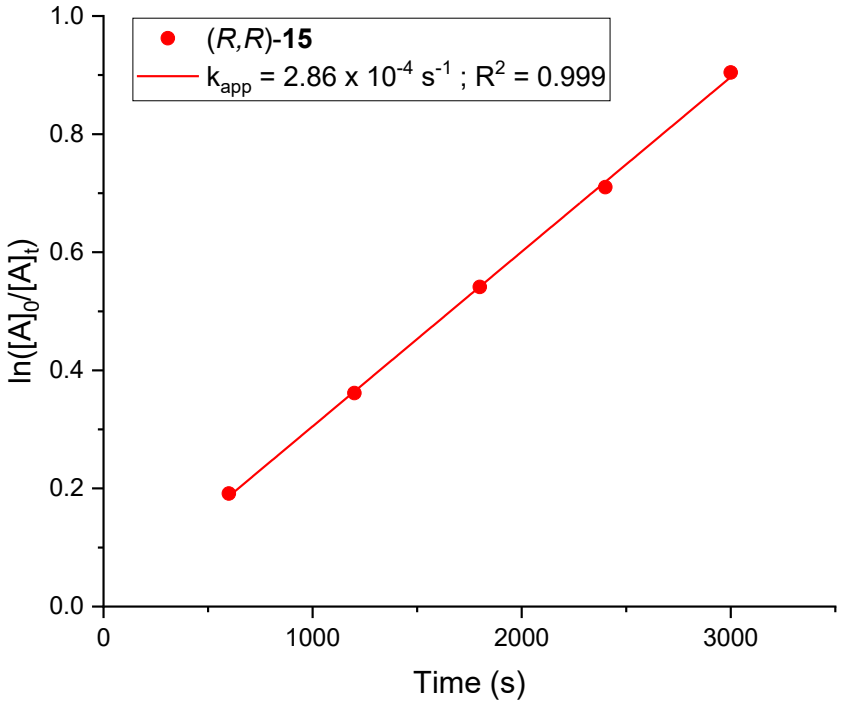


Figure B58. First-order plot (linear fit) for *rac*-LA ROP initiated by (*R,R*)-**15** as per conditions in Table 4, Entry 1.

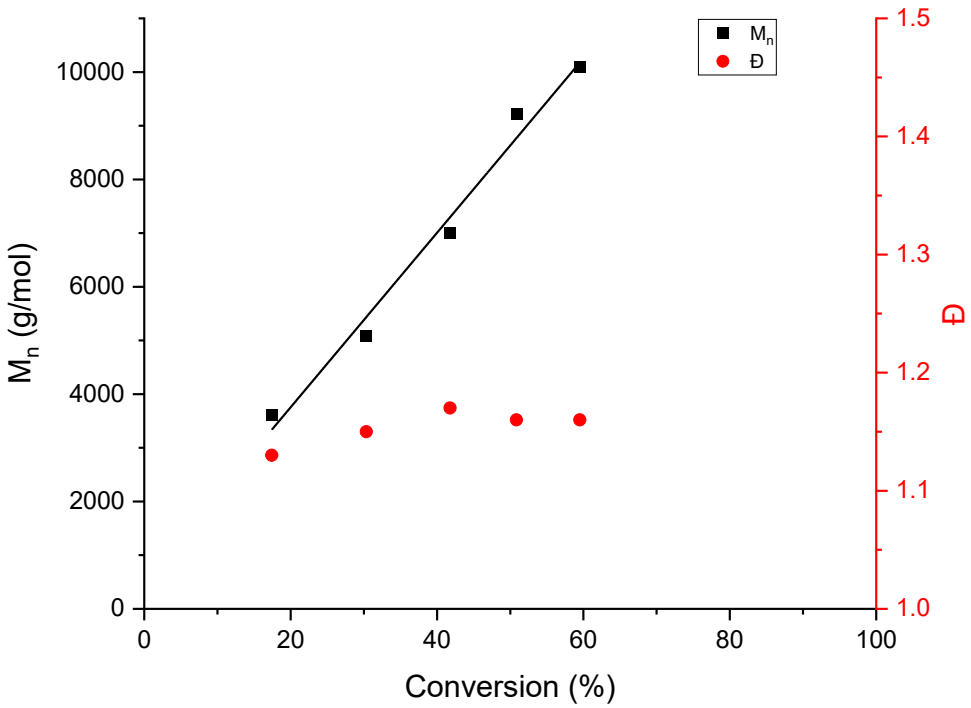


Figure B59. Plot of M_n *vs. rac*-LA conversion for *rac*-LA ROP as initiated by (*R,R*)-**15** as per conditions in Table 4, Entry 1.

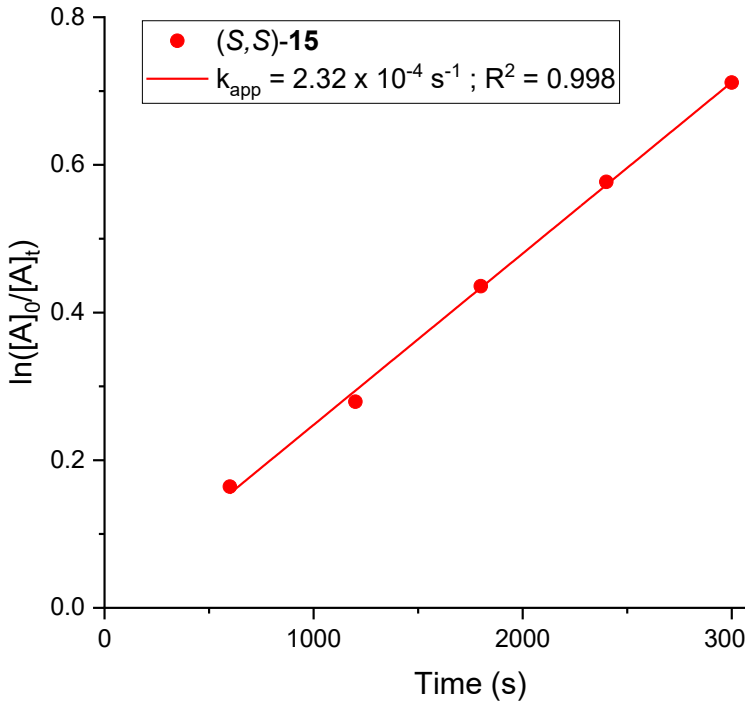


Figure B60. First-order plot (linear fit) for *rac*-LA ROP initiated by (*S,S*)-**15** as per conditions in Table 4, Entry 2.

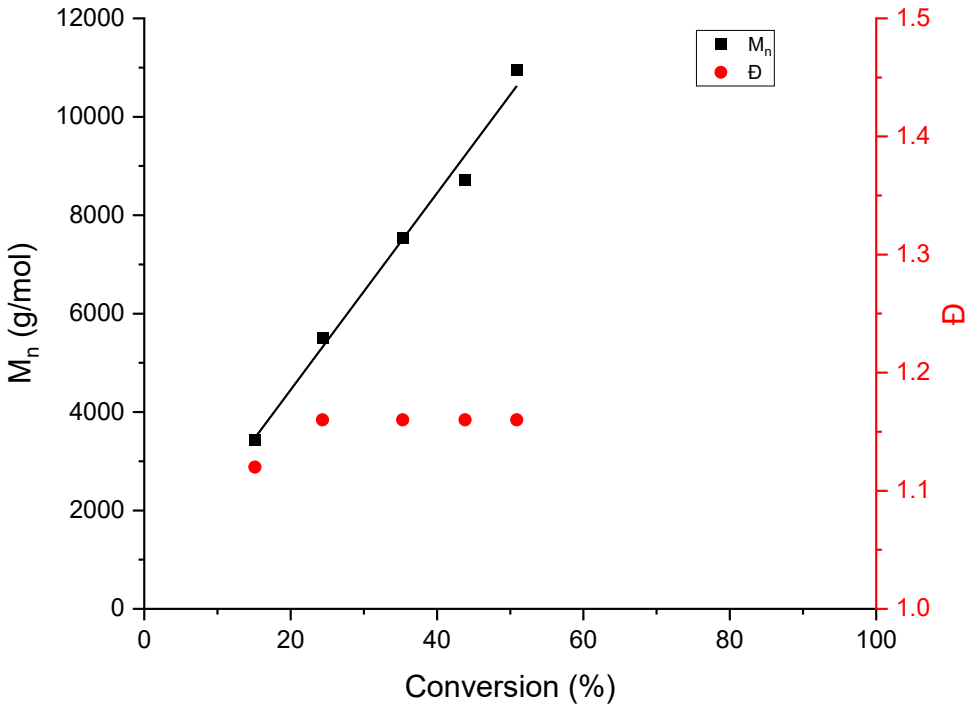


Figure B61. Plot of M_n *vs.* *rac*-LA conversion for *rac*-LA ROP as initiated by (*S,S*)-**15** as per conditions in Table 4, Entry 2.

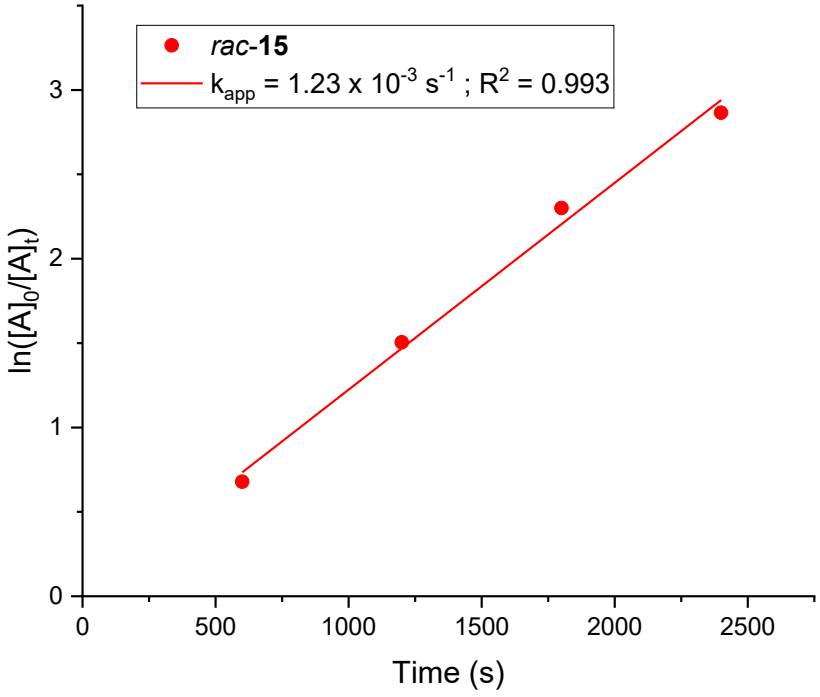


Figure B62. First-order plot (linear fit) for *rac*-LA ROP initiated by *rac*-**15** as per conditions in Table 4, Entry 3.

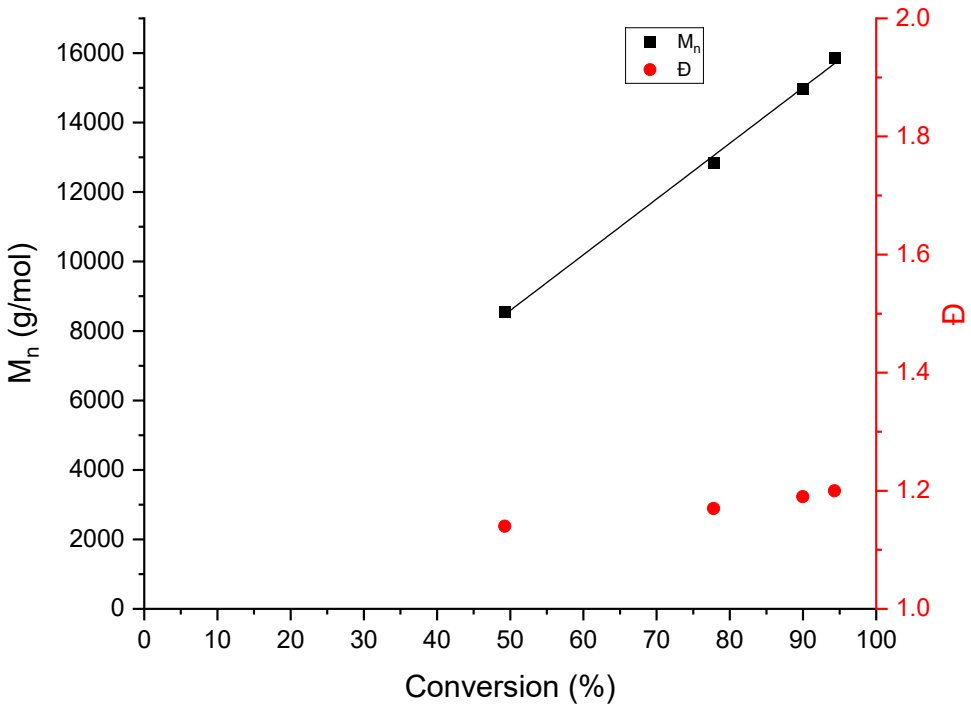


Figure B63. Plot of M_n *vs. rac*-LA conversion for *rac*-LA ROP as initiated by *rac*-**15** as per conditions in Table 4, Entry 3.

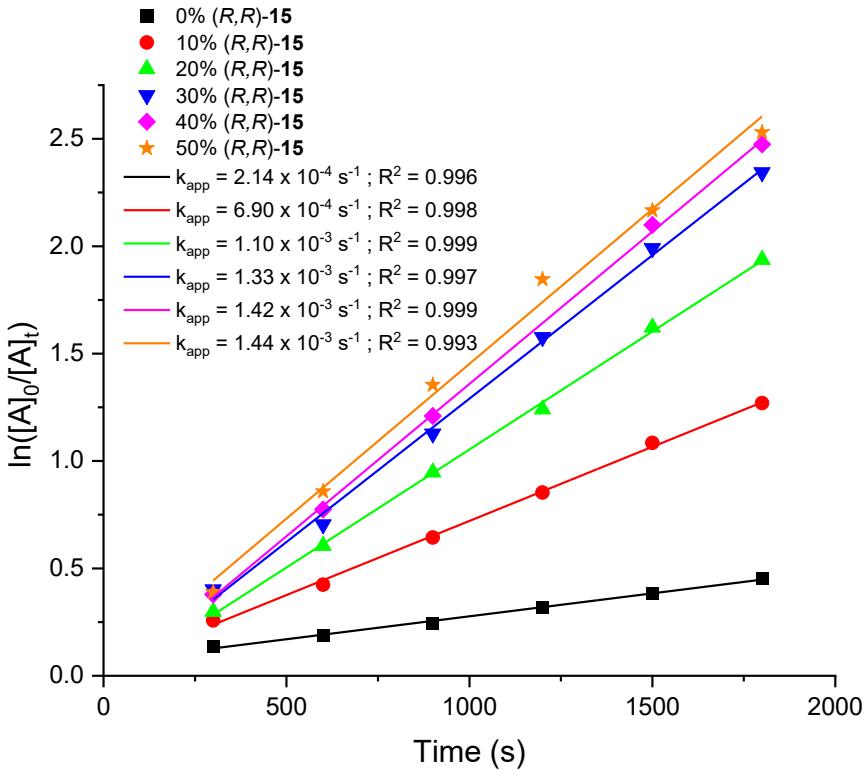


Figure B64. Superimposition of first-order log plots at various %ee$_{cat}$ (0-100 %) and their corresponding k_{app} for *rac*-LA ROP.

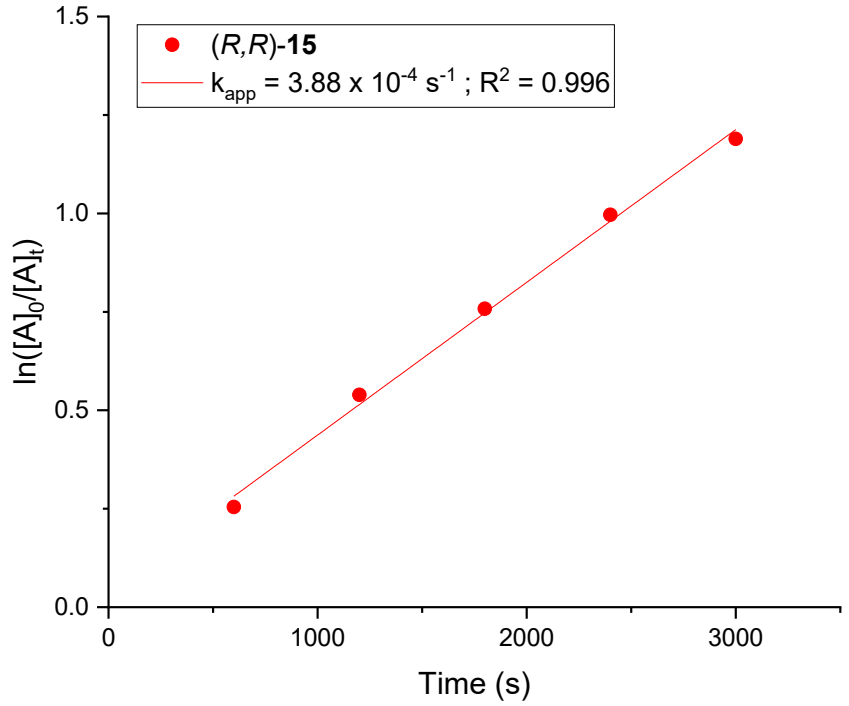


Figure B65. First-order plot (linear fit) for β-BL ROP initiated by (*R,R*)-**15** as per conditions in Table 5, Entry 1.

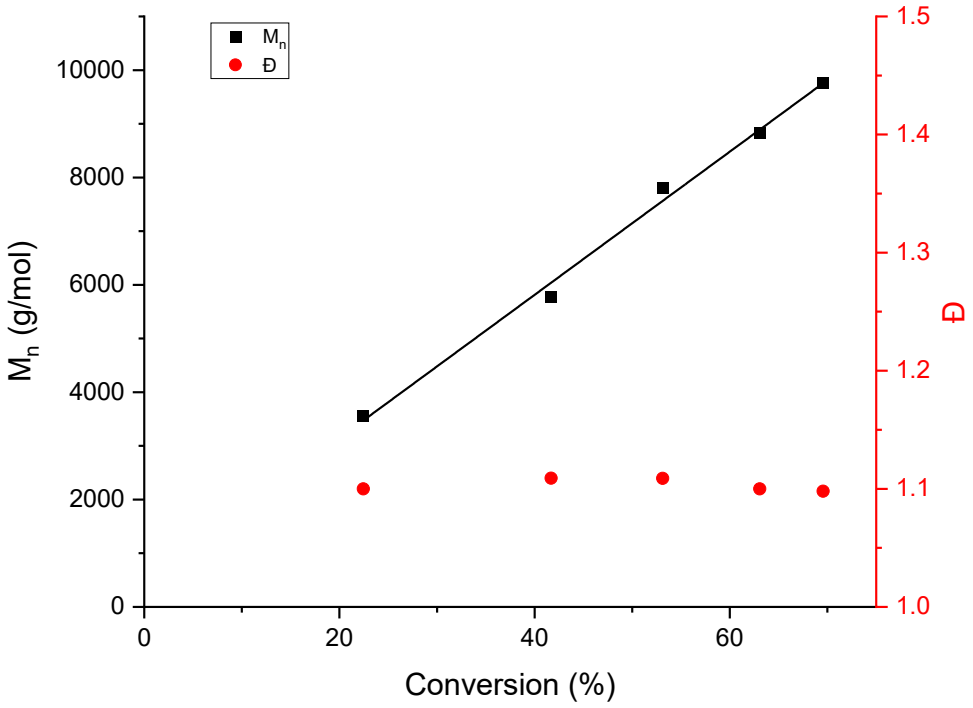


Figure B66. Plot of M_n *vs.* β-BL conversion for β-BL ROP as initiated by (*R,R*)-**15** as per conditions in Table 5, Entry 1.

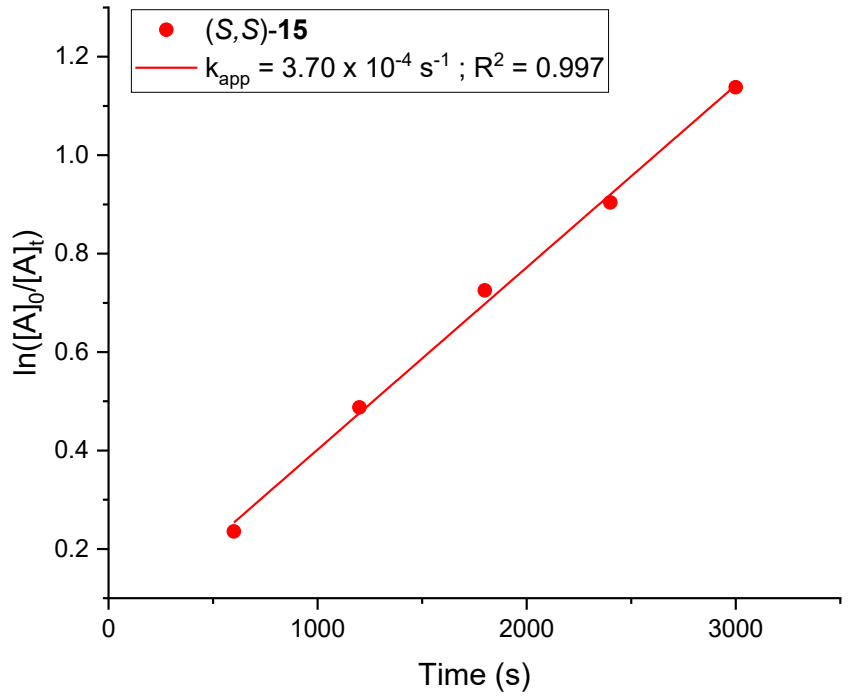


Figure B67. First-order plot (linear fit) for β-BL ROP initiated by (*S,S*)-**15** as per conditions in Table 5, Entry 2.

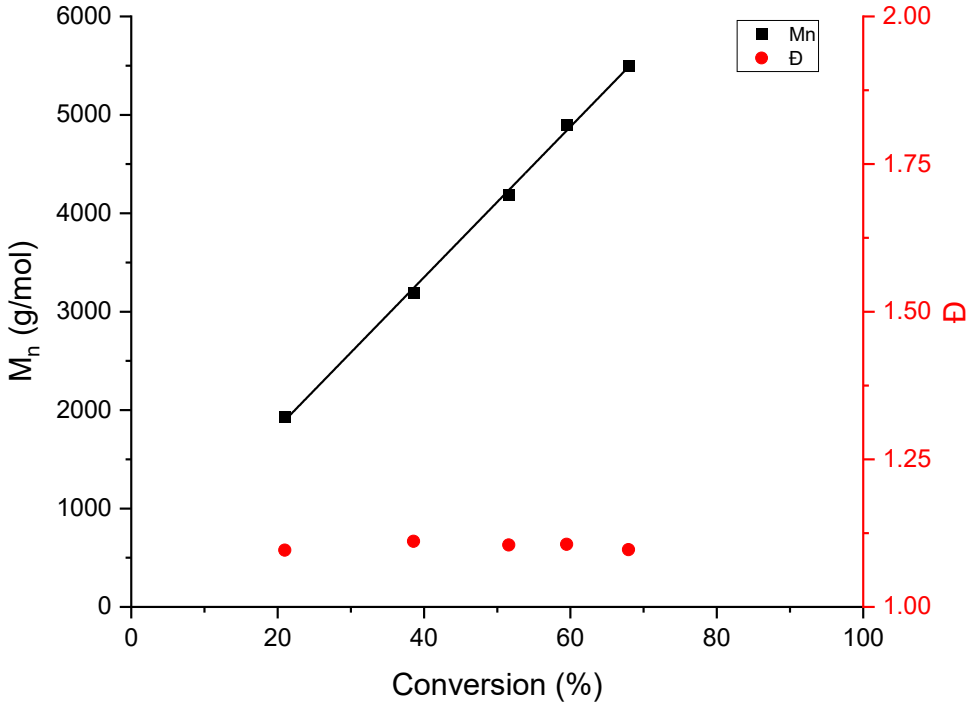


Figure B68. Plot of M_n *vs.* β-BL conversion for β-BL ROP as initiated by (*S,S*)-**15** as per conditions in Table 5, Entry 2.

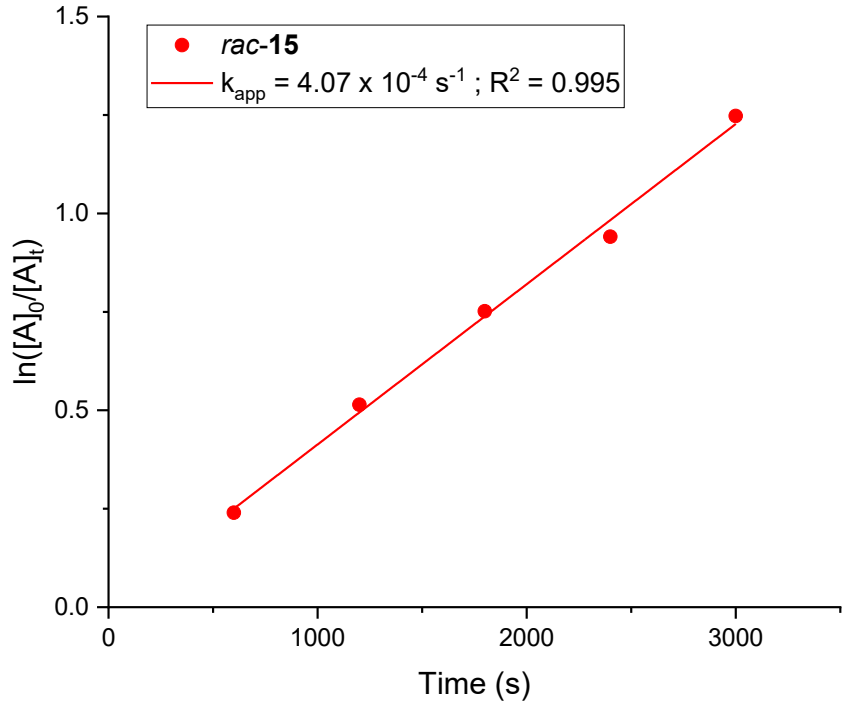


Figure B69. First-order plot (linear fit) for β-BL ROP initiated by *rac*-**15** as per conditions in Table 5, Entry 3.

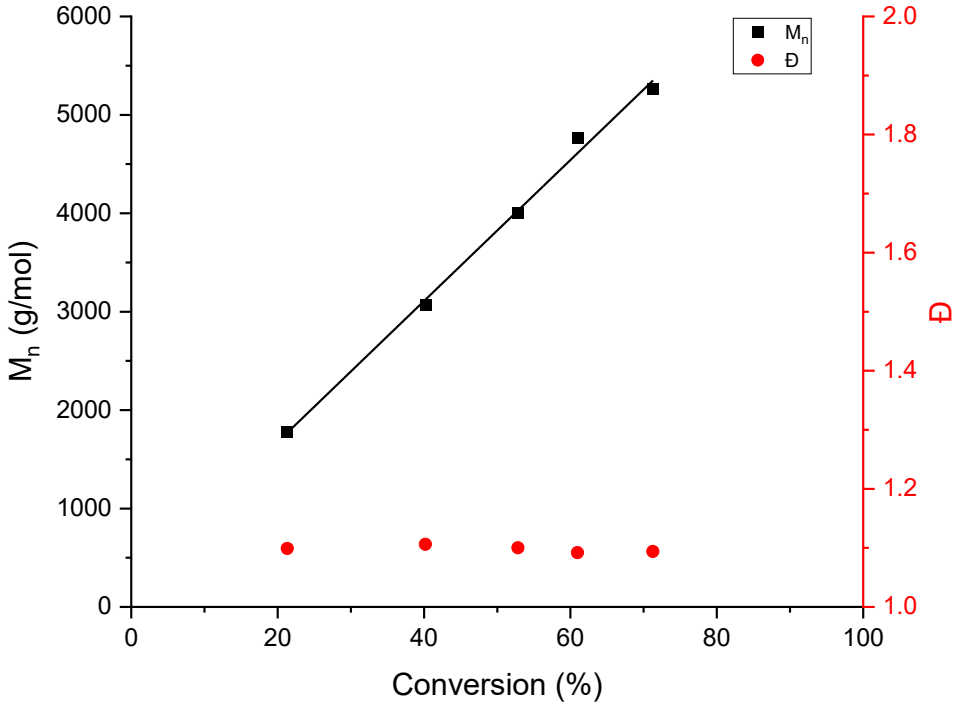


Figure B70. Plot of M_n *vs.* β-BL conversion for β-BL ROP as initiated by *rac*-**15** as per conditions in Table 5, Entry 3.

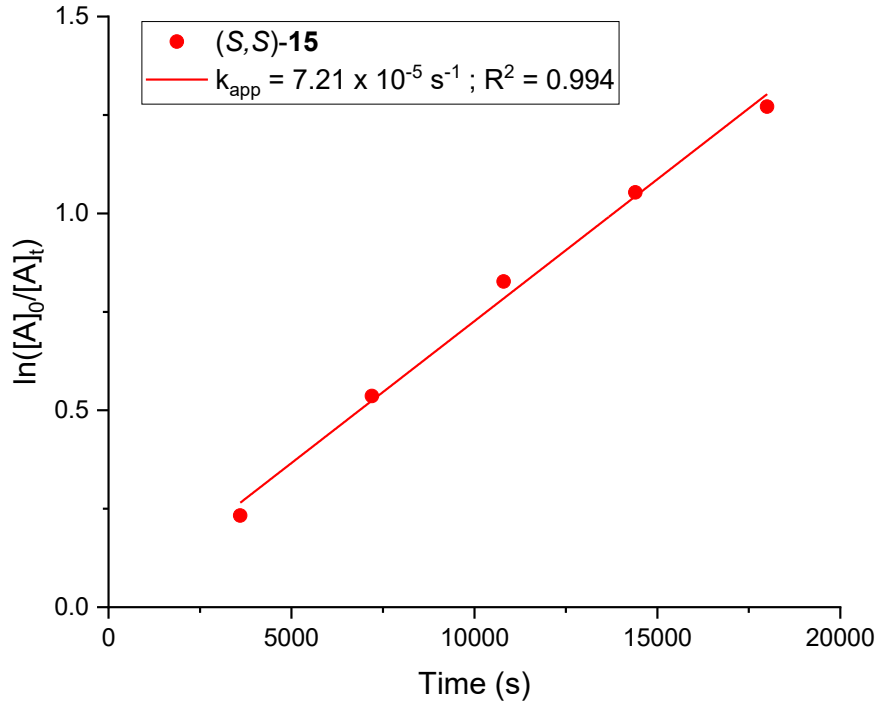


Figure B71. First-order plot (linear fit) for ε-DL ROP initiated by (*S,S*)-**15** as per conditions in Table 6, Entry 1.

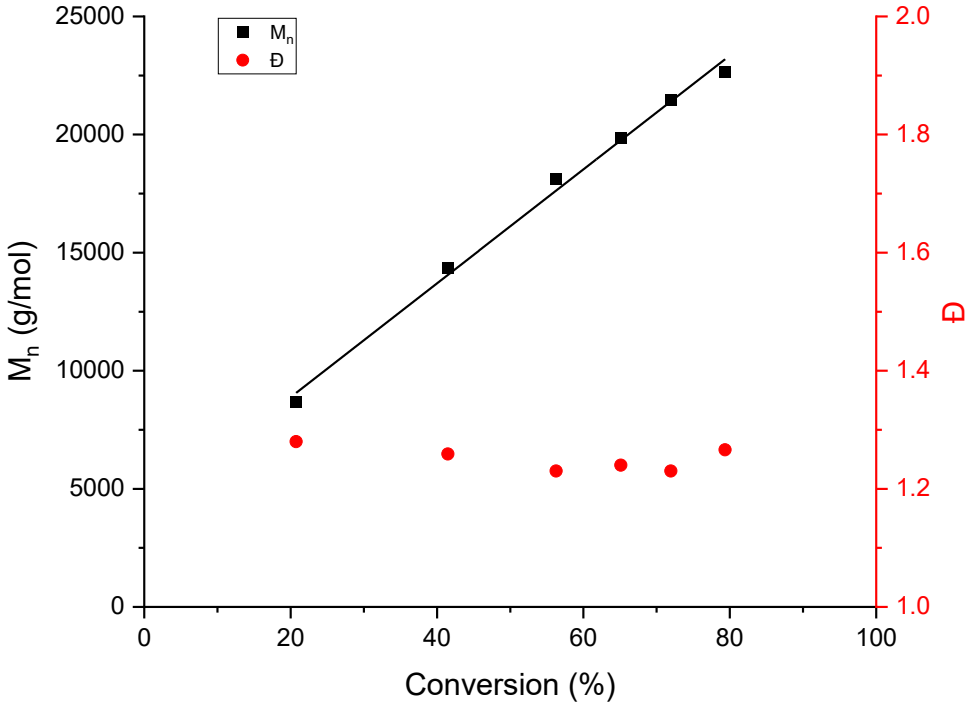


Figure B72. Plot of M_n *vs.* ε-DL conversion for ε-DL ROP as initiated by (*S,S*)-**15** as per conditions in Table 6, Entry 1.

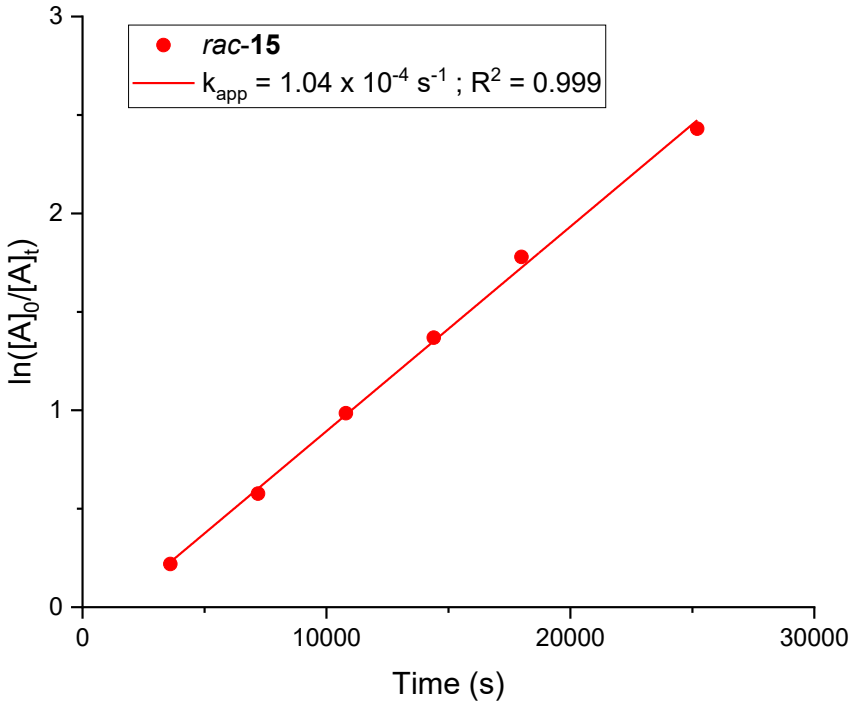


Figure B73. First-order plot (linear fit) for ε-DL ROP initiated by *rac*-**15** as per conditions in Table 6, Entry 2.

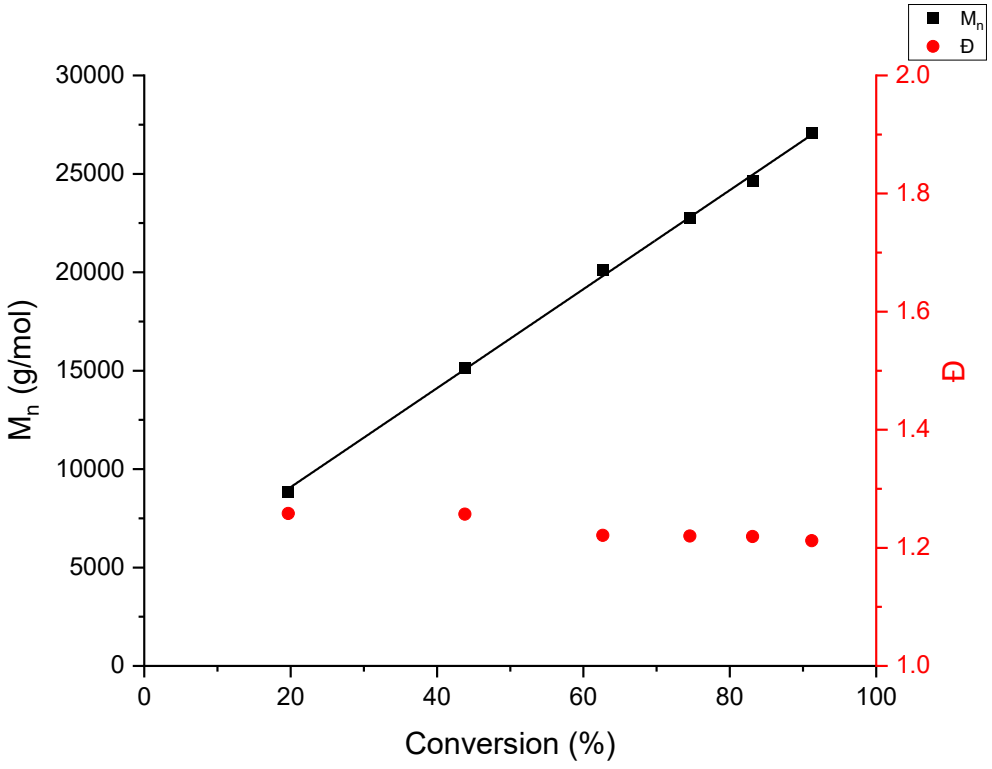


Figure B74. Plot of M_n *vs.* ε-DL conversion for ε-DL ROP as initiated by *rac*-**15** as per conditions in Table 6, Entry 2.

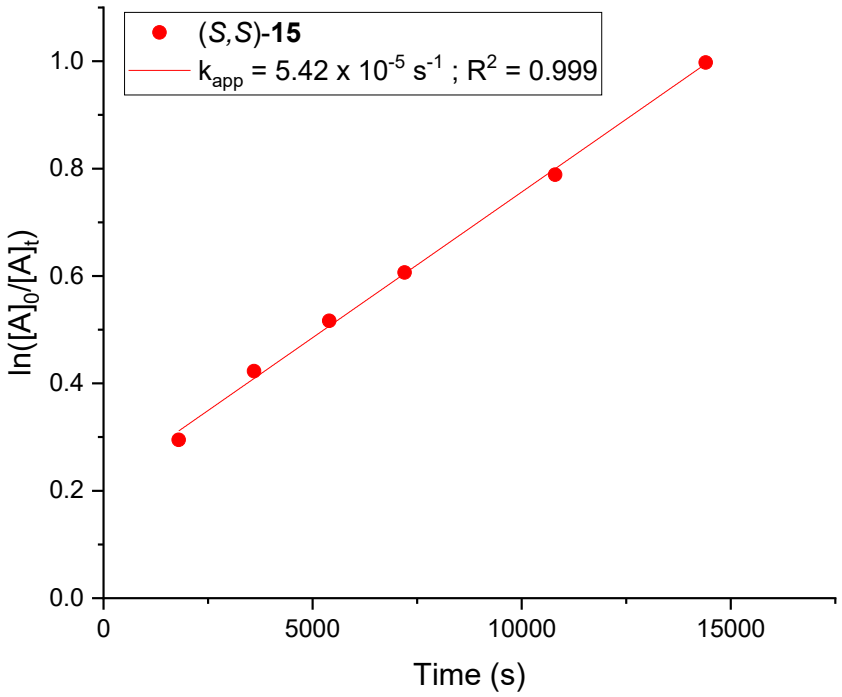


Figure B75. First-order plot (linear fit) for TMC ROP initiated by (*S,S*)-**15** as per conditions in Table 6, Entry 4.

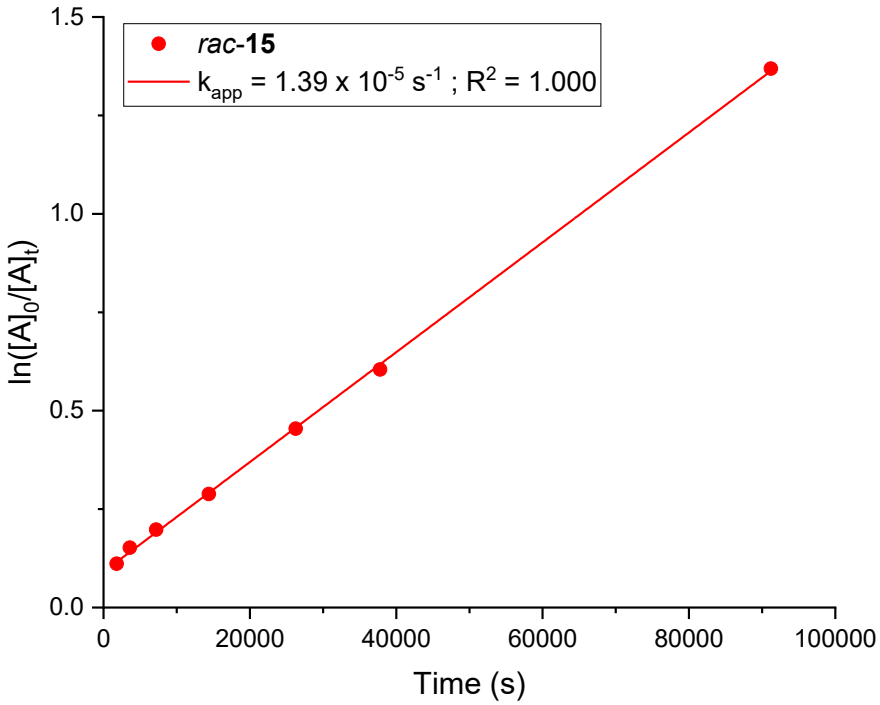


Figure B76. First-order plot (linear fit) for TMC ROP initiated by *rac*-**15** as per conditions in Table 6, Entry 5.

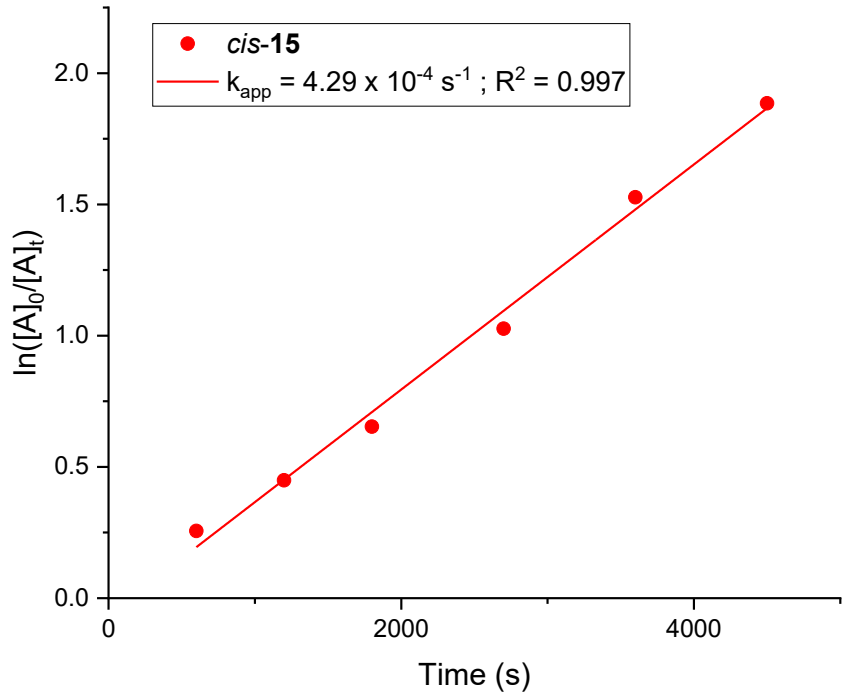


Figure B77. First-order plot (linear fit) for *rac*-LA ROP initiated by *cis*-**15** as per conditions in Table 7, Entry 1.

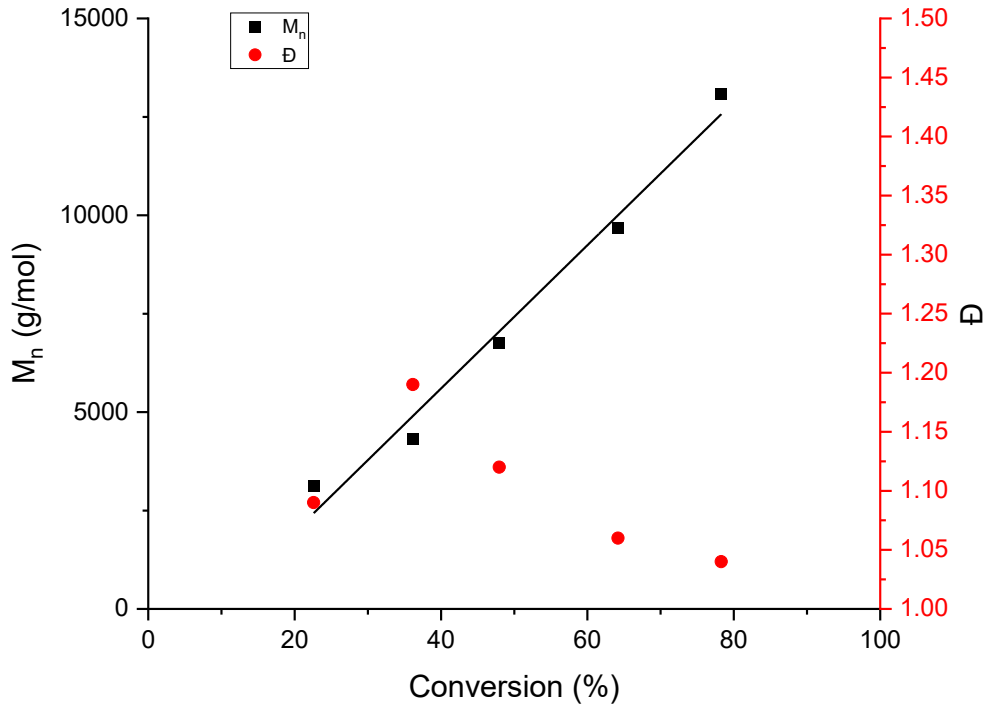


Figure B78. Plot of M_n *vs. rac*-LA conversion for *rac*-LA ROP as initiated by *cis*-**15** as per conditions in Table 7, Entry 1.

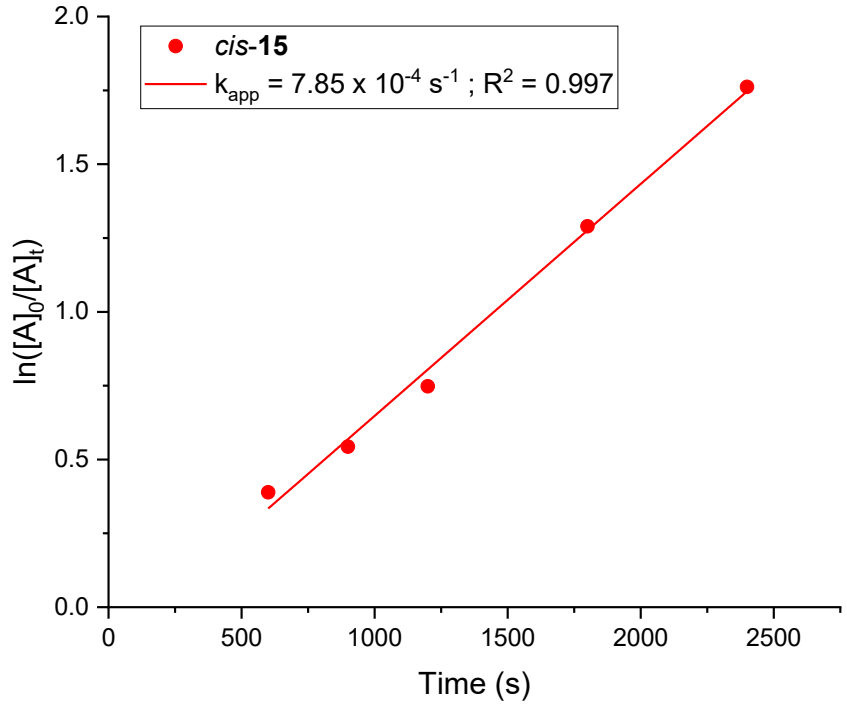


Figure B79. First-order plot (linear fit) for *L*-LA ROP initiated by *cis*-**15** as per conditions in Table 7, Entry 2.

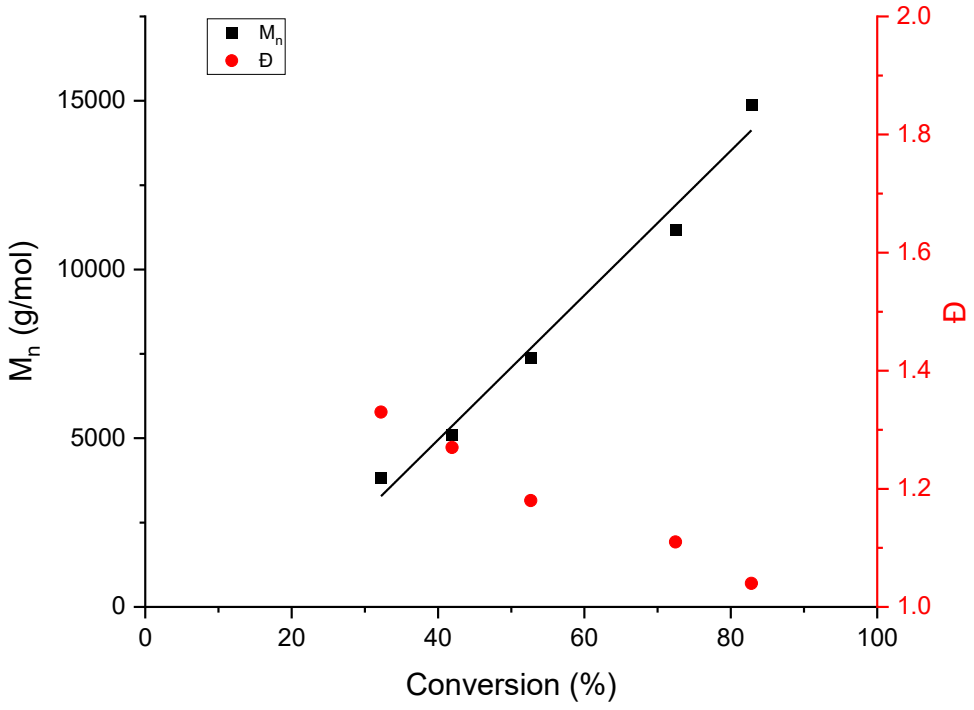


Figure B80. Plot of M_n *vs.* *L*-LA conversion for *L*-LA ROP as initiated by *cis*-**15** as per conditions in Table 7, Entry 2.

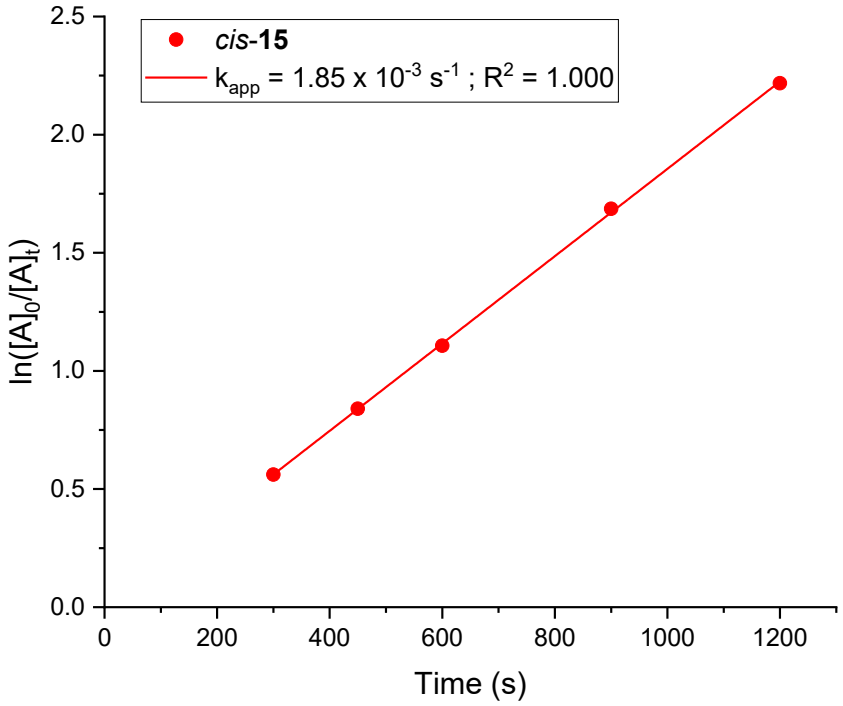


Figure B81. First-order plot (linear fit) for *meso*-LA ROP initiated by *cis*-**15** as per conditions in Table 7, Entry 3.

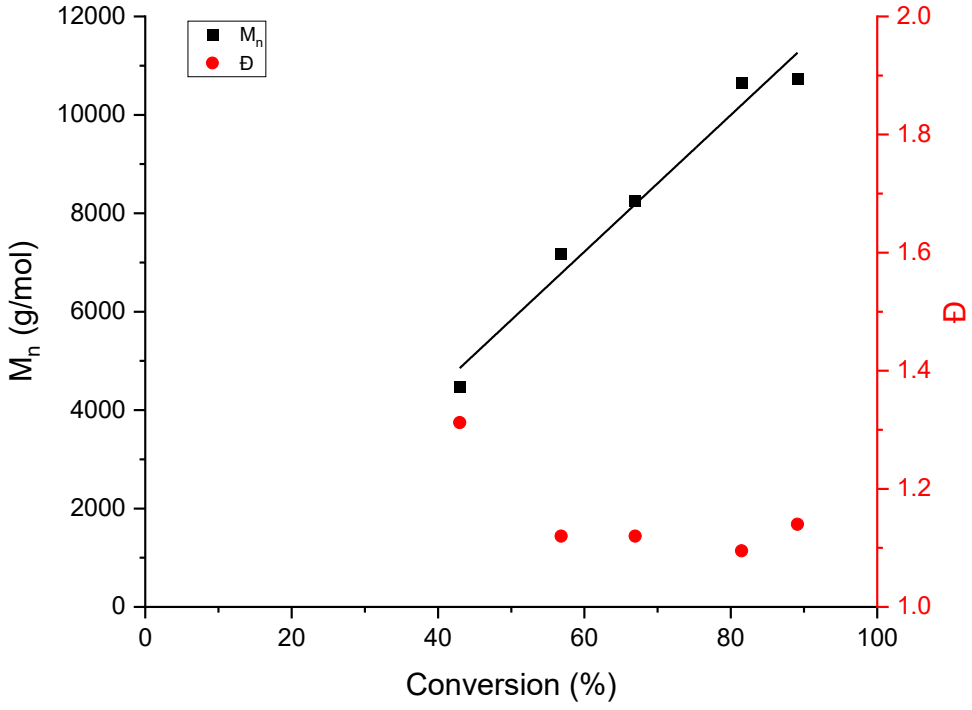


Figure B82. Plot of M_n *vs. meso*-LA conversion for *meso*-LA ROP as initiated by *cis*-**15** as per conditions in Table 7, Entry 3.

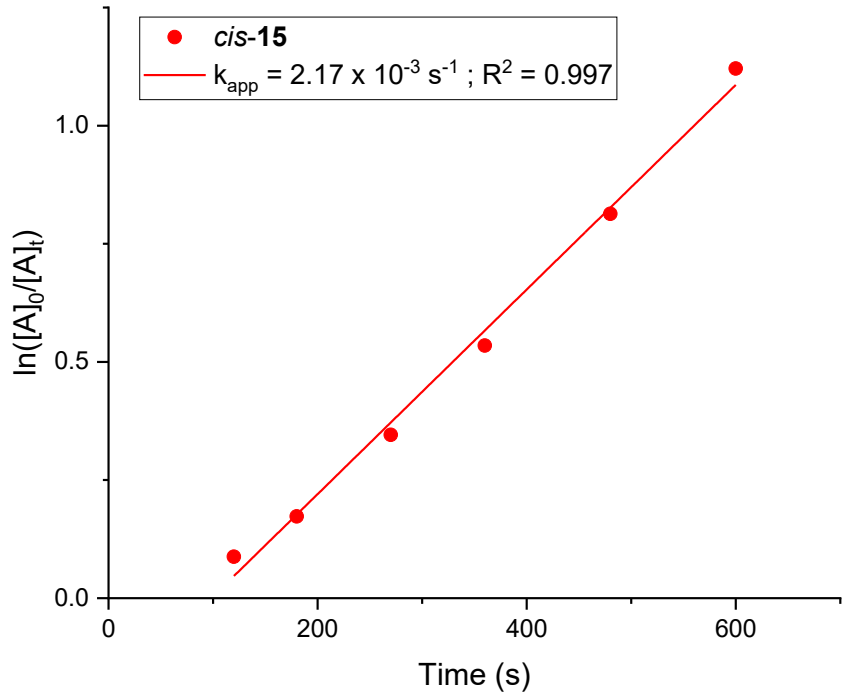


Figure B83. First-order plot (linear fit) for ε-CL ROP initiated by *cis*-**15** as per conditions in Table 7, Entry 4.

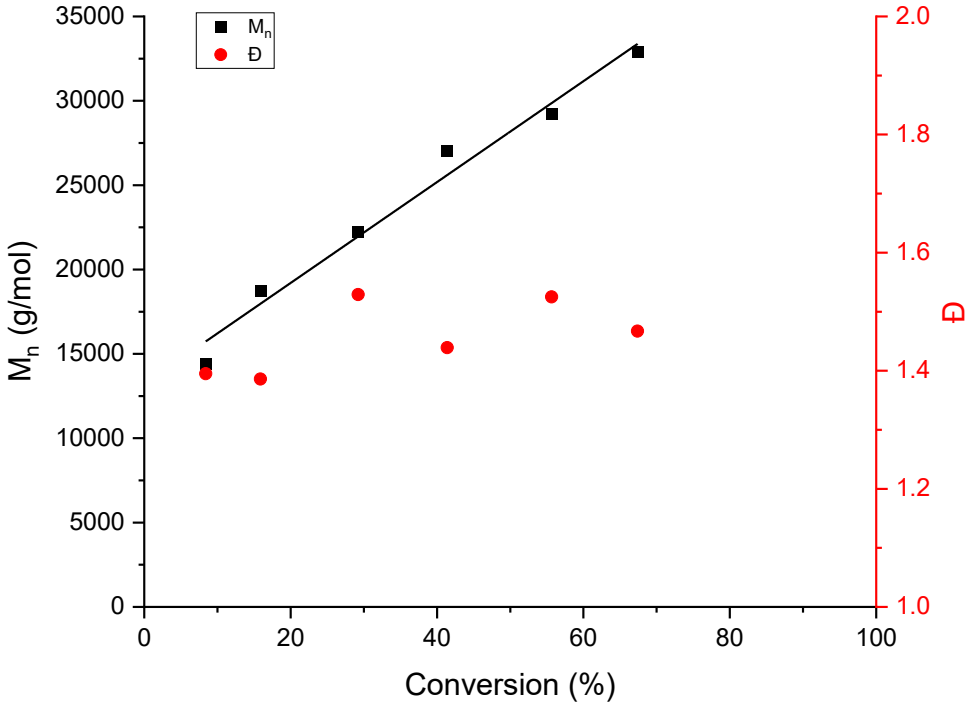


Figure B84. Plot of M_n *vs.* ε-CL conversion for ε-CL ROP as initiated by *cis*-**15** as per conditions in Table 7, Entry 4.

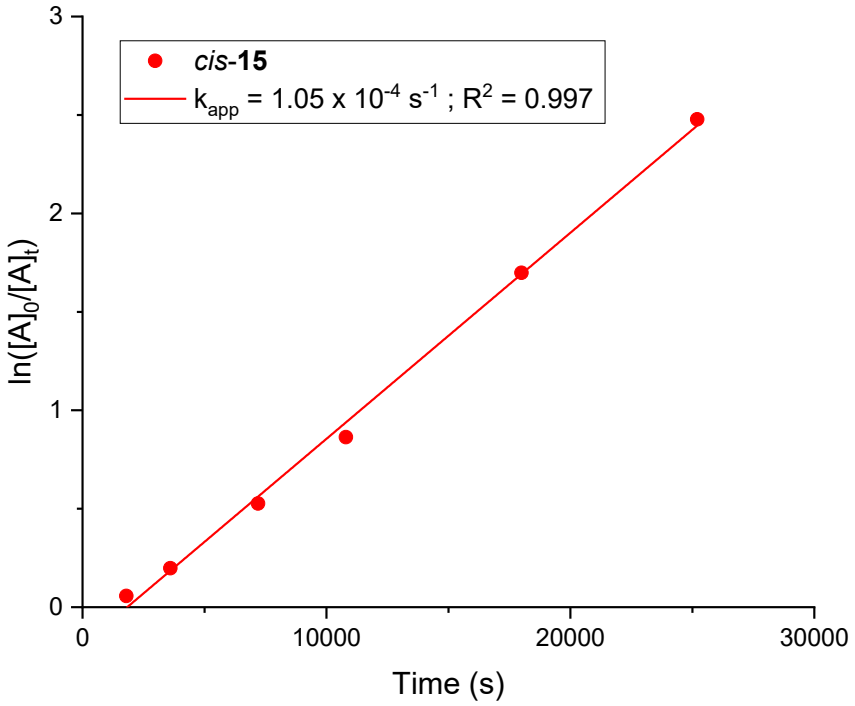


Figure B85. First-order plot (linear fit) for β-BL ROP initiated by *cis*-**15** as per conditions in Table 8, Entry 1.

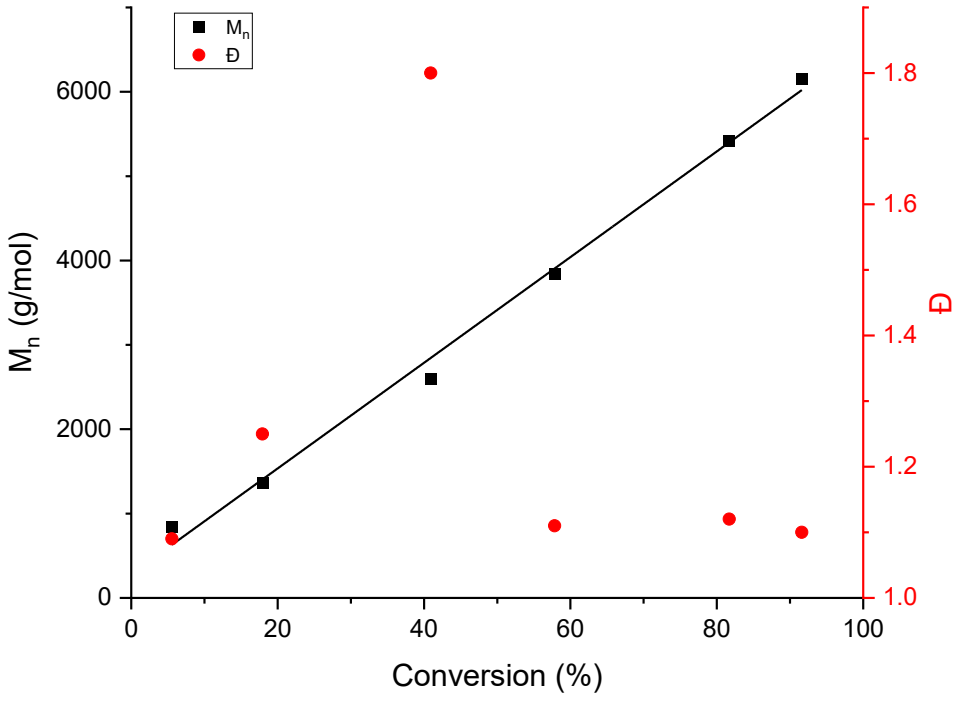


Figure B86. Plot of M_n *vs.* β-BL conversion for β-BL ROP as initiated by *cis*-**15** as per conditions in Table 8, Entry 1.

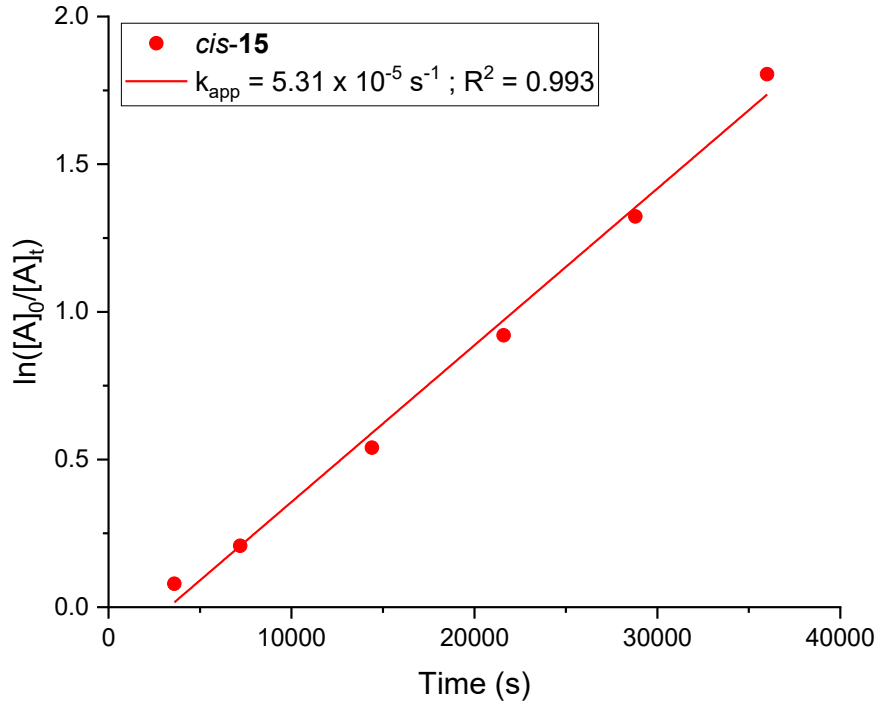


Figure B87. First-order plot (linear fit) for ε-DL ROP initiated by *cis*-**15** as per conditions in Table 8, Entry 2.

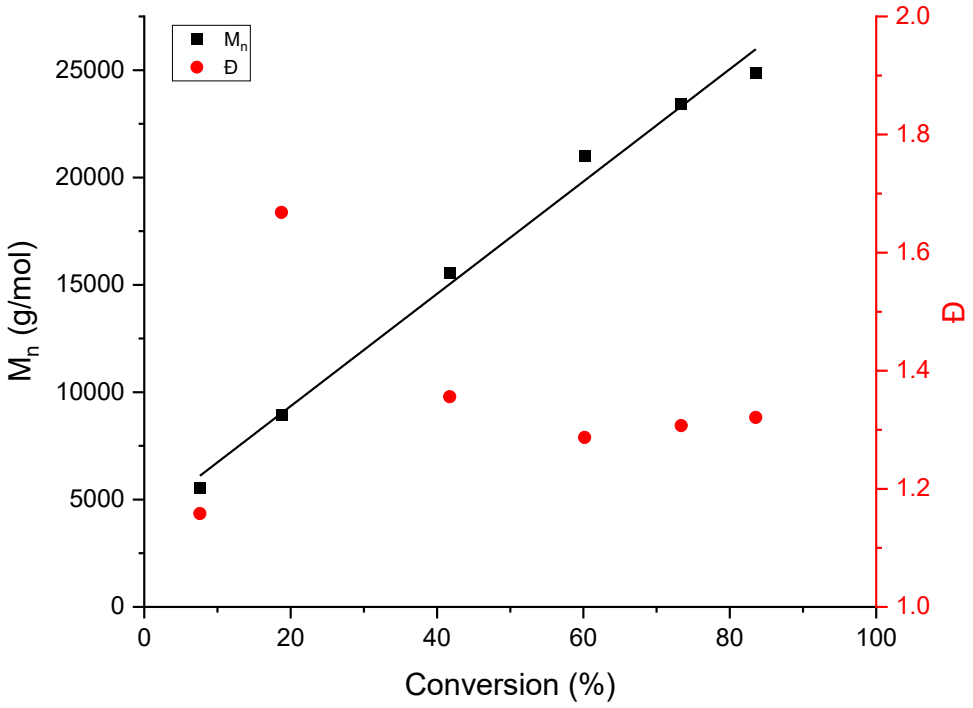


Figure B88. Plot of M_n *vs.* ε-DL conversion for ε-DL ROP as initiated by *cis*-**15** as per conditions in Table 8, Entry 2.

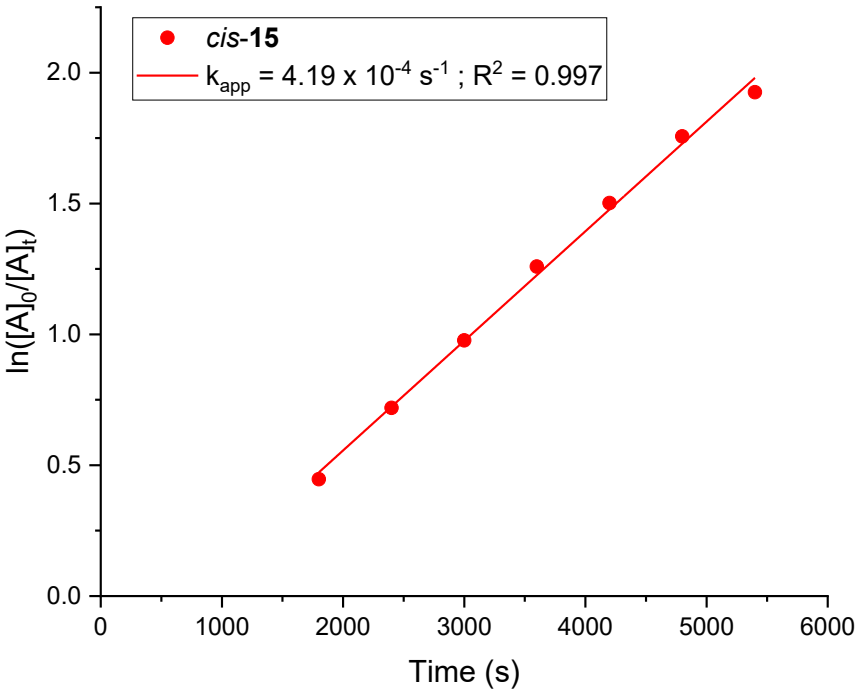


Figure B89. First-order plot (linear fit) for TMC ROP initiated by *cis*-**15** as per conditions in Table 8, Entry 3.

6.7.3 Chapter 4

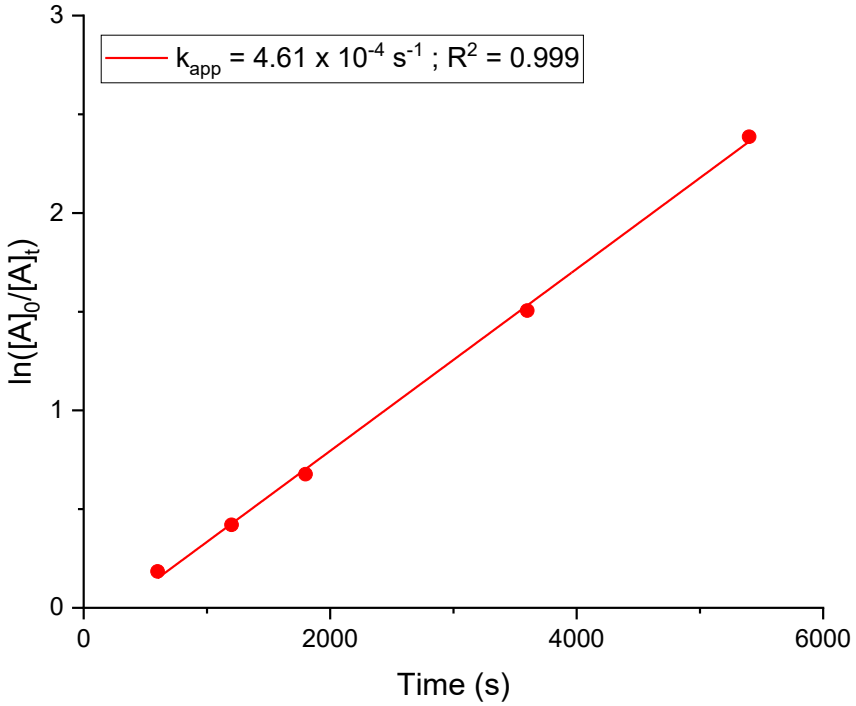


Figure B90. First-order plot (linear fit) for *rac*-LA ROP initiated by **18** as per conditions in Table 3, Entry 1.

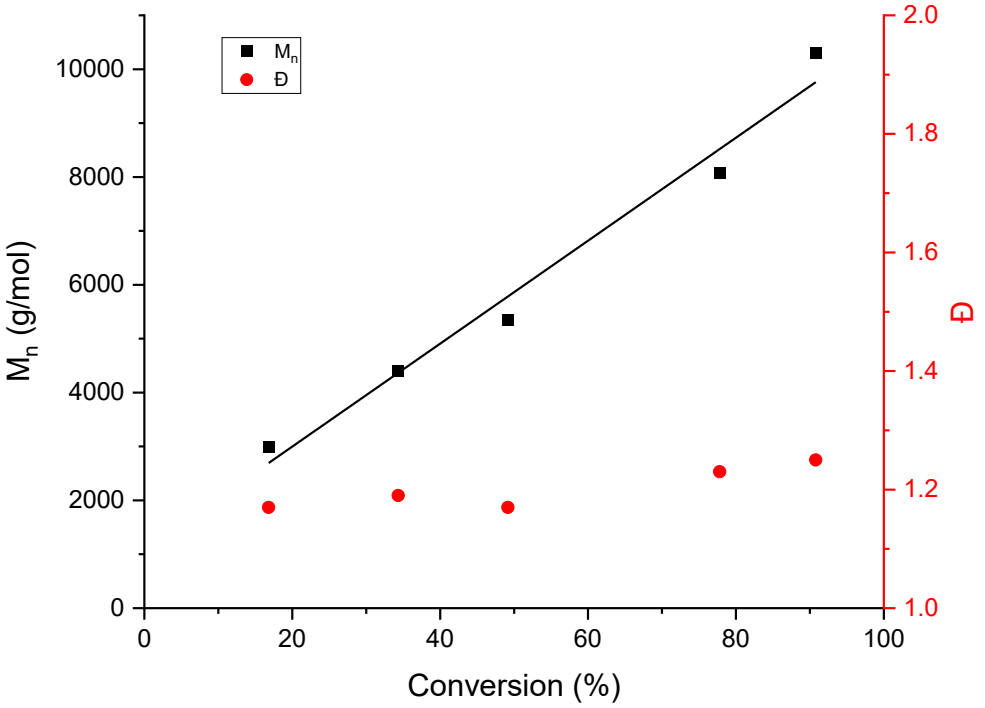


Figure B91. Plot of M_n *vs rac*-LA conversion for *rac*-LA ROP as initiated by **18**, as per conditions in Table 3, Entry 1.

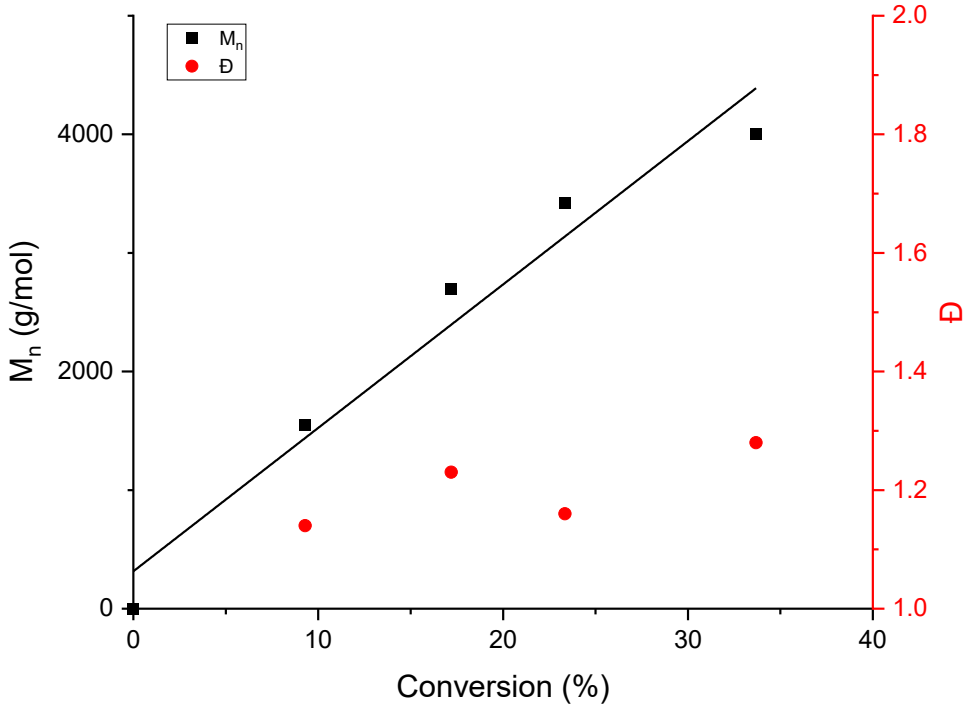


Figure B92. Plot of M_n *vs. rac*-LA conversion for *rac*-LA ROP as initiated by **18**, as per conditions in Table 3, Entry 4. There appears to be a linear molecular weight increase upon switching **18-ox** ($FcBAr^F$) back to **18** with $CoCp_2$.

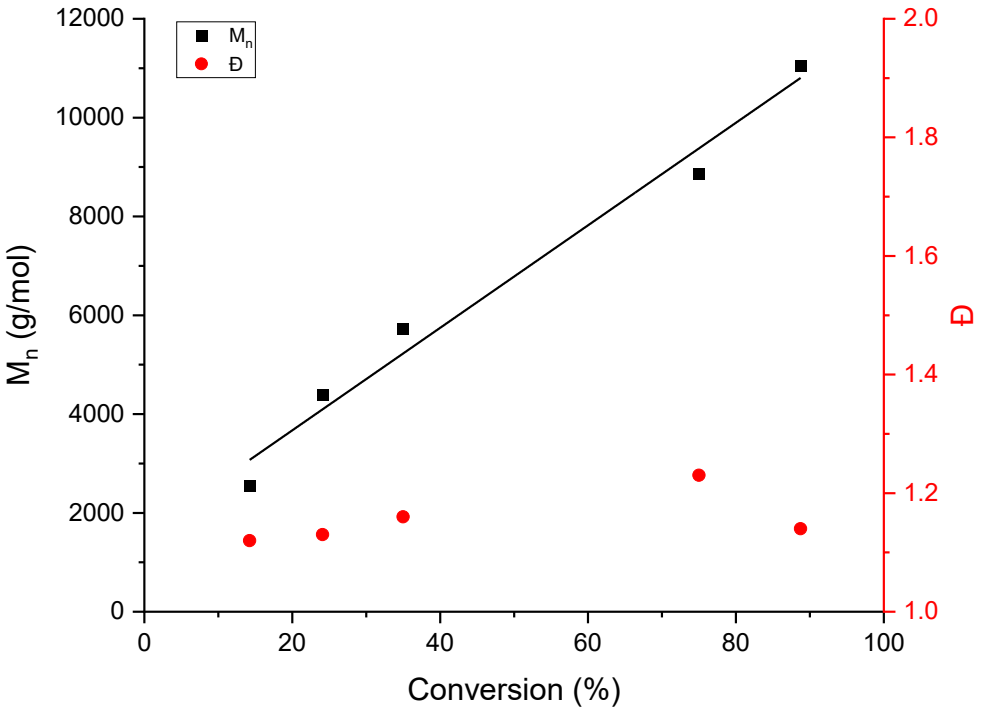


Figure B93. Plot of M_n *vs. rac*-LA conversion for *rac*-LA ROP as initiated by **18**, as per conditions in Table 3, Entry 6. There appears to be a linear molecular weight increase despite switching from **18** to **18-ox** (AgOTf) and back to **18** ($CoCp_2$).

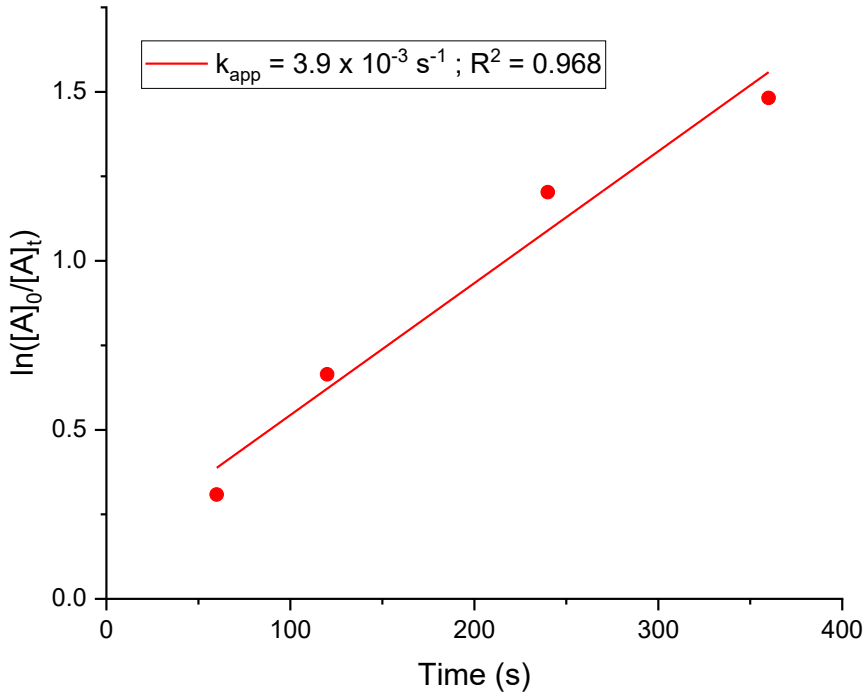


Figure B94. First-order plot (linear fit) for CHO ROP initiated by **18-ox** as per conditions in Table 4, Entry 3.

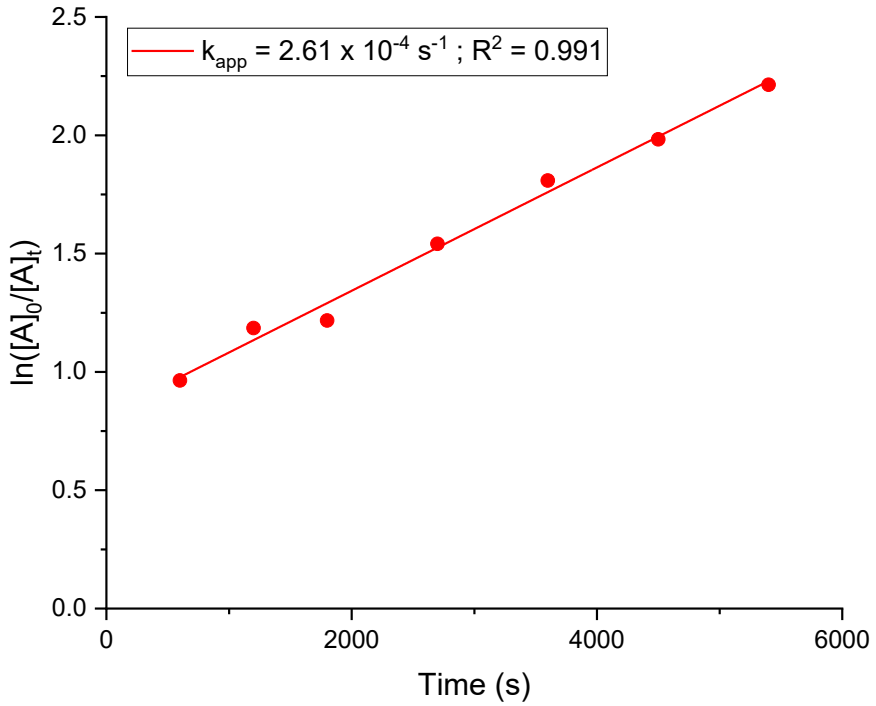


Figure B95. First-order plot (linear fit) for *meso*-LA ROP initiated by **18** as per conditions in Table 5, Entry 1.

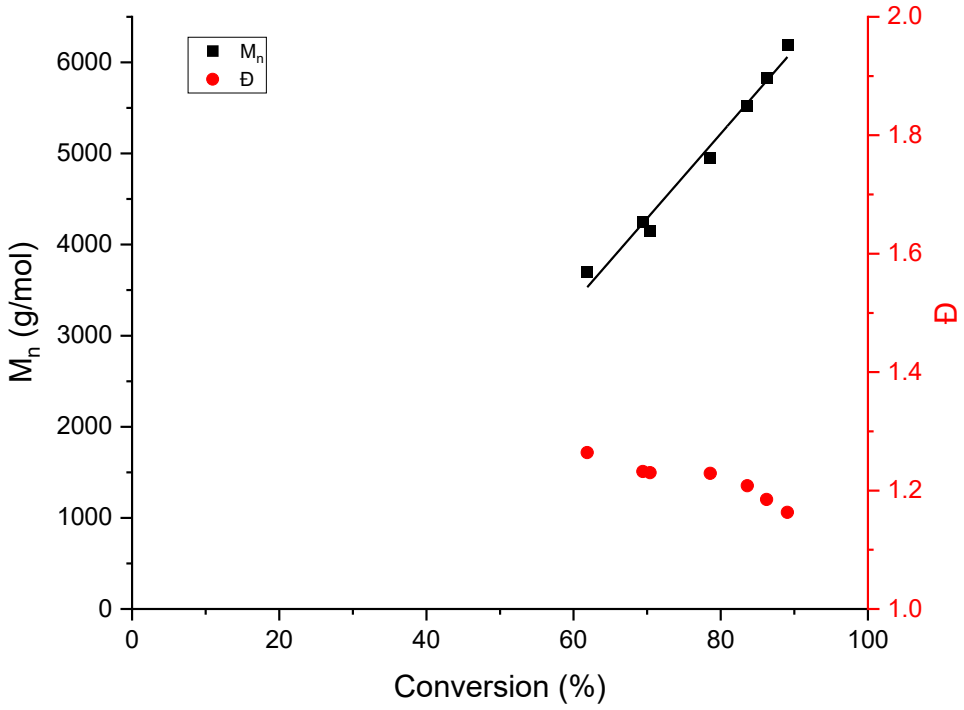


Figure B96. Plot of M_n *vs* *meso*-LA conversion for *meso*-LA ROP as initiated by **18**, as per conditions in Table 5, Entry 1.

B.2 Determination of Reaction Order

B.2.1 Determination of order in catalyst for ε-CL ROP:

All three experiments used to determine order in catalyst where ran at the same time, using the same stir plate and same batch of catalyst.
Sample preparation: the amount of catalyst [either (*R*,*R*)-**15**, *rac*-**15**, or *cis*-**15**] was weighed in three separate vials:

- For $[cat]_0$ = 0.005 M: 5 mg (0.008 mmol)
- For $[cat]_0$ = 0.0075 M: 7.5 mg (0.012 mmol)
- For $[cat]_0$ = 0.01 M: 10 mg (0.016 mmol)
- For $[cat]_0$ = 0.0125 M: 12.5 mg (0.02 mmol)
- For $[cat]_0$ = 0.02 M: 10 mg (0.032 mmol)

To each vial was added 178.5 µL of ε-CL (1.61 mmol) in 1.43 mL of THF (so that $[\varepsilon\text{-CL}]_0$ = 1 M)

Once the monomer solution was added to the catalyst-containing vial, timing was started. Aliquots were taken periodically and quenched in wet $CDCl_3$ to stop any further reaction. The samples were analysed by ^{1}H NMR spectroscopy to determine conversion by relative integration of monomer and polymer signals (see above). Once aliquots were collected and analysed for different concentration reactions, the concentration of monomer was plotted as a function of $[cat]^{\alpha}t$ (where **α** is the catalyst order). The value of **α** was changed in such a way to cause the three curves to overlap.

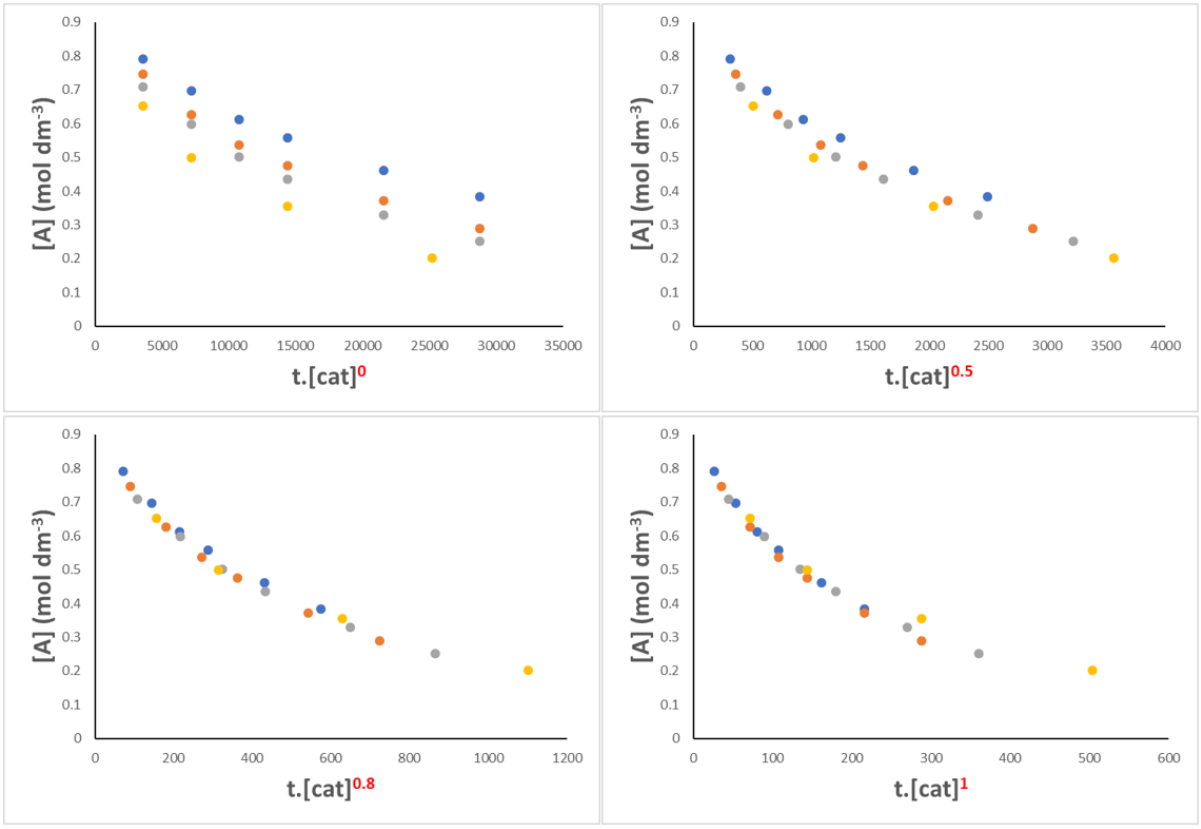


Figure B97. Variable Time Normalisation Analysis for the enantiopure catalyst (*R*,*R*)-**15** (ε-CL ROP) shows an order of 0.8 with [(*R*,*R*)-**15**] = 0.0125 (●), 0.01 (●), 0.0075 (●), 0.005 (●) mol.dm^{-3}.

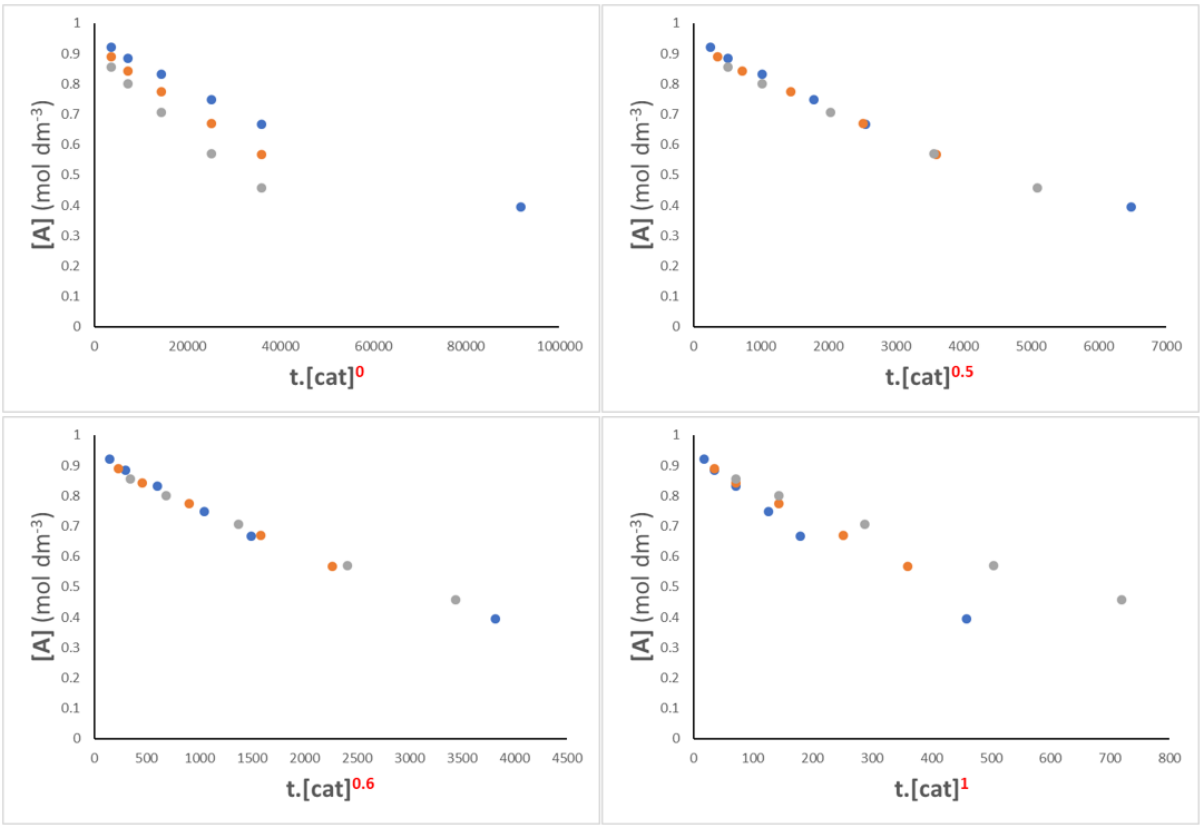


Figure B98. Variable Time Normalisation Analysis for the racemic catalyst *rac*-**15** (ε-CL ROP) shows an order between 0.5 and 0.6, with [*rac*-**15**] = 0.005 (●), 0.01 (●), 0.02 (●) mol.dm^{-3}.

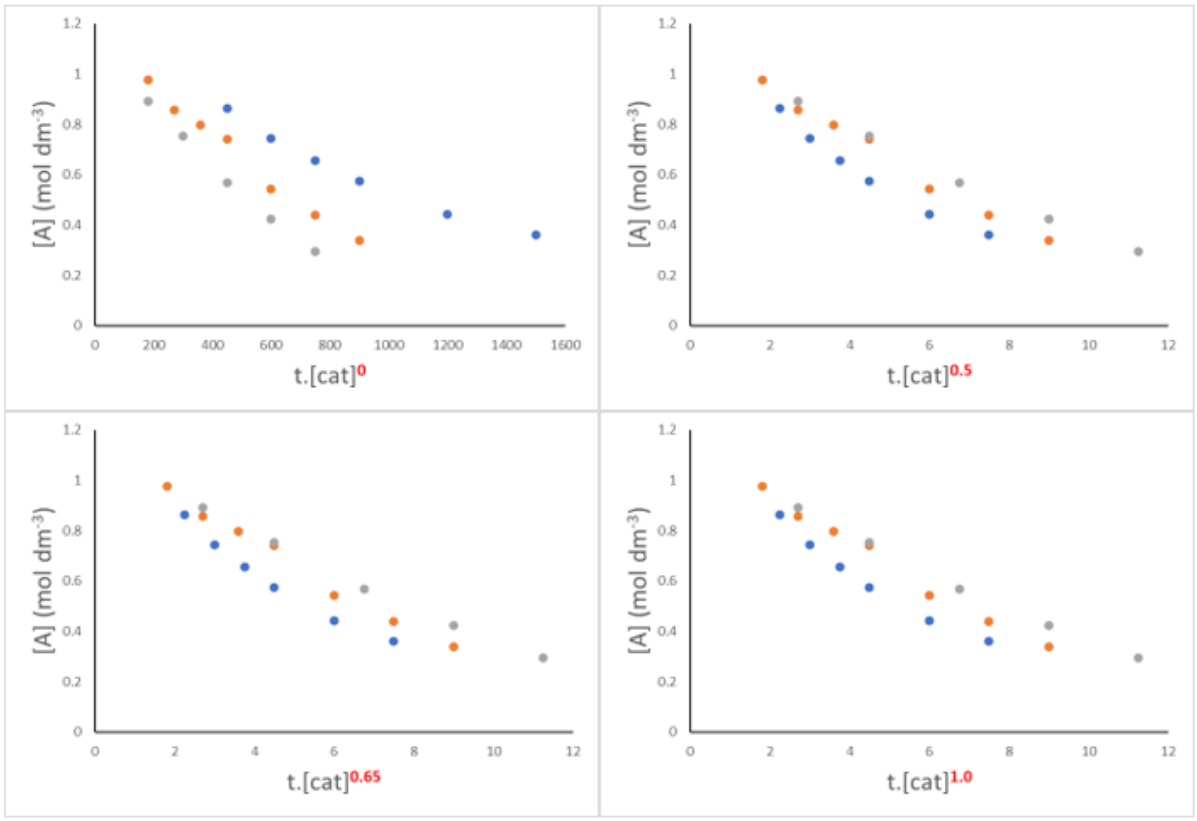


Figure B99. Variable Time Normalisation Analysis for complex *cis*-**15** (ε-CL ROP) shows an order of 0.65, with [*cis*-**15**] = 0.005 (●), 0.01 (●), 0.02 (●) mol.dm^{-3}.

B.2.2 Determination of order in catalyst for *rac*-LA/*L*-LA ROP:

All three experiments used to determine order in catalyst where ran at the same time, using the same stir plate and same batch of catalyst.
Sample preparation: the amount of catalyst [either **2**, **8c**, (*R,R*)-**15**, (*S,S*)-**15**, or *rac*-**15**] was weighed in three separate vials:

- For $[cat]_0$ = 0.005 M: 5 mg
- For $[cat]_0$ = 0.0075 M: 7.5 mg
- For $[cat]_0$ = 0.01 M: 10 mg
- For $[cat]_0$ = 0.0125 M: 12.5 mg
- For $[cat]_0$ = 0.02 M: 10 mg

To each vial was added the appropriate amount of LA in THF (so that $[LA]_0$ = 1 M):

- When using **2**: 242 mg of LA in 1.68 mL of THF
- When using **8c**: 240 mg of LA in 1.66 mL of THF
- When using (*R,R*)-, (*S,S*)-, or *rac*-**15**: 232 mg of LA in 1.61 mL of THF

Once the monomer solution was added to the catalyst-containing vial, timing was started. Aliquots were taken periodically and quenched in wet $CDCl_3$ to stop any further reaction. The samples were analysed by ^{1}H NMR spectroscopy to determine conversion by relative integration of monomer and polymer signals (see above). Once aliquots were collected and analysed for different concentration reactions, the concentration of monomer was plotted as a function of $[cat]^{\alpha}t$ (where **α** is the catalyst order). The value of **α** was changed in such a way to cause the three curves to overlap.

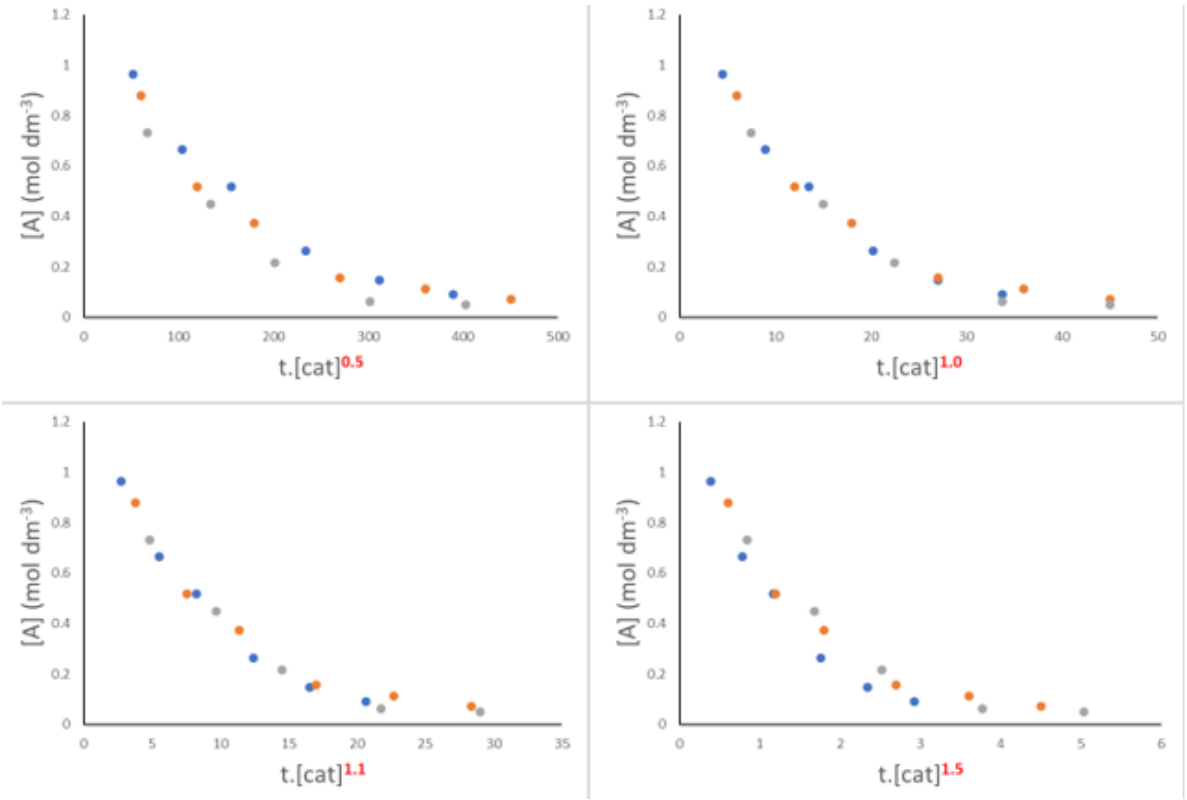


Figure B100. Variable Time Normalisation Analysis for complex **2** (*rac*-LA ROP) shows an order close to 1.0, with [**2**] = 0.0075 (●), 0.01 (●), 0.0125 (●) mol.dm^{-3}.

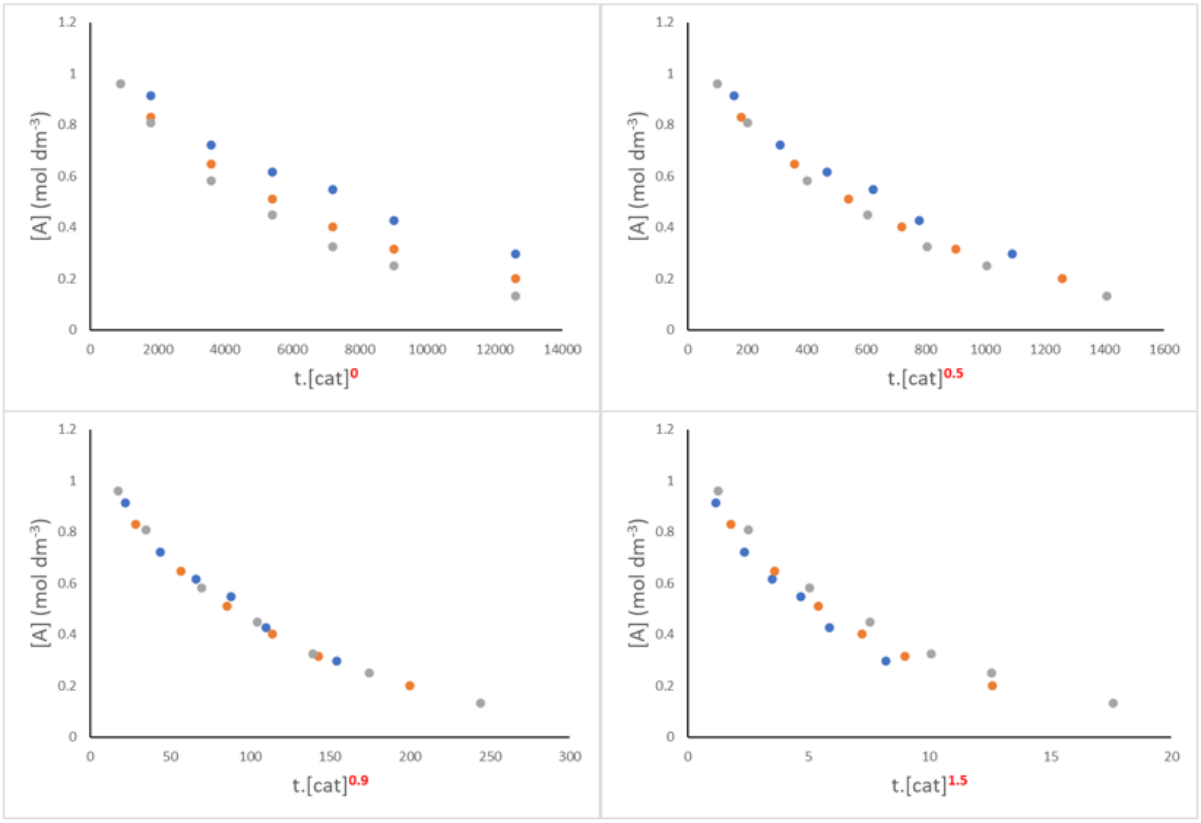


Figure B101. Variable Time Normalisation Analysis for complex **2** (*L*-LA ROP) shows an order of 0.9, with [**2**] = 0.0075 (●), 0.01 (●), 0.0125 (●) mol.dm^{-3}.

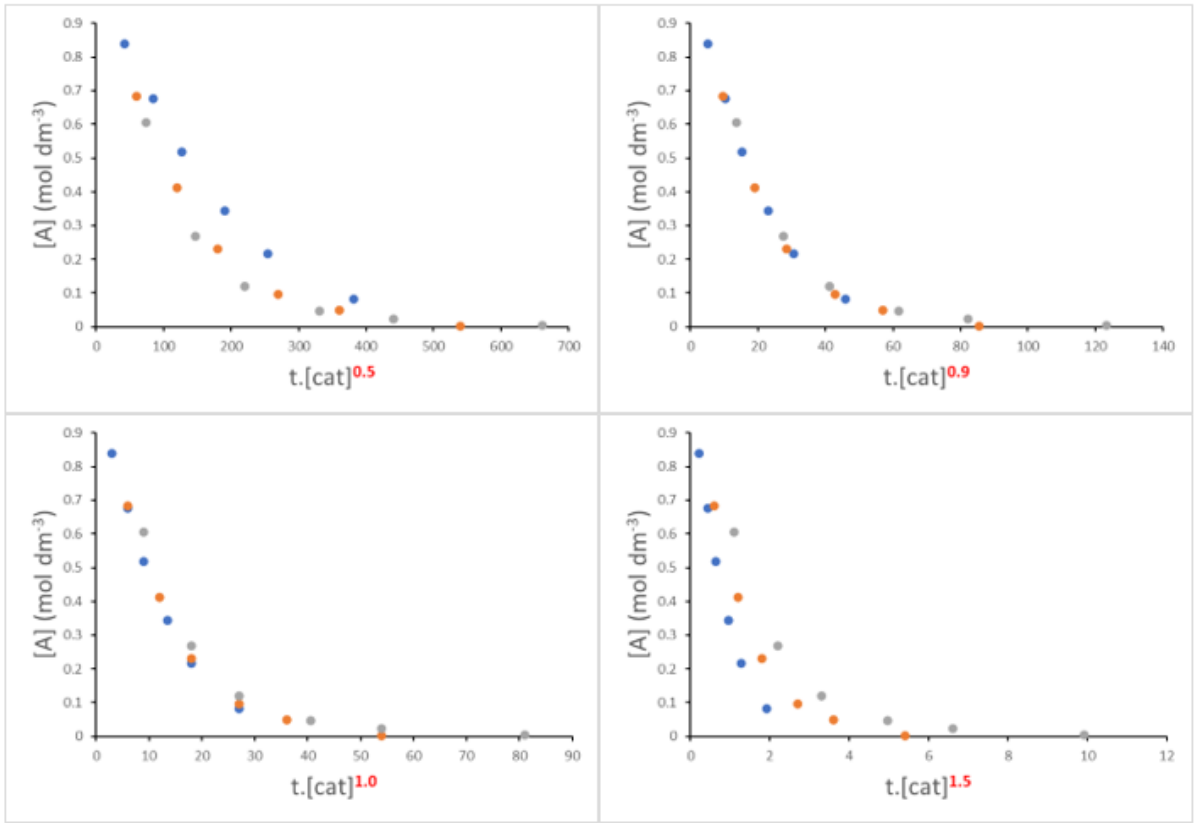


Figure B102. Variable Time Normalisation Analysis for complex **8c** (*rac*-LA ROP) shows an order close to 1.0, with [**8c**] = 0.005 (●), 0.01 (●), 0.02 (●) mol.dm^{-3}.

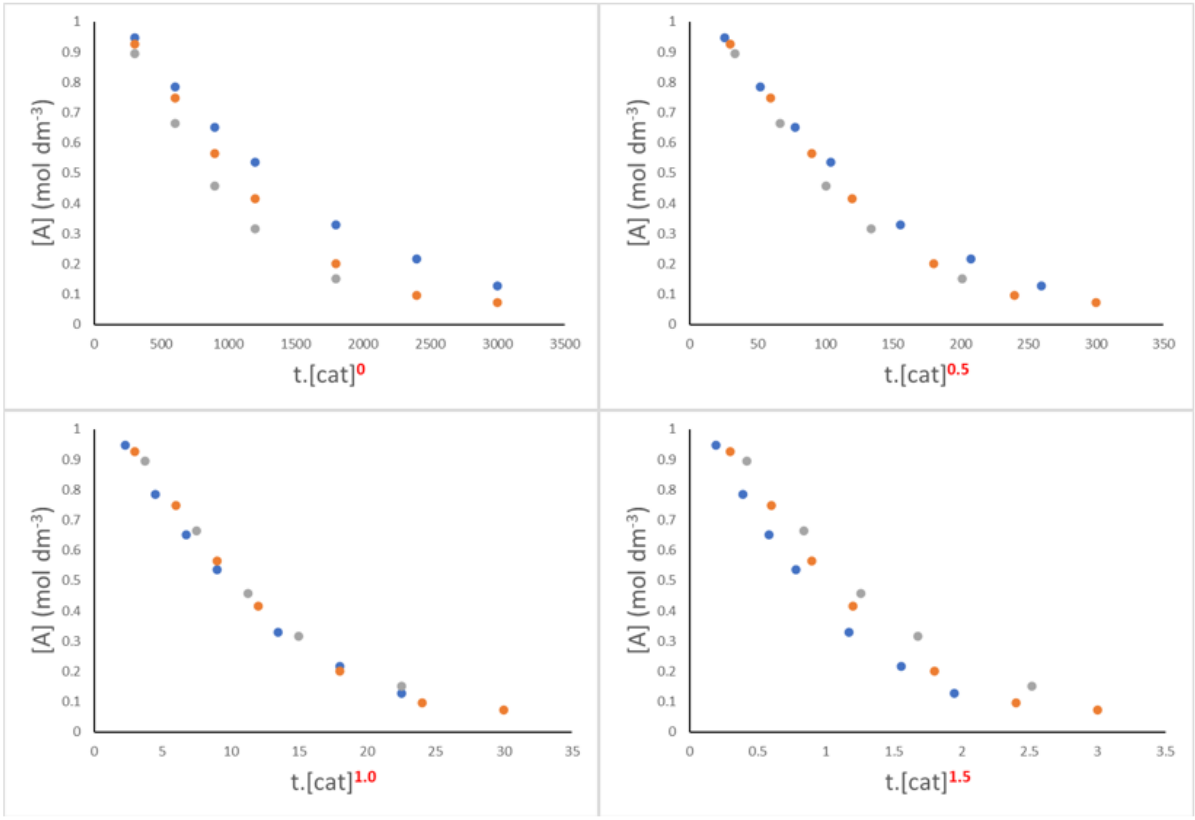


Figure B103. Variable Time Normalisation Analysis for complex **8c** (*L*-LA ROP) shows an order of 1.0, with [**8c**] = 0.0075 (●), 0.01 (●), 0.0125 (●) mol.dm^{-3}.

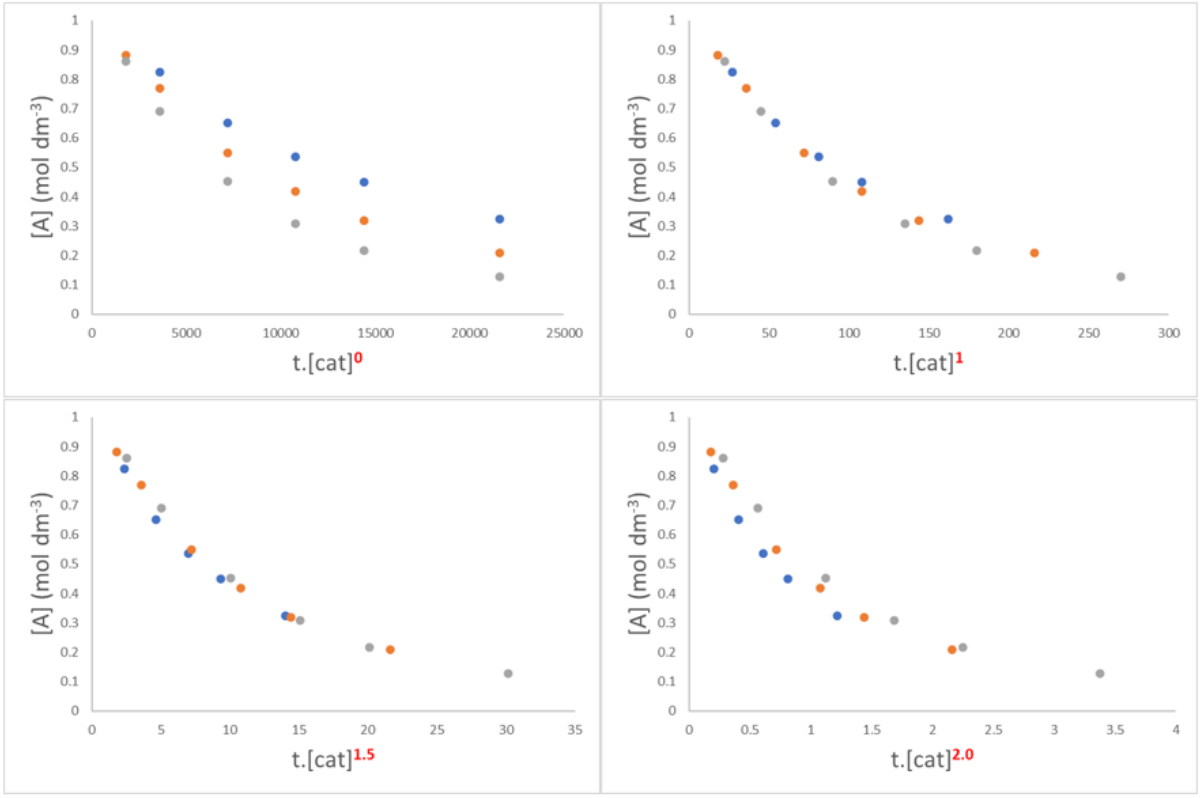


Figure B104. Variable Time Normalisation Analysis for the enantiopure catalyst (*R,R*)-**15** (*L*-LA ROP) shows an order of 0.8 with [(*R,R*)-**15**] = 0.0075 (●), 0.01 (●), 0.0125 (●) mol.dm^{-3}.

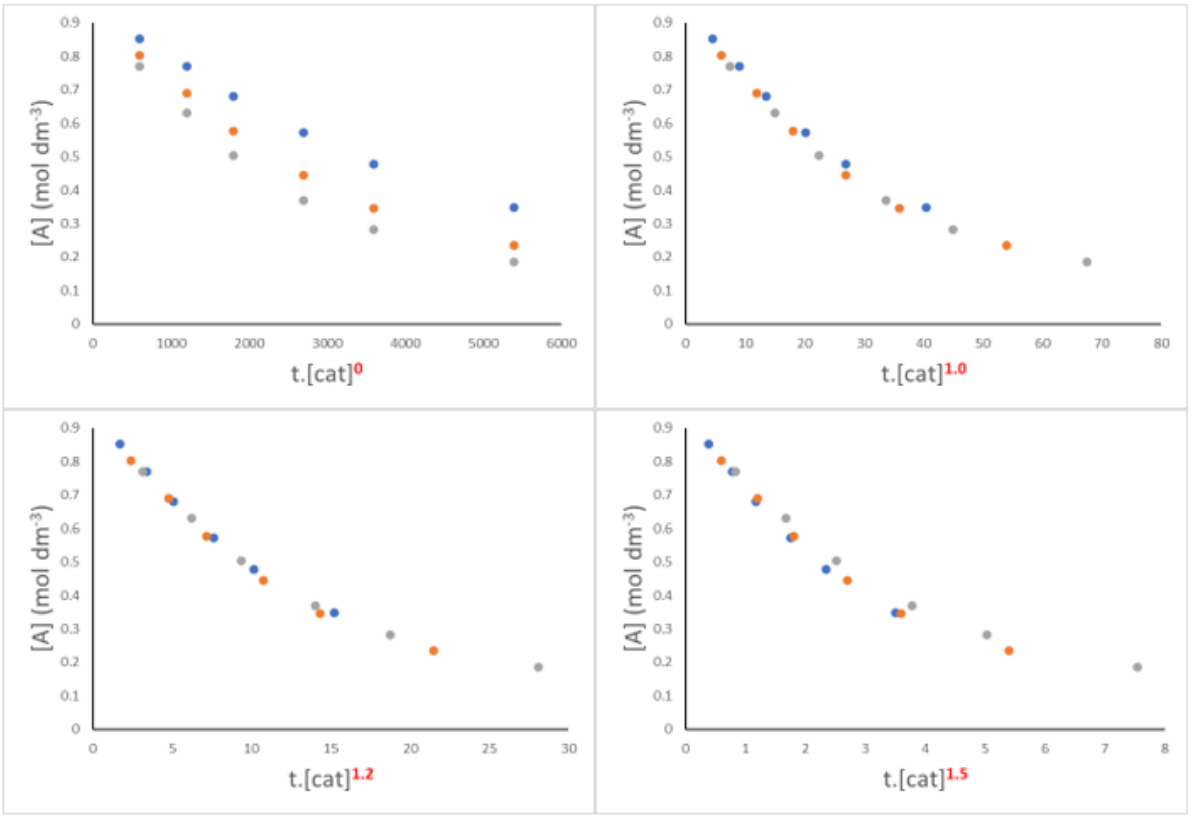


Figure B105. Variable Time Normalisation Analysis for the enantiopure catalyst (*S,S*)-**15** (*rac*-LA ROP) shows an order of 1.2 with [(*S,S*)-**15**] = 0.0075 (●), 0.01 (●), 0.0125 (●) mol.dm^{-3}.

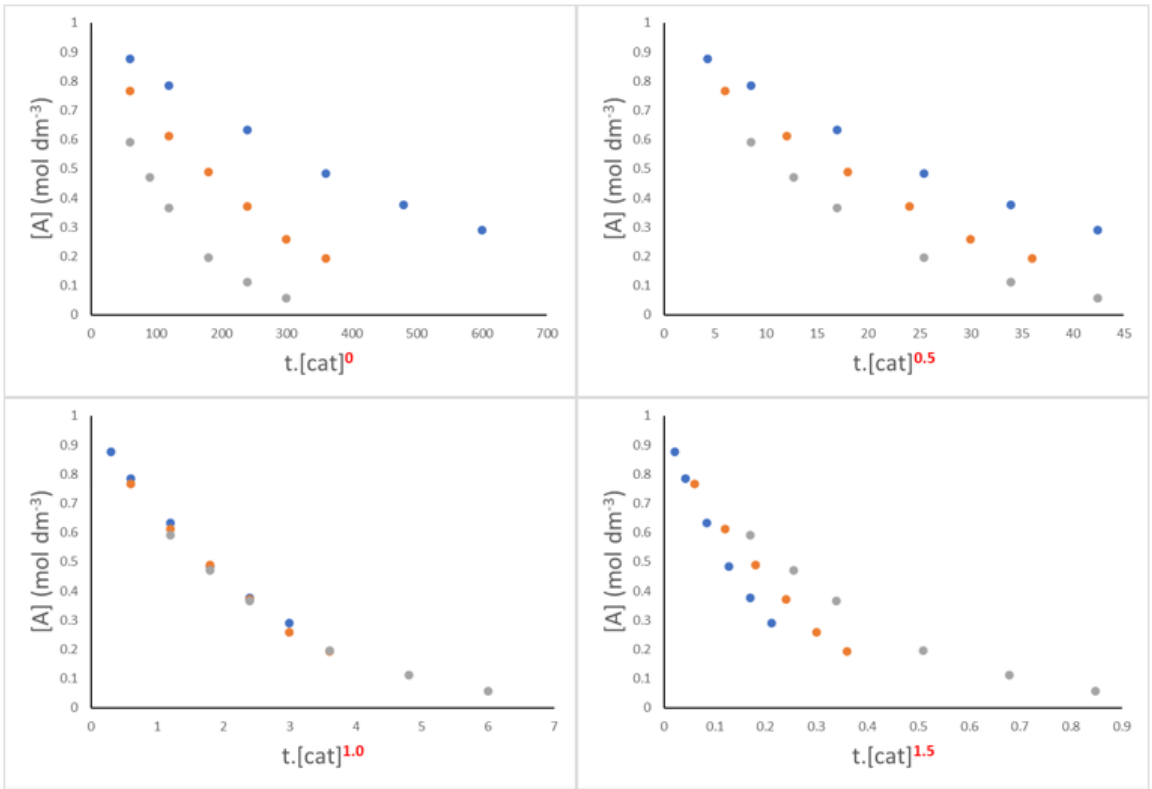


Figure B106. Variable Time Normalisation Analysis for the enantiopure catalyst (*S,S*)-**15** (*L*-LA ROP) shows an order of 1.0 with [(*S,S*)-**15**] = 0.005 (●), 0.01 (●), 0.02 (●) mol.dm^{-3}.

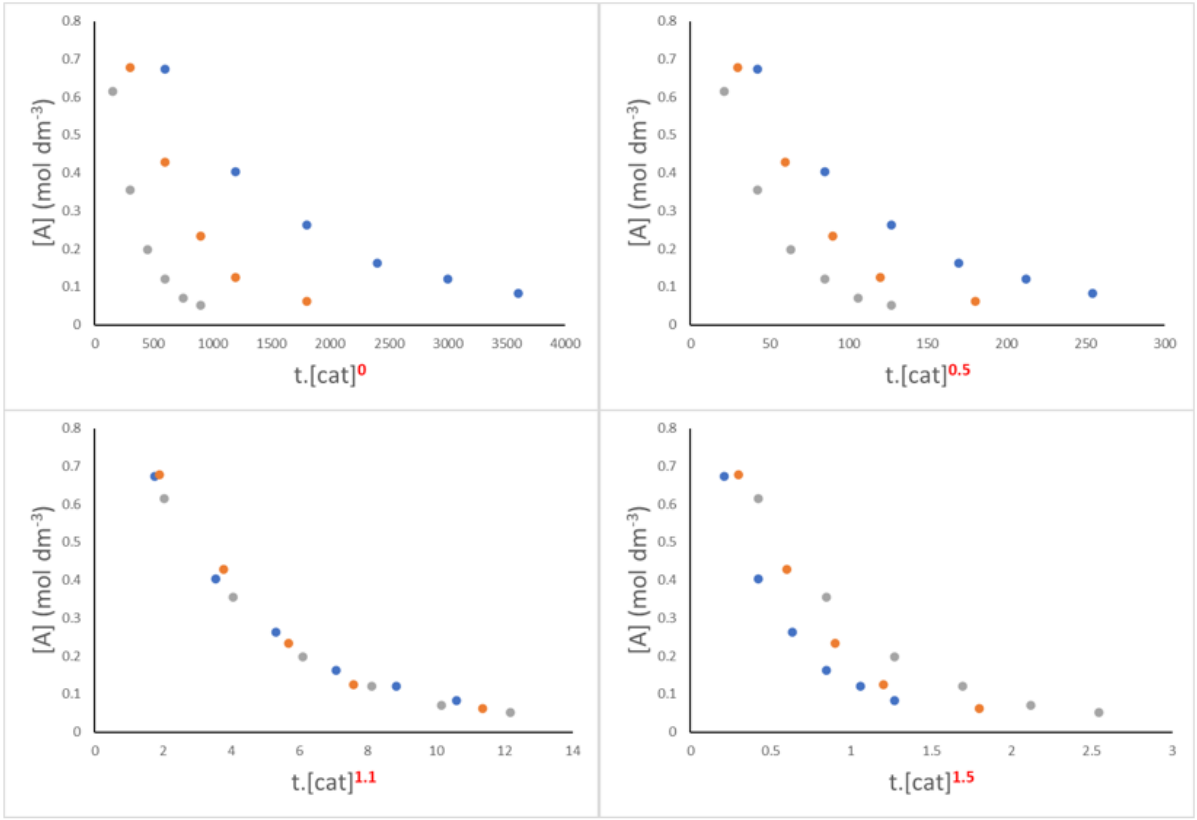


Figure B107. Variable Time Normalisation Analysis for the racemic catalyst *rac*-**15** (*rac*-LA ROP) shows an order of 1.1 with [*rac*-**15**] = 0.005 (●), 0.01 (●), 0.02 (●) mol.dm^{-3}.

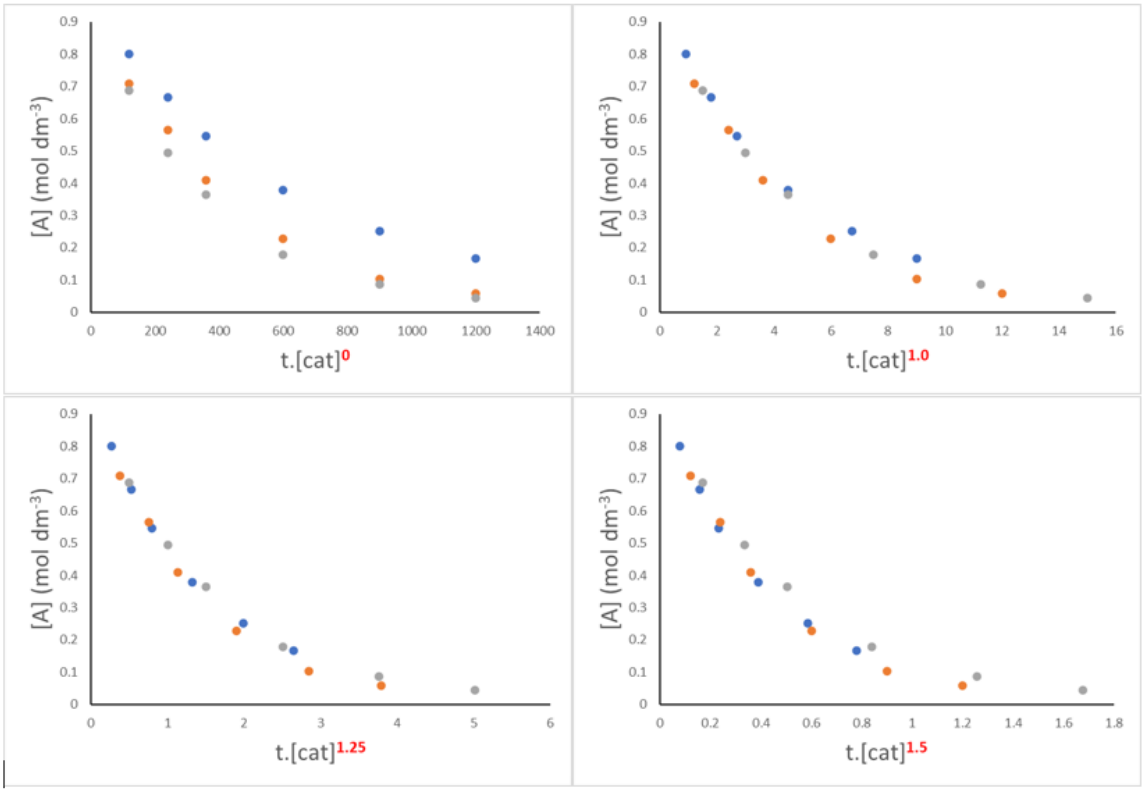


Figure B108. Variable Time Normalisation Analysis for the racemic catalyst *rac*-**15** (*L*-LA ROP) shows an order of 1.25 with [*rac*-**15**] = 0.0075 (●), 0.01 (●), 0.0125 (●) mol.dm^{-3}.

B.2.3 Determination of order in ε-CL:

Three experiments with three different initial concentration in ε-CL (i.e. [ε-CL]0 = 1.0 M, 1.5 M and 2.0 M) were monitored to determine the order in ε-CL.

Procedure: In a glovebox, the catalyst (10 mg, 0.016 mmol, either *R*,*R*-**1** or *rac*-**1**) was weighed in a vial. In a separate vial, the desired amount of ε-CL and THF were measured out to reach the considered $[\varepsilon\text{-CL}]_0$, i.e.:

- For $[\varepsilon\text{-CL}]_0$ = 1.0 M: 178.5 µL of ε-CL (1.61 mmol) in 1.43 mL of THF
- For $[\varepsilon\text{-CL}]_0$ = 1.5 M: 267.7 µL of ε-CL (2.42 mmol) in 1.34 mL of THF

The ε-CL solution was then added to the vial containing the catalyst and timing was started. Aliquots were taken periodically and quenched in wet $CDCl_3$ to stop any further reaction. These samples were analysed by ^{1}H NMR spectroscopy to determine conversion by relative integration of signals at 4.23 ppm (monomer) and 4.05 ppm (polymer). The temporal reaction concentration profiles are very similar when shifted to account for the different initial concentration of monomer, suggesting a close to zero order dependence on [ε-CL] at concentrations higher than 0.5 M.

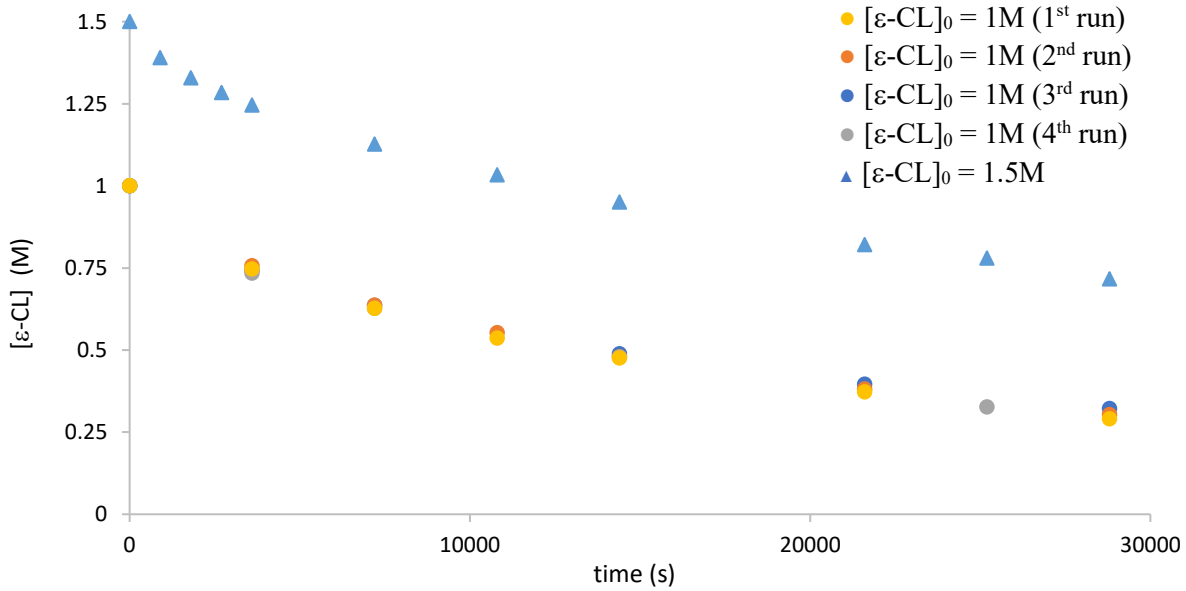


Figure B109: [ε-CL] versus time for multiple runs using $[\varepsilon\text{-CL}]_0$ = 1 M and $[\varepsilon\text{-CL}]_0$ = 1.5 M.

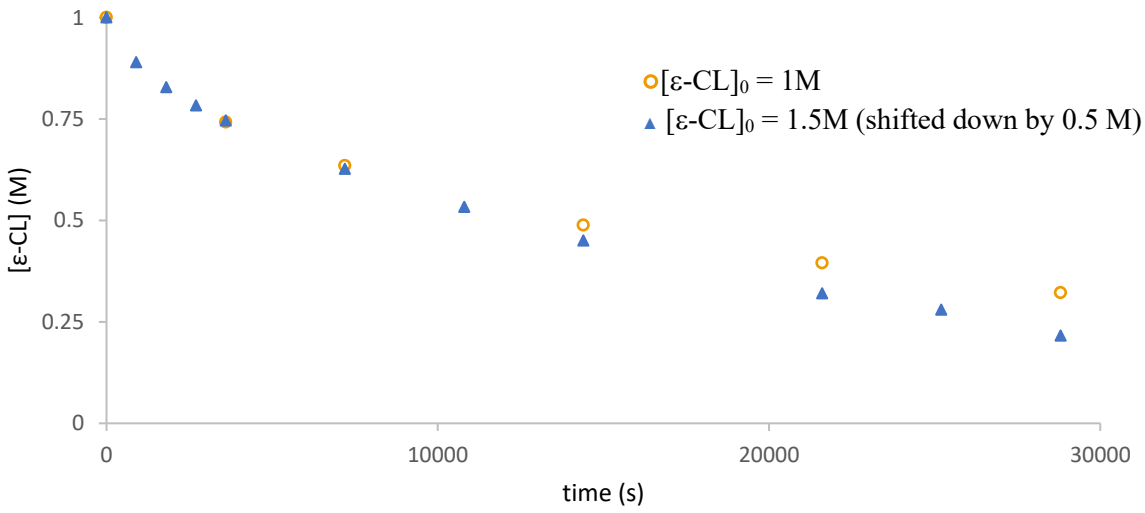


Figure B110: Similar temporal reaction profiles for $[\varepsilon\text{-CL}]_0$ = 1 M (○) and $[\varepsilon\text{-CL}]_0$ = 1.5 M (▲, shifted down by 0.5 M) suggesting a close to zero order dependence on [ε-CL] at concentrations higher than 0.5 M.

Appendix C: Homo- and Heteronuclear Decoupled NMR Spectra

C.1 General procedure

Determination of tacticity of PLA derived from *rac*-LA

The PLA tacticity (P_r) was determined using the homonuclear decoupled ^{1}H NMR spectrum (methine region). In the case of *rac*-lactide polymerisation, five possible tetrad sequences are possible. Thus, the decoupled NMR spectrum yields five peaks, each corresponding to a tetrad sequence, with their relative ratios determining the microstructure of the PLA through Bernoullian statistics (Figure C25).[1-3]

Example of calculation:

$[rmr] = P_r^2/2 \quad \rightarrow \quad P_r = \sqrt{\left[\frac{(2\times 21394)}{52457}\right]} = 0.90$

$[rmm] = P_r P_m/2 \quad \rightarrow \quad P_m = \frac{\left[\frac{(2\times 3146)}{52457}\right]}{0.90} = 0.13$ P_m = [(2 x 3146) / (52457)] / 0.90 = 0.13

$[mmr] = P_r P_m/2$

$[mmm] = P_m^2 + P_r P_m/2$

$[mrm] = (P_r^2 + P_r P_m)/2$

Although all five peaks are used in the calculations, only the equations corresponding to the *rmr* and *rmm* peaks are employed as these peaks are the only ones that can be integrated with accuracy. The MestReNova line fitting tool was used to deconvolute the spectrum and obtain the area below the peaks.

Determination of tacticity of PLA derived from *meso*-LA

In the case of *meso*-lactide polymerisation, five possible tetrad sequences are possible as well. However, only the *rmr* tetrad at 5.20 ppm can be integrated with confidence as the other tetrads overlap.[1]

Example of calculation:

$[rmr] = (P_m^2 + P_r P_m)/2 \quad \rightarrow \quad P_m = 2 \times [rmr]$

Determination of tacticity of P3HB derived from β-BL

In the case of β-BL polymerisation, the stereoregularity is analysed by examining the carbonyl regions in the quantitative ^{13}C NMR spectrum of P3HB. This region consists of two peaks which represent the *r* (169.2 ppm) and *m* dyad (169.1 ppm). Their intensity can be resolved by simple integration of the peaks.[4]

Example of calculation:

P_r = [r] / ([r] + [m])

C.2 Chapter 2 Decoupled NMR Spectra

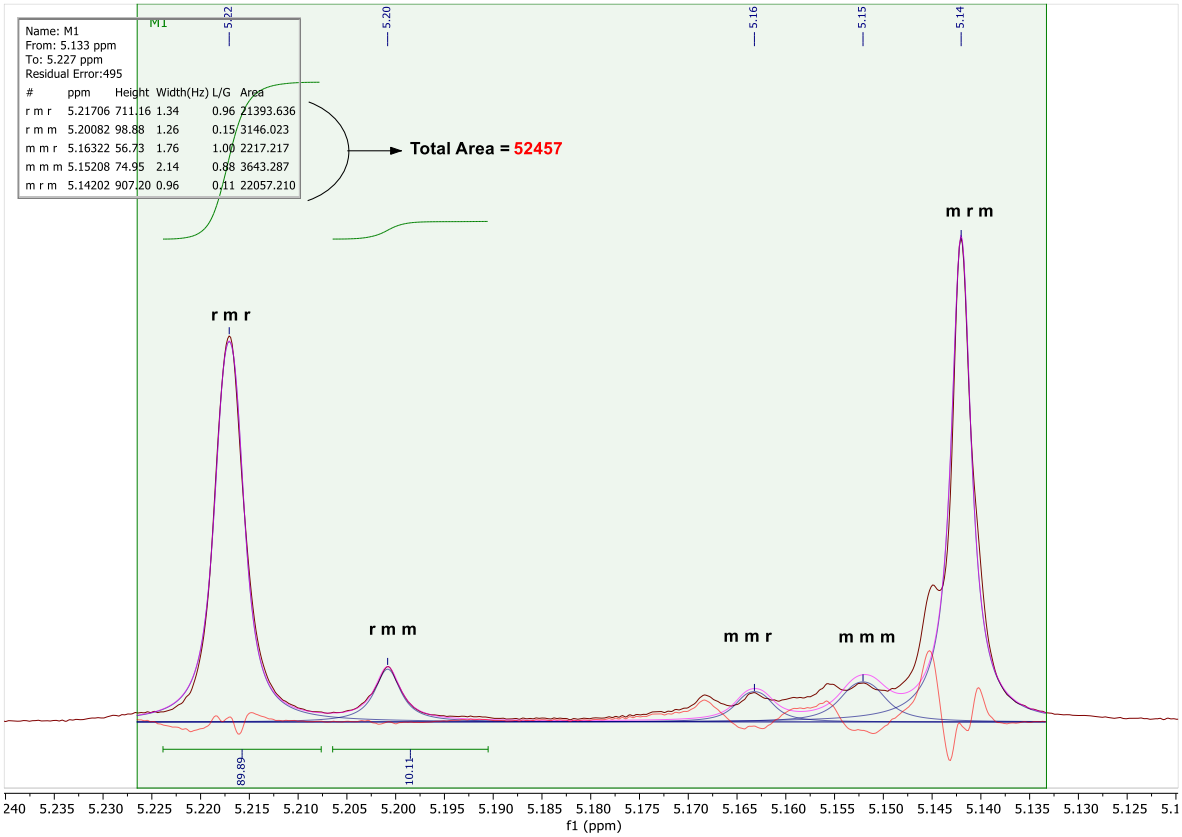


Figure C1. Methine region of the homonuclear decoupled $^{1}H\{^{1}H\}$ NMR spectrum for *rac*-LA ROP initiated by **1** showing P_r = 0.90 (reaction conditions as per Table 1, Entry 1).

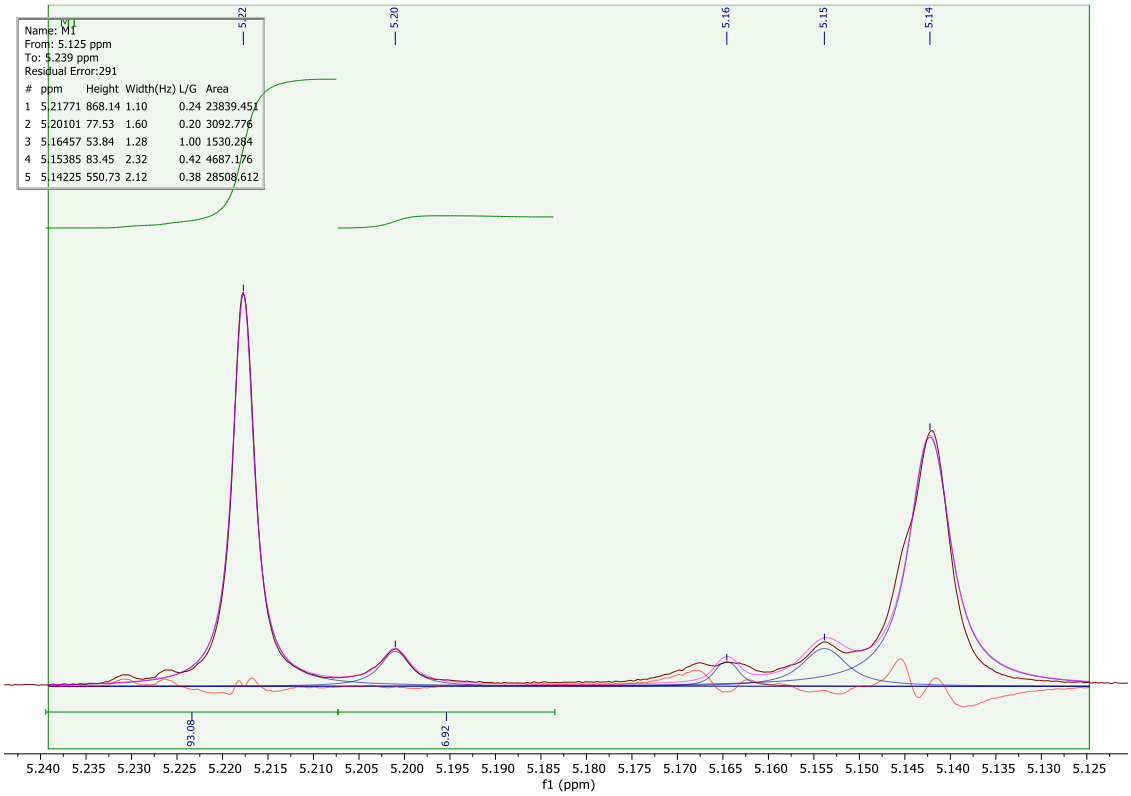


Figure C2. Methine region of the homonuclear decoupled $^{1}H\{^{1}H\}$ NMR spectrum for *rac*-LA ROP initiated by **1** showing P_r = 0.89 (reaction conditions as per Table 1, Entry 2).

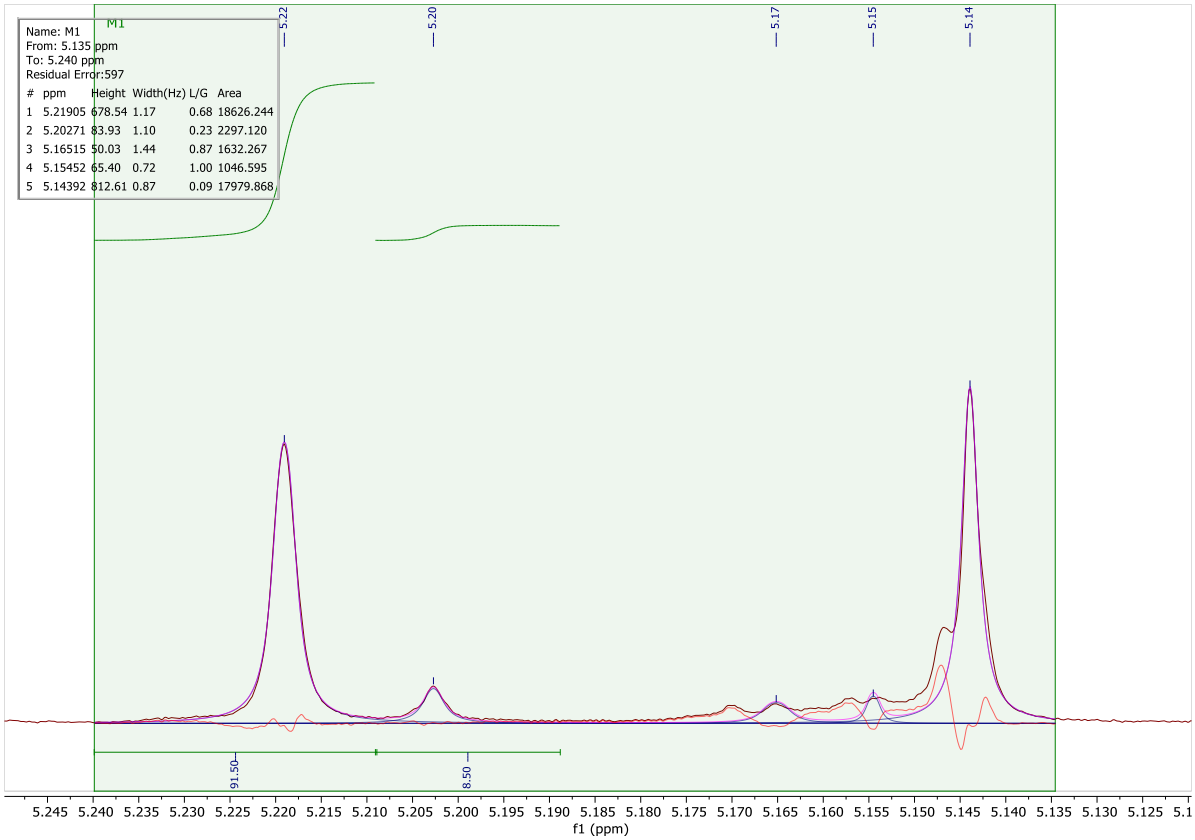


Figure C3. Methine region of the homonuclear decoupled $^{1}H\{^{1}H\}$ NMR spectrum for *rac*-LA ROP initiated by **2** showing P_r = 0.91 (reaction conditions as per Table 1, Entry 3).

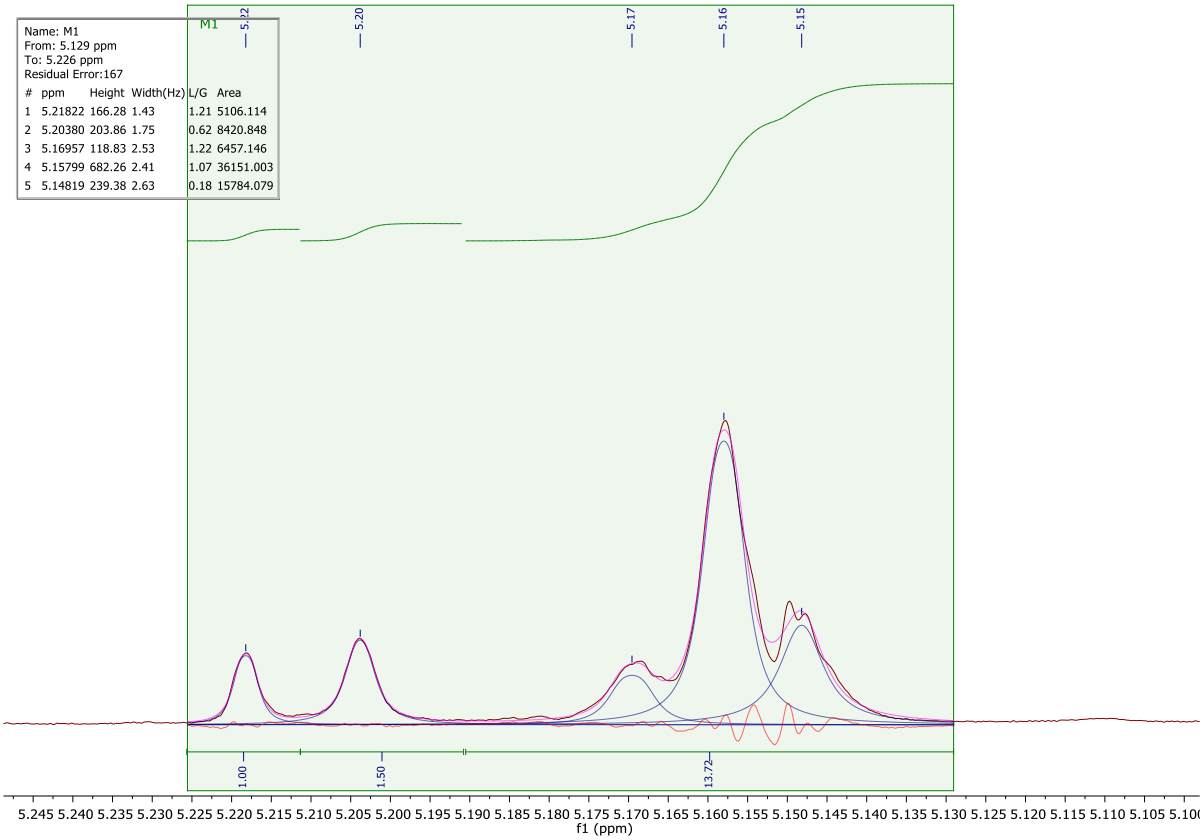


Figure C4. Methine region of the homonuclear decoupled $^{1}H\{^{1}H\}$ NMR spectrum for *rac*-LA ROP initiated by **6** showing P_m = 0.62 (reaction conditions as per Table 1, Entry 4).

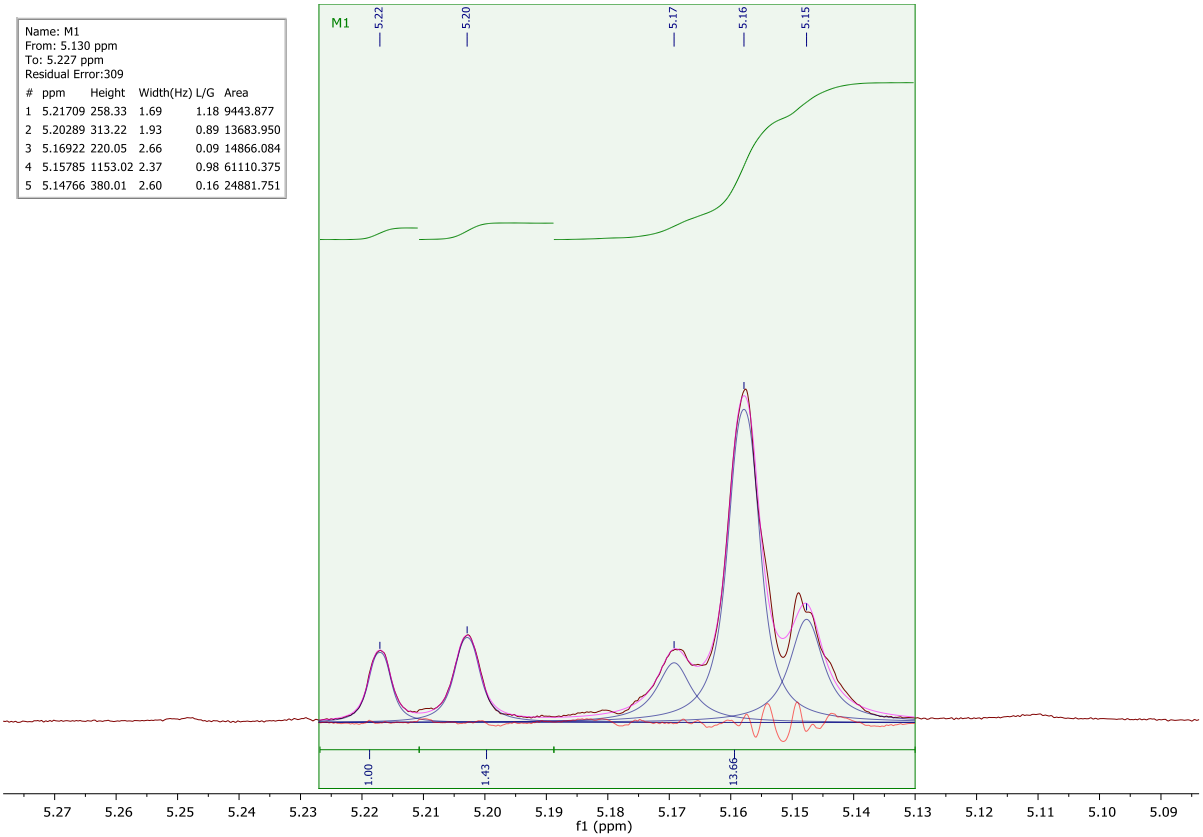


Figure C5. Methine region of the homonuclear decoupled $^{1}H\{^{1}H\}$ NMR spectrum for *rac*-LA ROP initiated by **6** showing P_m = 0.59 (reaction conditions as per Table 1, Entry 5).

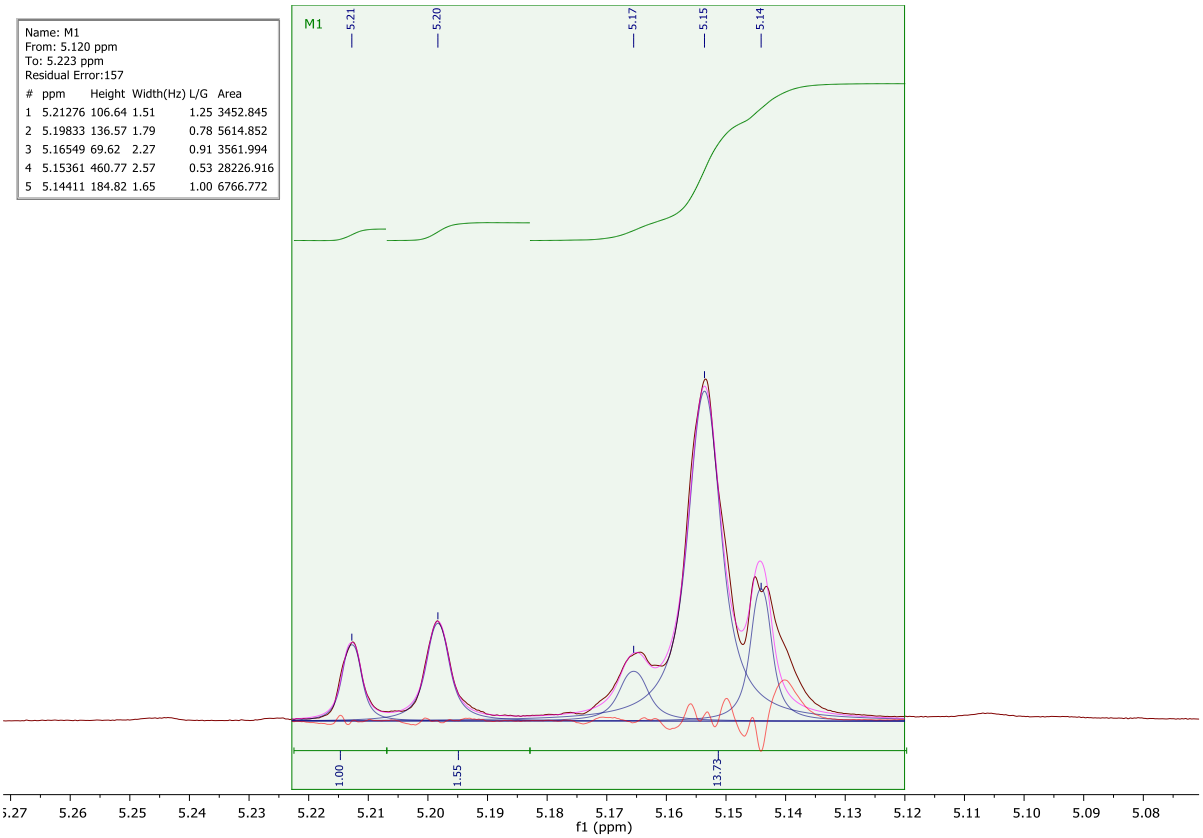


Figure C6. Methine region of the homonuclear decoupled $^{1}H\{^{1}H\}$ NMR spectrum for *rac*-LA ROP initiated by **7** showing P_m = 0.62 (reaction conditions as per Table 1, Entry 6).

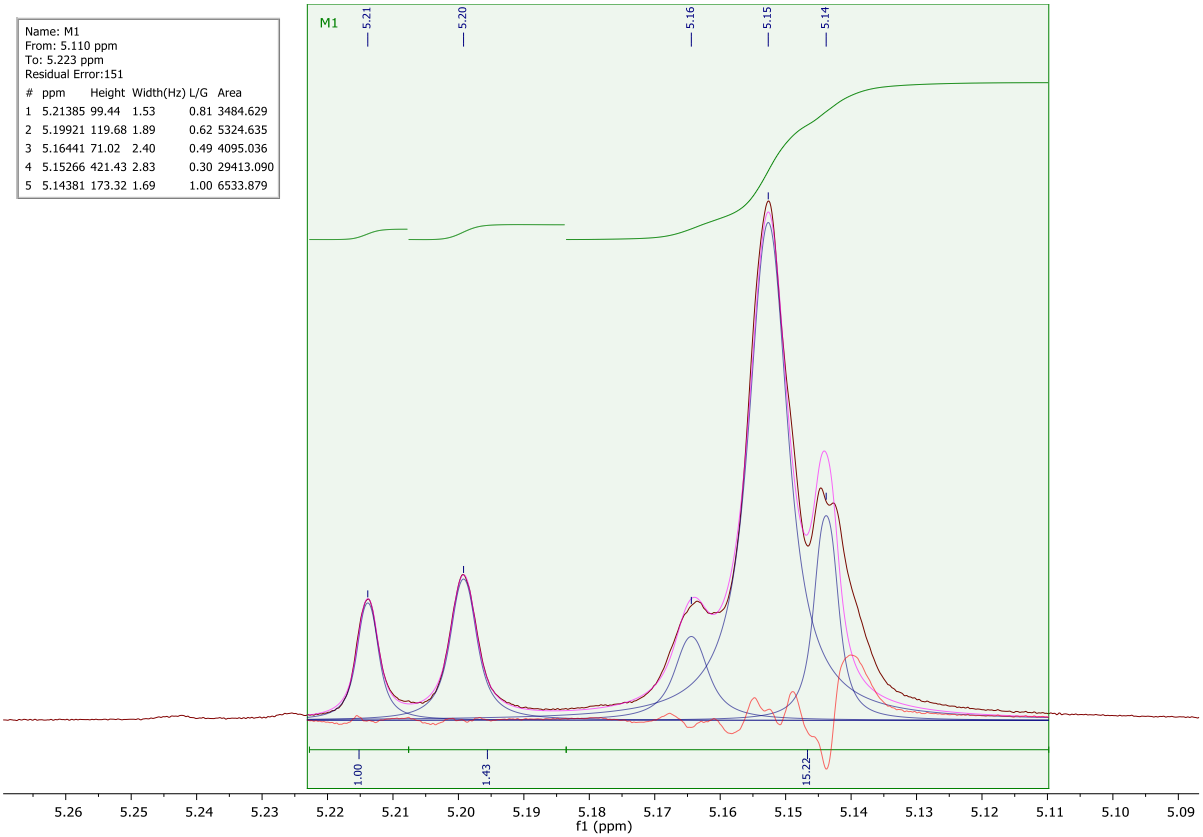


Figure C7. Methine region of the homonuclear decoupled $^{1}H\{^{1}H\}$ NMR spectrum for *rac*-LA ROP initiated by **8c** showing $P_m = 0.60$ (reaction conditions as per Table 1, Entry 7).

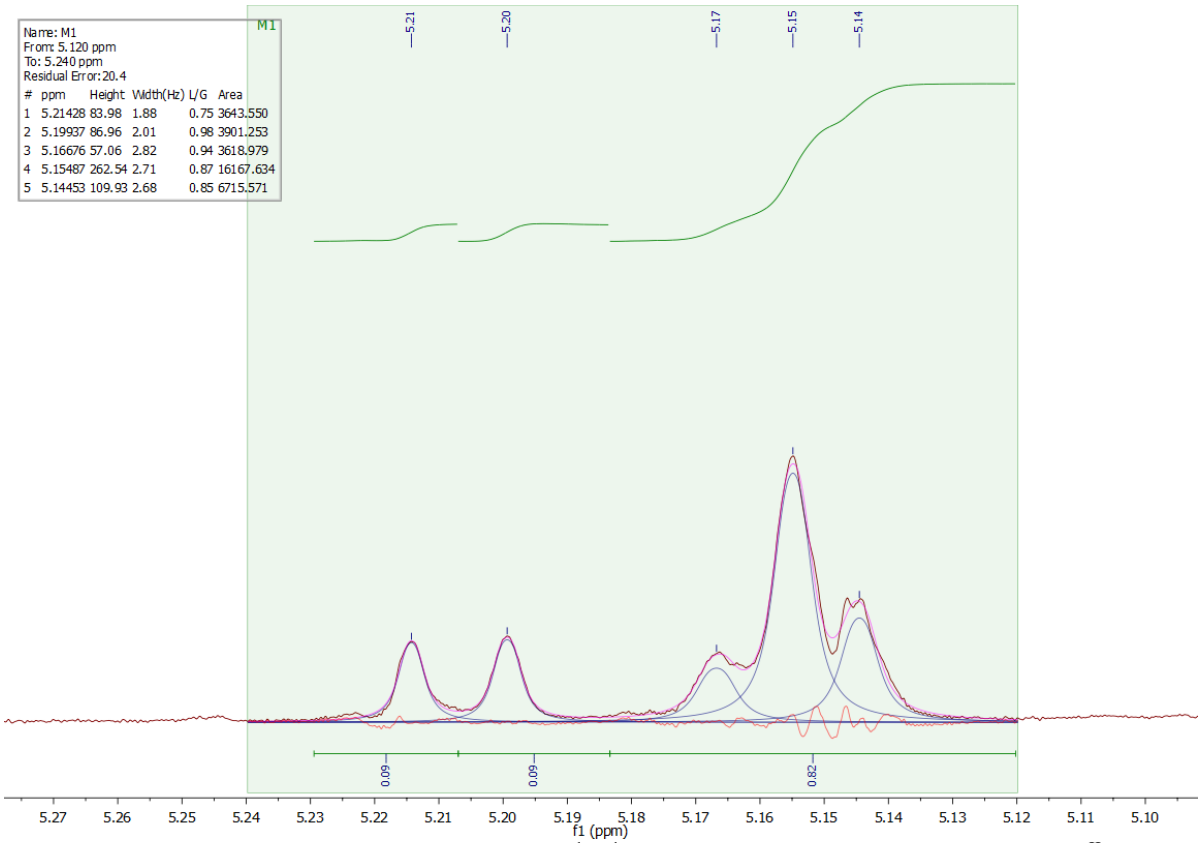


Figure C8. Methine region of the homonuclear decoupled $^{1}H\{^{1}H\}$ NMR spectrum for *rac*-LA ROP initiated by **^{H}salan**-Al showing $P_r = 0.54$ (reaction conditions as per Table 1, Entry 8).

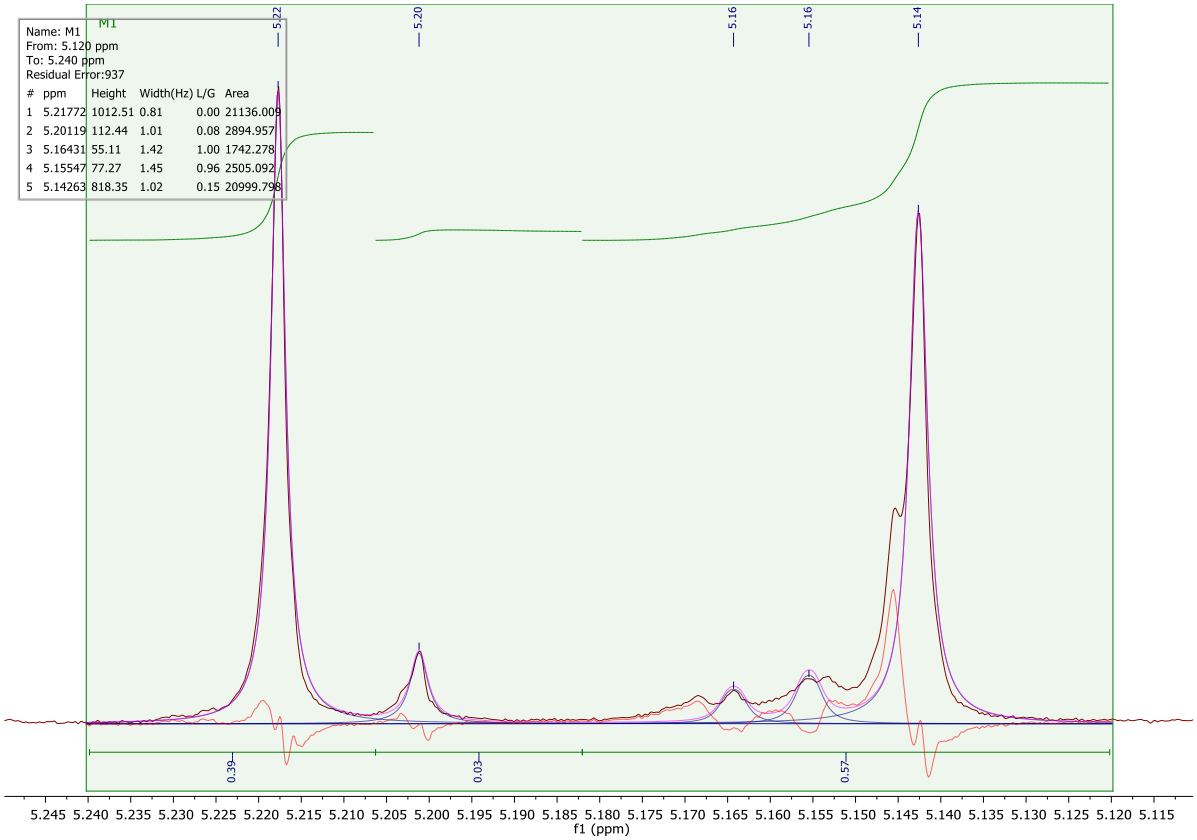


Figure C9. Methine region of the homonuclear decoupled $^{1}H\{^{1}H\}$ NMR spectrum for *rac*-LA ROP initiated by **4** showing P_r = 0.91 (reaction conditions as per Table 2, Entry 2).

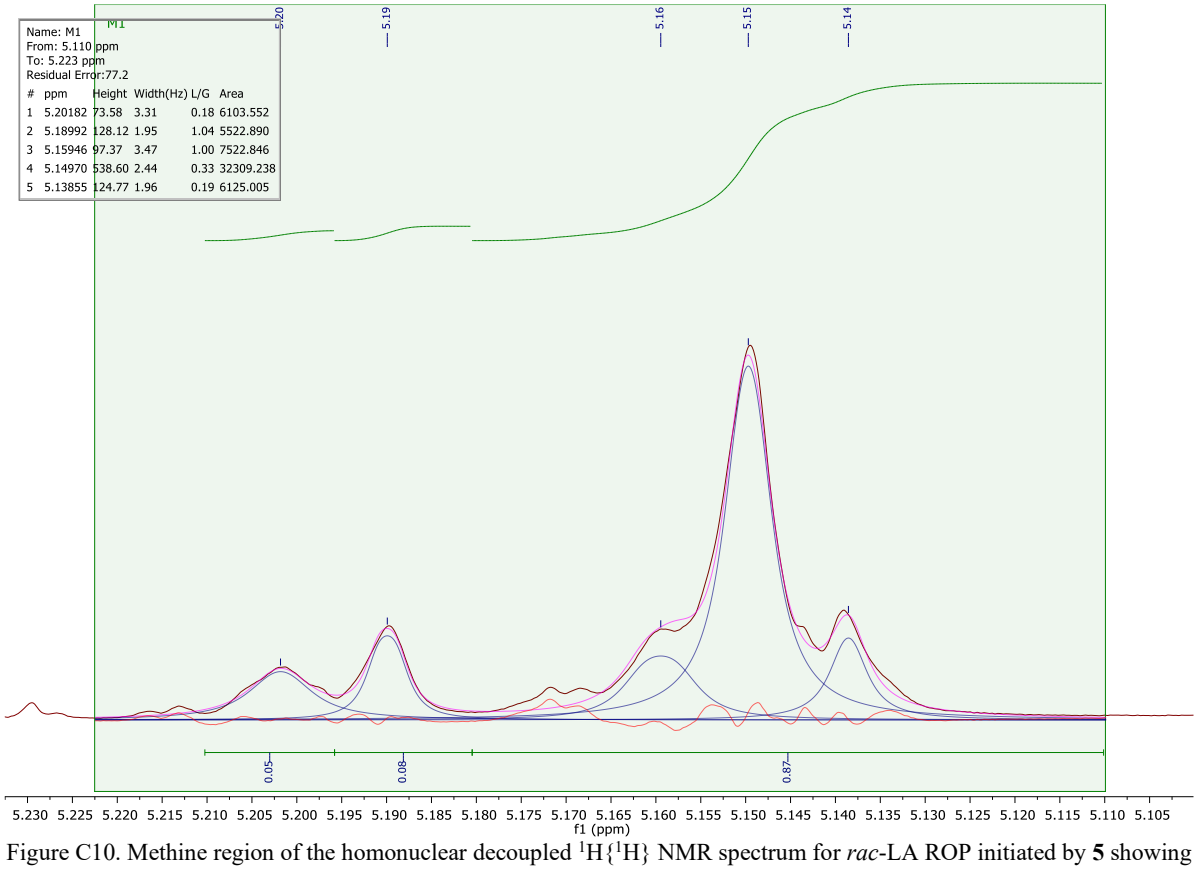


Figure C10. Methine region of the homonuclear decoupled $^{1}H\{^{1}H\}$ NMR spectrum for *rac*-LA ROP initiated by **5** showing P_r = 0.43 (reaction conditions as per Table 3, Entry 1).

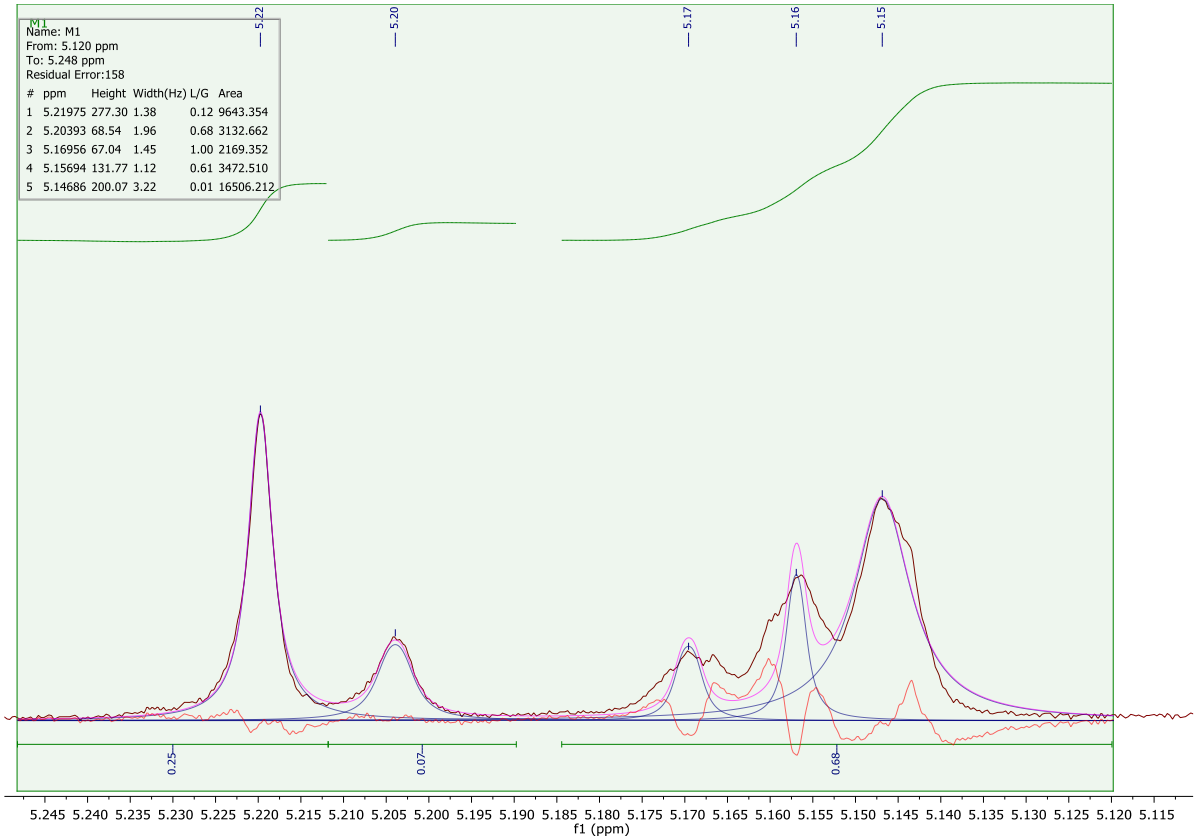


Figure C11. Methine region of the homonuclear decoupled $^{1}H\{^{1}H\}$ NMR spectrum for *rac*-LA ROP initiated by **2** showing $P_r = 0.69$ (reaction conditions as per Table 5, Entry 3).

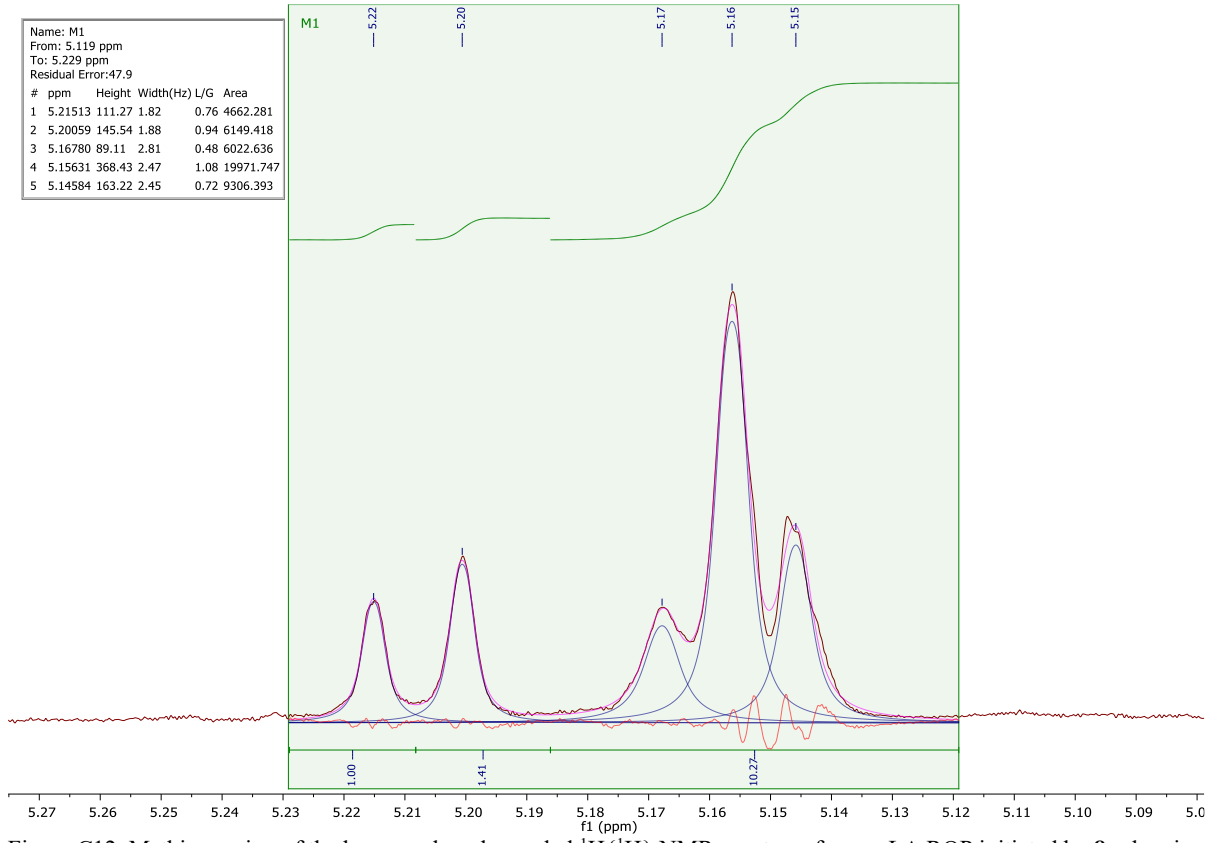


Figure C12. Methine region of the homonuclear decoupled $^{1}H\{^{1}H\}$ NMR spectrum for *rac*-LA ROP initiated by **8c** showing $P_m = 0.57$ (reaction conditions as per Table 5, Entry 4).

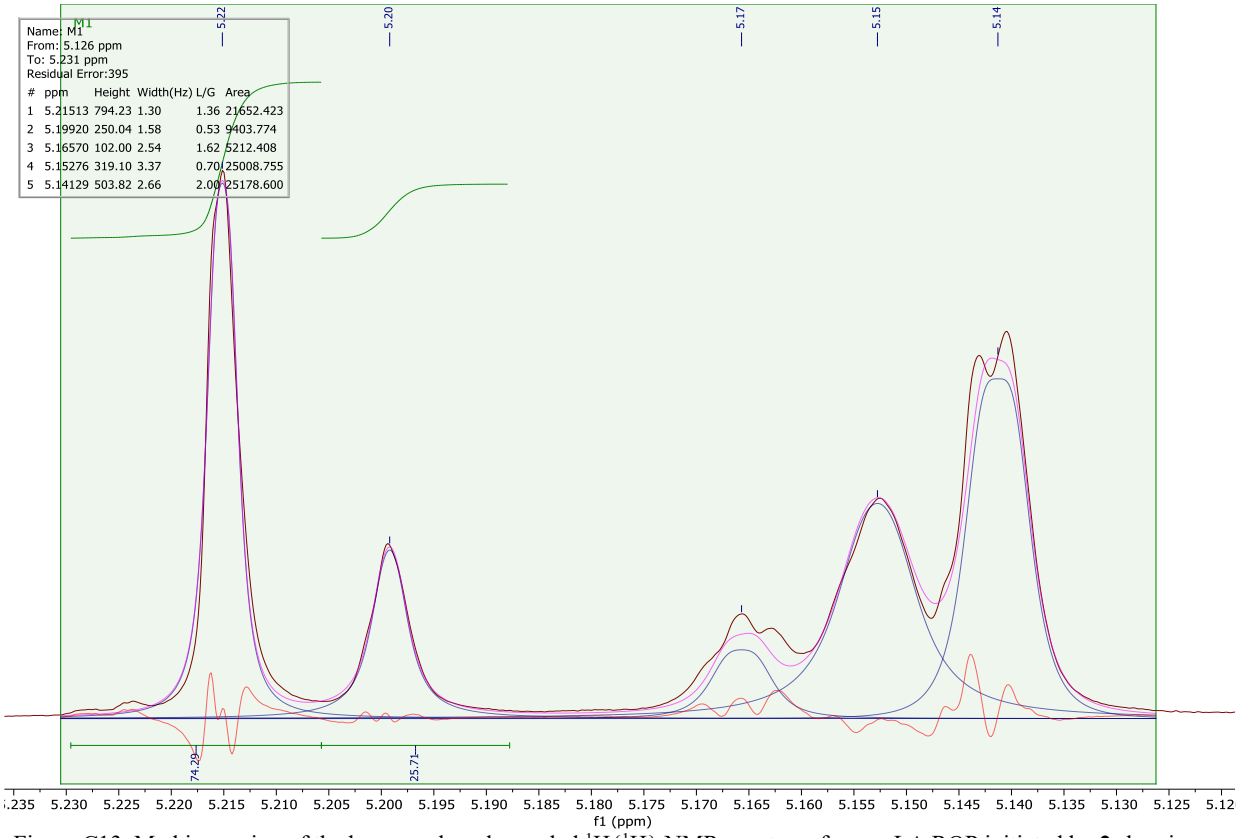


Figure C13. Methine region of the homonuclear decoupled $^{1}H\{^{1}H\}$ NMR spectrum for *rac*-LA ROP initiated by **2** showing $P_r = 0.61$ (reaction conditions as per Table 6, Entry 1).

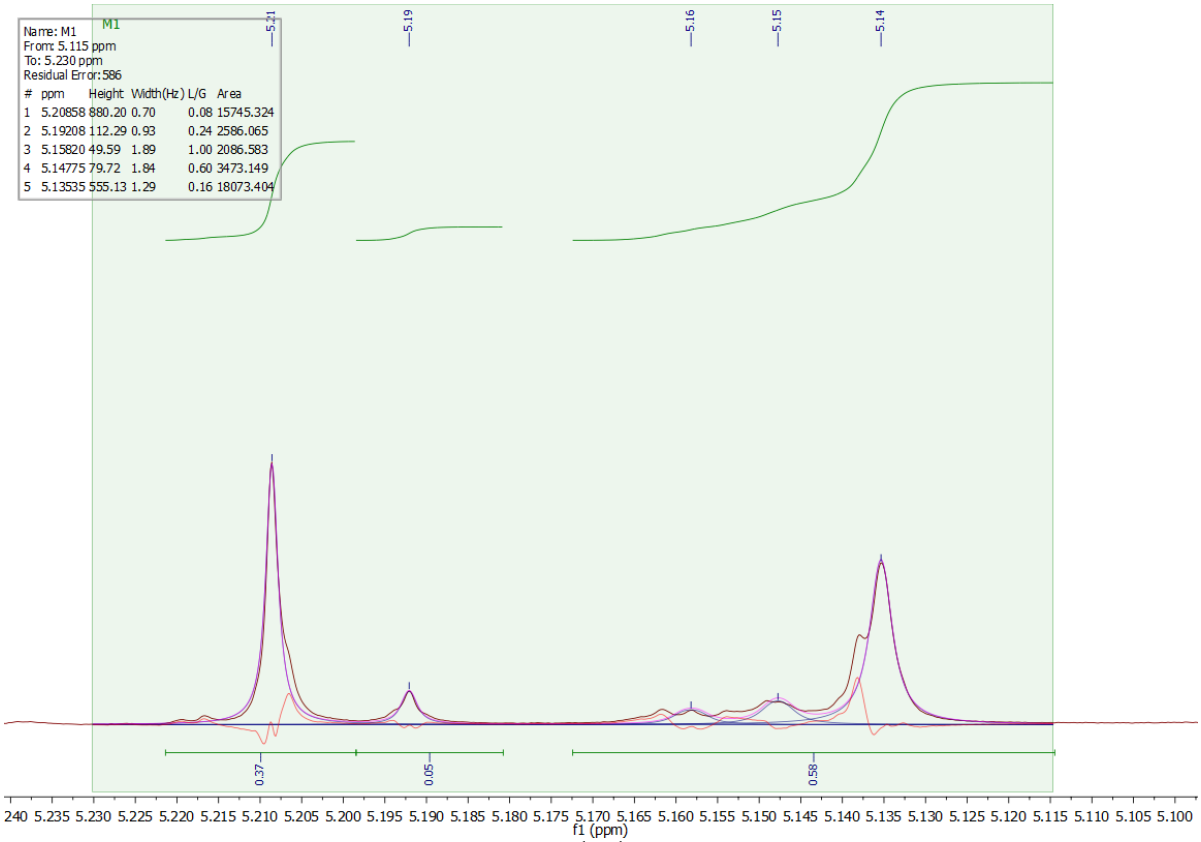


Figure C14. Methine region of the homonuclear decoupled $^{1}H\{^{1}H\}$ NMR spectrum for *rac*-LA ROP initiated by **2** showing $P_r = 0.85$ (reaction conditions as per Table 6, Entry 2).

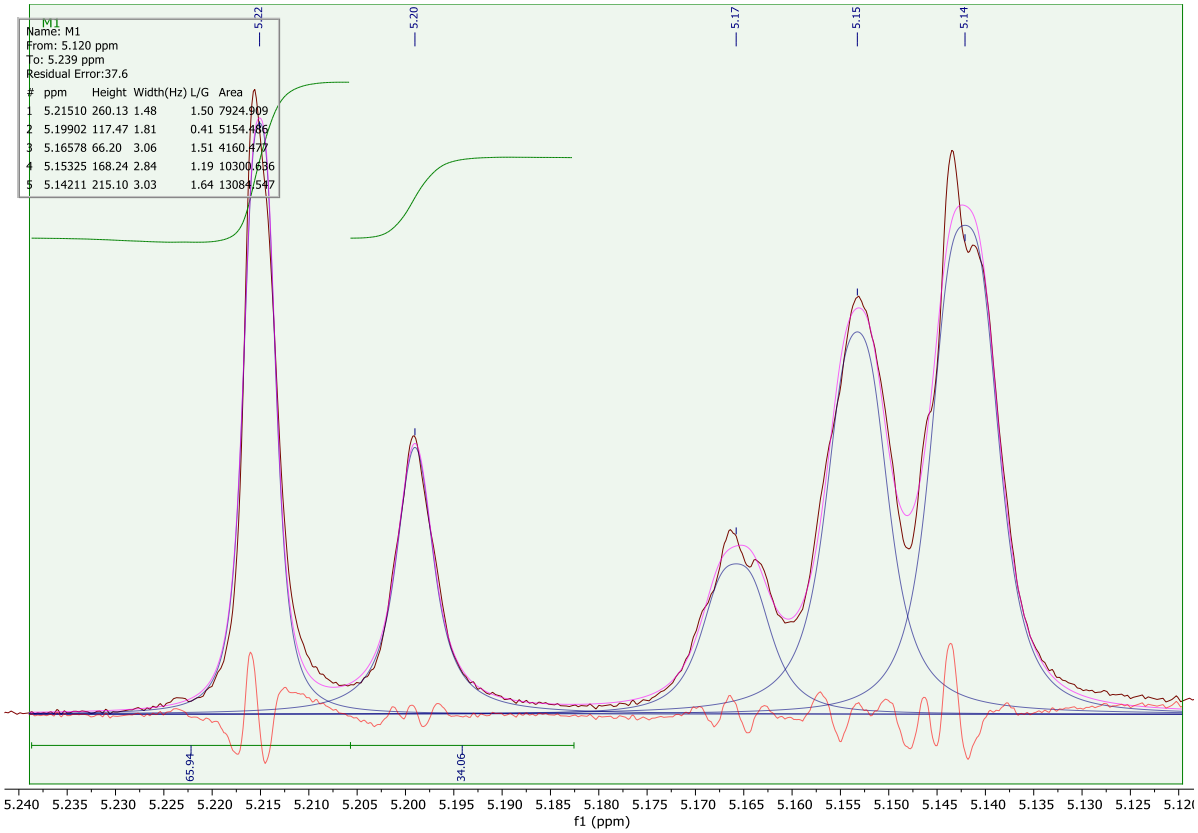


Figure C15. Methine region of the homonuclear decoupled $^{1}H\{^{1}H\}$ NMR spectrum for *rac*-LA ROP initiated by **2** showing $P_r = 0.61$ (reaction conditions as per Table 6, Entry 3).

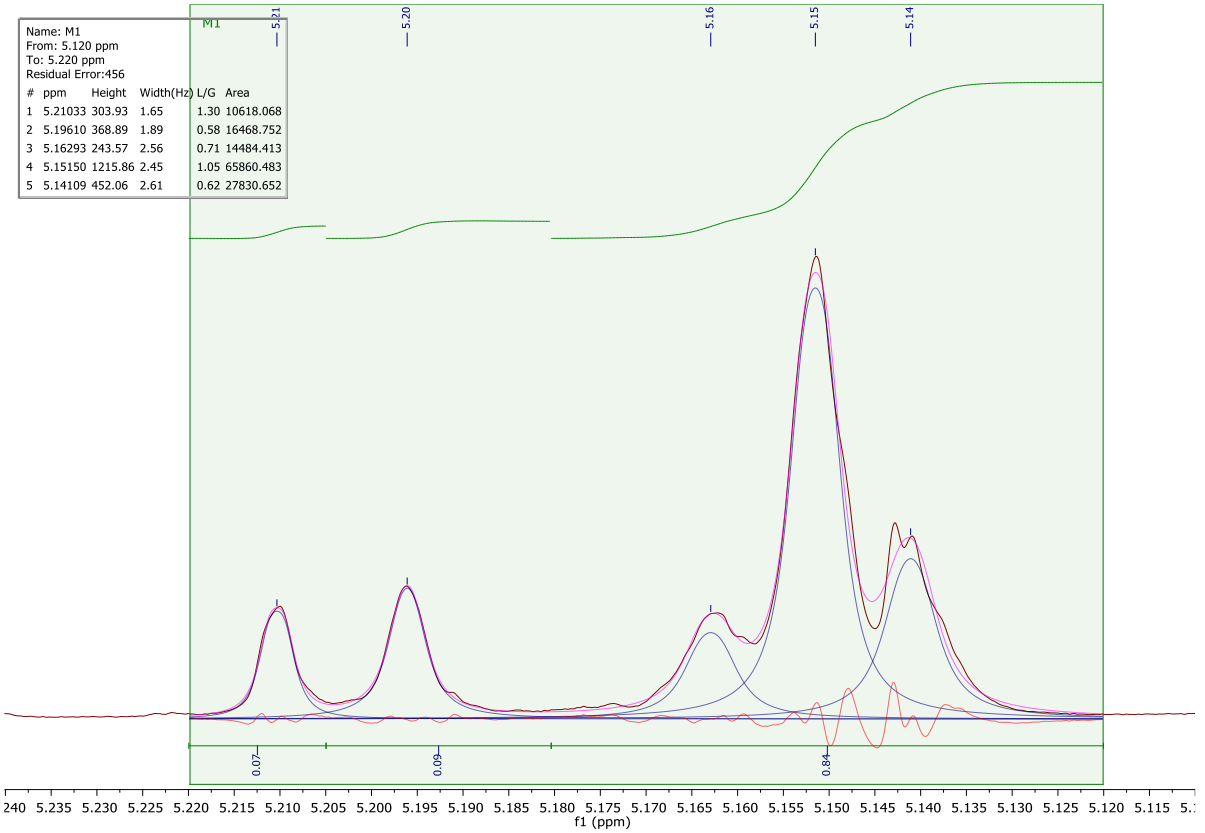


Figure C16. Methine region of the homonuclear decoupled $^{1}H\{^{1}H\}$ NMR spectrum for *rac*-LA ROP initiated by **8c** showing $P_m = 0.61$ (reaction conditions as per Table 6, Entry 5).

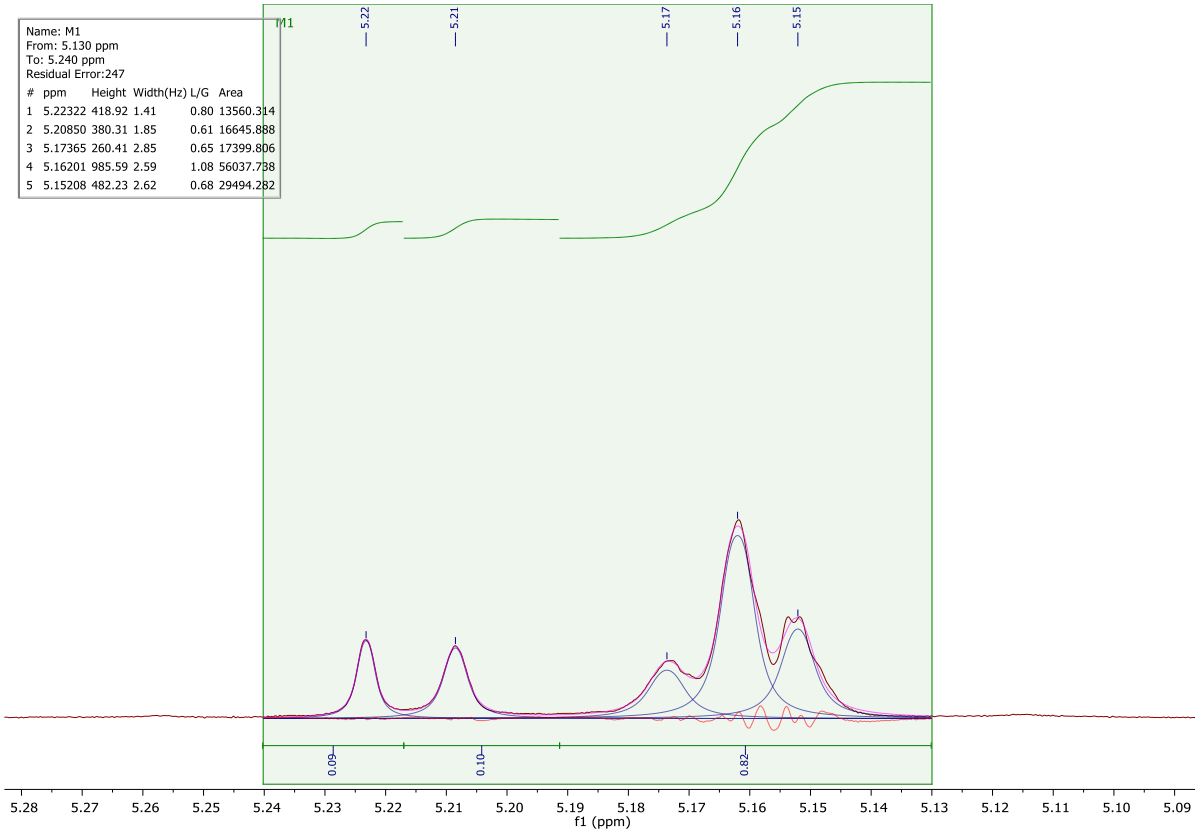


Figure C17. Methine region of the homonuclear decoupled $^{1}H\{^{1}H\}$ NMR spectrum for *rac*-LA ROP initiated by **8c** showing $P_m = 0.55$ (reaction conditions as per Table 6, Entry 6).

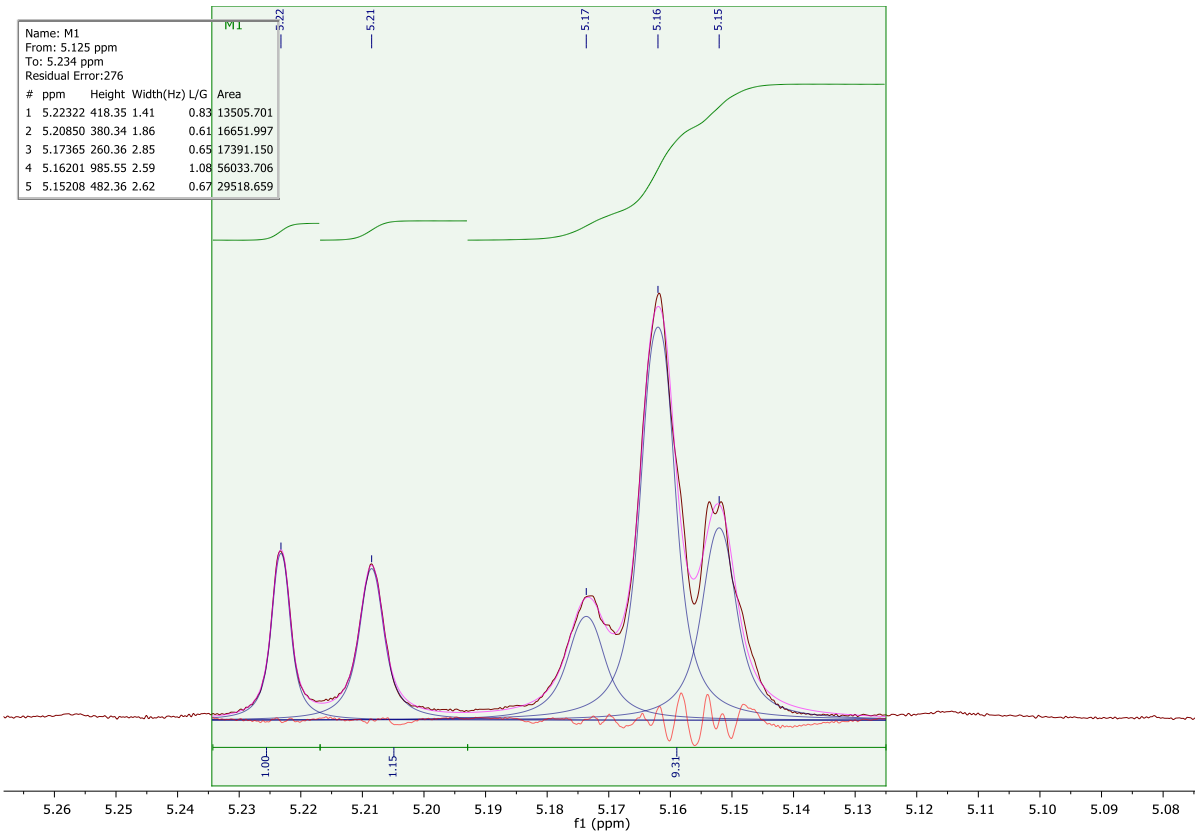


Figure C18. Methine region of the homonuclear decoupled $^{1}H\{^{1}H\}$ NMR spectrum for *rac*-LA ROP initiated by **8c** showing $P_m = 0.55$ (reaction conditions as per Table 6, Entry 7).

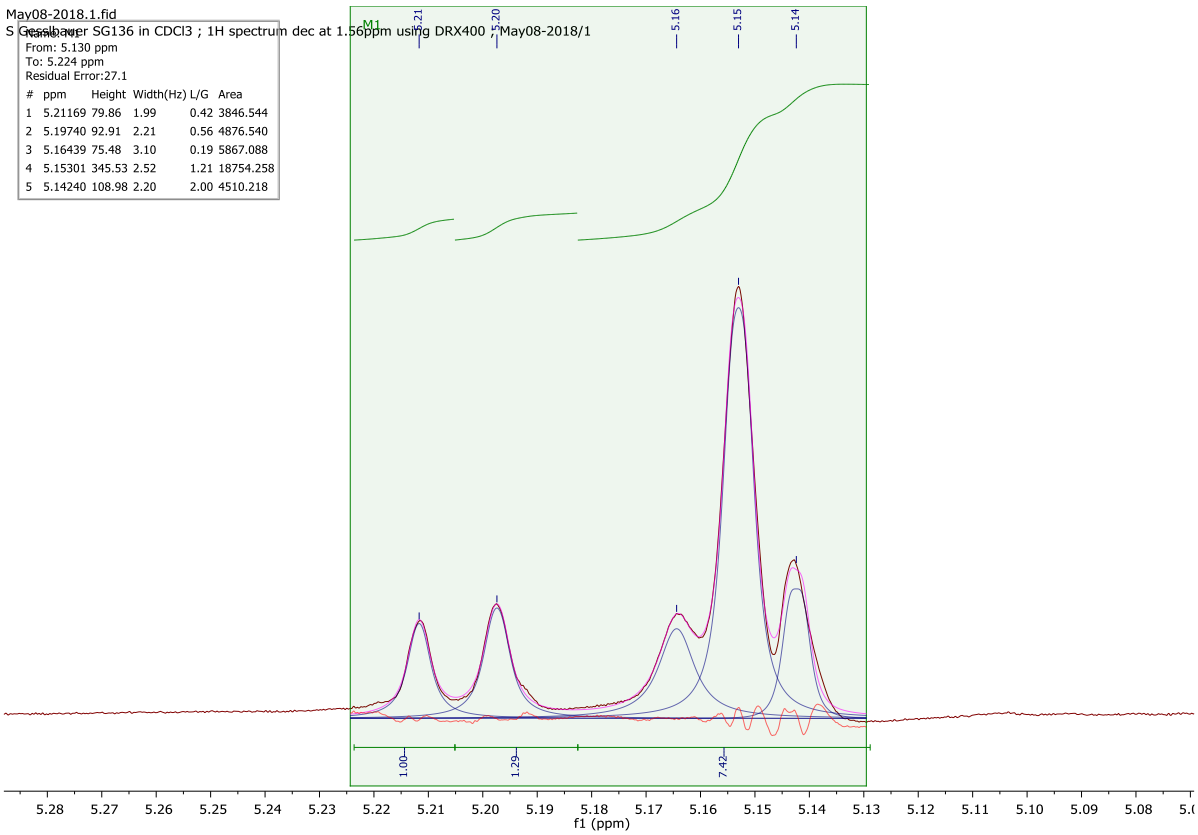


Figure C19: Methine region of the homonuclear decoupled $^{1}H\{^{1}H\}$ NMR spectrum for *rac*-LA ROP initiated by **8c** showing $P_m = 0.56$ (reaction conditions as per Table 6, Entry 8).

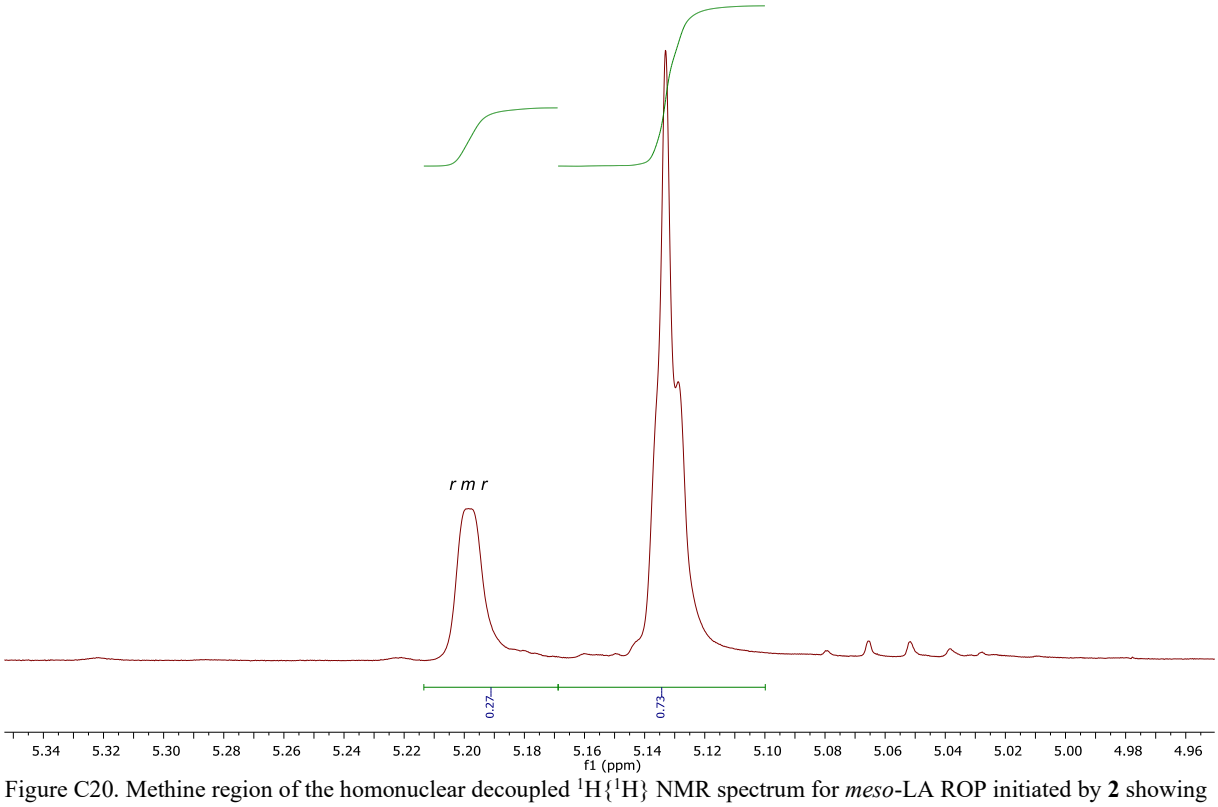


Figure C20. Methine region of the homonuclear decoupled $^{1}H\{^{1}H\}$ NMR spectrum for *meso*-LA ROP initiated by **2** showing $P_m = 0.54$ (reaction conditions as per Table 7, Entry 3).

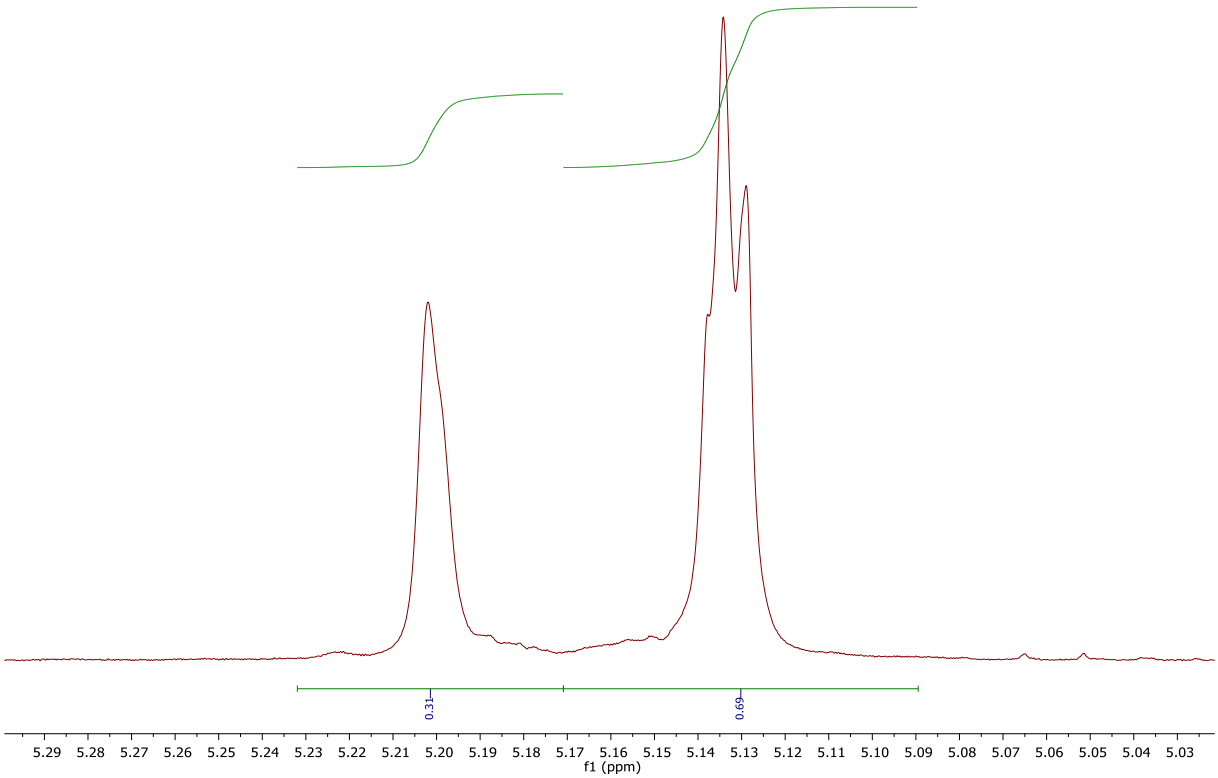


Figure C21. Methine region of the homonuclear decoupled 1H{1H} NMR spectrum for *meso*-LA ROP initiated by **8c** showing P_m = 0.62 (reaction conditions as per Table 7, Entry 4).

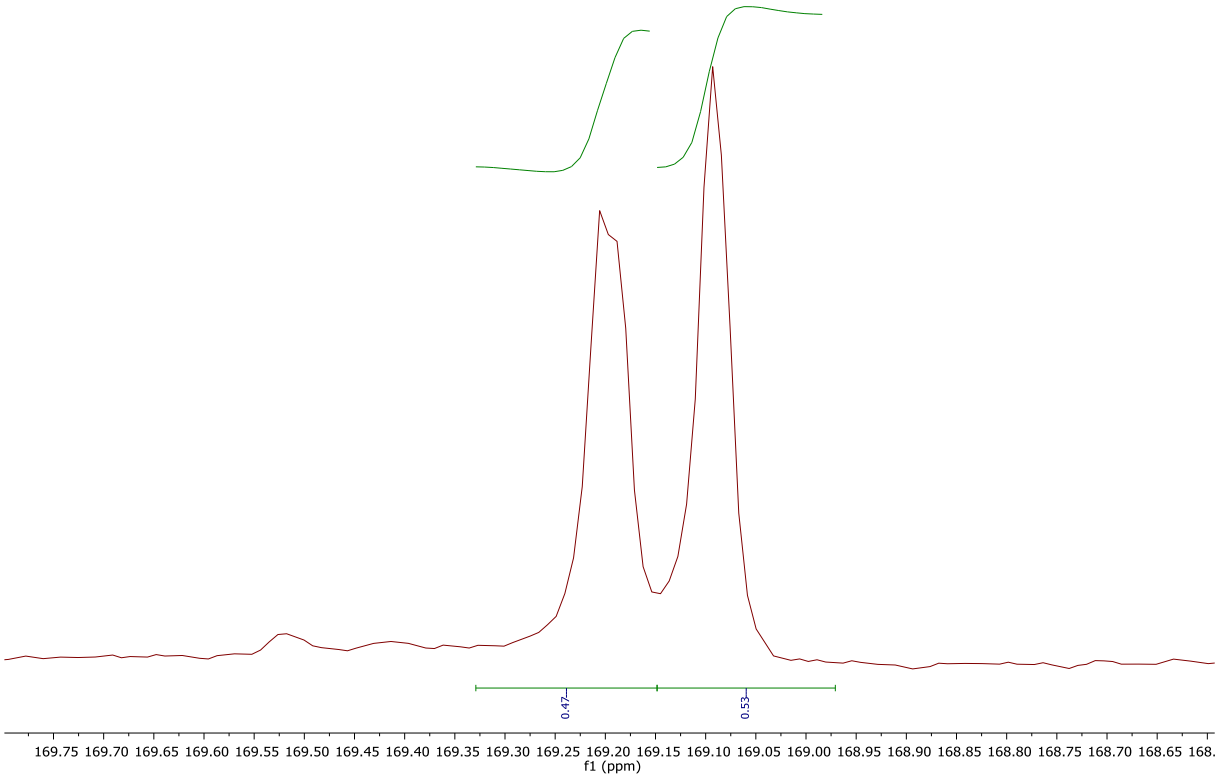


Figure C22. Methine region of the homonuclear decoupled 1H{1H} NMR spectrum for β-BL ROP initiated by **2** showing P_r = 0.47 (reaction conditions as per Table 9, Entry 1).

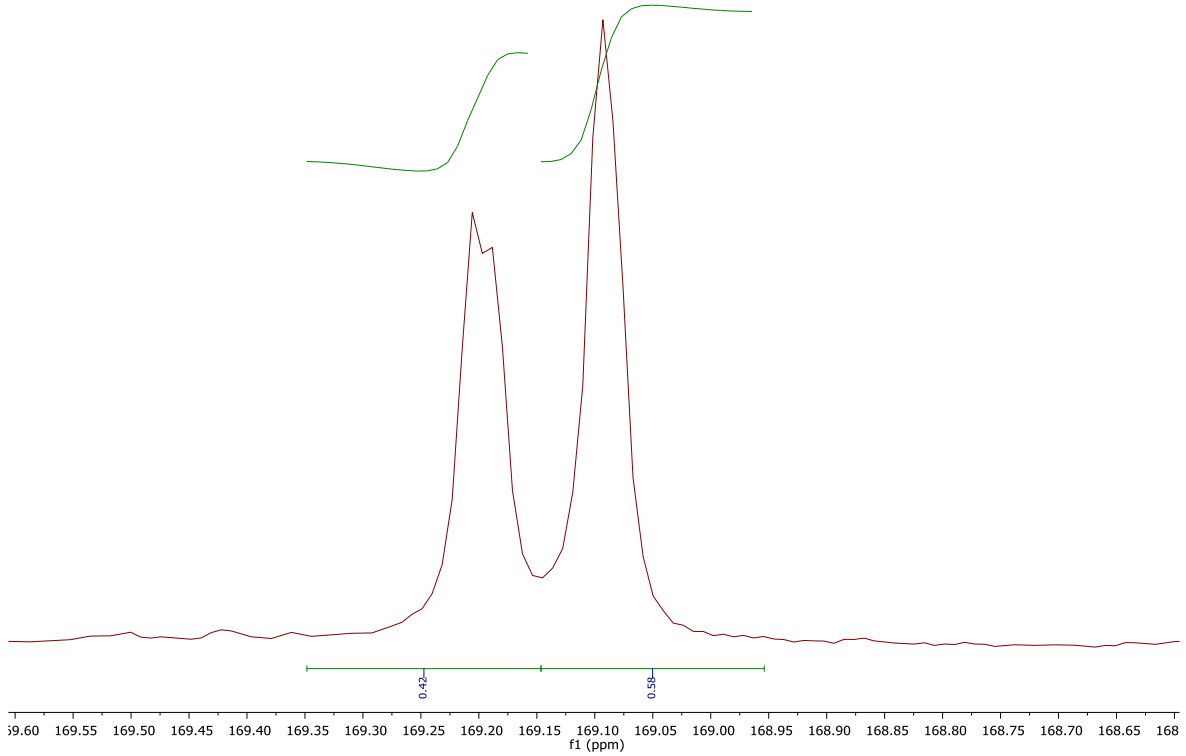


Figure C23. Methine region of the homonuclear decoupled 1H{1H} NMR spectrum for β-BL ROP initiated by **8c** showing P_r = 0.42 (reaction conditions as per Table 9, Entry 2).

C.3 Chapter 3 Decoupled NMR Spectra

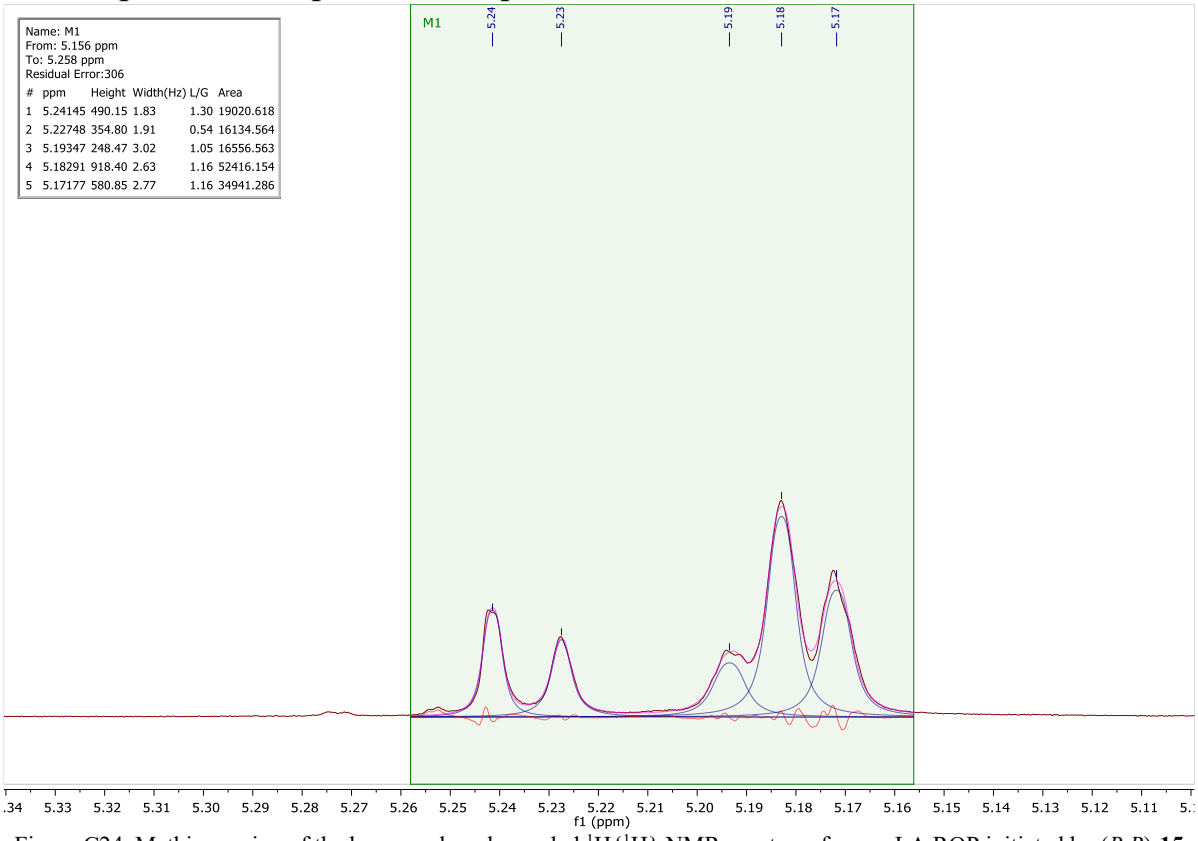


Figure C24. Methine region of the homonuclear decoupled $^1H\{^1H\}$ NMR spectrum for *rac*-LA ROP initiated by (*R,R*)-**15** showing P_m = 0.50 (reaction conditions as per Table 4, Entry 1).

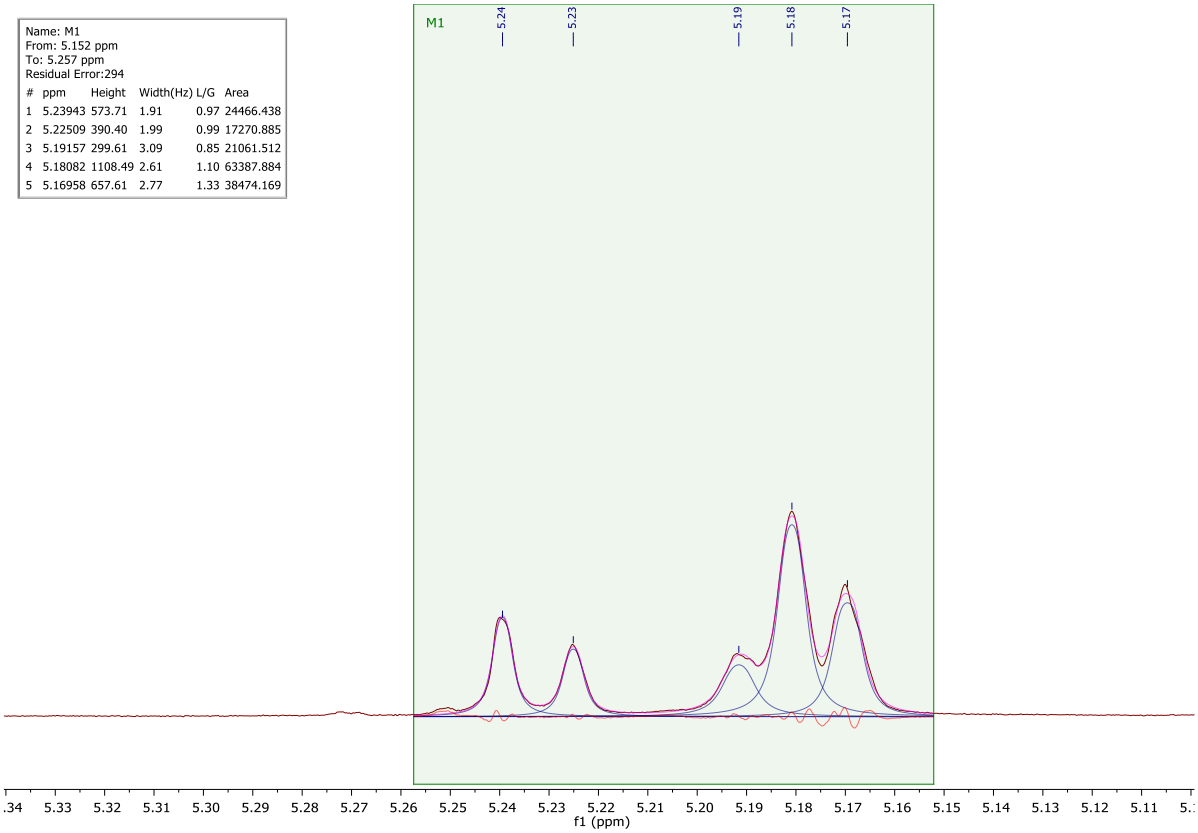


Figure C25. Methine region of the homonuclear decoupled $^{1}H\{^{1}H\}$ NMR spectrum for *rac*-LA ROP initiated by (*S,S*)-**15** showing P_m = 0.50 (reaction conditions as per Table 4, Entry 2).

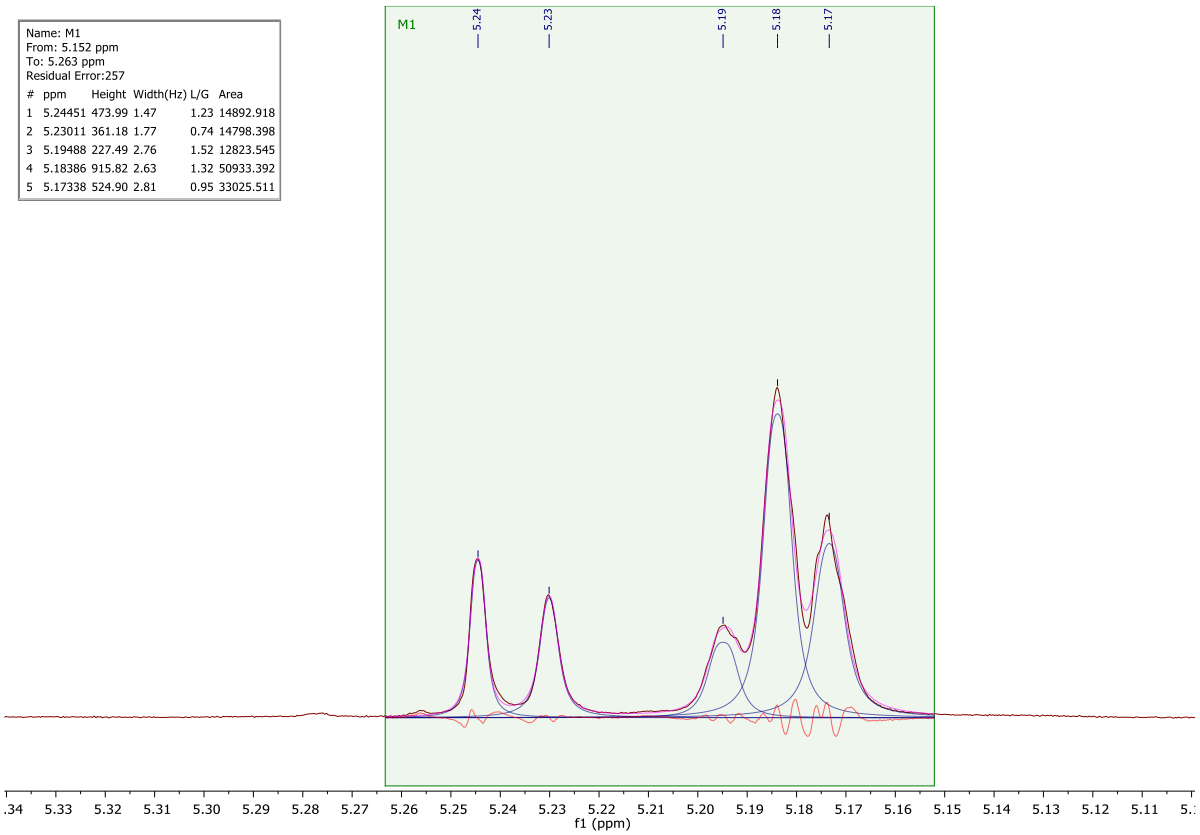


Figure C26. Methine region of the homonuclear decoupled $^{1}H\{^{1}H\}$ NMR spectrum for *rac*-LA ROP initiated by *rac*-**15** showing P_m = 0.50 (reaction conditions as per Table 4, Entry 3).

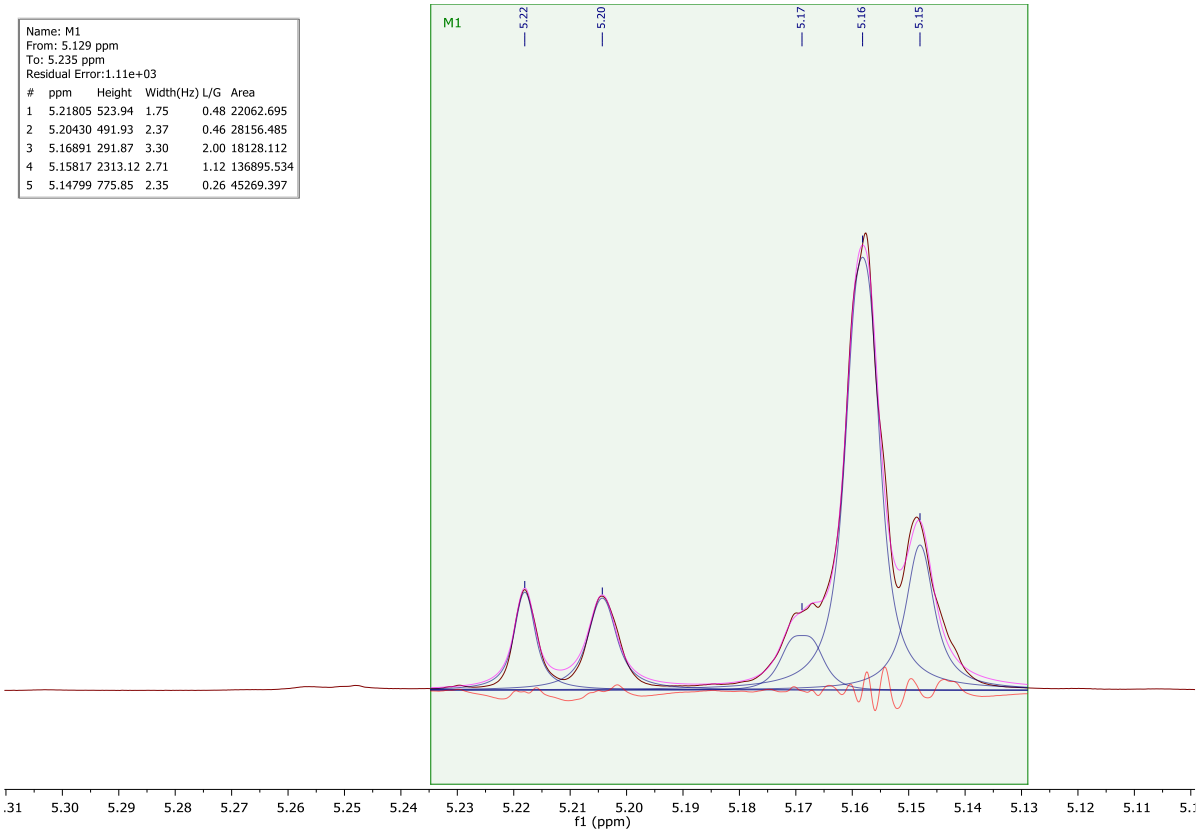


Figure C27. Methine region of the homonuclear decoupled $^{1}H\{^{1}H\}$ NMR spectrum for *rac*-LA ROP initiated by *cis*-**15** showing $P_m = 0.54$ (reaction conditions as per Table 7, Entry 1).

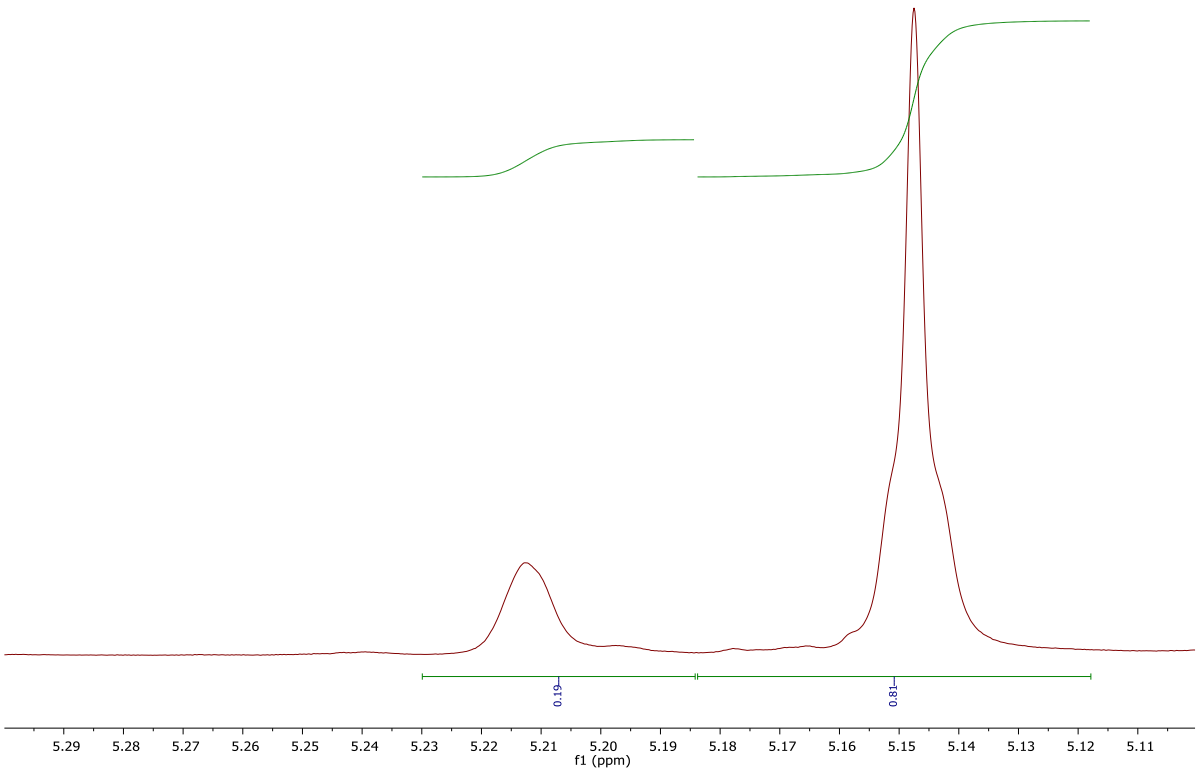


Figure C28. Methine region of the homonuclear decoupled $^{1}H\{^{1}H\}$ NMR spectrum for *meso*-LA ROP initiated by (*R,R*)-**15** showing $P_m = 0.38$ (reaction conditions as per Table 3, Entry 1).

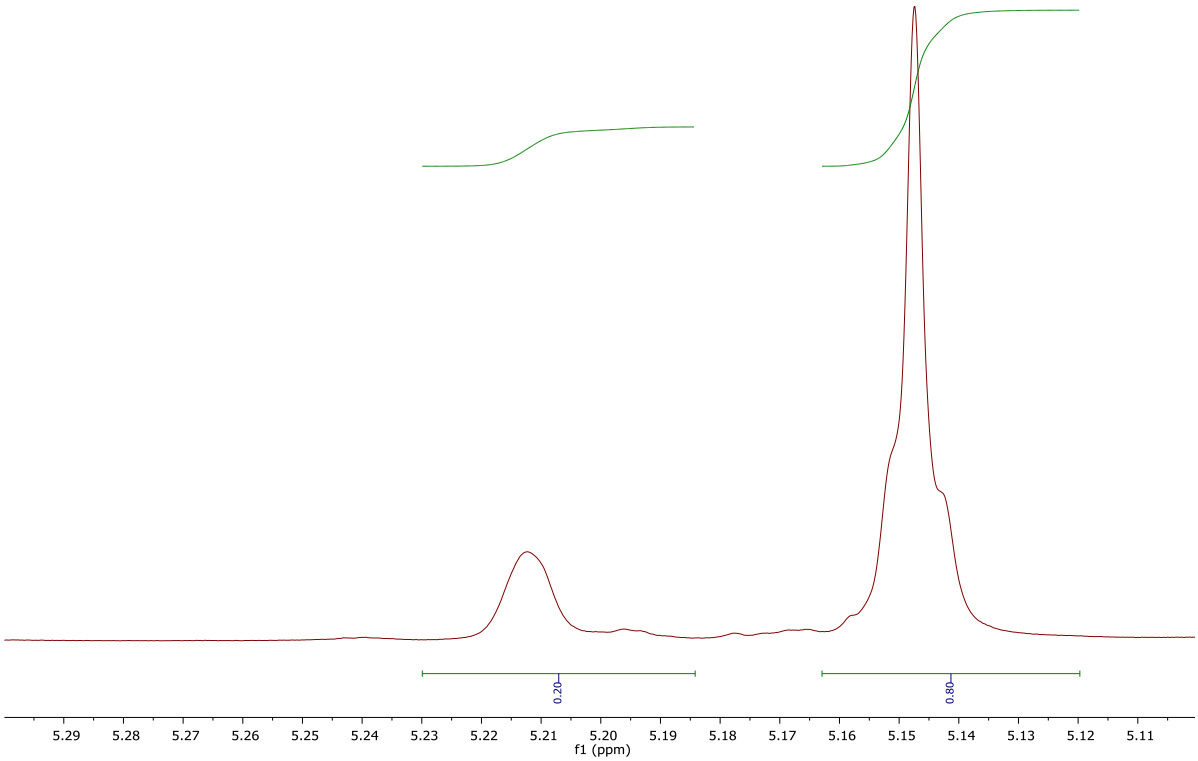


Figure C29. Methine region of the homonuclear decoupled $^{1}H\{^{1}H\}$ NMR spectrum for *meso*-LA ROP initiated by (*S,S*)-**15** showing $P_m = 0.40$ (reaction conditions as per Table 3, Entry 2).

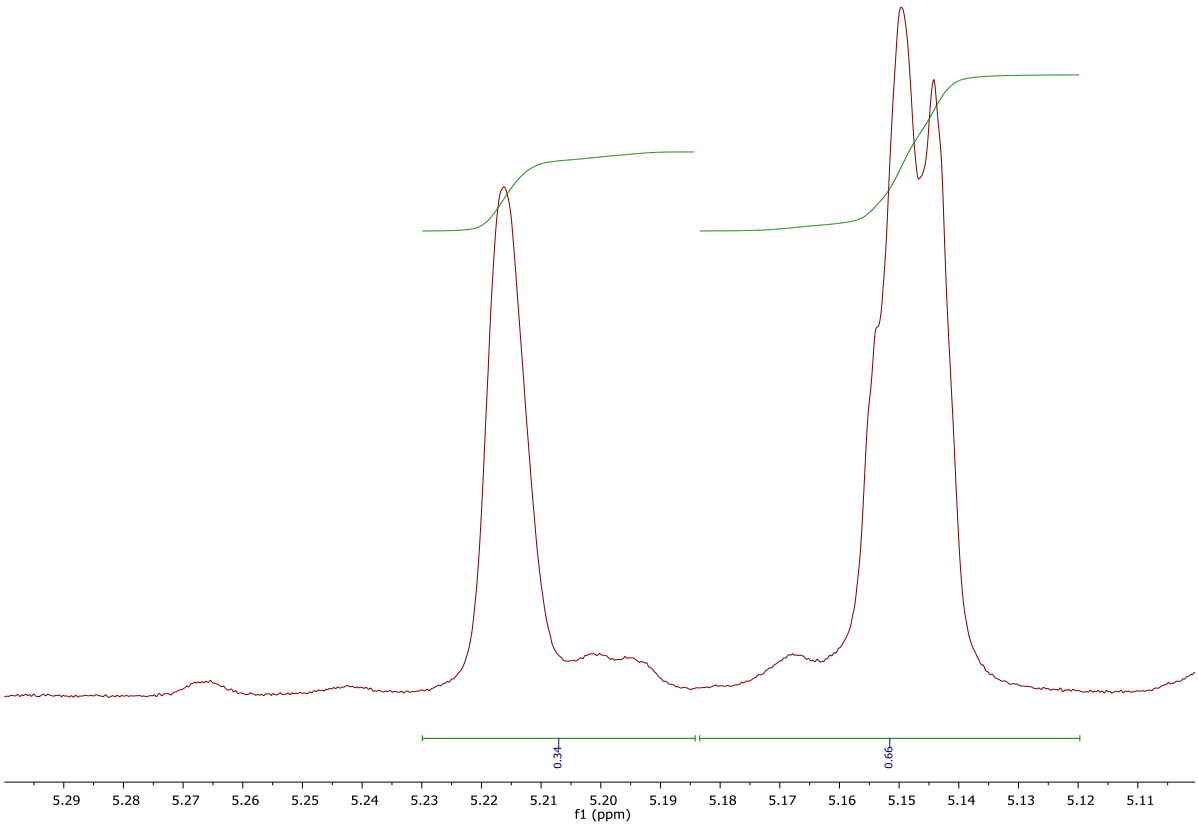


Figure C30. Methine region of the homonuclear decoupled $^{1}H\{^{1}H\}$ NMR spectrum for *meso*-LA ROP initiated by *rac*-**15** showing $P_m = 0.76$ (reaction conditions as per Table 3, Entry 3).

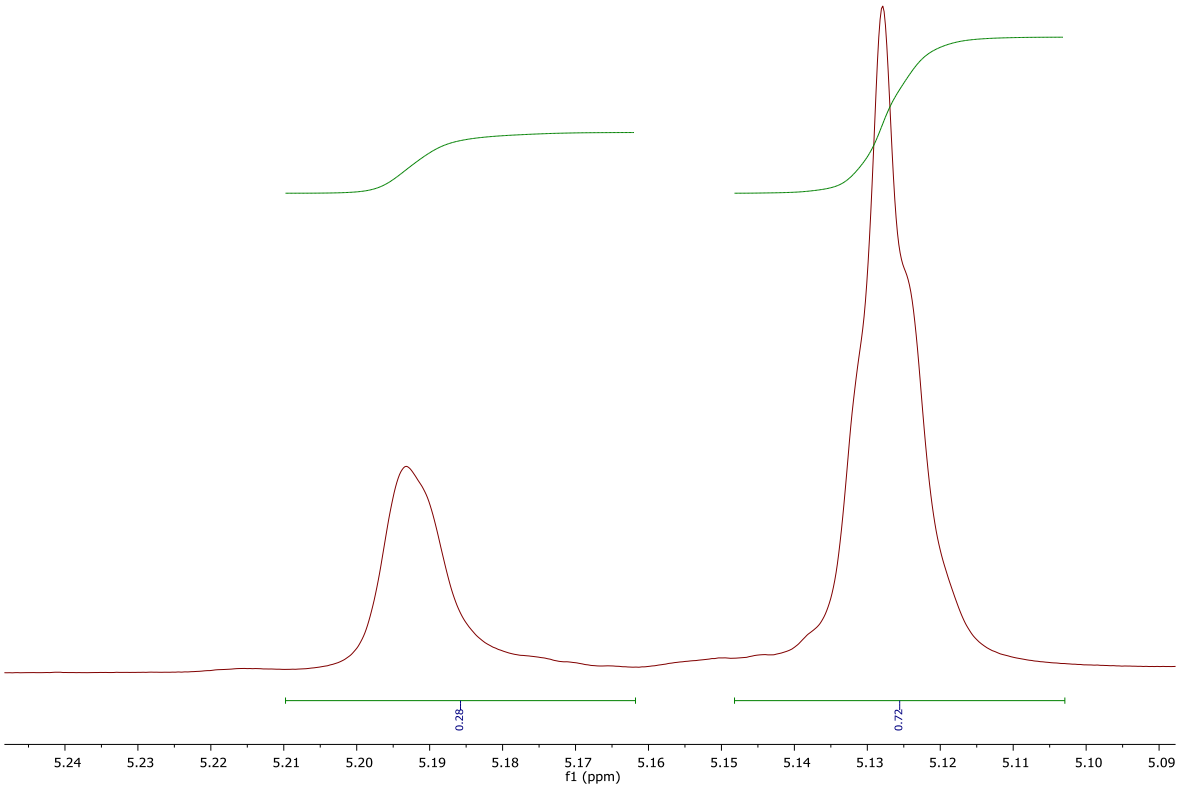


Figure C31. Methine region of the homonuclear decoupled $^{1}H\{^{1}H\}$ NMR spectrum for *meso*-LA ROP initiated by *cis*-**15** showing $P_m = 0.54$ (reaction conditions as per Table 7, Entry 3).

C.4 Chapter 4 Decoupled NMR Spectra

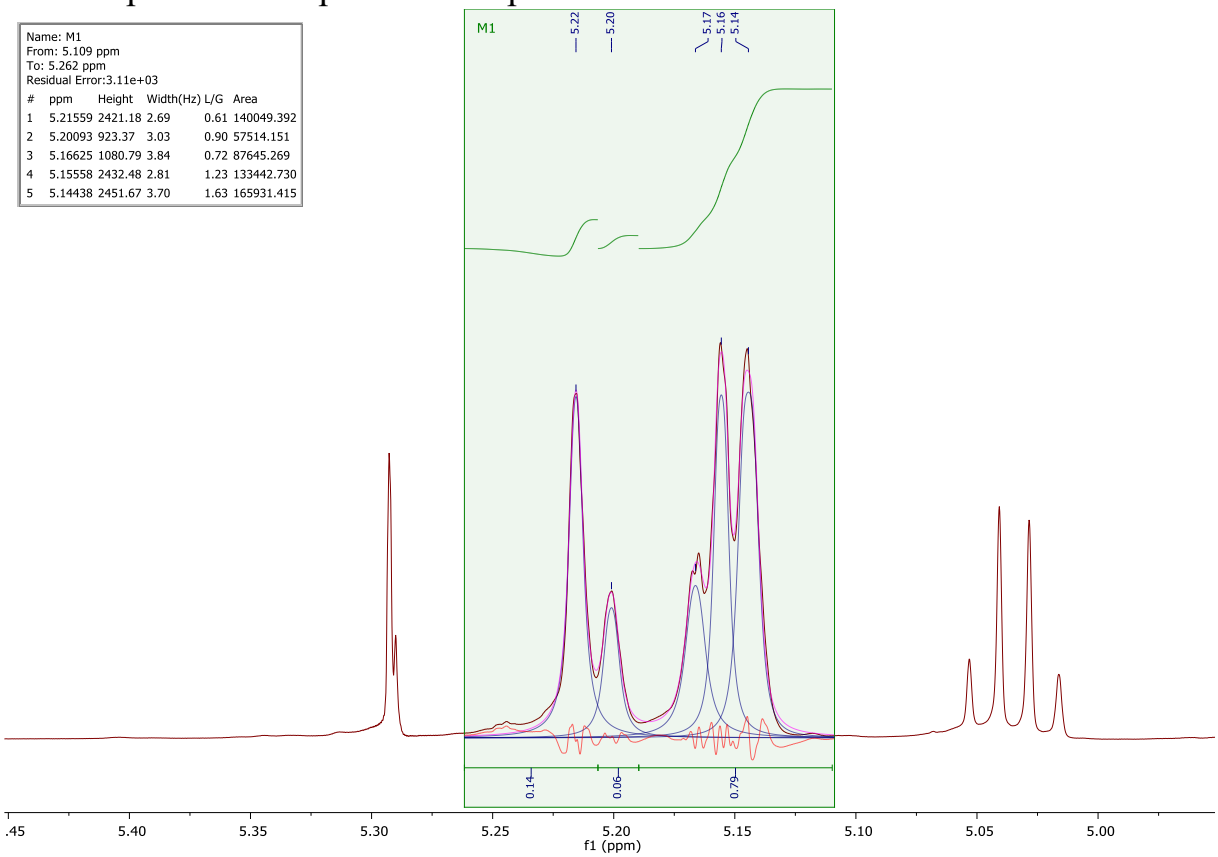


Figure C32. Methine region of the homonuclear decoupled $^{1}H\{^{1}H\}$ NMR spectrum for *rac*-LA ROP initiated by **18** showing $P_r = 0.70$ (reaction conditions as per Table 3, Entry 1).

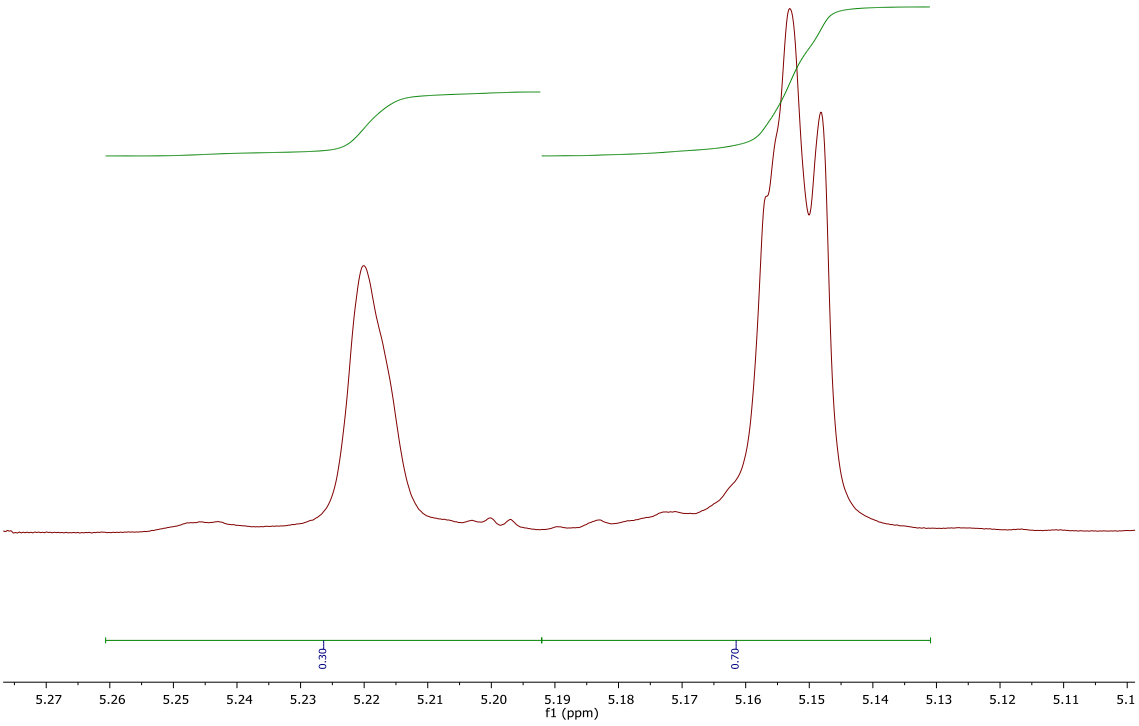


Figure C33. Methine region of the homonuclear decoupled $^{1}H\{^{1}H\}$ NMR spectrum for *meso*-LA ROP initiated by **18** showing $P_m = 0.60$ (reaction conditions as per Table 5, Entry 1).

1. Chamberlain, B. M.; Cheng, M.; Moore, D. R.; Ovitt, T. M.; Lobkovsky, E. B.; Coates, G. W., *J. Am. Chem. Soc.* **2001,** *123*, 3229-3238.
2. Orhan, B.; Tschan, M. J. L.; Wirotius, A.-L.; Dove, A. P.; Coulembier, O.; Taton, D., *ACS Macro Letters* **2018,** *7*, 1413-1419.
3. Aluthge, D. C.; Ahn, J. M.; Mehrkhodavandi, P., *Chem. Sci.* **2015,** *6*, 5284-5292.
4. García-Valle, F. M.; Tabernero, V.; Cuenca, T.; Mosquera, M. E. G.; Cano, J.; Milione, S., *Organometallics* **2018,** *37*, 837-840.

Appendix D: MALDI-ToF Mass Spectra

D.1 Chapter 2

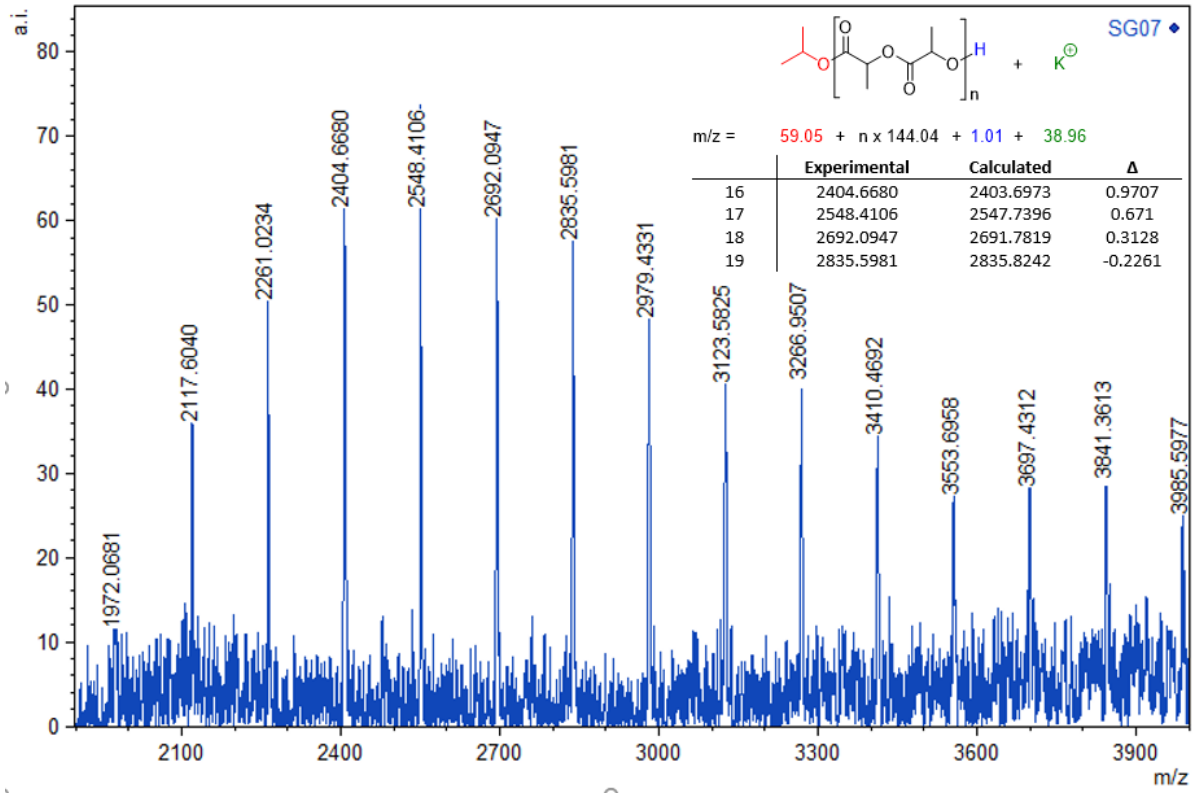


Figure D1: MALDI-ToF spectrum of PLA obtained using **2** (conditions as per Table 1).

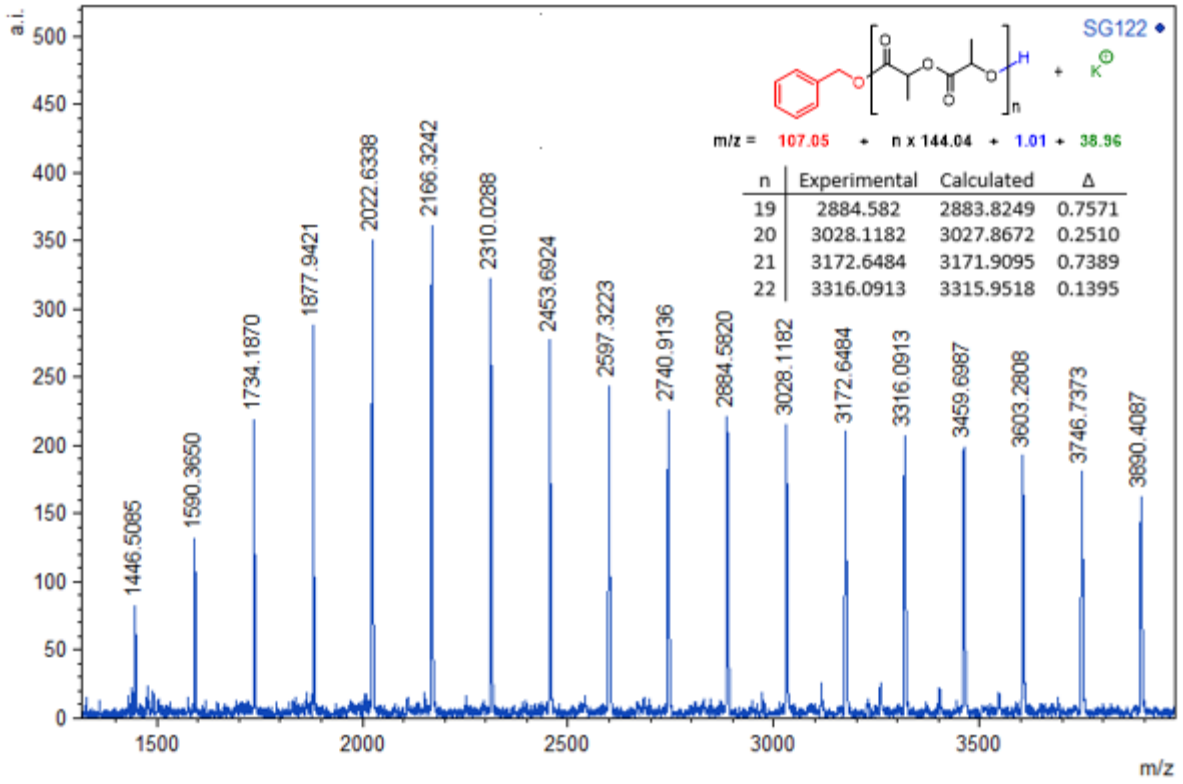


Figure D2. MALDI-ToF spectrum of PLA obtained using **8c** (conditions as per Table 1).

D.2 Chapter 3

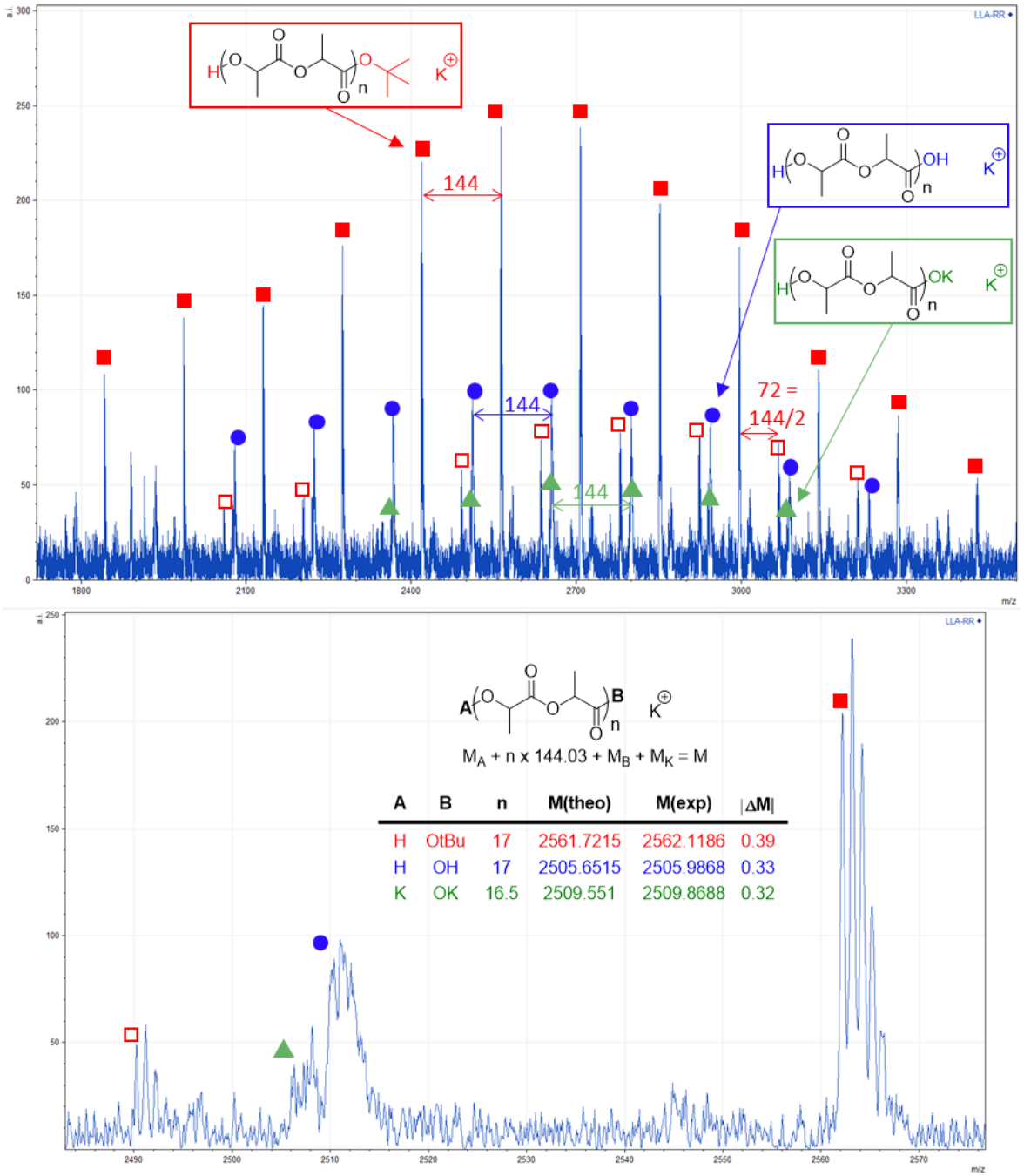


Figure D3: MALDI-ToF spectrum of a PLLA product initiated by (*R,R*)-**15** (conditions as per Table 2).

4 series of peak spaced by 144 a.u. were obtained corresponding to:

- Polymer chains initiated by O^{t}Bu (■) + corresponding transesterification (□)
- Hydrolysis of the *tert*-butyl ester end-groups leading to acid-terminated polymer chains (▲, ●), likely due to the use of KTFA during sample preparation (TFA can be used to deprotect *tert*-butyl esters)[11]

D.3 Chapter 4

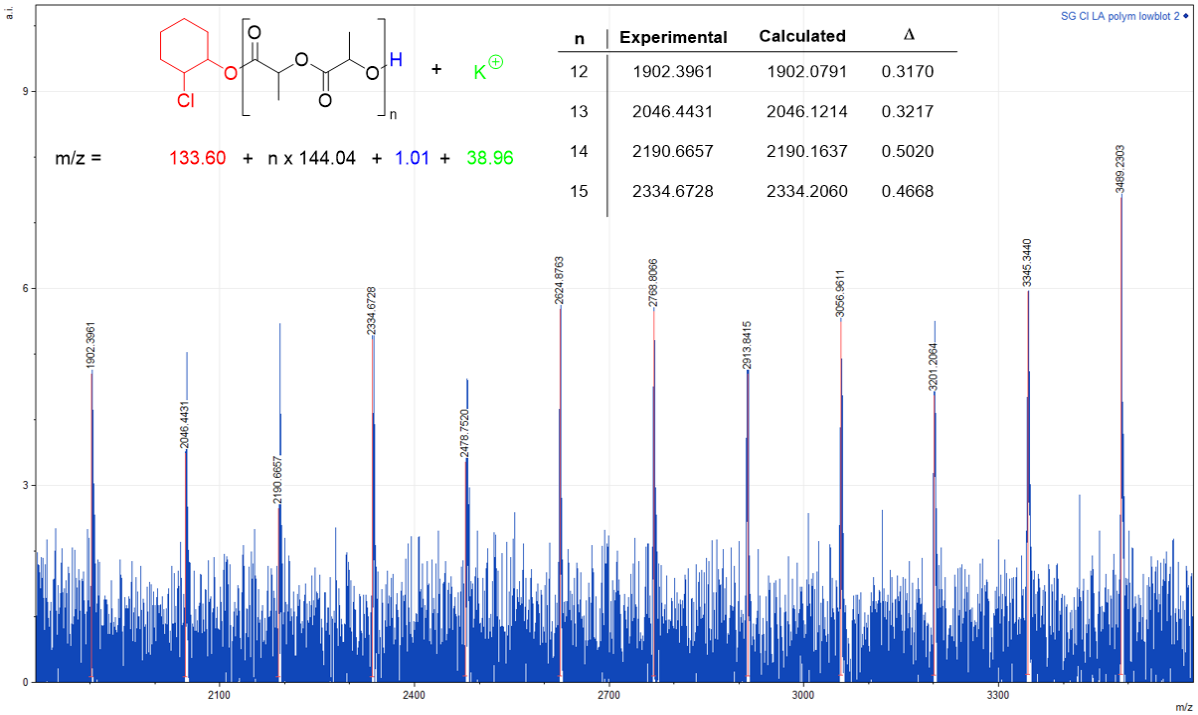


Figure D4. MALDI-ToF spectrum of a PLA product initiated by **18** showing the 2-chlorocyclohexano initiating group that is generated during the pre-activation period of **18**.

Appendix E: DFT Calculations

E.1 General Considerations

Computational details:

DFT calculations were performed using Gaussian 09 (revision D01). Unless stated otherwise, calculations used the ωB97xD density functional (which includes a second-generation dispersion and long-range corrections) with a 6-31G(d,p) basis set. Self-consistent reaction cavity continuum solvation model was used with THF as the solvent [scrf=(cpcm, solvent=THF)]. All calculations were performed with an ultrafine grid (integral=grid=ultrafine) and without restriction on symmetry (No Symm) at 298.15K (default). All transition states were characterized by normal coordinate analysis revealing precisely one imaginary mode corresponding to the intended reaction.

Non-covalent interactions (NCI): NCI surfaces were created using a script developed by Prof. Henry Rzepa available here http://doi.org/10.14469/hpc/3660.[1, 2] The following parameters were used to create the NCI surface:

```
isosurface parameters [0.5 1 0 0.05 0.95 1.00] NCI density.cube colorscheme
"bgyor";color isosurface range 0.04 -0.04.
```

Topograhic steric Map:[3] The topographic steric maps (TSM) were created using the SambVCa 2 tool. Atomic radii were selected to be Bondi radii scaled by 1.17, a mesh spacing of 0.10 was chosen and the hydrogen atoms were included in the calculations. All coordination spheres were centred on the Al atom with a radius of 5.0 Å.

Framework Distortion Energy (FDE):[4, 5] From the optimized TS structures, the reacting species (i.e lactide, alkoxide moiety) were removed and a single-point energy calculation was performed on the resulting cationic aluminium species. Similarly, the methoxide was removed from the optimized structure of the initial catalyst **I(c)** and a single-point energy calculation was carried out. The difference in energy determines the FDE.

Gaussian 09, Revision D.01, M. J. Frisch, G. W. Trucks, H. B. Schlegel, G. E. Scuseria, M. A. Robb, J. R. Cheeseman, G. Scalmani, V. Barone, G. A. Petersson, H. Nakatsuji, X. Li, M. Caricato, A. Marenich, J. Bloino, B. G. Janesko, R. Gomperts, B. Mennucci, H. P. Hratchian, J. V. Ortiz, A. F. Izmaylov, J. L. Sonnenberg, D. Williams-Young, F. Ding, F. Lipparini, F. Egidi, J. Goings, B. Peng, A. Petrone, T. Henderson, D. Ranasinghe, V. G. Zakrzewski, J. Gao, N. Rega, G. Zheng, W. Liang, M. Hada, M. Ehara, K. Toyota, R. Fukuda, J. Hasegawa, M. Ishida, T. Nakajima, Y. Honda, O. Kitao, H. Nakai, T. Vreven, K. Throssell, J. A. Montgomery, Jr., J. E. Peralta, F. Ogliaro, M. Bearpark, J. J. Heyd, E. Brothers, K. N. Kudin, V. N. Staroverov, T. Keith, R. Kobayashi, J. Normand, K. Raghavachari, A. Rendell, J. C. Burant, S. S. Iyengar, J. Tomasi, M. Cossi, J. M. Millam, M. Klene, C. Adamo, R. Cammi, J. W. Ochterski, R. L. Martin, K. Morokuma, O. Farkas, J. B. Foresman, and D. J. Fox, Gaussian, Inc., Wallingford CT, 2016.

E.2 Chapter 2

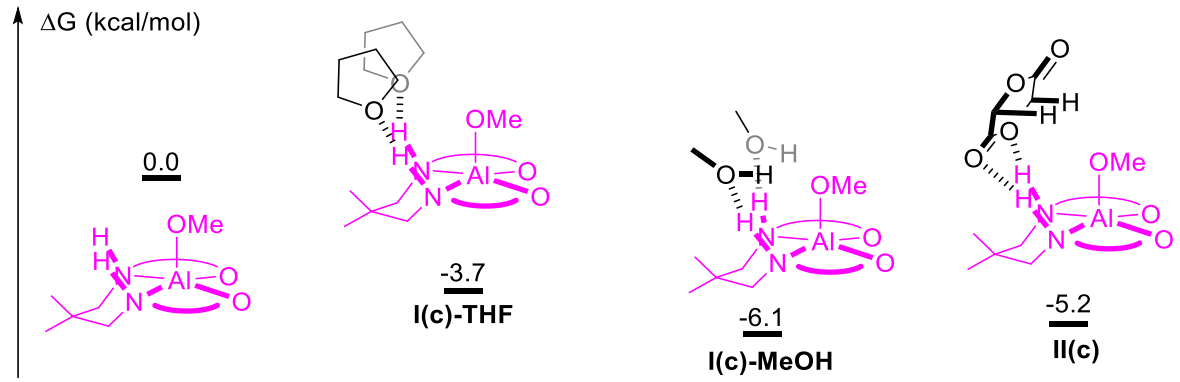


Figure E1: Relative Gibbs free energies ΔG_{298} of different Lewis base adducts of **I(c)**.

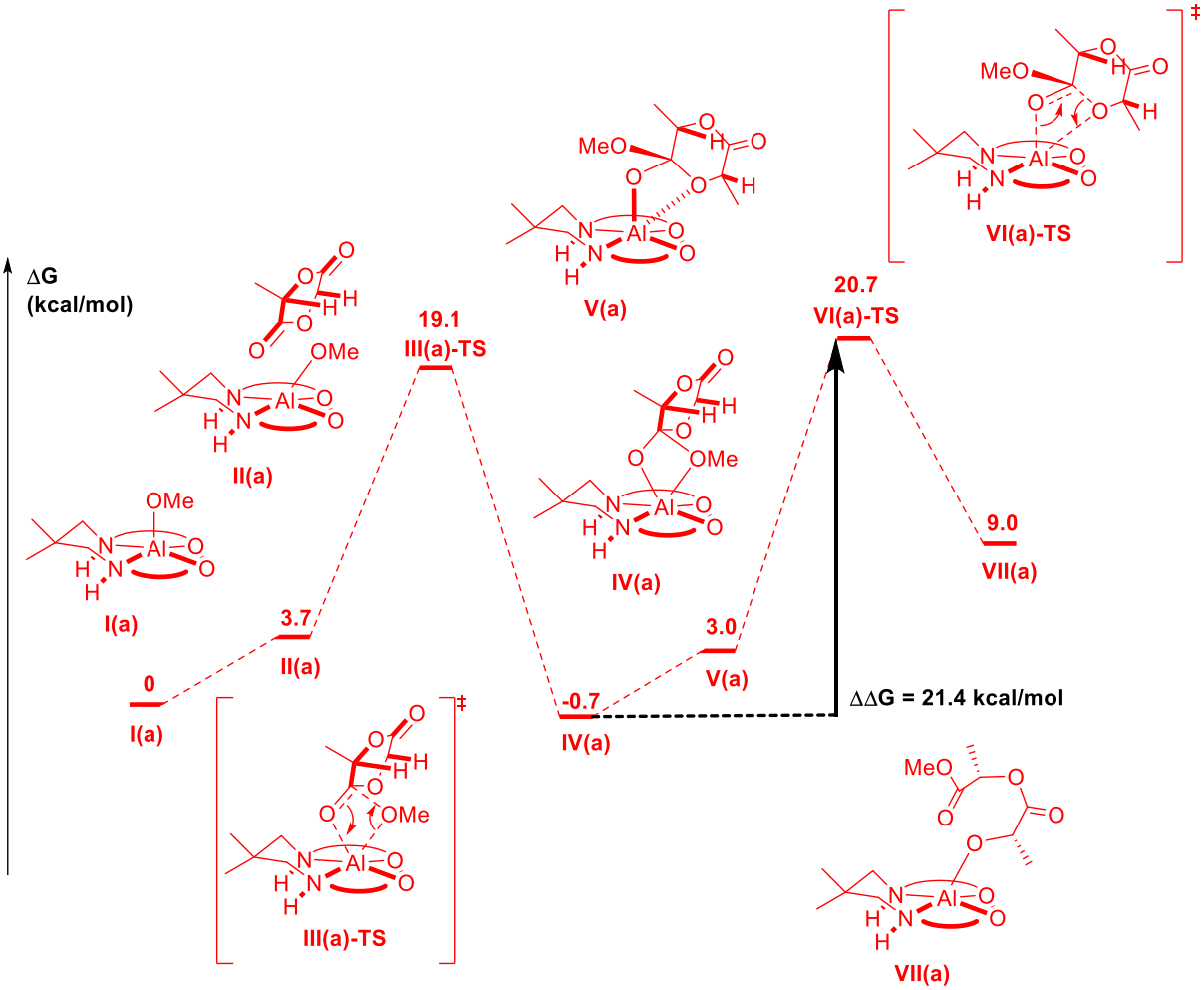


Figure E2. PES showing first insertion of a LA monomer into complex **2**-I(a). DFT protocol: # ωB97xD/6-31g(d,p) scrf=(cpcm, solvent = THF) nosymm integral=grid=ultrafine.

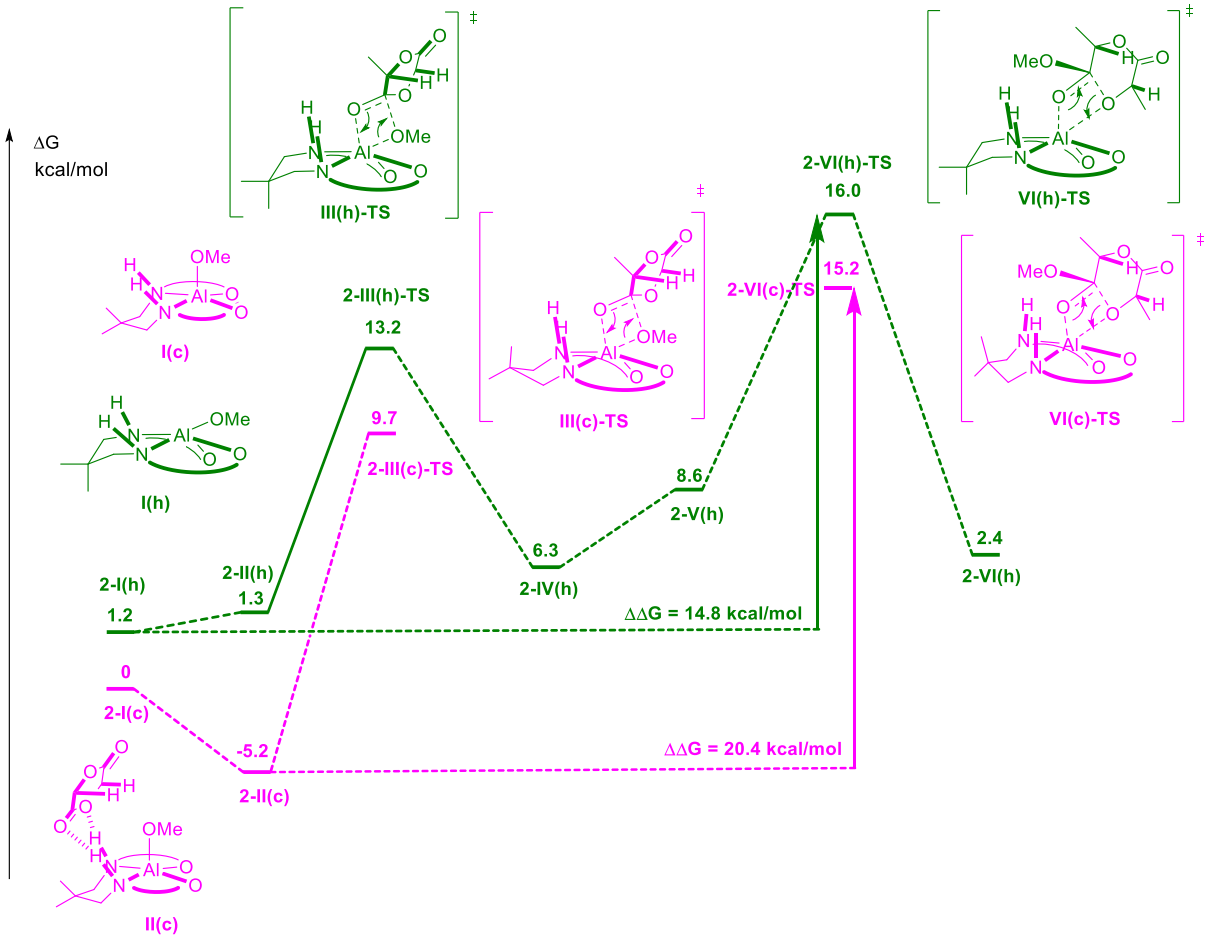


Figure E3. PES showing first insertion of a LA monomer into complex **2**-I(c) and **2**-I(h). DFT protocol: # ωB97xD/6-31g(d,p) scrf=(cpcm, solvent = THF) nosymm integral=grid=ultrafine.

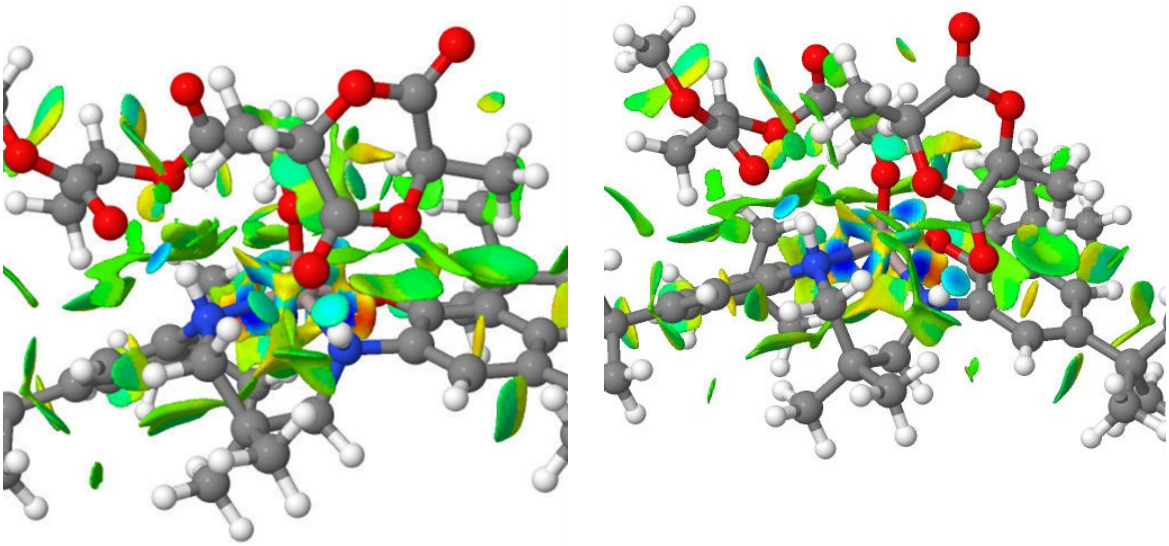


Figure E4: NCI surfaces of **IX(D)** [left] and **IX(L)** [right] showing H bonds (**bright blue spot**) between O atoms of the lactide and the growing polymer chain with the NH moieties of the ligands.

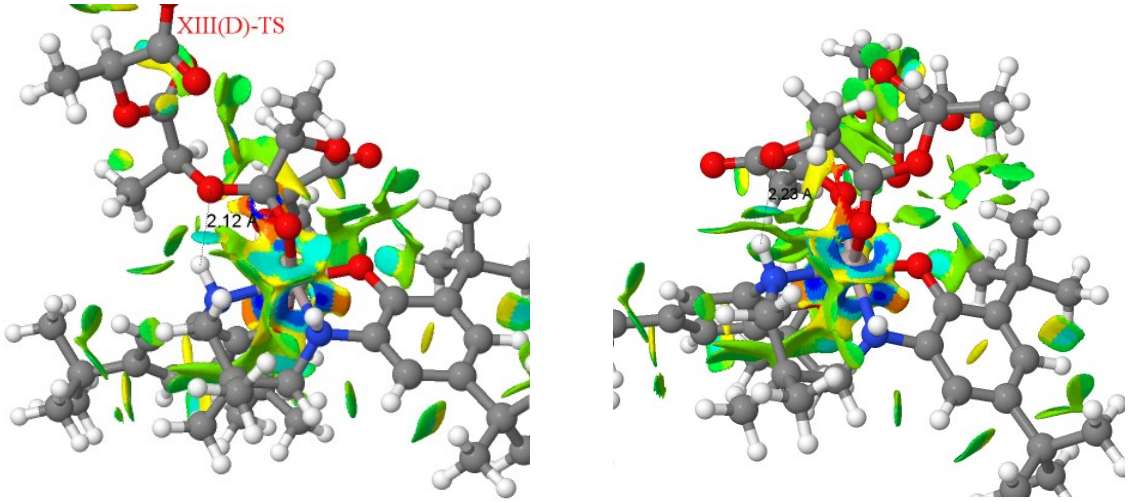


Figure E5: NCI surfaces of **XIII(D)-TS** [left] and **XIII(L)-TS** [right] showing H bonds (**bright blue spot**) between O atoms of the lactide and the growing polymer chain with the NH moieties of the ligands.

E.3 Chapter 3

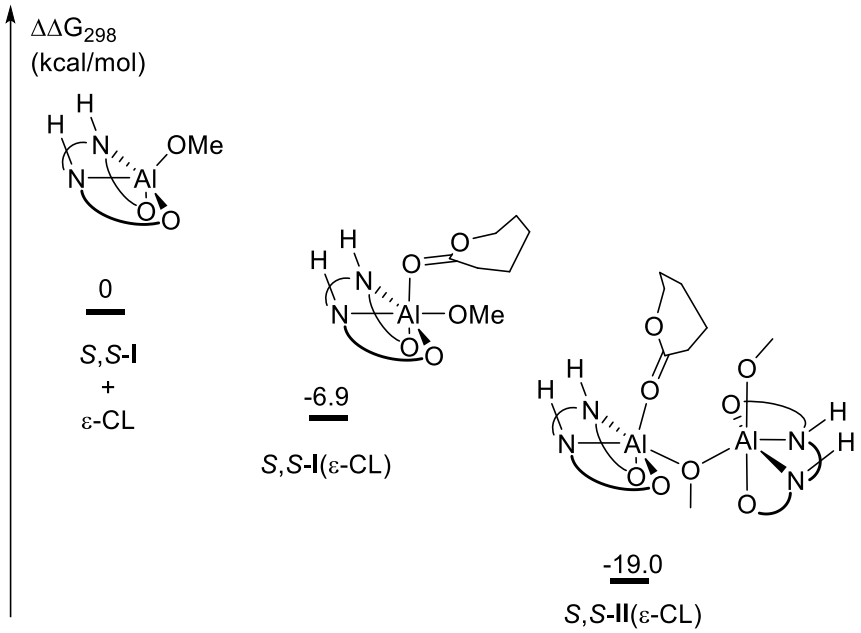


Figure E6: Relative Gibbs free energy for mononuclear and dinuclear Al complexes binding ε-CL.

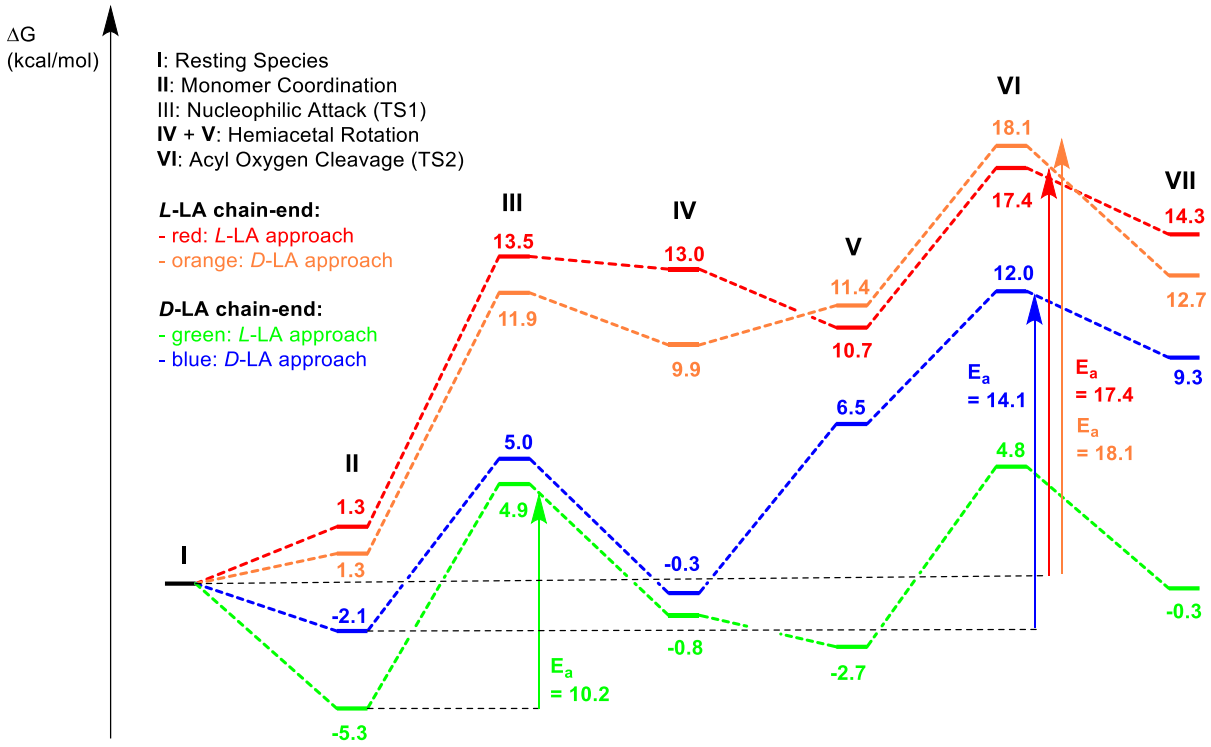


Figure E7. PES showing second insertion of a LA monomer into after an *L*-LA insertion (red and orange) and *D*-LA insertion (green and blue). DFT protocol: # ωB97xD/6-31g(d,p) scrf=(cpcm, solvent = THF) nosymm integral=grid=ultrafine.

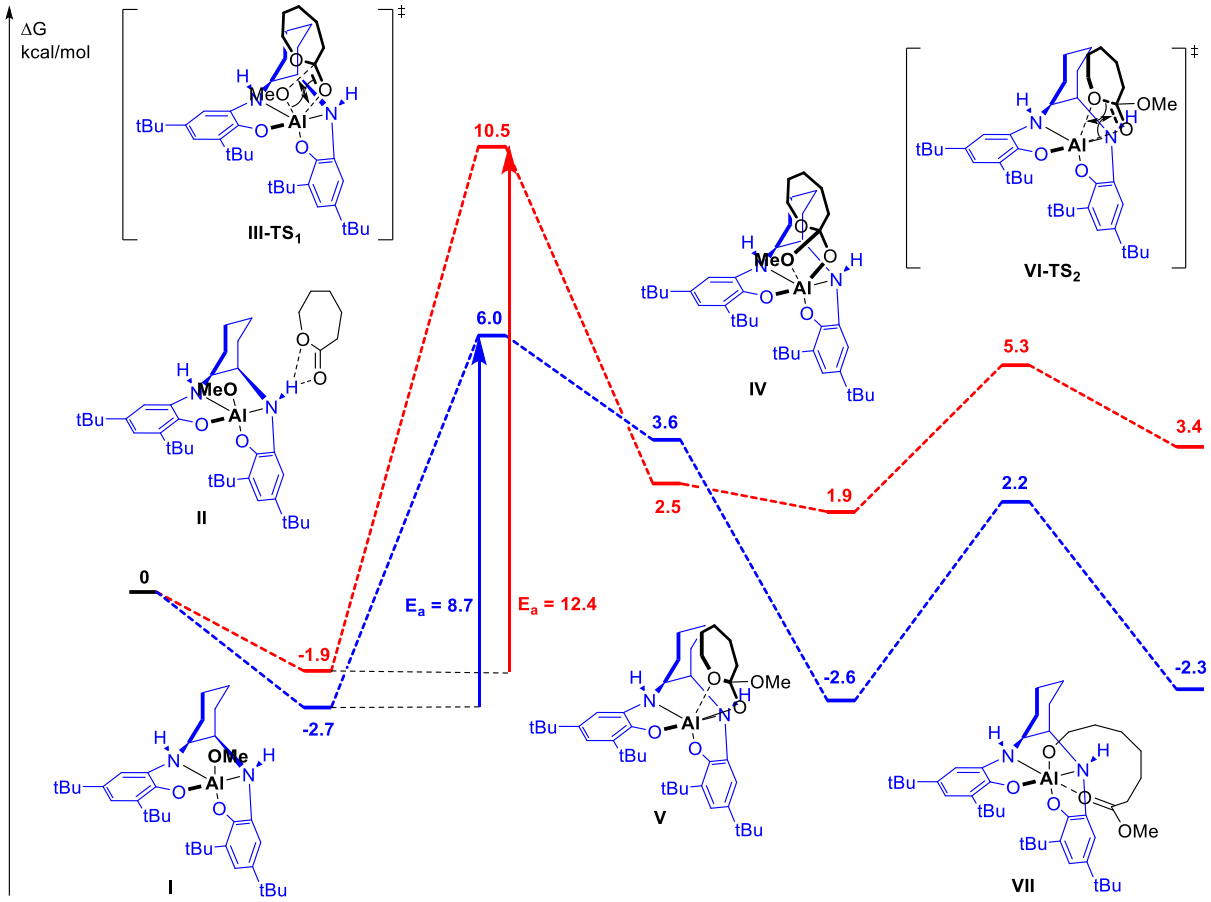


Figure E8. PES showing first insertion of a ε-CL monomer into *cis*-**15** (**I**). DFT protocol: # ωB97xD/6-31g(d,p) scrf=(cpcm, solvent = THF) nosymm integral=grid=ultrafine.

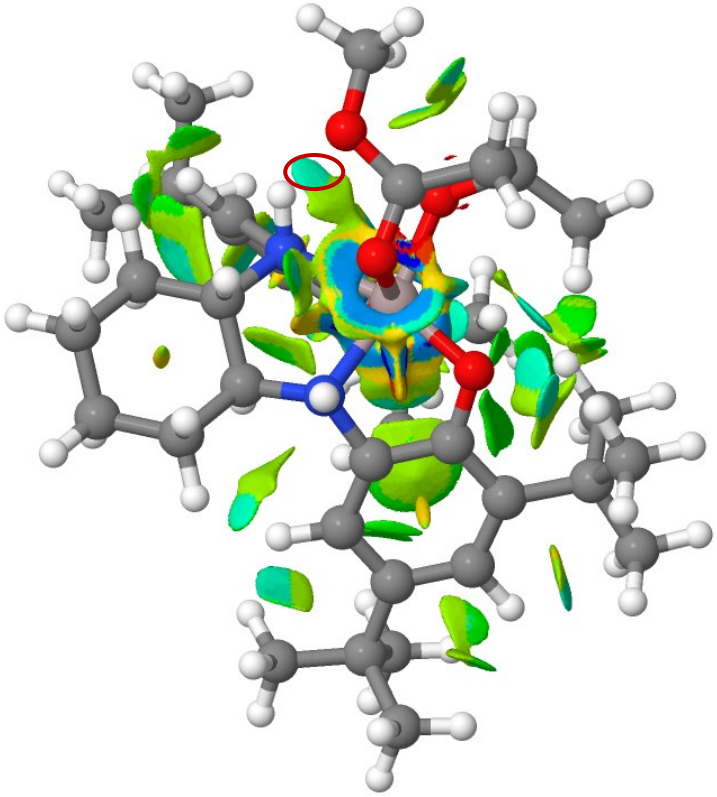


Figure E9. NCI surface of acyl oxygen cleavage TS of β-BL with (*S,S*)-**15** showing a hydrogen bond between the hemiacetal and NH moiety as a blue disc.

1. Contreras-García, J.; Johnson, E. R.; Keinan, S.; Chaudret, R.; Piquemal, J.-P.; Beratan, D. N.; Yang, W., *J. Chem. Theo. Comput.* **2011,** *7*, 625-632.
2. Johnson, E. R.; Keinan, S.; Mori-Sánchez, P.; Contreras-García, J.; Cohen, A. J.; Yang, W., *J. Am. Chem. Soc.* **2010,** *132*, 6498-6506.
3. Falivene, L.; Credendino, R.; Poater, A.; Petta, A.; Serra, L.; Oliva, R.; Scarano, V.; Cavallo, L., *Organometallics* **2016,** *35*, 2286-2293.
4. Marlier, E. E.; Macaranas, J. A.; Marell, D. J.; Dunbar, C. R.; Johnson, M. A.; DePorre, Y.; Miranda, M. O.; Neisen, B. D.; Cramer, C. J.; Hillmyer, M. A.; Tolman, W. B., *ACS Catal.* **2016,** *6*, 1215-1224.
5. Macaranas, J. A.; Luke, A. M.; Mandal, M.; Neisen, B. D.; Marell, D. J.; Cramer, C. J.; Tolman, W. B., *Inorg. Chem.* **2018,** *57*, 3451-3457.

Appendix F: Crystallography Data

Crystal data for 1: $C_{35}H_{57}AlN_2O_2 \cdot 2(C_4H_8O)$, M = 709.01, monoclinic, $P2_1/n$ (no. 14), a = 11.02907(12), b = 21.7628(3), c = 17.7351(2) Å, β = 91.0574(11)°, V = 4256.12(9) Å^3, Z = 4, D_c = 1.106 g cm^{-3}, μ(Cu-Kα) = 0.723 mm^{-1}, T = 173 K, colourless blocky needles, Agilent Xcalibur PX Ultra A diffractometer; 8215 independent measured reflections (R_{int} = 0.0272), F^2 refinement,[X1,X2] R_1(obs) = 0.0486, wR_2(all) = 0.1325, 6615 independent observed absorption-corrected reflections [$|F_o| > 4\sigma(|F_o|)$, completeness to θ_{full}(67.7°) = 98.5%], 489 parameters. **CCDC 1827520**.
Crystal not grown by the author.

The C22-based *t*-butyl group in the structure of **1** was found to be disordered. Two orientations were identified of *ca*. 71 and 29% occupancy, their geometries were optimised, the thermal parameters of adjacent atoms were restrained to be similar, and only the non-hydrogen atoms of the major occupancy orientation were refined anisotropically (those of the minor occupancy orientation were refined isotropically). The N–H hydrogen atoms on N7 and N11 were both located from ΔF maps and refined freely subject to an N–H distance constraint of 0.90 Å. These N–H groups are both involved in intermolecular N–H···O hydrogen bonds to the two included tetrahydrofuran solvent molecules with N···O and H···O distances (Å) and N–H···O angles (°) of 3.110(2), 2.231(4) and 165.6(13) for the N7···O40 contact, and 3.061(2), 2.181(4) and 165.4(12) for the N11···O50 contact.

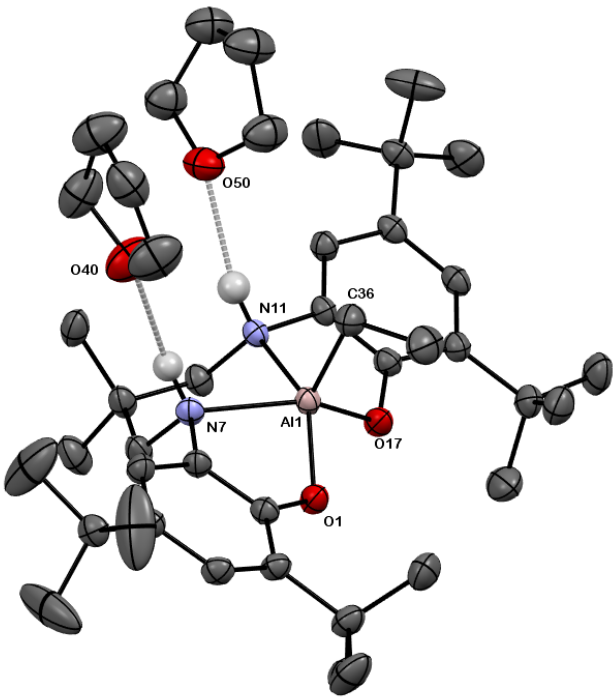


Figure F1: The crystal structure of **1** (ellipsoid plot, 50% probability) showing the N–H···O hydrogen bonds to the included tetrahydrofuran solvent molecules. The hydrogen bonding geometries [N···O and H···O (Å), and N–H···O (°)] are 3.110(2), 2.231(4) and 165.6(13) for the N7···O40 contact, and 3.061(2), 2.181(4) and 165.4(12) for the N11···O50 contact.

Crystal data for 3: $C_{37}H_{61}AlN_2O_2$, M = 592.85, orthorhombic, $Pna2_1$ (no. 33), a = 29.9888(18), b = 13.4133(8), c = 9.2213(5) Å, V = 3709.2(4) Å^3, Z = 4, D_c = 1.062 g cm^{-3}, μ(Mo-Kα) = 0.086 mm^{-1}, T = 173 K, colourless blocks, Agilent Xcalibur 3 E diffractometer; 4898 independent measured reflections (R_{int} = 0.0300), F^2 refinement,[X1,X2] R_1(obs) = 0.0523, wR_2(all) = 0.1367, 4120 independent observed absorption-corrected reflections [$|F_o| > 4\sigma(|F_o|)$, completeness to θ_{full}(25.2°) = 98.7%], 445 parameters. The structure was refined as a two component inversion twin [Flack parameter x = +0.3(3)]. **CCDC 1827521**.
Crystal not grown by the author.

The C22- and C30-based *t*-butyl groups in the structure of **3** were both found to be disordered, and in each case two orientations were identified, of *ca*. 70:30 and 71:29% occupancy respectively. For each pair of orientations the geometries were optimised, the thermal parameters of adjacent atoms were restrained to be similar, and only the non-hydrogen atoms of the major occupancy orientations were refined anisotropically (those of the minor occupancy orientations were refined isotropically).

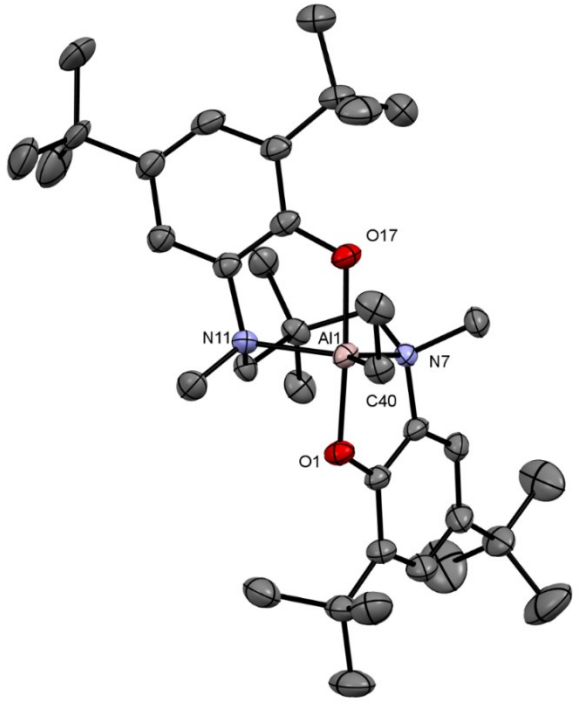


Figure F2: The crystal structure of **3** (ellipsoid plot, 50% probability).

Crystal data for 6: $C_{60}H_{90}Al_2N_4O_4$, M = 985.31, triclinic, *P-1* (no. 2), a = 10.3044(5), b = 10.3044(5), c = 14.5467(9) Å, α = 80.997(4), β = 72.376(5)°, γ = 83.181(4), V = 1478.84(14) Å^3, Z = 1, D_c = 1.106 g cm^{-3}, μ(Cu-Kα) = 0.798 mm^{-1}, T = 173 K, colourless tablets, Agilent Xcalibur PX Ultra A diffractometer; 5645 independent measured reflections (R_{int} = 0.0234), F^2 refinement,[X1,X2] R_1(obs) = 0.0416, wR_2(all) = 0.1142, 4759 independent observed absorption-corrected reflections [$|F_o| > 4\sigma(|F_o|)$, completeness to θ_{full}(67.7°) = 98.4%], 332 parameters. **CCDC 1836017**.
Crystal not grown by the author.

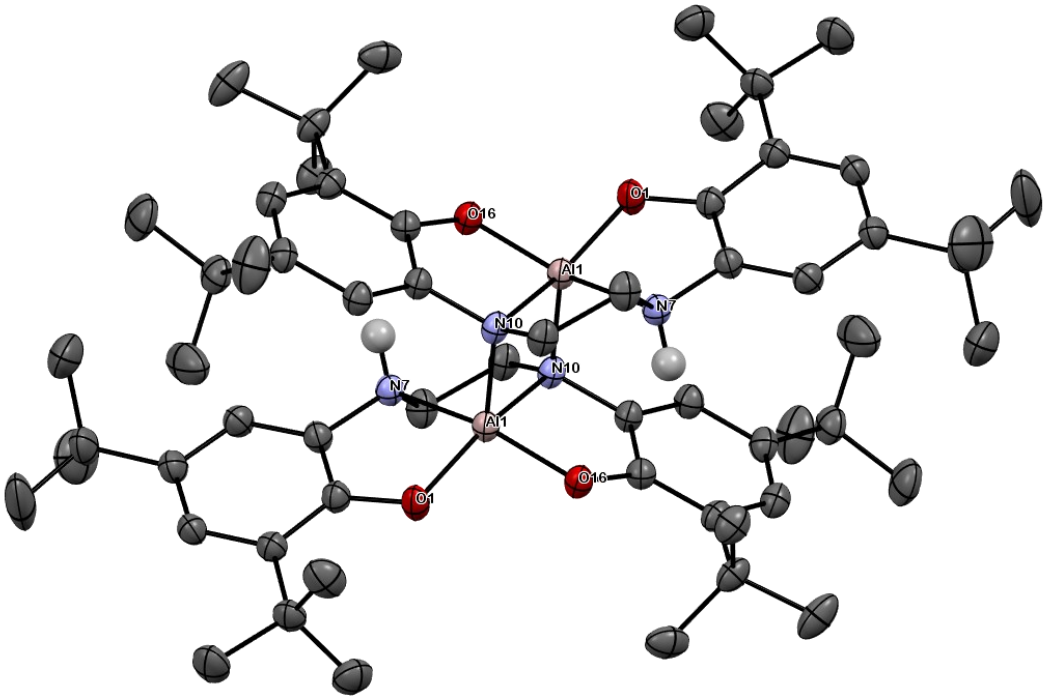


Figure F3. Crystal structure of **7** (ellipsoid plot, 50% probability).

Crystal data for 8c: $C_{74}H_{106}Al_2N_4O_6$, M = 1514.01, monoclinic, $P2_1/c$ (no. 14), a = 15.4213(4), b = 15.4213(5), c = 22.2668(5) Å, β = 93.350(2)°, V = 4603.5(2) Å^3, Z = 2, D_c = 1.092 g cm^{-3}, μ(Cu-Kα) = 0.084 mm^{-1}, T = 173 K, colourless blocks, Agilent Xcalibur 3 E diffractometer; 9164 independent measured reflections (R_{int} = 0.0225), F^2 refinement,[X1,X2] R_1(obs) = 0.0480, wR_2(all) = 0.1114, 6643 independent observed absorption-corrected reflections [$|F_o| > 4\sigma(|F_o|)$, completeness to θ_{full}(25.2°) = 98.7%], 517 parameters. **CCDC 1836019**.

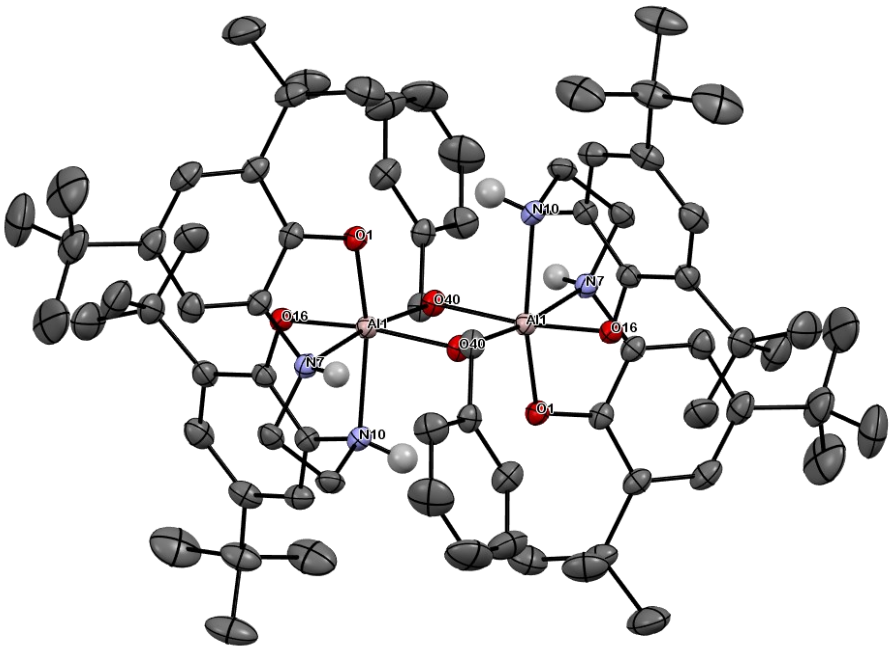


Figure F4. Crystal structure of **8c** (ellipsoid plot, 50% probability).

Crystal data for 11: $C_{68}H_{110}Al_2N_4O_4$, M = 1101.55, monoclinic, $P2_1/c$ (no. 14), a = 29.5098(6), b = 11.5958(2), c = 19.4955(5) Å, β = 95.297(2)°, V = 6642.7(3) Å^3, Z = 4, D_c = 1.101 g cm^{-3}, μ(Cu-Kα) = 0.084 mm^{-1}, T = 173 K, colourless blocks, Agilent Xcalibur 3 E diffractometer; 13303 independent measured reflections (R_{int} = 0.0220), F^2 refinement,[X1,X2] R_1(obs) = 0.0561, wR_2(all) = 0.1389, 10191 independent observed absorption-corrected reflections, 733 parameters.

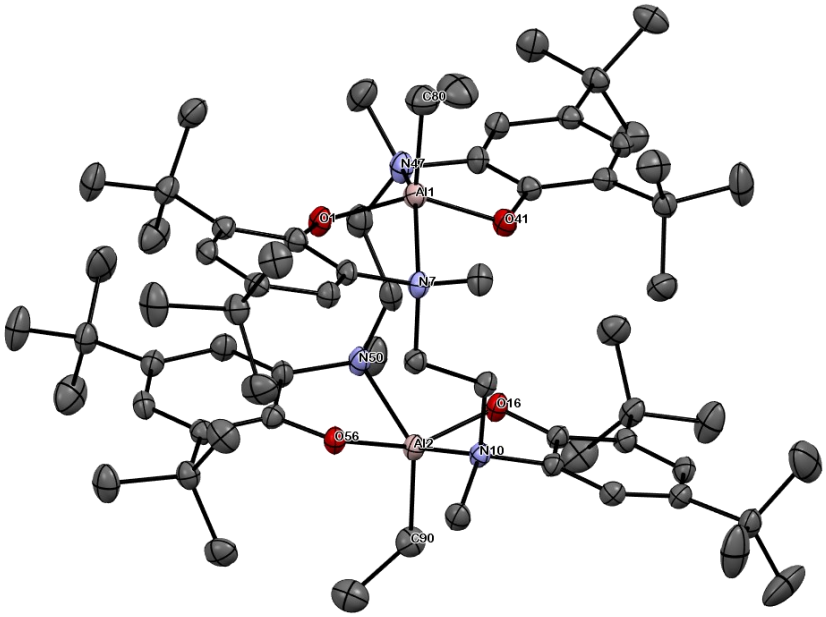


Figure F5. Crystal structure of **11** (ellipsoid plot, 50% probability).

Crystal data for 2-Cl: $C_{33}H_{52}AlClN_2O_2 \cdot C_{36}H_{30}NP_2 \cdot Cl$, M = 1301.41, triclinic, P-1, a = 15.3997(4), b = 15.4612(4), c = 16.8442(5) Å, α = 95.768(2), β = 107.098(2) γ = 102.551(2)°, V = 3683.15(18) Å^3, Z = 2, D_c = 1.173 g cm^{-3}, μ(Cu-Kα) = 0.084 mm^{-1}, T = 173 K, colourless blocky needles, Agilent Xcalibur 3 E diffractometer; 14518 independent measured reflections (R_{int} = 0.0191), F^2 refinement,[X1,X2] R_1(obs) = 0.0568, wR_2(all) = 0.1631, 10374 independent observed absorption-corrected reflections, 858 parameters.
Crystal not grown by the author.

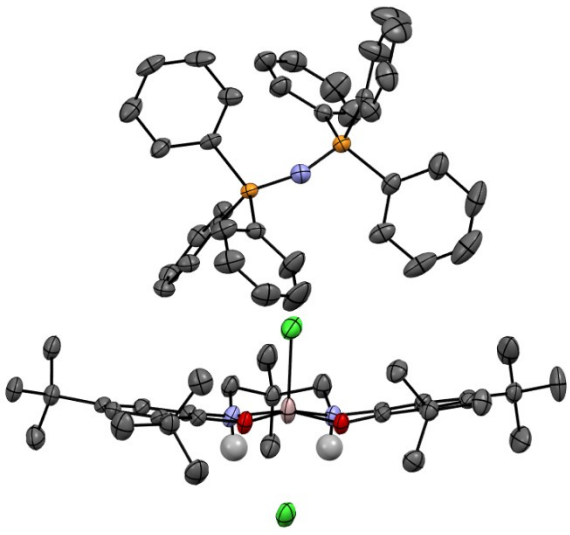


Figure F6. Crystal structure of **2-Cl** (ellipsoid plot, 50% probability).

Crystal data for *rac*-13: $C_{68}H_{102}Al_2N_4O_4$, M = 1178.4, triclinic, *P-1*, a = 10.5780(4), b = 12.2216(7), c = 13.9230(8) Å, α = 75.891(5), β = 71.532(4)°, γ = 87.632(4)° V = 1654.50(16) Å^3, Z = 1, D_c = 1.183 g cm^{-3}, μ(Cu-Kα) = 0.174 mm^{-1}, T = 173 K, colourless blocks, Agilent Xcalibur 3 E diffractometer; 6519 independent measured reflections (R_{int} = 0.0180), F^2 refinement,[1, 2] R_1(obs) = 0.0484, wR_2(all) = 0.1217, 5071 independent observed absorption-corrected reflections [$|F_o| > 4\sigma(|F_o|)$, completeness to θ_{full}(67.7°) = 98.2%], 395 parameters.

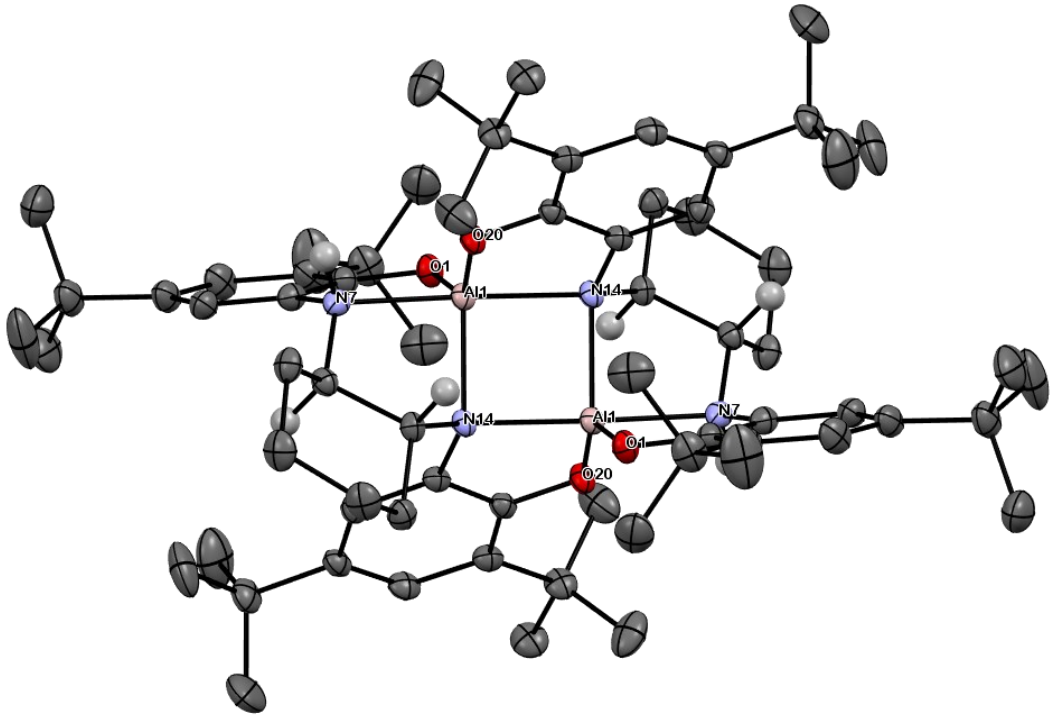


Figure F7. The crystal structure of *rac*-**13** (ellipsoid plot, 50% probability).

Crystal data for *rac*-14: $C_{82}H_{118}Al_2N_4O_6{\cdot}1.25(CH_2Cl_2)$, M = 1415.91, monoclinic, $P2_1/n$ (no. 14), a = 14.7009(5), b = 19.8009(6), c = 15.5738(6) Å, β = 112.532(4)°, V = 4187.3(3) Å^3, Z = 2 [C_i symmetry], D_c = 1.123 g cm^{-3}, μ(Mo-Kα) = 0.165 mm^{-1}, T = 173 K, colourless blocks, Agilent Xcalibur 3 E diffractometer; 8327 independent measured reflections (R_{int} = 0.0239), F^2 refinement,[1, 2] R_1(obs) = 0.0864, wR_2(all) = 0.2563, 6052 independent observed absorption-corrected reflections [$|F_o| > 4\sigma(|F_o|)$, completeness to θ_{full}(25.2°) = 98.6%], 487 parameters. **CCDC 1972760**.

The structure of *rac*-**14** was found to sit across a centre of symmetry at the middle of the central Al_2O_2 ring. The included solvent was found to be highly disordered, and the best approach to handling this diffuse electron density was found to be the SQUEEZE routine of PLATON.[3] This suggested a total of 110 electrons per unit cell, equivalent to 55 electrons per molecule. Before the use of SQUEEZE the solvent clearly resembled dichloromethane (CH_2Cl_2, 42 electrons), and 1.25 dichloromethane molecules corresponds to 52.5 electrons, so this was used as the solvent present. As a result, the atom list for the asymmetric unit is low by 0.625(CH_2Cl_2) = $C_{0.625}H_{1.25}Cl_{1.25}$ (and that for the unit cell low by $C_{2.5}H_5Cl_5$) compared to what is actually presumed to be present.

The *t*-Bu_2-C_6H_2 group between O1 and N7, the C33-based *t*-butyl group, and the benzyl portion of the O40-based bridging benzyloxide group were all found to be disordered, and two orientations were identified in each case of *ca*. 61:39, 92:8 and 71:29% occupancy respectively. The geometries of each pair of orientations were optimised, the thermal parameters of adjacent atoms were restrained to be similar, and only the non-hydrogen atoms of the major occupancy orientations were refined anisotropically (those of the minor occupancy orientations were refined isotropically). (As a test, the structure was solved and partially refined in the lower symmetry space group without the inversion

centre in the middle of the complex (*Pn*) to see if this would remove the extensive disorder. It did not, and so the higher symmetry space group was retained.) The N–H hydrogen atoms on N7 and N14 were located from Δ*F* maps and refined freely subject to an N–H distance constraint of 0.90 Å.

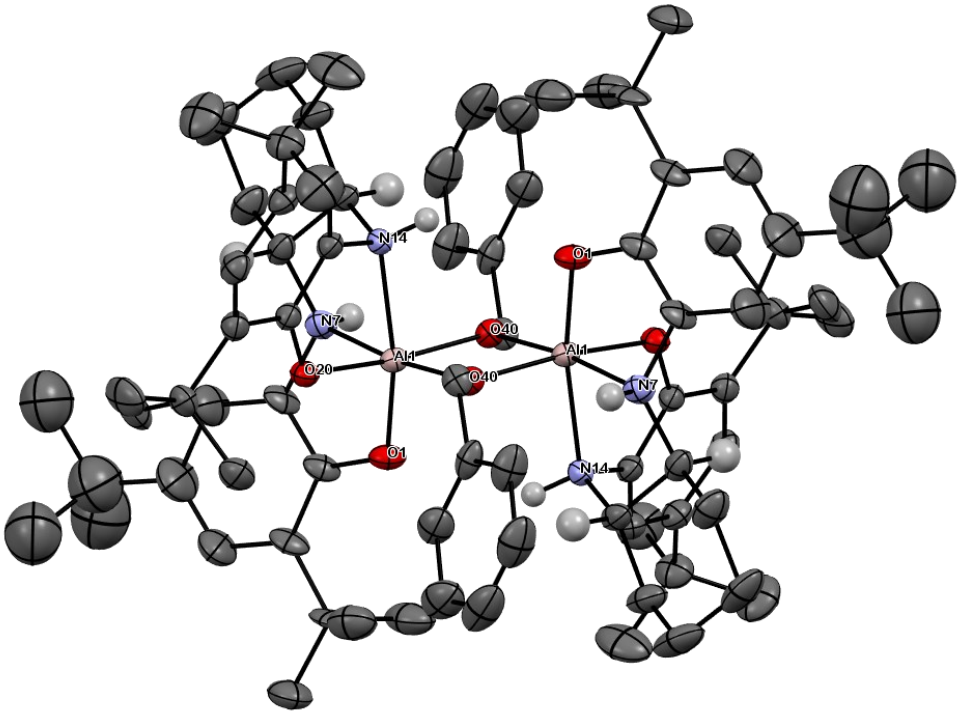


Figure F8: The crystal structure of *rac*-**14** (ellipsoid plot, 50% probability).

Crystal data for (*S*,*S*)-mix14: $C_{75}H_{112}Al_2N_4O_6 \cdot 2(C_6H_6)$, M = 1375.85, monoclinic, $P2_1$ (no. 4), a = 14.2817(3), b = 19.6139(2), c = 16.3139(3) Å, β = 112.131(2)°, V = 4233.15(13) Å^3, Z = 2, D_c = 1.079 g cm^{-3}, μ(Cu-Kα) = 0.702 mm^{-1}, T = 173 K, colourless tablets, Agilent Xcalibur PX Ultra A diffractometer; 10672 independent measured reflections (R_{int} = 0.0377), F^2 refinement,[1, 2] R_1(obs) = 0.0555, wR_2(all) = 0.1582, 9496 independent observed absorption-corrected reflections [$|F_o| > 4\sigma(|F_o|)$, completeness to θ_{full}(67.7°) = 98.3%], 966 parameters. The absolute structure of *S*,*S*-**2** was determined by use of the Flack parameter [x = 0.08(4)]. **CCDC 1972759**.

The C25- and C65-based *t*-butyl groups, and the C101- and C121-based included benzene solvent molecules in the structure of *S*,*S*-**1** were all found to be disordered, and two orientations were identified in each case of *ca*. 71:29, 89:11, 74:26 and 77:23% occupancy respectively. The geometries of each pair of orientations were optimised, the thermal parameters of adjacent atoms were restrained to be similar, and only the non-hydrogen atoms of the major occupancy orientations were refined anisotropically (those of the minor occupancy orientations were refined isotropically). The N–H hydrogen atoms on N7, N14, N47 and N54, and the O–H hydrogen atom on O90, were all located from Δ*F* maps and refined freely subject to an X–H distance constraint of 0.90 Å.

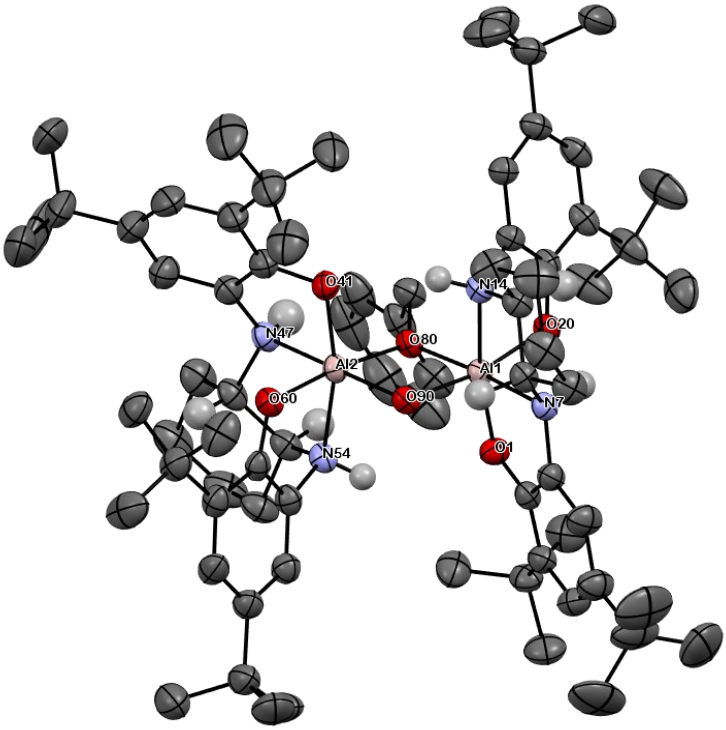


Figure F9: The crystal structure of (*S,S*)-**mix14** (ellipsoid plot, 50% probability).

Crystal data for (*S,S*)-15: $C_{38}H_{61}AlN_2O_3$, M = 620.86, monoclinic, $P2_1$ (no. 4), a = 10.5311(3), b = 12.1035(3), c = 14.8941(4) Å, β = 100.650(3)°, V = 1865.74(9) Å^3, Z = 2, D_c = 1.105 g cm^{-3}, μ(Cu-Kα) = 0.743 mm^{-1}, T = 173 K, colourless blocks, Agilent Xcalibur PX Ultra A diffractometer; 4705 independent measured reflections (R_{int} = 0.0351), F^2 refinement,[1,2] R_1(obs) = 0.0432, wR_2(all) = 0.1056, 4052 independent observed absorption-corrected reflections [$|F_o| > 4\sigma(|F_o|)$, completeness to θ_{full}(67.7°) = 98.2%], 450 parameters. The structure of *S*,*S*-**1** was refined as a two component inversion twin [Flack parameter x = 0.37(6)]. **CCDC 1972758**.

The C25- and C29-based *t*-butyl groups in the structure of *S*,*S*-**1** were both found to be disordered, and two orientations were identified in each case of *ca*. 75:25 and 79:21% occupancy respectively. The geometries of each pair of orientations were optimised, the thermal parameters of adjacent atoms were restrained to be similar, and only the non-hydrogen atoms of the major occupancy orientations were refined anisotropically (those of the minor occupancy orientations were refined isotropically). The N–H hydrogen atoms on N7 and N14 were located from ΔF maps and refined freely subject to an N–H distance constraint of 0.90 Å.

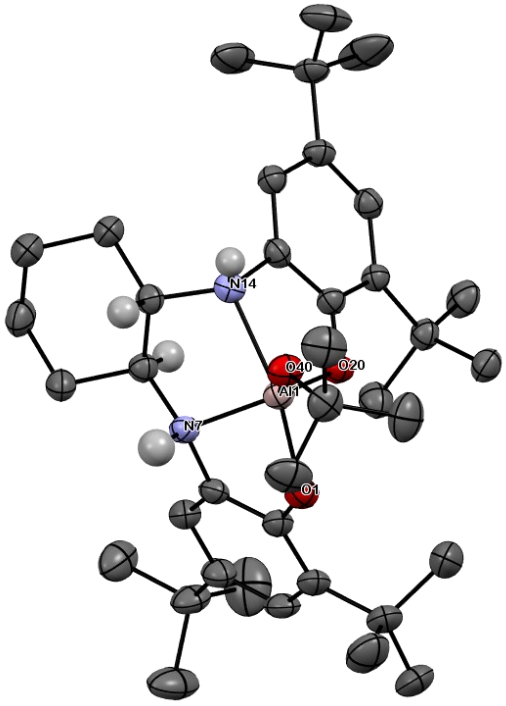


Figure F10: The crystal structure of (*S,S*)-**15** (ellipsoid plot, 50% probability).

Crystal data for *cis*-15: $C_{68}H_{106}Al_2N_4O_6$, M = 1363.84, monoclinic, $C_{2/c}$, a = 25.6952(5), b = 16.2237(2), c = 19.8057(4) Å, β = 100.650(3)°, V = 8256.3(3) Å^3, Z = 4, D_c = 1.097 g cm^{-3}, μ(Cu-Kα) = 0.716 mm^{-1}, T = 173 K, colourless tablets, Agilent Xcalibur PX Ultra A diffractometer; 8120 independent measured reflections (R_{int} = 0.0410), F^2 refinement,[1,2] R_1(obs) = 0.0538, wR_2(all) = 0.1670, 5942 independent observed absorption-corrected reflections [$|F_o| > 4\sigma(|F_o|)$, completeness to θ_{full}(67.7°) = 98.2%], 454 parameters.

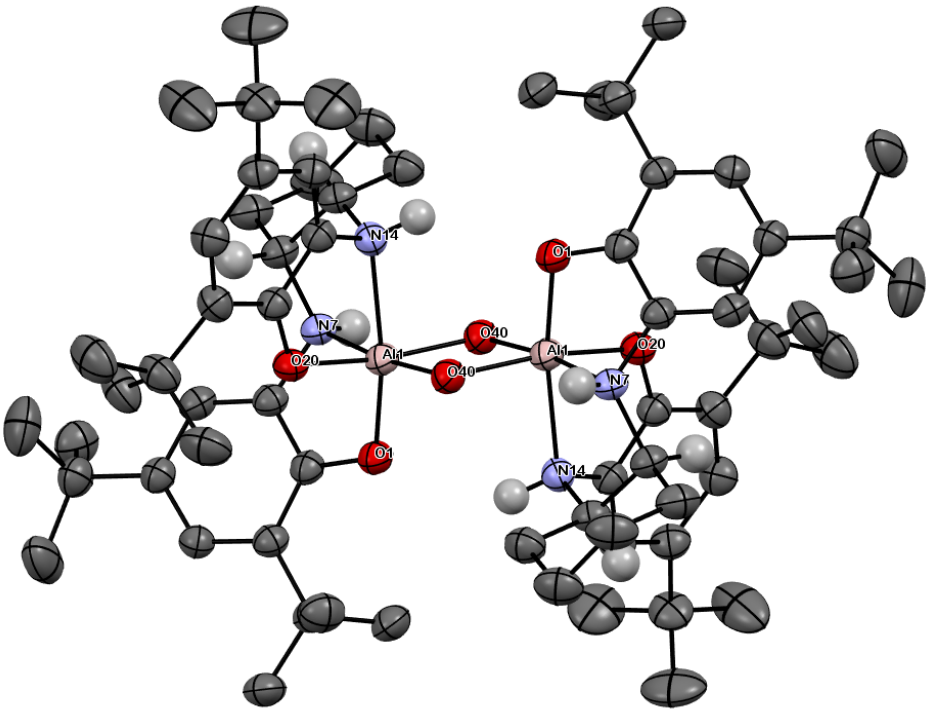


Figure F11. The crystal structure of *cis*-**15** (ellipsoid plot, 50% probability).

Crystal data for 18: $C_{34}H_{46}AlClN_2O_2$, M = 577.16, orthorhombic, *Pbca*, a = 21.8935(5), b = 9.3491(2), c = 32.4903(12) Å, α = 90°, β = 90°, γ = 90° V = 6650.3(3) Å^3, Z = 8, D_c = 1.153 g cm^{-3}, μ(Mo-Kα) = 1.504 mm^{-1}, T = 173 K, colourless needles, Agilent Xcalibur PX Ultra A diffractometer; 6469 independent measured reflections (R_{int} = 0.0498), F^2 refinement,[1, 2] R_1(obs) = 0.0496, wR_2(all) = 0.1218, 4594 independent observed absorption-corrected reflections [$|F_o| > 4\sigma(|F_o|)$, completeness to θ_{full}(25.2°) = 98.6%], 409 parameters.

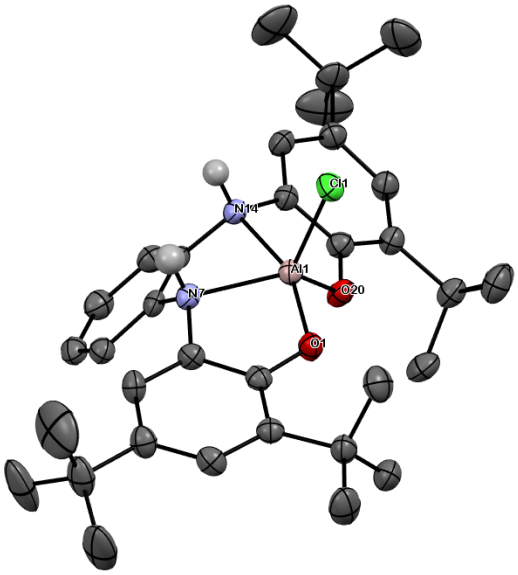


Figure F12. Crystal structure of **18** (ellipsoid plot, 50% probability).

Crystal data for [19 + 16]: $C_{74}H_{101}Al_2ClN_4O_5$, CH_2Cl_2 M = 1300.92, monoclinic, $P2_1/n$, a = 15.7048(3), b = 29.5260(4), c = 16.3308(2) Å, α = 90°, β = 104.4812(14)°, γ = 90° V = 7332.02(18) Å^3, Z = 4, D_c = 1.179 g cm^{-3}, μ(Mo-Kα) = 1.756 mm^{-1}, T = 173 K, colourless plates, Agilent Xcalibur PX Ultra A diffractometer; 13976 independent measured reflections (R_{int} = 0.0399), F^2 refinement,[1, 2] R_1(obs) = 0.0557, wR_2(all) = 0.1651, 9926 independent observed absorption-corrected reflections [$|F_o| > 4\sigma(|F_o|)$, completeness to θ_{full}(25.2°) = 98.6%], 877 parameters.

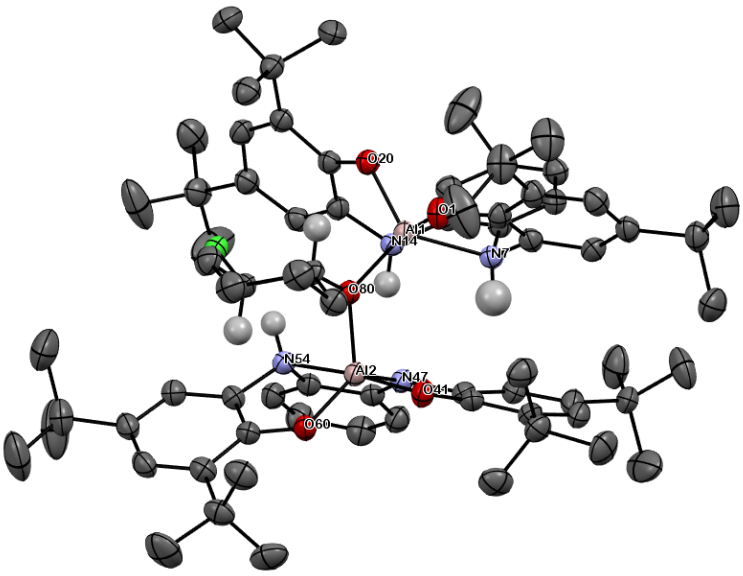


Figure F13. Crystal structure of [**19** + **16**] (ellipsoid plot, 50% probability).

1. SHELXTL v5.1, B. A., Madison, WI, 1998.
2. Sheldrick, G., *Act. Cryst. C* **2015,** *71*, 3-8.
3. Spek, A., *Act. Cryst. C* **2015,** *71*, 9-18.